

Falling Liquid Films in narrow  
geometries and other  
Thin Film Flows

Habilitation à diriger des recherches  
de l'Université Paris-Saclay

présentée et soutenue à Orsay, le 24/05/2022, par

**Georg F. DIETZE**

**Composition du jury**

**Jacques MAGNAUDET**

Directeur de recherche CNRS  
Institut de Mécanique des Fluides de Toulouse

Rapporteur

**Alexander ORON**

Professeur, Technion - Israel Institute of Technology

Rapporteur

**Maurice ROSSI**

Directeur de recherche CNRS  
Institut Jean Le Rond d'Alembert, Paris

Rapporteur

**Viswanathan KUMARAN**

Professeur, Indian Institute of Science

Examineur

**Frédéric MOISY**

Professeur, Université Paris-Saclay

Examineur

**Ranga NARAYANAN**

Professeur, University of Florida

Examineur

**Christian RUYER-QUIL**

Professeur, Université Savoie Mont Blanc

Examineur



**Titre :** Films liquides tombants au sein de géométries étroites et autres écoulements de films minces

**Mots clés :** Films liquides minces ; instabilités interfaciales ; modèles intégraux de couche limite

**Résumé :** Ce manuscrit d'habilitation résume mes recherches depuis que j'ai rejoint le Laboratoire FAST en tant que chargé de recherche CNRS en 2012. Mes travaux se sont principalement concentrés sur l'hydrodynamique des films liquides minces : (i) les films liquides tombants soumis à l'instabilité de Kapitza ; (ii) les films liquides annulaires au sein de géométries cylindriques soumis à l'instabilité de Plateau-Rayleigh ; (iii) films liquides ou couches de vapeur soumis aux instabilités de Rayleigh-Taylor et Marangoni ; et (iv) les films liquides s'étalant sur un substrat en interaction avec des microparticules. Pour les trois premières configurations, où l'écoulement est soumis à des instabilités interfaciales à ondes longues, j'ai développé des modèles à basse dimension fondés sur l'approche intégrale de couche limite aux résidus pondérés (WRIBL). Ma contribution a été d'étendre cette approche aux écoulements de films à deux fluides, où le film liquide est en contact avec un fluide extérieur actif, par exemple un film liquide tombant

cisailé par un contre-écoulement de gaz. En outre, j'ai appliqué des techniques de simulation numérique directe basées sur les équations complètes de Navier-Stokes.

Une partie importante de mon travail a été consacrée aux films liquides tombants et, en particulier, à la façon dont un écoulement de gaz affecte leur stabilité linéaire ainsi que la dynamique et la stabilité des ondes de surface non linéaires. Aussi, je me suis concentré sur des configurations fortement confinées, telles que les minicanaux ou les tubes étroits, et sur le rôle des ondes de surface dans l'occlusion/l'engorgement ainsi que dans l'intensification du transfert de chaleur et de masse. J'ai également travaillé sur l'occlusion des voies respiratoires pulmonaires par des films de mucus, l'accélération du mouillage à l'aide de microparticules et les instabilités secondaires au sein de films minces soumis à l'instabilité de Rayleigh-Taylor.

**Title :** Falling liquid films in narrow geometries and other thin film flows

**Keywords :** Thin liquid films; interfacial instabilities; integral boundary layer models

**Abstract :** The present habilitation document summarizes my research since joining Laboratoire FAST as a CNRS research associate in 2012. My work has mainly focussed on the hydrodynamics of thin liquid films: (i) falling liquid films subject to the Kapitza instability; (ii) annular liquid films in cylindrical geometries subject to the Plateau-Rayleigh instability; (iii) liquid films or vapour layers subject to the Rayleigh-Taylor and Marangoni instabilities; and (iv) spreading liquid films in interaction with microparticles. For the first three configurations, where the flow is subject to long-wave interfacial instabilities, I have developed low-dimensional models based on the weighted residual integral boundary layer (WRIBL) approach. My contribution has been to extend this approach to two-fluid film flows, where the liquid film is in contact with an active outer fluid, e.g. a falling liquid film sheared by a counter-current gas flow.

In addition, I have applied direct numerical simulation techniques based on the full Navier-Stokes equations.

A substantial part of my work has been dedicated to falling liquid films, and, in particular, how an adjacent gas flow affects their linear stability and the dynamics and stability of nonlinear surface waves. Thereby, I have focused on strongly-confined configurations, such as minichannels or narrow tubes, and the role of surface waves in causing occlusion/flooding events and heat/mass transfer intensification. I have also worked on the occlusion of pulmonary airways by mucus films, the acceleration of wetting via microparticles, and secondary instabilities in thin films subject to the Rayleigh-Taylor instability.



# **Falling Liquid Films in narrow geometries and other Thin Film Flows**

Georg F. Dietze

Chargé de recherche au CNRS  
Laboratoire Fluides, Automatique et Systèmes Thermiques (FAST)

February 17, 2022



# Acknowledgements

I am honoured that Jacques Magnaudet, Alexander Oron, Maurice Rossi, Viswanathan Kumaran, Frédéric Moisy, Ranga Narayanan, and Christian Ruyer-Quil have accepted to be part of my habilitation committee. I wish to thank them for their interest in my work and the time they have invested. I am also indebted to Jean-Pierre Hulin for proof reading this manuscript, as well as several of my research papers.

I came to Orsay in 2011, not long after defending my PhD. thesis at RWTH-Aachen University, in the context of a postdoctoral fellowship funded by DAAD (Deutscher Akademischer Austauschdienst). They gave me a large sum of money to extend my scientific horizon, no questions asked. I chose to come to laboratoire FAST to work with Christian Ruyer-Quil and learn about low-dimensional modelling. It was the best decision I could have made. I wish to thank DAAD for their support and trust. I also wish to thank Paul Manneville, who oriented me toward FAST.

I was recruited as a CNRS research associate in 2012. I consider this a great honour. Since that time, I have attempted to live up to the high standards that prevail within this research institution, and I must admit that comparison with my fellow researchers has often been challenging for my ego. My feeling is that I will never cease to learn and grow within this institution. I wish to thank CNRS and in particular the Comité national de la recherche scientifique for their trust.

I also wish to thank laboratoire FAST for having supported my CNRS candidacy in 2012 and for having welcomed me. In particular, I am indebted to Christian Ruyer-Quil, Sophie Mergui, Béatrice Guerrier, Neil Ribe, Marc Rabaud, Jean-Pierre Hulin, and Harold Auradou for teaching me the craft of being a professional researcher. I am very thankful to Pierre-Philippe Cortet for his advice and help in preparing my promotion and progress reports for CNRS. Also, I wish to thank Mai Guerrib for her kindness.

Throughout these years, I have been privileged to collaborate with esteemed colleagues in France and abroad. Christian Ruyer-Quil introduced me to hydrodynamic stability, bifurcation theory, long-wave theory, and low-dimensional modelling. He has been my mentor since I came to France and I have never stopped learning from him. I wish to thank him for his teachings, guidance, and continuing support. Having employed both numerical and experimental methods during my PhD. thesis, I have concentrated on theoretical work since my arrival at FAST. Thus, my work on falling liquid films has been complimentary to the experiments of Sophie Mergui, which have been very valuable in validating and challenging the theoretical work. I wish to thank her for our long-lasting

fruitful collaboration on this topic, which has involved many open discussions.

Since joining FAST, I have enjoyed a very inspiring collaboration with Air Liquide, who funded and participated in several research projects on falling liquid films. I wish to thank Guillaume Mougin and Jacopo Seiwert from Air Liquide for their continuing interest and support.

In 2015, I spent 4 months at the University of Florida as an invited scholar, where I gave a series of lectures on low-dimensional modelling in the group of Ranga Narayanan at the Department of Chemical Engineering. I wish to thank Ranga, as well as Farzam Zoueshtiagh, who's EU IRSES project funded my stay, and Marc Rabaud, who was director of FAST, for giving me this great opportunity. I also thank Ranga for our ongoing collaboration on thin films subject to the Rayleigh-Taylor and Marangoni instabilities, his continuing support, and for introducing me to many colleagues in the field.

Since 2016, I have been collaborating with Ichiro Ueno from Tokyo University of Science (TUS). Thanks to the funding from his international research network, which also involved Farzam Zoueshtiagh and Harunori Yoshikawa, I have been privileged to visit TUS several times. In this context, I have supervised several Japanese students from Ichiro's group, some of which did their masters thesis at FAST. In particular, I wish to acknowledge Motochika Inoue, who laid the groundwork for several research papers on liquid films in interaction with micro-particles. I am very thankful to Ichiro Ueno for this honest and productive collaboration.

Most recently, I have made a move into biological fluid dynamics. I wish to thank Marcel Filoche, Nicolas Grenier, and Anjishnu Choudhury for the very fruitful and productive working environment within the new Labex LaSIPS project *mucusFILM*. Also, I wish to thank Farzam Zoueshtiagh for welcoming me into his ANR project *FES*, which concerns hydrodynamics and bacteria.

A rewarding part of my work has been the supervision of and collaboration with masters students (8 since joining FAST), PhD. students (5), and post-doctoral fellows (3). I wish to thank all of them for their trust. In particular, I wish to thank Gianluca Lavallo, Motochika Inoue, Misa Ishimura, Hayate Nakamura, Jason Picardo, Wilko Rohlf, Yiqin Li, and Anjishnu Choudhury for their hard work, dedication, and ideas. I am very happy to continue working with Gianluca Lavallo, since his appointment as assistant professor at École des Mines de Saint Étienne.

I have enjoyed participating in the CNRS research networks *GDR3373* ("Ruissellement et films cisailés") and *GDR2042* ("TransINTER"). I wish to thank the organizers, Christian Ruyer-Quil and Michel Gradeck for fostering fruitful collaborations within these networks.

Throughout the years, I have received generous funding from DAAD, Forschungszentrum Jülich, Université Paris-Saclay, INSIS, the European Union, ANR, and Labex LaSIPS. I thank these institutions for entrusting me with tax-payer money. In particular, I was honoured to serve as the principal investigator of the ANR project *wavyFILM*, which involved Sophie Mergui, Guillaume Mougin, Nicolas Grenier, Gianluca Lavallo, and Yiqin Li. I cherish the memories of our four-year collaboration during this project between 2016 and 2020.

I also wish to thank Manfred Zeller for his continuing support and interest in my work



since I have left Germany.

Most of all, I wish to thank those closest to me, my parents Gertrud and Hartmut, who are my role models, my sister Charlotte and her family, James, Oliver, Eleanor, and Theodore, and Kerstin, Peter, and Bernadette, for their unconditional support and help. Without these, it would have been impossible for me to produce the current document and the research it contains. Finally, I thank Kerstin for always believing in me.

Orsay, February 17, 2022



# Abstract

The present habilitation document summarizes my research since joining Laboratoire FAST as a CNRS research associate in 2012. My work has mainly focussed on the hydrodynamics of thin liquid films: *(i)* falling liquid films subject to the Kapitza instability; *(ii)* annular liquid films in cylindrical geometries subject to the Plateau-Rayleigh instability; *(iii)* liquid films or vapour layers subject to the Rayleigh-Taylor and Marangoni instabilities; and *(iv)* spreading liquid films in interaction with microparticles. For the first three configurations, where the flow is subject to long-wave interfacial instabilities, I have developed low-dimensional models based on the weighted residual integral boundary layer (WRIBL) approach. My contribution has been to extend this approach to two-fluid film flows, where the liquid film is in contact with an active outer fluid, e.g. a falling liquid film sheared by a counter-current gas flow. In addition, I have applied direct numerical simulation techniques based on the full Navier-Stokes equations. A substantial part of my work has been dedicated to falling liquid films, and, in particular, how an adjacent gas flow affects their linear stability and the dynamics and stability of nonlinear surface waves. Thereby, I have focused on strongly-confined configurations, such as minichannels or narrow tubes, and the role of surface waves in causing occlusion/flooding events and heat/mass transfer intensification. I have also worked on the occlusion of pulmonary airways by mucus films, the acceleration of wetting via microparticles, and secondary instabilities in thin films subject to the Rayleigh-Taylor instability.



# Résumé

Ce manuscrit d'habilitation résume mes recherches depuis que j'ai rejoint le Laboratoire FAST en tant que chargé de recherche CNRS en 2012. Mes travaux se sont principalement concentrés sur l'hydrodynamique des films liquides minces : *(i)* films liquides tombants soumis à l'instabilité de Kapitza ; *(ii)* films liquides annulaires au sein de géométries cylindriques soumis à l'instabilité de Plateau-Rayleigh ; *(iii)* films liquides ou couches de vapeur soumis aux instabilités de Rayleigh-Taylor et Marangoni ; et *(iv)* films liquides s'étalant sur un substrat en interaction avec des microparticules. Pour les trois premières configurations, où l'écoulement est soumis à des instabilités interfaciales à ondes longues, j'ai développé des modèles à basse dimension fondés sur l'approche intégrale de couche limite aux résidus pondérés (WRIBL). Ma contribution a été d'étendre cette approche aux écoulements bicouche, où le film liquide est en contact avec un deuxième fluide actif, par exemple un film liquide tombant cisailé par un contre-écoulement de gaz. En outre, j'ai appliqué des techniques de simulation numérique directe basées sur les équations complètes de Navier-Stokes. Une partie importante de mon travail a été consacrée aux films liquides tombants et, en particulier, à la façon dont un écoulement de gaz modifie leur stabilité linéaire ainsi que la dynamique et la stabilité des ondes de surface non linéaires. Aussi, je me suis concentré sur des configurations fortement confinées, telles que les minicanaux ou les tubes étroits, et sur le rôle des ondes de surface dans l'occlusion/l'engorgement ainsi que dans l'intensification du transfert de chaleur et de masse. J'ai également travaillé sur l'occlusion des voies respiratoires pulmonaires par des films de mucus, l'accélération du mouillage à l'aide de microparticules et les instabilités secondaires au sein de films minces soumis à l'instabilité de Rayleigh-Taylor.



# Contents

<b>Acknowledgements</b>	<b>i</b>
<b>Abstract</b>	<b>v</b>
<b>Résumé</b>	<b>vii</b>
<b>Introduction</b>	<b>1</b>
<b>1 WRIBL models for two-fluid film flows</b>	<b>11</b>
1.1 Planar liquid films in rectangular channels . . . . .	13
1.2 Annular liquid films in cylindrical tubes . . . . .	23
1.3 Films subject to the Rayleigh-Taylor and Marangoni instabilities . . . . .	31
1.4 Falling liquid films sheared by a turbulent gas . . . . .	33
<b>2 WRIBL model computations</b>	<b>41</b>
2.1 Linear stability analysis . . . . .	41
2.1.1 Planar liquid films in rectangular channels . . . . .	41
2.1.2 Annular liquid films in cylindrical tubes . . . . .	45
2.1.3 Time-evolving base state: Rayleigh-Taylor instability . . . . .	49
2.1.4 Falling liquid films sheared by a turbulent gas . . . . .	51
2.2 Nonlinear computations . . . . .	52
2.2.1 Travelling-wave solutions (TWS) . . . . .	53
2.2.2 Transient periodic and spatio-temporal computations . . . . .	55
2.2.3 Liquid plugs in cylindrical tubes . . . . .	58
2.2.4 Falling liquid films sheared by a turbulent gas . . . . .	61
2.3 Validity range of our WRIBL models . . . . .	63
2.3.1 Planar model . . . . .	63
2.3.2 Cylindrical model . . . . .	70
<b>3 Orr-Sommerfeld linear stability analysis</b>	<b>81</b>
3.1 Planar liquid films in rectangular channels . . . . .	81
3.2 Annular liquid films in cylindrical tubes . . . . .	90

<b>4</b>	<b>Direct numerical simulation</b>	<b>93</b>
4.1	Continuum formulation . . . . .	93
4.1.1	Liquid films in planar geometries . . . . .	93
4.1.2	Liquid films in cylindrical geometries . . . . .	97
4.1.3	Drops spreading on rigid surfaces . . . . .	99
4.2	VOF and CSF methods . . . . .	100
4.3	Validation . . . . .	105
<b>5</b>	<b>Falling liquid films in a quiescent atmosphere</b>	<b>113</b>
5.1	On the origin of precursory capillary ripples . . . . .	115
5.2	Three-dimensional falling liquid films . . . . .	127
	Dietze, <i>J. Fluid Mech.</i> , 2016 . . . . .	134
	Dietze et al., <i>J. Fluid Mech.</i> , 2014 . . . . .	135
<b>6</b>	<b>Falling liquid films in narrow channels</b>	<b>137</b>
6.1	Gas-induced suppression of Kapitza instability . . . . .	141
6.2	Nonlinear waves and secondary instabilities . . . . .	146
6.2.1	Vertically-falling liquid films . . . . .	146
6.2.2	Inclined falling liquid films . . . . .	156
6.3	Scalar transfer and wall corrugations . . . . .	160
	Lavalle et al., <i>J. Fluid Mech.</i> , 2019 . . . . .	168
	Dietze and Ruyer-Quil, <i>J. Fluid Mech.</i> , 2013 . . . . .	169
	Lavalle et al., <i>Phys. Rev. Fluids</i> , 2020 . . . . .	170
	Lavalle et al., <i>J. Fluid Mech. Rapids</i> , 2021 . . . . .	171
	Dietze, <i>J. Fluid Mech.</i> , 2019 . . . . .	172
<b>7</b>	<b>Liquid films in narrow tubes</b>	<b>173</b>
7.1	Falling liquid films in vertical tubes . . . . .	177
7.2	Mucus films in pulmonary capillaries . . . . .	187
	Dietze, Lavalle and Ruyer-Quil, <i>J. Fluid Mech.</i> , 2020 . . . . .	192
	Dietze and Ruyer-Quil, <i>J. Fluid Mech.</i> , 2015 . . . . .	193
<b>8</b>	<b>Other thin film flows</b>	<b>195</b>
8.1	Films subject to the Rayleigh-Taylor instability . . . . .	195
8.2	Drops spreading around microparticles . . . . .	205
8.3	Pressure-driven liquid films in microgaps . . . . .	209
	Dietze, Picardo and Narayanan <i>J. Fluid Mech.</i> , 2018 . . . . .	213
	Nakamura et al. <i>J. Colloid Interface Sci.</i> , 2020 . . . . .	214
	Nakamura et al. <i>Langmuir</i> , 2020 . . . . .	215
<b>9</b>	<b>Ongoing work: falling liquid films sheared by a turbulent gas</b>	<b>217</b>
<b>10</b>	<b>Conclusions and outlook</b>	<b>225</b>



---

<b>A Coefficients of WRIBL models</b>	<b>233</b>
A.1 Planar model . . . . .	233
A.2 Cylindrical model . . . . .	239
<b>Curriculum vitæ</b>	<b>247</b>
<b>List of publications</b>	<b>253</b>
<b>Bibliography</b>	<b>261</b>



# Introduction

This habilitation document covers the research I have conducted since becoming a CNRS researcher at laboratoire FAST in 2012. During this time, I have worked on different thin film flows involving interfacial instabilities.

In particular, I have studied falling liquid films, which develop large-amplitude surface waves due to the inertia-driven Kapitza instability (Kapitza, 1948). My interest has been to understand the linear and nonlinear behavior of these waves and their effect on the velocity field within the liquid film, in particular when the latter is subjected to a strongly-confined and hydrodynamically active (counter-current) gas flow. Such a configuration is encountered in rectification columns used for cryogenic air separation, where oxygen-rich liquid air and nitrogen-rich gaseous air are put into contact within millimetric channels formed by structured packings (Valluri *et al.*, 2005). Even stronger confinement levels are achieved in falling-film micro-reactors (Lapkin & Anastas, 2018).

In such systems, surface waves play a dual role: on the one hand, they significantly intensify heat and mass transfer (Yoshimura *et al.*, 1996), on the other hand they can trigger catastrophic events associated with flooding, such as liquid arrest or a direct occlusion of the channel cross section (Vlachos *et al.*, 2001). My goal has been to elucidate the mechanisms underlying these opposing effects linked to surface waves, and to identify ways of producing optimal regimes that exploit the benefits of waviness while avoiding their risks. In this context, I have mostly focused on extreme confinement levels, where flow conditions in the gas are laminar, and which already produce a rich wave dynamics. However, in currently ongoing work, I have started to study configurations with intermediate confinement levels, where the gas flow is turbulent. These conditions are closest to those typically encountered in air separation units.

Another focus of my work have been annular liquid films in narrow cylindrical tubes, where the Plateau-Rayleigh instability (Plateau, 1849; Rayleigh, 1892) can produce liquid plugs occluding the tube cross section. Here, I have studied occlusion scenarios for two different flow configurations involving an active core fluid. The first concerns falling liquid films in vertical tubes, where the Plateau-Rayleigh and Kapitza instabilities are simultaneously active. This configuration is encountered in tubular multiphase heat exchangers, such as falling film evaporators for milk inspissation (Jebson & Chen, 1997), which have been successfully miniaturized (Seebauer *et al.*, 2012). Another example is surfactant replacement therapy in the human lung, where gravity determines the surfactant distribution within the respiratory network (Filoche *et al.*, 2015). The second

configuration concerns very narrow tubes, where the effect of gravity and thus the role of the Kapitza instability is negligible versus that of the Plateau-Rayleigh instability. This situation is encountered in the terminal bronchioles of the human lung, where the coating mucus film can cause airway occlusion accompanied by cell damage (Bian *et al.*, 2010). Such occlusion events may be triggered by the breathing-induced core air flow.

My work on these two topics has led me to study two related problems involving thin film flows. Firstly, I have studied liquid/gas flows in horizontal channels. Here, the mean flow is driven by an imposed pressure drop and not by gravity, and the Yih instability (Yih, 1967), due to the inter-phase viscosity contrast, generates large-amplitude surface waves, that are quite similar to waves on falling liquid films. Such flows are encountered in micro-gap coolers used for microprocessor cooling (Kabov *et al.*, 2011). Secondly, I have worked on fluid films subject to the Rayleigh-Taylor and Marangoni instabilities, where secondary instability can cause the spontaneous motion of liquid drops suspended from a ceiling or vapor blisters forming underneath a liquid layer. Such phenomena can cause defects in coating operations, and the sliding instability may also play a role in the spontaneous migration of Leidenfrost drops (Bouillant *et al.*, 2018). More generally, the sliding phenomenon seems to be linked to fluid films draining under the effect of an interfacial instability, as I have also observed it in annular liquid films, where it can trigger the occlusion of narrow tubes.

Finally, I have worked on a thin-film problem that is not directly linked to interfacial instabilities, i.e. the interaction between a liquid film spreading on a plane substrate and a micro-particle placed in its path. On the one hand, the addition of a micro-structure can accelerate the spreading rate of the liquid (Cazabat & Stuart, 1986; Bico *et al.*, 2001), which may be exploited in the design of heat pipes (Jouhara *et al.*, 2017) or labs on a chip (Blanchard *et al.*, 1996). On the other hand, the interaction between the contact line and the micro-particle can produce large forces acting on the latter, which may be exploited in the cleaning of contaminated surfaces (Aramrak *et al.*, 2013; Zoueshtiagh *et al.*, 2014; Khodaparast *et al.*, 2017).

The interfacial instabilities studied here all originate at zero wave number, and thus the underlying thin film flows are amenable to the so-called “long-wave” hypothesis, i.e. the characteristic wavelength of surface waves is much larger than the characteristic thickness of the film. I have exploited this property to describe the studied flows via high-fidelity low-cost computations based on low-dimensional models. In particular, I have applied the weighted residual integral boundary layer (WRIBL) method (Ruyer-Quil & Manneville, 1998; Kalliadasis *et al.*, 2012), which I learned from Christian Ruyer-Quil upon my arrival at FAST. My contribution has been to extend this approach to two-fluid film flows, in particular liquid/gas flows, e.g. falling liquid films in interaction with a strongly-confined counter-current gas flow. The development and detailed validation of these models has been a substantial part of my work. Further, they helped uncover several key physical phenomena associated with the linear and nonlinear dynamics of surface waves for the various two-fluid film flows studied.

In addition, I have applied numerical methods based on the full Navier-Stokes equations: Orr-Sommerfeld linear stability calculations, and nonlinear direct numerical simu-

lations (DNS). Depending on the problem studied, the DNS were performed with three different open-source numerical codes, which are all based on the volume of fluid (VOF) and continuum force (CSF) methods: **Gerris** (Popinet, 2009), **Basilisk** (Popinet, 2015), and **OpenFOAM** (Rusche, 2002). On the one hand, these computations based on first principles were used to validate our WRIBL models. On the other hand, they were employed to investigate phenomena outside the scope of these models, i.e. inter-phase scalar transfer in falling liquid films flowing on corrugated substrates, and spreading liquid drops interacting with micro-particles.

The current habilitation document does not cover my postdoctoral work before joining FAST, which was performed at the Institute of Heat and Mass Transfer at RWTH Aachen University, where I was group leader of the Film Group from 2010 to 2011 (Haustein *et al.*, 2013; Rohlfes *et al.*, 2013, 2012*a,b*; Dietze & Kneer, 2011). This work mainly concerned numerical and experimental investigations of wavy falling liquid films and their response to electric fields and heating.

The research presented here has involved several collaborations. Thus, where appropriate, I will privilege the impersonal “we” and “our” (Alley, 2018) versus “I” and “my”. The current document is self-contained, i.e. it presents in each chapter a summary of the salient features of our publications on a given topic. The title pages of these publications are appended at the end of each chapter, for reference.

As this document covers 9 years of research, the state of the art has evolved since the publication of our earliest papers. Thus, in chapters 5-9, which present our main physical findings, the literature overview is presented in two steps. At the start of a chapter, the state of the art at the time of publication of our papers is sketched, and we discuss our main novel contributions. Then, at the end of each individual section, we discuss relevant literature that has appeared since the publication of our papers, and how our work has impacted this.

Chapter 1 is dedicated to the derivation of four novel WRIBL models, which we have developed for and applied to the following two-dimensional flow configurations:

- Two-fluid film flows in narrow rectangular channels (Dietze & Ruyer-Quil, 2013), e.g. falling liquid films sheared by a counter-current gas flow, or pressure-driven two-layer Poiseuille flows.
- Two-fluid film flows in cylindrical geometries (Dietze & Ruyer-Quil, 2015), e.g. annular falling liquid films in narrow tubes or mucus films within the pulmonary airways.
- Thin films subject to the Rayleigh-Taylor and Marangoni instabilities in contact with an unconfined outer fluid (Dietze *et al.*, 2018), e.g. liquid films suspended from a ceiling or vapour films underneath a liquid layer.
- Falling liquid films in contact with a turbulent gas flow, where the liquid film is modelled via the WRIBL approach and the gas flow is represented via an asymptotic expansion approach based on a simple mixing-length model for representing turbulence.

Our respective models are introduced in sections 1.1, 1.2, 1.3, and 1.4. At the end of each section, we discuss how our models improved upon prior modelling works for predicting the studied flows, and how the state of the art has been impacted since their publication. We have deliberately chosen to write out our models first and to discuss the literature after, so that the reader can appreciate more precisely what novel contributions our modelling work involves. All four models, which were published in different papers, have been recast in a unified mathematical form for this habilitation document, and I have corrected two small mistakes that appeared in Dietze & Ruyer-Quil (2013) and Dietze & Ruyer-Quil (2015).

In chapter 2, we discuss the different numerical solutions that can be obtained with our WRIBL models. Therein, section 2.1 is dedicated to spatial and temporal linear stability calculations. Section 2.2 concerns nonlinear computations: numerical continuation of travelling-wave solutions (TWS), and spatio-temporal computations on periodic or open domains. Finally, in section 2.3, we establish the validity range of our models based on Orr-Sommerfeld linear stability predictions and DNS.

In chapter 3, we write out the Orr-Sommerfeld linear stability problems for the different flow configurations studied, and we discuss the employed numerical methods to solve them. Further, we demonstrate via stability calculations of this kind that only long-wave instability modes are relevant for the laminar gas-sheared liquid films studied in this habilitation document. Such instability modes can be accurately captured with our long-wave WRIBL models. Finally, we introduce a transient stability analysis method that we will use in section 8.1 to study the secondary instability of a slowly evolving film subject to the Rayleigh-Taylor instability.

Chapter 4 discusses our DNS. Therein, we start by writing the full governing equations and boundary conditions for the different problems studied. Further, we discuss the numerical methods underlying the three DNS codes employed (**Gerris**, **Basilisk**, and **OpenFOAM**), and we detail the computational setup for each type of simulation. At the end of the chapter, section 4.3 provides a validation of the employed codes based on experiments and analytical solutions for representative benchmark configurations.

Chapters 5, 6, 7, 8, and 9, are dedicated to the physical problems studied with the methods introduced in chapters 1 to 4. Chapters 5, 6, and 9 gather our work on falling liquid films in a quiescent atmosphere and in confined rectangular channels, and chapter 7 gathers our work on liquid films in cylindrical tubes. Finally, chapter 8 brings together several individual studies that are not closely linked to one another. At the start of each chapter (or section in the case of chapter 8), we provide a general introduction that establishes the context of our work, and we briefly summarize our main novel contributions to the state of the art. In the ensuing sections (subsections), we then detail the different studies that led to these results.

Chapter 5 concerns falling liquid films in a quiescent atmosphere, where the surrounding gas has no effect on the dynamics of the liquid film. Although this topic has been studied for a very long time, we have elucidated two unresolved problems: the origin of the so-called precursory capillary ripples preceding large-amplitude waves (Dietze, 2016), and the hydrodynamics within three-dimensional solitary waves (Dietze *et al.*, 2014).

Chapter 6 concerns falling liquid films in superconfined rectangular channels in contact with a counter-current laminar gas flow. In section 6.1, we discuss the implications of such a strong confinement on the linear stability of the liquid film (Lavalle *et al.*, 2019), whereas section 6.2 is dedicated to the effect of the gas flow on the dynamics of nonlinear waves. In particular, we focus on secondary instabilities and catastrophic events, such as wave reversal and occlusion (Dietze & Ruyer-Quil, 2013; Lavalle *et al.*, 2020, 2021). Section 6.3 concerns the intensification of inter-phase heat and mass transfer via surface waves and wall corrugations (Dietze, 2019).

Chapter 7 is dedicated to annular liquid films in narrow cylindrical tubes in contact with a core gas flow. In section 7.1, we focus on wave-induced occlusion scenarios in falling liquid films (Dietze *et al.*, 2020), whereas section 7.2 is dedicated to mucus films in the pulmonary airways, where the effect of gravity is negligible and the liquid film is subject to an oscillating air flow (Dietze & Ruyer-Quil, 2015).

Chapter 8 summarizes our work on several other thin film flows. Section 8.1 focusses on thin films subject to the Rayleigh-Taylor and Marangoni instabilities (Dietze *et al.*, 2018), section 8.1 on spreading liquid films in interaction with micro-particles (Nakamura *et al.*, 2020*b,a*), and section 8.2 on pressure-driven two-phase Poiseuille flow through narrow rectangular channels (Dietze & Ruyer-Quil, 2013).

Chapter 9 reports our ongoing work on falling liquid films sheared by a turbulent gas flow, which extends our work on strongly-confined falling liquid films (chapter 6) to flow conditions that are more representative of liquid/gas flows in cryogenic air separation units.

In chapter 10, we draw conclusions and discuss several routes for future work. Appendix A contains mathematical expressions for the coefficients of the WRIBL models derived in sections 1.1, 1.2, and 1.3. The document is completed by a curriculum vitae and a comprehensive list of publications.

The outcomes presented in this habilitation document have benefited from collaborations with distinguished colleagues, the work contributed by graduate and postdoctoral students, and the funding provided by government agencies and companies.

My work on low-dimensional modelling has benefited greatly from an ongoing and close collaboration with Christian Ruyer-Quil (Université Savoie Mont Blanc), who introduced me to this approach and has guided me at many stages. This modelling work has been a driving force in my research, yielding deep insight into the physical mechanisms governing the studied flows and helping to orient the choice of problems investigated.

The presented work on plane falling liquid films is quite relevant for cryogenic air separation units. In this context, I have collaborated since 2011 with Guillaume Mougin and Jacopo Seiwert, from “Paris Innovation Campus” at Air Liquide in Les Loges-en-Josas. A new CIFRE PhD. thesis on falling condensate films is supposed to start in 2022. Our theoretical and numerical investigations have been accompanied at many stages by the experiments of Sophie Mergui (Sorbonne Université), which were performed at Laboratoire FAST. Further, a very productive collaboration with Gianluca Lavalle (École des Mines Saint-Étienne) has been ongoing since his post-doctoral stay in Orsay between 2017 and 2018. Finally, I have collaborated on this topic with Nicolas Grenier

(Université Paris-Saclay) and Benoit Scheid (Université Libre de Bruxelles).

My work on annular liquid films in narrow cylindrical geometries was performed with Christian Ruyer-Quil and Gianluca Lavallo. It has proven that the WRIBL technique is a very promising approach for studying mucus flow in the pulmonary airways. In this context, I have started a new collaboration with Marcel Filoche (École Polytechnique) and Nicolas Grenier, via the LaSIPS project *mucusFILM*. This project, which funds a postdoctoral-fellow at laboratoire FAST, Anjishnu Choudhury, focusses on modelling mucociliary clearance of viscoelastic mucus (see section 10).

My work with Ranga Narayanan (University of Florida) and Jason Picardo (IIT Bombay) on thin films subject to the Rayleigh-Taylor and Marangoni instabilities was initiated in 2015 during a three-month stay at the University of Florida, as an invited researcher in the group of Ranga Narayanan. This stay was funded by an IRSES project led by Farzam Zoueshtiagh (Université de Lille). During that time, I gave a series of lectures on the WRIBL method to graduate students and researchers at the Department of Chemical Engineering. This led to an ongoing collaboration with Ranga Narayanan which is currently continuing through the PhD. thesis of Igin Ignatius (University of Florida), who has secured a four-month Chateaubriand fellowship to join FAST in March 2022. His work concerns thin films subject to the Marangoni instability and mechanical vibrations.

Our work on liquid films in interaction with micro-particles is part of a rich long-term collaboration with Ichiro Ueno (Tokyo University of Science). In particular, I have participated in an international exchange project funded by Tokyo University of Science, which also involved Farzam Zoueshtiagh (Université de Lille) and Harunori Yoshikawa (Université de Nice). This project has funded several visits by myself to Tokyo University of Science and two four-month stays of Japanese graduate students at FAST. The collaboration is ongoing and will intensify further following my joining of the ANR project *FEFS* (Fluid Engineering for Food Security), directed by Farzam Zoueshtiagh, which focuses on using multi-phase flows for cleaning surfaces that are contaminated by bacteria.

I have also been an active member of the CNRS research networks *GDR3373* (“Ruisselement et films cisailés”) and *GDR2042* (“TransINTER”), which brought/bring together researchers working on interfacial instabilities in fluid flows. The regular meetings organized by these networks greatly helped in fostering collaborations.

Several students and post-doctoral fellows have particularly contributed to the presented work:

- Gianluca Lavallo (École des Mines Saint-Étienne) was a post-doctoral fellow working between LIMSI and FAST from 2017 to 2018, as part of the ANR project *wavyFILM*, which I headed as PI. He contributed greatly to our work on superconfined falling liquid films discussed in chapter 6 (Lavallo *et al.*, 2019, 2020, 2021). Our collaboration has been ongoing since. In 2020, he was appointed assistant professor at École des Mines Saint-Étienne.
- Jason Picardo was a visiting Fulbright doctoral scholar at University of Florida and later a post-doctoral fellow at Tata Institute of Fundamental Research in Bangalore, when we worked together on thin films subject to the Rayleigh-Taylor and



Marangoni instabilities as discussed in section 8.1 (Dietze *et al.*, 2018). He is now a faculty member at IIT Bombay and we continue to collaborate.

- Yiqin Li was a post-doctoral fellow at FAST between 2017 and 2019 in the context of the ANR project wavyFILM. Her experiments allowed to confirm the strong stabilization observed in superconfined falling liquid films, which is discussed in section 6.1 (Lavalley *et al.*, 2019).
- Misa Ishimura is a PhD. student from Université Savoie Mont Blanc, whom I am currently co-supervising at FAST together with Sophie Mergui (Sorbonne Université) and Christian Ruyer-Quil (Université Savoie Mont Blanc). Her thesis, which will be completed in 2022, concerns our work on falling liquid films sheared by a turbulent gas flow discussed in section 1.4 and chapter 9.
- Wilko Rohlfes was a PhD. student at RWTH Aachen University when we worked on the hydrodynamics of three-dimensional falling liquid films as discussed in section 5.2 (Dietze *et al.*, 2014). Before my joining FAST, we had worked together on falling liquid films subject to electric fields and thermally-induced Marangoni stresses (Rohlfes *et al.*, 2012*b,a*, 2013).
- Motochika Inoue was a visiting Japanese master's student, who spent four months at laboratoire FAST in 2016. His hard work laid the basis for our numerical simulations of liquid-film/micro-particle interactions as discussed in section 8.1 (Nakamura *et al.*, 2020*b,a*).

I have received funding from several sources, which greatly helped in supporting and orienting the research presented in this habilitation document. The following list reports the different projects funded and my role in these projects:

PhD. co-supervisor <i>since 2018</i>	PhD. scholarship from Université Savoie Mont Blanc: <i>“Confined wavy liquid films on corrugated substrates: transfer intensification versus flooding”</i> PhD. candidate: Misa Ishimura Partners: Christian Ruyer-Quil (Université Savoie Mont Blanc), Sophie Mergui (Sorbonne Université)
Principal Investigator <i>2016-2019</i>	ANR project wavyFILM: <i>“Harnessing waves on liquid films to optimize distillation processes”</i> Partners: Sophie Mergui (Sorbonne Université), Nicolas Grenier (Université Paris-Saclay), Guillaume Mougin (Air Liquide), Gianluca Lavalley and Yiqin Li (postdoctoral fellows) Grant: 323.000 EUR
Project Partner <i>since 2016</i>	Tokyo University of Science exchange program: <i>“Fluid dynamics in the vicinity of a macroscopic contact line in interaction with microparticles.”</i>

	Partners: Ichiro Ueno (Tokyo University of Science), Farzam Zoueshtiagh (Université de Lille), Harunori Yoshikawa (Université de Nice)
Principal Investigator 2014-2015	INSIS project DYNAFILM: “ <i>Excitation spatiale de la dynamique non-linéaire d’un film liquide tombant : application à l’optimisation des échangeurs à films ruisselants</i> ” Partners: Christian Ruyer-Quil, Marguerite Gisclon, and Didier Bresch (Université Savoie Mont Blanc) Grant: 15.000 EUR
Principal Investigator 2017	Industrial consulting contract Partner: Air Liquide Grant: 4.000 EUR
Invited Researcher 2015	Fellowship funded by European Union IRSES project: “ <i>Patterns and Surfaces</i> ” Host institution: University of Florida Partners: Farzam Zoueshtiagh (Université de Lille), Ranga Narayanan (University of Florida)
Principal Investigator 2013	Industrial consulting contract Partner: Air Liquide Grant: 10.000 EUR
Principal Investigator 2013	Computation time on supercomputer JUROPA at Forschungszentrum Jülich Partners: Reinhold Kneer and Wilko Rohlf (RWTH Aachen University) Grant number: HAC27
Principal Investigator 2013	Junior researcher project funded by Université Paris-Sud: “ <i>Experimental study of the Poiseuille-Rayleigh-Bénard instability in complex fluids</i> ” Partners: Sophie Mergui (Université Pierre et Marie Curie) Grant: 15.000 EUR (unfortunately, this project did not yield publishable results)

Further, I have secured funding for several new projects, which will allow extending the work presented here, and to move toward new topics:

PhD. supervisor to start in 2022	CIFRE PhD. grant from Air Liquide: “ <i>Optimization of condensation channels in cryogenic vaporizer-condensers</i> ” Partners: Jacopo Seiwert and Nicolas Kofman (Air Liquide), Christian Ruyer-Quil (Université Savoie Mont Blanc), Sophie Mergui (Sorbonne Université) Candidate: currently soliciting applications
-------------------------------------	--

- 
- Project Partner  
*since October 2021*
- ANR project FEFS: “*Fluid Engineering for Food Security*”  
Partners: Farzam Zoueshtiagh (Université de Lille), Ichiro Ueno (Tokyo University of Science), and Harunori Yoshikawa (Université de Nice)  
Grant: 20.000 EUR
- Principal Investigator  
*since September 2021*
- LaSIPS project mucusFILM: “*Low-dimensional modelling of a viscoelastic mucus film in an individual pulmonary airway*”  
Partners: Nicolas Grenier (Université Paris-Saclay), Marcel Filoche (École Polytechnique), and Anjishnu Choudhury (post-doctoral fellow)  
Grant: 57.500 EUR



# Chapter 1

## WRIBL models for two-fluid film flows

We are interested in modelling thin liquid film flows subject to long-wave interfacial instabilities, which originate at wave number  $k=2\pi/\Lambda=0$ . In this case, the characteristic thickness of the liquid film  $h_0$  is much smaller than the characteristic wavelength  $\Lambda$  of surface waves resulting from instability. We are particularly interested in configurations where the liquid film is subject to an active outer fluid, usually a gas, which is confined by a narrow geometry. We designate these as two-fluid film flows, and we wish to predict the linear and nonlinear dynamics resulting from interfacial instability, through low-cost computations based on low-dimensional models.

Figure 1.1 shows several examples studied in this work. The aspect ratio of the graphical representations in the different panels is true to scale, allowing to appreciate the slenderness of the studied two-fluid film flows. The star superscripts, which mark the longitudinal coordinate  $x^*$  and the wall-normal coordinates  $y^*$  and  $r^*$ , denote dimensional quantities here and throughout this document. Panels 1.1a and 1.1b correspond to vertically falling liquid films in narrow planar channels (chapter 6) and cylindrical tubes (chapter 7), where surface waves form as a result of the Kapitza and Plateau-Rayleigh instability, respectively. In both cases, the outer fluid is air, which is either quiescent or flows counter-currently. Panel 1.1c corresponds to a highly viscous mucus film in a pulmonary airway, which is subject to the Plateau-Rayleigh instability (section 7.2). Panel 1.1d corresponds to a water film suspended from a ceiling, forming droplets due to the Rayleigh-Taylor instability (section 8.1).

These flows are amenable to the so-called *long-wave approximation*  $\epsilon=h_0/\Lambda \ll 1$ , under which the governing equations reduce in accordance with boundary layer theory (Schlichting & Gersten, 2001). Different modelling approaches may be applied to further simplify the resulting boundary layer equations, leading to low-dimensional models in terms of the film thickness  $h(x, t)$  and flow rate  $q(x, t)$ .

Long-wave asymptotic models (Oron *et al.*, 1997; Craster & Matar, 2009) rely on successively truncating the boundary layer equations at increasing orders of the long-wave parameter  $\epsilon$ , and developing the solution by asymptotic expansion of the primary flow

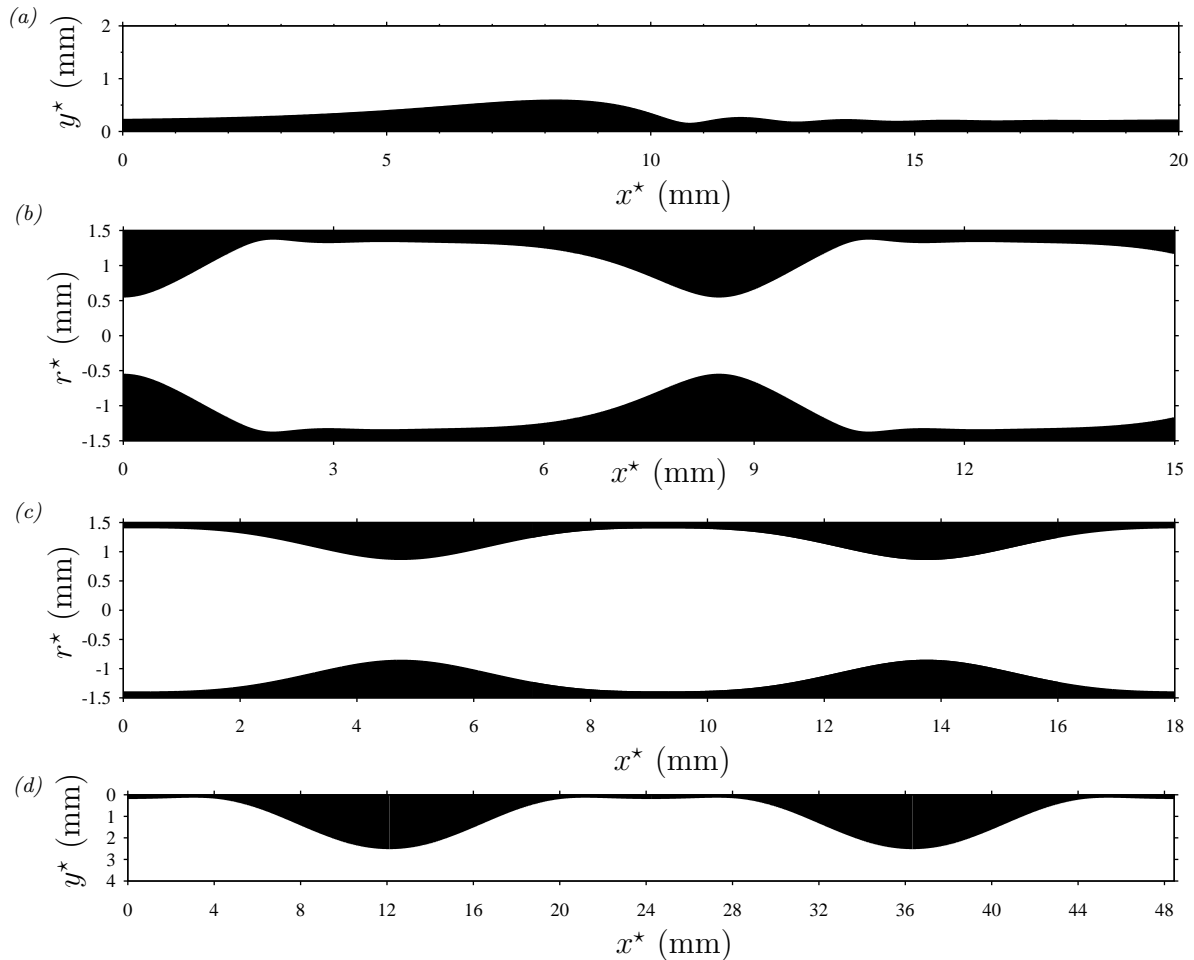


Figure 1.1: Examples of two-fluid film flows studied in this work: liquid film (black) in contact with an active gas (white) within a narrow geometry. The aspect ratio in all representations is true to scale. Here, the wall-adjacent film is always liquid and the outer fluid is always air, but liquid/liquid and vapour/liquid combinations have also been studied. (a) Falling liquid film of DMSO-water (flowing from left to right) in a vertical planar channel of height  $H^*=2$  mm; (b) falling liquid film of silicone-oil in a vertical cylindrical tube; (c) highly viscous model mucus film in a cylindrical model of a terminal bronchiole; (d) water film suspended from a ceiling forming droplets.

around the long-wave limit  $k=0$ . This approach yields a single evolution equation for the film thickness  $h(x, t)$ , capturing different physical effects, depending on the order of  $\epsilon$  at which the expansion is truncated. For example, at leading order, i.e. consistent at  $\epsilon^0$ , one obtains so-called lubrication models, which do not account for inertia nor streamwise viscous diffusion. The validity of long-wave asymptotic models is limited to regimes in the vicinity of the instability threshold, where the entire span of unstable wave numbers  $\kappa$  is small. Outside this validity range, high-order nonlinear terms in the evolution equa-

tion may cause unphysical behaviour, such as the finite-time blow-up observed for falling liquid films (Pumir *et al.*, 1983).

In the current work, we employ a different approach, the so-called integral boundary layer (IBL) method. Instead of expanding around the primary flow like the methods described above, this method relies on expanding around a leading-order base flow that varies dynamically with  $h(x, t)$  and  $q(x, t)$ . In this case, one obtains two coupled evolution equations for  $h$  and  $q$ , by integrating the boundary layer and continuity equations across the film. The approach is inspired by the integral method of von Kármán and Pohlhausen (von Kármán, 1921; Pohlhausen, 1921) for boundary layer flows. It was first applied to falling liquid films by Kapitza & Kapitza (1949), and later improved by Shkadov (1967). Subsequently, Ruyer-Quil & Manneville (2000) perfected the method, by introducing a weighted residual formalism to enforce that the model equations converge toward the linear long-wave limit of the Navier-Stokes equations, allowing to recover exactly the corresponding instability threshold. This constitutes the weighted residual integral boundary layer (WRIBL) method, which will be detailed in the current chapter.

When I was introduced to the WRIBL method by Christian Ruyer-Quil in 2011, it had been applied to many problems of liquid film flows where the outer fluid was not taken into account (Ruyer-Quil *et al.*, 2012; Ruyer-Quil & Manneville, 2002; Ruyer-Quil *et al.*, 2008; Scheid *et al.*, 2006; Trevelyan *et al.*, 2007; Kalliadasis *et al.*, 2012; Ruyer-Quil, 2012). My contribution has been to account for the effect of an additional active outer phase (either gas or liquid), by building on the works of Amaouche *et al.* (2007), Mehidi & Amatousse (2009), and Alba *et al.* (2011). Versus these works, I have extended the method so that counter-current two-phase flows with arbitrary density ratios and can be represented. In particular, I developed WRIBL models for four different configurations of two-fluid film flows (Dietze & Ruyer-Quil, 2013, 2015; Dietze *et al.*, 2018):

- Planar liquid films in rectangular channels (section 1.1)
- Annular liquid films in cylindrical tubes (section 1.2)
- Fluid films subject to the Rayleigh-Taylor and Marangoni instabilities (section 1.3)
- Falling liquid films sheared by a turbulent gas (section 1.4)

Most of our computations with these models have concerned systems where the outer fluid is air, but liquid/liquid systems and vapour films underneath a liquid layer have also been studied.

## 1.1 Planar liquid films in rectangular channels

We consider the configuration sketched in figure 1.2, a liquid film flowing along a plane wall in contact with a co- or counter-current gas flow confined by a second wall at a distance  $H^*$ . The two parallel plates form a 2-dimensional planar channel. The liquid film is either driven by gravity (panel 1.2a), in which case the channel is vertical (chapter

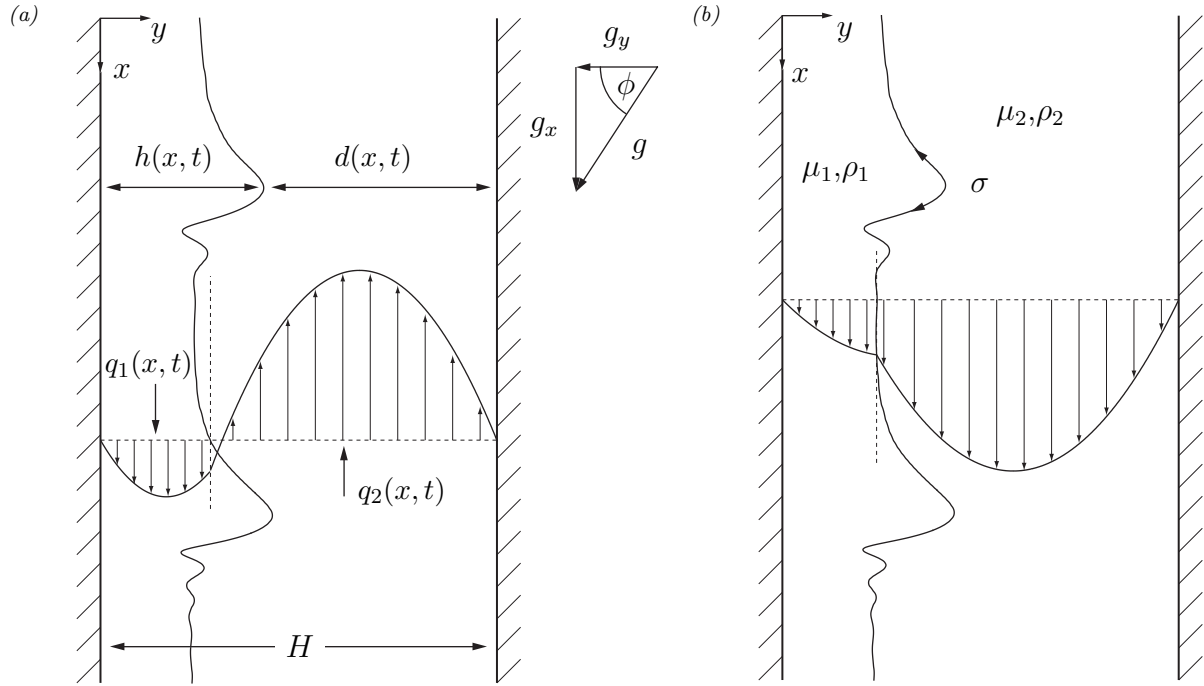


Figure 1.2: Liquid film (subscript 1) flowing on a planar wall subject to a strongly-confined co- or counter-current gas flow (subscript 2). (a) Gravity-driven falling liquid film; (b) pressure-driven liquid/gas channel flow (no **streamwise** gravity). The flows are laminar and all fluids are Newtonian.

6) or inclined at an angle  $\phi$ , or by an applied pressure gradient (panel 1.2b), in which case the channel is horizontal (section 8.3).

The liquid (subscript  $k=1$ ) and the gas (subscript  $k=2$ ) are assumed to be Newtonian fluids and their viscosity  $\mu$ , density  $\rho$ , and surface tension  $\sigma$  are assumed to be constant. Further,  $h$  denotes the film thickness and  $q$  the flow rate per unit width. The flow is assumed to be laminar and 2-dimensional. Although the planar WRIBL model is applied only to liquid/gas systems in this work, fluids 1 and 2 can be chosen freely. For example, liquid/liquid configurations can also be studied.

We introduce  $\mathcal{L}$  and  $\mathcal{U}_k$  to scale dimensional variables (denoted with a star):

$$u_k = \frac{u_k^*}{\mathcal{U}_k}, \quad v_k = \frac{v_k^*}{\epsilon \mathcal{U}_k}, \quad x = \epsilon \frac{x^*}{\mathcal{L}}, \quad y = \frac{y^*}{\mathcal{L}}, \quad t = \epsilon t^* \frac{\mathcal{U}_1}{\mathcal{L}}, \quad p_k = \frac{p_k^*}{\rho_k \mathcal{U}_k^2}, \quad (1.1)$$

where the length scale ratio  $\epsilon = \mathcal{L}/\Lambda^*$  is usually called long-wave parameter,  $\Lambda^*$  denoting a characteristic wavelength. For the length scale in y-direction  $\mathcal{L}$ , we choose the channel height,  $\mathcal{L} = H^*$ , and for the velocity scale  $\mathcal{U}_k$  we choose the phase-specific surface velocity,  $\mathcal{U}_k = \underline{q}_k^*/H^*$ , based on the corresponding signed nominal flow rate per unit width  $\underline{q}_k^*$ . Nominal refers to the fully-developed state (subscript  $\infty$ ) of a considered wavy-film solution. Depending on whether the solution evolves in time subject to periodicity conditions



(2.31), or in space subject to an inlet condition (2.35),  $\underline{q}_k^*$  is defined through a spatial average over the wavelength  $\Lambda$  or a temporal average over the wave period  $1/f$ :

$$\textit{spatially periodic solution} : \quad \underline{q}_k^* = \frac{1}{\Lambda^*} \int_0^{\Lambda^*} \{q_k^*\}_\infty dx^* \quad (1.2)$$

$$\textit{time periodic solution} : \quad \underline{q}_k^* = f^* \int_0^{\frac{1}{f^*}} \{q_k^*|_{x^*=0}\}_\infty dt^*. \quad (1.3)$$

Depending on the direction of the flow,  $\underline{q}_k^*$ , and thus  $\mathcal{U}_k$ , is positive or negative.

Our derivation is consistent at  $\epsilon^2$ , i.e. the governing equations are truncated at  $\epsilon^2$ , terms of order  $\epsilon^3$  and smaller dropping out. In that limit, the dimensionless Navier-Stokes and continuity equations for the liquid ( $k=1$ ) and gas ( $k=2$ ) reduce to<sup>1</sup>:

$$X_k \epsilon \partial_t u_k + \epsilon u_k \partial_x u_k + \epsilon v_k \partial_y u_k = -\epsilon \partial_x p_k + \frac{1}{\text{Re}_k} \{ \epsilon^2 \partial_{xx} u_k + \partial_{yy} u_k \} + \frac{X_k^2}{\text{Fr}^2} \sin(\phi), \quad (1.4a)$$

$$0 = -\epsilon \partial_y p_k + \epsilon^2 \frac{1}{\text{Re}_k} \partial_{yy} v_k - \epsilon \frac{X_k^2}{\text{Fr}^2} \cos(\phi), \quad (1.4b)$$

$$\partial_x u_k + \partial_y v_k = 0, \quad (1.4c)$$

where  $\text{Re}_k = \rho_k \mathcal{U}_k \mathcal{L} / \mu_k = \underline{q}_k^* \rho_k / \mu_k$  denote the phase-specific Reynolds numbers, and  $\text{Fr} = \mathcal{U}_1 / \sqrt{g \mathcal{L}}$  is the liquid Froude number. The parameter  $X_k$  accounts for the different velocity scales in the two phases:

$$X_1 = 1, \quad X_2 = \Pi_u^{-1}, \quad (1.5)$$

introducing the velocity scale ratio  $\Pi_u = \mathcal{U}_2 / \mathcal{U}_1$ . The inter-phase coupling conditions at  $y=h$  for the normal and tangential stresses truncated at  $\epsilon^2$  are:

$$\begin{aligned} \epsilon p_1 - \epsilon \text{We} \epsilon^2 \kappa + \frac{2 \epsilon^2}{\text{Re}_1} (-\partial_y v_1 + \partial_x h \partial_y u_1) = \\ \Pi_\rho \Pi_u^2 \epsilon p_2 + \Pi_\mu \Pi_u \frac{2 \epsilon^2}{\text{Re}_1} (-\partial_y v_2 + \partial_x h \partial_y u_2), \end{aligned} \quad (1.6a)$$

$$-(\partial_y u_1 + \epsilon^2 \partial_x v_1) + 4 \epsilon^2 \partial_x h \partial_x u_1 = \Pi_u \Pi_\mu \{ -(\partial_y u_2 + \epsilon^2 \partial_x v_2) + 4 \epsilon^2 \partial_x h \partial_x u_2 \}, \quad (1.6b)$$

where  $\text{We} = \sigma / \rho_1 / \mathcal{U}_1^2 / \mathcal{L}$  denotes the Weber number, relating capillary to liquid inertial effects. Note that this definition, commonly used in the falling film literature, is the reciprocal of the usual definition. We will also use the Kapitza number  $\text{Ka} = \sigma \rho_1^{-1} g^{-1/3} \nu_1^{-4/3}$ , which involves only fluid properties, and which is related to  $\text{We}$  via  $\text{Ka} = \text{We} \text{Fr}^{2/3} \text{Re}_1^{4/3}$ .

<sup>1</sup>See section 4.1.1 for full governing equations.

The term  $\kappa = -\partial_{xx}h$  in (1.6a) corresponds to the order  $\epsilon^0$  approximation of the (dimensionless) film surface curvature  $C$ :

$$C = \mathcal{L} C^* = \nabla \cdot \mathbf{n} = -\partial_{xx}h, \quad (1.7)$$

where  $\nabla = \mathcal{L} \nabla^* = [\epsilon \partial_x, \partial_y]$  and  $\mathbf{n}$ , both dimensionless, are the gradient operator and the normal vector (pointing from liquid,  $k=1$ , toward gas,  $k=2$ ) of the orthonormal surface coordinate system:

$$\mathbf{n} = [-\epsilon \partial_x h, 1] (1 + \epsilon^2 \partial_x h^2)^{-1/2}, \quad \boldsymbol{\tau} = [1, \epsilon \partial_x h] (1 + \epsilon^2 \partial_x h^2)^{-1/2}. \quad (1.8)$$

In (1.6a), the capillary pressure jump  $\epsilon \text{We} \epsilon^2 \kappa$  has been retained, and this implies  $\mathcal{O}(\epsilon \text{We})=1$ . Thus, our approach is restricted to flows where capillary effects dominate inertia, i.e. where  $\text{We}$  is large (Gjevik, 1970). Typical falling film liquids, such as water and different aqueous solutions, allow to satisfy this condition. For example,  $\text{We}=36.2$  for the case shown in panel 1.1a, which is the most unfavourable considered.

The system is completed by the kinematic inter-phase coupling conditions at  $y=h$ :

$$u_1 = \Pi_u u_2, \quad v_1 = \Pi_u v_2 \quad (1.9a)$$

$$X_k^{-1} v_k = \frac{dh}{dt} = \partial_t h + X_k^{-1} u_k \partial_x h, \quad (1.9b)$$

where the so-called kinematic condition (1.9b) results from the impermeability of the film surface assumed here, and the crosswise boundary conditions:

$$u_1|_{y=0} = v_1|_{y=0} = 0, \quad u_2|_{y=H} = v_2|_{y=H} = 0. \quad (1.10)$$

The streamwise boundary conditions depend on the type of computation (see section 2.2). They can either impose periodicity on a domain spanning one wavelength, e.g. for the computation of travelling-wave solutions, or they can mimic inlet/outlet conditions encountered in experiments of spatially developing films.

Equations (1.4) to (1.10) are the two-phase analog of the system obtained in classical boundary layer theory (Schlichting & Gersten, 2001). We further simplify these equations by recasting (1.4a) and (1.4b) into a single equation. Integrating (1.4b) between  $y$  and  $h$  and substituting the resulting expression for the pressure  $p_k$  into (1.4a), yields the (second-order) boundary layer equations BLE $_k$  for the liquid film and gas layer, respectively:

$$\begin{aligned} \text{BLE}_k : \quad X_k \epsilon \partial_t u_k + \epsilon u_k \partial_x u_k + \epsilon v_k \partial_y u_k = & \\ & - \epsilon \partial_x [p_k|_h] + \frac{X_k^2}{\text{Fr}^2} \{ \sin(\phi) - \epsilon \cos(\phi) \partial_x h \} \\ & - \epsilon^2 \frac{1}{\text{Re}_k} \partial_x [\partial_x u_k|_h] + \frac{1}{\text{Re}_k} \{ 2 \epsilon^2 \partial_{xx} u_k + \partial_{yy} u_k \}. \end{aligned} \quad (1.11)$$

The momentum equation of our WRIBL model is obtained by performing a weighted integration of  $\text{BLE}_k$  across the respective layers and summing the two results:

$$\text{ME} : \int_0^{h(x,t)} w_1(y) \text{BLE}_1 dy + \Pi_\rho \Pi_u^3 \int_{h(x,t)}^H w_2(y) \text{BLE}_2 dy, \quad (1.12)$$

where we have introduced the weight functions  $w_k$ , and where the multiplicative factor  $\Pi_\rho \Pi_u^3$  is a direct consequence of the chosen phase-specific scaling (1.1). These weight functions are tailored to produce several desired properties of the model. The first condition imposed on  $w_k$  is:

$$\Pi_u \int_h^H w_2(y) dy = - \int_0^h w_1(y) dy, \quad (1.13)$$

which allows to recast the pressure term in (1.12) as follows:

$$\begin{aligned} -\partial_x [p_1|_h] \int_0^h w_1(y) dy - \Pi_\rho \Pi_u^3 \partial_x [p_2|_h] \int_h^H w_2(y) dy = \\ -\partial_x [p_1|_h - \Pi_\rho \Pi_u^2 p_2|_h] \int_0^h w_1(y) dy. \end{aligned} \quad (1.14)$$

As a result, the pressure variable can be eliminated from (1.14) by substituting the normal stress balance (1.6a) for  $p_1|_h - \Pi_\rho \Pi_u^2 p_2|_h$ .

To perform the integration required in (1.12), we decompose the longitudinal velocity component  $u_k$  into an order  $\epsilon^0$  base profile  $\hat{u}_k$  and an order  $\epsilon^1$  correction  $u_k^{(1)}$ :

$$u_k(x, y, t) = \underbrace{\hat{u}_k(x, y, t)}_{\mathcal{O}(\epsilon^0)} + \underbrace{u_k^{(1)}(x, y, t)}_{\mathcal{O}(\epsilon^1)}, \quad (1.15)$$

implying that  $\hat{u}$  is sufficiently close to the exact solution  $u_k$  of (1.4)-(1.10), a condition to be checked a posteriori by comparing with direct numerical simulations (DNS). Following the WRIBL approach for single-fluid film flows (Samanta *et al.*, 2011), we require  $\hat{u}_k$  to satisfy the leading-order governing equations, i.e. (1.4)-(1.10) truncated at  $\epsilon^0$ :

$$\partial_{yy} \hat{u}_k = Z_k, \quad \partial_y \hat{u}_1|_h = \Pi_\mu \Pi_u \partial_y \hat{u}_2|_h, \quad \hat{u}_1|_h = \Pi_u \hat{u}_2|_h, \quad \hat{u}_1|_0 = \hat{u}_2|_H = 0, \quad (1.16a)$$

and to yield the phase-specific local instantaneous flow rates (per unit width)  $q_k(x, t)$  corresponding to the full system (1.4)-(1.10):

$$\int_0^{h(x,t)} \hat{u}_1 dy = q_1(x, t), \quad \int_{h(x,t)}^H \hat{u}_2 dy = q_2(x, t). \quad (1.16b)$$

This defines the constants  $Z_k$  and parametrizes the base profile  $\hat{u}_k$  in terms of  $h$ ,  $q_1$ , and  $q_2$ , which will emerge as the three dependent variables of the WRIBL model:

$$\hat{u}_k(x, y, t) = f_{ki}(y, h) q_i(x, t), \quad (1.17)$$

where  $f_{ki}$  are defined through the boundary value problem (1.16):

$$\int_0^h f_{11} dy = \int_h^H f_{22} dy = 1, \quad \int_0^h f_{12} dy = \int_h^H f_{21} dy = 0. \quad (1.18)$$

They are given explicitly in (A.4) of appendix A.1. Importantly, as a result of 1.16b, the integrals of the velocity corrections  $u_k^{(1)}$  vanish:

$$\int_0^h u_1^{(1)} dy = \int_h^H u_2^{(1)} dy = 0. \quad (1.19)$$

The wall-normal velocity component  $v_k$  is obtained from the continuity equation (1.4c):

$$v_k(x, y, t) = \underbrace{\hat{v}_k(x, y, t)}_{\mathcal{O}(\epsilon^0)} + \underbrace{v_k^{(1)}(x, y, t)}_{\mathcal{O}(\epsilon^1)}, \quad (1.20)$$

$$\hat{v}_k(x, y, t) = -\delta_{k1} \int_0^y \partial_x \hat{u}_1 d\tilde{y} + \delta_{k2} \int_y^H \partial_x \hat{u}_2 d\tilde{y}, \quad (1.21)$$

where we have introduced the Kronecker symbol  $\delta_{ij}$ , and the base profile  $\hat{v}_k(x, y, t)$  can be factorized as follows:

$$\hat{v}_k(x, y, t) = g_{k1}(y, h) q_1 \partial_x h + g_{k2}(y, h) q_2 \partial_x h + g_{k3}(y, h) \partial_x q_1 + g_{k4}(y, h) \partial_x q_2. \quad (1.22)$$

The coefficients  $g_{kj}$  are given explicitly in (A.5) of appendix A.1.

The last remaining step in the model derivation is to eliminate terms from the momentum equation (1.12) involving the velocity corrections  $u_k^{(1)}$  and  $v_k^{(1)}$ , which are unknown at this stage. This is done in three steps:

- Most terms involving  $u_k^{(1)}$  and  $v_k^{(1)}$  drop out because they are smaller than the truncation limit  $\epsilon^2$ .
- Inertial corrections of order  $\epsilon^2$ , such as  $\epsilon \int w_k \hat{u}_k \partial_x u_k^{(1)} dy$ , are dropped under the assumption that inertial effects are weak compared to capillary effects. This requires  $We \gg 1$  for the primary fluid and  $We/\Pi_\rho/\Pi_u^2 \gg 1$  for the outer fluid. Assuming  $We$  is at the low end, this would imply  $\mathcal{O}(\Pi_u) \geq \mathcal{O}(\Pi_\rho^{-1/2})$  for the outer fluid. For liquid-gas systems, where  $\mathcal{O}(\Pi_\rho)=10^{-3}$ , the characteristic gas velocity is thus allowed to be up to  $\sqrt{10^3}$  times greater than the liquid velocity, i.e.  $\mathcal{O}(\Pi_u)=10^{3/2}$ . We point out that order  $\epsilon^2$  inertial corrections can, in principle, be accounted for in the WRIBL approach, as has been shown by Ruyer-Quil & Manneville (2002) for the limiting case of a passive outer phase ( $\Pi_\rho=\Pi_\mu=0$ ). Although this would expand the range of validity of our model, it would also render it much more involved, in particular due to accounting for the active outer phase.

- The viscous correction terms  $\text{Re}_k^{-1} \int w_k \partial_{yy} u_k^{(1)} dy$ , which are of order  $\epsilon^0$ , can be recast through twofold integration by parts:

$$\begin{aligned} & \text{Re}_1^{-1} \left\{ \int_0^h w_1 \partial_{yy} u_1^{(1)} dy - \Pi_\mu \Pi_u^2 \int_h^H w_2 \partial_{yy} u_2^{(1)} dy \right\} = \\ & \text{Re}_1^{-1} \left\{ \int_0^h \partial_{yy} w_1 u_1^{(1)} dy - \Pi_\mu \Pi_u^2 \int_h^H \partial_{yy} w_2 u_2^{(1)} dy \right. \\ & \left. + \left[ u_1^{(1)} \partial_y w_1 \right]_0^h - \Pi_\mu \Pi_u^2 \left[ u_2^{(1)} \partial_y w_2 \right]_h^H + \left[ w_1 \partial_y u_1^{(1)} \right]_0^h - \Pi_\mu \Pi_u^2 \left[ w_2 \partial_y u_2^{(1)} \right]_h^H \right\}, \end{aligned} \quad (1.23)$$

where we have used the identity  $\Pi_\rho \Pi_u^3 \text{Re}_2^{-1} = \Pi_\mu \Pi_u^2 \text{Re}_1^{-1}$ . The different terms on the RHS of (1.23) can be eliminated or substituted step for step, by requiring the weight functions  $w_k$  to satisfy the boundary value problem:

$$\begin{aligned} \partial_{yy} w_k &= \underline{Z}_k, \quad w_1|_0 = w_2|_H = 0, \\ w_1|_h &= \Pi_u w_2|_h, \quad \partial_y w_1|_h = \Pi_\mu \Pi_u \partial_y w_2|_h, \end{aligned} \quad (1.24)$$

by invoking the gauge conditions (1.19), boundary conditions (1.10), and kinematic inter-phase coupling condition (1.9a) for  $u_k^{(1)}$ , and, finally, by substituting the expression:

$$w_1 \partial_y u_1^{(1)} \Big|_h - \Pi_\mu \Pi_u^2 w_2 \partial_y u_2^{(1)} \Big|_h = w_1|_h \left\{ \partial_y u_1^{(1)} \Big|_h - \Pi_\mu \Pi_u \partial_y u_2^{(1)} \Big|_h \right\}, \quad (1.25)$$

via the inter-phase tangential stress balance (1.6b), with the base profile velocity gradient jump  $\partial_y \hat{u}_1|_h - \Pi_\mu \Pi_u \partial_y \hat{u}_2|_h$ .

The weight functions  $w_k$  are defined through (1.24) and (1.13), up to an arbitrary constant, and thus one of the  $\underline{Z}_k$  in (1.24) can be chosen freely. The system (1.24) is identical to the boundary value problem (1.16a) defining the base profile  $\hat{u}_k$ . In the case of single-fluid films (Samanta *et al.*, 2011), this implies  $w = \hat{u}$ , similar to the Galerkin approach in finite element numerical integration (Zienkiewicz *et al.*, 2013). By contrast, in our two-phase configuration,  $w_k$  and  $\hat{u}_k$  are necessarily different, owing to the integral constraint (1.13). A suitable choice for  $w_k$  then is<sup>2</sup>:

$$w_k(y, h) = f_{k1}(y, h) - \Pi_u^{-1} f_{k2}(y, h). \quad (1.26)$$

As a result, the final form of our momentum equation is:

$$\begin{aligned} S_i \partial_t q_i + F_{ij} q_i \partial_x q_j + G_{ij} q_i q_j \partial_x h &= \text{We} \partial_{xx} h \\ &+ \frac{1}{\text{Fr}^2} (1 - \Pi_\rho) \{ \sin(\phi) - \cos(\phi) \partial_x h \} + C_i q_i \\ &+ J_i q_i \partial_x h^2 + K_i \partial_x q_i \partial_x h + L_i q_i \partial_{xx} h + M_i \partial_{xx} q_i, \end{aligned} \quad (1.27)$$

---

<sup>2</sup>This choice implies  $\int_0^h w_1 dr = 1$  and  $\int_h^R w_2 dr = 1$ .

where the subscripts  $i$  and  $j$  are to be permuted through the phase indicators 1 and 2 using Einstein summation, and the coefficients  $S_i$ ,  $F_{ij}$ ,  $G_{ij}$ ,  $C_i$ ,  $J_i$ ,  $K_i$ ,  $L_i$ , and  $M_i$  are known functions of the film thickness  $h$  and the control parameters, e.g.  $Re_i$ ,  $\Pi_\mu$ , and  $\Pi_\rho$ . They are given in appendix A.1.

The terms on the LHS of (1.27), with coefficients  $S_i$ ,  $F_{ij}$ , and  $G_{ij}$ , account for the effect of inertia. The first two terms on the RHS, respectively scaled by  $We$  and  $Fr$ , express the effect of surface tension forces and gravity. Streamwise gravity enters through  $\sin(\phi)$  and wall-normal gravity through  $\cos(\phi)$ . The remaining terms account for viscous stresses. Those with coefficients  $C_i$  express effects of order  $\epsilon$ , and those with coefficients  $J_i$ ,  $K_i$ ,  $L_i$ , and  $M_i$  express effects of order  $\epsilon^2$ .

Our model is closed with two additional equations obtained by integrating the continuity equation (1.4b) across the liquid and gas layer, and applying the kinematic condition (1.9b):

$$\partial_t h + \partial_x q_1 = 0, \quad (1.28a)$$

$$-\partial_t h + \Pi_u \partial_x q_2 = 0. \quad (1.28b)$$

Taking the sum of these two equations, yields that the total flow rate  $q_{\text{tot}} = q_1 + \Pi_u q_2$  is spatially invariant. From the perspective of solving (1.27) numerically, it is thus convenient to eliminate  $q_2$  from the problem via:

$$q_2 = \Pi_u^{-1} (q_{\text{tot}} - q_1). \quad (1.29)$$

Then, (1.28a), (1.27), and (1.29) constitute a closed system for the two unknowns  $q_1(x, t)$  and  $h(x, t)$ . The gas flow is controlled either by prescribing  $q_{\text{tot}}$  explicitly, or by imposing a condition on the gas pressure drop  $\Delta p_2$ .

For the second scenario, a pressure equation is derived by applying a different set of weight functions  $\tilde{w}_1$  and  $\tilde{w}_2$  to (1.12):

$$\text{PE : } \int_0^{h(x,t)} \tilde{w}_1(y) \text{BLE}_1 dy + \Pi_\rho \Pi_u^3 \int_{h(x,t)}^H \tilde{w}_2(y) \text{BLE}_2 dy, \quad (1.30)$$

where we choose:

$$\tilde{w}_k(y, h) = f_{k1}(y, h) + \Pi_u^{-1} f_{k2}(y, h). \quad (1.31)$$

As a result of this choice, the pressure term in (1.30) takes the form:

$$\begin{aligned} -\partial_x [p_1|_h] \int_0^h \tilde{w}_1(y) dy - \Pi_\rho \Pi_u^3 \partial_x [p_2|_h] \int_h^H \tilde{w}_2(y) dy = \\ -\partial_x [p_1|_h - \Pi_\rho \Pi_u^2 p_2|_h] \int_0^h \tilde{w}_1(y) dy \\ - 2\Pi_\rho \Pi_u^2 \partial_x [p_2|_h] \int_0^h \tilde{w}_1(y) dy. \end{aligned} \quad (1.32)$$

The first RHS term is once again eliminated through (1.6a) but the second term remains. As a result, (1.30) can be recast into a dynamic equation for the streamwise gas pressure gradient  $\partial_x [p_2|_h]$ :

$$\begin{aligned}
2\Pi_\rho\Pi_u^2 \partial_x [p_2|_h] &= -\tilde{S}_i\partial_t q_i - \tilde{F}_{ij}q_i\partial_x q_j - \tilde{G}_{ij}q_iq_j\partial_x h + \text{We} \partial_{xxx} h \\
&+ \frac{1}{\text{Fr}^2} (1 - \Pi_\rho) \{ \sin(\phi) - \cos(\phi)\partial_x h \} + \tilde{C}_i q_i \\
&+ \tilde{J}_i q_i \partial_x h^2 + \tilde{K}_i \partial_x q_i \partial_x h + \tilde{L}_i q_i \partial_{xx} h + \tilde{M}_i \partial_{xx} q_i \\
&= -\tilde{S}_i\partial_t q_i + \text{NLP}(x, t),
\end{aligned} \tag{1.33}$$

where the coefficients  $\tilde{S}_i$ ,  $\tilde{F}_{ij}$ ,  $\tilde{G}_{ij}$ ,  $\tilde{C}_i$ ,  $\tilde{J}_i$ ,  $\tilde{K}_i$ ,  $\tilde{L}_i$ , and  $\tilde{M}_i$  are defined through the same functions (given in appendix A.1) as their counterparts in (1.27), only that  $\tilde{w}_k$  instead of  $w_k$  are used. Equation (1.33) can be employed either to evaluate the pressure distribution a posteriori in a computation where  $q_{\text{tot}}$  is prescribed, or to impose  $\Delta p_2$  instead of  $q_{\text{tot}}$  through an integral condition:

$$\begin{aligned}
\Delta p_2 &= \int_0^L \partial_x [p_2|_h] dx = \frac{1}{2\Pi_\rho\Pi_u^2} \left\{ \int_0^L \text{NLP}(x, t) dx - \int_0^L \tilde{S}_i \partial_t q_i dx \right\} \\
&= \frac{1}{2\Pi_\rho\Pi_u^2} \left\{ \int_0^L \text{NLP}(x, t) dx - \int_0^L \left( \tilde{S}_1 - \Pi_u^{-1} \tilde{S}_2 \right) \partial_t q_1 dx - \partial_t q_{\text{tot}} \int_0^L \Pi_u^{-1} \tilde{S}_2 dx \right\},
\end{aligned} \tag{1.34}$$

where  $L$  designates the domain length of the computation. In the second case,  $\partial_t q_1$  is eliminated from (1.34) using the momentum equation (1.27), and  $\partial_t q_{\text{tot}}$  is adjusted to yield the desired  $\Delta p_2$ . In some situations, it is convenient to relate  $\Delta p_2$  to the weight of the gas column, and so we introduce the normalized pressure gradient  $M$ :

$$M = \frac{\Delta p_2^*}{\rho_2 g L^*}. \tag{1.35}$$

The limit  $M=\sin(\phi)$  corresponds to the reference case of an aerostatic pressure drop.

As a first basic consistency test, we have checked that (1.27) converges to equation (41) of Ruyer-Quil & Manneville (2000) in the appropriate limit of a passive gas phase ( $\Pi_\mu=\Pi_\rho=0$ ), after rescaling with the natural scales:

$$\mathcal{L}_\nu = \nu_l^{2/3} g^{-1/3}, \quad \mathcal{U}_\nu = (\nu_l g)^{1/3}, \quad \mathcal{T}_\nu = \mathcal{L}_\nu / \mathcal{U}_\nu, \tag{1.36}$$

where  $\nu_l$  is the liquid kinematic viscosity. Similarly, in the limit of a passive liquid ( $\Pi_\mu^{-1}=\Pi_\rho^{-1}=0$ ), and after appropriate rescaling (formulating the natural scales with the kinematic viscosity  $\nu_g$  of the gas), the same equation is obtained, only that the sign of the normal gravity term involving  $\cos(\phi)$  is reversed. A detailed validation of our model for the flow configurations studied in this work is provided in section 2.3.1.

**Relation to the state of the art and impact of our work:** At the time of its publication (Dietze & Ruyer-Quil, 2013), our planar two-phase WRIBL model, given by (1.28a), (1.28b), (1.27), and (1.33), extended the state of the art on modelling liquid film flows through narrow planar channels in several ways.

As far as the WRIBL method is concerned, our model extended the single-phase WRIBL model of Ruyer-Quil & Manneville (2000) (see also Oron *et al.* (2009)), by accounting for an active outer phase in contact with the liquid film. Further, it extended the two-phase model of Amaouche *et al.* (2007), which was derived (consistent at order  $\epsilon^2$ ) in the limit of zero pressure gradient  $\partial_x p_2=0$ . In this limit, it is not necessary to eliminate  $p_2$  through (1.13), (1.14), and (1.6a). However, without a driving pressure gradient, the configuration of a liquid film sheared by a counter-current gas flow cannot be represented. The idea for eliminating  $p_2$  through (1.13) was introduced later by Alba *et al.* (2011), who derived a WRIBL model consistent at order  $\epsilon^1$  for a pressure-driven two-phase channel flow. However, surface tension forces and gravity were neglected in that work, and equal densities were assumed for the two fluids ( $\Pi_\rho=1$ ). Our model improved upon the models of Amaouche *et al.* (2007) and Alba *et al.* (2011) by generalizing the two-phase WRIBL approach, so that counter-current flows with arbitrary density ratios (e.g. liquid-gas flows) and surface tension can be represented. Also, our pressure equation (1.33), which allows imposing the gas pressure drop or calculating the pressure distribution a posteriori, extended the WRIBL methodology.

Our WRIBL model (applied up to order  $\epsilon^2$ ) also improves upon other approaches that had been applied to liquid films in narrow channels. For example, asymptotic models (Jurman *et al.*, 1989; Jurman & McCreedy, 1989; Tilley *et al.*, 1994*b,a*), which are based on the approach of Benney (1966) and Gjevik (1970), i.e. a long-wave expansion around the primary flow<sup>3</sup>, are limited to the vicinity of the stability threshold, and, thus, only small-amplitude nonlinear waves can be represented. Outside this range, asymptotic models are prone to finite-time blow-up (Pumir *et al.*, 1983). Lubrication models (Pozrikidis, 1998) cannot account for the inertia-driven Kapitza instability, and IBL models (Sisoev *et al.*, 2009; Zakaria, 2012), which are based on the approach of Shkadov (1967), i.e. an unweighted integration of the boundary layer equations, cannot correctly predict the stability threshold for inclined configurations. Moreover, such models have been developed only up to order  $\epsilon$ , and thus do not account for streamwise viscous diffusion, which is known to significantly affect both the cut-off wave number of the instability and the amplitude of precursory capillary ripples in nonlinear solutions (Ruyer-Quil & Manneville, 2000). In some cases, the asymptotic approach was applied to one phase and the IBL approach to the other (Matar *et al.*, 2007).

Our WRIBL model accounts for the dynamic coupling between the two fluid phases via the full inter-phase coupling conditions. However, it is limited to rather low values of the Reynolds number ( $|\text{Re}_k| \leq 200$ ) as well as strong confinement levels. In that sense, our model complements weakly-coupled models that have been developed for liquid

---

<sup>3</sup>See Oron & Gottlieb (2004) for a discussion of the first- and second-order Benney equation applied to falling liquid films.



films sheared by high-speed gas flows (Demekhin, 1981; Alekseenko & Nakoryakov, 1995; Tseluiko & Kalliadasis, 2011). Such models relax the coupling conditions by assuming the film surface to be immobile relative to the gas. Although this assumption breaks down at low gas velocities, it is well suited to describe turbulent gas flows. In section 1.4, we will use this approach to derive a model for falling liquid films sheared by a turbulent gas flow.

Since its publication, our paper Dietze & Ruyer-Quil (2013), which introduced and validated our planar WRIBL model for two-fluid film flows through narrow channels, has been cited 45 times, according to *Web of Science*. Here, we focus only on citations that have referred to the methodological aspect of our paper, whereas section 6.2 will discuss the impact of the physics we have uncovered with our WRIBL model. Several works have acknowledged our paper as a seminal contribution to the modelling of two-phase film flows:

Vellingiri *et al.* (2015); Schmidt *et al.* (2016); Saleh & Ormiston (2017); Miao *et al.* (2017); Dandekar *et al.* (2018); Lavalley *et al.* (2015, 2017, 2018); Denner *et al.* (2018); Pillai & Narayanan (2018*b,a*); Tselodub & Bocharov (2017, 2018, 2020); Samanta (2013, 2020); Vakili-pour *et al.* (2021); Tselodub *et al.* (2021); Mohamed *et al.* (2021).

Some of these works have built upon our approach by incorporating additional physical effects. For example, Samanta (2013) extended our WRIBL model by accounting for variations in interfacial tension due to an insoluble surfactant, and used the model to study the role of the Marangoni effect in inclined liquid/liquid channel flows. Later, Pillai & Narayanan (2018*a*) incorporated heat transfer and phase change to study the dynamics of an unstable liquid/vapour bilayer within a narrow horizontal gap. Other works have used our benchmark data on pressure-driven two-layer channel flows and gas-sheared falling liquid films to validate their own low-dimensional models (Lavalley *et al.*, 2015; Miao *et al.*, 2017) and DNS solvers (Vakili-pour *et al.*, 2021).

## 1.2 Annular liquid films in cylindrical tubes

We consider the axisymmetric configuration sketched in figure 1.3, an annular liquid film coating the inner surface of a cylindrical tube of radius  $R^*$  in contact with an active core fluid. The liquid film is either driven by gravity (panel 1.3a), in which case the tube is vertical (section 7.1), or the tube is so narrow that capillarity dominates all other driving mechanisms (panel 1.3a), in which case the flow is entirely governed by the Plateau-Rayleigh instability, e.g. in the case of mucus films within the pulmonary airways (section 7.1). The core fluid may flow co- or counter-currently w.r.t the liquid film, or it may be quiescent. For example, we will consider an oscillating core gas flow in section 7.1, to mimic the air flow induced by breathing.

The derivation of our cylindrical model follows the WRIBL approach described for the planar configuration in section 1.1. From a physical point of view, the main differ-

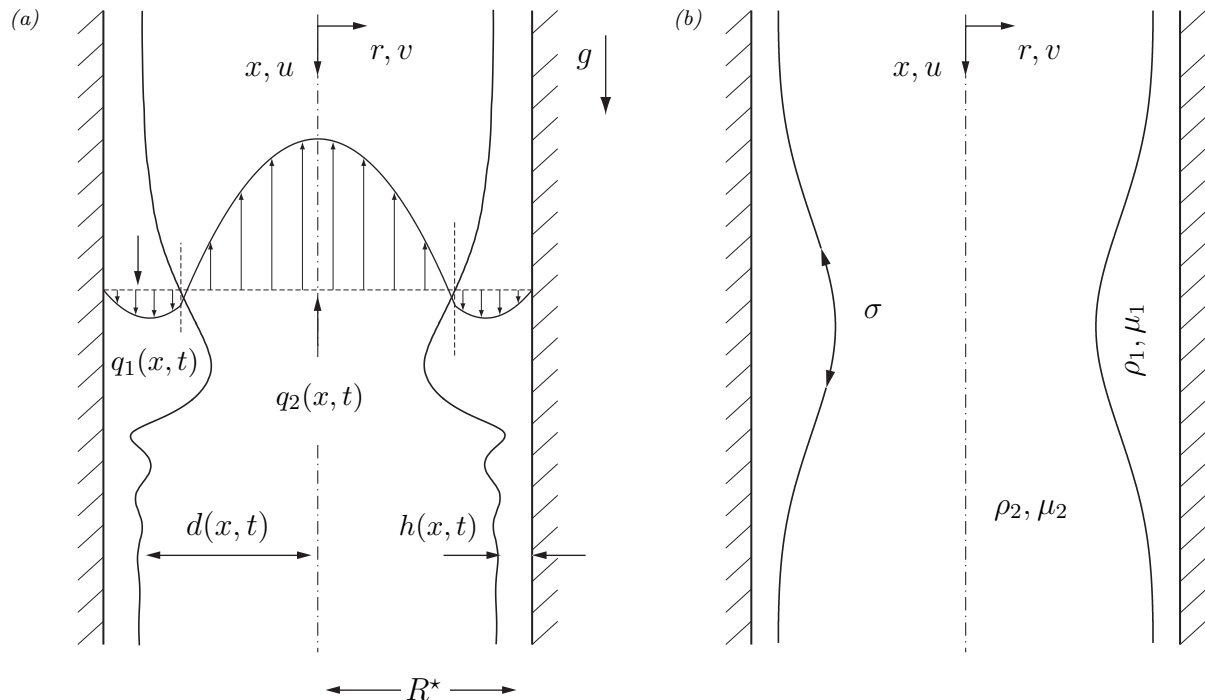


Figure 1.3: Axisymmetric annular liquid film (subscript 1) lining the inner surface of a narrow cylindrical tube and subject to an active core fluid (subscript 2). (a) Gravity-driven vertically falling liquid film in contact with a co- or counter-current gas flow; (b) gravity-free liquid film in contact with an oscillating gas flow (mucus films in pulmonary airways) or a quiescent core liquid (oil/water systems in porous media). The flows are laminar and both fluids are Newtonian. The star symbol denotes dimensional quantities.

ence versus the planar configuration is the azimuthal curvature of the film surface, which introduces the Plateau-Rayleigh instability. All other changes are due to moving from Cartesian differential operators to cylindrical ones. The liquid film (subscript  $k=1$ ) and core fluid (subscript  $k=2$ ) are again assumed to be Newtonian with constant fluid properties, and they are assumed to flow in a laminar two-dimensional (axisymmetric) manner. The core fluid is either a gas or a liquid, but we will focus on the former case<sup>4</sup>. We keep the same notations as in section 1.1, but  $q_k$  will now designate the cross-sectional flow rates:

$$q_1 = 2\pi \int_{d(x,t)}^R r u_1 dr, \quad q_2 = 2\pi \int_0^{d(x,t)} r u_2 dr \quad (1.37)$$

where we have introduced the core radius  $d$ , i.e. the radial distance between the tube axis and the film surface, which will be our main dependent variable instead of  $h$ . Variables are once again scaled according to (1.1), this time choosing the tube radius as the length scale  $\mathcal{L}=R^*$ . For the velocity scale  $\mathcal{U}$ , we distinguish between gravity-driven flow (panel

<sup>4</sup>Results for liquid/liquid combinations are discussed in Dietze & Ruyer-Quil (2015).

1.3a) and capillary-driven flow (panel 1.3b):

$$\text{gravity-driven flow : } \mathcal{U}_k = \frac{q_k^*}{\pi R^{*2}}, \quad (1.38)$$

$$\text{capillary-driven flow : } \mathcal{U}_k = \mathcal{U} = \frac{\sigma}{\mu_1}, \Pi_u = 1, \quad (1.39)$$

and the time scale is  $\mathcal{T} = \mathcal{L}/\mathcal{U}_1$ .

Compared to equations (1.4), (1.6), and (1.9) for the planar configuration, we obtain the following non-dimensional governing equations truncated at order  $\epsilon^2$  for the cylindrical configuration. The Navier-Stokes and continuity equations read:

$$X_k \epsilon \partial_t u_k + \epsilon u_k \partial_x u_k + \epsilon v_k \partial_r u_k = -\epsilon \partial_x p_k + \frac{1}{\text{Re}_k} \left\{ \epsilon^2 \partial_{xx} u_k + \frac{1}{r} \partial_r (r \partial_r u_k) \right\} + \frac{X_k^2}{\text{Fr}^2}, \quad (1.40a)$$

$$0 = -\epsilon \partial_r p_k + \epsilon^2 \frac{1}{\text{Re}_k} \partial_r \left\{ \frac{1}{r} \partial_r (r v_k) \right\}, \quad (1.40b)$$

$$\partial_x u_k + \frac{1}{r} \partial_r (r v_k) = 0, \quad (1.40c)$$

where, once again,  $X_1=1$  and  $X_2=\Pi_u^{-1}$ . The inter-phase coupling conditions for the normal<sup>5</sup> and tangential stresses at  $r=d$  are:

$$\epsilon p_1 + \epsilon \text{We} \epsilon^2 \kappa - \frac{2 \epsilon^2}{\text{Re}_1} \partial_r v_1 = \Pi_\rho \Pi_u^2 \epsilon p_2 - \Pi_\mu \Pi_u \frac{2 \epsilon^2}{\text{Re}_1} \partial_r v_2, \quad (1.41a)$$

$$\begin{aligned} & -(\partial_r u_1 + \epsilon^2 \partial_x v_1) + 2 \epsilon^2 \partial_x d (\partial_x u_1 - \partial_r v_1) = \\ & \Pi_u \Pi_\mu \left\{ -(\partial_r u_2 + \epsilon^2 \partial_x v_2) + 2 \epsilon^2 \partial_x d (\partial_x u_2 - \partial_r v_2) \right\}, \end{aligned} \quad (1.41b)$$

where  $\kappa$  again designates the order  $\epsilon^0$  approximation of the full curvature  $C = \nabla \cdot \mathbf{n}$  (4.19):

$$\kappa = \frac{1}{\epsilon^{-2} d} - \frac{1}{2} \frac{\partial_x d^2}{d} - \partial_{xx} d, \quad (1.42)$$

introducing the nabla operator  $\nabla = [\epsilon \partial_x, r^{-1} + \partial_r]$  in cylindrical coordinates, and the orthonormal surface coordinate system:

$$\mathbf{n} = [-\epsilon \partial_x d, 1] (1 + \epsilon^2 \partial_x d^2)^{-1/2}, \quad \boldsymbol{\tau} = [1, \epsilon \partial_x d] (1 + \epsilon^2 \partial_x d^2)^{-1/2}. \quad (1.43)$$

Further, we have the kinematic coupling conditions at  $r=d$ :

$$u_1 = \Pi_u u_2, \quad v_1 = \Pi_u v_2 \quad (1.44a)$$

---

<sup>5</sup>The sign of the We term in (1.41a) is inverted w.r.t (1.6a), because the normal vector  $\mathbf{n}$  (1.43) points into the liquid film.

$$X_k^{-1}v_k = \frac{dd}{dt} = \partial_t d + X_k^{-1}u_k \partial_x d, \quad (1.44b)$$

and the radial boundary conditions:

$$u_1|_{r=R} = v_1|_{r=R} = 0, \quad \partial_r u_2|_{r=0} = v_2|_{r=0} = 0. \quad (1.45)$$

The boundary layer equations for the annular liquid film and core fluid are obtained in the same way as (1.11):

$$\begin{aligned} \text{BLE}_k : \quad X_k \epsilon \partial_t u_k + \epsilon u_k \partial_x u_k + \epsilon v_k \partial_r u_k &= -\epsilon \partial_x [p_k|_d] + \frac{X_k^2}{\text{Fr}^2} \\ &- \epsilon^2 \frac{1}{\text{Re}_k} \partial_x [\partial_x u_k|_d] + \frac{1}{\text{Re}_k} \{2 \epsilon^2 \partial_{xx} u_k + \partial_{rr} u_k\}, \end{aligned} \quad (1.46)$$

and are combined as follows:

$$\text{ME} : \quad \int_{d(x,t)}^R r w_1(r) \text{BLE}_1 dr + \Pi_\rho \Pi_u^3 \int_0^{d(x,t)} r w_2(r) \text{BLE}_2 dr, \quad (1.47)$$

to construct the final integral momentum equation of our cylindrical WRIBL model (rescaled by setting  $\epsilon=1$ ):

$$\begin{aligned} S_i \partial_t q_i + F_{ij} q_i \partial_x q_j + G_{ij} q_i q_j \partial_x d &= \frac{\text{We}}{2\pi} \partial_x \kappa + \frac{1}{2\pi} \text{Fr}^{-2} (1 - \Pi_\rho) + \frac{1}{2\pi} C_i q_i \\ &+ J_i q_i \partial_x d^2 + K_i \partial_x q_i \partial_x d + L_i q_i \partial_{xx} d + M_i \partial_{xx} q_i, \end{aligned} \quad (1.48)$$

which is analogous to (1.27) of the planar model, and where  $\kappa$  is defined according to (1.42) (rescaled by setting  $\epsilon=1$ ). The model coefficients are known functions of  $d$  and the control parameters of the problem, e.g.  $\text{Re}_k$ ,  $\Pi_\mu$ , and  $\Pi_\rho$ . They are defined in terms of the base velocity profiles  $\hat{u}_k$  and  $\hat{v}_k$ :

$$\hat{u}_k(x, r, t) = f_{ki}(r, d) q_i(x, t), \quad (1.49)$$

$$\begin{aligned} \hat{v}_k(x, r, t) &= g_{k1}(r, d) q_1 \partial_x d + g_{k2}(r, d) q_2 \partial_x d \\ &+ g_{k3}(r, d) \partial_x q_1 + g_{k4}(r, d) \partial_x q_2, \end{aligned} \quad (1.50)$$

which satisfy:

$$\frac{1}{r} \partial_r (r \partial_r \hat{u}_k) = Z_k, \quad \partial_r u_1|_d = \Pi_\mu \Pi_u \partial_r u_2|_d, \quad u_1|_d = \Pi_u u_2|_d, \quad u_1|_R = \partial_r u_2|_0 = 0, \quad (1.51a)$$

$$2\pi \int_{d(x,t)}^R r \hat{u}_1 dr = q_1(x, t), \quad 2\pi \int_0^{d(x,t)} r \hat{u}_2 dy = q_2(x, t), \quad (1.51b)$$

$$\hat{v}_k(x, r, t) = \frac{1}{r} \delta_{k1} \int_r^R \tilde{r} \partial_x \hat{u}_1 d\tilde{r} - \frac{1}{r} \delta_{k2} \int_0^r \tilde{r} \partial_x \hat{u}_2 d\tilde{r}, \quad (1.51c)$$

and the weight functions  $w_k$ :

$$w_k(r, d) = f_{k1}(r, d) - \Pi_u^{-1} f_{k2}(r, d), \quad (1.52)$$

which satisfy:

$$\frac{1}{r} \partial_r (r \partial_r w_k) = \underline{Z}_k, \quad w_1|_R = \partial_r w_2|_0 = 0, \quad (1.53)$$

$$w_1|_d = \Pi_u w_2|_d, \quad \partial_r w_1|_d = \Pi_\mu \Pi_u \partial_r w_2|_d, \quad (1.54)$$

$$\Pi_u \int_0^{d(x,t)} r w_2(r) dr = - \int_{d(x,t)}^R r w_1(r) dr = -\frac{1}{2\pi} \quad (1.55)$$

All coefficients involved in (1.48), (1.49), and (1.50) are defined in appendix A.2.

The model is closed with the integral continuity equations:

$$\partial_t d - \frac{1}{2\pi d} \partial_x q_1 = 0, \quad (1.56)$$

$$\partial_t d + \frac{\Pi_u}{2\pi d} \partial_x q_2 = 0, \quad q_2 = \Pi_u^{-1} (q_{\text{tot}} - q_1), \quad (1.57)$$

and the pressure equation:

$$\begin{aligned} 2\Pi_\rho \Pi_u^2 \partial_x [p_2|_d] &= -\tilde{S}_i \partial_t q_i - \tilde{F}_{ij} q_i \partial_x q_j - \tilde{G}_{ij} q_i q_j \partial_x d \\ &+ \frac{\text{We}}{2\pi} \partial_x \kappa + \frac{1}{2\pi} \text{Fr}^{-2} (1 + \Pi_\rho) + \frac{1}{2\pi} \tilde{C}_i q_i \\ &+ \tilde{J}_i q_i \partial_x d^2 + \tilde{K}_i \partial_x q_i \partial_x d + \tilde{L}_i q_i \partial_{xx} d + \tilde{M}_i \partial_{xx} q_i \\ &= -\tilde{S}_i \partial_t q_i + \text{NLP}(x, t), \end{aligned} \quad (1.58)$$

which can be used to apply a condition on the pressure drop  $\Delta p_2$  through (1.34), and which is analogous to (1.33) for the planar model. The coefficients in (1.58) satisfy the same functions as their counterparts in (1.48), which are given in appendix A.2, only that the modified weight functions  $\tilde{w}_k$  are used:

$$\tilde{w}_k(r, d) = f_{k1}(r, d) + \Pi_u^{-1} f_{k2}(r, d). \quad (1.59)$$

To allow representing liquid plugs (see figure 2.19 for an example), where a singularity is reached as  $d \rightarrow 0$ , we augment our momentum equation (1.48) with a source term  $\Pi_\varphi$ :

$$\begin{aligned} S_i \partial_t q_i + F_{ij} q_i \partial_x q_j + G_{ij} q_i q_j \partial_x d &= \frac{\text{We}}{2\pi} \partial_x \kappa + \Pi_\varphi + \frac{1}{2\pi} \text{Fr}^{-2} (1 - \Pi_\rho) + \frac{1}{2\pi} C_i q_i \\ &+ J_i q_i \partial_x d^2 + K_i \partial_x q_i \partial_x d + L_i q_i \partial_{xx} d + M_i \partial_{xx} q_i, \end{aligned} \quad (1.60a)$$

which was introduced in Dietze *et al.* (2020):

$$\Pi_\varphi = -\frac{\text{We}}{2\pi}\Pi_{\text{CRL}} \exp\left[\lambda\left(1 - \frac{d(x,t)}{d_{\text{plug}}}\right)\right] \partial_x \kappa_\varphi, \quad (1.60b)$$

with  $\kappa_\varphi = \frac{1}{d} \left[1 - \frac{1}{2}(\partial_x d)^2\right]$ .

Here,  $\Pi_{\text{CRL}}$  sets the magnitude of  $\Pi_\varphi$ ,  $\lambda$  is a slope coefficient ( $\lambda=1$  in our computations), and  $d_{\text{plug}}$  designates the core radius of a *pseudo-plug*. By pseudo-plug, we mean a liquid annulus that fills the entire tube cross section except for an extremely thin filament of core fluid with  $d=d_{\text{plug}} \ll 1$  ( $d_{\text{plug}}=0.01$  in our computations). This way, liquid plugs can be represented without violating the requirement of a finite core radius  $d(x)$ .

Conceptually, the source term  $\Pi_\varphi$  is comparable to the disjoining pressure used for imposing a stable precursor film in lubrication models for contact line problems (Thiele *et al.*, 2001). At  $d=d_{\text{plug}}$  and  $\Pi_{\text{CRL}}=1$ ,  $\Pi_\varphi$  (1.60b) exactly cancels the azimuthal capillary term  $\frac{\text{We}}{2\pi}\partial_x \kappa_\varphi$  in (1.60a), which is responsible for the Plateau-Rayleigh instability, thus rendering the cylindrical surface of the pseudo-plug stable. For  $d \gtrsim d_{\text{plug}}$ ,  $|\Pi_\varphi| \lesssim \left|\frac{\text{We}}{2\pi}\partial_x \kappa_\varphi\right|$  and the Plateau-Rayleigh mechanism is dominant, whereas the opposite holds for  $d \lesssim d_{\text{plug}}$ . As a result, the film surface is attracted toward  $d=d_{\text{plug}}$  from both sides.

Because  $\Pi_\varphi$  varies very sharply around  $d_{\text{plug}}$ , this effect is felt only when  $d$  is close to  $d_{\text{plug}}$ , and it translates into a very strong repulsion of the film surface away from the tube axis as  $d \rightarrow 0$ . Moreover, the cylindrical surface  $d=d_{\text{plug}}$  can be rendered entirely stable even in the presence of a mean flow, via an appropriate choice of  $\Pi_{\text{CRL}} \geq 1$  (see discussion of panel 2.3d in section 2.1.2).

A discussion of how pseudo-plugs are constructed numerically is provided in section 2.2.3. And, we will show in section 2.3.2 that our augmented model (1.60) yields quite accurate predictions of real liquid plugs.

**Relation to the state of the art and impact of our work** At the time of its publication (Dietze & Ruyer-Quil, 2015), our cylindrical WRIBL model for core-annular flow, given by (1.56), (1.57), (1.48), and (1.58), extended the state of the art on modelling annular liquid films in narrow cylindrical geometries in several ways.

As far as the WRIBL method is concerned, our model extended the single-phase model of Ruyer-Quil *et al.* (2008) (see also Novbari & Oron (2009)) by accounting for an active core fluid<sup>6</sup>. Further, it extended the two-phase WRIBL model of Mehidi & Amatoousse (2009) beyond the limiting case of a zero core-fluid pressure gradient  $\partial_x p_2|_d=0$ , via an appropriate choice of weight functions (1.52). This allows to study pressure-driven core-annular flows and annular falling liquid films subject to a quiescent, co-, or counter-current core gas.

---

<sup>6</sup>The model of Ruyer-Quil *et al.* (2008) was written for a falling liquid film on the outside of a cylindrical fibre, but it can be transposed to the configuration in figure 1.3 by making the fibre radius negative.

By employing the WRIBL method, and developing our model up to order  $\epsilon^2$ , we were able to improve upon other modelling approaches that had been applied to annular liquid films. For example, thin-film models (Hammond, 1983; Lister *et al.*, 2006b) cannot represent the occlusion of the tube, lubrication models (Gauglitz & Radke, 1988; Camassa *et al.*, 2014) cannot account for the inertia-driven Kapitza instability, first-order IBL models (Johnson *et al.*, 1991; Trifonov, 1992; Zhou *et al.*, 2016; Liu & Ding, 2017; Ding *et al.*, 2019) cannot account for axial viscous diffusion, and quasi-static approaches (Jensen, 2000) constrain the shape of interfacial deformations.

In terms of representing the core fluid, our fully-coupled model complements the models of Halpern & Grotberg (2003) and Camassa *et al.* (2017), which are based on a relaxed form of the inter-phase coupling conditions in the limit of high-frequency core flow oscillations or large velocity contrasts between the two fluids. For example, the model of Camassa *et al.* (2017) was designed for turbulent gas core flows in contact with a laminar annular liquid film<sup>7</sup>. By contrast, our model covers the range of moderate velocity contrasts (strongly-confined laminar-laminar two-phase flows) and slow core flow oscillations (e.g. due to breathing in the pulmonary airways), where the models of Halpern & Grotberg (2003) and Camassa *et al.* (2017) are not applicable.

Our representation of liquid plugs through the source term (1.60b) in (1.60), which was introduced in Dietze *et al.* (2020), allows to continue computations past occlusion events. This has enabled us to perform fully developed computations of falling liquid films in narrow tubes beyond the occlusion limit, as opposed to other studies (Zhou *et al.*, 2016), where computations broke down at the first occlusion event. For example, we have successfully reproduced the occlusion experiment of Camassa *et al.* (2014) (see computation in figure 2.20 of section 2.3.2). In the future, we plan to use our augmented model to study the dynamics of gravity-driven liquid plugs (currently ongoing), in complement to the works of Suresh & Grotberg (2005) on plugs in planar channels, and Ubal *et al.* (2008) on pressure-driven plugs in tubes.

Wang (2016) studied core annular liquid-liquid systems with zero base flow via a two-phase lubrication model. He was able to continue computations quite far toward the formation of liquid plugs, without any special mathematical treatment. In his case, the core fluid was very viscous and thus the drainage of liquid from the thin cylindrical thread forming at the center of the tube was slow. This strongly delays the actual pinch-off of the core fluid, allowing a cascade of satellite droplets to form, as a result of the Plateau-Rayleigh instability.

We have not considered in this work pressure-driven core-annular flows, for which there is a vast body of literature (Aul & Olbricht, 1990; Chen & Joseph, 1991; Kerchman, 1995; Joseph *et al.*, 1997; Govindarajan & Sahu, 2014). Our model is capable of capturing long-wave instabilities in these flows (see figures 2.4 and 2.15d). This is another interesting prospect for future work, but care must be taken to avoid regimes where short wave instability modes are relevant.

---

<sup>7</sup>We will use the gas-side formalism introduced by Camassa *et al.* (2017) to develop a weakly-coupled WRIBL model for planar falling liquid films sheared by a turbulent gas in section 1.4.

Since their publication, our papers Dietze & Ruyer-Quil (2015), which introduced our cylindrical two-phase WRIBL model, and Dietze *et al.* (2020), which introduced our representation of liquid plugs (1.60), have been cited 25 and 5 times, respectively, according to *Web of Science*. Here, we focus only on citations that have referred to the methodological aspects of our papers, whereas sections 7.1 and 7.2 will discuss the impact of the physics we have uncovered. Several works have acknowledged our papers as seminal contributions to the modelling of annular liquid films and core-annular flows:

Wang (2016); Zhou *et al.* (2016); Lavallo *et al.* (2017); Liu & Ding (2017); Camassa *et al.* (2017); Wang & Papageorgiou (2018); Pillai & Narayanan (2018a); Sirwah & Zakaria (2019); Liu & Ding (2020); Camassa *et al.* (2021); Ogrosky (2021b,a); Rohlfis *et al.* (2021).

Some of these papers have noted the usefulness of our WRIBL model for predicting the occlusion limit of annular liquid films in narrow cylindrical tubes (Camassa *et al.*, 2021; Ogrosky, 2021b; Romano *et al.*, 2021; Ogrosky, 2021a). For example, we found in Dietze *et al.* (2020) that accounting for axial viscous diffusion within the liquid film is essential to accurately predict the occlusion limit in the case of highly-viscous fluids, such as Newtonian model liquids for mucus.

This was acknowledged by Ogrosky (2021a) as a motivation for developing his three-layer asymptotic model up to order  $\mathcal{O}(\epsilon^2)$ . That model consists of two coaxial annular liquid films lining the inner surface of a cylindrical tube, in contact with a gaseous core. Such a configuration is well suited for representing the serous-mucus bilayer coating the pulmonary airways (Grotberg, 1994, 2011).



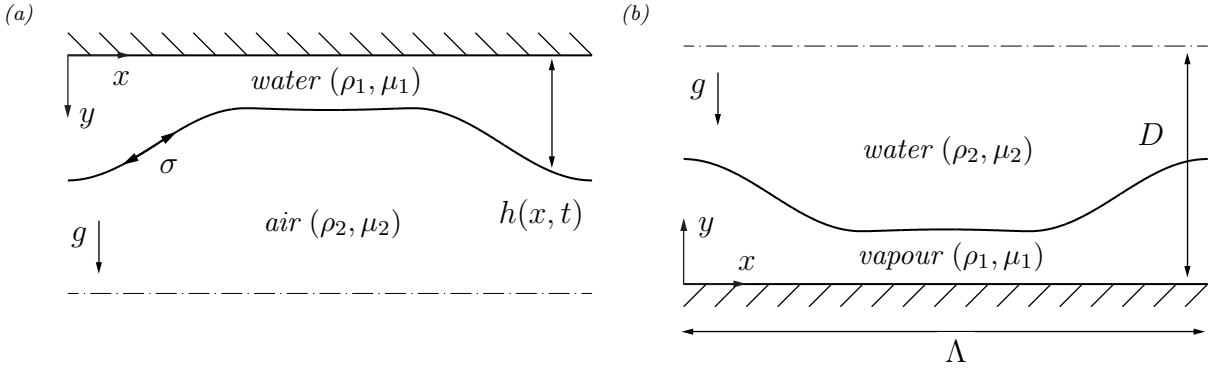


Figure 1.4: Fluid film (subscript 1) on a planar wall in contact with an active outer fluid (subscript 2) and subject to the Rayleigh-Taylor. If the wall-adjacent fluid is heated, the Marangoni instability also intervenes. (a) Water film suspended from a horizontal ceiling in contact with air; (b) gas film underneath a liquid layer (e.g. vapour underneath a Leidenfrost drop). At the boundary marked by the dot-dashed line, a slip boundary mimics an unconfined outer phase. All fluids are Newtonian.

### 1.3 Films subject to the Rayleigh-Taylor and Marangoni instabilities

We consider the planar configurations in figure 1.4, i.e. a liquid film suspended from a horizontal ceiling in contact with a gas (panel 1.4a), or a gas film trapped between a liquid and a wall (panel 1.4b). These configurations will be studied in section 8.1. In both cases, gravity acts from the liquid toward the gas and there is no mean base flow. Thus, the film is subject to the Rayleigh-Taylor instability in the presence of surface tension (Yiantsios & Higgins, 1989). If the wall-adjacent fluid is additionally heated, which we will consider only later in this section, the Marangoni instability also intervenes (Boos & Thess, 1999; Alexeev & Oron, 2007).

In contrast to the film flows in panel 1.2a, we impose a slip condition at the outer boundary  $y=D$ :

$$\partial_y u_2 = v_2 = 0. \quad (1.61)$$

The thickness of the outer phase is assumed sufficiently large to exclude confinement effects,  $D \gg h$ , but sufficiently small to satisfy the long-wave approximation,  $D \ll \Lambda$ .

Applying the two-phase WRIBL approach to the current problem, involves only two modifications w.r.t. section 1.1, which both result from the new boundary condition (1.61). Firstly, the base velocity profile now satisfies:

$$\begin{aligned} \partial_{yy} \hat{u}_k = Z_k, \quad \partial_y \hat{u}_1|_h = \Pi_\mu \Pi_u \partial_y \hat{u}_2|_h, \quad \hat{u}_1|_h = \Pi_u \hat{u}_2|_h, \quad \hat{u}_1|_0 = \partial_y \hat{u}_2|_D = 0, \\ \int_0^{h(x,t)} \hat{u}_1 dy = q_1(x,t), \quad \int_{h(x,t)}^D \hat{u}_2 dy = q_2(x,t), \end{aligned} \quad (1.62)$$

and, secondly, the weight functions now satisfy:

$$\begin{aligned} \partial_{yy} w_k &= \underline{Z}_k, & w_1|_0 &= \partial_y w_2|_D = 0, \\ w_1|_h &= \Pi_u w_2|_h, & \partial_y w_1|_h &= \Pi_\mu \Pi_u \partial_y w_2|_h. \end{aligned} \quad (1.63)$$

The final model equations have the same form as (1.27) and (1.28) in the limit  $\phi=0$ , only that the model coefficients, defined in appendix A.1, are now evaluated using  $\hat{u}_k$  and  $w_k$  according to (1.62) and (1.63):

$$\begin{aligned} S_i \partial_t q_i + F_{ij} q_i \partial_x q_j + G_{ij} q_i q_j \partial_x h &= \text{We} \partial_{xxx} h + \frac{1}{\text{Fr}^2} (1 - \Pi_\rho) + C_i q_i, \\ &+ J_i q_i \partial_x h^2 + K_i \partial_x q_i \partial_x h + L_i q_i \partial_{xx} h + M_i \partial_{xx} q_i, \end{aligned} \quad (1.64)$$

$$\partial_t h + \partial_x q_1 = 0, \quad -\partial_t h + \Pi_u \partial_x q_2 = 0. \quad (1.65)$$

Equation (1.26) remains a suitable choice for  $w_k$ , where the coefficients  $f_{ki}$ , which are defined through (1.17), are to be based on  $\hat{u}_k$  according to (1.62). The pressure equation is given by (1.33), where coefficients are to be evaluated with  $\tilde{w}_k$  according to (1.31), once again using coefficients  $f_{ki}$  based on  $\hat{u}_k$  according to (1.62).

We introduce scales that are more appropriate for the Rayleigh-Taylor problem:

$$\mathcal{L} = \bar{h}^*, \quad \mathcal{U}_1 = \mathcal{U}_2 = \mathcal{U} = \frac{\Delta \rho g \mathcal{L}^2}{\mu_1}, \quad \mathcal{T} = \mathcal{L}/\mathcal{U}, \quad (1.66)$$

where the overbar denotes a spatial average and  $\Delta \rho = \rho_1 - \rho_2$  is the density difference. As a result, the dimensionless groups appearing in (1.64) are recast as:

$$\text{Re}_1^{-1} = \text{Re}_2^{-1} \frac{\Pi_\rho}{\Pi_\mu} = \frac{1}{\text{Ar}}, \quad \text{Fr}^{-2} = \frac{1}{\text{At Ar}}, \quad \text{We} = \frac{1}{\text{Bo Ar}}, \quad (1.67)$$

where  $\text{At} = \Delta \rho / \rho = 1 - \Pi_\rho$  denotes the Atwood number,  $\text{Bo} = \Delta \rho g \mathcal{L}^2 / \sigma$  the Bond number, and  $\text{Ar} = \Delta \rho \rho_1 \mathcal{L}^3 g / \mu_1^2$  the Archimedes number. Thus, the governing groups are now  $\text{Ar}$ ,  $\text{Bo}$ ,  $\Pi_\rho$ , and  $\Pi_\mu$ .

In section 8.1, we will consider the current model in the lubrication limit, where  $S_i = F_{ij} = G_{ij} = J_i = K_i = L_i = M_i = 0$ , and we will assume a passive outer phase, i.e.  $\Pi_\mu = \Pi_\rho = 0$  and  $\text{At} = 1$ . In that case, the model reduces to:

$$\partial_t h = -\partial_x q_1, \quad (1.68a)$$

$$q_1 = \frac{1}{3} \left[ h^3 \partial_x h + \frac{1}{\text{Bo}} h^3 \partial_{xxx} h \right]. \quad (1.68b)$$

We have also investigated the additional effect of the Marangoni instability (Boos & Thess, 1999; Alexeev & Oron, 2007), produced by heating the wall-adjacent fluid layer from the wall. In that case, (1.68b) is augmented as:

$$q_1 = \frac{1}{3} \left[ h^3 \partial_x h + \frac{1}{\text{Bo}} h^3 \partial_{xxx} h \right] + \frac{1}{2} \frac{\text{Ma}}{\text{Bo}} h^2 \partial_x \theta|_h, \quad (1.69)$$

where  $\text{Ma} = \partial_T \sigma (T_w - T_\infty) / \sigma$  designates a modified Marangoni number, which is negative in our case, and  $\theta|_h$  denotes the dimensionless film surface temperature:

$$\theta|_h = \frac{T|_h - T_w}{T_w - T_\infty} = -\frac{\text{Bi } h}{1 + \text{Bi } h}. \quad (1.70)$$

Here,  $\text{Bi} = \mathcal{H} h_0 / k_1$  denotes the Biot number, and  $T_w$  and  $T_\infty$  denote the wall and ambient temperatures. The Biot number contains the inter-phase heat transfer coefficient  $\mathcal{H}$  and the thermal conductivity  $k_1$ .

**Relation to the state of the art and impact of our work** Our model was introduced in Dietze *et al.* (2018) to elucidate the sliding instability of thin fluid films subject to the Rayleigh-Taylor instability (section 8.1). In contrast to prior modelling works dedicated to the same configuration (Lister *et al.*, 2006b; Glasner, 2007; Alexeev & Oron, 2007), it accounts for the effect of inertia, which produces oscillations during the early evolution of a liquid film suspended from a ceiling (see panel 8.2b in section 8.1). However, our analysis of the sliding instability was mainly focused on the long-time evolution, where the lubrication approximation is valid and where our model collapses with that of Lister *et al.* (2006b) (1.68b) or, in the case of Rayleigh-Taylor-Marangoni instability, with that of Alexeev & Oron (2007) (1.69), at least in the passive-gas limit ( $\Pi_\rho = \Pi_\mu = 0$ ).

Our work Dietze *et al.* (2018) has been cited 3 times. Pillai & Narayanan (2018a) applied our approach to model a confined liquid-gas bilayer subject to the Rayleigh-Taylor instability and additional evaporation, and Pillai & Narayanan (2020) to the problem of a bilayer of dielectric fluids subject to electrostatic forcing. Most-recently, Dinesh *et al.* (2022) have extended the approach to account for a corrugated bounding wall.

## 1.4 Falling liquid films sheared by a turbulent gas

Many industrial applications involve a laminar falling liquid film sheared by a counter-current gas flow within a plane channel of intermediate confinement, i.e.  $H^* \geq 5$  mm (Vlachos *et al.*, 2001; Valluri *et al.*, 2005). Although the long-wave approximation  $\epsilon \ll 1$  may still apply to such flows, the large  $\text{Re}_2$  values associated with these regimes increase the importance of second-order inertial corrections  $\epsilon \text{Re}_2 \hat{u}_2 \partial_x u_2^{(1)}$ , which we have neglected in our two-layer WRIBL approach introduced in section 1.1. Nonetheless, in the case of turbulent flows, Reynolds stresses may become the dominant inertial terms in the Reynolds-averaged Navier-Stokes (RANS) equations. Invoking the Boussinesq hypothesis, these can be expressed via diffusional terms of the form:

$$\text{Re}_2^{-1} \partial_y \left( \frac{\mu_t}{\mu_2} \partial_y \bar{u}_2 \right), \quad (1.71)$$

where  $\mu_t$  is the turbulent viscosity and the overbar indicates averaging over a time span that is large versus the turbulent time scale but small versus the wave period (Reynolds averaging).

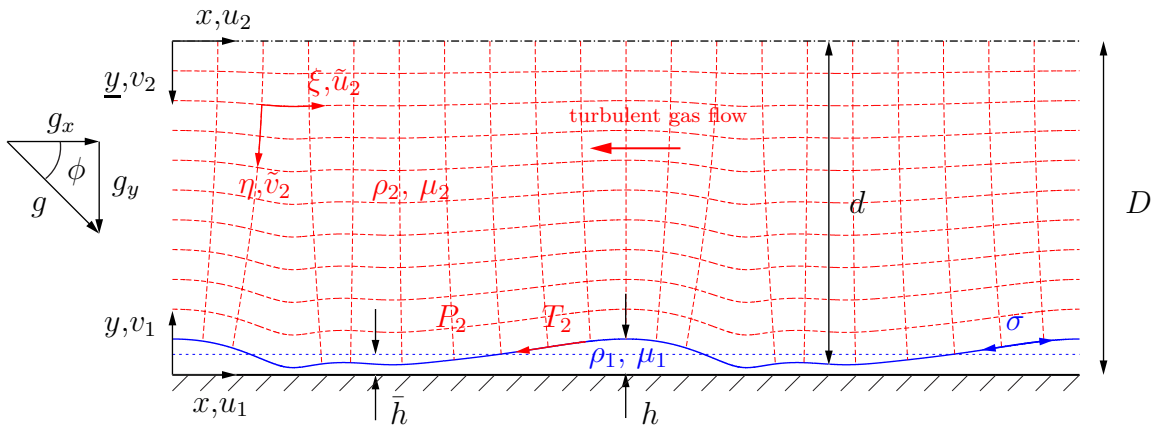


Figure 1.5: Falling liquid film (index 1) on an inclined wall subject to a counter-current turbulent gas flow (index 2). The flow is confined by an upper wall at  $y=H=H^*/\mathcal{L}_1$  (not shown) and a symmetry condition is imposed at the centreline of the average gas layer, i.e.  $y=0$  or  $y=D^*/\mathcal{L}_1=\Pi_L D$ , where  $\Pi_L=\mathcal{L}_2/\mathcal{L}_1$  accounts for the different scaling in the liquid (1.1) and gas (1.78). Gas-liquid coupling is expressed through the tangential gas shear stress  $T_2$  and the gas pressure  $P_2$  at the film surface  $y=h$ . Red dashed lines illustrate the orthogonal curvilinear coordinate system  $(\eta, \xi)$  for the gas flow, where  $\eta=y\bar{d}/d$ .

Such diffusional terms can be dealt with readily in the WRIBL framework, through an appropriate choice of the weight function  $w_2$  in the integral momentum equation (1.12). This is an enticing prospect for future work. Here, we introduce a simpler modelling approach, which we have implemented in the context of the PhD. thesis of Misa Ishimura and which is the focus of ongoing work. We briefly outline this approach next and preliminary results will be discussed in chapter 9.

We consider the flow in figure 1.5. A laminar falling liquid film (index 1) flows along an inclined plane under the action of gravity and interacts with a counter-current turbulent gas flow (index 2). At  $y=H=H^*/\mathcal{L}_1$ , the flow is confined by a second wall (not shown), and we impose a symmetry condition at the centreline of the average gas layer. i.e. at  $y=0$  or  $y=D^*/\mathcal{L}_1=\Pi_L D$ , where  $\Pi_L=\mathcal{L}_2/\mathcal{L}_1$  accounts for the different scalings used in the liquid (1.1) and gas (1.78). In the case of a symmetrical vertical configuration with liquid films lining both walls (Vlachos *et al.*, 2001), the symmetry condition is satisfied analytically and we have  $D=H/\Pi_L/2$ . In the case of an inclined configuration with a dry upper wall, the symmetry condition in the gas remains a good approximation in the limit  $H \gg \bar{h}$  (Tseluiko & Kalliadasis, 2011), which is the one we are interested in here. In that case,  $D=(H+\bar{h})/\Pi_L/2$ .

Following several previous works (Halpern & Grotberg, 2003; Tseluiko & Kalliadasis, 2011; Samanta, 2014; Camassa *et al.*, 2017), we apply a weakly-coupled treatment of the two phases by relaxing the full kinematic inter-phase coupling conditions (4.1c).

The liquid film is modelled via the WRIBL method introduced in section 1.1, where the effect of the gas enters via the gaseous tangential shear stress  $T_2$  and gas pressure  $P_2$

at the film surface  $y=h^8$  (figure 1.5). The coupling quantities  $T_2$  and  $P_2$ , which constitute approximations of the RHS of equations (1.6a) and (1.6b), are obtained from the gas-side model (1.98), which will be introduced later in this section<sup>9</sup>. These quantities are scaled with the gas-side scales  $\mathcal{L}_2$  and  $\mathcal{U}_2$  defined in (1.79):

$$T_2 = T_2^* \frac{\mathcal{L}_2}{\mu_2 \mathcal{U}_2}, \quad P_2 = p_2|_{\underline{y}=d} = P_2^* \frac{\mathcal{L}_2}{\mu_2 \mathcal{U}_2} \underline{\epsilon}, \quad (1.72)$$

where  $\underline{\epsilon}=\mathcal{L}_2/\Lambda^*$  is the long-wave parameter for the gas layer. In this one-sided WRIBL formulation, the weighted integral momentum equation (1.12) reduces to:

$$\text{ME} : \quad \int_0^{h(x,t)} w_1(y) \text{BLE}_1 \, dy, \quad (1.73)$$

where the base velocity profile  $\hat{u}_1$  now satisfies:

$$\begin{aligned} \partial_{yy}\hat{u}_1 = Z_1, \quad \partial_y\hat{u}_1|_h = \frac{\Pi_\mu\Pi_u}{\Pi_L}T_2, \quad \hat{u}_1|_0 = 0, \\ \int_0^{h(x,t)} \hat{u}_1 \, dy = q_1(x, t), \end{aligned} \quad (1.74)$$

introducing the length scale ratio  $\Pi_L=\mathcal{L}_2/\mathcal{L}_1$ . Further, the weight function  $w_1$  now satisfies:

$$\partial_{yy}w_1 = \underline{Z}_1, \quad w_1|_0 = 0, \quad \partial_yw_1|_h = 0, \quad (1.75)$$

where  $\underline{Z}_1$  is an arbitrary constant. This yields the following integral momentum equation for the liquid film:

$$\begin{aligned} \partial_t q_1 + \frac{17}{7} \frac{q_1}{h} \partial_x q_1 - \frac{9}{7} \frac{q_1^2}{h^2} \partial_x h = \frac{5}{6} \text{We} h \partial_{xxx} h + \frac{5}{6} \text{Fr}^{-2} h \{ \sin(\phi) - \cos(\phi) \partial_x h \} \\ + \text{Re}_1^{-1} \left\{ -\frac{5}{2} \frac{q_1}{h^2} + 4 \frac{q_1}{h^2} \partial_x h^2 - \frac{9}{2h} \partial_x q_1 \partial_x h - 6 \frac{q_1}{h} \partial_{xx} h + \frac{9}{2} \partial_{xx} q_1 \right\} \\ + \frac{\Pi_\mu \Pi_u}{\Pi_L} T_2 \left\{ \text{Re}_1^{-1} \left[ \frac{5}{4} + \frac{h}{6} \partial_{xx} h + \frac{1}{2} \partial_x h^2 \right] - \frac{5}{112} q_1 \partial_x h - \frac{19}{336} \partial_x q_1 h \right\} \\ - \frac{19}{672} \frac{\Pi_\mu^2 \Pi_u^2}{\Pi_L^2} h^2 \partial_x h T_2^2 - \frac{5}{6} \text{Re}_2^{-1} \frac{\Pi_\rho \Pi_u^2}{\Pi_L} h \partial_x P_2 \\ + \frac{\Pi_\mu \Pi_u}{\Pi_L} \left\{ \partial_x T_2 \left[ \text{Re}_1^{-1} \frac{3}{4} h \partial_x h - \frac{15}{224} h q_1 \right] - \frac{25}{1344} \frac{\Pi_\mu \Pi_u}{\Pi_L} h^3 T_2 \partial_x T_2 - \frac{h^2}{48} \partial_t T_2 \right\}, \end{aligned} \quad (1.76)$$

to which is added the integral continuity equation (1.28a). Following Tseluiko & Kalliadasis (2011), we will neglect the terms involving  $\partial_x T_2$  and  $\partial_t T_2$ ,

<sup>8</sup>Normal gaseous viscous stresses are neglected.

<sup>9</sup>The gas-side model is based on a mixing-length approach to describe the turbulent viscosity  $\mu_t$  in (1.71).

but we will account for the space and time dependence of  $T_2$  and  $\partial_x P_2$  in the remaining terms, via the gas model (1.98). This amounts to a quasi-steady approximation. In the limit  $T_2 = \partial_x P_2 = 0$ , (1.76) reduces to equation (41) in Ruyer-Quil & Manneville (2000). In the limit  $\partial_x T_2 = \partial_t T_2 = \partial_x P_2 = 0$ , it collapses with equation (3.9) of Samanta (2014)<sup>10</sup>.

The turbulent gas flow is governed by the continuity and Navier-Stokes equations (4.1), written in the gas coordinates  $x$  and  $\underline{y}$  (figure 1.5), then Reynolds-averaged, and truncated at order  $\underline{\epsilon}$ :

$$\partial_x u_2 + \partial_{\underline{y}} v_2 = 0, \quad (1.77a)$$

$$\underline{\epsilon} u_2 \partial_x u_2 + \underline{\epsilon} v_2 \partial_{\underline{y}} u_2 = -\frac{1}{\text{Re}_2} \partial_x p_2 + \frac{1}{\text{Re}_2} \left\{ \partial_{\underline{y}\underline{y}} u_2 + \partial_{\underline{y}} \left[ \frac{\mu_t}{\mu_2} \partial_{\underline{y}} u_2 \right] \right\} + \frac{1}{\text{Fr}_2^2} \sin(\phi), \quad (1.77b)$$

$$0 = -\frac{1}{\text{Re}_2} \partial_{\underline{y}} p_2 + \underline{\epsilon} \frac{1}{\text{Fr}_2^2} \cos(\phi), \quad (1.77c)$$

where we have omitted the overbar designating Reynolds-averaged quantities,  $\mu_t$  is the (dimensional) turbulent viscosity,  $\text{Fr}_2 = \mathcal{U}_2 / \sqrt{g \mathcal{L}_2}$ ,  $\text{Re}_2 = \mathcal{U}_2 \mathcal{L}_2 / \nu_2$ , and where we have used the following scaling:

$$u_2 = \frac{u_2^*}{\mathcal{U}_2}, \quad v_2 = \frac{v_2^*}{\underline{\epsilon} \mathcal{U}_2}, \quad x = \underline{\epsilon} \frac{x^*}{\mathcal{L}_2}, \quad \underline{y} = \frac{y^*}{\mathcal{L}_2}, \quad p_2 = p_2^* \frac{\underline{\epsilon} \mathcal{L}_2}{\mu_2 \mathcal{U}_2}, \quad (1.78)$$

based on the gas-side reference scales:

$$\mathcal{L}_2 = H^*, \quad \mathcal{U}_2 = \frac{q_2^*}{\mathcal{L}_2} = \frac{q_2^*}{H^*}. \quad (1.79)$$

We have chosen to scale pressure using a measure for the viscous shear stress, in contrast to (1.1), where the dynamic pressure was used. This choice is more appropriate in a weakly-confined setting.

Time derivatives in (1.77b) have been neglected under the assumption  $\Pi_u = \mathcal{U}_2 / \mathcal{U}_1 \gg 1$ , which yields:

$$\mathcal{O} \left\{ \frac{\partial_t^* u_2^*}{u_2^* \partial_x^* u_2^*} \right\} = \frac{1}{\Pi_u} \ll 1, \quad (1.80)$$

assuming that the time scale is dictated by the waviness of the liquid film  $\mathcal{T}_1 = \Lambda^* / \mathcal{U}_1$ . This amounts to a quasi-steady representation of the film surface.

The turbulent viscosity  $\mu_t$  is formulated with Prandtl's mixing-length approach (Prandtl, 1925):

$$\frac{\mu_t}{\mu_2} = \text{Re}_2 l_t^2 \left| \partial_{\underline{y}} u_2 \right|, \quad (1.81)$$

where  $l_t = l_t^* / \mathcal{L}_2$  denotes the dimensionless mixing length. Finally,  $\Pi_u \gg 1$  also implies that the film surface can be approximated as a wavy wall with adherence and no-penetration conditions at  $\underline{y} = d$  (Tseluiko & Kalliadasis, 2011):

$$u_2 = v_2 = 0. \quad (1.82a)$$

---

<sup>10</sup>There is a typo in the  $T_2 \partial_x h^2$  term in equation (3.9) of Samanta (2014).

In addition, we impose symmetry at  $\underline{y}=0$ :

$$\partial_{\underline{y}}u_2 = v_2 = 0. \quad (1.82b)$$

We now introduce the curvilinear coordinates  $\eta$  and  $\xi$ :

$$\eta = \underline{y} \frac{\bar{d}}{d}, \quad \xi = x + \underline{\epsilon} F(\xi, \eta), \quad (1.83)$$

where orthogonality implies:

$$\partial_{\eta}F = \underline{\epsilon} \frac{d}{\bar{d}^2} \partial_{\xi}d \frac{1}{\underline{\epsilon} \partial_{\xi}F - 1}. \quad (1.84)$$

Red dashed lines in figure 1.5 constitute curves of constant  $\eta$  and  $\xi$ , where<sup>11</sup>:

$$\partial_x \underline{y} \Big|_{\eta} = - \partial_{\underline{y}} x \Big|_{\xi} = \frac{\bar{d}}{d} \partial_x d. \quad (1.85)$$

Following Camassa *et al.* (2017), we recast the governing equations (1.77) in terms of these coordinates, while maintaining the same truncation limit  $\underline{\epsilon}$ , and we eliminate the pressure variable  $p_2$  via an appropriate integration of (1.77c):

$$\frac{\partial_{\xi}d}{d} \partial_{\xi} \tilde{u}_2 + \partial_{\xi} \tilde{u} + \frac{\bar{d}}{d} \partial_{\eta} \tilde{v}_2 = 0, \quad (1.86a)$$

$$\begin{aligned} \underline{\epsilon} \tilde{u}_2 \partial_{\xi} \tilde{u}_2 + \underline{\epsilon} \frac{\bar{d}}{d} \tilde{v}_2 \partial_{\eta} \tilde{u}_2 = & - \frac{1}{\text{Re}_2} \partial_{\xi} P_2 + \frac{1}{\text{Fr}_2^2} (\sin(\phi) + \underline{\epsilon} \cos(\phi) \partial_{\xi} d) \\ & + \frac{1}{\text{Re}_2} \frac{\bar{d}^2}{d^2} \left\{ \partial_{\eta\eta} \tilde{u}_2 + \partial_{\eta} \left[ \frac{\tilde{\mu}_t}{\mu_2} \partial_{\eta} \tilde{u}_2 \right] \right\}, \end{aligned} \quad (1.86b)$$

where we have invoked the projection rules:

$$u_2 = \tilde{u}_2 + \mathcal{O}(\underline{\epsilon}^2), \quad v_2 = \tilde{v}_2 + \frac{\partial_{\xi}d}{d} \eta \tilde{u}_2 + \mathcal{O}(\underline{\epsilon}), \quad (1.87)$$

$$\partial_x = \partial_{\bar{x}} - \eta \frac{\partial_{\xi}d}{d} \partial_{\eta} + \mathcal{O}(\underline{\epsilon}), \quad \partial_{\underline{y}} = \frac{\bar{d}}{d} \partial_{\eta} + \mathcal{O}(\underline{\epsilon}^2), \quad (1.88)$$

and where  $\tilde{\mu}_t$  satisfies:

$$\frac{\tilde{\mu}_t}{\mu_2} = \frac{d}{\bar{d}} \text{Re}_2 \tilde{l}_t^2 |\partial_{\eta} \tilde{u}|, \quad (1.89)$$

with  $\tilde{l}_t = l_t \bar{d} / d$ . In this curvilinear formulation, the spatial variation of the mixing length  $\tilde{l}_t$  is expressed in terms of  $\eta$ , i.e. normal to the film surface, and thus correlations developed

---

<sup>11</sup>From equations (1.85) and (1.83), we obtain:  $F(\xi = \text{const}) = \xi - x = \frac{\bar{d}}{2d} \partial_x d$ .

for parallel flows can be used. Here, we employ the van Driest equation (Van Driest, 1956):

$$\tilde{l}_t = \kappa (\bar{d} - \eta) \left\{ 1 - \exp \left[ \sqrt{\left| \partial_\eta \tilde{u}_2^{(0)} \right|_{\bar{d}} \text{Re}_2 \frac{\eta - \bar{d}}{A}} \right] \right\}, \quad (1.90)$$

where  $A=26$ , and  $\kappa=0.41$  denotes the von Karman constant. The square root in the exponential argument results from rescaling the traditional formulation, which is based on the friction velocity  $\mathcal{U}^+$ :

$$\mathcal{L}^+ = \frac{\mu_2}{\rho_2 \mathcal{U}^+}, \quad \mathcal{U}^+ = \left\{ \frac{\mu_2}{\rho_2} \left| \partial_\eta \tilde{u}_2^{(0)} \right|_{\bar{d}} \right\}^{\frac{1}{2}}, \quad (1.91)$$

in terms of our scales (1.78), introducing the zeroth-order velocity  $\tilde{u}_2^{(0)}$  according to (1.93a). Finally, the boundary conditions (1.82) become:

$$\tilde{u}_2|_{\eta=\bar{d}} = \tilde{v}_2|_{\eta=\bar{d}} = 0, \quad \partial_\eta \tilde{u}_2|_{\eta=0} = \tilde{v}_2|_{\eta=0} = 0. \quad (1.92)$$

Following Camassa *et al.* (2017), we solve the BVP given by (1.86) and (1.92) order by order based on the following asymptotic expansions in  $\underline{\epsilon}$ :

$$\tilde{u}_2 = \tilde{u}_2^{(0)} + \underline{\epsilon} \tilde{u}_2^{(1)} + \mathcal{O}(\underline{\epsilon}^2), \quad (1.93a)$$

$$\tilde{v}_2 = \tilde{v}_2^{(0)} + \underline{\epsilon} \tilde{v}_2^{(1)} + \mathcal{O}(\underline{\epsilon}^2), \quad (1.93b)$$

$$P_2 = P_2^{(0)} + \underline{\epsilon} P_2^{(1)} + \mathcal{O}(\underline{\epsilon}^2). \quad (1.93c)$$

The zeroth-order problem is obtained by inserting (1.93a) into (1.86) and (1.92) and then truncating at  $\underline{\epsilon}^0$ . We anticipate a solution in the form of the product ansatz:

$$\tilde{u}_2^{(0)} = g_0(\xi) U_0(\eta) = \frac{\bar{d}}{d} U_0(\eta), \quad (1.94)$$

which leads to the variable-separated zeroth-order momentum equation:

$$\frac{d^3}{d\bar{d}^3} \left\{ \frac{1}{\text{Re}_2} \partial_\xi P_2^{(0)} - \frac{1}{\text{Fr}_2^2} \sin(\phi) \right\} = \frac{1}{\text{Re}_2} \partial_{\eta\eta} U_0 + \partial_\eta \left\{ \tilde{l}_t^2 \mathbf{sgn}(\partial_\eta U_0) (\partial_\eta U_0)^2 \right\} = C_0, \quad (1.95a)$$

subject to the boundary conditions:

$$U_0|_{\eta=\bar{d}} = \partial_\eta U_0|_{\eta=0} = 0, \quad (1.95b)$$

where we have employed the signum function  $\mathbf{sgn}$  to substitute  $|\partial_\eta U_0| = \mathbf{sgn}(\partial_\eta U_0) \partial_\eta U_0$ , and where the separation constant  $C_0$  is subject to the gauge condition:

$$\int_0^{\bar{d}} \tilde{u}_2^{(0)} d\tilde{y} = \int_0^{\bar{d}} U_0 d\eta = \frac{q_2}{2}. \quad (1.95c)$$



At the next order, i.e.  $\underline{\epsilon}^1$ , we obtain:

$$\frac{d^2}{d^2} \left\{ \frac{1}{\text{Re}_2} \partial_\xi P_2^{(1)} \frac{d}{d\xi} - \frac{1}{\text{Fr}_2^2} \cos(\phi) d \right\} = U_0^2 + \frac{1}{\text{Re}_2} \partial_{\eta\eta} U_1 \quad (1.96a)$$

$$+ \partial_\eta \left\{ \tilde{l}_t^2 \text{sgn}(\partial_\eta U_0) \partial_\eta U_0 \partial_\eta U_1 \right\} = C_1,$$

$$U_1|_{\eta=\bar{d}} = \partial_\eta U_1|_{\eta=0} = 0, \quad (1.96b)$$

$$\int_0^{\bar{d}} \tilde{u}_2^{(1)} d\tilde{y} = \int_0^{\bar{d}} U_1 d\eta = 0, \quad (1.96c)$$

where we have employed the product ansatz:

$$\tilde{u}_2^{(1)} = g_1(\xi) U_1(\eta) = \frac{\partial_\xi d}{d} U_1(\eta). \quad (1.97)$$

The augmented BVPs (1.95) and (1.96) are solved numerically for  $U_0$ ,  $U_1$ ,  $\partial_\xi P_2^{(0)}$ ,  $\partial_\xi P_2^{(1)}$ ,  $C_0$ , and  $C_1$  via the continuation software `Auto07P` (see section 2.2.4). Importantly, this numerical solution needs to be computed only once for a given  $\bar{d}$  on a fixed domain spanning  $0 \leq \eta \leq \bar{d}$ . Based on this, the coupling quantities  $T_2$  and  $\partial_x P_2$ , which appear in the liquid-side model (1.76), are readily constructed at order  $\underline{\epsilon}^1$ :

$$\begin{aligned} T_2 &= -\frac{\bar{d}}{d} \left\{ \partial_\eta \tilde{u}_2^{(0)} \Big|_{\eta=\bar{d}} + \underline{\epsilon} \partial_\eta \tilde{u}_2^{(1)} \Big|_{\eta=\bar{d}} \right\} + \mathcal{O}(\underline{\epsilon}^2), \\ &= -\frac{\bar{d}^2}{d^2} \left\{ \partial_\eta U_0 \Big|_{\eta=\bar{d}} + \frac{\partial_{x^*} d^*}{\bar{d}} \partial_\eta U_1 \Big|_{\eta=\bar{d}} \right\} + \mathcal{O}(\underline{\epsilon}^2), \end{aligned} \quad (1.98a)$$

$$\begin{aligned} \partial_x P_2 &= \partial_\xi P_2^{(0)} + \underline{\epsilon} \partial_\xi P_2^{(1)} + \mathcal{O}(\underline{\epsilon}^2) \\ &= \text{Re}_2 \left\{ \frac{\bar{d}^3}{d^3} \left( C_0 + C_1 \frac{\partial_{x^*} d^*}{\bar{d}} \right) + \frac{1}{\text{Fr}_2^2} (\sin(\phi) + \cos(\phi) \partial_{x^*} d^*) \right\} + \mathcal{O}(\underline{\epsilon}^2). \end{aligned} \quad (1.98b)$$

Importantly, for a fixed  $\bar{d}$ , the inter-phase coupling quantities  $T_2$  and  $\partial_x P_2$  depend solely on  $d=D-h/\Pi_L$ .

For completeness, the solution for the velocity expansion (1.93a) up to order  $\mathcal{O}(\underline{\epsilon})$  is:

$$\tilde{u}_2 = \frac{\bar{d}}{d} U_0 + \frac{\partial_{x^*} d^*}{d} U_1 + \mathcal{O}(\underline{\epsilon}^2). \quad (1.99)$$

**Relation to the state of the art and impact of our work** Our model (which has not been published yet), given by equations (1.28a), (1.76), and (1.98), extends the work of Samanta (2014), who considered the limit of a constant  $T_2$  and neglected  $\partial_x P_2$  altogether. Further, it extends the model of Tseluiko *et al.* (2013), who considered the

limit of zero confinement, i.e.  $H \rightarrow \infty$ . It thus opens the possibility to study falling liquid films at intermediate confinement levels, where the dynamics of the gas-liquid interaction is still strongly affected by the channel height  $H$ , but the gas flow is already turbulent. Such conditions are typically encountered in flooding experiments (Vlachos *et al.*, 2001).

Our representation of the gas flow follows the seminal work of Camassa *et al.* (2017), who inspired our work. However, our account of the liquid phase represents an improvement w.r.t that paper. Camassa *et al.* (2017) considered the inertialess limit, which was sufficient in their study of low  $\text{Re}_1$  co-current pressure-driven liquid-gas flows. However, in the case of falling liquid films, inertia is essential for the Kapitza instability mechanism (Brooke Benjamin, 1957; Yih, 1963), as will be discussed in section 5.1. Our model, which applies the WRIBL approach to the liquid film, accounts for this effect via the LHS terms in (1.76).

# Chapter 2

## WRIBL model computations

### 2.1 Linear stability analysis

Our WRIBL models introduced in sections 1.1, 1.2, and 1.3 are designed to capture exactly the neutral stability threshold of long-wave instabilities. Also, they accurately predict, within a certain validity range, the dispersion of the spatial (temporal) linear growth rate in terms of the angular frequency  $\omega$  (wave number  $k$ ) of a perturbation. In the current section, we outline the methods of linear stability analysis applied to our WRIBL models. We also demonstrate their consistency in the long-wave limit  $\omega \rightarrow 0$  ( $k \rightarrow 0$ ). Orr-Sommerfeld (OS) linear stability calculations based on the full Navier-Stokes equations will be discussed in chapter 3. In section 2.3, we will establish the validity range of our WRIBL models based on such OS calculations.

Sections 2.1.1 and 2.1.2 are dedicated to the planar and cylindrical configurations sketched in figures 1.2 and 1.3, where the primary flow is steady and subject to the Kapitza and Plateau-Rayleigh instabilities. In section 2.1.3, we will apply transient linear stability approaches to the configuration in figure 1.4, where secondary instability can cause the spontaneous sliding of suspended liquid drops forming as a result of the Rayleigh-Taylor instability.

#### 2.1.1 Planar liquid films in rectangular channels

We apply linear stability analysis to the planar WRIBL model given by (1.27) and (1.28), corresponding to the configuration in figure 1.2. First, the film thickness  $h$  and flow rates  $q_1$  and  $q_2$  are perturbed around their steady primary-flow values  $h_0$ ,  $q_{10}$ , and  $q_{20}$ :

$$\begin{aligned} h &= h_0 + h' = h_0 + \hat{h} \exp \{i(kx - \omega t)\} \\ q_1 &= q_{10} + q'_1 = q_{10} + \hat{q}_1 \exp \{i(kx - \omega t)\} \\ q_2 &= q_{20} + q'_2 = q_{20} + \hat{q}_2 \exp \{i(kx - \omega t)\}, \end{aligned} \tag{2.1}$$

where the infinitesimal perturbations  $h'$ ,  $q'_1$ , and  $q'_2$  are assumed to grow exponentially in time/space, starting from their initial amplitudes  $\hat{h}$ ,  $\hat{q}_1$ , and  $\hat{q}_2$ . Using the continuity

equations (1.28a) and (1.28b),  $\hat{q}_1$  and  $\hat{q}_2$  can be expressed in terms of  $\hat{h}$ :

$$\hat{q}_1 = -\hat{h} \frac{\omega}{k}, \quad \hat{q}_2 = \hat{h} \frac{\omega}{k} \Pi_u^{-1}. \quad (2.2)$$

Inserting (2.1) into the momentum equation (1.27) and then linearizing, yields the dispersion relation of the WRIBL model:

$$\begin{aligned} \text{DR} &= i \omega^2 \{S_2 - S_1\} + i k \omega \{-F_{22} q_2 + F_{21} q_2 - F_{12} q_1 + F_{11} q_1\} \\ &+ i k^2 \{G_{22} q_2^2 + 2 G_{12} q_2 q_1 + G_{11} q_1^2\} \\ &+ i k^2 \text{Fr}^{-2} \{\cos(\phi) - \Pi_\rho \cos(\phi)\} - i^3 k^4 \text{We} \\ &- \{C_1 \omega + \partial_h C_1 k q_1\} + \{C_2 \omega - \partial_h C_2 k q_2\} \\ &- i^2 k^3 \{L_1 q_1 + L_2 q_2\} + i^2 k^2 \omega \{M_2 - M_1\} = 0, \end{aligned} \quad (2.3)$$

where all variables and coefficients correspond to the primary flow, i.e.  $h=h_0$ ,  $q_1=q_{10}$ , and  $q_2=q_{20}$ , and where the coefficient derivatives  $\partial_h C_1$  and  $\partial_h C_2$  newly appear. This (complex) algebraic equation can be solved for  $k$  in terms of  $\omega$  (or vice versa). We will do this based on two different formulations:

- In the case of a spatial stability formulation, we assume  $\omega \in \mathbb{R}$  and  $k=k_r+i k_i$ . Here,  $-k_i$  is the spatial growth rate and  $\omega$  the angular frequency of a linear perturbation. This is the most adequate formulation for convectively unstable flows, such as falling liquid films (chapters 5 to 7). It breaks down however, when the liquid film succumbs to absolute instability (AI), e.g. due to a counter-current gas flow (Vellingiri *et al.*, 2015). Beyond the AI limit, perturbations grow in time at every position and solutions with  $\text{Im}(\omega)=\omega_i=0$  no longer exist. The loss of solutions within a spatial stability calculation can thus be used to identify the AI threshold. For this, we track the  $\partial_\omega(-k_i)=0$  maximum of the growth rate dispersion curve  $-k_i(\omega)$ , which degenerates into a pinch point<sup>1</sup>  $\partial_\omega(-k_i) \rightarrow \infty$  at AI (see panels 2.11d and 2.15d).
- In the case of a temporal stability formulation, we assume  $k \in \mathbb{R}$  and  $\omega=\omega_r+i \omega_i$ , or  $c=\omega/k=c_r+i c_i$ . Here,  $k c_i=\omega_i$  is the temporal growth rate and  $c_r=\omega_r/k$  is the wave celerity of the linear perturbation. This formulation is adequate for problems where there is no mean primary flow, such as the classical Rayleigh-Taylor (section 8.1) and Plateau-Rayleigh (section 7.2) configurations.

Although falling liquid films flowing in a passive atmosphere ( $\Pi_\mu=\Pi_\rho=0$ ) are convectively unstable, many studies have applied the temporal formulation to study their instability. This is because the Gaster transformation (Gaster, 1962):

$$\frac{\omega_i}{k_i} = -\partial_{k_r} \omega_r \quad (2.4)$$

---

<sup>1</sup>Strictly-speaking, the AI limit corresponds to a pinch point in the  $-k_i(k_r)$  curve. Whether this coincides with a pinch point in the  $-k_i(\omega)$  curve, depends on the group velocity  $\partial_{k_r} \omega = \partial_{k_r} k_i / \partial_\omega k_i$ . We have checked for all our configurations that  $\partial_{k_r} \omega$  does not diverge at AI. Thus,  $\partial_{k_r}(-k_i) \rightarrow \infty$  necessarily implies  $\partial_\omega(-k_i) \rightarrow \infty$ , and the AI limit can be obtained from the degeneration of the  $\partial_\omega k_i=0$  maximum.

applies in this limit (Brevdo *et al.*, 1999).

We solve the algebraic dispersion relation (2.3) numerically with the continuation software `Auto07P`. As only long-wave instabilities are considered here, the solution in the limit of infinitely long perturbations can be used as a starting point:

$$\begin{aligned} \text{Temporal formulation: } k = 0, \quad c_i = 0, \quad c_r = \frac{q_1 \partial_h C_1 + q_2 \partial_h C_2}{C_2 - C_1}, \\ \text{Spatial formulation: } \omega = 0, \quad k_i = 0, \quad k_r = 0. \end{aligned} \quad (2.5)$$

Starting from this solution, the dispersion curve of the spatial growth rate  $-k_i(\omega)$  (temporal growth rate  $\omega_i(k)$ ) is obtained by numerically advancing  $\omega(k)$ . Panel 2.1a shows examples of  $-k_i(\omega)$  curves for a weakly-inclined falling water film in contact with a counter-current air flow (configuration in panel 1.2a). The two sets of curves correspond respectively to  $\text{Re}_1=20$  (circles), which is supercritical, and  $\text{Re}_1=10$  (diamonds), which is subcritical. Curves with symbols correspond to the WRIBL dispersion relation (2.3) and solid lines without symbols were obtained from OS linear stability calculations based on the full Navier-Stokes equations, which will be discussed in section 3.1.

The WRIBL and OS data sets in panel 2.1a converge exactly as  $\omega \rightarrow 0$ . In that limit, the wave number  $k \in \mathbb{C}$  can be expanded asymptotically in terms of  $\omega$ :

$$k = k_0 + k_1 \omega + k_2 \omega^2 + \dots \quad (2.6)$$

Successively truncating (2.3) at orders  $\omega^0$ ,  $\omega^1$  and  $\omega^2$ , we obtain:

$$k_0 = k_1 = 0, \quad (2.7a)$$

and a purely complex solution for  $k_2$ :

$$\begin{aligned} k_2 = i \left\{ \text{Fr}^{-2} \cos(\phi) (1 - \Pi_\rho) \frac{\Psi^2}{\Xi^3} + q_2 (F_{21} - F_{22}) \frac{\Psi}{\Xi^2} + q_1 (F_{11} - F_{12}) \frac{\Psi}{\Xi^2} \right. \\ \left. - q_1 q_2 2 G_{12} \frac{\Psi^2}{\Xi^3} + q_1^2 G_{11} \frac{\Psi^2}{\Xi^3} + q_2^2 G_{22} \frac{\Psi^2}{\Xi^3} - \frac{S_2}{\Xi} + \frac{S_1}{\Xi} \right\}, \end{aligned} \quad (2.7b)$$

$$\text{with } \Psi = C_2 - C_1, \quad \text{and } \Xi = q_1 \partial_h C_1 + q_2 \partial_h C_2. \quad (2.7c)$$

Curves for  $-k_i(\omega)$  based on (2.6) and (2.7) are represented with dot-dashed lines in panel 2.1a. Because  $k_1, k_2 \in \mathbb{R}$ , the sign of  $\text{Im}(k_2)$  decides over instability ( $\text{Im}(k_2) < 0$ ) or stability ( $\text{Im}(k_2) > 0$ ).

The neutral stability bound  $k_2=0$  is predicted exactly by our WRIBL model. We have checked that (2.7) collapses analytically with the result obtained from the OS problem (see (3.7) in chapter 3). This is shown graphically in panel 2.1b, representing curves of the angular cut-off frequency  $\omega_c$  in terms of  $\text{Re}_1$ . As the neutral stability threshold is approached,  $\omega_c \rightarrow 0$ , predictions of the WRIBL model (curves with symbols)

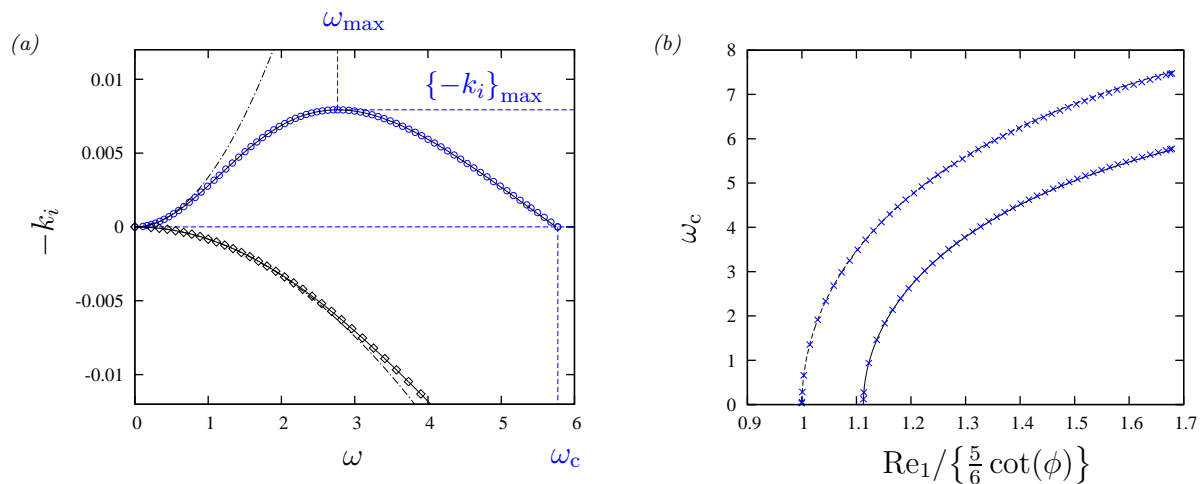


Figure 2.1: Spatial linear stability predictions for a falling water film in contact with a counter-current gas flow:  $\phi=4^\circ$ ,  $Ka=3406.9$  (water II and air IV in table 2.1),  $H^*=3$  mm,  $Re_2=-20$ . Symbols: WRIBL model; solid/dashed lines without symbols: OS calculations. (a) Dispersion curves of the linear growth rate  $-k_i$ . Circles:  $Re_1=20$ ; diamonds:  $Re_1=10$ ; dot-dashed lines: asymptotic expansion (2.6); (b) angular cut-off frequency and neutral stability threshold  $Re_1^{\text{crit}} = \lim_{\omega_c \rightarrow 0} Re_1$ . Dashed line: passive-gas limit ( $\Pi_\mu=\Pi_\rho=0$ ).

and OS analysis (lines without symbols) converge. In the special case of a passive atmosphere ( $\Pi_\mu=\Pi_\rho=0$ , dashed curves), both predictions yield the well known threshold  $Re_1^{\text{crit}} = \frac{5}{6} \cot(\phi)$  (Brooke Benjamin, 1957; Yih, 1963).

Figure 2.2 compares predictions of the neutral stability bound  $k_2=0$  in terms of the principal control parameters for the two planar configurations represented in figure 1.2. For the falling liquid film configuration (panel 2.2a), instability is either helped (large  $H^*$ ) or hindered (small  $H^*$ ) by an increasingly strong counter-current gas flow (controlled by  $M$ ), depending on the confinement level. However, for a large enough normalized gas pressure drop  $M$ , all curves are bounded by a limit point, beyond which the flow is either unconditionally unstable (large  $H^*$ ) or unconditionally stable (small  $H^*$ ), with the exception of the blue curve, which corresponds to the passive gas limit. We have investigated the stability of strongly confined planar falling liquid films in Lavalle *et al.* (2019) and our results will be discussed in detail in section 6.1.

Panel 2.2b corresponds to the configuration of pressure-driven plane Poiseuille flow of two superimposed fluids. In the limit  $\Pi_\rho=1$ , our WRIBL (dot-dashed blue curve) and OS (blue open circles) predictions exactly recover the well-known stability bound  $1/\Pi_\mu=(h_0/d_0)^2$  (Yiantsios & Higgins, 1988). This result subsumes the special case  $\Pi_\mu=1$  obtained in the limit  $h_0/d_0=1$  (Yih, 1967). The other curves in panel 2.2b correspond to lower density ratios, evidencing a stabilization of the flow as  $\Pi_\rho$  decreases.

The WRIBL prediction of the growth rate dispersion curve  $-k_i(\omega)$  (respectively  $\omega_i(k)$ ) deteriorates as  $\omega$  (respectively  $k$ ) increases and linear perturbations become shorter, al-

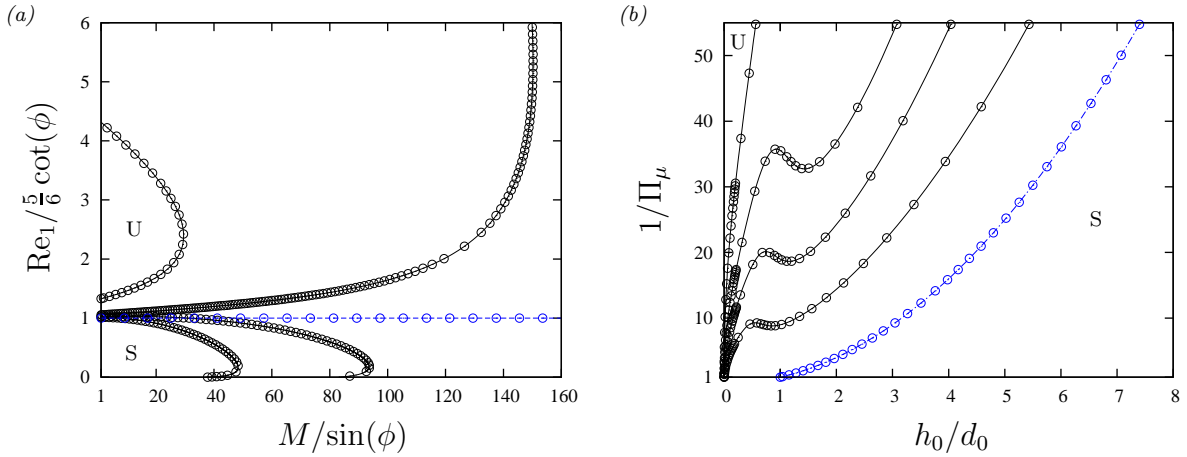


Figure 2.2: Neutral linear stability bound  $\text{Im}(k_2)=\text{Im}(\partial_{\omega\omega}k_i|_{\omega=0})=0$  according to (2.6) for long-wave instability modes. Lines: WRIBL model (2.7b); symbols: OS problem (3.29). (a) Configuration in panel 1.2a. Inclined water film in contact with an increasingly strong counter-current air flow:  $\text{Ka}=3406.9$  (air IV and water II in table 2.1). Solid curves from top to bottom:  $H^*=1, 2, 3,$  and  $4$  mm; (b) configuration in panel 1.2b. Poiseuille flow of two superimposed fluids:  $\phi=0^\circ$ . Solid curves from top to bottom:  $\Pi_\rho=0.1, 0.15, 0.2,$  and  $0.3$ . The dashed (panel a) and dot-dashed (panel b) blue lines correspond to  $\Pi_\mu=\Pi_\rho=0$  and  $\Pi_\rho=1$ , respectively. “S” indicates stability, and “U” indicates instability.

though this effect is very weak in the particular case represented in panel 2.1a. This limitation follows from the long-wave approximation underlying our modelling approach. In section 2.3, we will establish the validity range of our different WRIBL models, which is determined by their ability to accurately predict the linear growth rate  $-k_i$  (respectively  $\omega_i$ ) and wave celerity ( $c_r$ ) over the entire range of unstable frequencies  $\omega$  (respectively wave numbers  $k$ ).

Short-wave instabilities cannot be captured by our WRIBL models. In principle, such instabilities can occur in the planar configurations of two-fluid film flow studied in this work. However, we have checked that short-wave instability modes are always stable for the flow conditions considered here. These tests were performed based on a solution of the OS problem using Chebyshev polynomials, and they will be presented in section 3.1. Thus, for the flows considered in this work only long-wave instability modes are relevant.

### 2.1.2 Annular liquid films in cylindrical tubes

We apply the same linear stability formulations discussed in section 2.1.1 also to our cylindrical model (1.56), (1.57), (1.48), and (1.58), only that  $q_1$  and  $q_2$  now express the cross sectional flow rates, and that the core radius  $d$  now defines the interface position (configuration in figure 1.3). Thus, the amplitudes of the linear perturbations (2.1) are now related by:

$$\hat{q}_1 = -2\pi d_0 \hat{d} \frac{\omega}{k}, \quad \hat{q}_2 = 2\pi d_0 \Pi_u^{-1} \hat{d} \frac{\omega}{k}, \quad (2.8)$$

and the dispersion relation is:

$$\begin{aligned}
\text{DR} &= i \omega^2 2\pi d \left\{ \Pi_u^{-1} S_2 - S_1 \right\} \\
&+ i k \omega 2\pi d \left\{ -\Pi_u^{-1} F_{22} q_2 + F_{21} q_2 - \Pi_u^{-1} F_{12} q_1 + F_{11} q_1 \right\} \\
&+ i k^2 \left\{ G_{22} q_2^2 + 2 G_{12} q_2 q_1 + G_{11} q_1^2 \right\} \\
&- \left\{ \omega C_1 d + k \frac{1}{2\pi} \partial_d C_1 q_1 \right\} + \left\{ \omega \Pi_u^{-1} C_2 d - k \frac{1}{2\pi} \partial_d C_2 q_2 \right\} \\
&- i^2 k^3 \left\{ L_1 q_1 + L_2 q_2 \right\} + i^2 k^2 \omega 2\pi d \left\{ \Pi_u^{-1} M_2 - M_1 \right\} \\
&- i^3 k^4 \text{We} \frac{1}{2\pi} - i k^2 \text{We} \frac{1}{2\pi} \frac{1}{d^2} \left\{ 1 - \Pi_{\text{CRL}} \exp \left[ \lambda \left( 1 - \frac{d}{d_{\text{plug}}} \right) \right] \right\} = 0,
\end{aligned} \tag{2.9}$$

where  $d$  and  $q_k$  again correspond to the primary flow (the subscript 0 has been dropped for convenience). The capillary term proportional to  $i k^2 \text{We}$  is due to the azimuthal curvature of the film surface, and it includes the source term  $\Pi_\varphi$  introduced in (1.60b). Through the parameter  $\Pi_{\text{CRL}}$ , this term can be tuned to fully stabilize a cylindrical surface at  $d=d_{\text{plug}} \ll 1$ , allowing to represent stable pseudo-plugs in nonlinear computations (see section 2.2.3).

In the classical Plateau-Rayleigh configuration (panel 1.3b), where  $q_k=\Pi_\mu=\Pi_\rho=0$ , assuming temporally growing modes, i.e.  $k \in \mathbb{R}$  and  $\omega=i\omega_i \in \mathbb{C}$ , the cut-off wave number  $k_c$  is given by:

$$k_c = \frac{1}{d} \left\{ 1 - \Pi_{\text{CRL}} \exp \left[ \lambda \left( 1 - \frac{d}{d_{\text{plug}}} \right) \right] \right\}^{1/2}. \tag{2.10}$$

In this case, full stabilization ( $k_c=0$ ) is achieved for  $\Pi_{\text{CRL}}=1$  at  $d/d_{\text{plug}}=1$ . Conversely, in the limit  $\Pi_{\text{CRL}}=0$ , which is the default setting, our WRIBL model correctly retrieves the well-known analytical cut-off  $k_c=1/d$ . Further, as shown in panel 2.3a, our model (solid curves) accurately predicts the growth rate dispersion curve  $\omega_i(k)$  versus the solution of the OS problem<sup>2</sup> (symbols) for various real fluid combinations, including liquid-liquid pairings.

In the falling liquid film configuration (panel 1.3a),  $\Pi_{\text{CRL}} > 1$  may be required to fully stabilize a pseudo-plug at  $d=d_{\text{plug}}$ , due to the additional contribution of the inertia-driven convective Kapitza instability. In this case, we choose a spatial stability formulation, i.e.  $k = k_r + ik_i \in \mathbb{C}$  and  $\omega \in \mathbb{R}$ . Panel 2.3a compares growth rate dispersion curves  $-k_i(\omega)$  obtained from (2.9) (symbols) with OS predictions (solid curves), for three examples of annular falling liquid films in contact with air. For all three working liquids, which correspond to real experiments (Camassa *et al.*, 2014; Dao & Balakotaiah, 2000; Piroird *et al.*, 2011) and cover a wide Ka range, our WRIBL model predictions are in good agreement with the OS results.

---

<sup>2</sup>Section 3.2 introduces the OS linear stability problem for the cylindrical configuration.



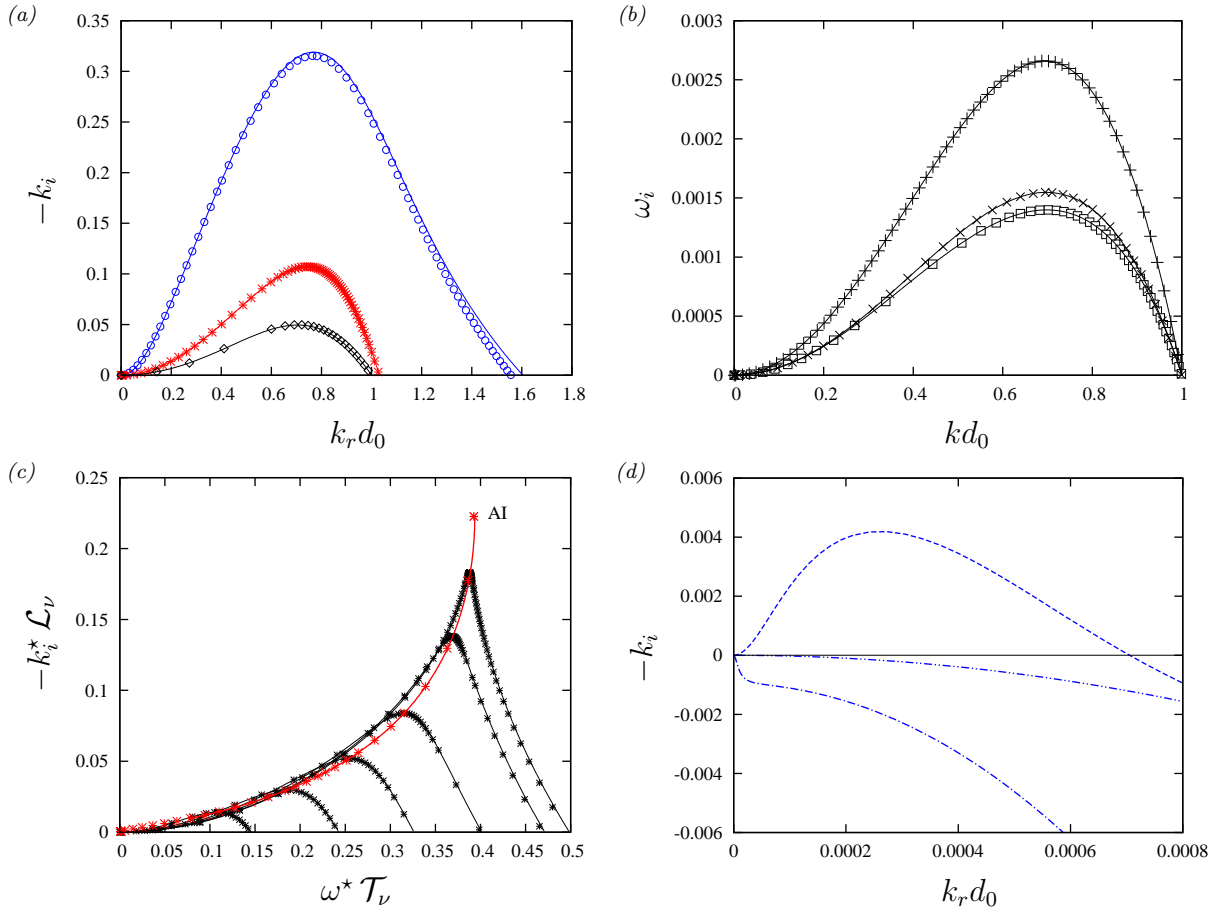


Figure 2.3: Spatial and temporal linear stability of an annular liquid film in contact with an active core fluid (figure 1.3). Symbols: WRIBL; solid lines: OS. (a) Falling liquid film. Circles:  $R^*=1.5$  mm,  $Ka=121.4$  (silicone oil III/air I in table 2.1),  $Re_1=15.4$ ,  $M=1$ ; asterisks: run 13 in Dao & Balakotaiah (2000),  $R^*=3.175$  mm,  $Ka=3.532$  (glycerol(89%)-water/air I),  $Re_1=0.258$ ,  $M=1$ ; (b) Static liquid film:  $Re_1=0$ ,  $M=0$ ,  $Fr^{-1}=0$ . Squares: panel 5b in Johnson *et al.* (1991),  $La=5314.3$  (mucus I/air I),  $d_0=0.8$ ; crosses: panel 4b in Tai *et al.* (2011),  $La=76.9$  (mucus II/air I),  $d_0=0.8$ ; plus signs: figure 4 in Bian *et al.* (2010),  $La=0.0280$  (glycerol(96%)-water/silicone oil I),  $d_0=0.77$ ; (c) transition to absolute instability (AI). Falling film from panel a (glycerol-water):  $Re_1=0.1, 0.2, 0.3, 0.4, 0.5$ , and  $0.54$  (from left to right); (d) stability of a pseudo-plug according to (1.60b). Silicone oil film from panel a:  $d_0=d_{\text{plug}}=0.01$ ,  $\lambda=1$ . Dashed:  $\Pi_{\text{CRL}}=1$ ,  $\Pi_\mu=\Pi_\rho=0$ ; dot-dashed:  $\Pi_{\text{CRL}}=1.01$ ,  $\Pi_\mu=\Pi_\rho=0$ ; dot-dot-dashed:  $\Pi_{\text{CRL}}=1$  ( $-k_i$  has been multiplied by  $10^3$ ).

In the case of the low-viscosity silicone oil (blue open circles), the cut-off wave number  $k_c d_0$  is shifted w.r.t. the classical Plateau-Rayleigh solution  $k_c d_0=1$ , as a result of the Kapitza instability. Thus, in the passive-core limit ( $\Pi_\mu=\Pi_\rho=0$ ),  $\Pi_{\text{CRL}} > 1$  is required to fully stabilize a pseudo-plug at  $d=d_{\text{plug}}$ . We show this in panel 2.3d, which represents  $-k_i(\omega)$  curves for a pseudo-plug of  $d=d_{\text{plug}}=0.01$ . Comparing the dashed and dot-dashed

curves, we see that full stabilization is achieved by changing  $\Pi_{\text{CRL}}$  from 1 to 1.01. In the case of an active core fluid, e.g. air, full stabilization is already achieved at  $\Pi_{\text{CRL}}=1$  (solid curve), but the growth rate magnitude is very small in this case ( $-k_i$  has been multiplied by  $10^3$  in the graph).

In the falling liquid film configuration, the interfacial instability is not always convective, even in the absence of a counter-current gas flow. There can be a transition from convective instability to absolute instability (AI) when the Plateau-Rayleigh mechanism overpowers the Kapitza mechanism. In panel 2.3c, this is achieved (for one of the working liquids from panel 2.3a) by reducing the core radius  $d_0$ , via an increase of the liquid Reynolds number  $\text{Re}_1$ . Our WRIBL model (symbols) accurately predicts the transition to AI versus OS calculations (solid lines). The AI limit coincides with the loss of solutions within a spatial stability formulation (see section 2.1.1). It was identified by tracking the  $\partial_\omega(-k_i)=0$  maximum in terms of the continuation parameter  $d_0$ , until reaching a limit point (red curve in panel 2.3c), where the  $-k_i(\omega)$  curve produces a pinch point<sup>3</sup>.

Our cylindrical WRIBL model captures exactly the long-wave neutral stability bound for both configurations in figure 1.3. Based on the spatial stability formulation and the asymptotic expansion in (2.6), this bound is once-again given by  $\text{Im}(k_2)=0$  (as  $k_0=k_1=0$ ), where  $k_2$  satisfies:

$$\begin{aligned}
 k_2 = i & \left[ 4\pi^2 d \{ \Pi_u S_1 - S_2 \} \frac{1}{\Xi} \right. \\
 & + 8\pi^3 d^2 \{ q_2 (\Pi_u F_{21} - F_{22}) + q_1 (\Pi_u F_{11} - F_{12}) \} \frac{\Psi}{\Xi^2} \\
 & + 16\pi^3 d^2 \Pi_u \{ q_1 q_2 G_{12} + q_1^2 G_{11} + q_2^2 G_{22} \} \frac{\Psi^2}{\Xi^3} \\
 & \left. + 4\pi^2 \text{We} \Pi_u \left\{ 1 - \Pi_{\text{CRL}} \exp \left[ \lambda \left( 1 - \frac{d}{d_{\text{plug}}} \right) \right] \frac{\Psi^2}{\Xi^3} \right\} \right],
 \end{aligned} \tag{2.11}$$

$$\text{with } \Psi = C_2 - C_1 \Pi_u, \quad \text{and} \quad \Xi = \Pi_u \{ q_1 \partial_d C_1 + q_2 \partial_d C_2 \}. \tag{2.12}$$

We demonstrate this graphically in figure 2.4, which compares WRIBL (lines) and OS (symbols) predictions. For the case of a falling liquid film in contact with a counter-current gas flow (panel 2.4a), the stable portion of the stability diagram shrinks very rapidly when increasing the Kapitza number  $\text{Ka}$  from  $\text{Ka}=0$ . Thus, for realistic values of  $\text{Ka}$ , the falling liquid film is always unstable. This is due to the surface tension term  $4\pi^2 \Pi_u \text{We}$  in (2.11), which does not appear in the planar problem (2.7b).

For the case of a pressure-driven core annular flow (panel 2.4b), our model reproduces the well-known islands of stability (Preziosi *et al.*, 1989) for liquid/liquid ( $\Pi_\rho=1$ , blue lines and circles) and liquid/gas (green lines and crosses) combinations.

---

<sup>3</sup>See panel 2.15c in section 2.3.2 for a validation of this approach versus applying full spatio-temporal stability analysis (Salin & Talon, 2019).

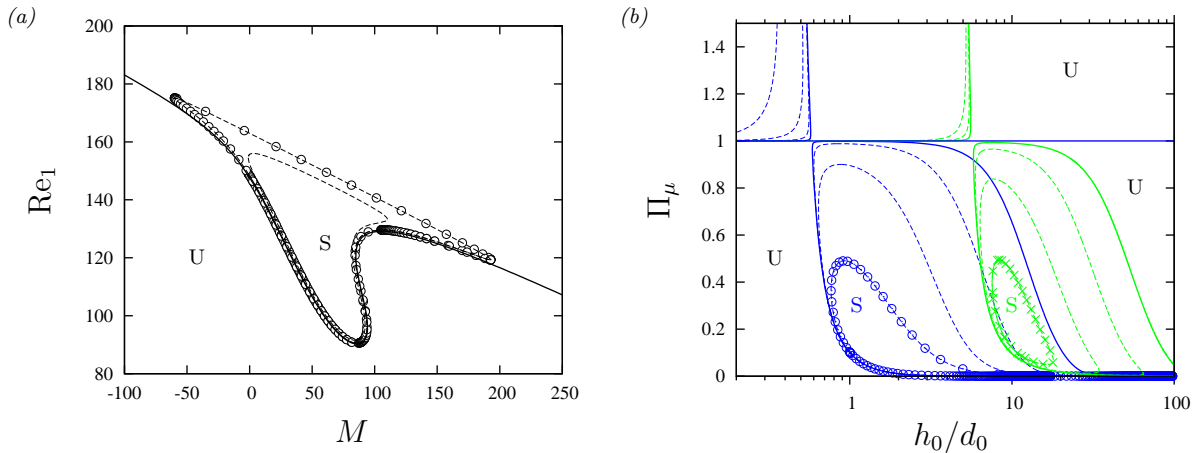


Figure 2.4: Neutral stability bound  $\text{Im}(k_2)=0$  for the cylindrical configurations in figure 1.3. Lines: WRIBL model (2.11); symbols: OS problem (3.29). (a) Falling liquid film in contact with a counter-current gas (panel 1.3a):  $R^*=1.5$  mm,  $\Pi_\rho=1.3 \cdot 10^{-3}$ ,  $\Pi_\mu=4 \cdot 10^{-3}$ . From solid to inner dashed curve:  $\text{Ka}=0, 1,$  and  $4.4$ ; (b) gravity-free core-annular flow (panel 1.3b):  $R^*=1.5$  mm. Green lines and crosses:  $\Pi_\rho=1.3 \cdot 10^{-3}$ ,  $\text{Ka} \cdot 10^9=2, 10, 50,$  and  $191$  (from solid to inner dashed line); blue lines and circles:  $\Pi_\rho=1$ ,  $\text{Ka}=0.1, 1, 10,$  and  $121.4$  (from solid to inner dashed line). “S” indicates stability, and “U” indicates instability.

### 2.1.3 Time-evolving base state: Rayleigh-Taylor instability

We now consider the configuration in panel 1.4a, where a horizontal liquid film is subject to the Rayleigh-Taylor instability. Our planar WRIBL model for this configuration is given by (1.64), with scales according to (1.66). Because there is no mean flow in this case, a temporal stability formulation is required. The standard linear stability approach outlined in section 2.1.1 also applies here and we will not repeat it. We simply point out that our WRIBL model predicts exactly the cut-off wave number  $k_c=\sqrt{\text{Bo}}$  (Yiantsios & Higgins, 1989) in the limit of a passive atmosphere ( $\Pi_\mu=\Pi_\rho=0$ ).

In section 8.1, we will study a suspended water film draining into liquid drops due to the Rayleigh-Taylor instability, which starts to spontaneously slide as the result of a secondary instability, before it has reached static equilibrium (see figure 8.2 for a sequence of the events). We apply linear stability analysis to elucidate the nature of this secondary instability, based on the lubrication model (1.68). We employ two different approaches to account for the time-dependent nature of the base state, which is a transient nonlinear solution of the model equations. First, a frozen-time approach, where the nonlinear base state is assumed to evolve much slower than the instability. Second, a transient stability analysis, where the time evolution of the base state is incorporated into the linear stability problem (Schmid, 2007; Balestra *et al.*, 2016).

In the frozen-time approach, we assume a quasi-steady base state profile  $\mathcal{H}(x)=\mathcal{H}(x, t_i)$ , corresponding to a particular time  $t=t_i$  in the nonlinear evolution of the liquid film. This

is obtained a priori via a nonlinear numerical computation based on (1.68) on a domain of length  $L=\Lambda/2$ , using symmetry conditions. As a result, the base state is perfectly symmetrical, precluding any bias in predicting symmetry-breaking instability modes. Next, we perturb  $\mathcal{H}(x)$ , introducing the linear film thickness perturbation  $h'(x,t)$ , which is assumed to grow exponentially:

$$h(x,t) = \mathcal{H}(x) + h'(x,t) = \mathcal{H}(x) + \hat{h}(x) \exp(\eta t). \quad (2.13a)$$

Upon inserting (2.13a) into (1.68) and linearising in terms of  $\hat{h}$ , an eigenvalue problem with eigenvalue  $\eta$  and eigenfunction  $\hat{h}$  is obtained:

$$\eta \hat{h} = -\partial_x \left[ \frac{\mathcal{H}^3}{3} \left( \partial_x \hat{h} + \frac{1}{\text{Bo}} \partial_{xxx} \hat{h} \right) + \mathcal{H}^2 \left( \partial_x \mathcal{H} + \frac{1}{\text{Bo}} \partial_{xxx} \mathcal{H} \right) \hat{h} \right]. \quad (2.13b)$$

We choose a Fourier series ansatz with  $N = 100$  for the eigenfunction  $\hat{h}$ :

$$\hat{h}(x) = \sum_{j=1}^N A_j \cos(j 2\pi x/\Lambda) + B_j \sin(j 2\pi x/\Lambda), \quad (2.13c)$$

and solve the eigenvalue problem with the Galerkin approach (Boyd, 1989). We then identify the most-unstable (greatest  $\eta$ ) eigenfunctions for two perturbation types: (i) asymmetric perturbations, when  $A_j=0$ ; and (ii) symmetric perturbations, when  $B_j=0$ .

For the transient stability analysis (Schmid, 2007), we follow the approach of Balestra *et al.* (2016), which allows to study rapidly-evolving base states. We start by linearizing (1.68) around the time-evolving nonlinear base state  $\mathcal{H}=\mathcal{H}(x,t)$ :

$$\begin{aligned} \partial_t h' + \partial_x q'_1 &= 0, \\ q'_1 &= \frac{1}{3} \mathcal{H}^3 \left[ \partial_x h' + \frac{1}{\text{Bo}} \partial_{xxx} h' \right] + h' \mathcal{H}^2 \left[ \partial_x \mathcal{H} + \frac{1}{\text{Bo}} \partial_{xxx} \mathcal{H} \right], \end{aligned} \quad (2.14a)$$

where  $h'$  and  $q'_1$  denote linear perturbations. The system (2.14a) allows to compute the linear response w.r.t to a perturbation applied at  $t=t_i$  over a time horizon  $T$ . This direct problem is repeatedly solved starting from an iteratively improved initial condition:

$$h'(x, t_i) = \frac{1}{2} h^\dagger(x, t_i) G(T) \int_0^L h'_{\text{old}}(x, t_i)^2 dx, \quad (2.14b)$$

where  $L$  denotes the domain length. This initial condition is obtained by solving the adjoint problem:

$$\begin{aligned} \partial_t h^\dagger - \frac{1}{3} \left[ \partial_x (q_1 \mathcal{H}^3) + \frac{1}{\text{Bo}} \partial_{xxx} (q_1 \mathcal{H}^3) \right] + q_1 \mathcal{H}^2 \left[ \partial_x \mathcal{H} + \frac{1}{\text{Bo}} \partial_{xxx} \mathcal{H} \right] &= 0, \\ q_1 &= \partial_x h^\dagger, \end{aligned} \quad (2.14c)$$

starting from the end condition:

$$h^\dagger(x, t_i + T) = 2 \frac{h'(x, t_i + T)}{\int_0^L h'(x, t_i)^2 dx}, \quad (2.14d)$$

and stepping backwards in time from  $t_i + T$  to  $t_i$ . The iterative procedure converges to a solution with maximal gain:

$$G(T) = \frac{\int_0^L h'(x, t_i + T)^2 dx}{\int_0^L h'(x, t_i)^2 dx}, \quad (2.14e)$$

which quantifies growth over the time horizon  $T$ .

The direct problem (2.14a) can also be solved to determine the linear noise response of the time evolving nonlinear base state. In that case, computations are started from a noisy initial condition  $h'(x, t_i) = h_{\text{noise}}$ :

$$h_{\text{noise}} = \epsilon \sum_{j=1}^N \cos(j \Delta k x - \varphi_{\text{rand}}), \quad \Delta k = 100 k_c / N, \quad k_c = \sqrt{\text{Bo}}, \quad (2.15)$$

Such computations always yield the most-amplified instability mode over a given time horizon  $T$ . These can be compared with the linear response to the maximum-gain solution obtained from the transient stability analysis (2.14), and with the most-unstable mode obtained from the frozen-time approach (2.13c).

### 2.1.4 Falling liquid films sheared by a turbulent gas

We now consider the configuration in figure 1.5, where a falling liquid film is subject to a turbulent gas flow. Our WRIBL model for this configuration is given by (1.76), (1.28a), and (1.98). Applying linear stability analysis to this model, entails only a slight difference w.r.t. section 2.1.1. It concerns the treatment of the inter-phase coupling quantities  $T_2$  (1.98a) and  $\partial_x P_2$  (1.98b), which express the effect of the gas flow. Linear expansion of  $T_2$  and  $\partial_x P_2$  yields:

$$T_2 = T_{20} + \partial_h T_2|_{h_0} (h - h_0) = T_{20} + \partial_d T_2|_{d_0} \frac{h'}{\Pi_L}, \quad (2.16a)$$

$$\partial_x P_2 = \partial_x P_{20} + \partial_h (\partial_x P_2)|_{h_0} (h - h_0) = \partial_x P_{20} + \partial_d (\partial_x P_2)|_{d_0} \frac{h'}{\Pi_L}, \quad (2.16b)$$

where we have made use of (2.1), and where the derivatives  $\partial_d T_2$  and  $\partial_d (\partial_x P_2)$  can be readily obtained from (1.98). In the linear limit,  $\bar{h} = h_0$  and  $\bar{d} = d_0$ , and so the base flow around which we have developed our gas-side model in section 1.4 corresponds to the primary flow.

Introducing (2.16) and (2.1) into the WRIBL model (1.76) and (1.28a), we obtain the following dispersion relation for the linear stability problem:

$$\begin{aligned}
\text{DR} = & -i\omega^2 + ik\omega \frac{17q_1}{7h} - ik^2 \frac{9q_1^2}{7h^2} + \frac{5}{6}\text{Fr}^{-2} \{ik^2 \cos(\phi)h - k \sin(\phi)\} \\
& - i^3 k^4 \frac{5}{6}\text{We} + \frac{5}{2} \frac{1}{\text{Re}_1} \frac{1}{h^2} \left\{ \omega - k 2 \frac{q_1}{h} \right\} + i^2 k^3 \frac{6}{\text{Re}_1} \frac{q_1}{h} - i^2 k^2 \omega \frac{9}{2} \frac{1}{\text{Re}_1} \\
& - \frac{5}{6} \Pi_\rho \frac{\Pi_u^2}{\Pi_L} \left\{ ik^2 \left[ C_1 \frac{h}{d} + \frac{\cos(\phi)}{\text{Fr}_2^2} h \right] - k \left[ C_0 \left( 1 + \frac{3}{2} \frac{1}{\Pi_L} \frac{h}{d} \right) + \frac{\sin(\phi)}{\text{Fr}_2^2} \right] \right\} \\
& + \Pi_\mu \frac{\Pi_u}{\Pi_L} \left\{ i^2 k^3 \frac{1}{6} \frac{1}{\text{Re}_1} h \partial_\eta U_0|_d - ik^2 \left[ \frac{5}{112} q_1 \partial_\eta U_0|_d + \frac{5}{4} \frac{1}{\text{Re}_1} \frac{1}{d} \partial_\eta U_1|_d \right] \right. \\
& \left. - ik\omega \frac{19}{336} h \partial_\eta U_0|_d + k \frac{5}{4} \frac{1}{\text{Re}_1} \frac{1}{\Pi_L} \frac{1}{d} \partial_\eta U_0|_d \right\} + ik^2 \frac{19}{672} \Pi_\mu^2 \frac{\Pi_u^2}{\Pi_L^2} h^2 (\partial_\eta U_0|_d)^2 = 0,
\end{aligned} \tag{2.17}$$

where we have dropped the index 0 referring to the primary flow, for convenience, and where the last three lines correspond to the contribution due to the gas flow. The inter-phase coupling quantities  $\partial_\eta U_0|_d$ ,  $\partial_\eta U_1|_d$ ,  $C_0$ , and  $C_1$  are obtained by solving the BVPs (1.95) and (1.96) numerically via the continuation software `Auto07P` (see section 2.2.4).

## 2.2 Nonlinear computations

We will perform three types of nonlinear computations based on our WRIBL models derived in sections 1.1, 1.2, 1.3, and 1.4:

- Construction of travelling-wave solutions (TWS), which are stationary in the reference frame of the wave, using the continuation software `Auto07P` (Doedel, 2008).
- Transient periodic computations on a domain spanning the streamwise wavelength  $\Lambda$ , using our own finite differences `Fortran` code.
- Spatio-temporal computations on an open domain of length  $L$  with inlet/outlet conditions, using our own finite differences `Fortran` code.

In the next two sections, we will detail these numerical procedures based on our fully-coupled planar WRIBL model, which is given by (1.27), (1.28a), (1.29), and (1.33), and applies to the configuration in figure 1.2. In section 2.2.3, we will then point out differences in the treatment of the cylindrical WRIBL model, which is given by (1.48), (1.56), (1.57), and (1.58), and applies to the configuration in figure 1.3. In particular, we will discuss the computation of pseudo-plugs based on our augmented model formulation (1.60).

### 2.2.1 Travelling-wave solutions (TWS)

To construct TWS, we introduce the wave celerity  $c$ , and express the space and time derivatives in our model equations (1.27), (1.28a), and (1.33) in terms of the wave coordinate  $\xi$ :

$$\xi = x - ct, \quad \partial_x = \partial_\xi, \quad \partial_t = -c \partial_\xi, \quad (2.18)$$

thus transforming the system of partial differential equations (PDEs) into a system of ordinary differential equations (ODEs):

$$h''' = \text{NL}(h, h', h'', q_1^{\text{MF}}, q_{\text{tot}}), \quad (2.19a)$$

$$q_1 - hc = \bar{q}_1 - \bar{h}c = q_1^{\text{MF}}, \quad (2.19b)$$

$$q_{\text{tot}} = q_1 + \Pi_u q_2 = \bar{q}_1 + \Pi_u \bar{q}_2, \quad (2.19c)$$

where primes denote differentiation w.r.t.  $\xi$ , bars signify averaging over the wavelength  $\Lambda$  in terms of  $\xi$ , the subscript MF refers to the moving reference frame, and where we have used (1.28) to replace derivatives  $q_k^{(j)}$  by derivatives  $h^{(j)}$  in (2.19a). Further, (2.19b) and (2.19c) are the integral forms of (1.28a) and (1.29), which we have used to eliminate  $q_k$  from (2.19a). The system is closed through the periodicity boundary conditions:

$$h^{(j)}|_{\xi=0} = h^{(j)}|_{\xi=\Lambda}, \quad j = 0, 1, 2, \quad (2.19d)$$

and it is solved for fixed values of  $\bar{q}_1$ , which is enforced through an integral condition:

$$\bar{q}_1 = \Lambda^{-1} \int_0^\Lambda q_1 d\xi, \quad (2.20)$$

and  $q_{\text{tot}}$ , which is imposed either explicitly, or indirectly through an integral condition on the pressure drop (1.34):

$$\Delta p_2 2\Pi_\rho \Pi_u^2 = \int_0^\Lambda \text{NLP}(h, h', h'', h''', q_1^{\text{MF}}, q_{\text{tot}}) d\xi - \int_0^\Lambda \left( \tilde{S}_1 - \Pi_u^{-1} \tilde{S}_2 \right) h' c d\xi. \quad (2.21)$$

In order to solve (2.19) with `Auto07P`, (2.19a) is recast into a dynamical system of three first-order ODEs for the dependent variables  $U_1=h$ ,  $U_2=h'$ , and  $U_3=h''$ :

$$U_3' = \text{NL}(U_1, U_2, U_3, \bar{q}_1, q_{\text{tot}}), \quad U_2' = U_3, \quad U_1' = U_2. \quad (2.22)$$

Solutions are obtained through numerical continuation, involving three steps. First, we seek fixed points  $U_1=h=\text{const}$  of the dynamical system by solving  $U_2=U_3=0$  (setting `IPS=1` in `Auto07P`) under the condition  $q_1^{\text{MF}}=q_1-hc=q_{10}-h_0c$ , which ensures connecting to the analytical primary-flow solution  $h=h_0$ ,  $q_1=q_{10}$ , and  $q_2=q_{20}$ , from which the continuation is

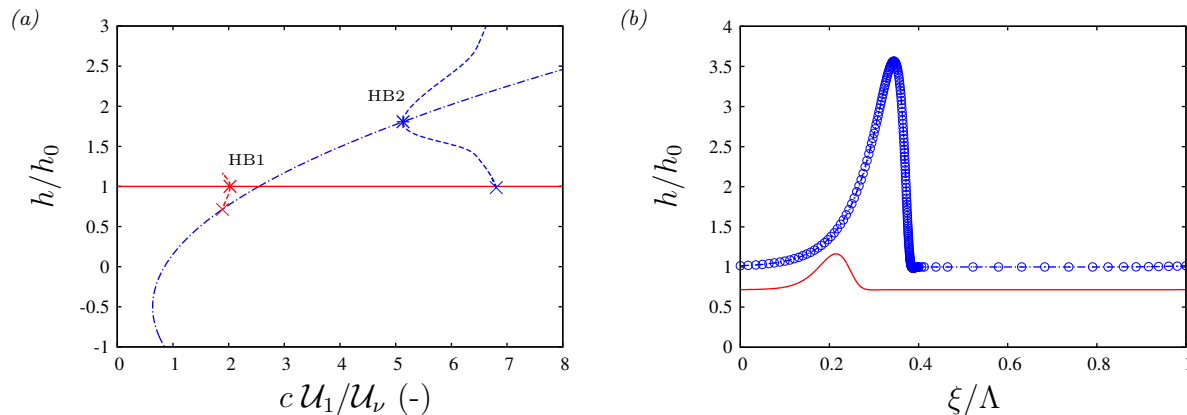


Figure 2.5: First steps in the construction of the TWS of panel 2.12a with Auto07P. Parameters correspond to panel 2.12a except for  $Ka=509.5/100$  and  $h_0=H/10$ , which will be adjusted in subsequent steps. (a) Fixed point solution branches (solid red and dot-dashed blue lines) according to (2.23), and periodic solutions continued from the Hopf bifurcation points HB1 and HB2 (dashed lines); (b) profiles of TWS corresponding to the periodic solutions in panel a in the limit of a homoclinic orbit (endpoints of the dashed lines). The symbols indicate the adaptively refined grid discretization.

started. We vary the wave celerity  $c$  as principal continuation parameter while maintaining  $h_0=\text{const}$ ,  $q_{10}=\text{const}$ , and  $q_{\text{tot}}=q_{10}+\Pi_u q_{20}=\text{const}$ . In this limit, (2.19a) reduces to:

$$0 = \frac{1}{Fr^2} (1 - \Pi_\rho) \sin(\phi) + C_1(h) \{q_{10} + c(h - h_0)\} + \frac{C_2(h)}{\Pi_u} \{q_{\text{tot}} - q_{10} - c(h - h_0)\}, \quad (2.23)$$

which has two solutions for  $h$ . The first corresponds to the primary flow  $h=h_0$ , and the second represents a uniform perturbation w.r.t.  $h_0$  travelling at celerity  $c$ . The two solutions are plotted in panel 2.5a as a function of  $c$  (solid red and dot-dashed blue lines). Each of the two branches exhibits a Hopf bifurcation (marked by HB), from which non-uniform periodic solutions  $h(\xi)$  emanate.

Next, we continue these periodic solutions in terms of  $c$ , starting from the Hopf bifurcation points (IPS=2 in Auto07P). The dashed lines in panel 2.5a represent the envelopes  $h_{\min}$  and  $h_{\max}$  for the two periodic solutions, and panel 2.5b represents the corresponding travelling wave profiles at the points where they have attained homoclinic orbits, i.e. where the dashed lines in panel 2.5a intersect one of the fixed-point solution branches (crosses). In terms of deviations from the primary flow, the wave profile corresponding to HB2 (dot-dashed blue line in panel 2.5b) represents a positively-humped wave, whereas the profile corresponding to HB1 (solid red line in panel 2.5b) a negatively-humped one. The former are usually encountered in experiments and thus our TWS solutions are constructed from HB2.



In the final step for constructing TWS, integral conditions such as (2.20) and (2.21) are activated (IPS=4 in Auto07P) and control parameters are continued one by one to their target values. In the case of the planar configuration (figure 1.2), there are 3 control parameters, i.e.  $\bar{q}_1$  and  $M$  (or  $q_{\text{tot}}$ ), for defining the primary flow, plus a measure for selecting the TWS, e.g. the wavelength  $\Lambda$ , the wave celerity  $c$ , or the wave frequency  $f$ .

In particular, our TWS codes allow imposing the spatially most-amplified frequency  $f=f_{\text{max}}$ . To determine  $f_{\text{max}}$ , which changes with the control parameters varied in a given continuation run, we additionally solve the dispersion relation (2.3) of the spatial linear stability problem for  $\omega_{\text{max}}=2\pi f_{\text{max}}$ :

$$\text{DR}(\omega_{\text{max}}, k) = 0, \quad \partial_{\omega} k_i|_{\omega=\omega_{\text{max}}} = 0, \quad (2.24)$$

where the relation for  $\partial_{\omega} k_i$  is obtained through rearranging  $\partial_{\omega} \text{DR}=0$ . In a given continuation run, the linear stability problem (2.24) is solved for the primary flow  $\{q_{10}, q_{20}\}=\{\bar{q}_1, \bar{q}_2\}$ , which is fixed by the mean flow rates  $\bar{q}_1$  and  $\bar{q}_2$  of the current TWS. For example, this procedure was applied to construct the results in panel 2.12a.

### 2.2.2 Transient periodic and spatio-temporal computations

In our transient periodic computations, we solve the WRIBL model equations (1.27) and (1.28) iteratively by numerically advancing the solution in time. Upon eliminating  $q_2$  with (1.29), the model equations are recast into:

$$\partial_t q_1 + S_2 (\Pi_u S_1 - S_2)^{-1} \partial_t q_{\text{tot}} = \text{NL}(\partial_{x^j} h, \partial_{x^i} q_1), \quad (2.25a)$$

$$\partial_t h = \partial_x q_1, \quad (2.25b)$$

and integrated over the time increment  $\Delta_t$ :

$$q_1|_{\text{new}} - q_1|_{\text{old}} + S_2 (\Pi_u S_1 - S_2)^{-1} \partial_t q_{\text{tot}} \Delta_t = \int_{t_{\text{old}}}^{t_{\text{new}}} \text{NL} dt, \quad (2.26a)$$

$$h_{\text{new}} - h_{\text{old}} = \int_{t_{\text{old}}}^{t_{\text{new}}} \partial_x q_1 dt, \quad (2.26b)$$

where the time evolution of the RHS terms is represented with a semi-implicit Crank-Nicolson formulation (Patankar, 1980):

$$\text{NL} = \text{NL}|_{\text{old}} + \frac{t - t_{\text{old}}}{\Delta_t} \{ \text{NL}|_{\text{new}} - \text{NL}|_{\text{old}} \}, \quad (2.27a)$$

$$\partial_x q_1 = \partial_x q_1|_{\text{old}} + \frac{t - t_{\text{old}}}{\Delta_t} \{ \partial_x q_1|_{\text{new}} - \partial_x q_1|_{\text{old}} \}, \quad (2.27b)$$

and all spatial derivatives are approximated with first-order central finite differences. Further, it is assumed in (2.26) that the model coefficients,  $S_i$ ,  $F_{ij}$ ,  $G_{ij}$ ,  $C_i$ ,  $J_i$ ,  $K_i$ ,  $L_i$ ,

and  $M_i$  (evaluated at  $t_{\text{old}}$ ), as well as  $\partial_t q_{\text{tot}}$  are constant over the time step. The nonlinear operator  $\text{NL}|_{\text{new}}$  of the momentum equation at  $t_{\text{new}}=t_{\text{old}} + \Delta_t$  is linearized in terms of the dependent variables  $h$  and  $q_1$ , and their derivatives  $h^{(j)}$  and  $q_1^{(i)}$ :

$$\begin{aligned} \text{NL}|_{\text{new}} &= \text{NL}|_{\text{old}} + \frac{\partial \text{NL}|_{\text{old}}}{\partial h^{(j)}} \{ h^{(j)}|_{\text{new}} - h^{(j)}|_{\text{old}} \} \\ &+ \frac{\partial \text{NL}|_{\text{old}}}{\partial q^{(i)}} \{ q^{(i)}|_{\text{new}} - q^{(i)}|_{\text{old}} \}, \end{aligned} \quad (2.28)$$

where the bracketed superscripts denote the power of differentiation w.r.t.  $x$ . The thus obtained discretized evolution equations are evaluated at the  $N_x-1$  points of an equidistant grid spanning from  $x=\Delta_x$  to  $x=\Lambda$  with grid spacing  $\Delta_x=\Lambda/(N_x - 1)$ . The point  $x=0$  is excluded as it coincides with  $x=\Lambda$  due to streamwise periodicity, yielding a linear system of  $N_x-1$  algebraic difference equations:

$$\underline{\mathbf{A}}\mathbf{x} = \mathbf{b}, \quad (2.29)$$

$$\mathbf{x} = [h|_{i_x=2}, q_1|_{i_x=2}, \dots, h|_{i_x=N_x}, q_1|_{i_x=N_x}]^T, \quad (2.30)$$

where the solution vector  $\mathbf{x}$  contains the solutions at the grid points  $i_x$ ,  $\underline{\mathbf{A}}$  is the coefficient matrix, and  $\mathbf{b}$  the inhomogeneity. The periodicity conditions:

$$h^{(j)}|_{x=0} = h^{(j)}|_{x=\Lambda}, \quad (2.31a)$$

$$q^{(i)}|_{x=0} = q^{(i)}|_{x=\Lambda}, \quad (2.31b)$$

are imposed directly by making use of the nodes at and downstream of  $x=0$  in the formulation of spatial derivatives at and upstream of  $x=\Lambda$ , and vice versa. As a result,  $\underline{\mathbf{A}}$  loses its pentadiagonal shape through entries in its upper right and lower left corners. The system (2.29) is referred to as a cyclic or periodic pentadiagonal system and can be recast into a form that requires solving a series of purely pentadiagonal subsystems (Navon, 1987). These subsystems are solved through LU decomposition with the **Fortran** routine **DGBSV**, which is part of the **LAPACK** library. Using this procedure, we iteratively solve (2.29) at each time step, starting from the initial condition:

$$h(x, t = 0) = \bar{h} [1 + \epsilon_1 \sin(2\pi x/\Lambda)], \quad q_1(x, t = 0) = q_{10} (q_{\text{tot}}(t = 0), \bar{h}), \quad (2.32)$$

where the control parameters of the computation,  $\bar{h}$ ,  $\Lambda$ , and  $q_{\text{tot}}$ , naturally appear, and where  $\epsilon_1$  denotes the initial perturbation amplitude. Alternatively, the computation can be started from a the result of a previous run, or from a TWS constructed with **Auto07P**. The latter option will be used to study the linear stability of TWS (see e.g. figure 6.8 in section 6.2).

The time evolution of the total flow rate  $q_{\text{tot}}$  is either prescribed explicitly<sup>4</sup>), or obtained from an integral conditions on the pressure drop (1.34). In the second case, (1.34)

---

<sup>4</sup>In our **Fortran** codes,  $q_{\text{tot}}$  can be varied in time according to a sigmoid function, allowing to gradually increase the gas flow rate.

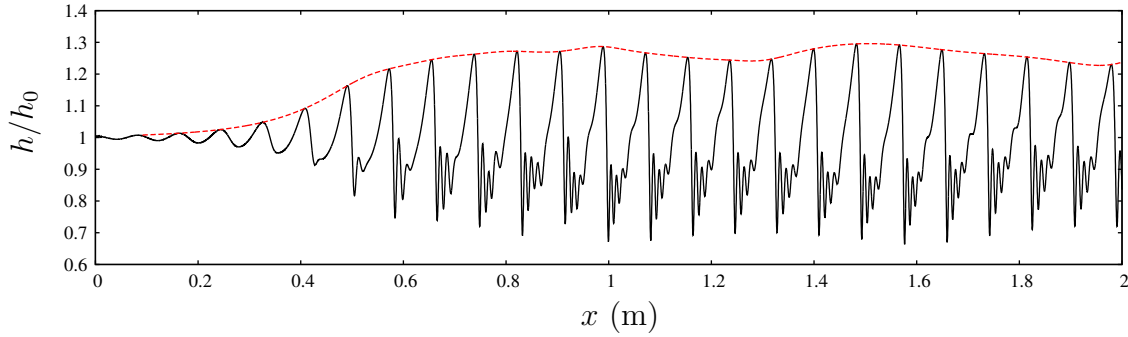


Figure 2.6: Benchmark computation on an open domain with inlet/outlet conditions using our `Fortran` solver based on the planar WRIBL model (1.27). Inclined falling liquid film flowing in a passive atmosphere ( $\Pi_\rho = \Pi_\mu = 0$ ), according to the experiments in figure 6 of Liu & Gollub (1994):  $\phi = 5^\circ$ ,  $\text{Re}_1 = 58/3$ ,  $f^* = 3.0$  Hz,  $\text{Ka} = 253.0$  (glycerol(54%)-water mixture in table 2.1). The domain is discretized with  $N_x = 13000$  points and we have used  $\epsilon_1 = 0.01$  as the forcing amplitude (2.38). The red dashed line tracks the Lagrangian path of one of the wave crests, evidencing a secondary instability (Liu & Gollub, 1993).

is recast to isolate  $\partial_t q_{\text{tot}}$ :

$$\begin{aligned} \partial_t q_{\text{tot}} \frac{1}{\Pi_u} \left\{ \int_0^L S_2 \frac{\Pi_u \tilde{S}_1 - \tilde{S}_2}{\Pi_u S_1 - S_2} dx - \int_0^L \tilde{S}_2 dx \right\} &= 2\Pi_\rho \Pi_u^2 \Delta p_2 - \int_0^L \text{NLP}(x, t) dx \\ &+ \int_0^L \left( \tilde{S}_1 - \frac{\tilde{S}_2}{\Pi_u} \right) \text{NL}(x, t) dx, \end{aligned} \quad (2.33)$$

having eliminated  $\partial_t q_1$  through (2.25), and then used to update  $q_{\text{tot}}$  at each time step:

$$q_{\text{tot}}|_{\text{new}} = q_{\text{tot}}|_{\text{old}} + \partial_t q_{\text{tot}}|_{\text{old}} \Delta t. \quad (2.34)$$

Our `Fortran` code for open-domain computations (see example in figure 2.6) relies on the same numerical procedure as the transient periodic code. The only difference resides in the use of inlet and outlet conditions at the left ( $x=0$ ) and right ( $x=L$ ) boundaries, respectively. The linear system (2.29) is now set up for the grid points ranging from  $i_x=1$  ( $x=0$ ) to  $i_x=N_x$  ( $x=L$ ) and  $\underline{A}$  takes a purely pentadiagonal form.

Inlet conditions are set by explicitly prescribing  $h$  and  $q_1$  at the first two grid points ( $i_x=1,2$ ) based on the primary flow:

$$h|_{i_x=1} = h|_{i_x=2} = h_0, \quad (2.35a)$$

$$q_1|_{i_x=1} = q_1|_{i_x=2} = q_{10} [1 + F(t)], \quad (2.35b)$$

which is implemented in (2.29) through:

$$\underline{A}_{1i} = \delta_{1i} + \delta_{2i}, \quad \underline{A}_{2i} = \delta_{3i} + \delta_{4i}, \quad (2.36)$$

$$b_1 = b_3 = h|_{i_x=1} = h|_{i_x=2}, \quad b_2 = b_4 = q_1|_{i_x=1} = q_1|_{i_x=2}. \quad (2.37)$$

The function  $F(t)$  in (2.35b) allows to apply a tailored inlet forcing:

$$F(t) = \epsilon_1 \sin(2\pi f t) + \epsilon_2 \sum_{k=1}^N \sin(2\pi k \Delta f t + \varphi_{\text{rand}}), \quad \Delta f = 2 f_c / N. \quad (2.38)$$

The first term in (2.38) constitutes a harmonic perturbation of frequency  $f$  and the second one mimics white noise through a series of  $N=1000$  Fourier modes that are shifted by a random phase shift  $\varphi_{\text{rand}} = \varphi_{\text{rand}}(k) \in [0, 2\pi]$  and that span a frequency range of twice the linear cut-off frequency  $f_c$  (Chang *et al.*, 1996a). All our computations were run with the same  $\varphi_{\text{rand}}(k)$  number series, which was generated once and for all with the pseudo random number generator `RandomReal` in Mathematica (2014). The strength of the two terms in (2.38) is determined through their amplitudes  $\epsilon_1$  and  $\epsilon_2$ . When  $\epsilon_1=0$ , the inlet perturbation consists of only white noise. This setting will be used to simulate the natural, noise-driven, evolution of a wavy film as it would occur in an experiment. In other computations, we will apply coherent inlet forcing by setting  $\epsilon_1 > 0$ , thus adding a monochromatic harmonic perturbation to the inlet noise.

At the outlet, we apply the boundary conditions of Richard *et al.* (2016), which ensure that liquid is always sufficiently drained from the domain, by introducing two downstream ghost nodes at  $i_x = N_x + 1, N_x + 2$ :

$$h|_{i_x=N_x+1} = h|_{i_x=N_x+2} = h|_{i_x=N_x}, \quad (2.39a)$$

$$q_1|_{i_x=N_x+1} = q_{10} \frac{q_{10}^{\text{PG}}(h|_{i_x=N_x})}{q_{10}^{\text{PG}}(h_0)}, \quad (2.39b)$$

where  $q_{10}^{\text{PG}}(h) = q_{10}(\Pi_\rho = \Pi_\mu = 0, h)$  is the passive-gas limit of the primary flow rate  $q_{10}$  for a given  $h$ . These ghost nodes are used to evaluate the finite differences approximations of spatial derivatives at  $i_x = N_x - 1, N_x$ . Thereby,  $q_1|_{i_x=N_x+2}$  is not needed because derivatives of  $q_1$  not higher than second-order intervene in (1.27), (1.28), and (1.33).

Our open-domain computations were always started from the initial condition:

$$h(x, t = 0) = h_0, \quad q_1(x, t = 0) = q_{10}. \quad (2.40)$$

Figure 2.6 represents a snapshot of such a computation reproducing the experiments in figure 6 of Liu & Gollub (1994), which were performed in a quiescent gas. Accordingly, we have set  $\Pi_\rho = \Pi_\mu = 0$ . The inlet forcing amplitude is  $\epsilon_1 = 0.01$ , following the work of Samanta (2014), who had previously simulated this experiment. Agreement between our data and the two references is good, our computation exhibiting spatial oscillations of the wave height (highlighted by the red dashed line), which result from a secondary instability of the saturated wave train (Liu & Gollub, 1993).

### 2.2.3 Liquid plugs in cylindrical tubes

We employ the same numerical approaches described in sections 2.2.1 and 2.2.2 to solve our cylindrical model given by (1.56), (1.57), (1.48), and (1.58). Formally, all relations

written for the planar configuration also apply to the cylindrical configuration, upon replacing the film thickness  $h$  by the core radius  $d$ . For example, the initial condition (2.32) becomes in the cylindrical formulation:

$$d(x, t = 0) = d_0 [1 + \epsilon_1 \sin(2\pi x/\Lambda)], \quad q_1(x, t = 0) = q_{10} (q_{\text{tot}}(t = 0), \bar{d}), \quad (2.41)$$

where  $d_0$  is used instead of  $\bar{d}$ , because  $\bar{d}$  changes over time even when the liquid volume  $V_1$  is fixed. The only substantial difference w.r.t. the formalism for the planar configuration arises when computing liquid pseudo-plugs via the augmented momentum equation (1.60a). In the case of TWS, we then solve the dynamical system:

$$d''' = \text{NL}_{\text{CRL}}(d, d', d'', q_1^{\text{MF}}, q_{\text{tot}}, \Pi_{\text{CRL}}, \lambda, d_{\text{plug}}), \quad (2.42a)$$

$$q_1 - \pi d^2 c = \bar{q}_1 - \pi \bar{d}^2 c = q_1^{\text{MF}}, \quad (2.42b)$$

$$q_{\text{tot}} = q_1 + \Pi_u q_2 = \bar{q}_1 + \Pi_u \bar{q}_2, \quad (2.42c)$$

where (2.42a) is obtained by recasting (1.60a) in terms of the moving-frame coordinate  $\xi = x - ct$ , and  $\Pi_{\text{CRL}}$ ,  $\lambda$ , and  $d_{\text{plug}}$  represent the pseudo-plug parameters, the limit  $\Pi_{\text{CRL}}=0$  allowing to recover the standard model.

By contrast, the pressure drop  $\Delta p_2$  is computed via the standard equation (1.58):

$$\Delta p_2 2\Pi_\rho \Pi_u^2 = \int_0^\Lambda \text{NLP}(d, d', d'', d''', q_1^{\text{MF}}, q_{\text{tot}}) d\xi - \int_0^\Lambda (\tilde{S}_1 - \Pi_u^{-1} \tilde{S}_2) \partial_t q_1 d\xi, \quad (2.43)$$

where  $\partial_t q_1$  is obtained from the standard momentum equation (1.48), rearranged with the help of (2.42c) in order to eliminate  $q_2$ .

Figure 2.7 represents TWS obtained from (2.42) and (2.43) for an annular falling liquid film within a cylindrical vertical tube in contact with air under an aerostatic pressure drop  $M=1$ . We see that non-occluding TWS are bounded by a first limit point (LP1) and that pseudo-plug solutions (blue solid line) branch off from the standard model (red dashed line) in the vicinity of a second limit point (LP2). We will show in section 2.3.1 that these pseudo-plug solutions are in good agreement with DNS data.

In the case of transient computations, we solve:

$$\partial_t q_1 + S_2 (\Pi_u S_1 - S_2)^{-1} \partial_t q_{\text{tot}} = \text{NL}(\partial_{x^j} d, \partial_{x^i} q_1) + \Pi_\varphi (\Pi_u S_1 - S_2)^{-1}, \quad (2.44a)$$

$$\partial_t d = \frac{1}{2\pi d} \partial_x q_1, \quad (2.44b)$$

where (2.44a) corresponds to the augmented momentum equation (1.60a) upon substituting  $q_2 = \Pi_u (q_{\text{tot}} - q_1)$ , which collapses to the standard form (1.48) in the limit  $\Pi_\varphi = 0$ . The total flow rate  $q_{\text{tot}}$  is either prescribed explicitly or updated according to:

$$\begin{aligned} \partial_t q_{\text{tot}} \frac{1}{\Pi_u} \left\{ \int_0^L S_2 \frac{\Pi_u \tilde{S}_1 - \tilde{S}_2}{\Pi_u S_1 - S_2} dx - \int_0^L \tilde{S}_2 dx \right\} &= 2\Pi_\rho \Pi_u^2 \Delta p_2 - \int_0^L \text{NLP}(x, t) dx \\ &+ \int_0^L \left( \tilde{S}_1 - \frac{\tilde{S}_2}{\Pi_u} \right) \text{NL}(x, t) dx, \end{aligned} \quad (2.44c)$$

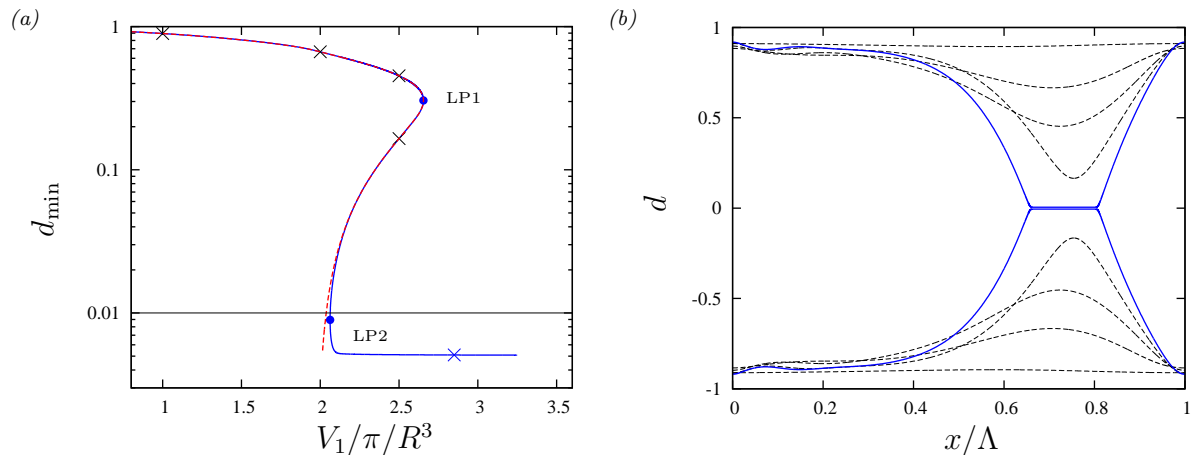


Figure 2.7: TWS obtained with the augmented cylindrical model (1.60a), which allows to represent liquid pseudo-plugs. Falling liquid film in contact with air within a vertical cylindrical tube (panel 1.3a):  $Ka=121.4$  (silicone oil III and air I in table 2.1),  $R^*=1.5$  mm,  $M=1$ ,  $\Lambda=5.4$ . (a) Minimal core radius  $d_{\min}$  in terms of the normalized liquid volume. Solid blue:  $\Pi_{\text{CRL}}=\lambda=1$ ,  $d_{\text{plug}}=0.01$ ; dashed red:  $\Pi_{\text{CRL}}=0$ ; (b) profiles of TWS corresponding to crosses in panel a. From bottom to top:  $V_1/\pi/R^3=1, 2, 2.5, 2.5, 2.85$ .

which allows imposing the pressure drop  $\Delta p_2$ . This equation is obtained by integrating the standard pressure equation (1.58) and substituting  $\partial_t q_1$  based on the standard momentum equation (1.48).

Figure 2.8 demonstrates the formation of a liquid plug obtained from a transient periodic computation based on (2.44) and started from the initial condition (2.41) with perturbation amplitude  $\epsilon_1=0.013$ . Parameters correspond to figure 2.7 and the liquid volume was fixed at  $V_1/\pi/R^3=2.85$ . In panel 2.8a, we see that the instantaneous liquid and gas Reynolds numbers converge quite closely to the final values of our DNS (marked by green dot-dashed lines), which will be introduced later (panel 2.19b). Further, panel 2.8b shows that the liquid plug from our transient computation converges to the corresponding TWS from panel 2.7b (dashed blue line in panel 2.8b).

Open-domain computations of liquid plugs based on the augmented momentum equation (1.60) can be costly, because a fine spatial resolution is required to resolve the plug fronts (panel 2.20f). Thus, we will employ a less costly approach in some computations, where only the dynamics upstream of the occlusion zone is of interest (panel 7.3). In that case,  $d \geq d_{\text{crit}}$  is enforced numerically at each time step via:

$$\forall d_{\text{old}} < d_{\text{crit}} : d_{\text{old}} = d_{\text{crit}}. \quad (2.45)$$

This alternative approach is to be understood as a numerical trick to continue computations past occlusion events, in order to reach a developed state.

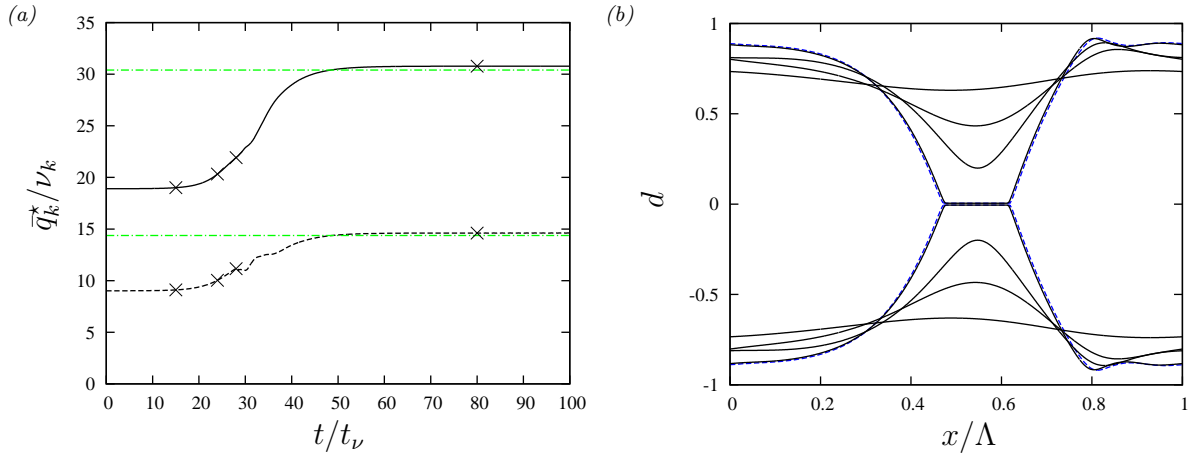


Figure 2.8: Transient periodic computation of a pseudo-plug forming by occlusion of a vertical cylindrical tube. Parameters as in figure 2.7:  $V_1/\pi/R^3=2.85$ . (a) Time traces of the instantaneous Reynolds numbers  $\bar{q}_k^*/\nu_k$  in the liquid (solid) and gas (dashed), with  $\bar{q}_k=\Lambda^{-1}\int_0^\Lambda q_k dx$ . Dot-dashed green lines mark final values for the DNS represented in panel 2.19b; (b) profiles corresponding to crosses in panel a (solid black curves) and to the TWS in panel 2.7b (dashed blue curve).

### 2.2.4 Falling liquid films sheared by a turbulent gas

Numerical solution of the nonlinear equation system (1.76) and (1.28a) follows the same principles discussed in sections 2.2.1 and 2.2.2, only that the treatment of the gas is different. To obtain the inter-phase coupling quantities  $T_2$  and  $\partial_x P_2$ , which enter (1.76) and are governed by (1.98), the augmented nonlinear BVPs (1.95) and (1.96) need to be solved for  $\partial_\eta U_0|_{\eta=\bar{d}}$ ,  $\partial_\eta U_1|_{\eta=\bar{d}}$ ,  $C_0$ , and  $C_1$ . We do this numerically via the continuation software `Auto07P`, starting from the analytical solution in the laminar limit ( $\mu_t=0$ ):

$$U_0 = \frac{1}{2}C_0\text{Re}_2(\eta^2 - \bar{d}^2), \quad (2.46)$$

$$C_0 = -\frac{3}{2}\frac{1}{\text{Re}_2}\frac{q_2}{\bar{d}^3}, \quad (2.47)$$

$$U_1 = \frac{1}{120}\text{Re}_2(\bar{d} - \eta)(\bar{d} + \eta)\{C_0^2\text{Re}_2^2(11\bar{d}^4 - 4\bar{d}^2\eta^2 + \eta^4) - 60C_1\}, \quad (2.48)$$

$$C_1 = \frac{6}{35}C_0^2\bar{d}^4\text{Re}_2^2. \quad (2.49)$$

In the case of TWS computations, equations (1.95) and (1.96) are solved with `Auto07P` in conjunction with the film-model equations (1.76) and (1.28a), as well as the linear stability problem (2.24), based on the dispersion relation (2.17). This allows to impose the linearly most-amplified frequency  $f=f_{\max}$ . Importantly, (1.95) and (1.96) have been

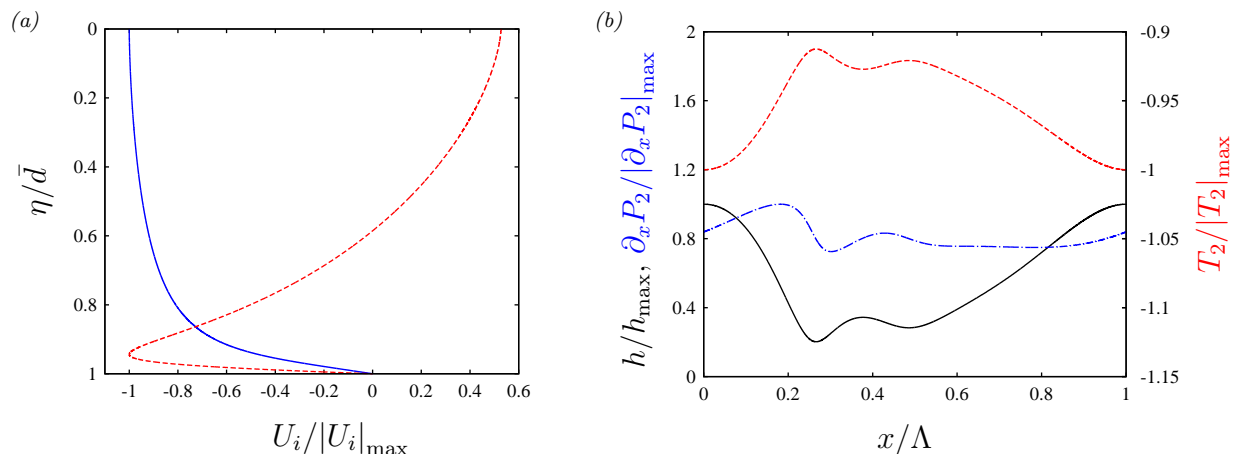


Figure 2.9: Vertically-falling liquid film sheared by a turbulent air flow (figure 1.5):  $Ka=509.5$  (DMSO-water in table 2.1),  $H^*=10$  mm,  $Re_1=15$ ,  $Re_2=-4123$ ,  $f=f_{\max}$ . (a) Velocity profiles  $U_0$  (solid blue) and  $U_1$  (dashed red) from (1.99) obtained via numerical solution of (1.95) and (1.96) using `Auto07P`; (b) nonlinear surface wave (solid black, left ordinate) and corresponding profiles of  $T_2$  (dashed red, right ordinate) and  $\partial_x P_2$  (dot-dashed blue, left ordinate) according to (1.98).

developed around  $d=\bar{d}$ , i.e. the spatial average of the nonlinear film surface position, whereas (2.24) has been developed around the primary flow  $d=d_0$ . These two reference states are not necessarily the same, and thus (1.95) and (1.96) are solved twice, once for  $\bar{d}$  corresponding to the nonlinear TWS and once for  $\bar{d} \equiv d_0$ .

Figure 2.9 shows an example of such a fully-coupled TWS computation. Panel 2.9a represents profiles of the velocity contributions  $U_0$  and  $U_1$  in (1.99), which display the typical shapes associated with turbulent flow, and panel 2.9b represents the associated (normalized) profiles of  $T_2$  (dashed red) and  $\partial_x P_2$  (dot-dashed blue) according to (1.98) for a representative surface wave (solid black line).

In the case of transient computations on an open domain with inlet/outlet conditions, the inter-phase coupling quantities  $\partial_\eta U_0|_{\eta=\bar{d}}$ ,  $\partial_\eta U_1|_{\eta=\bar{d}}$ ,  $C_0$ , and  $C_1$  are provided via an external look-up table. This table is generated by solving (1.95) and (1.96) via numerical continuation using `Auto07P`. Choosing  $Re_2$  as the continuation parameter for the look-up table, allows to vary the gas flow rate in a given open-domain computation, e.g. to reproduce a particular experimental protocol. In contrast to our TWS computations, it is not straightforward to define a representative  $\bar{d}$  for the solution of the gas-side problem, as surface waves evolve spatially in an open-domain computation and may undergo dramatic alterations, e.g. via coalescence. We thus choose  $\bar{d}=d_0$ , assuming that the average film thickness of the nonlinear wavy film remains close to that of the primary flow.



## 2.3 Validity range of our WRIBL models

In this section, we check the consistency of the planar (1.27) and cylindrical (1.48) WRIBL models derived in sections 1.1 and 1.2 for the configurations in figures 1.2 and 1.3, and we ascertain their range of validity. This is done in two steps for each of the two models<sup>5</sup>.

First, we confront linear stability predictions obtained from our WRIBL models with solutions of the corresponding OS problem, as obtained from the full linearized Navier-Stokes equations (see chapter 3). We use both spatial and temporal stability formulations, depending on the situation. Numerical details of the different linear stability calculations are given in section 2.1 and chapter 3. Second, we compare nonlinear WRIBL computations with DNS based on the full Navier-Stokes equations (see chapter 4). Details of the employed numerical procedures are given in section 2.2 and chapter 4. Physical properties for all fluids used in our computations are given in table 2.1.

Section 2.3.1 is dedicated to our planar WRIBL model and section 2.3.2 to our cylindrical one.

### 2.3.1 Planar model

Figure 2.10 reports linear stability predictions for two benchmark cases from the literature, corresponding to the two configurations in figure 1.2:

- (i) A falling liquid film flowing down an inclined plane in a passive atmosphere (Brevdo *et al.*, 1999), where  $\Pi_\rho = \Pi_\mu = 0$ . The flow is gravity-driven (panel 1.2a) and subject to the convective Kapitza instability (Brooke Benjamin, 1957; Yih, 1963).
- (ii) Plane Poiseuille flow of two superimposed equal-density fluids through a rectangular channel without gravity (Yiantsios & Higgins, 1988). The flow is pressure-driven (panel 1.2b) and subject to the convective Yih instability (Yih, 1967).

Panels 2.10a and 2.10b report spatial linear stability predictions for case (i). They represent dispersion curves for the spatial growth rate  $-k_i$  and wave number  $k_r$  in terms of the purely real angular velocity  $\omega$ . Four values of the liquid Reynolds number  $\text{Re}_1$  are considered. For small to moderate  $\text{Re}_1$ , our WRIBL predictions (dashed lines) are in excellent agreement with the OS data (solid lines) over the entire range of unstable wave frequencies<sup>6</sup>. At larger values ( $\text{Re}_1 \geq 40$ ), agreement starts to deteriorate due to the increasing relevance of order  $\epsilon^2$  inertial corrections, e.g.  $\epsilon \text{Re}_k \int w_k \hat{u}_k \partial_x u_k^{(1)} dy$  in (1.12), which we have neglected.

As mentioned in section 1.1, our WRIBL model collapses to the model of Ruyer-Quil & Manneville (2002) in the limit of a passive outer phase ( $\Pi_\rho = \Pi_\mu = 0$ ). That model having been checked versus the OS stability data of Brevdo *et al.* (1999), our comparisons in panels 2.10a and 2.10b do not add anything new. They simply verify that we have not made any implementation errors.

<sup>5</sup>See Denner *et al.* (2018) for the validity range of single-phase WRIBL models.

<sup>6</sup>We have verified that our OS calculations match those reported in figure 9 of Brevdo *et al.* (1999).

Liquids (fluid 1)	$\rho$ (kg/m <sup>3</sup> )	$\mu$ (Pas)	$\nu$ (m <sup>2</sup> /s)	$\sigma$ (N/m)	Ka
Water I	1000.0	$1.00 \cdot 10^{-3}$	$1.00 \cdot 10^{-6}$	0.0769	3592.3
Water II	998.2	$1.00 \cdot 10^{-3}$	$1.00 \cdot 10^{-6}$	0.0728	3406.9
Water III	997.07	$0.89 \cdot 10^{-3}$	$0.893 \cdot 10^{-6}$	0.07201	3923.2
Water IV	998.3	$1.03 \cdot 10^{-3}$	$1.035 \cdot 10^{-6}$	0.071	3174.4
DMSO(83.11%)-water	1098.3	$3.13 \cdot 10^{-3}$	$2.85 \cdot 10^{-6}$	0.0484	509.5
Glycerol(54%)-water	1070	$6.71 \cdot 10^{-3}$	$6.27 \cdot 10^{-6}$	0.067	253.0
Glycerol(89%)-water	1223.9	0.167	$1.36 \cdot 10^{-4}$	0.065	3.532
Glycerol(99%)-water	1260.7	1.049	$8.32 \cdot 10^{-4}$	0.064	0.303
Alcohol I	1000	$2.02 \cdot 10^{-3}$	$2.02 \cdot 10^{-6}$	$\rho 29 \cdot 10^{-6}$	530.5
Mucus I	1098.3	$3.1 \cdot 10^{-3}$	$2.8 \cdot 10^{-6}$	0.031	330.5
Mucus II	1000	$13 \cdot 10^{-3}$	$1.3 \cdot 10^{-5}$	0.020	30.6
Mucus III	1000	$1 \cdot 10^{-3}$	$1 \cdot 10^{-6}$	0.020	934.3
Mucus IV	1223.9	0.01	$8.2 \cdot 10^{-6}$	0.025	58.0
Silicone oil I	924.3	$10.7 \cdot 10^{-3}$	$11.6 \cdot 10^{-6}$	0.01887	36.32
Silicone oil II	873	$1.75 \cdot 10^{-3}$	$2.0 \cdot 10^{-6}$	0.0183	388.6
Silicone oil III	900	$4.5 \cdot 10^{-3}$	$5 \cdot 10^{-6}$	0.020	121.4
Silicone oil IV	970	12.9	$1.33 \cdot 10^{-3}$	0.0215	$3.29 \cdot 10^{-3}$
Gases (fluid 2)	$\rho$ (kg/m <sup>3</sup> )	$\mu$ (Pas)	$\nu$ (m <sup>2</sup> /s)	$\sigma$ (N/m)	Ka
Air I	1.200	$1.80 \cdot 10^{-5}$	$15.00 \cdot 10^{-6}$	-	-
Air II	1.185	$1.85 \cdot 10^{-5}$	$15.58 \cdot 10^{-6}$	-	-
Air III	1.000	$1.00 \cdot 10^{-5}$	$10.00 \cdot 10^{-6}$	-	-
Air IV	1.205	$1.82 \cdot 10^{-5}$	$15.13 \cdot 10^{-6}$	-	-
Air V	1.209	$1.81 \cdot 10^{-5}$	$14.93 \cdot 10^{-6}$	-	-
Liquid/liquid	$\rho$ (kg/m <sup>3</sup> )	$\mu$ (Pas)	$\nu$ (m <sup>2</sup> /s)	$\sigma_{12}$ (N/m)	Ka <sub>k</sub>
1 Glycerol(96%)-water	1251	0.624	$5.00 \cdot 10^{-4}$	0.030	0.2832
2 Silicone oil V	1191	$6.24 \cdot 10^{-3}$	$5.24 \cdot 10^{-6}$	0.030	129.3
1 Water IV	997.1	$0.89 \cdot 10^{-3}$	$0.89 \cdot 10^{-6}$	0.035	1908.0
2 Silicone oil VI	1191	0.005	$4.20 \cdot 10^{-6}$	0.035	202.7
1 Glycerol(80%)-water	1180	0.034	$28.8 \cdot 10^{-6}$	0.01227	2.57
2 SAE 30 oil	850	0.103	$1.21 \cdot 10^{-4}$	0.01227	1.12
1 Water	995	0.001	$1.0 \cdot 10^{-6}$	0.026	1212.5
2 Oil	905	0.601	$6.64 \cdot 10^{-4}$	0.026	0.23

Table 2.1: Properties of liquids and gases used in our computations. For liquid/gas combinations, we give  $Ka = \sigma \rho_1^{-1} g^{-1/3} \nu_1^{-4/3}$ , where  $\sigma$  is the surface tension of the liquid. For liquid/liquid combinations, we give  $Ka_k = \sigma_{12} \rho_k^{-1} g^{-1/3} \nu_k^{-4/3}$ , where  $\sigma_{12}$  is the interfacial tension between the two liquids.

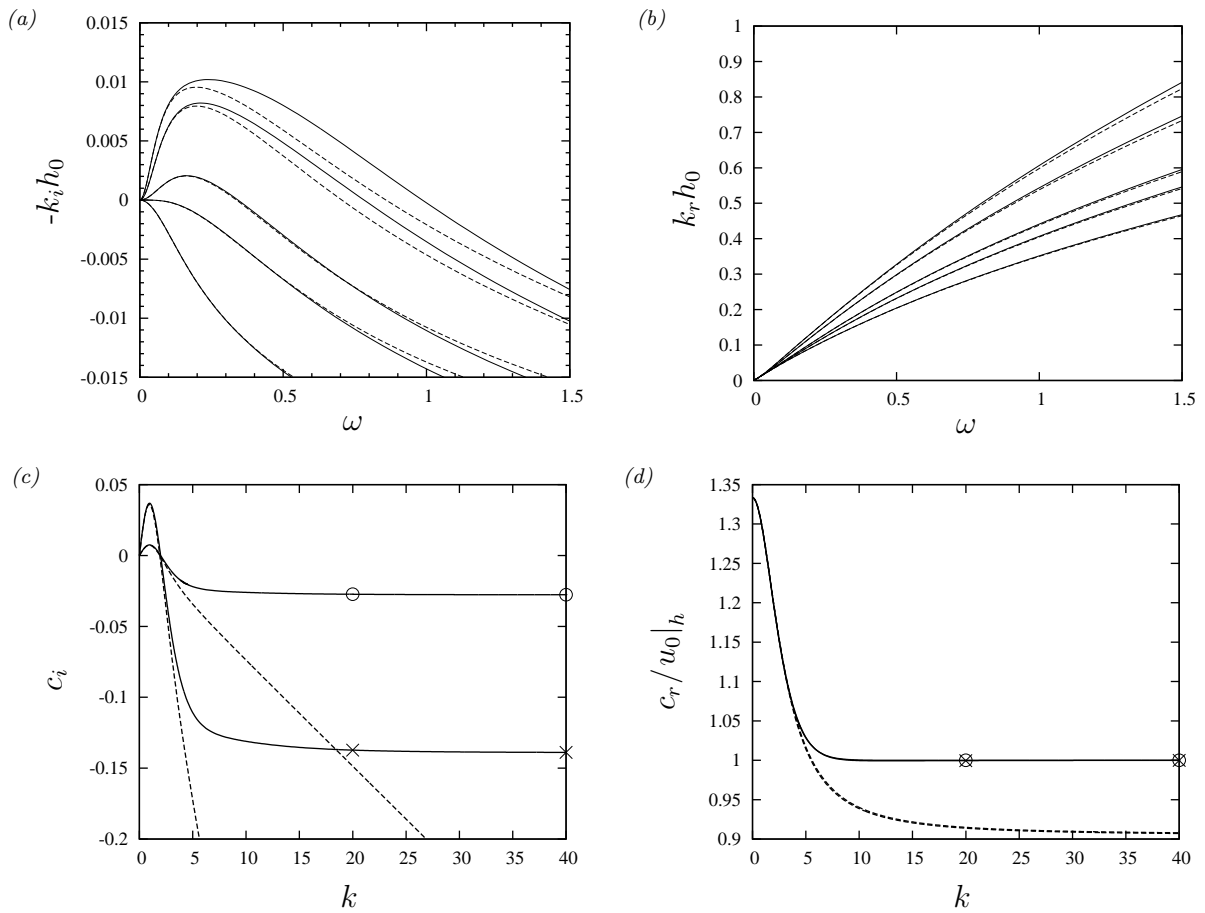


Figure 2.10: Linear stability predictions for two benchmark cases from the literature corresponding to the configurations in figure 1.2. Dashed lines: WRIBL model; solid lines: OS problem. (a,b) Spatial stability calculations. Inclined falling liquid film in a passive atmosphere according to figure 9 in Brevdo *et al.* (1999):  $\Pi_\rho = \Pi_\mu = 0$ ,  $\phi = 4.6^\circ$ ,  $\text{Ka} = 331.85$ . From bottom to top:  $(3/2)\text{Re}_1 = 10$ ,  $(5/4)\cot(\phi)$ , 20, 40, and 60; (c,d) temporal stability calculations. Pressure-driven two-layer channel flow:  $h_0 = 0.5$ ,  $\Pi_\rho = 1$ ,  $\Pi_\mu = 0.2$ . Symbols: OS data reported by Tilley *et al.* (1994a). Crosses:  $\text{La} = \sigma H^* \rho_1 / \mu_1^2 = 0.2$ ,  $q_{\text{tot}} \text{Re}_1 = 1.6$ ; open circles:  $\text{La} = 0.008$ ,  $q_{\text{tot}} \text{Re}_1 = 0.32$ .

In case (ii), the second fluid plays an essential role in the instability mechanism, and thus the two-phase nature of our WRIBL model comes into play. Panels 2.10c and 2.10d report linear stability predictions for two parameter sets considered in the OS calculations of Yiantsios & Higgins (1988) and Tilley *et al.* (1994b). In accordance with these works, we use a temporal stability formulation, even though the instability is convective. The two panels represent dispersion curves of the imaginary part  $c_i$  and real part  $c_r$  of the complex wave celerity  $c = \omega/k$  in terms of the purely real wave number  $k$ . Two different values of the total flow rate  $q_{\text{tot}}$  are considered. Dashed lines represent predictions of our WRIBL model, solid lines our OS calculations, and symbols mark numeric values of OS

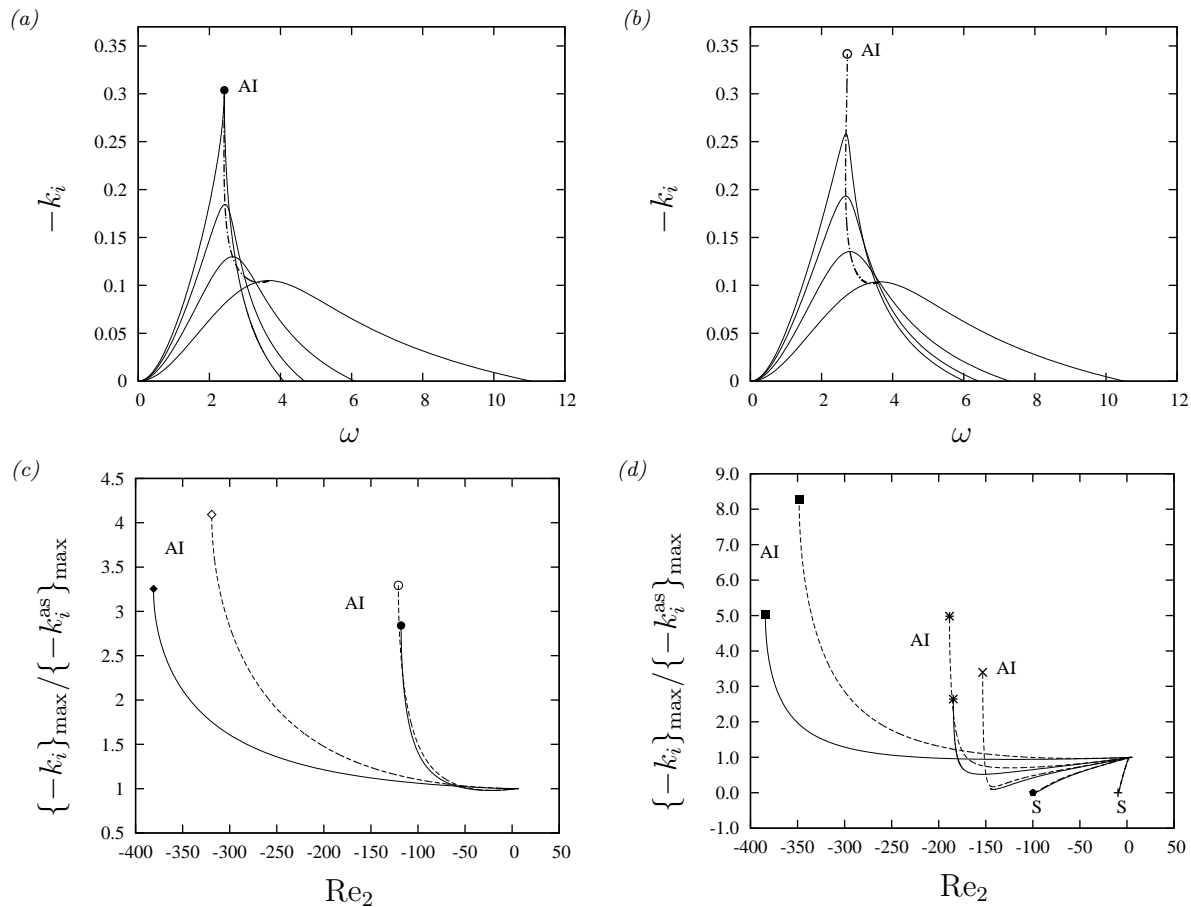


Figure 2.11: Spatial linear stability predictions for the configuration in panel 1.2a. Vertical (panels *a-c*) or inclined (panel *d*) falling liquid film in contact with an increasingly strong counter-current gas flow:  $Ka=509.5$  (DMSO-water and air II in table 2.1),  $Re_1=15$ . (*a*) Dispersion curves (solid lines) of the spatial growth rate  $-k_i$ , from OS calculations. From right to left:  $M=1$ ,  $Re_2=-90$ ,  $-110$ , and  $-118$ . The dot-dashed curve traces the locus of  $\{-k_i\}_{\max}$ , up to the onset of absolute instability (AI); (*b*) corresponding WRIBL predictions; (*c-d*) maximal growth rate in terms of  $Re_2$ , in relation to the aerostatic ( $M=1$ ) limit  $\{-k_i^{as}\}_{\max}$ . Dashed: WRIBL; solid: OS; (*c*) vertical film:  $\phi=90^\circ$ . Circles:  $H^*=1$  mm; diamonds:  $H^*=1.5$  mm; (*d*) inclined film:  $\phi=10^\circ$ . Squares:  $H^*=2.35$  mm; asterisks:  $H^*=1.88$  mm; crosses:  $H^*=1.78$  mm; pentagons:  $H^*=1.69$  mm; plus signs:  $H^*=1.22$  mm. “S” indicates linear suppression of the Kapitza instability.

calculations reported in Tilley *et al.* (1994a). Agreement between our WRIBL and OS calculations is very good over the entire range of unstable wave numbers ( $c_i > 0$ ). For greater values of  $k$ , the long-wave approximation breaks down and our WRIBL predictions deteriorate. This occurs beyond  $k \approx 5$ , where the wavelength  $\Lambda$  has become comparable to the channel height.

We turn now to two liquid-gas flows that will be studied in sections 6.2 and 8.3. First,

figure 2.11 reports spatial linear stability predictions for a vertical/inclined falling liquid film subject to a strongly confined counter-current laminar gas flow (configuration in panel 1.2a). The liquid corresponds to an aqueous solution of dimethylsulfoxide (DMSO) typically used in experiments (Dietze *et al.*, 2009) and the gas is ambient air. The liquid Reynolds number is constant at  $Re_1=15$ , while the gas Reynolds number  $Re_2$ , which is negative for counter-current flow, is varied such as to produce an increasingly strong counter-current gas flow.

Panels 2.11a (OS) and 2.11b (WRIBL) represent dispersion curves (solid lines) of the spatial growth rate obtained for a vertically falling liquid film. Different curves correspond to different values of  $Re_2$ . The dashed line in each of the panels traces the locus of the maximum growth rate  $\{-k_i\}_{\max}$ . As the magnitude of  $Re_2$  increases,  $\{-k_i\}_{\max}$  becomes greater and eventually diverges, indicating the onset of AI. Vellingiri *et al.* (2015) and Schmidt *et al.* (2016) have demonstrated with OS calculations the transition from convective to absolute instability for essentially the same problem. However, Vellingiri *et al.* (2015) considered turbulent flow in the gas, and Schmidt *et al.* (2016) considered only moderate density ( $\Pi_\rho=10$ ) and viscosity ( $\Pi_\mu=5$ ) contrasts. Our OS calculations in panel 2.11b thus complete this picture for laminar liquid-gas flows.

Our WRIBL model (panel 2.11b) reproduces the OS data (panel 2.11a) quite accurately, except for the decrease of the cut-off wave number  $k_c$  with increasingly negative  $Re_2$ , which is predicted only qualitatively. This stabilizing effect coincides with an increase in  $\{-k_i\}_{\max}$ , which implies a destabilization. The coincidence of stabilizing and destabilizing effects has been reported by Alekseenko *et al.* (2009) for falling liquid films subject to a turbulent counter-current gas flow. Our model captures this intricate behaviour well. Direct comparison between the maximum growth rate curves in panels 2.11a and 2.11b is made in panel 2.11c, where they have been plotted in terms of  $Re_2$ , for two different channel heights  $H^*$ . In both cases, agreement is very good up to  $Re_2 \approx -120$ . For  $H^*=1$  mm (curves with circles), AI sets in within this range and thus the WRIBL model accurately predicts this limit. For the less confined case ( $H^*=1.5$  mm, diamonds), absolute instability sets in at much greater  $|Re_2|$ , where the model prediction has deteriorated due to the increasing relevance of inertial corrections. Nonetheless, our WRIBL prediction remains in qualitative agreement.

Panel 2.11d represents similar curves for a falling liquid film inclined at  $\phi=10^\circ$  over a wide range of confinement levels. For the weakest confinement (squares), the growth rate increases monotonically with  $|Re_2|$ . In this sense, the effect of the counter-current gas flow is destabilizing. For intermediate confinement levels (asterisks and crosses), the effect of the gas is non-monotonic, stabilization occurring at low flow rates and destabilization at greater flow rates<sup>7</sup>. For strong confinement (pentagons and plus signs), the gas monotonically stabilizes the film, up to the full suppression of the Kapitza instability (S). We have studied this phenomenon in Lavalley *et al.* (2019), which will be discussed in section 6.1. The different behaviours observed in panel 2.11d are captured by our WRIBL model

---

<sup>7</sup>Vellingiri *et al.* (2015) and Trifonov (2017a) have also demonstrated a non-monotonic behaviour, however, based on the cut-off wave number  $k_c$

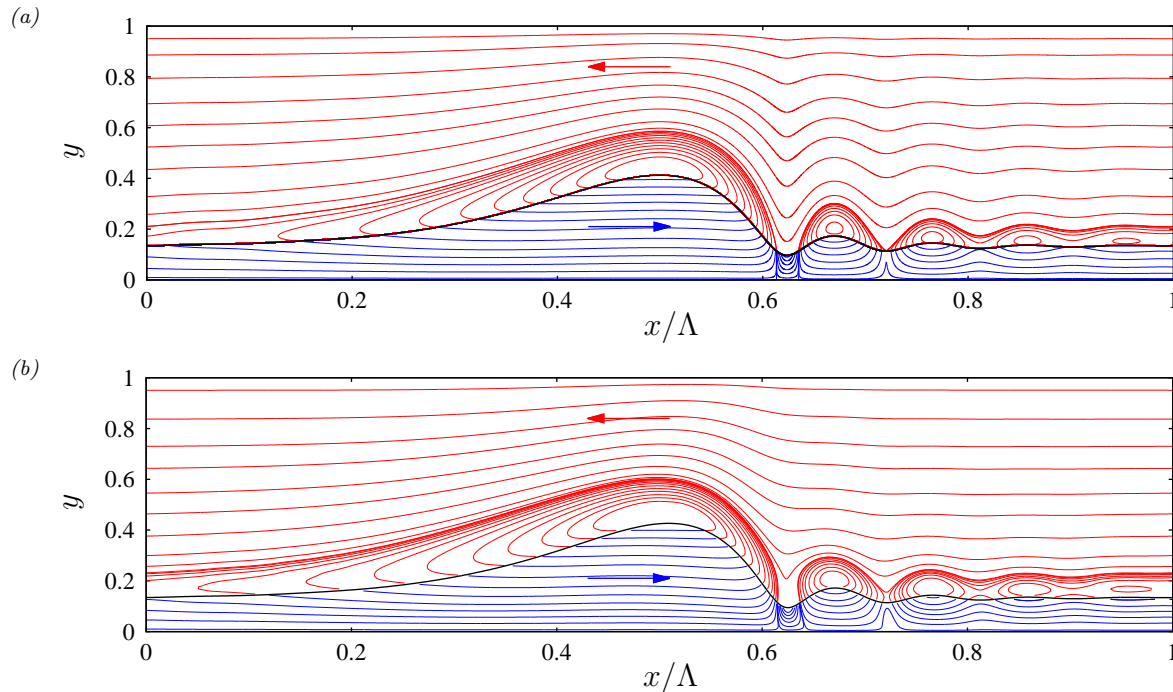


Figure 2.12: Nonlinear travelling wave for the configuration in panel 1.2a. Vertically falling liquid film in contact with a counter-current air flow:  $H^*=1.5$  mm,  $f^*=15.86$  Hz,  $Ka=509.5$  (DMSO-water and air II in table 2.1),  $Re_1=15.07$ ,  $Re_2=-54.46$ . Streamlines in the wall-fixed reference frame. (a) WRIBL computation of TWS with `Auto07P`:  $\Lambda=13.75$ , liquid holdup  $\bar{h}=0.200$ . Streamfunction constructed with (1.17) and (1.22); (b) transient DNS with periodicity boundary conditions:  $\Lambda=13.67$ , liquid holdup  $\bar{h}=0.201$ .

(dashed lines) in good agreement with the OS predictions (solid lines). Again, agreement improves as the confinement increases and the long-wave approximation becomes more accurate.

Figure 2.12 compares computations of a nonlinear saturated-amplitude travelling wave on a vertically falling liquid film sheared by a counter-current gas flow. The WRIBL prediction (panel 2.12a) was obtained via numerical continuation of TWS with `Auto07P` (see section 2.2) and the transient periodic DNS (panel 2.12b) was done with `Gerris` (see chapter 4). The control parameters  $f$ ,  $Re_1$ , and  $Re_2$  in the WRIBL continuation were set according to the converged values of the DNS. Blue (liquid phase) and red (gas phase) lines represent streamlines in the wall-fixed reference frame<sup>8</sup>. We see that our WRIBL model accurately predicts the different vortical structures generated by the surface wave. These will be discussed in section 6.2.

Our second example of liquid-gas flows concerns the pressure-driven plane Poiseuille flow of two superimposed layers of water and air without gravity (configuration in panel

<sup>8</sup>For the WRIBL prediction, these were computed with the base flow velocity components  $\hat{u}$  (1.17) and  $\hat{v}$  (1.22).

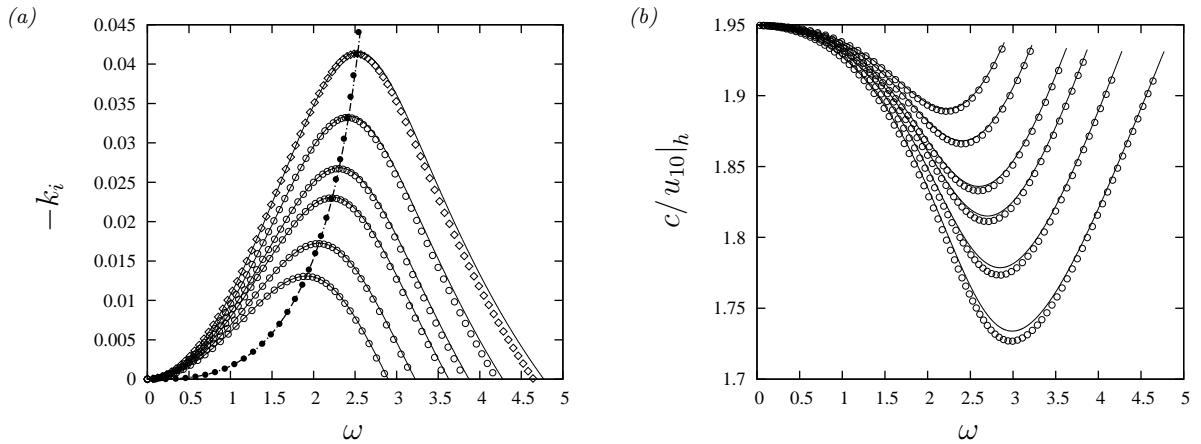


Figure 2.13: Spatial linear stability predictions for the configuration in panel 1.2b. Pressure-driven gravity-free plane Poiseuille flow of two superimposed layers of water (lower layer) and air (upper layer). Conditions according to figure 7 in Frank (2008):  $h_0=1/3$ ,  $Ka=3592.3$  (water I and air III in table 2.1),  $\Pi_\rho=10^{-3}$ ,  $\Pi_\mu=10^{-2}$ . Lines: OS; symbols: WRIBL. (a) Dispersion curves (solid lines; open symbols) of the spatial growth rate  $-k_i$ . From lowest to greatest growth rate:  $Re_1|Re_2=3.5|28.8$ ,  $3.9|32.1$ ,  $4.4|36.1$ ,  $4.7|38.6$ ,  $5.2|42.7$ , and  $5.8|47.7$ . Dot-dashed line and filled circles trace the locus of maximum growth rate; (b) corresponding dispersion curves of the wave celerity  $c=\omega/k_r$  normalized with the liquid surface velocity  $u_{10}|_h$ .

1.2b), according to the conditions in Frank (2008). Here, the Yih instability, which results from the viscosity contrast between the two fluids, is responsible for generating surface waves. Figure 2.13 reports spatial linear stability predictions for this case, as obtained from our WRIBL (symbols) and OS (lines) calculations for different values of  $Re_1$ . Our model accurately predicts the dispersion curves of the growth rate  $-k_i$  and wave celerity  $c=\omega/k_r$ , as well as the variation of the maximal growth rate (dot-dashed line and filled circles).

Finally, figure 2.14 confronts WRIBL (panel 2.14a) and DNS (panel 2.14b) predictions of a nonlinear travelling wave for the same configuration at  $Re_1=5.8$ ,  $\Lambda^*=26.0$  mm, and  $\bar{h}=1/3$ . Blue (liquid) and red (gas) lines again represent streamlines in the wall-fixed reference frame. Our WRIBL model accurately predicts the shape and amplitude of the wave as well as the flow structure in the liquid and gas. In particular, the flow separation zone at the first capillary trough is captured correctly. Such zones are typically observed in falling liquid films (figure 2.12), and it is interesting to note that they also occur in pressure-driven films. We will discuss surface waves resulting from the Yih instability in section 8.2.

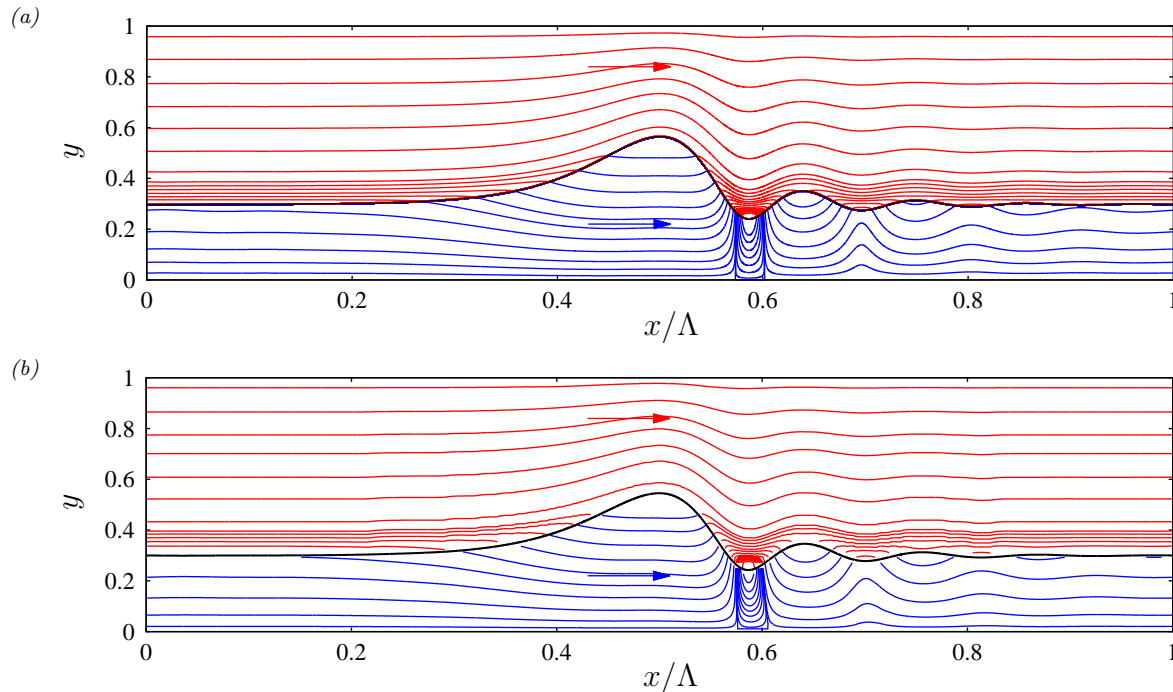


Figure 2.14: Nonlinear travelling waves for the configuration in panel 1.2b. Pressure-driven plane Poiseuille flow of two superimposed layers of water and air without gravity:  $H^*=0.39$  mm,  $Ka=3592.3$  (water I and air III in table 2.1),  $\Lambda=200/3$ ,  $Re_1=5.97$ ,  $\bar{h}=1/3$ . Streamlines in the wall-fixed reference frame. (a) WRIBL continuation of TWS with Auto07P:  $M=-256.0$ ,  $Re_2=33.86$ . Streamfunction constructed with (1.17) and (1.22); (b) transient DNS with periodicity boundary conditions:  $M=-244.8$ ,  $Re_2=31.46$ .

### 2.3.2 Cylindrical model

We start by confronting our cylindrical WRIBL model with OS linear stability predictions for several benchmark configurations from the literature in figure 2.15. The first three panels correspond to the vertical configuration (sketched in panel 1.3a), where a falling liquid film is in contact with a gas (panel 2.15a) or a liquid (panels 2.15b and 2.15c) core. Agreement for the liquid/gas combination (Camassa *et al.*, 2014) is excellent, whereas for the liquid/liquid free-fall experiment of Chen *et al.* (1990) it deteriorates rather quickly with increasing  $q_{tot}$  (decreasing  $d_0$  in panel 2.15b)<sup>9</sup>. In panel 2.15c, we have reproduced with our WRIBL model two curves from figure 3 in Hickox (1971). These represent  $c_1$  from the asymptotic expansion of the complex celerity  $c=c_0 + c_1k + \mathcal{O}(k^2)$  in the framework of temporal stability analysis. Agreement with the data of Hickox (not shown here) is good, but not perfect, as a slight discrepancy occurs for the dashed curve. Because our WRIBL model is designed to predict  $c_1$  exactly, we attribute this discrepancy to numerical errors.

<sup>9</sup>However, we believe that liquid/liquid systems can be studied with our WRIBL model, by focussing on narrower tubes. We point out that the dominant instability mode for the conditions in panel 2.15b is a long-wave mode (Preziosi *et al.*, 1989).



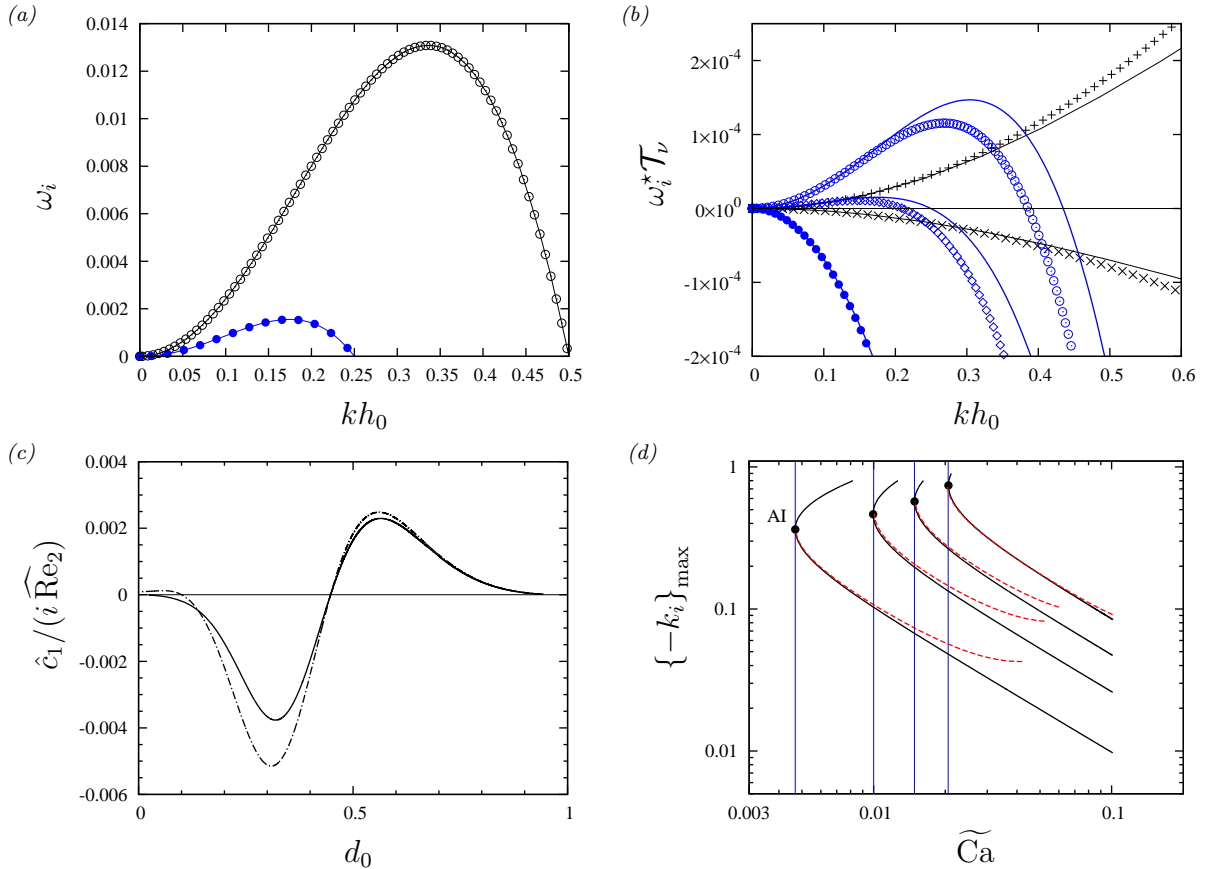


Figure 2.15: Linear stability of core-annular flows through cylindrical tubes (configuration in figure 1.3). Symbols: OS, lines: WRIBL. (a) Falling liquid film (Camassa *et al.*, 2014):  $\text{Ka}=3.29 \cdot 10^{-3}$  (silicone oil IV, air I in table 2.1),  $R^*=5$  mm,  $M=1$ . Filled circles:  $d_0=2/3$ , open circles:  $d_0=4/5$ ; (b,c) vertical liquid/liquid flows according to Chen *et al.* (1990) and Hickox (1971); (b)  $\text{Ka}_1=2.57$ ,  $\Pi_\mu=3.03$ ,  $\Pi_\rho=0.72$  (glycerol(80%)-water, SAE 30 oil),  $R^*=3.175$  mm,  $M=0$ . Filled circles:  $d_0^{-1}=1.67$ , diamonds:  $d_0^{-1}=1.86$ , open circles:  $d_0^{-1}=1.9$ . Crosses ( $\Pi_\rho^{-1}=1.1$ ) and plus signs ( $\Pi_\rho^{-1}=0.8$ ):  $\text{We}=0$ ,  $\Pi_\mu=1$ ,  $R_g=d_0^*(d_0^*g)^{1/2}/\nu_2=10$ ; (c)  $\Pi_\mu^{-1}=20$ ,  $R^*=25.4$  mm,  $M=0.049$ ,  $\text{We}=0$ . Coefficient  $c_1$  in asymptotic expansion of wave speed  $c=c_0+c_1k$ . Hat symbol indicates rescaling with  $\mathcal{L}=d_0^*$  and  $\mathcal{U}=u^*|_{r^*=0}$ . Solid:  $\Pi_\rho=1$ , dashed:  $\Pi_\rho^{-1}=0.75$ ; (d) pressure-driven flow (Salin & Talon, 2019):  $\text{Fr}^{-1}=0$ ,  $\Pi_\mu^{-1}=10$ ,  $\Pi_\rho=1$ ,  $R^*=150$   $\mu\text{m}$ ,  $\text{Ka}=1.98$ . Dashed: full WRIBL model, solid: inertialess limit. From top to bottom:  $d_0=0.4, 0.5, 0.6$ , and  $0.75$ . Vertical lines: AI limit from Salin & Talon (2019) for different  $\widetilde{\text{Ca}}=(q_{\text{tot}}^*/\pi/R^{*2})\mu_2/\sigma$ .

As  $d_0$  intervenes both in the ordinate and abscissa values of panel 2.15c, the presented curves are quite sensitive to such errors.

Panel 2.15d corresponds to pressure-driven core-annular flow without gravity. This case allows to check the AI bound predicted by our WRIBL model based on a spatial stability formulation (following the approach outlined in section 2.1.1) against the full

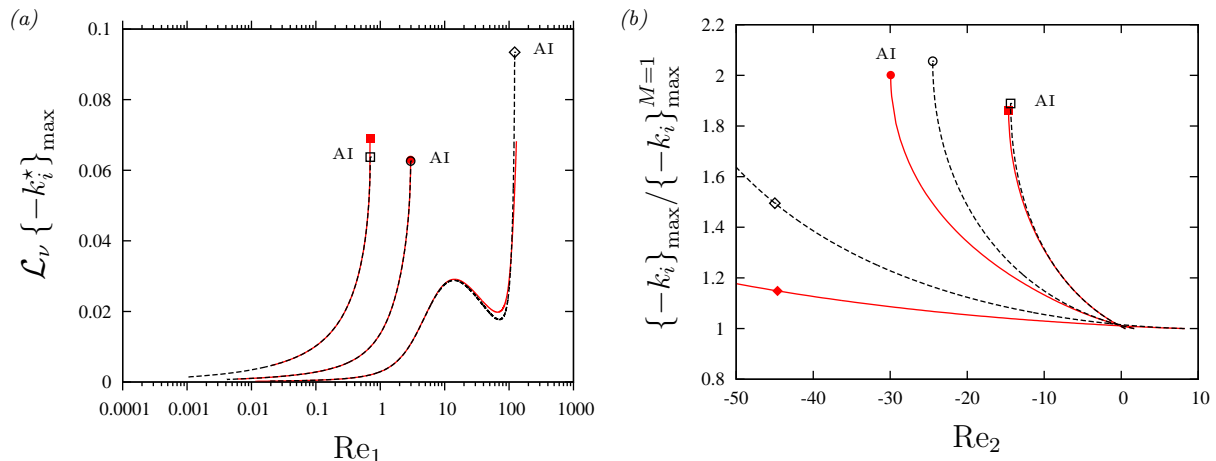


Figure 2.16: Validity range of our cylindrical WRIBL model (1.48). Annular falling liquid film in contact with air within a vertical cylindrical tube (panel 1.3a):  $Ka=121.4$  (silicone oil III and air I in table 2.1). Maximum spatial growth rate from WRIBL (dashed black lines) and OS (solid red lines) linear stability calculations. (a) Aerostatic pressure drop:  $M=1$ . Diamonds:  $R^*=1.5$  mm; circles:  $R^*=1$  mm; squares:  $R^*=0.75$  mm; (b) counter-current gas. Diamonds:  $Re_1=15$ ,  $R^*=1.5$  mm; circles:  $Re_1=2$ ,  $R^*=1$  mm; squares:  $Re_1=0.5$ ,  $R^*=0.75$  mm.

spatio-temporal analysis of Salin & Talon (2019), who studied liquid/liquid flows. The limit points (filled circles) of our  $\partial_\omega(-k_i)=0$  maximum growth rate curves in panel 2.15d are in excellent agreement with the AI bounds obtained by Salin and Talon (vertical blue lines in panel 2.15d)<sup>10</sup>.

We turn now to flow conditions that have been studied in this work. Figure 2.16 establishes the validity range of our cylindrical WRIBL model in terms of  $R^*$ ,  $Re_1$ , and  $Re_2$  for a vertically falling liquid film in contact with a quiescent or counter-current air flow. The working liquid is a low-viscosity silicone oil, which is the most challenging of all studied liquids<sup>11</sup>. In the case of a quiescent gas (panel 2.16a), our WRIBL model accurately predicts the increase of the maximum growth rate  $\{-k_i\}_{\max}$  with increasing liquid Reynolds number  $Re_1$  versus OS calculations. This agreement holds up to the AI limit (marked by symbols) and for tube radii up to  $R^*=1.5$  mm. Before reaching the AI bound, the variation of  $\{-k_i\}_{\max}$  with increasing  $Re_1$  can be non-monotonic (curve with diamond), which is the result of two competing effects: an increase in the flow rate  $q_{10}$ , which favours convective instability and spatial growth, versus a decrease in core radius  $d_0$ , which favours AI and temporal growth.

A second effect favouring AI comes into play when the liquid film is subject to a counter-current gas flow, as shown in panel 2.16b, where we have varied the gas Reynolds

<sup>10</sup>We thank Dominique Salin for providing the data underlying figure 3 in Salin & Talon (2019).

<sup>11</sup>The other liquids all exhibit large viscosities and thus neither inertia nor the effect of the gas are relevant. Water/air systems were not considered here, because the Bond number  $Bo=\rho_1 g R^{*2}/\sigma$  for narrow tubes is very high, causing an early transition to AI.

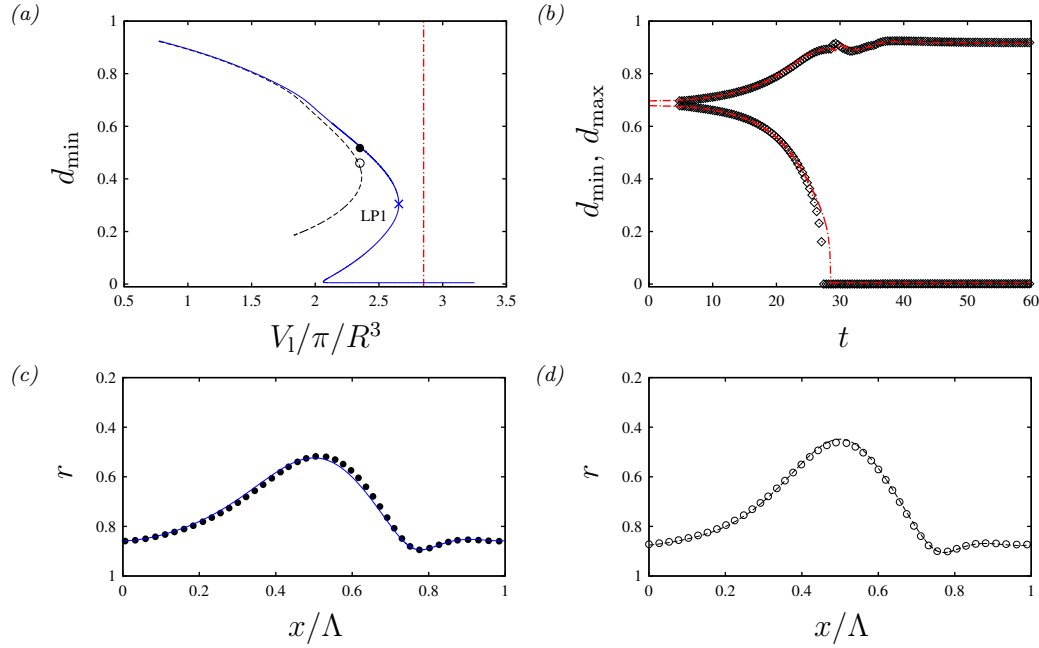


Figure 2.17: Annular falling liquid film in contact with an active core gas within a vertical cylindrical tube:  $Ka=121.4$  (silicone oil III and air I in table 2.1),  $R^*=1.5$  mm,  $\Lambda=5.4$ . (a) TWS obtained from WRIBL model (lines) and DNS with **Gerris** ( $V_1/\pi/R^3=2.35$ , circles). Blue solid line and filled circle:  $M=1$ ; dashed black line and open circle:  $Re_2=-17.3$ ; (b) occlusion and plug formation in transient periodic computations:  $M=1$  and  $V_1/\pi/R^3=2.85$  (vertical line in panel a). Red dot-dashed line: augmented WRIBL model (1.60); diamonds: DNS; (c-d) profiles of TWS from panel a:  $V_1/\pi/R^3=2.35$ . Lines: WRIBL; circles: DNS.

number  $Re_2$ . However, because the Kapitza number of the silicone oil is quite low ( $Ka=We Fr^{2/3} Re_1^{4/3}=121.4$ ), accuracy of our WRIBL model cannot be maintained up to the  $\|Rey_2$  values corresponding to AI, unless  $R^*$  is very small (curves with squares in panel 2.16b). Thus, we have limited our investigations to  $|Re_2|<17.5$ .

Nonetheless, figure 2.17 shows that such small gas flow rates suffice to significantly affect the nonlinear dynamics of a falling liquid film. For example, the gas can considerably precipitate the occlusion limit of TWS, as evidenced by the LPs of the dashed and solid blue curves in panel 2.17a. Our WRIBL model accurately predicts the TWS associated with these curves. This is shown in panels 2.17c ( $M=1$ ) and 2.17d ( $Re_2=-17.3$ ), which compare TWS profiles obtained from our WRIBL model with DNS data obtained with **Gerris** for the aerostatic and counter-current configurations at  $V_1/\pi/R^3=2.35$ . Figure 2.18 represents streamlines (in the wave-fixed reference frame) for the TWS in panels 2.17c and 2.17d. Both for the aerostatic configuration ( $M=1$ , panel 2.18a) and for the counter-current configuration ( $Re_2=-17.3$ , panel 2.18b), the streamline patterns predicted by our WRIBL model (upper halves of the graphs) are in good agreement with the DNS

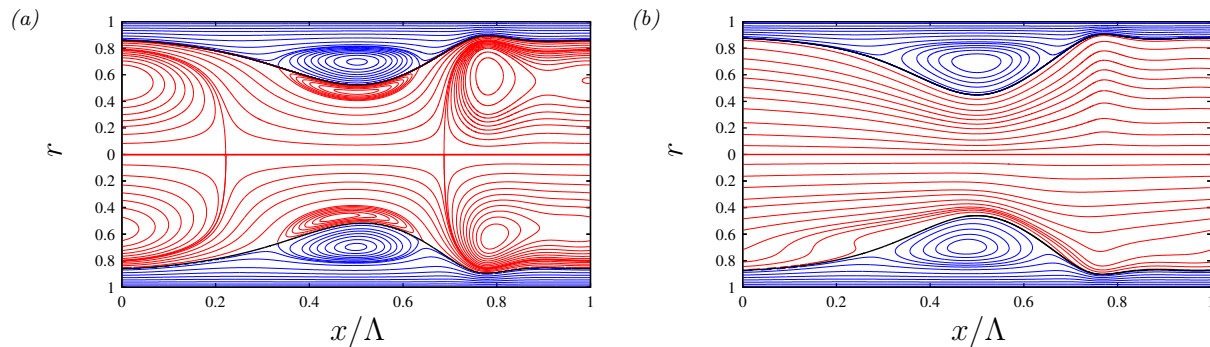


Figure 2.18: Streamlines in the wave-fixed reference frame corresponding to the TWS in panels 2.17c and 2.17d. Upper halves: WRIBL model; lower halves: DNS with **Gerris**. (a) Aerostatic gas pressure drop:  $M=1$ ; (b) counter-current gas flow:  $\text{Re}_2=-17.3$ .

(lower halves of the graphs).

Good agreement extends beyond the occlusion limit given by LP1 in panel 2.17a and the formation of liquid plugs. This is shown in panel 2.17b, which confronts transient periodic computations performed with our augmented WRIBL model (1.60) (dashed red line) and with **Gerris** (symbols), for  $M=1$  and  $V_1/\pi/R^3=2.35$  in panel 2.17a (vertical dot-dashed line there). As evidenced by the  $d_{\min}$  and  $d_{\max}$  time traces in panel 2.17b, our WRIBL model accurately predicts the dynamics of occlusion. The liquid plugs resulting from this occlusion are represented in figure 2.19. Here, we have represented streamlines in the moving reference frame within the liquid plugs (blue) and within the gas bubbles (red) trapped between two plugs. Our WRIBL model (panel 2.19a) accurately predicts the different vortices forming within the liquid and gas versus our DNS (panel 2.19b). The shapes of the plug and bubble are also predicted quite well, only that the ends of the gas bubble are much less steep in the WRIBL computation, which is a hard limitation imposed by the long-wave approximation underlying our model. Nonetheless, a spherical-cap approximation (Lamstaes & Eggers, 2017) can be employed to mitigate this discrepancy. In panel 2.19a (green dashed lines), we have applied the spherical-cap approximation for  $|\partial_x d| \geq 0.75$ , whereby the radius  $R_{\text{sc}}$  and center  $x_{\text{sc}}$  of the spherical cap are obtained by imposing continuity of  $d$  and  $\partial_x d$  across the patching point  $(x_p, d_p)$ , which is marked by crosses in panel 2.19a:

$$d_p^2 = R_{\text{sc}}^2 - (x_p - x_{\text{sc}})^2, \quad (2.50)$$

$$\partial_x d|_{x=x_p} = -\frac{(x_p - x_{\text{sc}})}{\{R_{\text{sc}}^2 - (x_p - x_{\text{sc}})^2\}^{1/2}}. \quad (2.51)$$

In our computations from figure 2.19,  $\Lambda$  and  $V_1$  were fixed, and, thus,  $\text{Re}_1$ ,  $\text{Re}_2$ , and the plug speed  $c$  are outcomes. The values obtained for these measures from our WRIBL computation ( $\text{Re}_1=30.8$ ,  $\text{Re}_2=14.6$ ,  $c^*=0.31$  m/s) are in excellent agreement with those of the DNS ( $\text{Re}_1=30.4$ ,  $\text{Re}_2=14.4$ ,  $c^*=0.30$  m/s).

Further validation of our augmented WRIBL model (1.60a) is provided in figure 2.20,

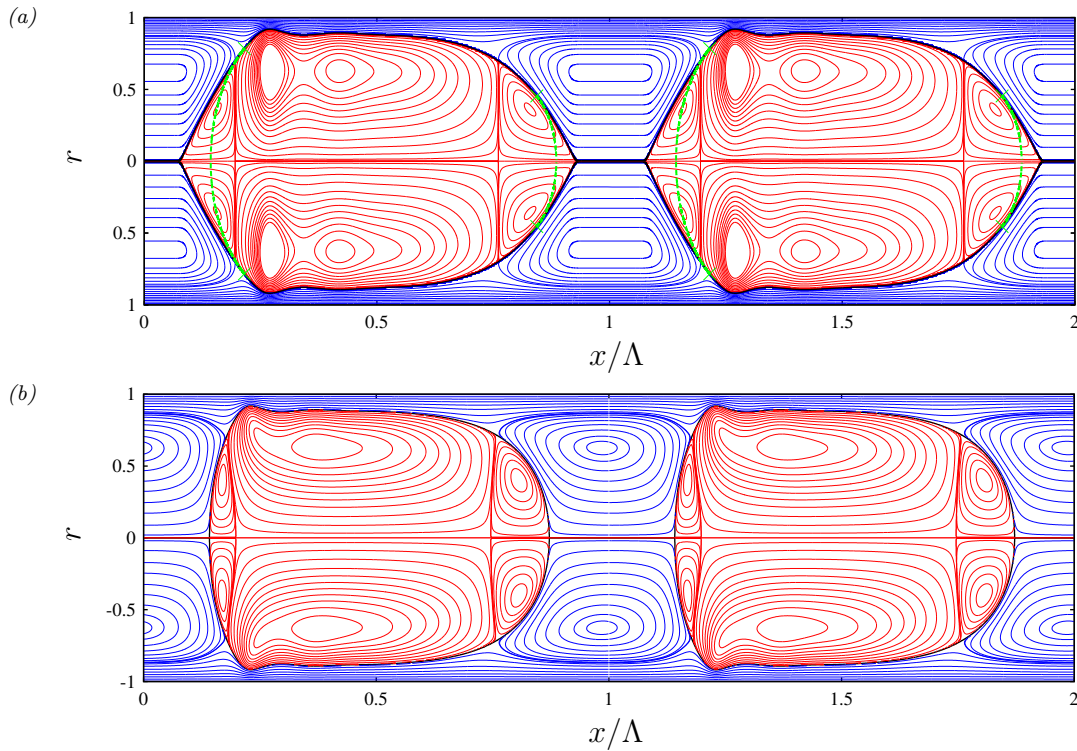


Figure 2.19: Liquid plugs forming in a vertical cylindrical tube. Streamlines in the reference frame moving with the plug speed  $c$ . Parameters according to panel 2.17b:  $\Lambda=5.4$ ,  $V_1/\pi/R^3=2.85$ ,  $M=1$ . (a) Transient periodic computation with our augmented WRIBL model (1.60):  $Re_1=30.8$ ,  $Re_2=14.6$ ,  $c^*=0.31$  m/s. Dashed green lines correspond to spherical-cap approximation (2.50) patched at points with  $|\partial_x d|=0.75$  (green crosses); (b) periodic DNS with `Gerris`:  $Re_1=30.4$ ,  $Re_2=14.4$ ,  $c^*=0.30$  m/s.

where we have reproduced numerically the experimental runs in panels 3a, 3b, and 3c of Camassa *et al.* (2014), who used a high-viscosity silicone oil in contact with air. Our WRIBL computations were performed on an open domain using a noisy inlet perturbation (2.38). Comparing the upper (experiment) and lower (WRIBL) graphs in panels 2.20a, 2.20b, and 2.20c, we conclude that our model correctly predicts all three experimental regimes. In particular, the number of liquid plugs in panel 2.20f, which are produced by occlusion events in the upper part of the tube and then convected downstream, is correctly predicted.

Several measures of these liquid plugs can be predicted quite accurately by TWS based on the linearly most-amplified frequency  $f=f_{\max}$ . This is shown in figure 2.21. Both the wavelength  $\Lambda$  (combined length of liquid plug and gas bubble), panel 2.21b, and the plug speed  $c=\Lambda f_{\max}$ , panel 2.21c, lie within the error bars of the experiments in panels 3c and 3d<sup>12</sup> of Camassa *et al.* (2014). These error bars were determined graphically from the

<sup>12</sup>The experiments from panel 3d in Camassa *et al.* (2014) are not shown in figure 2.20.

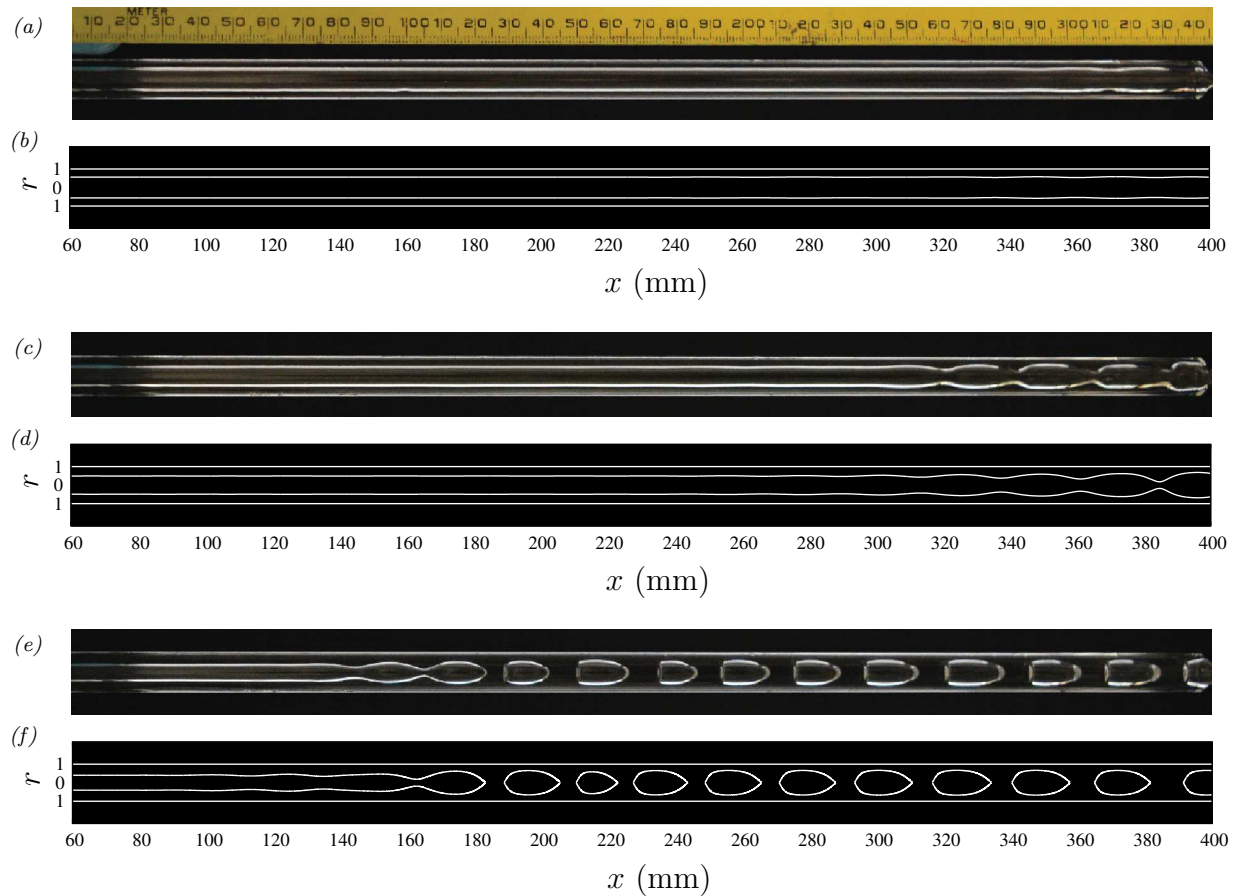


Figure 2.20: Highly-viscous falling liquid film in contact with air:  $Ka=3.29 \cdot 10^{-3}$  (silicone oil IV and air I in table 2.1),  $R^*=5$  mm,  $M=1$ . (a,c,e) Experiments from panels 3a, 3b, and 3c of Camassa *et al.* (2014); (b,d,f) open-domain computations (true to scale representation) based on our augmented WRIBL model (1.60a) for the representation of liquid plugs, using inlet noise (2.38):  $\epsilon_1=0$ ,  $\epsilon_2=10^{-4}$ ,  $d_{\text{crit}}=0.01$ . (a)  $Re_1=2.3 \cdot 10^{-4}$ , (b)  $Re_1=4.5 \cdot 10^{-4}$ , (c)  $Re_1=9.4 \cdot 10^{-4}$ .

variation of  $\Lambda$  between different plug/bubble pairs in the experimental photographs.

We point out that our computation in panel 2.20f was run with an imposed total flow rate  $Q_{\text{tot}}$ , obtained from the corresponding TWS in panel 2.21a. For this particular working liquid, our augmented WRIBL model did not behave well in open-domain or transient periodic computations with imposed gas pressure drop  $M=1$  beyond the occlusion limit. This seems to be linked to a degeneration of the pressure equation (2.43) in this special case, where the viscosity ratio is extremely small ( $\Pi_\mu=1.4 \cdot 10^{-6}$ ). The problem did not arise for other working liquids.

The gravity-free cylindrical configuration sketched in panel 1.3b is encompassed by the vertical configuration sketched in panel 1.3a. Nonetheless, it provides a valuable analytically tractable benchmark: Delaunay unduloids (Delaunay, 1841). These are sur-

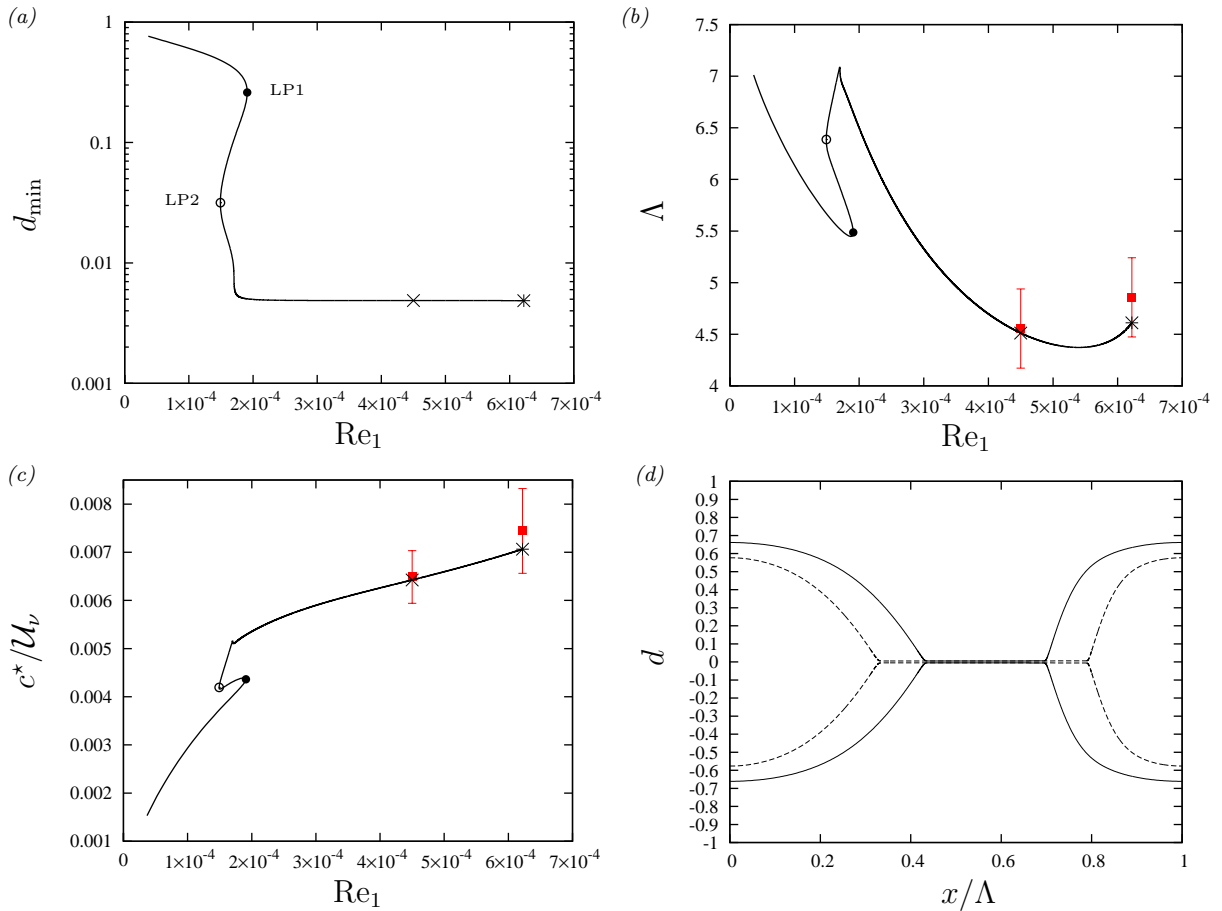


Figure 2.21: TWS at  $f=f_{\max}$  and  $M=1$  for the configuration in figure 2.20. Pseudo-plugs (lower branch beyond LP2 in panel *a*) obtained with our augmented model (1.60) versus experiments (filled squares) from panels 3c ( $Re_1=4.5 \cdot 10^{-4}$ ) and 3d ( $Re_1=6.22 \cdot 10^{-4}$ ) in Camassa *et al.* (2014). (*a*) Minimal core radius; (*b*) wavelength; (*c*) wave/plug speed; (*d*) plug profiles corresponding to crosses and asterisks in panels *a*, *b*, and *c*. Solid:  $Re_1=4.5 \cdot 10^{-4}$ ,  $f_{\max}^*=0.145$  Hz; dashed:  $Re_1=6.22 \cdot 10^{-4}$ ,  $f_{\max}^*=0.155$  Hz.

faces of revolution with constant curvature  $C$  (4.19). This benchmark allows to establish the validity range of the long-wave approximation underlying our WRIBL model, which results in the truncated curvature  $\kappa$  (1.42). Figure 2.22 represents unduloids obtained from numerical continuation with **Auto07P** based on the full curvature  $C$  (solid lines) and its long-wave approximation  $\kappa$  (dashed lines), following Everett & Haynes (1972). Good agreement is observed up to the limit point (LP) bounding the existence of unduloids. For liquid volumes  $V_1$  beyond this point, the only possible equilibrium shape is that of a liquid plug separated by two spherical bubbles. Those solutions lie on the y-axis at  $C=2$ . Between that branch and the LP, lies a branch of unstable unduloids, and it is here that our WRIBL model deteriorates. Such solutions contain increasingly steep portions of the interface as  $C$  increases (panel 2.22b), up to the formation of spherical bubbles at  $C=2$ ,

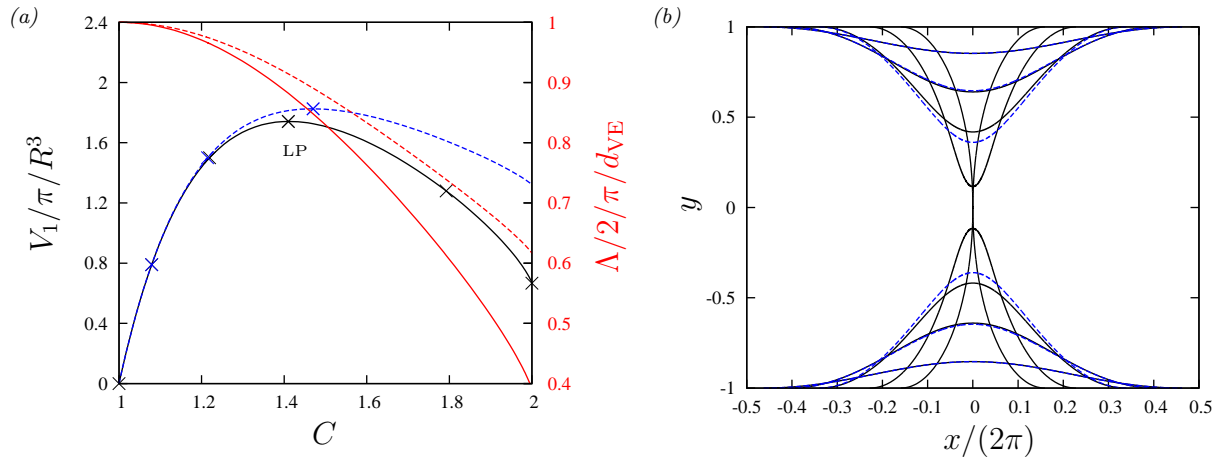


Figure 2.22: Delaunay unduloids (Delaunay, 1841): surfaces of revolution with constant curvature. (a) Family of solutions with  $d|_{-\Lambda/2}=1$ ,  $\partial_x d|_{-\Lambda/2}=0$  (Everett & Haynes, 1972). Solid: using full curvature  $C$  (4.19); dashed: using long-wave approximation  $C=\kappa$  (1.42). Lines with/without symbols correspond to left/right ordinate, and  $d_{VE}=(1 - V_1/\Lambda/\pi/R^3)^{1/2}$  is the volume-equivalent core radius; (b) profiles corresponding to crosses in panel a.

where  $\partial_x d$  diverges.

The unduloids represented in figure 2.22 belong to a particular family of solutions, which satisfy the boundary conditions:

$$d|_{-\Lambda/2} = 1, \quad (2.52)$$

$$\partial_x d|_{-\Lambda/2} = 0. \quad (2.53)$$

This implies that the film surface at the left unduloid trough connects smoothly to the tube wall at  $r=1$  (due to symmetry, the same applies at the right trough), which is the physically most-relevant configuration. According to panel 2.22b, the unduloid wavelength is always inferior or equal to the cut-off wavelength of the Plateau-Rayleigh instability ( $\Lambda=\Lambda^*/R^* \leq 2\pi$ ). Thus, unduloids can only form in a real system when the liquid film trough produced by primary instability fully drains, leaving behind a dry patch that increases in width until the film has retracted to the equilibrium length of the unduloid.

In figure 2.23, we have reproduced with our WRIBL model the transient periodic computations of Johnson *et al.* (1991), who considered a liquid film of Newtonian model mucus in contact with air within a pulmonary airway. Panels 2.23a and 2.23b correspond to a liquid volume of  $V_1/\Pi/R^3=1.14$ , i.e. below the unduloid threshold, and panels 2.23c and 2.23d correspond to  $V_1/\Pi/R^3=2.16$ , i.e. above the unduloid threshold. For both cases, our WRIBL computations (lines) agree well with our own DNS (symbols), correctly reproducing the unduloid/occlusion transition.

To conclude this chapter, figure 2.24 represents a similar comparison as in figure 2.23 for a liquid/liquid oil combination used in the experiments of Piroird *et al.* (2011).



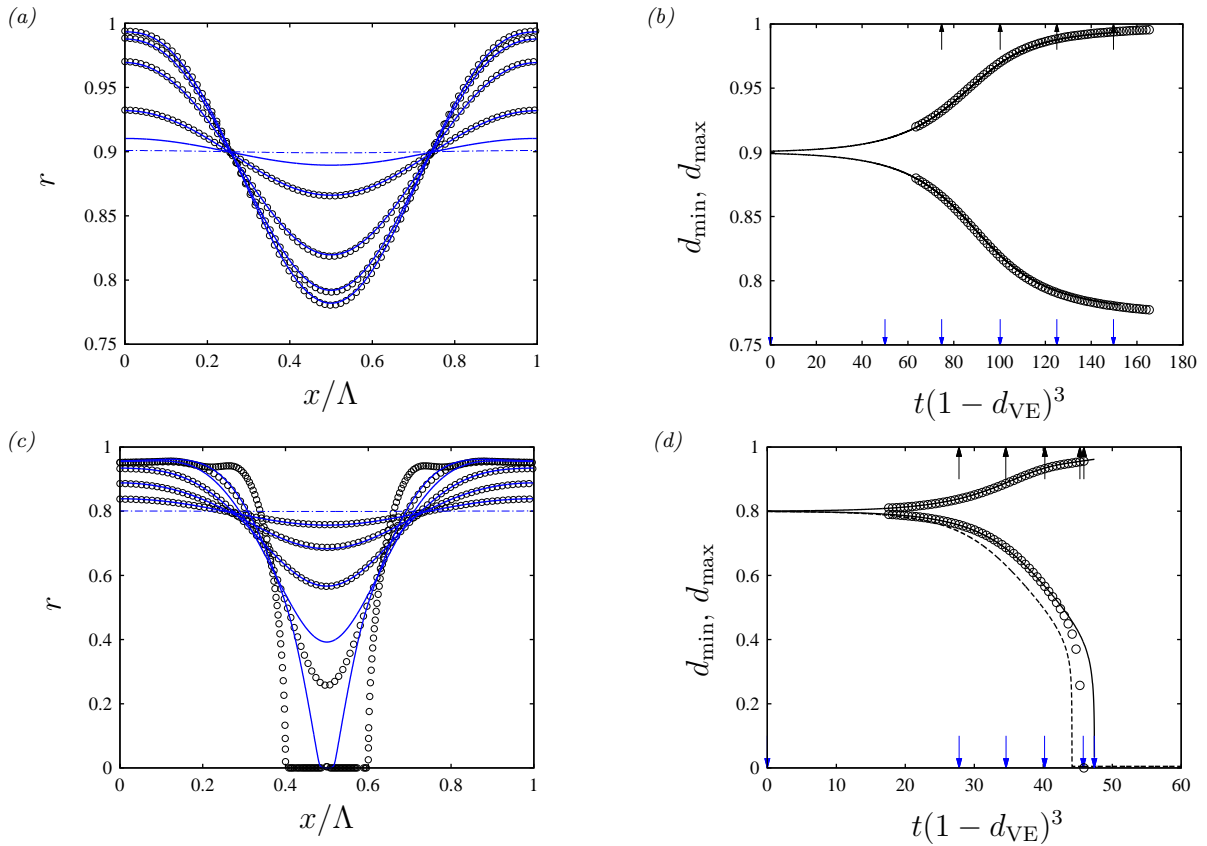


Figure 2.23: Time evolution of a gravity-free annular liquid film in contact with air within a cylindrical capillary, according to figure 5 in Johnson *et al.* (1991):  $La=5000$  (mucus III and air I in table 2.1),  $R^*=0.25$  mm,  $\Lambda^*=1.5$  mm,  $Fr^{-1}=0$ ,  $M=0$ . Lines: WRIBL model; symbols: DNS with **Gerris**. (a,b) Unduloid:  $V_1/\pi/R^3=1.14$ ,  $d_{VE}=0.9$ ; (c,d) occlusion:  $V_1/\pi/R^3=2.16$ ,  $d_{VE}=0.8$ . Dashed: inertialess limit ( $S_i=F_{ij}=G_{ij}=0$  in equation 1.60). Dot-dashed lines in panels a and c represent initial condition. Arrows in panels b and d mark time points for profiles in panels a and c.

Agreement between our WRIBL model and our own DNS is again good, confirming that cylindrical liquid/liquid configurations subject to long-wave instability are within the reach of our modelling approach.

Accounting for inertia is necessary in order to accurately predict the dynamics of occlusion, both for liquid/gas (panel 2.23d) and liquid/liquid (panel 2.24b) systems. This can be ascertained by comparing the dashed (inertialess limit) and solid (full WRIBL model) lines in panels 2.23d and 2.24b.

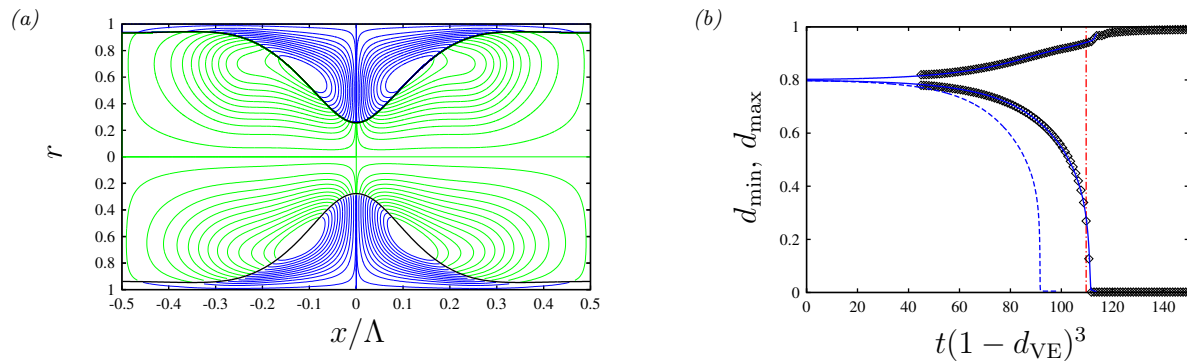


Figure 2.24: Gravity-free liquid/liquid system in a cylindrical tube: water IV/silicone oil VI in table 2.1 (Piroird *et al.*, 2011),  $R^*=1.5$  mm,  $\Lambda=7$ ,  $V_1/\pi/R^3=\Lambda(1-d_{VE}^2)=2.52$ ,  $M=0$ . (a) Streamlines at  $t(1-d_{VE})^3=110$  (red dot-dashed line in panel b). Top half: WRIBL; bottom half: DNS with **Gerris**; (b) time traces of  $d_{\min}$  and  $d_{\max}$ . Symbols: DNS; solid blue: WRIBL; dashed blue: inertialess limit ( $S_i=F_{ij}=G_{ij}=0$  in equation 1.60).

# Chapter 3

## Orr-Sommerfeld linear stability analysis

As a reference for testing the WRIBL models introduced in sections 1.1 and 1.2, we apply normal-mode linear stability analysis (Chandrasekhar, 1981) to the full two-phase Navier-Stokes equations. As far as long-wave instabilities are concerned, the Orr-Sommerfeld eigenvalue problem governing stability is solved via numerical continuation using `Auto07P`. Such calculations have allowed us to ascertain the validity range of our WRIBL models in sections 2.3.1 and 2.3.1.

In addition, we have written a Chebyshev collocation code to check for short-wave instability modes that our long-wave WRIBL models cannot capture. Such modes can arise in plane two-phase channel flows (Floryan *et al.*, 1987; Yiantsios & Higgins, 1988; Tilley *et al.*, 1994*b*; Trifonov, 2017*a*) as well as core annular flows through cylindrical tubes (Preziosi *et al.*, 1989). However, we have applied the analysis only to the planar configuration (figure 1.2) here. Among the liquid-gas flows studied in chapters 5 to 8, this configuration was the most susceptible to short-wave instability modes (only small gas velocities were studied for the cylindrical configuration).

### 3.1 Planar liquid films in rectangular channels

We start with the full governing equations for the planar configuration (figure 1.2), which are written in (4.1) of section 4.1.1. Next, we shift the coordinate system to the fluid/fluid interface of the primary flow,  $y=h_0$ , by introducing the new normal coordinate  $s$  (Yih, 1967):

$$s = y - h_0. \tag{3.1}$$

The primary-flow velocity profiles then read:

$$u_{k0} = b_k s^2 + a_k s + c_k, \tag{3.2}$$

with coefficients:

$$b_1 = -6 q_{10} \frac{(n + \Pi_\mu)}{h_0^3 \Delta} + \frac{3}{2} \Gamma \frac{n^2}{\Delta}, \quad a_1 = 6 q_{10} \frac{(n^2 - \Pi_\mu)}{h_0^2 \Delta} + 2 \Gamma \frac{h_0 n^2}{\Delta}, \quad (3.3a)$$

$$c_1 = 6 q_{10} \frac{n(1+n)}{h_0 \Delta} + \Gamma \frac{h_0^2 n^2}{2 \Delta}, \quad (3.3b)$$

$$b_2 = -q_{10} \frac{6}{h_0^3 \Delta} \frac{(n + \Pi_\mu)}{\Pi_\mu \Pi_u} - \frac{1}{2} \Gamma \frac{4n + \Pi_\mu}{\Delta} \frac{1}{\Pi_\mu \Pi_u}, \quad a_2 = \Pi_\mu^{-1} \Pi_u^{-1} a_1, \quad c_2 = c_1 \Pi_u^{-1}, \quad (3.3c)$$

where  $q_{10}=1$  is the dimensionless primary-flow liquid flow rate, and where we have introduced the thickness ratio  $n=d_0/h_0$ ,  $\Delta=\Pi_\mu + n(4 + 3n)$ , and  $\Gamma=(\Pi_\rho - 1)\sin(\phi)\text{Re}_1/\text{Fr}^2$ . Next, we introduce the stream functions  $\Phi$  (fluid 1) and  $\Psi$  (fluid 2):

$$u_1 = \partial_s \Phi, \quad v_1 = -\partial_x \Phi, \quad (3.4a)$$

$$u_2 = \partial_s \Psi, \quad v_2 = -\partial_x \Psi, \quad (3.4b)$$

and eliminate the pressure variable through cross-differentiation of the Navier-Stokes equations (4.1a). Then, we perturb the system around the primary flow:

$$h = h_0 + h'(x, t), \quad \Phi = \Phi_0 + \Phi'(x, s, t), \quad \Psi = \Psi_0 + \Psi'(x, s, t), \quad (3.5)$$

and linearize the governing equations in the perturbations, for which we seek solutions in terms of normal modes:

$$\begin{bmatrix} h' \\ \Phi' \\ \Psi' \end{bmatrix} = \begin{bmatrix} \hat{h} \\ \phi(s) \\ \psi(s) \end{bmatrix} \exp \{ik(x - ct)\}, \quad (3.6)$$

where the scale for  $c$  is  $\mathcal{U}_1$ , which follows directly from the choice of the time scale in (1.1). Although (3.6) resembles the typical temporal stability formulation ( $k \in \mathbb{R}$ ,  $c \in \mathbb{C}$ ), we can easily recover the spatial formulation ( $k \in \mathbb{C}$ ,  $\omega \in \mathbb{R}$ ) through the constraint  $kc=\omega \in \mathbb{R}$ . We thus obtain the familiar Orr-Sommerfeld equations for two-fluid (inclined) channel flow (Tilley *et al.*, 1994a):

$$\phi^{iv} - 2k^2 \phi'' + k^4 \phi = i \text{Re}_1 k \{ (c - u_{10}) (k^2 \phi - \phi'') - \phi u_{10}'' \}, \quad (3.7a)$$

$$\psi^{iv} - 2k^2 \psi'' + k^4 \psi = i \text{Re}_2 k \{ (\Pi_u^{-1} c - u_{20}) (k^2 \psi - \psi'') - \psi u_{20}'' \}, \quad (3.7b)$$

and the associated boundary, kinematic, and dynamic coupling conditions:

$$s = -h_0 : \quad \phi = \phi' = 0, \quad (3.7c)$$

$$s = d_0 : \quad \psi = \psi' = 0, \quad (3.7d)$$

$$s = 0 : \quad \phi' - \Pi_u \psi' = \frac{\phi}{\tilde{c}} (\Pi_u a_2 - a_1), \quad (3.7e)$$

$$s = 0 : \quad \phi = \Pi_u \psi, \quad (3.7f)$$

$$s = 0 : \quad \phi'' + k^2 \phi - 2\phi' \Omega = \Pi_\mu \Pi_u \{ \psi'' + k^2 \psi \} - 2\Pi_u \psi' \Omega, \quad (3.7g)$$

$$s = 0 : \quad -\phi''' + 3k^2 \phi' + \Pi_u \Pi_\mu \{ \psi''' - 3k^2 \psi' \} - ik\text{Re}_1 \{ \tilde{c} \phi' + a_1 \phi \} \\ + ik\text{Re}_1 \Pi_\rho \Pi_u \{ \tilde{c} \psi' + a_2 \Pi_u \psi \} = \frac{ik\text{Re}_1}{\tilde{c}} \phi \left\{ \frac{\cos(\phi)}{\text{Fr}^2} (\Pi_\rho - 1) - k^2 \text{We} \right\}, \quad (3.7h)$$

where primes denote differentiation w.r.t.  $s$ , and where we have introduced  $\tilde{c} = c - u_{10}|_{s=0}$  and  $\Omega = (b_1 - b_2 \Pi_\mu \Pi_u) / (a_1 - \Pi_u a_2)$ . Equations (3.7) reduce to equations 4 and 5 in Yiantsios & Higgins (1988) in the limit  $\sin(\phi)=0$  (horizontal flow), upon setting  $\Pi_u=1$  and interchanging the phase indices (Yiantsios and Higgins designated the upper layer as fluid 1). In particular, the third term on either side of (3.7g), which is associated with streamwise gravity, will vanish in that limit. Taking the further limit  $\Pi_\rho=1$  and  $h_0=1/2$ , our equations collapse to those of Yih (1967).

For the interfacial coupling conditions (3.7e)-(3.7h), we recall that the linear perturbation  $f'^1$  of the interfacial value  $f(h) = F|_{h(x,t)}$  of a field variable  $F(x, y, t)$  comprises one contribution due to changing the position  $y$  at constant interface height  $h$  and another due to changing  $h$  at constant  $y$  (Yih, 1967):

$$dF = \partial_y F|_h dy + \partial_h F|_y dh, \\ f' = df = f(h_0 + h') - f(h_0) = \partial_y F|_{h=h_0} h' + \partial_h F|_{y=h_0} dh, \\ \Rightarrow f' = \partial_y F_0|_{y=h_0} h' + F'|_{y=h_0},$$

where  $F_0$  and  $F' = \hat{F}(y) \exp \{ ik(x - ct) \}$  are the primary-flow and perturbation quantities of the field variable  $F$ , which are both defined on the domain of the primary flow.

We solve the fourth-order eigenvalue problem (3.7) numerically using two different methods. The first method makes use `Auto07P` (Doedel, 2008) to track long-wave instability modes through numerical continuation, starting from the analytically tractable

---

<sup>1</sup>Primes do not denote differentiation in this paragraph.

limit  $\omega=k=0$ , where  $c_i=0$  and:

$$\tilde{c} = c_r - u_{10}|_{s=0} = \Xi d_0^2 h_0^2 \{d_0^4 + 2\Pi_\mu d_0 h_0 (2d_0^2 + 3d_0 h_0 + 2h_0^2) + \Pi_\mu^2 h_0^4\}^{-1}, \quad (3.8)$$

$$\phi = \frac{12}{\Upsilon} (h_0 + s)^2 \left\{ d_0^3 + 2\Pi_\mu h_0^2 s + \Pi_\mu d_0 h_0 \left[ -h_0 + 2s + s \frac{h_0}{\tilde{c}} (a_1 - \Pi_u a_2) \right] \right\}, \quad (3.9)$$

$$\psi = \frac{12}{\Upsilon} \frac{h_0}{\Pi_u d_0} (d_0 - s)^2 \left\{ -\Pi_\mu h_0^3 + 2d_0 h_0 s + d_0^2 \left[ h_0 + 2s + s \frac{h_0}{\tilde{c}} (a_1 - \Pi_u a_2) \right] \right\}, \quad (3.10)$$

having introduced:

$$\Xi = 2\Pi_\mu a_1 H + b_1 (d_0^2 - \Pi_\mu h_0^2) + \Pi_\mu \Pi_u \{ -b_2 d_0^2 - 2a_2 H + \Pi_\mu b_2 h_0^2 \}, \quad (3.11)$$

$$\Upsilon = 4d_0^3 h_0^3 - 2\Pi_\mu h_0^6 + \Pi_\mu d_0 h_0^5 \left\{ -6 + \frac{h_0}{\tilde{c}} (-a_1 + \Pi_u a_2) \right\}, \quad (3.12)$$

and which is valid both in the spatial and temporal formulations.

To exclude the trivial solution  $\phi=\psi=0$  from consideration, and to fix the arbitrary integration constant arising from the fourth derivative in (3.7a), (3.7) is augmented by an integral condition on  $\phi$ :

$$\int_{-h_0}^0 \phi ds = 1. \quad (3.13)$$

In the case of spatial stability calculations, it has proven practical to introduce  $\omega$  into (3.6) indirectly through an additional equation  $\omega=kc \in \mathbb{R}$ . This forces  $k$  to become non-zero, as soon as the control parameter  $\omega$  is moved from its starting value (because  $c_r \neq 0$  at the starting point). Otherwise, when introducing  $\omega$  directly in (3.6), our continuations erred around the immediate vicinity of the starting point, where  $\omega=k=0$ .

The second solution method is based on expanding  $\phi$  and  $\psi$  in terms of Chebyshev polynomials (Boomkamp *et al.*, 1997; Barmak *et al.*, 2016):

$$\phi(\xi) = c_{10} + \sum_{j=1}^{N_p} c_{1j} T_j(\xi), \quad \psi(\xi) = c_{20} + \sum_{j=1}^{N_p} c_{2j} T_j(\xi), \quad (3.14)$$

where  $T_j$  are  $j$ th-degree Chebyshev polynomials of the first kind, defined on the interval  $\xi \in [-1, 1]$ , with  $\xi=2s/h_0 + 1$  in fluid 1 and  $\xi=2s/d_0 - 1$  in fluid 2. Thus, there are  $2(N_p + 1)$  unknown coefficients  $c_{kj}$ , which are fixed by the 8 conditions in (3.7c)-(3.7h), and  $2(N_p + 1) - 8$  additional constraints obtained by evaluating the ODEs (3.7a) at the inner collocation points  $\xi_2, \dots, \xi_{N_p-2}$ , defined according to:

$$\xi_i = \cos \left[ \frac{i \pi}{N_p} \right] \quad \forall i \in [0, N_p]. \quad (3.15)$$

Instead of solving for the coefficients  $c_{kj}$ , we solve directly for the  $2(N_p + 2)$  unknowns  $\phi(\xi_i)$  and  $\psi(\xi_i)$ , arranged into the solution vectors:

$$\boldsymbol{\phi} = [\phi(\xi_0), \dots, \phi(\xi_{N_p})]^T, \quad \boldsymbol{\psi} = [\psi(\xi_0), \dots, \psi(\xi_{N_p})]^T. \quad (3.16)$$

Then, by making use of the Chebyshev differentiation matrix  $\mathbf{D}$  (Trefethen, 2000):

$$[\phi^{(i)}(\xi_0), \dots, \phi^{(i)}(\xi_{N_p})]^T = \mathbf{D}^i [\phi(\xi_0), \dots, \phi(\xi_{N_p})]^T, \quad (3.17)$$

$$[\psi^{(i)}(\xi_0), \dots, \psi^{(i)}(\xi_{N_p})]^T = \mathbf{D}^i [\psi(\xi_0), \dots, \psi(\xi_{N_p})]^T, \quad (3.18)$$

where  $i=1, 2, 3, 4$ , and  $(i)$  indicates the order of differentiation w.r.t.  $\xi$ , (3.7) is cast into a generalized eigenvalue problem in matrix form:

$$\underline{A}\mathbf{x} = \tilde{c}\underline{B}\mathbf{x}, \quad (3.19)$$

with the coefficient matrices  $\underline{A}$  and  $\underline{B}$  and the concatenated solution vector  $\mathbf{x}=[\boldsymbol{\phi}, \boldsymbol{\psi}]^T$ . We solve (3.19) for the eigenvalues  $\tilde{c}$  and eigenvectors  $\mathbf{x}$ , using the function `eig` in MATLAB (MATLAB, 2015)<sup>2</sup>. We have applied the Chebyshev collocation method in the framework of the temporal stability formulation ( $k \in \mathbb{R}$ ,  $c \in \mathbb{C}$ ).

In contrast to the continuation method, the full set of eigenmodes is computed at once. Thus, short-wave instability modes, i.e. modes with  $k_i, c_i \neq 0$  at  $k=\omega=0$ , can be readily obtained. Once a mode has been identified at a given wavenumber  $k$ , it can be tracked by advancing  $k$ , using the function `eigs`, which searches for eigenvalues in the vicinity of a previous solution.

To validate our two numerical OS approaches, we have confronted in figure 3.1 our predictions of the most-unstable eigenmode for the two cases of horizontal two-phase Poiseuille flow reported in panels 16a and 16b of Yiantsios & Higgins (1988). In accordance with Yiantsios & Higgins (1988), our data were rescaled with  $\underline{\mathcal{L}}=d_0^*$  and  $\underline{\mathcal{U}}=u_{10}^*|_{s=0}$ . In the first case (panels 3.1a and 3.1c), the most-unstable mode is a long-wave interfacial mode. Both our OS calculations, using numerical continuation (solid red lines) and using the Chebyshev collocation method (symbols), accurately predict the growth rate dispersion curve  $kc_i(k)$  (panel 3.1a) and the associated eigenfunctions  $\phi$  and  $\psi$  (panel 3.1c), in accordance with Yiantsios & Higgins (1988). In the second case (panels 3.1b and 3.1d), the most-unstable mode is a short-wave mode. This mode is accurately captured by our Chebyshev collocation calculation, versus the data of Yiantsios & Higgins (1988), evidencing a Tollmien-Schlichting type eigenfunction in fluid 1.

Next, we apply our thus validated Chebyshev collocation approach to check for short-wave instability modes within the liquid-gas flows studied in chapters 5, 6, and 8. In short, only long-wave eigenmodes are unstable for the flow conditions investigated here (see figures 3.2 to 3.4), and thus our long-wave WRIBL models can accurately describe the linear dynamics of the studied two-phase flows.

Nonetheless, we briefly discuss the different short-wave instability modes that can arise for the two configurations sketched in figure 1.2. For falling liquid films (panel 1.2a) in a passive outer phase ( $\Pi_\mu=\Pi_\rho=0$ ), Floryan *et al.* (1987) identified a short-wave shear mode, with an eigenfunction similar to the Tollmien-Schlichting instability, for  $\text{Re}_1 > \text{Re}_1^{\text{SM}}$ . However,  $\text{Re}_1^{\text{SM}}$  is of the order of several thousands, and thus this mode becomes relevant only at extremely small inclination angles  $\phi$ , when the flow is quasi-horizontal and the

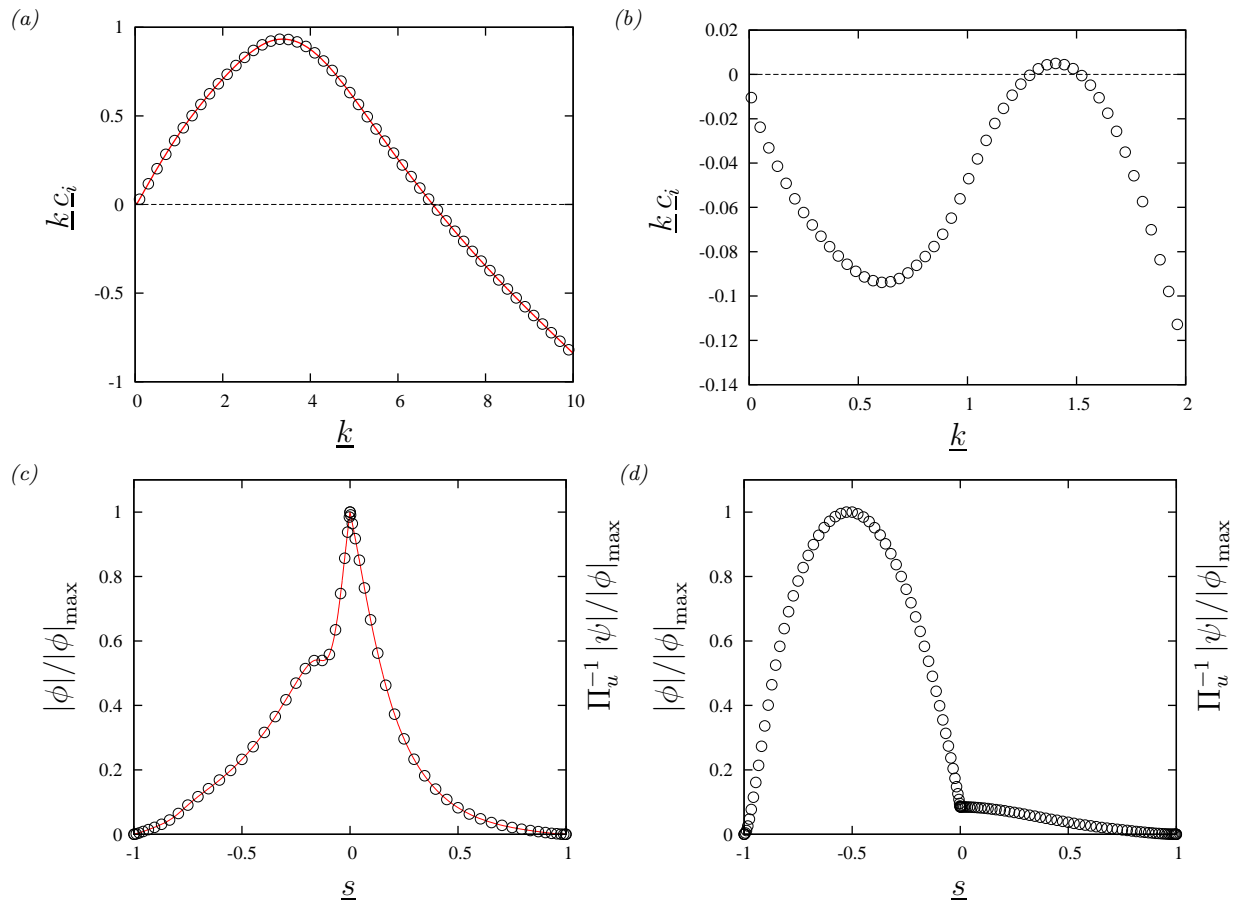


Figure 3.1: Numerical solutions of the Orr-Sommerfeld eigenvalue problem (3.7) for two cases of the configuration in panel 1.2b ( $\phi=0^\circ$ ), corresponding to figures 15 and 16 in Yiantsios & Higgins (1988):  $m=\Pi_\mu^{-1}=0.05$ ,  $r=\Pi_\rho^{-1}=1.16$ ,  $n=h_0/d_0=1$ ,  $F=(r-1)g\underline{\mathcal{L}}/\underline{\mathcal{U}}^2=5903/\text{Re}^2$ , and  $S=\sigma/\rho_1/\underline{\mathcal{L}}/\underline{\mathcal{U}}^2=829/\text{Re}^2$ , where  $\underline{\mathcal{L}}=d_0^*$  and  $\underline{\mathcal{U}}=u_{10}^*|_{s=0}$ , which have also been used to rescale underscored quantities. Solid red lines: continuation from  $k=0$  using Auto07P; symbols: solution based on Chebyshev polynomials (3.14). (a,c)  $\text{Re}=\rho_2 u_{10}^*|_{s=0} d_0^*/\mu_2=80$ : long-wave “interfacial mode”; (b,d)  $\text{Re}=230$ : short-wave “shear mode”. Eigenfunctions in panels c and d correspond to  $\underline{k}=5$  and  $\underline{k}=1.40$ , respectively. Chebyshev polynomials of degree  $N_p=60$  were used.

threshold of the interfacial mode  $\text{Re}_1^{\text{crit}}=(5/6)\cot(\phi)$  is itself very large. For the inclination angles and  $\text{Re}_1$  studied in this work, the long-wave interfacial Kapitza instability always dominates.

In the case of an active outer phase, e.g. a counter-current gas flow, additional long- and short-wave instability modes come into play, both in the falling film (panel 1.2a) and pressure-driven horizontal (panel 1.2b) configurations (Boomkamp & Miesen, 1996;

<sup>2</sup>The Matlab script provided by Singh (2014) was a useful starting point for our code.



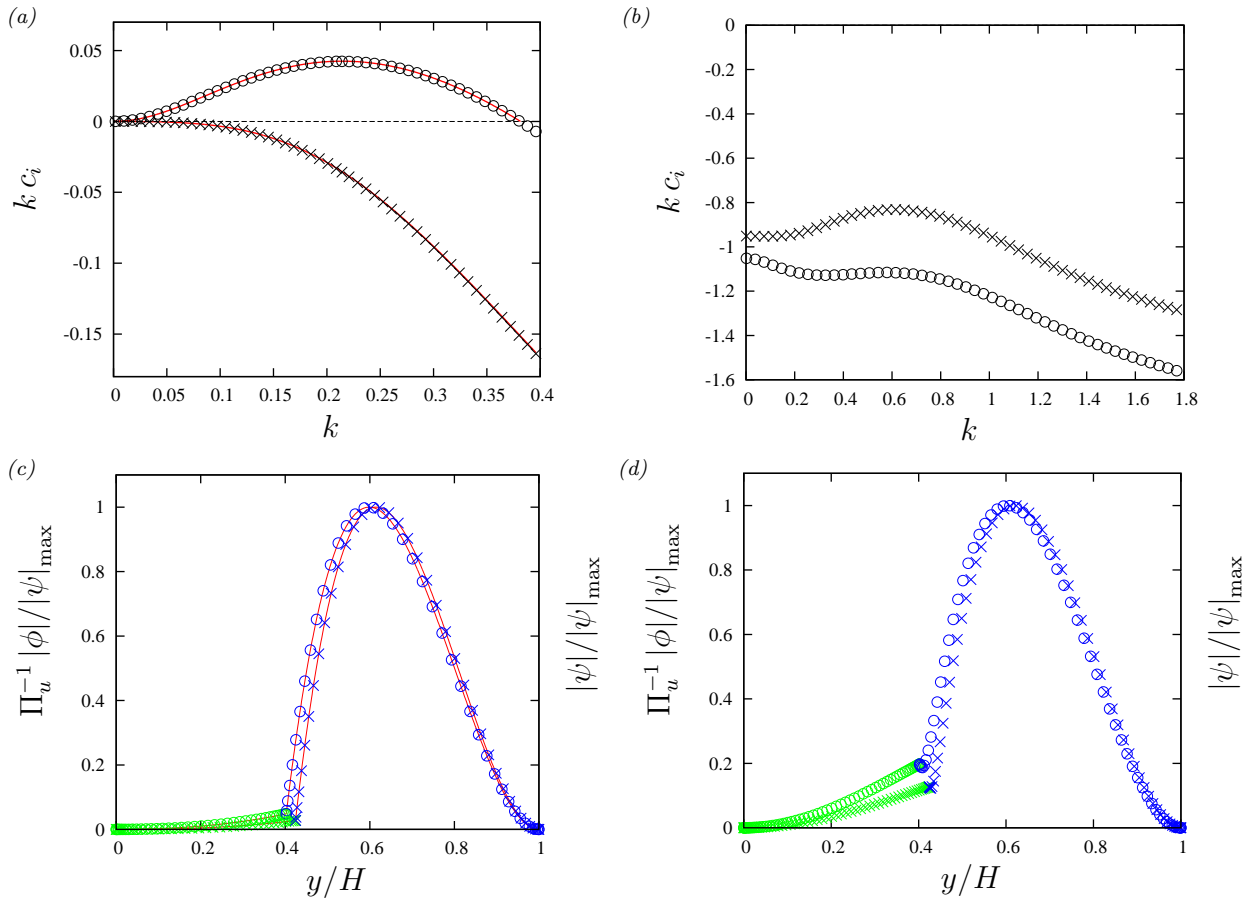


Figure 3.2: Numerical solutions of the OS eigenvalue problem (3.7) in the temporal formulation ( $k \in \mathbb{R}$ ,  $c \in \mathbb{C}$ ). Inclined falling liquid film subject to a counter-current gas flow according to panel 2.11d:  $Ka=509.5$  (DMSO-water and air II in table 2.1),  $\phi=10^\circ$ ,  $H^*=1.69$  mm,  $Re_1=15$ . Solid red lines: numerical continuation with Auto07P starting from  $k=0$ ; symbols: Chebyshev collocation method (3.14) with  $N_p=80$ . Open circles:  $Re_2=-80$ ; crosses:  $Re_2=-100$ . (a,c) Most-unstable long-wave mode; (b,d) most-unstable short-wave mode. Eigenfunctions in panels c and d are evaluated at  $k=0.214$ . Green symbols: liquid; blue symbols: gas.

Barthelet *et al.*, 1995; Charru & Hinch, 2000). One of these is the previously discussed long-wave interfacial mode resulting from the viscosity contrast between the two fluids (Yih, 1967). Another, short-wave, interfacial mode takes hold in the limit of zero surface tension ( $We=0$ ) (Hooper & Boyd, 1983; Hinch, 1984). Finally, a short-wave Tollmien-Schlichting mode can arise also in the outer phase (Yiantsios & Higgins, 1988; Tilley *et al.*, 1994a; Renardy, 1985; Trifonov, 2017a). It is this mode in particular that we have kept an eye on with our Chebyshev collocation calculations.

Figures 3.2 and 3.3 report results of such calculations for the strongly-confined falling liquid films considered in panel 2.11d. The left column in these figures corresponds to the

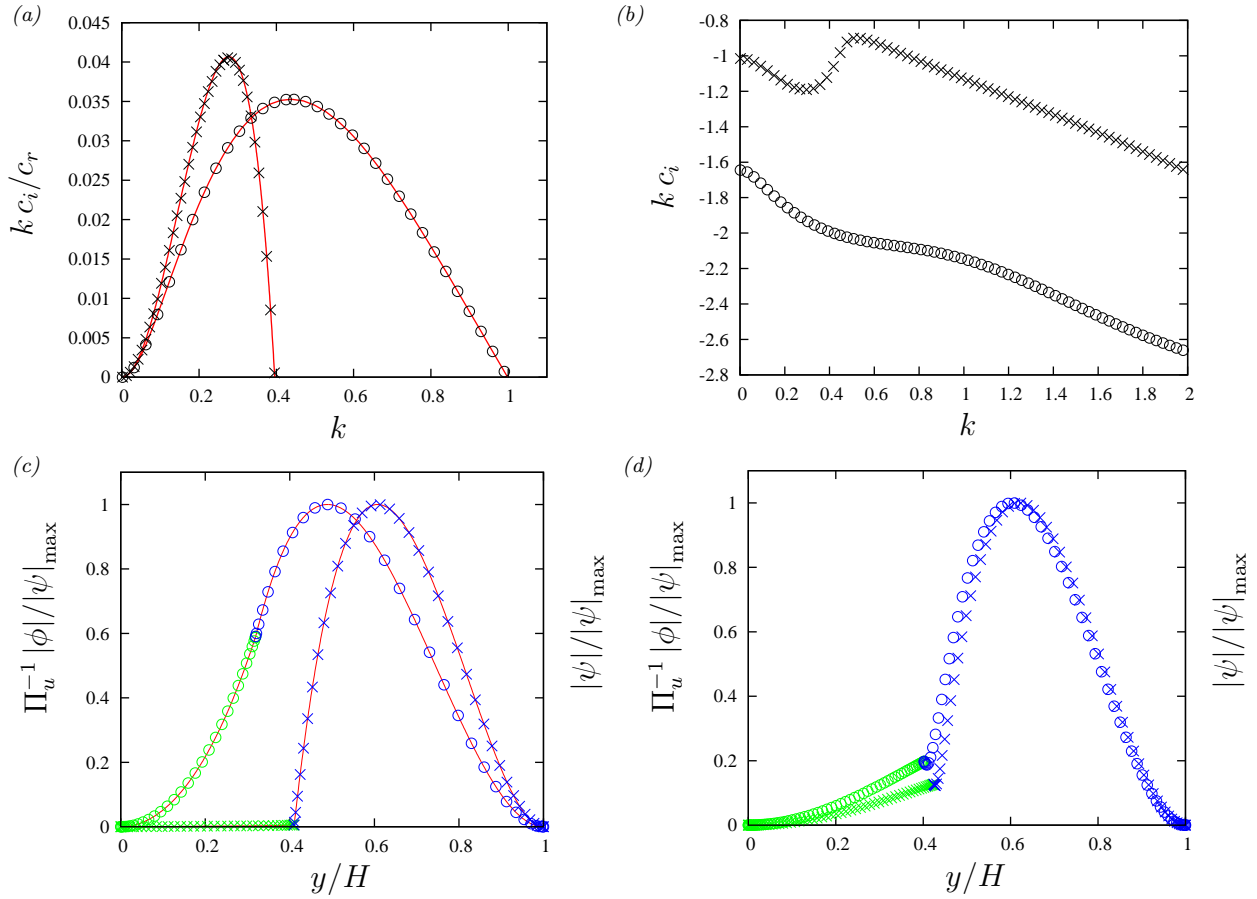


Figure 3.3: Same as figure 3.2, but for conditions in the vicinity of the absolute instability threshold according to panel 2.11d:  $Ka=509.5$  (DMSO-water and air II in table 2.1),  $\phi=10^\circ$ ,  $H^*=1.878$  mm,  $Re_1=15$ . Open circles:  $M=\sin(\phi)$ ; crosses:  $Re_2=-184$ . (a, c) Most-unstable long-wave mode; (b, d) most-unstable short-wave mode. Eigenfunctions in panels c and d are evaluated at  $k=0.264$ . Chebyshev polynomials with  $N_p=120$  were used.

most-unstable eigenmode, which is always a long-wave mode, whereas the right column represents the second-most-unstable eigenmode, which is always a stable short-wave mode (with a Tollmien-Schlichting type eigenfunction in the gas phase). In figures 3.2 and 3.3, we have varied  $Re_2$  in order to reproduce the two gas-induced effects observed with our WRIBL calculations in panel 2.11d: the suppression of the long-wave Kapitza instability (figure 3.2), and the build-up to absolute instability (figure 3.3). In both cases, short-wave instability modes play no role.

Finally, figure 3.4 represents OS calculations for the falling liquid film and pressure-driven water-air flow represented in figures 2.12 and 2.14. Once again, only the long-wave eigenmode of the Kapitza instability is unstable.

In summary, we may conclude that our long-wave WRIBL models are adequate for pre-

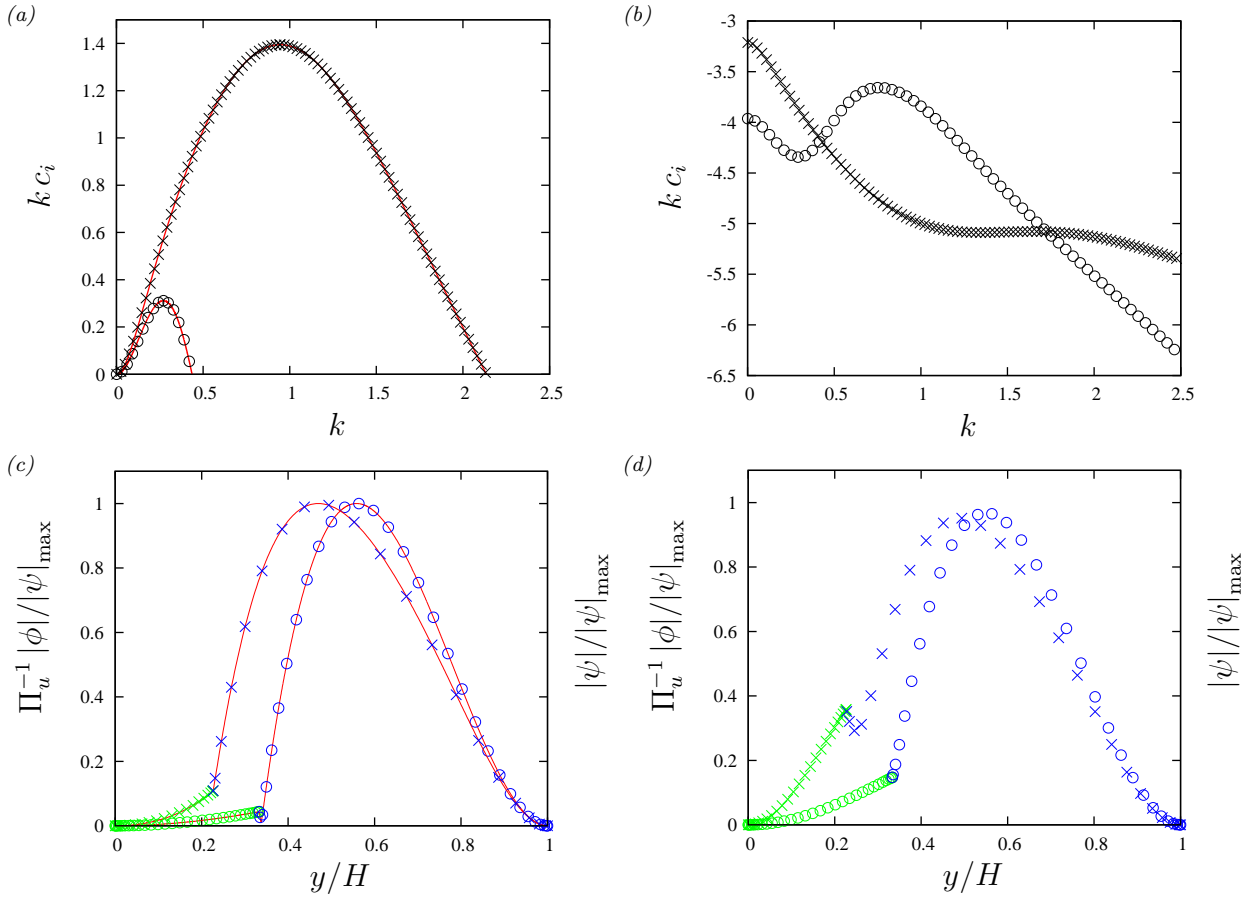


Figure 3.4: Long- and short-wave linear stability modes for the vertical and horizontal configurations in panels 2.12 and 2.14. Assignments as in figure 3.2. Crosses: vertically falling liquid film.  $Ka=509.5$  (DMSO-water and air II in table 2.1),  $\phi=90^\circ$ ,  $H^*=1.5$  mm,  $Re_1=15.07$ ,  $Re_2=-54.46$ ; circles: horizontal pressure-driven two-fluid plane Poiseuille flow.  $Ka=3592.3$  (water I and air III in table 2.1),  $\phi=0^\circ$ ,  $H^*=0.39$  mm,  $Re_1=5.8$ ,  $h_0=1/3$ . Eigenfunctions in panels *c*, *d* were obtained at  $k=0.94$  (crosses) and  $k=0.27$  (circles). Chebyshev polynomials (3.14) of degree  $N_p=80$  (crosses) and  $N_p=120$  (circles) were used.

dicting all instability modes that are relevant for the liquid-gas flows studied in chapters 5 to 8. Short-wave instability modes play no role, because Tollmien-Schlichting eigenmodes set in at large values of  $Re_1$  and  $|Re_2|$ , which lie outside the range of applicability of our models anyhow (see section 2.3). Nonetheless, even though we consider only low to moderate  $|Re_2|$  in our work (except for chapter 9), the effect of the gas flow is still significant, as a result of the strong confinement levels studied. This is expressed in the eigenfunction profiles of panels 3.2c, 3.3c and 3.4c, where, except for the aerostatic case (open circles in panel 3.3c), the eigenfunctions of the long-wave instability mode evidence very large perturbations in the gas. Interestingly, their shape is similar to that of the (stable) short-wave eigenmodes (3.2c, 3.3c and 3.4c).

In the case of falling liquid films sheared by a turbulent gas flow (section 1.4 and chapter 9), which we are studying in ongoing work, it remains to be verified whether short-wave instability modes play a role. For this, the Chebyshev collocation approach must be extended to account for turbulence in the gas (Nàraigh *et al.*, 2011). Nonetheless, we will show in chapter 9 that our long-wave WRIBL model accurately captures the effect of a counter-current turbulent gas flow on the shape and amplitude of nonlinear surface waves versus experiments.

## 3.2 Annular liquid films in cylindrical tubes

The full governing equations for the cylindrical configuration (figure 1.3) are written in section 4.1.2. Using the scales for the gravity-driven scenario (1.38) defined in section 1.2, i.e.  $\mathcal{L}=R^*$  and  $\mathcal{U}_k=q_k^*/\pi/R^{*2}$ , the primary flow is given by:

$$u_{k0} = a_k r^2 + b_k \ln(r) + c_k, \quad (3.20)$$

in terms of the core radius  $d_0$  and pressure derivative  $\partial_x p_{20}$ , which intervene via the coefficients  $a_k$ ,  $b_k$ , and  $c_k$ :

$$a_1 = 2\Xi \frac{C_1}{\Delta_1}, \quad b_1 = 4d_0^2 \frac{C_2}{\Delta_1}, \quad c_1 = -a_1, \quad (3.21)$$

$$a_2 = -2\frac{C_3}{\Delta_2}, \quad b_2 = 0, \quad c_2 = \frac{1}{d_0^2} - \frac{1}{2}d_0^2 a_2, \quad (3.22)$$

where we have substituted:

$$\Xi = \frac{\partial_{x^*} p_1^* - \rho_1 g}{\partial_{x^*} p_2^* - \rho_2 g} = \frac{\partial_x p_2 - \text{Fr}^{-1} \Pi_\rho^{-1} \Pi_u^{-2}}{\partial_x p_2 - \text{Fr}^{-1}}, \quad (3.23)$$

$$C_1 = (\Pi_\rho \Pi_u^2 - 1), \quad C_2 = (\Xi - 1)(\Pi_\rho - 1), \quad C_3 = C_2 - \Xi C_1, \quad (3.24)$$

$$\Delta_1 = (d_0^2 - 1) \left\{ \Xi C_1 (d_0^2 - 1) + 2d_0^2 C_2 \right\} - 4C_2 d_0^4 \ln(d_0), \quad (3.25)$$

$$\Delta_2 = d_0^4 C_3 + 2\Pi_\mu (C_2 - C_3) d_0^2 (d_0^2 - 1) - 4\Pi_\mu C_2 d_0^4 \ln(d_0). \quad (3.26)$$

Above, and in the remainder of this section, we have made use of  $\text{Re}_2 = \text{Re}_1 \Pi_\rho \Pi_u \Pi_\mu^{-1}$  to simplify expressions.

Next, we introduce the Stokes stream functions  $\Phi$  (fluid 1) and  $\Psi$  (fluid 2):

$$u_1 = \frac{1}{r} \partial_r \Phi, \quad v_1 = -\frac{1}{r} \partial_x \Phi, \quad (3.27a)$$

$$u_2 = \frac{1}{r} \partial_r \Psi, \quad v_2 = -\frac{1}{r} \partial_x \Psi, \quad (3.27b)$$

and apply the same steps to obtain the linearized governing equations as for the planar configuration in section 3.1, only that the core radius  $d$  is used instead of the film thickness  $h$ :

$$d = d_0 + d' = d_0 + \hat{d} \exp \{ik(x - ct)\}. \quad (3.28)$$

We thus obtain the Orr-Sommerfeld equations for axisymmetric core-annular flow through a cylindrical tube:

$$\begin{aligned} \phi^{iv} - 2r^{-1}\phi''' + 3r^{-2}\phi'' - 2k^2r\partial_r [r^{-1}\phi'] + k^4\phi = \\ i\text{Re}_1k \left\{ (c - u_{10}) (k^2\phi - r\partial_r [r^{-1}\phi']) - \phi r\partial_r [r^{-1}u'_{10}] \right\}, \end{aligned} \quad (3.29a)$$

$$\begin{aligned} \psi^{iv} - 2r^{-1}\psi''' + 3r^{-2}\psi'' - 2k^2r\partial_r [r^{-1}\psi'] + k^4\psi = \\ i\text{Re}_2k \left\{ (\Pi_u^{-1}c - u_{10}) (k^2\psi - r\partial_r [r^{-1}\psi']) - \psi r\partial_r [r^{-1}u'_{10}] \right\}, \end{aligned} \quad (3.29b)$$

and the associated boundary, kinematic, and dynamic coupling conditions:

$$r = 1 : \quad \phi = \phi' = 0, \quad (3.29c)$$

$$r = 0 : \quad \psi = \psi' = 0, \quad (3.29d)$$

$$r = d_0 : \quad \phi' - \Pi_u\psi' = \frac{\phi}{\tilde{c}} (\Pi_u u'_{20} - u'_{10}), \quad (3.29e)$$

$$r = d_0 : \quad \phi = \Pi_u\psi, \quad (3.29f)$$

$$r = d_0 : \quad \phi'' - d_0^{-1}\phi' + k^2\phi - \phi'\Omega = \Pi_\mu\Pi_u \{ \psi'' - d_0^{-1}\psi' + k^2\psi \} - \Pi_u\psi'\Omega, \quad (3.29g)$$

$$r = d_0 : \quad -\phi''' + \phi''d_0^{-1} - \phi'd_0^{-2} + k^2(3\phi' - 2\phi d_0^{-1}) \quad (3.29h)$$

$$+ \Pi_u\Pi_\mu \{ \psi''' - \psi''d_0^{-1} + \psi'd_0^{-2} - k^2(3\psi' - 2\psi d_0^{-1}) \} \quad (3.29i)$$

$$- ik\text{Re}_1 \{ \tilde{c}\phi' + u'_{10}\phi \} + ik\text{Re}_1\Pi_\rho\Pi_u \{ \tilde{c}\psi' + u'_{20}\Pi_u\psi \} \quad (3.29j)$$

$$= \frac{i\text{Re}_1\text{We}}{\tilde{c}}\phi \{ k^3 - kd_0^{-2} \},$$

where primes denote differentiation w.r.t.  $r$ , and where we have introduced  $\tilde{c} = c - u_{10}|_{d_0}$  and  $\Omega = (u''_{10}|_{d_0} - \Pi_\mu\Pi_u u''_{20}|_{d_0}) / (u'_{10}|_{d_0} - \Pi_u u'_{20}|_{d_0})$ . Compared to the planar configuration (3.7h), the sign of the  $\text{We}k^3$  term in the normal coupling condition (3.29j) has switched, because the radial coordinate points toward the liquid phase, and a new  $-\text{We}k$  term appears due to the azimuthal curvature.

The eigenvalue problem (3.29) is solved via numerical continuation using Auto07P, starting from the analytical solution  $c_i=0$ ,  $c_r=c_{r0}$ ,  $\phi=\phi_0$ , and  $\psi=\psi_0$  in the long-wave limit  $\omega=k=0$ . The algebraic relations for  $c_{r0}$ ,  $\phi=\phi_0$ , and  $\psi=\psi_0$  are obtained by solving  $\lim_{k \rightarrow 0} \{(3.29)\}$  using the ansatz functions:

$$\phi = L_0 + L_1 r^2 + L_2 r^4 + L_3 r^2 \ln(r), \quad (3.30)$$

$$\psi = G_0 + G_1 r^2 + G_2 r^4 + G_3 r^2 \ln(r), \quad (3.31)$$

subject to the additional gauge condition:

$$\int_0^1 \phi dr = 1. \quad (3.32)$$

Our calculations with `Auto07P` allow tracking only long-wave instability modes. In contrast to the planar configuration, we have not checked explicitly for short wave modes. Such modes can generally arise in core-annular flows (Preziosi *et al.*, 1989), but usually not in liquid/gas systems, unless the magnitude of  $\text{Re}_1$  and/or  $\text{Re}_2$  is large. In all our computations for the cylindrical configuration,  $|\text{Re}_1|$  and  $|\text{Re}_2|$  were much smaller than in our computations for the planar configuration. For the latter case, we have shown via calculations with the Chebyshev collocation method that long-wave instability modes dominate (see section 3.1).

Short-wave instability modes in core-annular flows are most relevant when the core fluid is denser and more viscous (Chen *et al.*, 1990), e.g. in liquid/liquid systems, although regimes dominated by long-wave modes can be found even there. Applying our WRIBL models to such regimes is an enticing route for future work.

We conclude with a technical remark. For the center line velocity  $u|_{r=0} = \lim_{r \rightarrow 0} \{\psi'/r\}$  to remain finite,  $\lim_{r \rightarrow 0} \{\psi'\}$  must converge toward zero at the same rate as  $\lim_{r \rightarrow 0} \{r^{-1}\}$ . This is not necessarily satisfied in a numerical calculation, where  $\psi(r)$  is approximated, and this lead to convergence problems in our calculations with `Auto07P`. We remedied this by formulating the boundary conditions of the OS problem at  $r=r_0$ , where  $r_0$  was chosen very small, typically  $r_0/R=10^{-4}$ .

Our OS calculations using the approaches outlined in this chapter, have allowed us to identify the validity range of the WRIBL models developed in sections 1.1 and 1.2. Within this validity range, which we have determined in section 2.3, linear predictions of our WRIBL models, such as growth rate dispersion curves, are accurate. Further, we have made sure that short-wave instability modes, which cannot be captured by our long-wave WRIBL models, play no role in these regimes. Moreover, our experience has shown that nonlinear predictions are usually accurate when linear predictions are, and this is confirmed by our validation with DNS, which will be discussed in the next section.

# Chapter 4

## Direct numerical simulation

For most of the problems studied in this work, we have performed direct numerical simulations (DNS) based on the full Navier-Stokes equations. On the one hand, these DNS were used as benchmarks (see section 2.3) to validate the WRIBL models developed in sections 1.1 to 1.3. On the other hand, DNS were used to investigate physical effects that were not accounted for in our models, such as three-dimensional falling liquid films (section 5.2), heat transfer in falling liquid films flowing on corrugated substrates (section 6.3), or liquid films spreading around micro-particles (section 8.2).

Our DNS were performed with three Navier-Stokes solvers based on the finite-volume discretization method (Patankar, 1980). The first solver, **Gerris** (Popinet, 2009), was used for most of our simulations, in particular those involving interfacial instabilities, owing to its excellent precision in representing the effect of surface tension forces. The second, the **interFOAM** solver of the **OpenFOAM** package (Rusche, 2002), was used for two particular cases where **Gerris** could not be employed, large-scale simulations of 3-dimensional falling liquid films on a supercomputer (section 5.2) and spreading droplets interacting with microparticles (section 8.2). We have also performed a few simulations with the solver **Basilisk** Popinet (2015), which is the successor of **Gerris** and relies on similar numerical methods. We will not discuss this solver in detail.

We will start in section 4.1 by casting the continuum mathematical formulation for the problems studied. Then, in section 4.2, we will introduce the main numerical approaches used for our two-phase simulations, i.e. the volume of fluid (VOF) and continuum surface force (CSF) methods. Finally, in section 4.3, we will validate the two codes **Gerris** and **interFOAM** based on representative benchmark simulations.

### 4.1 Continuum formulation

#### 4.1.1 Liquid films in planar geometries

The flows represented in figures 4.1 and 4.2 are governed by the full Navier-Stokes and continuity equations, written here in 3 dimensions using Einstein notation ( $i, j = 1, 2, 3$

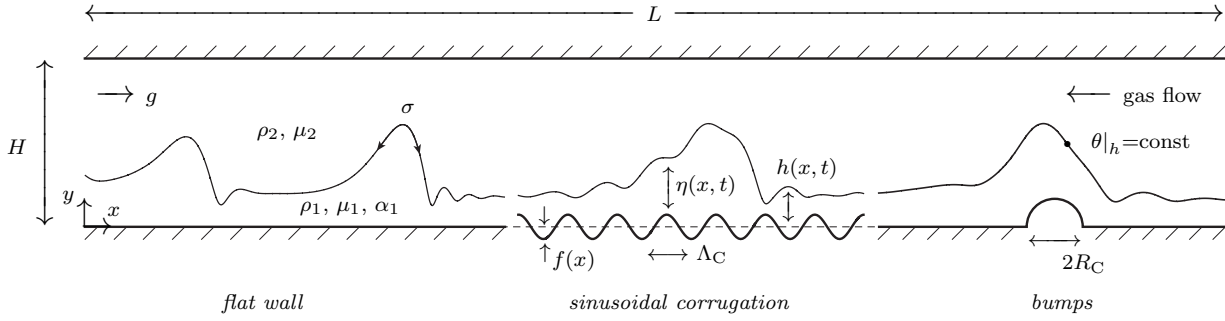


Figure 4.1: Setup of our 2-dimensional DNS of strongly-confined liquid films on an open domain with inlet/outlet conditions, using the finite volume solver **Gerris** (Popinet, 2009). The profile function  $f(x)$  allows applying a corrugation to the lower wall (Dietze, 2019), and  $\theta$  designates a passive scalar transported by the convection-diffusion equation (4.1j).

corresponding to coordinates  $x, y, z$  and velocity components  $u, v, w$ ):

$$X_k \partial_t u_i + u_j \partial_{x_j} u_i = -\partial_{x_i} p + \frac{1}{\text{Re}_k} \partial_{x_j x_j} u_i + \frac{X_k^2}{\text{Fr}^2} (1 - \delta_{i3}) [\delta_{i1} \sin(\phi) - \delta_{i2} \cos(\phi)], \quad (4.1a)$$

$$\partial_{x_j} u_j = 0, \quad (4.1b)$$

where  $\delta_{ij}$  denotes the Kronecker symbol and where we have omitted the phase index  $k$  on the field variables  $u_i$  and  $p$ . We use the scaling defined in (1.1) with  $\epsilon=1$  and recall that  $X_1=1$  (fluid 1) and  $X_2=\Pi_u^{-1}$  (fluid 2). The inter-phase kinematic coupling conditions and stress balances at  $y=h(x, z, t)$  are:

$$u_1 = \Pi_u u_2, \quad v_1 = \Pi_u v_2 = \partial_t h + u_1 \partial_x h + w_1 \partial_z h, \quad w_1 = \Pi_u w_2, \quad (4.1c)$$

$$p_1 + [S_{ij}^1 \cdot n_j] \cdot n_i = \Pi_\rho \Pi_u^2 p_2 + \Pi_\mu \Pi_u [S_{ij}^2 \cdot n_j] \cdot n_i + \text{We} C, \quad (4.1d)$$

$$[S_{ij}^1 \cdot n_j] \cdot \tau_i = \Pi_\mu \Pi_u [S_{ij}^2 \cdot n_j] \cdot \tau_i, \quad (4.1e)$$

$$[S_{ij}^1 \cdot n_j] \cdot t_i = \Pi_\mu \Pi_u [S_{ij}^2 \cdot n_j] \cdot t_i, \quad (4.1f)$$

where  $S_{ij}^k = \frac{1}{2} (\partial_{x_j} u_i + \partial_{x_i} u_j)$  denotes the rate of strain tensor (Whitaker, 1968),  $\boldsymbol{\tau}, \mathbf{t}, \mathbf{n}$  span the orthonormal surface coordinate system:

$$\boldsymbol{\tau} = [1, \partial_x h, 0] (1 + \epsilon^2 \partial_x h^2)^{-1/2}, \quad \mathbf{t} = [0, \partial_z h, 1] (1 + \epsilon^2 \partial_z h^2)^{-1/2}, \quad (4.1g)$$

$$\mathbf{n} = [-\partial_x h, 1, -\partial_z h] (1 + \partial_x h^2 + \partial_z h^2)^{-1/2}, \quad (4.1h)$$

and  $C$  is the full surface curvature:

$$C = \partial_{x_i} n_i = \frac{2 \partial_x h \partial_z h \partial_{xz} h - \partial_{xx} h (1 + \partial_z h^2) - \partial_{zz} h (1 + \partial_x h^2)}{(1 + \partial_x h^2 + \partial_z h^2)^{3/2}}. \quad (4.1i)$$



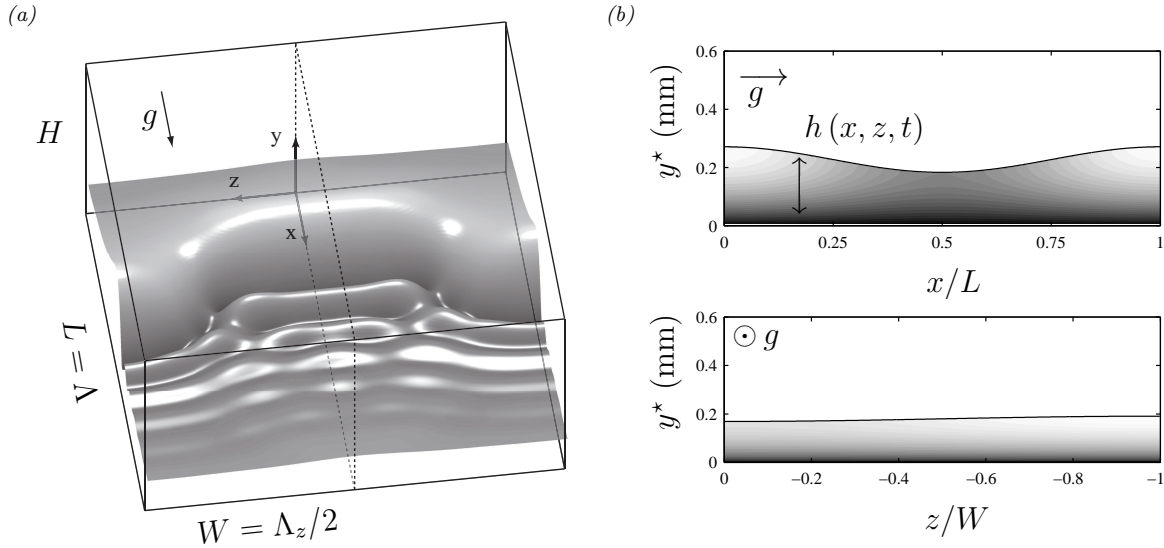


Figure 4.2: Setup of our 3-dimensional DNS (Dietze *et al.*, 2014) of a vertical liquid film falling in a quiescent gas (section 5.2), using the `interFOAM` solver of the `OpenFOAM` package (Rusche, 2002). Periodicity and symmetry are imposed in streamwise and spanwise directions. The domain spans one streamwise wavelength  $\Lambda$  and half of a spanwise wavelength  $\Lambda_z$  (half of the depicted box). (a) 3-dimensional view; (b) initial condition in the  $z=0$  and  $x = \Lambda_x/2$  planes. Contours correspond to the streamwise velocity component  $u(x, y, z, t = 0)$ .

In section 6.3, we will consider the liquid-controlled transfer of a passive scalar  $\vartheta_k$ , e.g. temperature or mass fraction, between a gas and a falling liquid film. In that limit, the gas is assumed ideally-mixed and the transfer problem reduces to solving the liquid-side convection-diffusion equation:

$$\partial_t \theta + u_j \partial_{x_j} \theta = \frac{1}{\text{Pe}} \partial_{x_j x_j} \theta, \quad (4.1j)$$

subject to a Dirichlet condition at the film surface:

$$\theta|_{y=h} = 1, \quad (4.1k)$$

where  $\text{Pe} = \mathcal{U}_1 \mathcal{L} / \alpha_1$  denotes the Péclet number, containing the diffusivity  $\alpha$ , and where  $\theta = (\vartheta_1 - \vartheta_1^0) / (\vartheta|_{y=h} - \vartheta_1^0)$  is the normalized liquid-side scalar  $\vartheta_1$  based on its inlet and interfacial values  $\vartheta_1^0$  and  $\vartheta|_{y=h}$ , which are both fixed.

We distinguish two sets of boundary conditions at the upper and lower boundaries:

(i) In our 2-dimensional DNS of strongly confined liquid films (figure 4.1), we use:

$$u_1|_{y=f} = v_1|_{y=f} = u_2|_{y=H} = v_2|_{y=H} = 0, \quad [(\partial_y - \partial_x f \partial_x) \theta]_{y=f} = 0, \quad (4.2)$$

where  $f(x) = \eta(x, t) - h(x, t)$  defines a corrugation profile for the lower wall (section 6.3).

- (ii) In our DNS of liquid films falling in a quiescent atmosphere (e.g. the 3-dimensional case in figure 4.2), we use:

$$u_1|_{y=0} = v_1|_{y=0} = w_1|_{y=0} = \partial_y u_2|_{y=H} = \partial_y v_2|_{y=H} = \partial_y w_2|_{y=H} = 0, \quad (4.3)$$

so that the gas is virtually unconfined by the upper boundary  $y=H$ .

In terms of streamwise boundary conditions, we distinguish:

- (i) Periodic DNS on a domain spanning the streamwise wavelength  $\Lambda$ , where we impose periodicity on the velocity field:

$$u_k|_{x=0} = u_k|_{x=\Lambda}, \quad v_k|_{x=0} = v_k|_{x=\Lambda}, \quad w_k|_{x=0} = w_k|_{x=\Lambda}, \quad (4.4)$$

while allowing for a non-zero pressure drop  $\Delta p_2$ , through an additional source term  $\Gamma_k$  on the RHS of the x-component of (4.1a):

$$\Gamma_k = \frac{\Delta p_k}{\Lambda}, \quad \Delta p_1 = \Pi_\rho \Pi_u^2 \Delta p_2. \quad (4.5)$$

In our 3-dimensional DNS (figure 4.2), additional spanwise symmetry conditions are imposed at  $z=0$  and  $z=\Lambda_z/2$ :

$$\partial_z u_k = \partial_z v_k = w_k = \partial_z p_k = 0, \quad (4.6)$$

whereby we have simulated only half of the domain depicted in panel 4.2a.

- (ii) Open-domain DNS according to figure 4.1 with inlet/outlet conditions on an extended domain of length  $L$ . At the liquid inlet  $x=0$ , we impose parabolic velocity profiles corresponding to Poiseuille flow in both phases:

$$u_1 = 6 \frac{\bar{q}_1}{h_0} [1 + F_1(t)] (\xi - \xi^2), \quad \xi = y - f|_{x=0}, \quad (4.7)$$

$$u_2 = 6 \frac{\bar{q}_2}{H - h_0} [1 + F_2(t)] (\xi - \xi^2), \quad \xi = \frac{y - h_0}{H - h_0}, \quad (4.8)$$

where  $\bar{q}_1$  and  $\bar{q}_2$  are the nominal flow rates,  $0 \leq \xi \leq 1$  denotes the relative position within the liquid and gas, and  $h_0 = \eta|_{x=0} + f|_{x=0}$  is the inlet film height. Further, at  $x=0$ :

$$v_k = 0, \quad \partial_x p_k = 0, \quad \theta = 0. \quad (4.9)$$

The liquid inlet flow rate  $q_1 = \int_{f|_{x=0}}^{h_0} u_1|_{x=0} dy$  is perturbed in time through the function  $F_1(t)$ , intervening in (4.7). This function is used to excite surface waves, either through sinusoidal monochromatic forcing:

$$F_1(t) = \epsilon_1 \sin(2\pi f t), \quad (4.10)$$

where  $f$  is the wave frequency and  $\epsilon_1$  the perturbation amplitude, or through “random” noise, mimicked through a Fourier series (Chang *et al.*, 1996a):

$$F_1(t) = \epsilon_1 \sum_{k=1}^N \sin(2\pi k \Delta f t + \varphi_{\text{rand}}), \quad \Delta f = 2 f_c/N, \quad (4.11)$$

where  $N=1000$ ,  $f_c$  designates the linear cut-off frequency of the Kapitza instability, and  $\varphi_{\text{rand}}$  is a random phase shift.

The gas flow rate  $q_2 = \int_{h_0}^H u_2|_{x=0} dy$  at  $x=0$  is kept constant in most of our DNS, i.e.  $F_2(t)=0$  in (4.7). However, in some cases of monochromatically forced surface waves, we require a constant total flow rate  $q_{\text{tot}}=q_1+q_2$ , and thus the time variation of  $q_1$  needs to be compensated by a time variation of  $q_2$ :

$$F_2(t) = \epsilon_2 \sin(2\pi f t), \quad \epsilon_2 = \epsilon_1 \frac{\bar{q}_1}{\bar{q}_2} \frac{H - h_0}{h_0}. \quad (4.12)$$

At the end of the computational domain,  $x = L$ , homogeneous Neumann conditions are imposed for the velocities and the passive scalar  $\theta$ :

$$\partial_x u_k = \partial_x v_k = \partial_x \theta = 0, \quad (4.13)$$

whereas the pressure is fixed by a Dirichlet condition:

$$u_1 > 0 : \quad p_k = 0 \quad (4.14)$$

$$u_1 \leq 0 : \quad \begin{cases} p_1 = -\frac{1}{2}(u^2 + v^2) \\ p_2 = 0 \end{cases} \quad (4.15)$$

where  $p_1$  is set depending on the sign of the liquid velocity  $u_1$  (Dietze & Ruyer-Quil, 2013), which may change due to flow reversal underneath the troughs of the precursory capillary ripples typically forming in falling liquid films (Malamataris & Balakotaiah, 2008; Dietze *et al.*, 2008). When  $u_1 < 0$ , the value of  $p_1$  is reduced below its usual value  $p_1=0$  by an increment corresponding to the local instantaneous dynamic pressure. This ensures that the flow reversal zones are advected out of the domain. Otherwise, they would be blocked at the domain outlet and continually suck liquid into the domain.

### 4.1.2 Liquid films in cylindrical geometries

The flow in figure 1.3 is governed by the full Navier-Stokes and continuity equations in cylindrical coordinates, written here in two dimensions (axial and radial coordinates and

components are denoted by  $x$ ,  $u$  and  $r$ ,  $v$ ), assuming axisymmetry about the tube axis  $r=0$ :

$$X_k \partial_t u_k + u_k \partial_x u_k + v_k \partial_r u_k = -\partial_x p_k + \frac{1}{\text{Re}_k} \left\{ \partial_{xx} u_k + \frac{1}{r} \partial_r (r \partial_r u_k) \right\} + \frac{X_k^2}{\text{Fr}^2}, \quad (4.16a)$$

$$X_k \partial_t v_k + v_k \partial_r v_k + u_k \partial_x v_k = -\partial_r p_k + \frac{1}{\text{Re}_k} \left\{ \partial_{xx} v_k + \partial_r \left[ \frac{1}{r} \partial_r (r v_k) \right] \right\}, \quad (4.16b)$$

$$0 = \frac{1}{r} \partial_r (r v_k) + \partial_x u_k, \quad (4.16c)$$

where we have used the scaling introduced in (1.38) and  $X_1=1$  and  $X_2=\Pi_u^{-1}$ . The coupling conditions at the film surface  $r=d(x,t)$  take the same form as for the planar configuration (see equations 4.1c to 4.1f), only that the third dimension is dropped and  $h$  is replaced by  $d$  in the kinematic condition:

$$v_1 = \Pi_u v_2 = \partial_t d + u_1 \partial_x v_1. \quad (4.17)$$

The stress tensor is again given by  $S_{ij}^k = \frac{1}{2} (\partial_{x_j} u_i + \partial_{x_i} u_j)$ , using Einstein notation ( $i,j=1$  and  $i,j=2$  correspond to the axial and radial dimensions), and the orthonormal surface coordinate system  $\tau$ ,  $\mathbf{n}$ , and surface curvature  $C$  take the form:

$$\boldsymbol{\tau} = [1, \partial_x d] (1 + \epsilon^2 \partial_x d^2)^{-1/2}, \quad \mathbf{n} = [-\partial_x d, 1] (1 + \partial_x d^2)^{-1/2}, \quad (4.18)$$

$$C = \nabla \cdot \mathbf{n} = \frac{1 + \partial_x d^2 - d \partial_{xx} d}{d (1 + \partial_x d^2)^{3/2}}, \quad (4.19)$$

where  $\nabla = [\partial_x, r^{-1} + \partial_r]$  again denotes the nabla operator in cylindrical coordinates. The radial boundary conditions are:

$$u_1|_{r=R} = v_1|_{r=R} = \partial_r u_2|_{r=0} = v_2|_{y=0} = 0. \quad (4.20)$$

All our DNS of the cylindrical configuration were performed with **Gerris** on a domain spanning the wavelength  $\Lambda$ , using periodic boundary conditions in axial direction:

$$u_k|_{x=0} = u_k|_{x=\Lambda}, \quad v_k|_{x=0} = v_k|_{x=\Lambda}, \quad (4.21)$$

and, as in the planar configuration, we add the additional source term  $\Gamma_k$  (4.5) to the RHS of (4.16a), to apply a non-zero pressure drop. Simulations were started from the initial condition:

$$d(x, t=0) = \bar{d} [1 + \epsilon_1 \sin(2\pi x/\Lambda)], \quad u_1(x, r, t=0) = u_{10}|_{d_0=d(x,t=0)}, \quad (4.22)$$

$$u_2 = v_1 = v_2 = 0, \quad (4.23)$$

In these simulations, there are 3 control parameters, i.e.  $\Lambda$ ,  $M$ , and the liquid volume  $V_1$ :

$$V_1 = \pi \Lambda \left\{ R^2 - \frac{1}{2} \bar{d}^2 (2 + \epsilon_1^2) \right\}. \quad (4.24)$$

Thus, the values of the Reynolds numbers  $\text{Re}_k$  are outcomes.

### 4.1.3 Drops spreading on rigid surfaces

In section 8.2, we will discuss numerical simulations that reproduce the experimental configuration in figure 8.7, which was studied at Tokyo University of Science in the group of Ichiro Ueno. In this configuration, a liquid drop of silicone oil spreads on an otherwise smooth horizontal substrate and comes into contact with an isolated micro-particle, which leads to an acceleration of the spreading rate.

Versus the simulations discussed in sections 4.1.1 and 4.1.2, there is one additional ingredient here, i.e. the presence of a contact line at the front of the spreading droplet, which moves onto and past the particle (figure 8.8). We account for this through an appropriate boundary condition at solid boundaries that come into contact with the liquid-gas interface. There, we prescribe the macroscopic contact angle  $\beta$  between the liquid-gas interface and the wall surface, according to the Cox-Voinov relation (Snoeijer & Andreotti, 2013):

$$\beta^3 = \beta_0^3 + 9 \text{Ca} \ln \left( \frac{c L_e^*}{L_i^*} \right), \quad (4.25)$$

where  $\beta_0$  denotes the static contact angle,  $\text{Ca} = U_{\text{CL}}^* \mu_1 / \sigma$  denotes the Capillary number, containing the local instantaneous contact line velocity  $U_{\text{CL}}$ ,  $c=10$  is a non-universal constant,  $L_e^* = R_0^*$  is an external length scale, which we set to the volume-equivalent drop radius  $R_0^*$ , and  $L_i^* = 100 \mu\text{m}$  is an internal length scale. The contact angle  $\beta$  according to (4.25) is enforced through a condition on the normal vector  $\mathbf{n}$  of the orthonormal surface coordinate system (4.1g):

$$\mathbf{n} \cdot \mathbf{n}^{\text{w}} = \cos(\beta), \quad (4.26)$$

where  $\mathbf{n}^{\text{w}}$  designates the normal unit vector of the orthonormal wall coordinate system. Further, we apply adherence and no-penetration conditions for the velocity at solid boundaries:

$$\mathbf{u} \cdot \mathbf{n}^{\text{w}} = \mathbf{u} \cdot \boldsymbol{\tau}_1^{\text{w}} = \mathbf{u} \cdot \boldsymbol{\tau}_2^{\text{w}} = 0, \quad (4.27)$$

where  $\mathbf{u}$  denotes the velocity vector, and  $\boldsymbol{\tau}_1^{\text{w}}$  and  $\boldsymbol{\tau}_2^{\text{w}}$  denote the tangential unit vectors of the orthonormal wall coordinate system.

In a continuum context, the adherence condition (4.27) implies that the contact line cannot move freely. This problem can be circumvented by applying a Navier slip condition for the tangential velocity components (Sui *et al.*, 2014; Gründing *et al.*, 2020). However, in simulations based on the volume of fluid method, the displacement of the contact line (via the liquid volume fraction  $\phi$ ) is governed by the tangential liquid velocity in the wall-adjacent contact cell  $u_{\text{cc}}$ , which is non-zero due to finite spatial discretization (see section 4.2). Thus, the contact line is free to move and  $u_{\text{cc}}$  is a good approximation for  $U_{\text{CL}}$ . This is in line with the derivation of Tanner (1979), who also assumed wall adherence.

Most of our contact line simulations reported in section 8.2 were performed at Tokyo University of Science, using the `interFOAM` solver, and my role was only a supervising one. The exact set-up of these simulations, including boundary conditions, is reported in Nakamura *et al.* (2020*b,a*). In addition, we have performed two simulations using `Gerris`. The first (figure 4.11), represents an axisymmetric liquid drop spreading on a smooth plane

substrate. This simulation was used to validate our representation of moving contact lines. The second (figure 8.10), represents a two-dimensional drop spreading toward and climbing up a vertical wall. This is a benchmark to study how the contact line moves from a substrate onto a particle. Further details of these simulations are given at the appropriate places.

## 4.2 VOF and CSF methods

Both employed codes, `Gerris` and `interFOAM`, rely on the volume of fluid (VOF) approach (Hirt & Nichols, 1981) and the continuum surface force (CSF) method (Brackbill *et al.*, 1992). We outline these methods for the planar 2-dimensional example in figure 4.1, based on equations (4.1). We focus first on their implementation in `Gerris`, before noting the differences in `interFOAM`. Extension to 2-dimensional axisymmetric and 3-dimensional Cartesian geometries is straightforward.

The Navier-Stokes equations are solved for an effective single-fluid defined on the entire computational domain, along with the purely-convective conservation equation for the liquid volume fraction  $\phi$ , while enforcing a divergence-free velocity field:

$$\bar{\rho} \partial_t u_i + \bar{\rho} u_j \partial_{x_j} u_i = -\partial_{x_i} p + \bar{\rho} g_i + \bar{\mu} \partial_{x_j x_j} u_i + F_{\sigma i}''', \quad (4.28)$$

$$\partial_t \phi + u_i \partial_{x_i} \phi = 0, \quad (4.29)$$

$$\partial_{x_j} u_j = 0, \quad (4.30)$$

where all quantities are dimensional (here and throughout this section), and the hydrodynamical properties of the single-fluid are computed from the pure-phase properties through a geometrically-weighted average:

$$\bar{\rho} = \phi \rho_l + (1 - \phi) \rho_g, \quad \bar{\mu} = \phi \mu_l + (1 - \phi) \mu_g. \quad (4.31)$$

Equation (4.29) is discretized based on a piecewise linear reconstruction of the interface (Youngs, 1982), which relies on the values of  $\phi$  in the computational cell itself and its immediate neighbours. The source term  $F_{\sigma i}'''$  in equation (4.28) accounts for the contribution of capillary forces in the normal coupling condition (4.1d):

$$F_{\sigma i}''' = \sigma \hat{\kappa} \delta_s \hat{n}_i, \quad (4.32)$$

where  $\hat{\kappa}$  and  $\hat{n}_i$  denote (dimensional) numerical estimates of the interfacial curvature  $C$  (4.1i) and normal vector  $\mathbf{n}$  (4.1g), while the Dirac distribution function  $\delta_s$  restricts treatment to the liquid-gas interface. The term  $\delta_s \hat{n}_i$  is computed from the gradient of the  $\phi$  field:

$$\delta_s \hat{n}_i = \hat{\partial}_{x_i} \phi, \quad (4.33)$$

where the discrete approximation  $\hat{\partial}_{x_i}$  of the differential operator is chosen to be compatible with that of the pressure gradient in (4.28), ensuring that the inter-phase pressure jump

is exactly recovered in the static limit (Renardy & Renardy, 2002; Francois *et al.*, 2006). The interface curvature  $\hat{\kappa}$  is computed from the height function  $\hat{h}$ , a numerical estimate of the film height  $h$  obtained from the integral  $\int \phi dy$  over a column of computational cells (Rudman, 1997):

$$\hat{\kappa} = -\hat{\partial}_{xx}\hat{h} \left\{ 1 + \hat{\partial}_x\hat{h}^2 \right\}^{-3/2}, \quad (4.34)$$

where the spatial derivatives are discretized appropriately (Popinet, 2009).

The transport and inter-phase transfer of a passive scalar  $\vartheta$  is computed through the single-fluid convection-diffusion equation:

$$\bar{\rho} \partial_t \vartheta + \bar{\rho} u_j \partial_{x_j} \vartheta = \partial_{x_j} (\bar{\alpha} \partial_{x_j} \vartheta), \quad (4.35)$$

where we construct the single-fluid diffusivity  $\bar{\alpha}$  as follows:

$$\bar{\alpha}^{-1} = \begin{cases} \alpha_1^{-1}, & y < \hat{h} - \frac{\Delta_x}{2} \\ \phi \alpha_1^{-1} + (1 - \phi) \alpha_2^{-1}, & \hat{h} - \frac{\Delta_x}{2} \leq y \leq \hat{h} + \frac{\Delta_x}{2} \\ \alpha_2^{-1}, & y > \hat{h} + \frac{\Delta_x}{2} \end{cases}, \quad (4.36)$$

where  $\Delta_x$  is the (dimensional) height of a cell containing the interface. This leads to a sharp representation of scalar transport (panel 4.3c), even though the volume fraction field  $\phi$  itself is not sharp. The middle relation in (4.36) constitutes a harmonic average and ensures that the diffusional resistance of interfacial cells is physically consistent (Patankar, 1980). For example, in the limit  $\alpha_2 \rightarrow \infty$ , which is the one we are interested in ( $\alpha_2/\alpha_1 > 10^3$  in our DNS),  $\bar{\alpha}^{-1}$  correctly reduces to the sole liquid contribution, whereas geometric averaging would yield a diffusional resistance of zero. See figure 4.3 for a comparison of  $\bar{\alpha}$  fields obtained by geometric (panel 4.3a) and harmonic (panel 4.3b) averaging. Our approach allows an accurate prediction of scalar transfer through the film surface (see figure 4.9 in section 4.3) while remaining within the VOF framework. Albert *et al.* (2014) used a different approach by approximating the scalar profile near the interface with an analytical solution.

In the case of liquid films flowing over corrugated substrates (section 6.3), the corrugation profile  $f(x)$  (figure 4.1) is represented through an embedded solid boundary (panel 4.4a) at which the boundary conditions are directly applied through interpolation (Calhoun, 1999).

The **Gerris** solver discretizes the computational domain into a Cartesian quadtree grid, which can be adaptively-refined based on user-defined solution variables. The (dimensional) cell size at a given refinement level  $RL$  is:

$$\Delta_x^* = \frac{L^*}{2^{RL}}, \quad (4.37)$$

where  $L^*$  is the length scale of the DNS (usually the domain height). In our simulations, we have systematically refined the grid around the liquid-gas interface, and within the bulk phases based on the vorticity. The maximal refinement level  $RL_{FS}$  at the liquid-gas

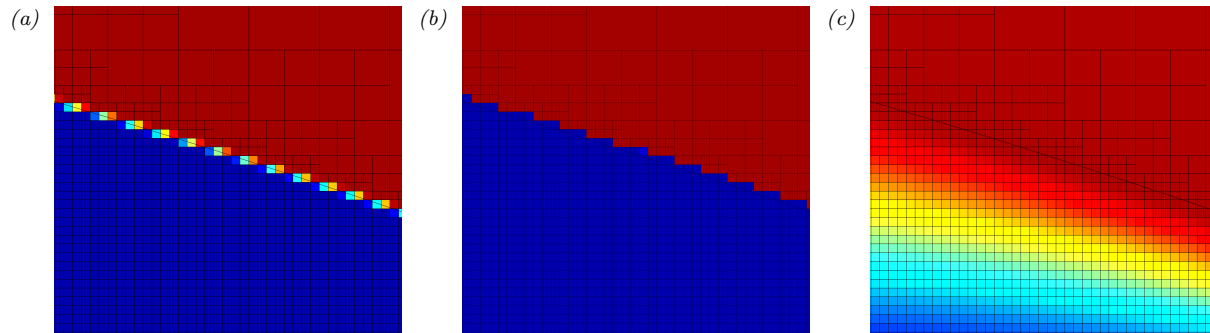


Figure 4.3: Geometric versus harmonic averaging of the single-fluid diffusivity  $\bar{\alpha}$  in (4.35) for simulating inter-phase scalar transfer based on the VOF approach, using the finite-volume solver **Gerris** (Popinet, 2009). (a) Geometrically averaged diffusivity:  $\bar{\alpha} = \phi\alpha_1 + (\phi - 1)\alpha_2$ . Blue corresponds to  $\alpha_1$  and red to  $\alpha_2$ ; (b) Harmonically averaged diffusivity:  $\bar{\alpha} = \alpha_1\alpha_2(\phi\alpha_2 + (\phi - 1)\alpha_1)^{-1}$ ; (c) field of the passive scalar  $\theta$  in the vicinity of the liquid-gas interface, as obtained with harmonic averaging (Dietze, 2019).

interface was usually larger by one unit than  $RL$  in the bulk ( $RL = RL_{FS} - 1$ ), except in our scalar transfer computations at large  $Pe$  (section 6.3), where a very fine uniform grid was imposed within the entire liquid phase ( $RL = RL_{FS}$ ). In that case, the grid in the vicinity of the corrugated wall was additionally refined ( $RL = RL_{FS} + 2$ ), in order to accurately capture the shape of the corrugations (panel 4.4a). We will use the interface refinement level  $RL_{FS}$  to characterize the grid resolution of our DNS. In terms of time discretization, **Gerris** employs a fractional-step projection method (Chorin, 1968) that leads to a formally second-order accurate discretisation (Popinet, 2009). The time step  $\Delta_t$  is dynamically adapted so that  $CFL = u^* \Delta_t / \Delta \leq 0.8$  in each cell ( $u^*$  denotes the magnitude of the dimensional velocity in a given cell). Results of grid dependence analyses are presented in section 4.3.

In the case of contact line simulations (section 8.2) with **Gerris**, the contact angle  $\beta$  (4.25) is imposed by orienting the liquid-gas interface in the contact cell (see panel 4.4b), according to the condition (4.26) on the interface normal  $\mathbf{n}$ . Syntactically, this is achieved by using the boundary condition type **BcAngle**. In 2-dimensional simulations, (4.26) is unambiguous, but in a 3-dimensional setting, the interface segment in the contact cell can be oriented in many ways without violating (4.26). In that case,  $\mathbf{n}$  is oriented according to (Afkhani & Bussmann, 2009):

$$\mathbf{n} = \frac{\underline{\mathbf{n}}}{|\underline{\mathbf{n}}|}, \quad \underline{\mathbf{n}} = [1, |\mathbf{n}^p| \tan(\beta)^{-1}, s_{CL}^w]^T, \quad (4.38)$$

$$\mathbf{n}^p = [1, 0, s_{CL}^w]^T, \quad s_{CL}^w = \nabla \cdot \boldsymbol{\tau}_2^w (\mathbf{r}^{CL} \cdot \boldsymbol{\tau}_1^w), \quad (4.39)$$

where  $\mathbf{n}^p$  is the projection of  $\underline{\mathbf{n}}$  onto the solid surface,  $\mathbf{r}_{CL}$  denotes the position vector of the contact line, and  $s_{CL}^w$  is the slope of the contact line in the solid-surface coordinate system  $(\boldsymbol{\tau}_1^w, \boldsymbol{\tau}_2^w)$ , which is evaluated at the old time step. In the 2-dimensional limit,



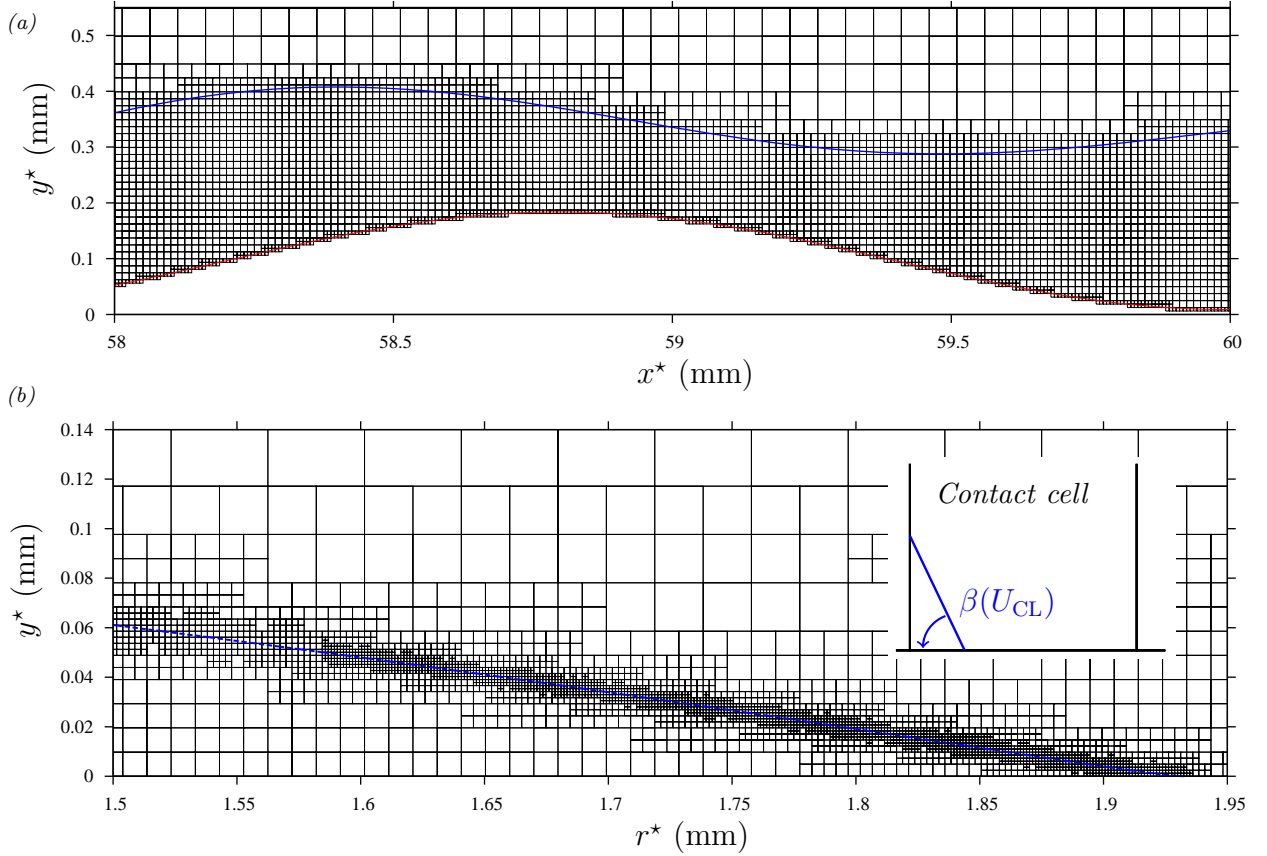


Figure 4.4: Examples of our DNS with **Gerris** using the VOF and CSF methods on an adaptively refined quadtree grid. (a) Falling liquid film (liquid-gas interface in blue) flowing over a sinusoidal corrugation represented by an immersed boundary (red line). Parameters as in panel 6.16d; (b) Axisymmetric silicone-oil drop spreading on a smooth substrate with  $\beta(U_{CL})$  according to (4.25) and  $\beta_0=1^\circ$ . Parameters as in figure 4.11.

$s_{CL}^w=0$  and (4.38) collapses to:

$$\mathbf{n} = \frac{\mathbf{n}}{|\mathbf{n}|}, \quad \mathbf{n} = [1, \tan(\beta)^{-1}]^T. \quad (4.40)$$

We use the tangential cell-centred fluid velocity within the contact cell  $u_{cc}$ :

$$u_{cc} = \pm \{(\boldsymbol{\tau}_1^w \cdot \mathbf{u}_{cc})^2 + (\boldsymbol{\tau}_2^w \cdot \mathbf{u}_{cc})^2\}^{1/2}, \quad (4.41)$$

as the contact line velocity in the Cox-Voinov relation (4.25), i.e.  $U_{CL}=u_{cc}$ , whereby the sign of  $u_{cc}$  depends on whether the contact line is advancing or receding.

When the grid resolution is coarse,  $u_{cc}$  is quite large, notwithstanding the adherence condition at the wall (4.27). Thus, the contact line slips freely. By contrast, in the limit of very fine grids,  $u_{cc}$  tends to zero. This causes the dynamic part in (4.25) to drop, which is physically consistent, as the static contact angle  $\beta_0$  should be recovered in that limit. Secondly, it imposes a pinning condition on the contact line in the contact cell. In

that case, we have observed that the contact line in our simulations moves in a stick-slip motion (at the scale of the grid resolution), whereby its macroscopic speed  $U_{\text{CL}}$  agrees well with the theoretical spreading rate (figure 4.11). During a pinning sequence, the liquid-gas interface around the pinning point (assuming it has not attained equilibrium) evolves such as to produce a strong positive curvature there. This causes a large pressure minimum, which increasingly sucks liquid toward the contact cell, thus increasing  $u_{\text{cc}}$  and eventually forcing the contact line to slip by one increment.

Implementation of the VOF and CSF methods in the `interFOAM` solver differs in two main respects. Firstly, the advection equation (4.29) for  $\phi$  is discretized without accounting for the orientation of the liquid-gas interface in interfacial cells. To mitigate the creation of flotsam due to numerical diffusion of  $\phi$  (Prosperetti & Tryggvason, 2007), an ad hoc *compression velocity*  $\mathbf{U}^c$ , which is directed normal to and toward the interface, is applied by augmenting the advection equation (4.29) as follows:

$$\partial_t \phi + u_i \partial_{x_i} \phi + \partial_{x_i} \{U_i^c \phi (1 - \phi)\} = 0. \quad (4.42)$$

Secondly, the curvature of the liquid-gas interface  $\hat{\kappa}$  is not computed based on the numerically integrated surface height (4.34), but through:

$$\hat{\kappa} = \hat{\partial}_{x_i} \hat{n}_i, \quad \hat{n}_i = \frac{\hat{\partial}_{x_i} \phi}{\left[ \hat{\partial}_{x_i} \phi \hat{\partial}_{x_j} \phi \right]^{\frac{1}{2}}}. \quad (4.43)$$

In the case of contact line simulations (section 8.2), (4.26) is recast as a boundary condition on the wall-normal gradient of the volume fraction  $\hat{\partial}_{x_i} \phi \hat{n}_i^w$ , by introducing the approximated interface normal  $\hat{n}_i$  (4.43). This condition is applied in all wall-adjacent cells with intermediate volume fractions ( $0 < \phi < 1$ ), which results in a less sharp representation of the contact line dynamics compared to `Gerris`. Finally, the velocity dependence of the contact angle  $\beta$  is prescribed via a hard-coded internal function:

$$\beta = \beta_0 + (\beta_a - \beta_r) \tanh \left( \frac{u_{\text{cc}}}{u_\beta} \right). \quad (4.44)$$

In our simulations, the parameters  $\beta_a$ ,  $\beta_r$ , and  $u_\beta$  were fitted in order to emulate (4.25) in the studied velocity range.

In all our simulations with `interFOAM`, a fixed grid was used. Regions of the computational domain containing the liquid phase and the liquid-gas interface were resolved with a better resolution than regions that always contain only gas. We will quantify the grid resolution in the finer region based on the minimum spatial increment  $\Delta_y^*|_{\min}$  normal to the main flow direction. The increment in flow direction always satisfies  $\Delta_x^*|_{\min} \geq \Delta_y^*|_{\min}$ .

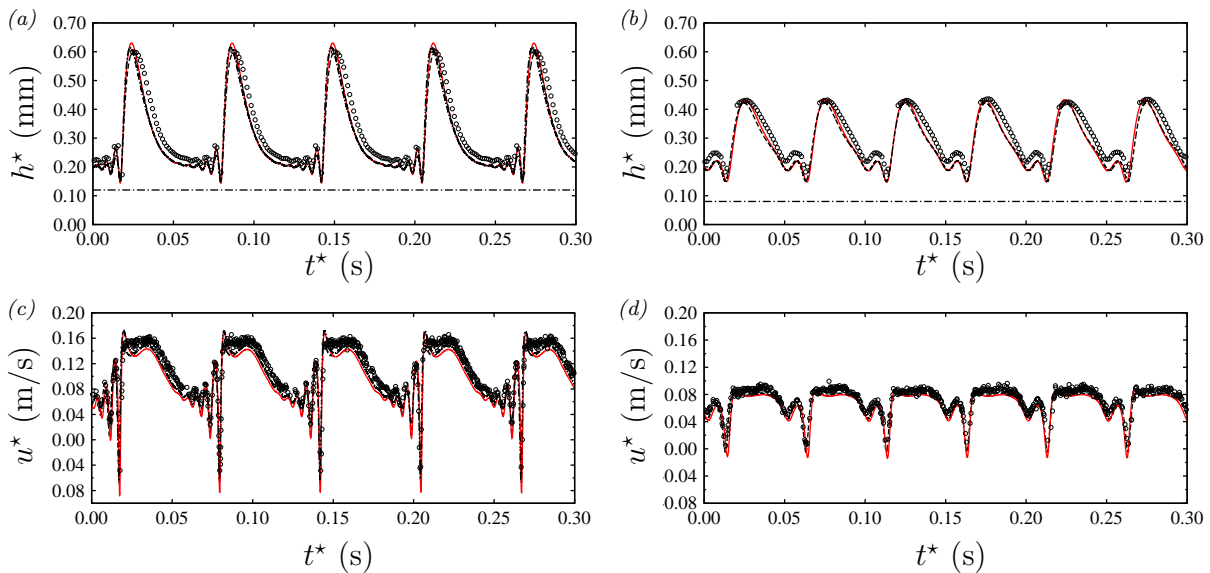


Figure 4.5: Benchmark DNS of a vertically falling liquid film, according to the experiments in panels 16b and 19b of Dietze *et al.* (2009):  $\phi=90^\circ$ ,  $\text{Re}_1=15$ ,  $\text{Ka}=509.5$  (DMSO-water in table 2.1). The gas phase is quiescent and has no significant effect. Symbols: experimental data; solid (red) lines: DNS with `Gerris` using  $RL_{\text{FS}}=9$  based on  $\underline{L}^*=1.49$  mm (4.37); dot-dot-dashed: DNS with `interFOAM` using  $\Delta_y^*|_{\text{min}}=10$   $\mu\text{m}$ ; dashed: WRIBL model (1.27). (a,c) Large-amplitude solitary waves:  $f^*=16$  Hz; (b,d) high-frequency shallow waves:  $f^*=20$  Hz. Dot-dashed lines in panels a,b mark y-position of velocity time-traces in panels c,d.

## 4.3 Validation

We have performed several benchmark DNS to validate the employed Navier-Stokes solvers, `Gerris` and `interFOAM`, against experiments from the literature and analytical solutions.

We start with the case of a vertically falling liquid film consisting of a 83% by weight aqueous solution of dimethylsulfoxide (DMSO, see table 2.1) flowing in quiescent ambient air, according to the experiments of Dietze *et al.* (2009). In that reference, 2-dimensional surface waves were excited by way of coherent inlet forcing. Figure 4.5 compares numerical data obtained from our periodic DNS using `Gerris` (Dietze, 2016) and `interFOAM` (Dietze *et al.*, 2014) with the experimental data for two different forcing frequencies. In addition, the dot-dashed lines represent TWS obtained with our WRIBL model (1.27). All numerical computations accurately capture the wave amplitude, the number of capillary waves, and the occurrence of flow reversal zones underneath the capillary troughs.

The second benchmark concerns a vertically falling water film flowing in quiescent air, according to the experiments of Park & Nosoko (2003), where a series of immersed needles was used, in addition to temporal inlet forcing, to excite regular 3-dimensional

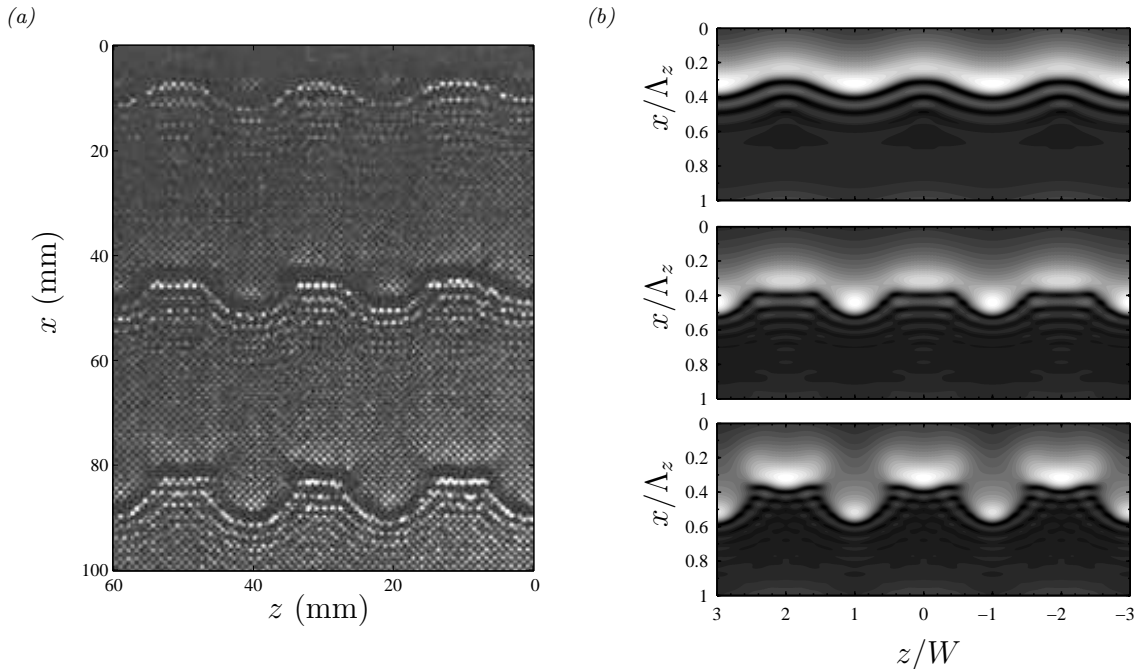


Figure 4.6: Benchmark DNS using **interFOAM** of a vertically-falling water film based on experiments by Park & Nosoko (2003):  $\phi=90^\circ$ ,  $Re_1 = 59.3$ ,  $f^*=17$  Hz,  $Ka=3923.2$  (water III in table 2.1). The ambient air is quiescent. (a) Experimental shadowgraph from panel 7d of Park & Nosoko (2003) reproduced here with permission from John Wiley & Sons, Inc; (b) snapshots of periodic DNS for successive periods during the evolution of a 3-dimensional surface wave:  $\Lambda_z^*=25$  mm;  $W^*=\Lambda_z^*/2=10$  mm;  $\Delta_y^*|_{\min}=10$   $\mu\text{m}$ .

surface waves of prescribed lateral wavelength  $\Lambda_z$  and frequency  $f$ . Figure 4.6 compares our DNS data, obtained from a periodic large-scale DNS<sup>1</sup> using **interFOAM** (Dietze *et al.*, 2014), with the experimental data for a representative case. The simulation reproduces all main features of the 3-dimensional wave structure, consisting of horseshoe-shaped solitary waves preceded by several capillary ripples.

The third benchmark concerns a liquid film of silicone oil falling over an inclined wall with a sinusoidal corrugation, according to the experiments of Wierschem *et al.* (2010). Figure 4.7 compares streamline plots obtained from our periodic DNS using **Gerris** (Dietze, 2019) with experimental photographs showing tracer particle pathlines. The film is stable for both  $Re_1$  values considered and thus the flow is steady. Thus, pathlines and streamlines should coincide. Our DNS accurately reproduce the size and position of the separation vortices forming in the corrugation troughs.

The fourth benchmark concerns an upward pressure-driven core-annular flow of oil (fluid 2) and water (fluid 1) through a vertical cylindrical tube, according to the experiment in panel 6b of Bai *et al.* (1996) and the corresponding DNS in figure 4 of

<sup>1</sup>The simulation was run on the supercomputer JUROPA (grant number HAC27) at Forschungszentrum Jülich.

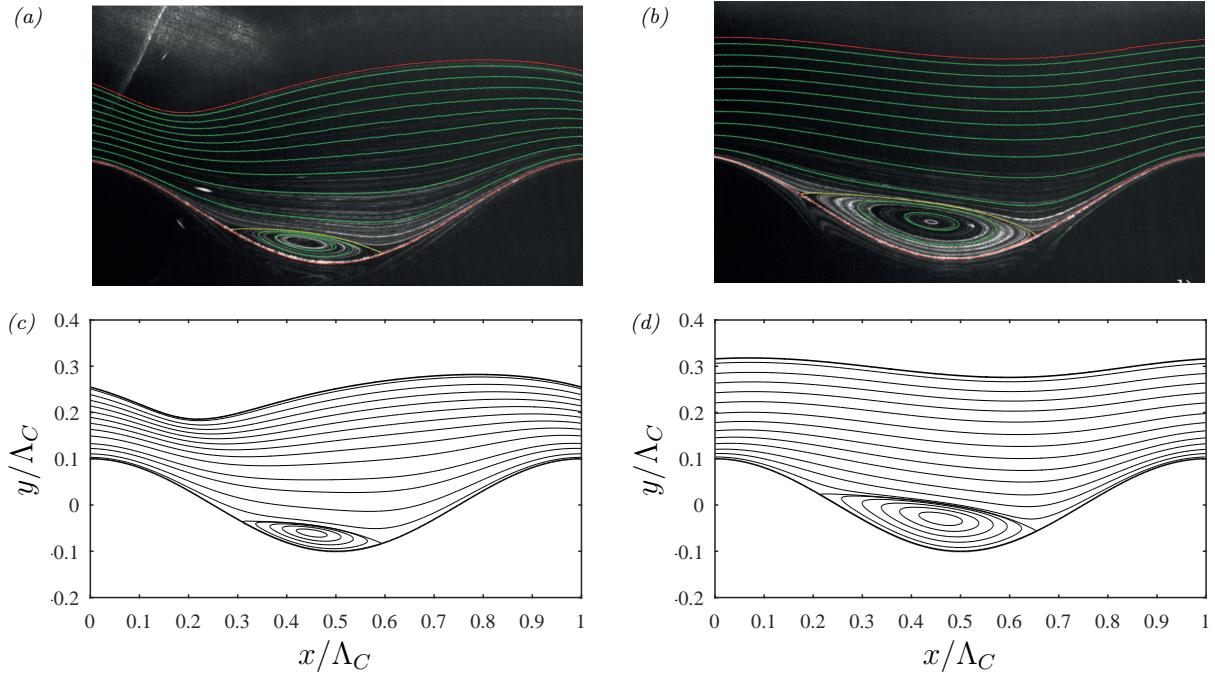


Figure 4.7: Benchmark DNS with *Gerris* of a liquid film falling over an inclined sinusoidal corrugation of wavelength  $\Lambda_C^*=10$  mm and amplitude  $\hat{h}_C^*=1$  mm (panel 4.1), according to the experiments in panels 3b and 3d of Wierschem *et al.* (2010):  $\phi=8^\circ$ ,  $Ka=36.3$  (silicone oil I in table 2.1). The gas phase is quiescent and has no significant effect. (a,b) experimental data; (b,d) periodic DNS with  $RLF_S=9$  based on  $\underline{L}^*=10$  mm (4.37); (a,c)  $Re_1=16.10$ ,  $\bar{h}/\Lambda_C=0.244$ ; (b,d)  $Re_1=47.95$ ,  $\bar{h}/\Lambda_C=0.297$ .

Kouris & Tsamopoulos (2001). We have reproduced this experiment with our own transient periodic DNS using *Gerris*, where we have set the wavelength  $\Lambda^*=12.25$  mm and the water volume  $V_1/(\pi R^2 \Lambda)=0.3932$  according to the experiment, and tuned the normalized pressure drop  $M$  to match the experimental target value for the oil Reynolds number  $Re_2=-0.714$ . Our simulation reproduces correctly the shape of the so-called bamboo waves forming on the water-oil interface (figure 4.8). However, there is a 30% error in the computed water Reynolds number  $Re_1$ . An error of this magnitude was also observed by Kouris & Tsamopoulos (2001), when comparing their DNS with the experiment. These authors attributed the error to an ambiguity in the surface tension values reported in different accounts of the experiments of Bai *et al.* (1996).

The fifth benchmark concerns the transport of a passive scalar in a hydrodynamically developed stable falling liquid film (figure 4.9), in the limit of a passive gas ( $\Pi_\mu=\Pi_\rho=0$ ). In this limit, the liquid streamwise velocity profile is given by:

$$u_0 = \frac{Re_1}{Fr^2} h_0^2 \left\{ \frac{y}{h_0} - \frac{1}{2} \frac{y^2}{h_0^2} \right\}, \quad (4.45)$$

where the index 0 refers to the primary flow. Further, we consider scalar transfer across the film surface by applying the boundary conditions in (4.1k) and (4.2), and focus on

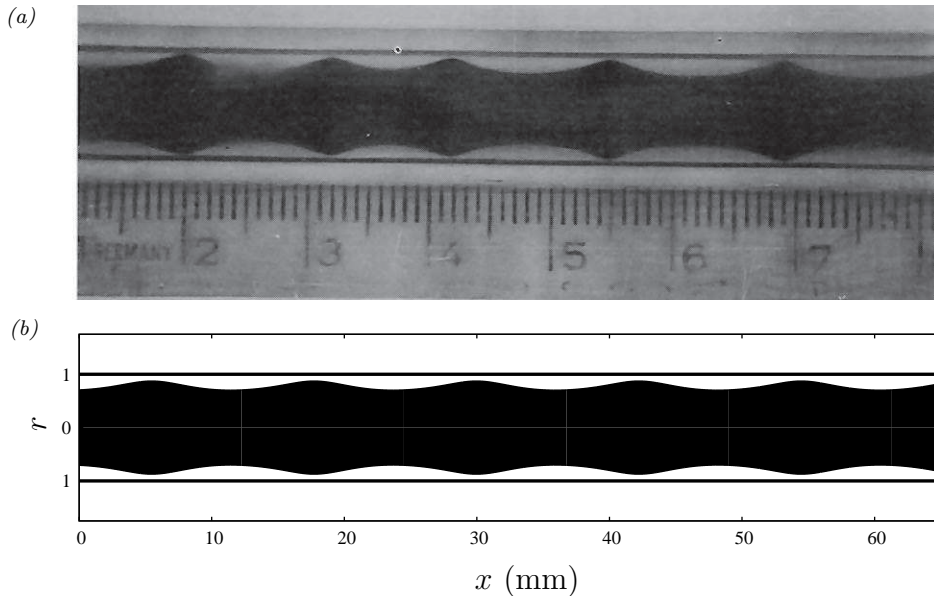


Figure 4.8: Benchmark simulation of bamboo waves in an upward pressure-driven liquid/liquid core-annular flow through a vertical cylindrical tube:  $R^*=4.8$  mm,  $\Pi_\mu=601$ ,  $\Pi_\rho=0.91$ ,  $Ka=1212.5$  (water/oil in table 2.1),  $V_1/(\pi R^2 \Lambda)=0.3932$ . (a) Experiment from panel 6b in Bai *et al.* (1996):  $Re_1=-219.9$ ,  $Re_2=-0.714$ ; (b) periodic DNS using **Gerris**:  $\Lambda^*=12.25$  mm,  $M=1.04$ ,  $Re_1=-153.7$ ,  $Re_2=-0.746$ .

the limit of large  $Pe$ , where the interfacial boundary layer is thin (panel 4.9a). In this limit, the local rate of convection  $\dot{H}(x)$  of the scalar within the liquid can be obtained analytically from penetration theory (Higbie, 1935):

$$\dot{H}(x) = \int_0^h u(y) \theta(x, y) dy, \quad \dot{H} = \left(\frac{6}{\pi}\right)^{1/2} \left(\frac{x}{Pe}\right)^{1/2}. \quad (4.46)$$

Panel 4.9b compares this analytical result with our open-domain DNS using **Gerris** (Dietze, 2019) for three resolution variants. For all three cases, there is a region near the inlet, where the boundary layer is under-resolved by the employed grid. However, the length of this inevitable<sup>2</sup> blind zone decreases drastically with increasing spatial resolution and the subsequent growth of the boundary layer is accurately captured by all three DNS. Panel 4.9c represents the streamwise profile of the boundary layer thickness  $h_{BL}$ :

$$h_{BL} = 3.6 \left[\frac{x}{Pe}\right]^{1/2}, \quad (4.47)$$

which is fixed by the  $\theta=0.01$  isoline in the scalar field  $\theta(x, y)$ :

$$\theta = 1 - \operatorname{erf} \left\{ \frac{h_0 - y}{2} \left(\frac{x}{Pe}\right)^{-1/2} \right\}. \quad (4.48)$$

<sup>2</sup>The thickness of the boundary layer tends to zero as  $x \rightarrow 0$ .

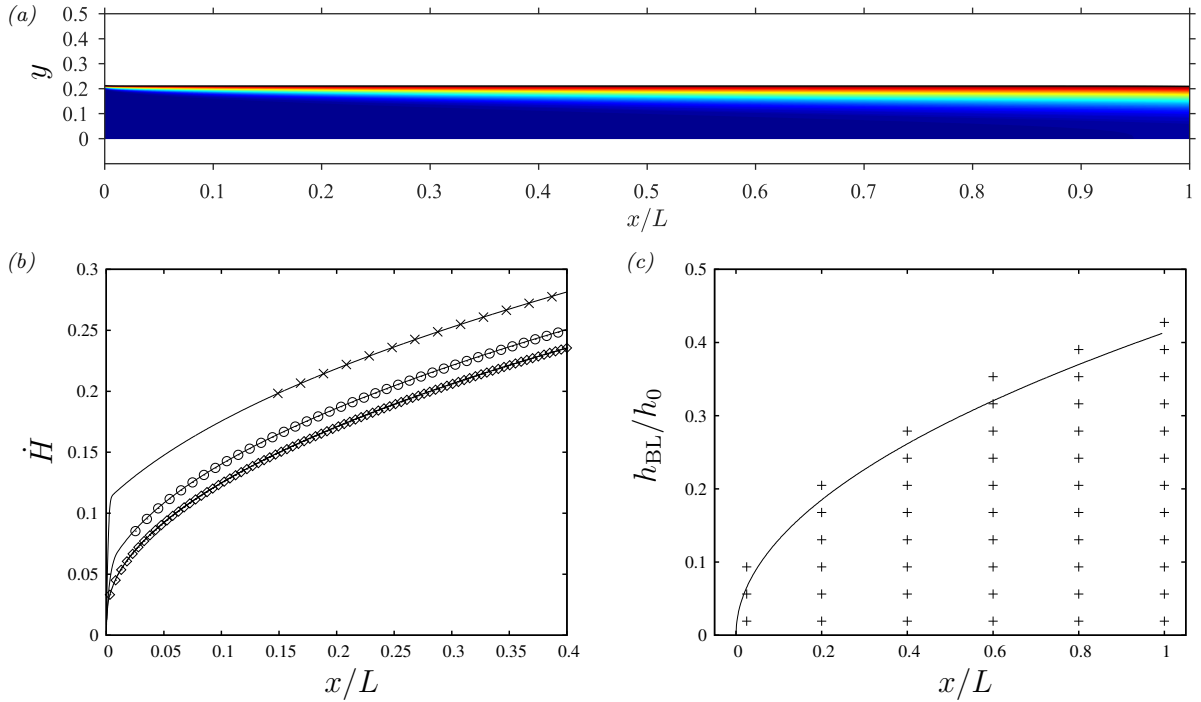


Figure 4.9: Benchmark DNS of scalar transfer to a steady hydrodynamically-developed falling liquid film:  $\phi=90^\circ$ ,  $\text{Re}_1=15$ ,  $\text{Pe}=4590$ ,  $\text{Ka}=509.5$  (DMSO-water in table 2.1). The gas phase is quiescent and has no significant effect. (a) Contours of the transported scalar  $\theta$  (blue:  $\theta=0$ ; red:  $\theta=1$ ); (b) rate of convection  $\dot{H}(x)$  of  $\theta$  within the liquid (4.46). Symbols: analytical solution (4.46) from penetration theory (Higbie, 1935); solid lines: DNS with coarse ( $RL=6$ , crosses), reference ( $RL=7$ , open circles), and fine ( $RL=8$ , diamonds) grid based on  $\underline{L}^*=1.59$  mm (4.37); (c) solid line: boundary layer thickness  $h_{\text{BL}}$  (4.47); plus signs: vertices of the reference grid ( $RL=7$ ) at selected x-positions.

In the same graph, we have represented via plus signs the wall-normal spatial resolution for the reference grid ( $RL_{\text{FS}}=8$ , open circles in panel 4.9b) at selected x-positions. This reference grid was used in the scalar transport investigations presented in section 6.3. The grid dependence analysis in figure 4.10 shows that it resolves all relevant features of the flow field and passive-scalar field within a nonlinear wavy falling liquid film flowing on a smooth substrate.

The final benchmark concerns an axisymmetric drop of silicone oil spreading on a smooth substrate with a static contact angle  $\beta_0=1^\circ$ . Conditions correspond to the experiment from figure 8.7, only that there is no micro-particle here. We use the axisymmetric version of **Gerris**, impose the macroscopic contact angle  $\beta$  according to (4.25), and start the simulation from a hemispherical-drop initial condition (see panel 4.11b). The grid, which is represented in panel 4.4b, is substantially refined near the contact line ( $RL_{\text{max}}=9$  based on  $\underline{L}^*=5$  mm). As a result, the dynamic contribution in (4.25), where we have used  $U_{\text{CL}}=u_{\text{cc}}$ , is small and the contact line moves from cell to cell in a stick-slip motion (at the scale of the grid resolution). During this intermittent motion, the contact angle also

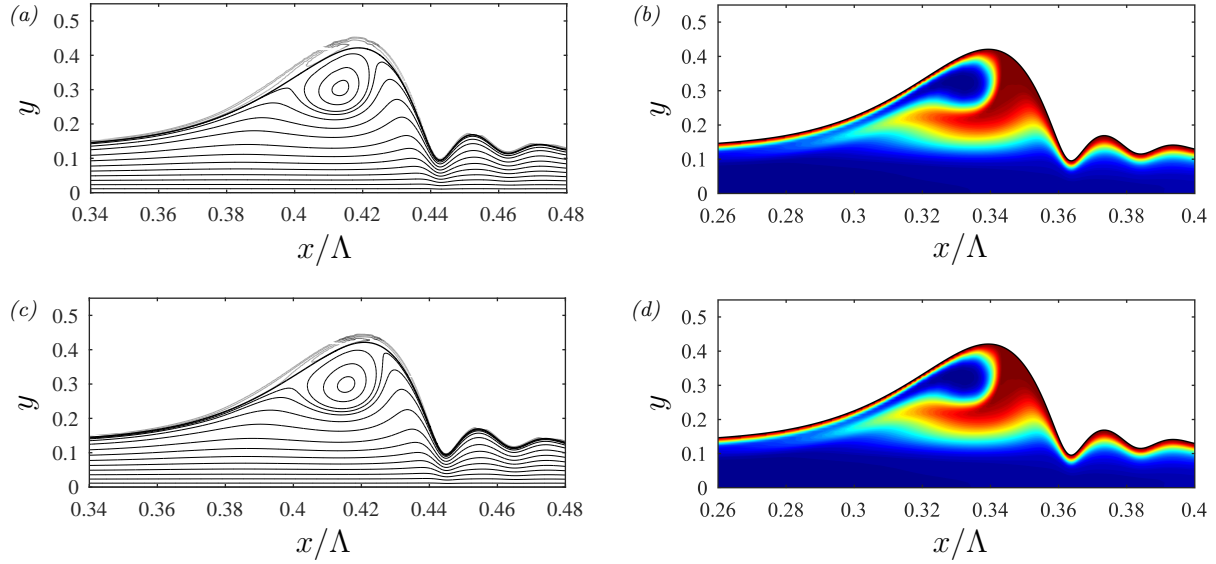


Figure 4.10: Grid dependence analysis using **Gerris**. Scalar transfer to a wavy falling liquid film in contact with a strongly-confined counter-current gas flow (panel 4.1):  $\phi=90^\circ$ ,  $\text{Re}_1=15$ ,  $\text{Re}_2=-57$ ,  $\text{Pe}=4590$ ,  $\text{Ka}=509.5$  (DMSO-water and air I in table 2.1). Streamlines (panels *a*, *c*) and Contours of the transported scalar  $\theta$  (panels *b*, *d*). (*a*,*b*) Reference grid:  $RL_{\text{FS}}=7$ ; (*c*,*d*) fine grid:  $RL_{\text{FS}}=8$ . Refinement level  $RL$  is based on  $\underline{L}^*=1.6$  mm (4.37).

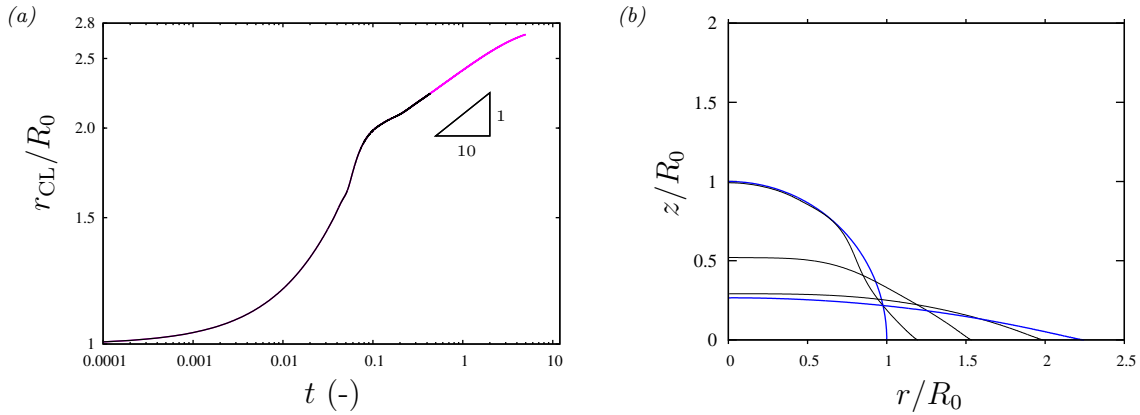


Figure 4.11: Benchmark DNS using **Gerris**. Axisymmetric liquid drop of silicone oil spreading on an oleophilic substrate:  $\beta_0=1^\circ$ ,  $V_1=1.8 \mu\text{l}$ ,  $R_0^*=7.5 \mu\text{m}$ ,  $\text{Bo}=2.6 \cdot 10^{-5}$  (silicone oil II in table 2.1). Dynamic contact angle  $\beta$  prescribed according to (4.25) with  $c=10$ ,  $L_e^*=R_0^*$ , and  $L_i^*=100 \mu\text{m}$ . Adaptive grid refinement with  $RL_{\text{max}}=9$  based on  $\underline{L}^*=5$  mm (see panel 4.4b). (*a*) Time trace of the radial contact line position  $r_{\text{CL}}$  in a double logarithmic plot. The drop spreads at the rate of  $t^{1/10}$  in accordance with the capillary spreading regime (Tanner, 1979; Cazabat & Stuart, 1986); (*b*) snapshots of drop profiles at selected time points. Thick blue curves correspond to initial and final states.



varies, its minimum reaching  $\beta=3^\circ$ , which is a bit larger than  $\beta_0$ .

Nonetheless, the obtained macroscopic contact line velocity  $U_{\text{CL}}$  agrees well with the appropriate theoretical spreading rate. This is shown in panel 4.11a, which represents the time evolution of the radial contact line position  $r_{\text{CL}}$ . Following an early stage of rapid growth, where the initial condition plays an important role, the drop radius reaches a regime where it evolves at the rate of  $t^{1/10}$ . This corresponds to the analytical prediction of Tanner (1979) for the axisymmetric 3-dimensional problem and the experimental observations of Cazabat & Stuart (1986) in the capillary regime.

The Navier-Stokes solvers introduced in this chapter, in particular **Gerris**, allow a very accurate description of the interfacial dynamics occurring in the two-phase flows studied in this work. This has allowed us to determine the validity of our WRIBL models from sections 1.1 to 1.3 for the studied regimes (section 2.3), and to elucidate the physics of flows involving phenomena that are not accounted for in these models (sections 5.2, 6.3, and 8.2).



# Chapter 5

## Falling liquid films in a quiescent atmosphere

Falling liquid films have been continually investigated<sup>1</sup> since the seminal work of Wilhelm Nusselt on the condensation of steam (Nusselt, 1916) and his later paper on predicting heat transfer in falling film coolers (Nusselt, 1923), where he derived the velocity profile and thickness of an unperturbed falling film flowing on a plane in a passive atmosphere, i.e. for the configuration in panel 1.2a in the passive-gas limit  $\Pi_\mu=\Pi_\rho=0$ :

$$u_{\text{Nu}} = 3 \left\{ y - \frac{1}{2}y^2 \right\}, \quad h_{\text{Nu}} = 1. \quad (5.1)$$

In equation (5.1), which is often designated as Nusselt solution (subscript “Nu”), we have scaled lengths with  $\mathcal{L}=h_{\text{Nu}}^*=(\frac{3q^*\nu}{g\sin(\phi)})^{1/3}$  instead of  $\mathcal{L}=H^*$  and velocities with  $\mathcal{U}=q^*/h_{\text{Nu}}^*=h_{\text{Nu}}^{*2}g\sin(\phi)/3/\nu$ . This is more appropriate when the gas is considered to be virtually unconfined and quiescent, in which case it does not significantly affect the liquid film and  $H^*$  does not enter the problem. We make this assumption and use the associated new scaling throughout this chapter. For the same reasons, we have dropped the phase index  $k$  here and throughout this chapter.

The limiting case underlying (5.1) is mainly of academic interest, as in most industrial applications the gas flow *does* play an important role, e.g. because it is strongly confined, and we will discuss these in chapters 6 and 7. Also, in applications where the gas is quiescent, the geometry is usually not planar and/or other effects such as phase change come into play. This is the case for tube-bank condensers/evaporators used e.g. in absorption chillers (Killion & Garimella, 2004), closed-circuit cooling towers (Xie *et al.*, 2019), or for milk inspissation (Åkesjö *et al.*, 2018), where the liquid film flows over a series of horizontal tubes placed one above the other, or vertical tubes placed side by side.

Nonetheless, many studies have focused on the planar quiescent-gas configuration considered in this chapter, as it already displays a very rich dynamics and associated phenomena of heat/mass transfer. Most of the state of the art is summarized in several

---

<sup>1</sup>Typing the search term “falling liquid film” in Google Scholar yields over 250,000 results.

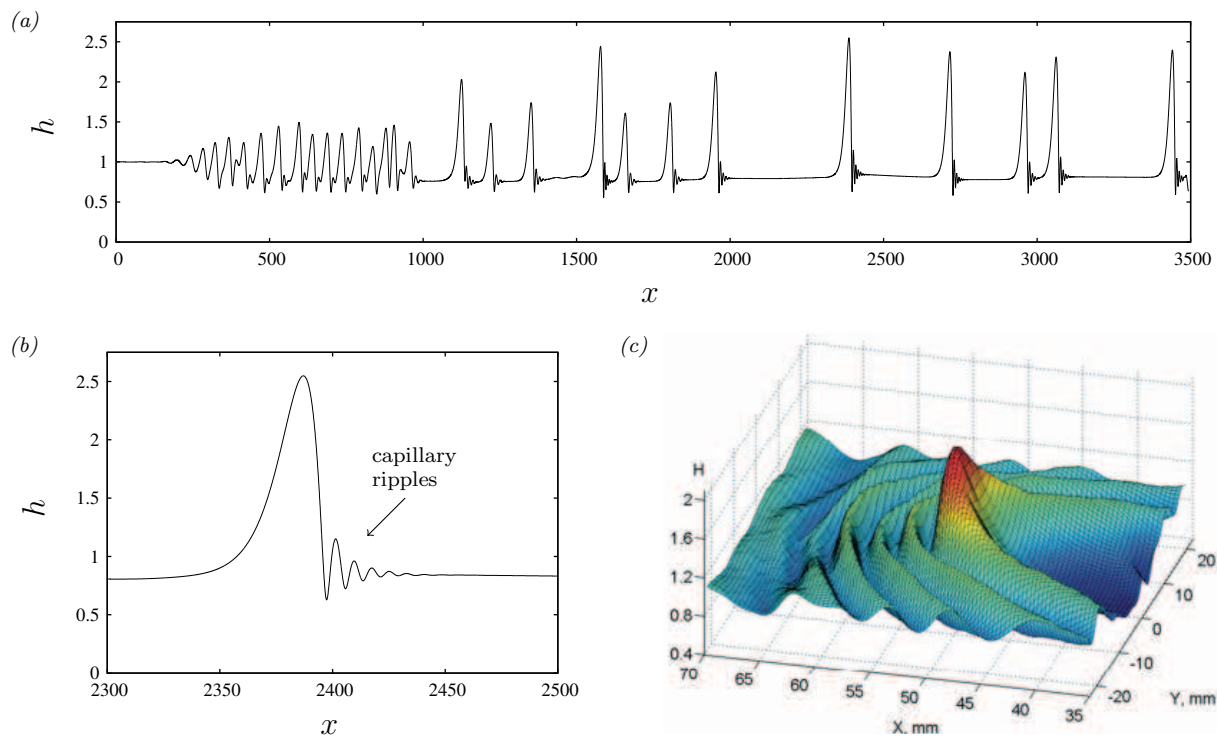


Figure 5.1: Liquid film falling down a vertical wall in a quiescent atmosphere. (a) Two-dimensional WRIBL computation (based on (1.27) with  $\Pi_\mu = \Pi_\rho = 0$ ) of the experiment in panel 42d of Kapitza & Kapitza (1965):  $Ka = 530.5$  (alcohol I in table 2.1),  $Re_1 = 6.09$ , inlet noise according to (2.38) with  $\epsilon_1 = 0$  and  $\epsilon_2 = 10^{-4}$ ; (b) blown-up view of a solitary wave from panel a, showing precursory capillary ripples; (c) experimental snapshot of a 3-dimensional horseshoe wave reproduced from Alekseenko *et al.* (2007a).

review articles (Chang, 1994; Craster & Matar, 2009) and monographs (Alekseenko *et al.*, 1994; Chang & Demekhin, 2002; Dietze, 2010; Kalliadasis *et al.*, 2012).

Here, we focus on a brief discussion of the main physics of surface waves, which are arguably the most important feature of falling liquid films. Such waves were first reported by Kapitza (1948)<sup>2</sup>, who observed them experimentally through shadowgraphy. Later, Brooke Benjamin (1957) and Yih (1963) demonstrated via (temporal) linear stability analysis that waves result from a long-wave instability of the primary flat-film flow (5.1), giving rise to a supercritical Hopf bifurcation (panel 2.5a). The instability is purely convective (Brevdo *et al.*, 1999) and subject to Squire’s theorem (Yih, 1955), i.e. two-dimensional perturbations are the most unstable versus three-dimensional ones. As we have reported in section 2.1.1, the neutral stability bound is given by  $Re = q^* / \nu = \frac{5}{6} \cot(\phi)$ .

In a typical experiment (Nosoko *et al.*, 1996), the Kapitza instability produces 2-dimensional surface waves of the linearly most-amplified frequency  $f_{\max}$  near the liquid inlet, which subsequently grow (spatially) and saturate nonlinearly under the stabiliz-

<sup>2</sup>See Kapitza & Kapitza (1965) for a translation from Russian.

ing effect of surface tension (Gjevik, 1970; Pumir *et al.*, 1983). The resulting travelling waves, with  $f \approx f_{\max}$ , are subject to a 2-dimensional subharmonic secondary instability (Liu & Gollub, 1993), leading to spatial amplitude modulations (figure 2.6) and wave coalescence, which eventually gives rise to a cascaded coarsening dynamics (Chang *et al.*, 1996*b*) producing large-amplitude solitary waves that travel on a flat residual film (panel 5.1a). At the same time, 3-dimensional secondary instability induces spanwise deformations of the wave fronts (Liu *et al.*, 1995; Kofman *et al.*, 2014; Demekhin *et al.*, 2007*a*), which eventually leads to independently-travelling horseshoe-shaped solitary waves (Petviashvili & Tsveldub, 1978; Alekseenko *et al.*, 2005; Demekhin *et al.*, 2007*b*), the final state of the film (panel 5.1c).

In the current work, we have conducted two studies that complete this physical picture:

- (i) The nonlinear evolution of Kapitza waves is accompanied by the formation of precursory capillary ripples travelling in front of the main wave humps (panel 5.1b). These generate extreme capillary pressure gradients (Dietze *et al.*, 2008) that can reverse the flow even in vertical falling films (Salamon *et al.*, 1994; Miyara, 1999; Malamataris *et al.*, 2002; Tihon *et al.*, 2006; Malamataris & Balakotaiah, 2008; Dietze *et al.*, 2009), and they play an important role in the interaction between successive large waves (Malamataris *et al.*, 2002; Pradas *et al.*, 2013).

In Dietze (2016), we have elucidated the mechanism by which these capillary ripples form, and how it is achieved that they may travel in group with the much larger main wave humps. These results are discussed in section 5.1.

- (ii) Three-dimensional surface waves are known to dramatically increase heat and mass transfer in falling liquid films (Alekseenko *et al.*, 1994; Kunugi & Kino, 2005; Demekhin *et al.*, 2007*a*). Also, the film's (3-dimensional) waviness plays an important role in the transition to turbulence, shifting its onset to significantly lower  $Re_1$  values compared to single-phase plane Poiseuille flow (Ishigai *et al.*, 1972; Adomeit & Renz, 2000).

In Dietze *et al.* (2014), we have elucidated some of the underlying mechanisms via high-performance DNS of 3-dimensional falling liquid films. These simulations reveal how surface waves shape and interact with the flow field. Results are discussed in section 5.2.

## 5.1 On the origin of precursory capillary ripples

Precursory capillary ripples are a nonlinear consequence of the Kapitza instability and, for a given wavelength  $\Lambda$ , arise when  $Re$  is sufficiently greater than  $Re^{\text{crit}}(\Lambda)$ . Closer to criticality ( $Re \gtrsim Re^{\text{crit}}$ ), saturated nonlinear Kapitza waves remain single-peaked, yet they already contain the basic ingredients for forming capillary ripples. We thus start by sketching the nonlinear evolution of single-peaked Kapitza waves (see figures 5.2, 5.3 and

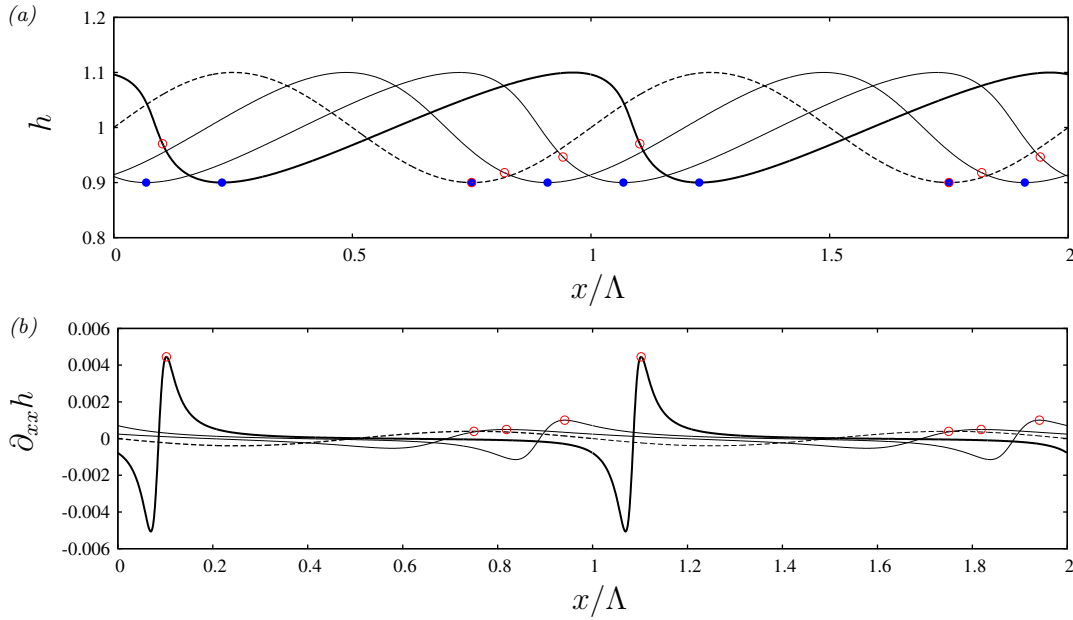


Figure 5.2: Kinematic waves evolving from a sinusoidal initial perturbation  $h|_{t=0}=1 + 0.1 \sin(2\pi x/\Lambda)$  (dashed profiles). Numerical solution of (5.2) in the limit  $\text{Re}_1=0$ ,  $1/\text{Bo}=0$ , using periodic boundary conditions:  $\Lambda=100$ ,  $h_{\text{Nu}}^*=0.1$  mm. The wave moves from left to right. (a) Film height  $h$ ; (b) film surface curvature  $\partial_{xx}h$ . Filled blue and open red circles mark loci of  $h_{\min}$  and  $\{\partial_{xx}h\}_{\max}$ , respectively.

5.4). We do this based on the well-known Benney equation (Benney, 1966; Gjevik, 1970), which is appropriate in that limit<sup>3</sup>:

$$\partial_t h = \underbrace{-3h^2 \partial_x h}_{\text{gravity}} - \underbrace{\frac{3}{5} \text{Re} \{12h^5 (\partial_x h)^2 + 2h^6 \partial_{xx} h\}}_{\text{inertia}} - \underbrace{\frac{h^2}{\text{Bo}} \{3\partial_x h \partial_{xxx} h + h \partial_{xxxx} h\}}_{\text{capillarity}}. \quad (5.2)$$

The new scaling used in this chapter gives  $\text{Re}=h_{\text{Nu}}^3 g \sin(\phi)/3\nu^2$  and the Bond number  $\text{Bo}=3/\text{We}/\text{Re}=\rho g h_{\text{Nu}}^2/\sigma$ , and RHS terms in (5.2) represent the effects of gravity, inertia, and surface tension. This evolution equation for  $h$  is obtained from asymptotic expansion around the primary flow (up to order  $\epsilon^1$ ), and implies the following relation for the flow rate  $q$ :

$$q = h^3 \left[ 1 + \frac{6}{5} \text{Re} h^3 \partial_x h + \frac{1}{\text{Bo}} \partial_{xxx} h \right]. \quad (5.3)$$

<sup>3</sup>See figure 22e in Dietze (2016) for a validation.

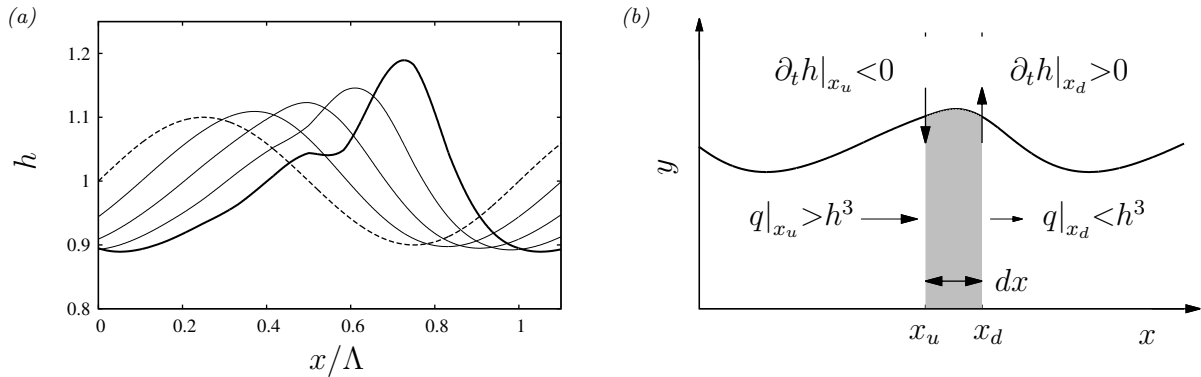


Figure 5.3: Dynamic wave on a vertically-falling liquid film evolving from a sinusoidal initial perturbation  $h|_{t=0}=1+0.1 \sin(2\pi x/\Lambda)$  (dashed line). (a) Numerical solution of (5.2) in the limit  $1/\text{Bo}=0$ , using periodic boundary conditions:  $\Lambda=100$ ,  $h_{\text{Nu}}^*=0.1$  mm,  $\text{Re}=3.27$ . Wave profiles at different times growing from left to right; (b) growth mechanism of the Kapitza instability: inertia-induced flow rate imbalance across the wave crest.

Further, in the case of travelling waves (superscript  $\infty$ ), the celerity  $c_{\text{ex}}^\infty$  at the wave extrema ( $x=x_{\text{ex}}$ ,  $\partial_x h|_{x=x_{\text{ex}}}=0$ ) can be expressed as:

$$\begin{aligned} c_{\text{ex}}^\infty &= \left. \frac{dx_{\text{ex}}}{dt} \right|_{dh=0} = -\frac{\partial_t h}{\partial_x h} = \partial_h q \\ &= 3h^2 + \frac{6}{5}\text{Re} h^6 \frac{\partial_{xxx} h}{\partial_{xx} h} + \frac{1}{\text{Bo}} \left\{ 3h^2 \partial_{xxx} h + h^3 \frac{\partial_{xxxx} h}{\partial_{xx} h} \right\}, \end{aligned} \quad (5.4)$$

where we have made use of the continuity equation (1.28a).

In the limit of inertialess flow and no surface tension ( $\text{Re}=1/\text{Bo}=0$ ), only gravity and viscous diffusion are active, producing kinematic waves that neither grow nor decay from their initial amplitude (figure 5.2). Nonetheless, their shape is distorted by gravity, which causes wave crests to travel faster than wave troughs (through the  $3h^2$  term in (5.4)), leading to a steepening of the wave front and an elongation of the wave back (panel 5.2a). In the process, the magnitude of the curvature at the crests ( $\partial_{xx} h < 0$ ) and troughs ( $\partial_{xx} h > 0$ ) increases (panel 5.2b), and, importantly, reaches a maximum positive value within the wave front (open red circles in panels 5.2a and 5.2b). This will turn out to be a key ingredient for the formation of capillary waves.

The growth of Kapitza waves is caused by inertia, as evidenced by adding this effect in our computation ( $\text{Re}=3.27$ ), while maintaining  $1/\text{Bo} \rightarrow 0$  (panel 5.3a). Focusing on the wave extrema ( $\partial_x h=0$ ), where the growth rate<sup>4</sup>  $dh/dt$  reduces to  $\partial_t h$ , we see that it is the surface curvature  $\partial_{xx} h$ , through the inertial term  $-(6/5)\text{Re}h^6 \partial_{xx} h$  in (5.2), that decides over growth or decay, causing  $h$  to increase at wave crests and decrease at wave troughs.

<sup>4</sup>The precise definition of a growth rate is  $h^{-1}dh/dt$ . However, we will sometimes refer to  $dh/dt$  as growth rate.

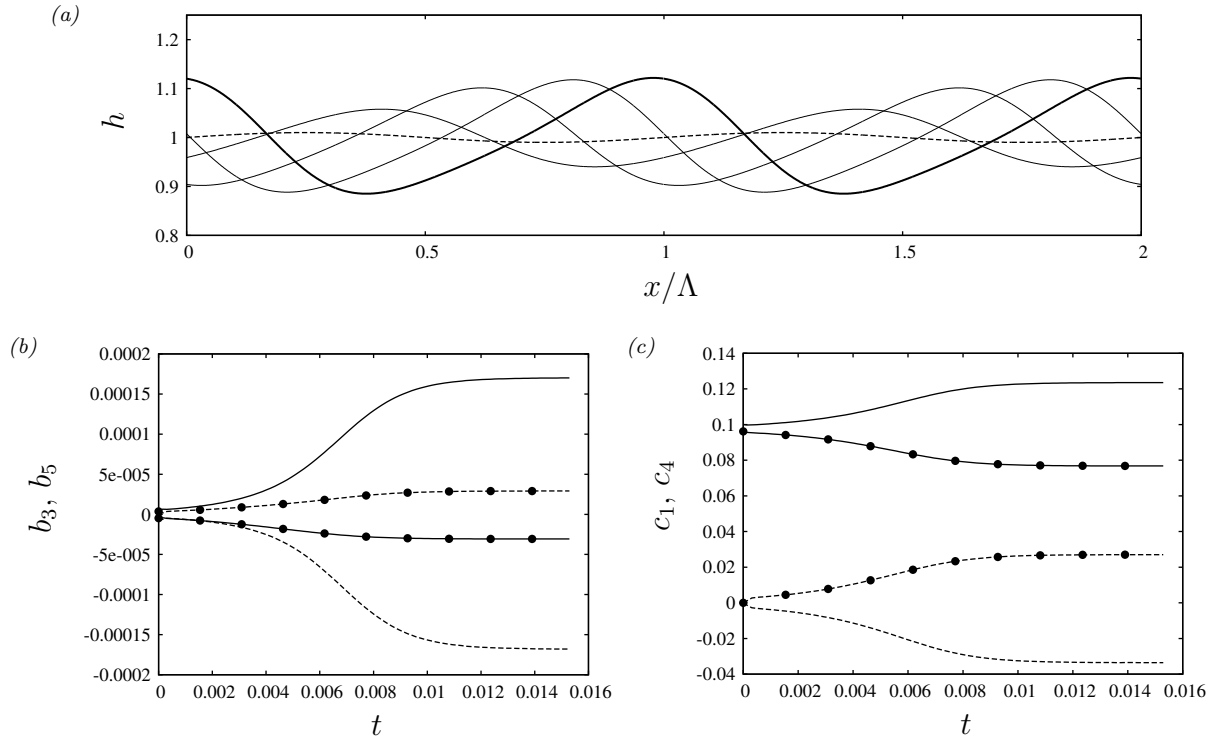


Figure 5.4: Saturating wave on a vertically-falling liquid film evolving from a sinusoidal initial perturbation  $h|_{t=0}=1+0.01 \sin(2\pi x/\Lambda)$  (dashed line in panel *a*). Numerical solution of (5.2) using periodic boundary conditions:  $\Lambda=100$ ,  $h_{\text{Nu}}^*=0.1$  mm,  $\text{Re}=3.27$ ,  $\text{Bo}=1.36 \cdot 10^{-3}$ . (*a*) Wave profiles at different times growing from left to right; (*b*) time evolution of the dominant terms  $b_3=-\frac{6}{5}\text{Re}h^6\partial_{xx}h$  (solid lines) and  $b_5=-\frac{h^3}{\text{Bo}}\partial_{xxxx}h$  (dashed lines) in (5.2) evaluated at the wave crest (lines without symbols) and wave trough (symbols); (*c*) corresponding plots of the dominant celerity contributions  $c_1=3h^2$  (solid lines) and  $c_4=\frac{h^3}{\text{Bo}}\partial_{xxxx}h/\partial_{xx}h$  (dashed lines) in (5.4).

The underlying growth mechanism is illustrated in panel 5.3b, where we consider the flow rate  $q$  (5.3) on either side of a wave crest. On the upstream side ( $x=x_u$ ), where  $h$  is in the process of decreasing due to the passage of the wave ( $\partial_t h < 0$ ), inertia causes  $q$  to lag slightly above its inertialess limit ( $q|_{x_u} > h^3$ ). The opposite holds on the downstream side ( $q|_{x_u} < h^3$ ), resulting in a flow rate imbalance across the wave crest ( $q|_{x_u} > q|_{x_d}$ ) that causes the latter to grow. The mechanism is inverted at the wave troughs, where  $\partial_{xx}h > 0$ , causing them to deepen, and this mechanism will turn out to be responsible for the inception of capillary waves within the wave front (figure 5.5).

In a real liquid film, the inertia-induced growth of Kapitza waves is eventually checked by the effect of capillarity ( $1/\text{Bo} \neq 0$ ), which grows in weight as the wave shape increasingly distorts under the effect of gravity (figure 5.4). Panel 5.4b shows this by comparing the time evolution of the growth rate contributions owing to inertia  $b_3=-\frac{6}{5}\text{Re}h^6\partial_{xx}h$  (solid lines) and capillarity  $b_5=-\frac{h^3}{\text{Bo}}\partial_{xxxx}h$  (dashed lines) at the wave crest (lines



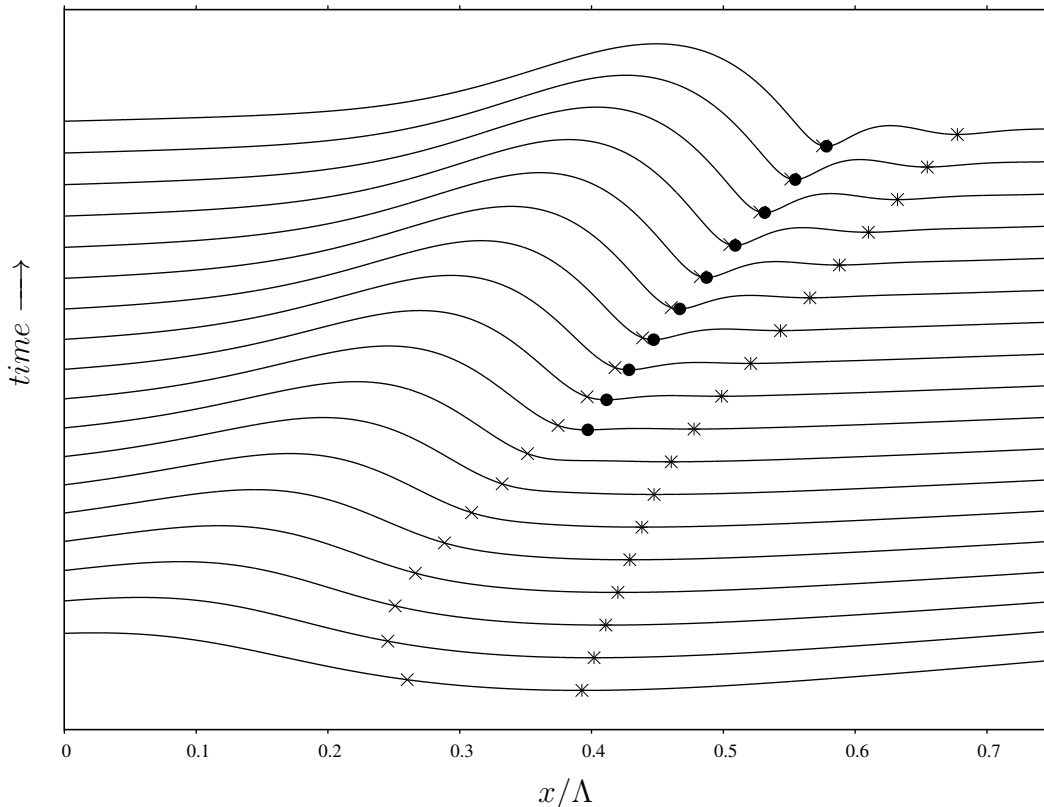


Figure 5.5: Inception of the first capillary trough within the front of the main wave. DNS with **Gerris** using periodic boundary conditions. vertically-falling liquid film:  $Ka=509.5$  (DMSO-water in table 2.1),  $Re=10.87$ ,  $h_{Nu}^*=0.300$  mm,  $\Lambda=69.33$ ,  $h|_{t=0}=1 + 0.4 \sin(2\pi x/\Lambda)$ . Film height profiles over the time span  $t \in [2.27, 12.32]$  shifted vertically to produce a spatio-temporal plot. Crosses: locus of  $\{h_{xx}\}_{max}$ ; asterisks: original global minimum of the wave; filled circles: first capillary trough. The minimal film height is resolved with approx. 25 grid cells.

without symbols) and wave trough (symbols), respectively. Capillarity is also responsible for compensating the initial gravity-induced celerity mismatch between wave hump and wave trough (panel 5.4c), slowing down the former and speeding up the latter through the term  $c_4=(h^3/Bo)\partial_{xxxx}h/\partial_{xx}h$  in (5.4). Here again, it is the gravity-induced distortion of the interface due to the compaction of the wave hump and trough, that produces the effect, and this mechanism will turn out to control also the speed of capillary ripples (figure 5.7).

Figure 5.5 demonstrates the formation of capillary ripples, which occur at  $Re$  outside the range of the Benney equation (5.2). Thus, we have performed a periodic DNS with **Gerris** of a vertically-falling liquid film at  $Re=10.87$ . The first capillary trough (filled circles) is seen to form within the main wave front, close to the point of maximal  $\partial_{xx}h$  (crosses), as the front increasingly steepens. This in turn generates a capillary hump enclosed between the new capillary trough (filled circles) and the original global wave

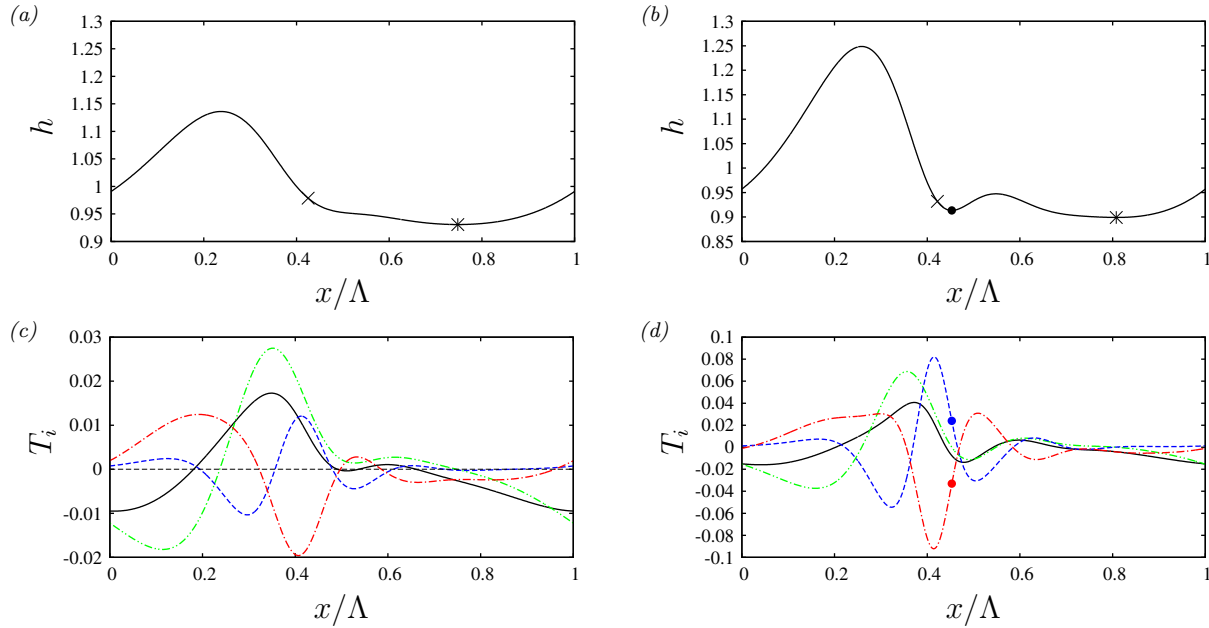


Figure 5.6: Inertia-induced inception of the first capillary trough within the main wave front. Periodic WRIBL computation based on (1.27) in the passive-gas limit ( $\Pi_\mu = \Pi_\rho = 0$ ). Parameters correspond to figure 5.5. (a, b) Film surface profiles at two characteristic times; (b) corresponding profiles of the growth rate contributions  $T_i$  according to (5.8). Solid: total growth rate  $h^{-1}dh/dt$ ; dashed blue: capillary term  $T_\sigma$ ; dot-dashed red: inertial term  $T_\rho$ ; dot-dot-dashed green: gravity term  $T_g$ .

minimum (asterisks), which changes to a local minimum. The mechanism underlying the generation of capillary ripples is identified by evaluating the relative growth rate contributions of inertia, capillarity, and streamwise viscous diffusion in relation to viscous drag. For this, we deconstruct the flow rate  $q$  through integration of (1.4a):

$$q = \underbrace{\operatorname{Re} \int_0^h \int_0^y \int_y^h -\frac{du}{dt} dy^3}_{q_\rho} + \underbrace{\operatorname{Re} \int_0^h \int_0^y \int_y^h -\partial_x p dy^3}_{q_\sigma} + 3 \underbrace{\int_0^h \int_0^y \int_y^h dy^3}_{q_g} + \underbrace{\int_0^h \int_0^y \int_y^h \partial_{xx} u dy^3}_{q_\mu}, \quad (5.5)$$

where  $\partial_x p$  is obtained by integrating (1.4b) subject to (1.6a). Then, we apply the kinematic condition (1.9b) to obtain the growth rate  $h^{-1}dh/dt$ :

$$\frac{1}{h} \frac{dh}{dt} = \frac{1}{h} \partial_t h + \frac{1}{h} u|_h \partial_x h, \quad (5.6)$$

$$\partial_t h = -\partial_x q = -\partial_x q_\rho - \partial_x q_\sigma - \partial_x q_g - \partial_x q_\mu. \quad (5.7)$$

A reasonable estimate of the different terms in (5.5) can be obtained from our WRIBL

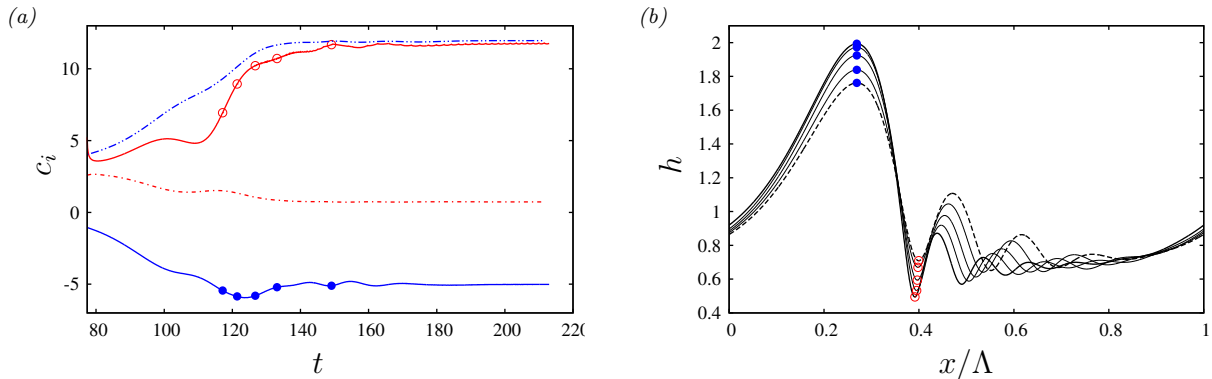


Figure 5.7: A compression-based capillary mechanism speeds up the capillary ripples and slows down the main hump, until a phase-locked travelling state is reached. Parameters as in figure 5.6. (a) Time traces of capillary (solid lines with symbols) and gravity-based (discontinuous lines) celerity contributions  $c_\sigma$  and  $c_g$  according to (5.9). Red dot-dashed line and solid line with open symbols: first capillary trough; blue dot-dot-dashed line and solid line with filled symbols: main wave crest; (b) snapshots of wave profiles (shifted so that wave maxima align) at times corresponding to symbols in panel a.

model (1.27) in the passive-gas limit ( $\Pi_\mu = \Pi_\rho = 0$ ) based on the leading-order<sup>5</sup> velocity profile  $\hat{u}$  (1.17), which yields  $u|_h = \frac{3}{2} \frac{q}{h}$ , and thus:

$$\frac{1}{h} \frac{dh}{dt} = T_\rho + T_\sigma + T_g + T_\mu, \quad T_i = \frac{3}{2} \frac{q_i}{h^2} \partial_x h - \frac{1}{h} \partial_x q_i, \quad i = \rho, \sigma, g, \mu. \quad (5.8)$$

Figure 5.6 represents profiles of the different growth rate contributions  $T_i$  in (5.8) for two representative time points during the formation of the first capillary ripple, as obtained from a periodic WRIBL computation with parameters according to our DNS in figure 5.5.

Based on panels 5.6a and 5.6b, we may conclude that inertia is responsible for generating the first capillary trough within the main wave front, i.e. through the negative growth rate contribution  $T_\rho$  (dot-dot-dashed red lines), which is large in the vicinity of the  $\partial_{xx} h$  maximum (crosses). Once a capillary trough has formed (filled circle in panel 5.6b), a local maximum of negative  $\partial_{xx} h$  and positive  $T_\rho$  develops slightly further downstream, and this generates the first capillary hump. In turn, this will initiate the next capillary trough and so on and so forth. The final number of capillary ripples is fixed by the condition that they must connect smoothly to the back of the next main wave, and travel at the same speed.

<sup>5</sup>See Dietze (2016) for a reconstruction based on velocity data from the DNS in panel 5.5. We have checked that our WRIBL predictions are in qualitative agreement with the DNS, but the  $\mathcal{O}(\epsilon^0)$  approximation  $\hat{u}$  remains coarse even within the context of our second-order model. Thus, quantitative agreement cannot be expected. Nonetheless, we elect to use our WRIBL data here, because they yield very smooth profiles for the complicated terms in (5.5) and (5.9).

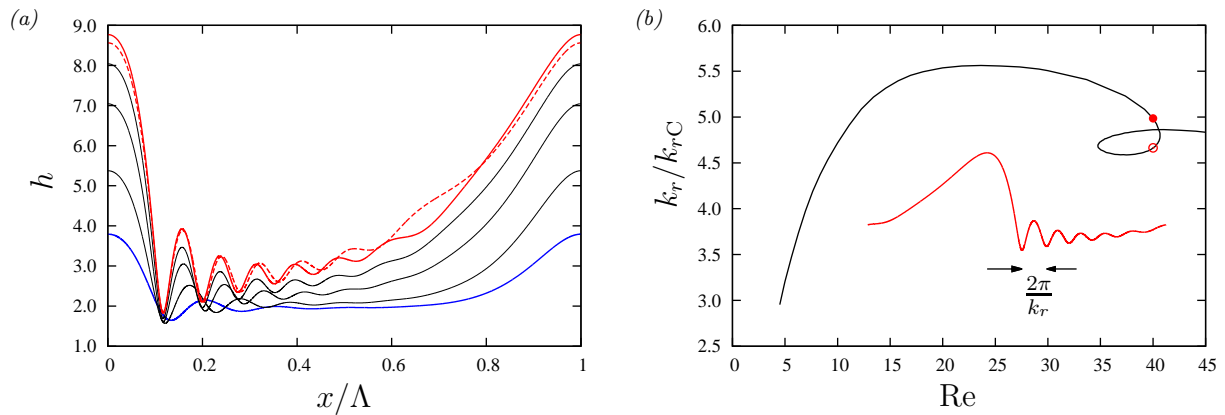


Figure 5.8: Capillary ripples within saturated TWS constructed with `Auto07P` (2.19). Effect of the Reynolds number  $Re$ . Other parameters according to figure 5.5. (a) Wave profiles for  $Re=5, 10, 20, 30$ , and  $40$  (two solutions); (b) wave number  $k_r$  of the first capillary wave related to the linear cut-off wave number  $k_{rC}(h)$  for  $h_0=h_{\min}(Re)$ . Capillary waves are much shorter than the linear cut-off wavelength of the Kapitza instability. Symbols in panel *b* mark the two solutions at  $Re=40$  from panel *a*.

By contrast, capillarity, through the growth rate contribution  $T_\sigma$  represented with dashed blue lines in panels 5.6a and 5.6b, counteracts deformations of the film surface. It is ultimately responsible for saturating the growth of the main wave and capillary ripples. Its weight grows with increasing distortion of the interface, as the main wave grows and the wave profile is increasingly compressed, due to the gravity-induced celerity discrepancy between wave maxima and minima (discussed in panel 5.2a). By compression, we mean that wave maxima and minima move closer to one another and their curvatures increase (panel 5.7b).

This compression-based capillary mechanism not only saturates the wave amplitude, but also speeds up the capillary ripples and slows down the main hump, so that a phase-locked travelling state is eventually reached. This is shown in panel 5.7a, where we have plotted time traces of the capillary contribution  $c_\sigma$  (solid lines with symbols) and the gravity-induced contribution  $c_g$  (discontinuous lines) to the extremal celerity  $c_{\text{ex}}^\infty$ :

$$c_{\text{ex}}^\infty = c_\rho + c_\sigma + c_g + c_\mu, \quad c_i = \lim_{x \rightarrow x_{\text{ex}}} \left\{ \frac{\partial_x q_i}{\partial_x h} \right\} = \left. \frac{\partial_{xx} q_i}{\partial_{xx} h} \right|_{x=x_{\text{ex}}}, \quad (5.9)$$

evaluated at the main wave crest (blue dot-dot-dashed line and solid line with filled symbols) and capillary trough (red dot-dashed line and solid line with open symbols). Symbols in panel 5.7a correspond to the wave profile snapshots represented in panel 5.7b. Comparing the solid and discontinuous curves in panel 5.7a for the two extrema, we see that  $c_\sigma$  substantially increases the speed of the capillary wave versus  $c_g$ , whereas it reduces that of the main wave hump<sup>6</sup>.

<sup>6</sup>Inertia and streamwise viscous diffusion slow down the capillary trough and speed up the main hump.

As a result, the wave reaches a TWS, where precursory capillary ripples travel in phase with the main wave hump. The degree of compression of the capillary ripples is dictated by the final speed of the TWS, which is controlled by the amplitude of the main wave hump. In turn, this dictates the number of precursory ripples, as the degree of compression of the first ripple fixes how many ripples are required to relax the interface toward the next main hump. Thus, the greater the main hump, the greater the number of capillary ripples. This is shown in panel 5.8a, representing TWS obtained with `Auto07P` based on (2.19) for different values of  $Re$ , all other parameters corresponding to figure 5.5.

When the Kapitza number  $Ka$  is small, streamwise viscous diffusion, which affects the speed and growth of capillary waves in a similar fashion to capillarity, becomes increasingly important. This reduces the amplitude of the fully-developed ripples (Ruyer-Quil & Manneville, 2000) while maintaining very large curvature variations there (Dietze, 2016).

Precursory capillary ripples are a nonlinear phenomenon, i.e. they are kept alive by an energy transfer from the fast-moving main hump that continually compresses them. This is evidenced by the fact that their wavelength is much shorter than the linear cut-off wavelength of the Kapitza instability<sup>7</sup>. We show this in panel 5.8b, where we have plotted, for the range of TWS in panel 5.8a, the actual wave number  $k_r$  of the first capillary wave compared to the linear cut-off wave number  $k_{rC}$  based on the corresponding minimal film height, i.e.  $h_0 = h_{\min}(Re)$ . According to this, capillary ripples are more than 3 times shorter than the linear cut-off wavelength of the Kapitza instability. Thus, they could not exist in a purely linear sense.

**Impact of the work and relation to the current state of the art** Our paper Dietze (2016) has been cited 16 times according to *Web of Science*.

Our finding, that the wavelength of capillary ripples is much shorter than the linear cut-off wavelength of the Kapitza instability (panel 5.8b), contradicts the conjecture of Chang (1994), who suggested that the two wavelengths should roughly correspond. Thus, capillary ripples in falling liquid films are linearly stable. This changes the physical interpretation of these ripples, as they require an active energy transfer from the main wave in order to exist. This is comparable to capillary wakes of objects travelling on liquid surfaces (Raphaël & de Gennes, 1996; Moisy & Rabaud, 2014). In some sense, one could compare the problem to the energy cascade in turbulence, where energy is also transferred from large structures to small dissipative structures. Further, the mechanism we have identified, which links the speed of the main wave humps to the number of capillary ripples, allows to explain why capillary ripples are reduced in number when subjecting the liquid film to a counter-current gas flow (Trifonov, 2010; Dietze & Ruyer-Quil, 2013; Kofman *et al.*, 2017), as the latter slows down the main wave.

Pfennig (2018) has cited our work in suggesting that the formation of capillary ripples

---

<sup>7</sup>Which is determined by the competition between the stabilizing effects of surface tension and streamwise viscous diffusion versus the destabilizing effect of inertia.

on gravity-driven liquid films may have a more fundamental analogue at molecular level, as a result of Lyapunov instability, gravity, and elasticity. Zhou & Prosperetti (2020*b*) have confirmed the DNS in figure 22 of our paper Dietze (2016), and Wang *et al.* (2020) have used our conclusions to formulate a physical argument for the threshold of flow reversal in falling liquid films.

Zhou & Prosperetti (2020*a*) have revisited our work by performing DNS of capillary ripples in falling liquid films for a large range of operating conditions encountered in the literature, and by comparing these with linear stability predictions. Importantly, their results confirm our finding that capillary ripples are linearly stable, i.e. the growth rate  $-k_i$  of linear waves with the same wave number  $k_r$  is negative for all studied conditions. Unfortunately, the authors did not acknowledge this agreement in their paper. Instead, they write:

*“Reference [23] describes a detailed study of capillary waves focusing on the mechanism of their formation and their speed, wavelength, and attenuation. The author argues that these small capillary waves are quite different from conventional capillary waves and owe their formation and characteristics to inherently nonlinear phenomena. By an analysis of wave patterns computed by the present authors and others from the literature, the present paper shows that nonlinear effects, while present, are not the determining factor. A linear approximation is adequate to satisfactorily account for these small ripples, which actually bear a strong similarity to linear viscocapillary waves on a horizontal liquid film of finite depth.”*

We disagree with this statement. As capillary ripples are linearly stable, they cannot attain nor maintain a finite amplitude without non-linearity. Thus, in our view, it is conceptually wrong to say that nonlinear effects are not the determining factor. The very existence of capillary ripples depends on it. The authors base their argument on a careful comparison of capillary wave trains from nonlinear computations with linear stability predictions. In particular, they fit the film height evolution for a linear wave train:

$$h = \bar{h} + A \exp(-\hat{k}_i x) \cos(\hat{k}_r x), \quad (5.10)$$

to their DNS data using a least-squares fit, and compare the values of  $\hat{k}_r$  and  $\hat{k}_i$  with their counterparts  $k_r$  and  $k_i$  obtained from spatial linear stability analysis at  $h_0 = \bar{h}$  and  $c = c_{\text{DNS}}$ , where  $c_{\text{DNS}}$  denotes the nonlinear wave speed from the DNS. The authors conclude from their data that  $\hat{k}_r$  and  $\hat{k}_i$  agree well with  $k_r$  and  $k_i$ .

No actual comparison of the linear wave profile from (5.10) with a DNS profile was shown in Zhou & Prosperetti (2020*a*). Thus, we have plotted our own comparison in figure 5.9. The thick solid red curve in panel 5.9a represents the nonlinear TWS at  $\text{Re}=40$  from panel 5.8a (solid red line there). The thin solid black curve corresponds to the linear wave train according to (5.10), where we have fitted  $\bar{h}=2.9$  and  $A=1.6$  to the first capillary hump of the nonlinear TWS, and set  $\hat{k}_r=k_r$  and  $-\hat{k}_i=-k_i$  according to the wave number  $k_r$  and growth rate  $-k_i$  of a linear wave travelling at speed  $c=c_{\text{TWS}}$  on a film of thickness  $h_0=\bar{h}$ , where  $c_{\text{TWS}}$  is the wave speed of the nonlinear TWS. Panel 5.9b shows how  $k_r$  is obtained from linear stability analysis. Its value  $k_r=0.376$  is more than three times greater than the cutoff wave number of the Kapitza instability.

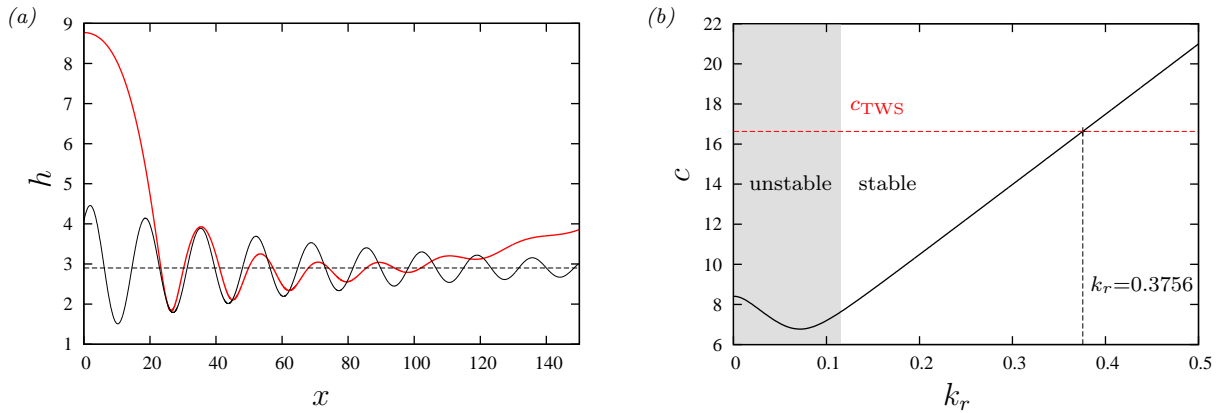


Figure 5.9: Linear approximation of capillary ripples following Zhou & Prosperetti (2020a):  $Ka=509.5$ ,  $\phi=90^\circ$ . (a) Wave profiles for conditions corresponding to panel 5.8a:  $Re=40$ . Thick solid red: nonlinear TWS; thin solid black: linear approximation according to equation (10) in Zhou & Prosperetti (2020a):  $h=\bar{h} + A \exp(-k_i x) \cos(k_r x)$ , where  $k_r$  and  $k_i$  are obtained from linear stability analysis at  $h_0=\bar{h}$  and  $c=c_{TWS}$  (panel b), and  $A=1.6$  and  $\bar{h}=2.9$  were fitted to the first capillary hump of the TWS; dashed black:  $h=\bar{h}$ ; (b) linear wave speed from spatial stability analysis:  $h_0=2.9$ .

Comparing the two capillary wave trains in panel 5.9a, it seems exaggerated to claim that a “linear approximation is adequate to satisfactorily account for these small ripples”. Although the first nonlinear capillary hump is approximated quite well by the linear wave number  $k_r$ , the error is 12% nonetheless, and this accumulates to a phase shift of roughly half a wavelength by the fifth capillary ripple between the thick solid red and thin solid black curves<sup>8</sup>. Also, the linear spatial growth rate  $-k_i$  does not predict the amplitude reduction of the capillary ripples, which seems to be in contradiction with the claim of Zhou & Prosperetti (2020a) regarding their figure 7b. However, we believe that no such agreement should be expected. The individual capillary ripples represented by the red curve in panel 5.9a are part of a TWS, and, thus, each one of them maintains a constant amplitude while propagating downstream, whereas a linear argument would imply a spatial attenuation. This, once again, underlines the importance of nonlinear effects.

Of course, because the amplitude of capillary ripples is rather small, a linear approximation should give a reasonable estimate of their wave number  $k_r$  for a known (nonlinear) wave speed. Also, a linear argument can explain, in principle, why capillary ripples speed up while being compressed. This effect results from the ascending branch of the celerity curve of panel 5.9b, as has been pointed out (Dietze, 2016). However, this argument cannot explain why ripples maintain a finite amplitude in a TWS although being linearly stable. For this, non-linearity needs to be taken into account. Consider slightly reducing the amplitude of a capillary ripple within a TWS, while maintaining  $k_r$  constant. This

<sup>8</sup>Accounting for the smaller value of  $\bar{h}$  for the second to fourth capillary ripple would further increase the error.

would reduce streamwise variations in surface curvature and weaken the effect of surface tension, which we have shown to be responsible for speeding up the capillary ripples (panel 5.7a). As a result, the capillary trough would slow down w.r.t. to the main wave hump, thus re-initiating the compression mechanism responsible for the growth and speed-up of capillary ripples in the first place<sup>9</sup>. Denner *et al.* (2018) have pointed out that this is qualitatively different from the behaviour of classical capillary waves in viscous fluids, which travel slower, the greater the initial amplitude is (Denner, 2016; Denner *et al.*, 2017).

Zhou & Prosperetti (2020a) also introduced a DNS-based thought experiment, where a surface wave was allowed to grow in the absence of surface tension, after which surface tension was suddenly activated. Capillary ripples were seen to form only after that event. The authors concluded from his:

*“This simulation shows that it is the initial surface distortion caused by the instability of the primary flow that, through the action of surface tension, generates the entire train of capillary ripples. Thus, it appears that not only the dynamics, but the very formation of the ripples are entirely dependent on the action of surface tension and its interaction with inertia and viscosity.”*

This statement is misleading. Surface tension in a planar film flow is always stabilizing, i.e. it tends to suppress surface deformations. It cannot be the driving mechanism at the origin of the capillary ripples. As we have shown in figure 5.6, inertia, via its destabilizing role in the Kapitza instability, causes the formation of the first capillary trough within the wave front against the resistance of surface tension. Thus, it is wrong to claim that “the entire train of capillary ripples” is generated “through the action of surface tension”. Nonetheless, surface tension plays an important role in the Kapitza instability. As we have shown in figure 5.4, it is the (stabilizing) counterweight to inertia, causing the saturation of surface waves, and reducing the celerity discrepancy between wave humps and wave troughs. This effect, which is responsible for steepening the leading wave front, may explain why capillary ripples occur only after activating surface tension in the numerical thought experiment of Zhou & Prosperetti (2020a). Before that, the steepening of the wave front must be so rapid that it drowns out the efforts of inertia to form the first capillary wave trough there.

To the thought experiment of Zhou & Prosperetti (2020a) we may oppose our low-Re computation in figure 5.4, where inertia is weak and surface tension is strong, but capillary ripples do not form. From these two thought experiments, we may conclude that both inertia and surface tension are relevant for the formation of capillary ripples, the first effect being direct (according to figure 5.6, inertia causes  $\partial_t h < 0$  at the origin of the first capillary trough within the main wave front) and the second being indirect (surface tension slows down the steepening of the wave front).

Given that the claims made by Zhou & Prosperetti (2020a) question some of our conclusions from Dietze (2016), I would have preferred to have been given a chance to respond to their findings before publication of their paper, especially as these claims turn

---

<sup>9</sup>By contrast, such a feedback loop does not exist in the linear argument, as the linear speed of the ripples would remain constant at constant  $k_r$ .



out to be questionable.

## 5.2 Three-dimensional falling liquid films

In Dietze *et al.* (2014), we have performed DNS of three-dimensional vertically-falling liquid films on the supercomputer JUROPA, using the `interFOAM` solver (Rusche, 2002) of the `OpenFOAM` package (version 2.0.1). Three-dimensional solitary waves were simulated in a box-shaped domain spanning one streamwise wavelength  $\Lambda_x$  in x-direction and half a spanwise wavelength  $\Lambda_z$  in z-direction (see figure 4.2 in section 4.1.1). Figure 5.10 shows snapshots of the film surface for the four cases simulated, which correspond to three working liquids, water, water-DMSO, and silicone oil, spanning a wide range of the Kapitza number  $Ka$ , and flow conditions from different experimental works (Park & Nosoko, 2003; Dietze *et al.*, 2009; Rohlfis *et al.*, 2012a).

Most of the liquid is concentrated into large horseshoe-shaped main wave humps, consisting of a protruding and a trailing portion, which are separated by a thin residual film covered by capillary ripples that espouse the shape of the main wave front. In panels 5.10a, 5.10b, and 5.10c, these ripples produce an interference pattern in the region between the protruding humps. The greater  $Ka$ , the more intricate the interference pattern and the greater the amplitude of the ripples. For the silicone oil film (panel 5.10d), where  $Ka=17.8$  is the lowest, only a single small-amplitude capillary ripple is observed, owing to the increased relevance of streamwise viscous diffusion (see section 5.1).

The three-dimensional wave structure is associated with a pronounced segregation of the flow field, which we characterize through the local Reynolds and inverse Weber numbers based on the local film height  $h$  and streamwise liquid flow rate  $q_x$ :

$$\hat{Re} = \frac{\rho |q_x^*|}{\mu}, \quad \hat{We}^{-1} = \frac{\rho q_x^{*2}}{\sigma h^*}, \quad q_x^* = \int_0^{h^*} u^* dy^*. \quad (5.11)$$

Panel 5.11a represents contours of  $\hat{We}^{-1}$  (right) and the corresponding film height  $h(x, t)$  (left) for the water film in panel 5.10b. The contours of  $\hat{We}^{-1}$ , which relates inertia to capillarity, demarcate an inertia-dominated region within the main humps, where  $\hat{We}^{-1}$  is large, and a visco-capillary region<sup>10</sup> in the residual film, where  $\hat{We}^{-1}$  is small. In the inertia-dominated region, the maximal local Reynolds number reaches  $\hat{Re}=300$ , which is more than five times greater than the nominal value  $Re=59.3$ .

Although the flow in our simulations is still fully laminar, this observation sheds some light on the transition to turbulence in falling liquid films. Based on dye experiments in such flows, Ishigai *et al.* (1972) reported onsets of wave-induced turbulence for  $Re \geq 2.2Ka^{3/10}$  ( $Re=26.3$  for water), wall-induced turbulence for  $Re \geq 75$ , and fully turbulent flow dominated by turbulence production at the wall for  $Re \geq 400$  (Brauer, 1956). These thresholds are much lower than the critical value for the transition of single phase channel

<sup>10</sup>Viscous diffusion comes into play when  $Ka$  is small, e.g. in panel 5.10d.

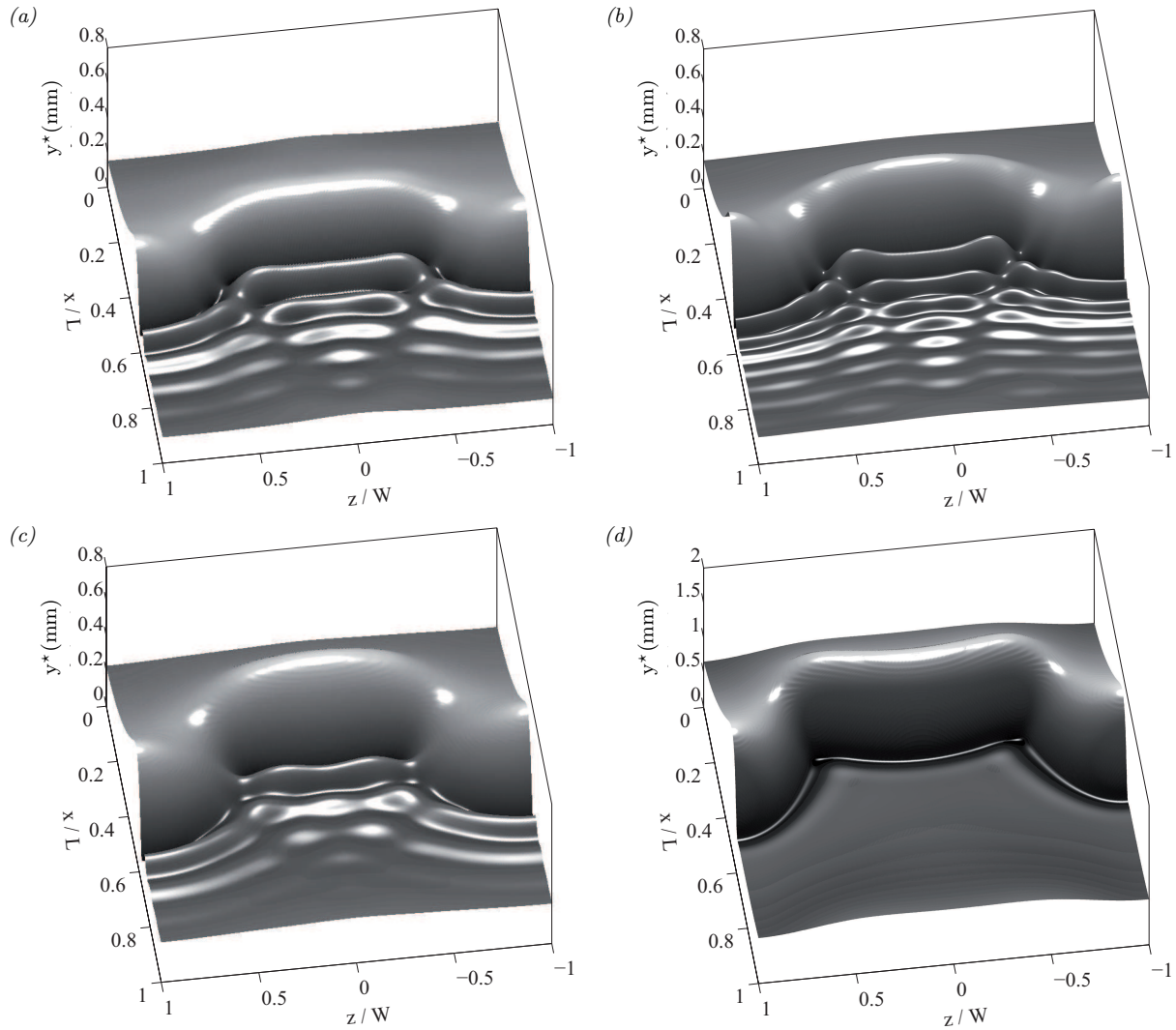


Figure 5.10: Three-dimensional solitary waves on a vertically-falling liquid film in quiescent, unconfined air. DNS on the supercomputer JUROPA using the `interFOAM` solver of the `OpenFOAM` package (see section 4.2). (a,b) Conditions according to experiments in figures 7c/7d of Park & Nosoko (2003): water ( $Ka=3923$ ),  $Re=40.8/59.3$ ,  $f^*=19.1$  Hz/17.0 Hz,  $\Lambda_x^*=20$  mm/25 mm,  $\Lambda_z^*=20$  mm; (c) according to two-dimensional experiments of Dietze *et al.* (2009) with additional  $\Lambda_z^*=20.7$  mm: water-DMSO ( $Ka=509.5$ ),  $Re=15.0$ ,  $f^*=16$  Hz,  $\Lambda_x^*=20.7$  mm; (d) according to experiments in Rohlfs *et al.* (2012a): silicone oil ( $Ka=17.8$ ),  $Re=6.2$ ,  $f^*=16.6$  Hz,  $\Lambda_x^*=22$  mm,  $\Lambda_z^*=30$  mm.

flow  $Re=675$  (Pope, 2000), where we have constructed  $Re$  with the mean velocity and half the channel height  $H^*/2$ . Our observations suggest that this discrepancy may result from the fact that the flow conditions (characterized through  $\hat{Re}$ ) within the large wave humps can be significantly closer to turbulence than the overall value of  $Re$  suggests. This view is also supported by the experiments of Adomeit & Renz (2000), who observed turbulent

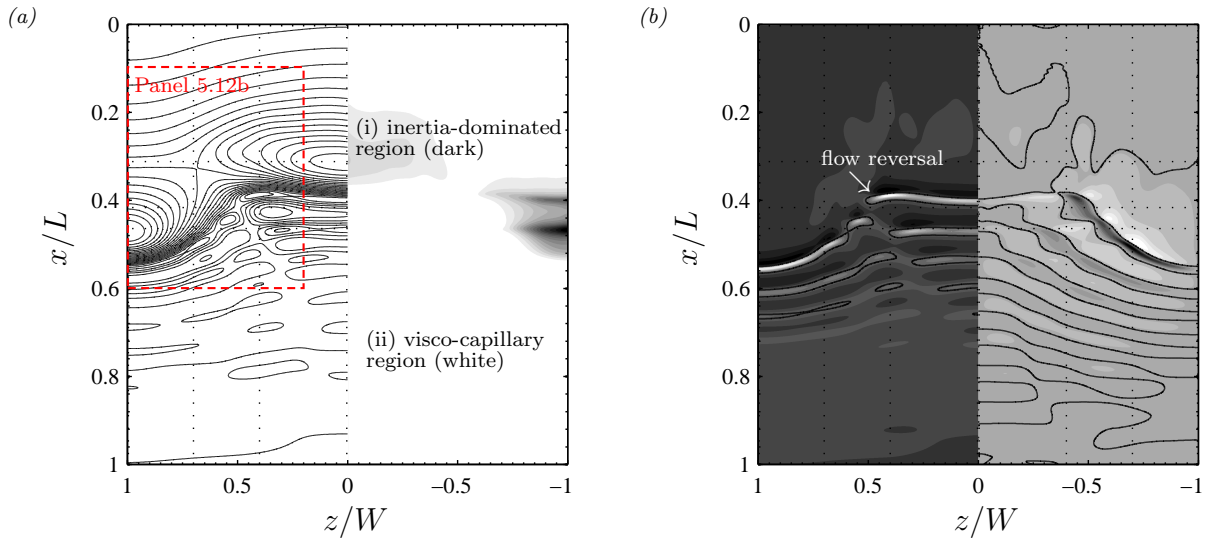


Figure 5.11: Segregation of the flow within a three-dimensional falling water film. Parameters according to panel 5.10b. (a) Contours of the film height  $h(x, z)$  (left) and the local inverse Weber number (5.11)  $We^{-1}$  (right; from white to black  $We^{-1} \in [0, 1.7]$ ); (b) contours of the streamwise and spanwise wall-shear stress components  $\tau_{wx}^* = -\mu \partial_{y^*} u^*|_{y^*=0}$  (left;  $\tau_{wx}^* \in [-7.7, 13.9]$  Pa) and  $\tau_{wz}^* = -\mu \partial_{y^*} w^*|_{y^*=0}$  (right;  $\tau_{wz}^* \in [-8, 3.8]$  Pa).

spots within the main wave humps (for  $Re=72$  and  $Ka=1042$ ).

In the visco-capillary region, the flow pattern is mainly governed by the film surface shape through the effect of curvature-induced capillary pressure gradients (see figures 15 and 20 in Dietze *et al.* (2014) for details). Panel 5.11b represents contours of the streamwise (left) and spanwise (right) wall shear stress components  $\tau_{wx}^*$  and  $\tau_{wz}^*$ , which we confront with the corresponding film thickness contours in panel 5.11a. Solid lines in panel 5.11b correspond to  $\tau_{wx}^*=0$  (left) and  $\tau_{wz}^*=0$  (right), and thus mark changes in flow direction. In the visco-capillary region, the flow direction is dictated by the film surface curvature, i.e. from the capillary humps to the capillary troughs. This produces several zones of upward flow underneath the capillary troughs, similar to the capillary flow separation observed in two-dimensional falling liquid films (Dietze *et al.*, 2008).

By contrast, in the inertia-dominated region, e.g. in the trailing portion of the main hump, sign changes in  $\tau_{wz}^*$  occur even in the absence of corresponding changes in surface curvature (panel 5.11b). Panel 5.12a represents a cross-sectional view of the velocity field in the  $y$ - $z$  plane for the water film in panel 5.11b, evidencing a cellular pattern of vortical structures filling the entire film height. These initially form at the wall as a result of capillary pressure gradients, but, as they grow, increasingly interact with the inertia-dominated mean flow, resulting in an increasing misalignment with the passing surface wave. Supplemental movies `Case1_DNS_TH.avi` and `Case2_DNS_TH.avi` from Dietze *et al.* (2014) show this process in action. It may be related to the wave-induced turbulence observed by Ishigai *et al.* (1972) at very low  $Re$ .

In the leading portion of the main wave hump (top view in panel 5.12b), large-

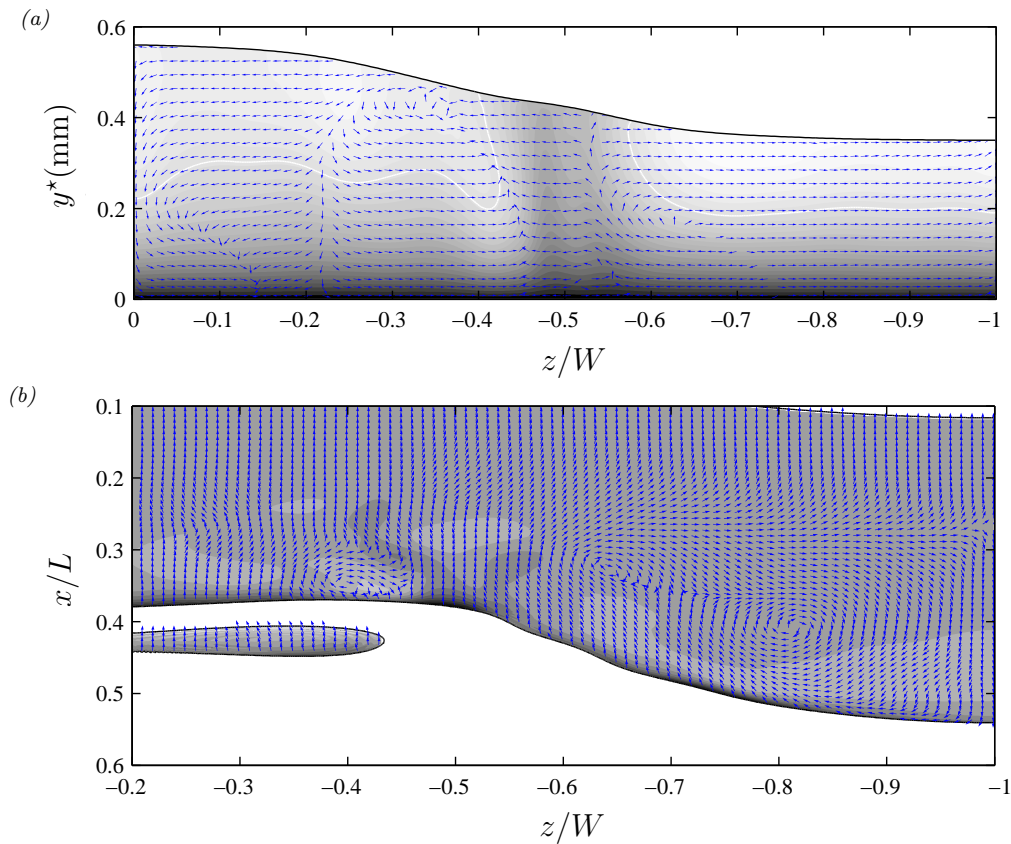


Figure 5.12: Cross-sectional views of the velocity field within the main wave hump of panel 5.11a. (a) Front view of  $y$ - $z$  cross section at  $x/L=0.31$  (trailing hump), evidencing vortical structures misaligned with the film surface shape. White solid lines mark  $u=c$ ; (b) top view of velocity field in a  $x$ - $z$  cross section moving with wave speed  $c$  at  $y^*=0.2$  mm (dashed red box in panel 5.11a), evidencing large-scale moving-frame vortices carrying wall-normal vorticity. Gray-scale contours indicate the third velocity component.

scale vortical structures carrying wall-normal vorticity are observed in the wave-fixed  $x$ - $z$  reference frame. These moving-frame vortices intensify lateral mixing within the liquid film, and thus further increase the wave-induced intensification of scalar transport w.r.t. two-dimensional falling liquid films (section 6.3), where a two-dimensional moving-frame vortex (see panel 4.10a) is already observed in the main hump (Miyara, 2001; Alekseenko *et al.*, 2007b).

The inertia-dominated and visco-capillary regions interact and this can produce self-sustained oscillatory states, where the wave front varies between a distinctly three-dimensional horseshoe shape (panel 5.13a) and a more two-dimensional structure (panel 5.13b). This is shown in figure 5.13 for the water-DMSO film in panel 5.10c, where oscillations are most regular (larger-amplitude oscillations, discussed in Dietze *et al.* (2014), are observed for water films). Panel 5.13c represents time traces of the streamwise and spanwise surface deformation energies  $E_x$  and  $E_z$  (Joo & Davis, 1992; Scheid *et al.*, 2008):

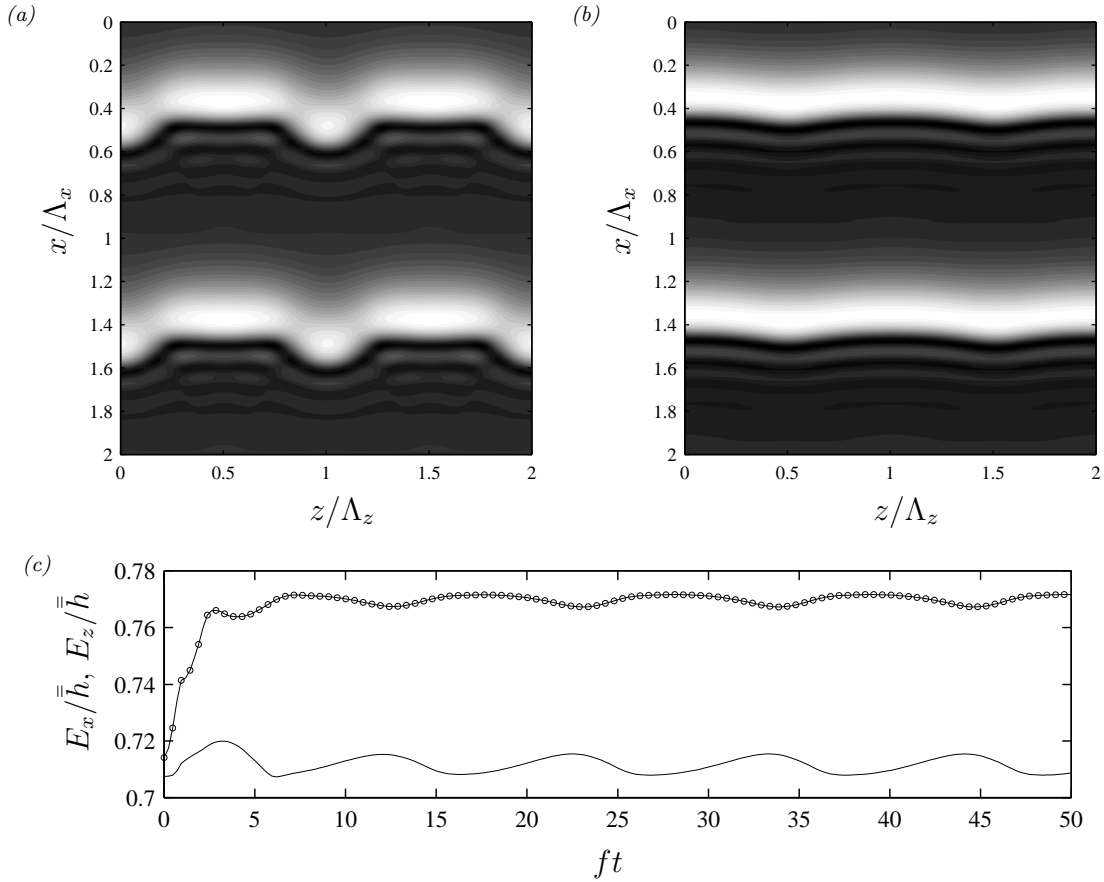


Figure 5.13: Self-sustained oscillations displaying a time-periodic transition between three- and two-dimensional wave fronts. Computations with the three-dimensional WRIBL model of Scheid *et al.* (2006) for parameters corresponding to the DMSO-water film in panel 5.10c. The computational domain spans two wavelengths in both dimensions. (a) Snapshot of a three-dimensional wave front:  $ft=4.6$ ; (b) more two-dimensional wave front:  $ft=15.5$ ; (c) time trace of the streamwise and spanwise surface deformation energies  $E_x$  (symbols) and  $E_z$  (solid line without symbols), according to (5.12), normalized with the mean wave height  $\bar{h} = \frac{1}{4} \Lambda_x^{-1} \Lambda_z^{-1} \int_0^{2\Lambda_x} \int_0^{2\Lambda_z} h \, dx \, dz$ .

$$E_x(t) = \frac{1}{N_x N_z} \sum_{j=1}^{N_z} \left[ \sum_{m=1}^{\frac{N_x}{2}-1} |A_m(z_j, t)|^2 \right]^{\frac{1}{2}}, \quad A_m(z, t) = \sum_{l=0}^{N_x-1} h(x_l, z, t) \exp\left[\frac{i 2\pi m l}{N_x}\right], \quad (5.12a)$$

$$E_z(t) = \frac{1}{N_x N_z} \sum_{l=1}^{N_x} \left[ \sum_{n=1}^{\frac{N_z}{2}-1} |B_n(x_l, t)|^2 \right]^{\frac{1}{2}}, \quad B_n(x, t) = \sum_{j=0}^{N_z-1} h(x, z_j, t) \exp\left[\frac{i 2\pi n j}{N_z}\right], \quad (5.12b)$$

where  $N_x$  and  $N_z$  denote the number of discrete grid points at which  $h$  is evaluated. The

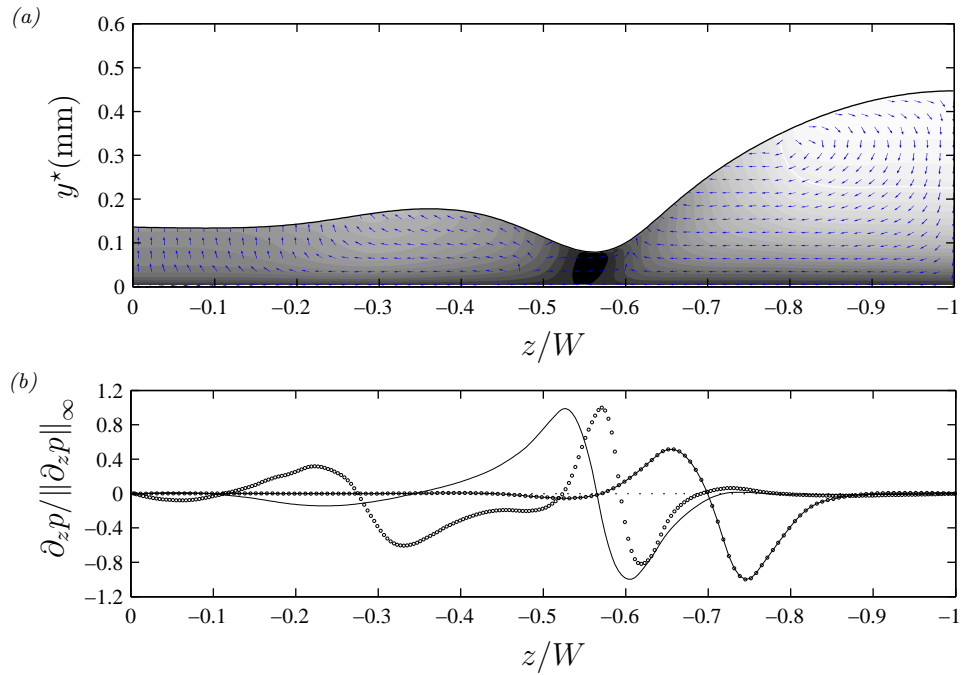


Figure 5.14: Spanwise drainage from the leading main hump toward the capillary trough. Parameters according to water film in panel 5.10a. (a) Velocity vectors within a  $y$ - $z$  cross section passing through the leading main hump; (b) profiles of the normalized spanwise wall pressure gradient. Solid line without symbols corresponds to panel a.

$E_x$  and  $E_z$  time traces evidence a periodic exchange between three- and two-dimensional interfacial deformations.

The underlying mechanism relies on a spanwise capillary pressure gradient forming as the leading portion of the main hump protrudes into the residual film, as has been invoked by Georgantaki *et al.* (2011) to explain the stabilization of curved wave fronts in laterally confined films. This gradient is unopposed by gravity and sucks liquid from the inner region of the protruding main humps toward the outlining capillary trough (see figure 5.14). As a result, the amplitude and celerity of the protruding hump is reduced, upon which the trailing portion of the main wave hump catches up once again. The draining mechanism relies on the large spanwise curvature gradient between the capillary trough and the protruding main hump, and is particularly effective when one or several capillary ridges dock onto the main humps, as seen in panels 5.10a, 5.10b, and 5.10c. Once the main wave front has retracted toward a two-dimensional shape, the draining mechanism subsides and the three-dimensional inertial mode of the Kapitza instability (Kofman *et al.*, 2014) restores the horseshoe-shaped wave structure.

The interaction between capillary ripples and main wave humps, has also been reported to produce oscillatory states in two-dimensional falling liquid films (Pradas *et al.*, 2011, 2012, 2013). It requires sufficiently strong capillary effects and breaks down for the low  $Ka$  silicone oil film in panel 5.10d. In that case, the leading humps continue to protrude and eventually break the spanwise connectivity of the main wave front, upon

which they repeatedly overtake the original trailing portions (see supplemental movie `Case4_WRIBL.avi` from Dietze *et al.* (2014)). This has been observed experimentally in a spatially developing water film (Alekseenko *et al.*, 2012).

**Impact of the work and relation to the current state of the art** Our paper Dietze *et al.* (2014) has been cited 27 times according to *Web of Science*.

Our observation, that solitary waves can increase the local Reynolds number  $\hat{Re}$  up to fivefold, and our conjecture that this may explain the very early transition to turbulence in falling liquid films (see discussion of panel 5.11a), have motivated Mukhopadhyay *et al.* (2017) to develop a transitional WRIBL model, where turbulence is accounted for via an eddy viscosity based on  $\hat{Re}$ . This model accurately predicts experimental roll waves in turbulent open-channel flows (Brock, 1970).

Kharlamov *et al.* (2015) have confirmed experimentally the oscillatory states we have uncovered in figure 5.13. Their figures 17 and 18, which are based on film thickness measurements through laser-induced fluorescence, clearly show the alternating protrusion (our panel 5.13a) and retraction (our panel 5.13b) of the leading humps.

Guzanov *et al.* (2018) have experimentally identified wavy rivulets forming on an isothermal falling liquid film, which seem to correspond to the wave regime observed in our periodic simulation of the silicone-oil film (panel 5.10d). As shown in the supplementary movie `Case4_WRIBL.avi` of Dietze *et al.* (2014), the long-time evolution for this case exhibits leading humps that disconnect from the rest of the wave front and overtake its trailing portions.

Feldmann *et al.* (2020) have suggested that the three-dimensional surface waves studied here may play a role in the de-wetting of falling liquid films.

Transverse mixing generated by the moving-frame vortices in panel 5.12b may explain the significant intensification of heat and mass transfer in three-dimensional falling liquid films (Alekseenko *et al.*, 1994). Kvon *et al.* (2016) and A. *et al.* (2022) have confirmed these vortices (and the lateral drainage of liquid toward the capillary trough) via depth-resolved particle tracking velocimetry with a light-field camera. Interestingly, the fluorescent dye used in these experiments makes visible plume-shaped flow structures in the trailing main hump.

# On the Kapitza instability and the generation of capillary waves

Georg F. Dietze<sup>†</sup>

Laboratoire FAST, Univ. Paris-Sud, CNRS, Université Paris-Saclay, F-91405, Orsay, France

(Received 30 April 2015; revised 29 August 2015; accepted 10 December 2015)

We revisit the classical problem of a liquid film falling along a vertical wall due to the action of gravity, i.e. the Kapitza paradigm (Kapitza, *Zh. Eksp. Teor. Fiz.*, vol. 18, 1948, pp. 3–28). The free surface of such a flow is typically deformed into a train of solitary pulses that consists of large asymmetric wave humps preceded by small precursory ripples, designated as ‘capillary waves’. We set out to answer four fundamental questions. (i) By what mechanism do the precursory ripples form? (ii) How can they travel at the same celerity as the large-amplitude main humps? (iii) Why are they designated as ‘capillary waves’? (iv) What determines their wavelength and number and why do they attenuate in space? Asymptotic expansion as well as direct numerical simulations and calculations with a low-dimensional integral boundary-layer model have yielded the following conclusions. (i) Precursory ripples form due to an inertia-based mechanism at the foot of the leading front of the main humps, where the local free-surface curvature is large. (ii) The celerity of capillary waves is matched to that of the large humps due to the action of surface tension, which speeds up the former and slows down the latter. (iii) They are justly designated as ‘capillary waves’ because their wavelength is systematically shorter than the visco-capillary cutoff wavelength of the Kapitza instability. Due to a nonlinear effect, namely that their celerity decreases with decreasing amplitude, they nonetheless attain/maintain a finite amplitude because of being continuously compressed by the pursuing large humps. (iv) The number and degree of compression of capillary waves is governed by the amplitude of the main wave humps as well as the Kapitza number. Large-amplitude main humps travel fast and strongly compress the capillary waves in order for these to speed up sufficiently. Also, the more pronounced the first capillary wave becomes, the more (spatially attenuating) capillary waves are needed to allow a smooth transition to the back of the next main hump. These effects are amplified by decreasing the Kapitza number, whereby, at very small values, streamwise viscous diffusion increasingly attenuates the amplitude of the capillary waves.

**Key words:** capillary waves, thin films

---

## 1. Introduction

We consider a Newtonian viscous liquid film flowing down a vertical wall due to the action of gravity in a two-dimensional setting. As shown in figure 1 and

<sup>†</sup> Email address for correspondence: [dietze@fast.u-psud.fr](mailto:dietze@fast.u-psud.fr)



## Three-dimensional flow structures in laminar falling liquid films

Georg F. Dietze<sup>1,†</sup>, W. Rohlf<sup>2</sup>, K. Nährich<sup>2</sup>, R. Kneer<sup>2</sup> and B. Scheid<sup>3</sup>

<sup>1</sup>Laboratoire FAST, CNRS, UPMC Université Paris 06, et Université Paris-Sud, Bâtiment 502, Campus Universitaire d'Orsay, 91405 Orsay, France

<sup>2</sup>Institute of Heat and Mass Transfer, RWTH Aachen University, Aachen 52056, Germany

<sup>3</sup>Laboratoire TIPS, Université Libre de Bruxelles, Bruxelles 1050, Belgium

(Received 14 June 2013; revised 29 September 2013; accepted 19 December 2013;  
first published online 4 March 2014)

Full numerical simulations of the Navier–Stokes equations for four cases of vertically falling liquid films with three-dimensional surface waves have been performed. Flow conditions are based on several previous experimental studies where the streamwise and spanwise wavelengths were imposed, which we exploit by simulating periodic wave segments. The considered flows are laminar but approach conditions at which intermittent wave-induced turbulence has been observed elsewhere. Working liquids range from water to silicone oil and cover a large interval of the Kapitza number ( $Ka = 18\text{--}3923$ ), which relates capillary to viscous forces. Simulations were performed on a supercomputer, using a finite-volume code and the volume of fluid and continuum surface force methods to account for the multiphase nature of the flow. Our results show that surface waves, consisting of large horseshoe-shaped wave humps concentrating most of the liquid and preceded by capillary ripples on a thin residual film, segregate the flow field into two regions: an inertia-dominated one in the large humps, where the local Reynolds number is up to five times larger than its mean value, and a visco-capillary region, where capillary and/or viscous forces dominate. In the inertial region, an intricate structure of different-scale vortices arises, which is more complicated than film thickness variations there suggest. Conversely, the flow in the visco-capillary region of large- $Ka$  fluids is entirely governed by the local free-surface curvature through the action of capillary forces, which impose the pressure distribution in the liquid film. This results in flow separation zones underneath the capillary troughs and a spanwise cellular flow pattern in the region of capillary wave interference. In some cases, capillary waves bridge the large horseshoe humps in the spanwise direction, coupling the two aforementioned regions and leading the flow to oscillate between three- and two-dimensional wave patterns. This persists over long times, as we show by simulations with the low-dimensional model of Scheid *et al.* (*J. Fluid Mech.*, vol. 562, 2006, pp. 183–222) after satisfactory comparison with our direct simulations at short times. The governing mechanism is connected to the bridging capillary waves, which drain liquid from the horseshoe humps, decreasing their amplitude and wave speed and causing them to retract in the streamwise direction. Overall, it is observed that spanwise flow structures (not accounted for in two-dimensional investigations) are particularly complex due to the absence of gravity in this direction.

**Key words:** interfacial flows (free surface), thin films

---

† Email address for correspondence: [dietze@fast.u-psud.fr](mailto:dietze@fast.u-psud.fr)



# Chapter 6

## Falling liquid films in narrow channels

Falling liquid films intervene in many applications involving inter-phase heat and mass transfer (Alekseenko *et al.*, 1994; Azzopardi *et al.*, 2011), where they are often subject to a strongly-confined counter-current gas flow. For example, structured packings in rectification columns for cryogenic air separation are typically designed to minimize the spacing between individual corrugated sheets (of the order of several millimetres) which form the small channels where the liquid and gas are put into contact (Fair & Bravo, 1990). Even stronger confinement levels are encountered in falling film micro-reactors (Lapkin & Anastas, 2018), where the channel height  $H^* < 1$  mm (Zhang *et al.*, 2009).

A lower bound for  $H^*$  is dictated by the onset of flooding, which can manifest itself either through an obstruction of the channel by the liquid film (Vlachos *et al.*, 2001), a gas-induced reversal of surface waves (Tseluiko & Kalliadasis, 2011), liquid arrest (Trifonov, 2010), or the disintegration of the liquid film into droplets (Zapke & Kröger, 2000). Surface waves travelling on the liquid film, and in particular their interaction with the gas flow, play an important role in triggering such events (panel 6.1a). On the other hand, surface waves are beneficial for heat and mass transfer (Miyara, 1999; Albert *et al.*, 2014), allowing to increase inter-phase transfer rates by more than 100% (Yoshimura *et al.*, 1996; Rastaturin *et al.*, 2006).

Structuring the bounding wall allows to act on the wavy falling liquid film (panel 6.1c). For example, structured packings in rectification columns typically consist of sheets that are corrugated at different levels (Valluri *et al.* (2005)). Large-scale corrugations force the falling liquid film to meander through the packing, thus increasing its residence time (while modulating its inclination). Additional small-scale texturing (panel 6.1b), with amplitudes of the order of  $100 \mu\text{m}$  (Trifonov, 2011), is said to promote turbulence. Although liquid flow rates in industrial devices are usually far removed from turbulent conditions, texturing is known to modify the stability and waviness of falling liquid films (Aksel & Schörner, 2018).

The above observations reveal a research challenge: find optimal wave regimes that maximize scalar transfer while avoiding flooding, and we have addressed this by studying

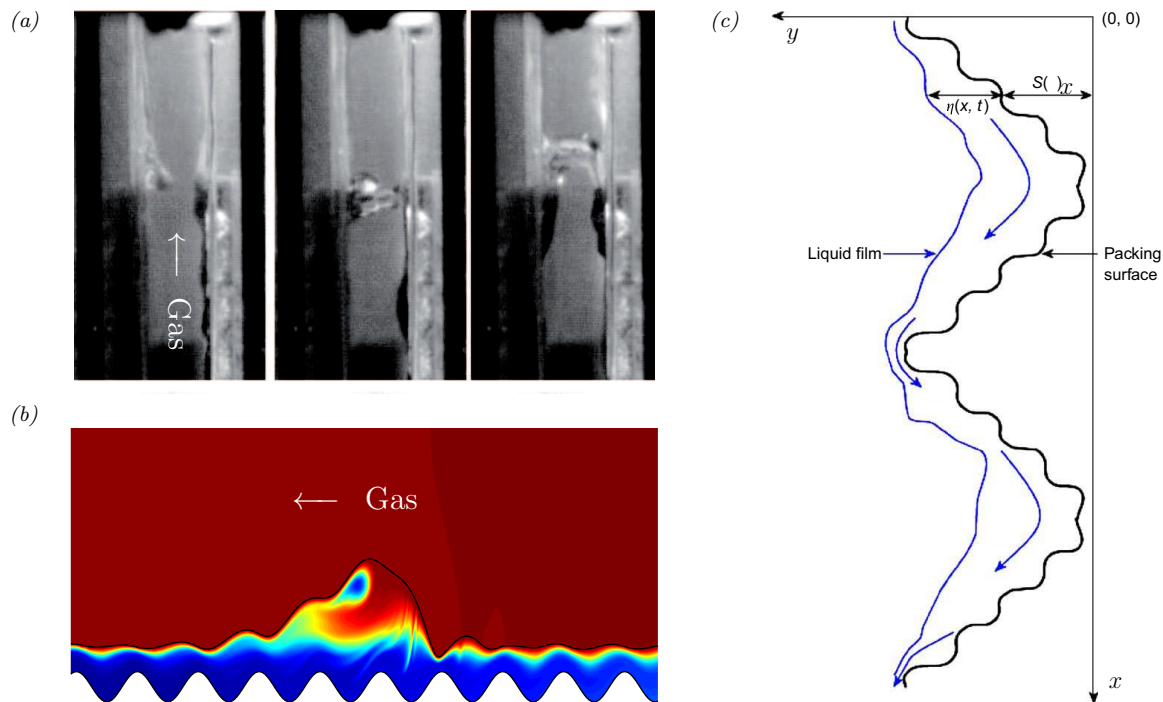


Figure 6.1: Planar falling liquid films in narrow (corrugated) channels subject to a counter-current gas flow. (a) Wave-induced flooding of the channel, adapted from Vlachos *et al.* (2001); (b) effect of wall corrugations on hydrodynamics and mixing within the liquid film, adapted from Dietze (2019); (c) sketch of a corrugated sheet from a structured packing, adapted from Valluri *et al.* (2005).

the two model problems represented in panel 1.2a and figure 4.1, i.e. a planar falling liquid film in contact with a counter-current gas flow within a planar possibly corrugated channel. These can be considered as elementary prototypes for the applications discussed above. Thereby, we have focused on strong confinement levels<sup>1</sup>, i.e. channel heights that are only several times greater than the mean film thickness ( $H/\bar{h} \leq 5$ ).

Such conditions, where the gas Reynolds number remains moderate ( $|\text{Re}_2| \leq 200$ ), are ideal for deploying our planar WRIBL model (1.27), allowing high-fidelity predictions at low computational cost. From a physical perspective, the limit of strong confinement promotes the pressure coupling (1.6a) between the liquid and gas, entailing several new phenomena. Our work has uncovered four novel phenomena that have extended the state of the art in the following ways:

- Linear stability analysis of falling liquid films subject to a counter-current gas had mainly focused on weak confinement levels, where turbulent conditions are required

<sup>1</sup>In ongoing work (chapter 9), we have used our hybrid WRIBL model of section 1.4 to study falling liquid films sheared by a turbulent counter-current gas flow within moderately confined channels.

for the gas effect to be significant. In that case, the maximum growth rate increases with increasing gas velocity (Alekseenko *et al.*, 2009), while the cut-off wave number diminishes or varies non-monotonically (Vellingiri *et al.*, 2015; Trifonov, 2017a). Moreover, increasing the gas velocity can lead to a convective/absolute/upward-convective transition of the primary instability (Vellingiri *et al.*, 2015). These observations suggest a mainly destabilizing effect of the gas flow.

However, Tilley *et al.* (1994a) pointed out the possibility of suppressing the long-wave interfacial instability in falling liquid films by strongly confining the gas phase, and suggested a stabilizing mechanism due to the tangential gas shear stress exerted at the film surface. But, the authors concluded for the studied parameter range that this stabilizing effect is weak for water-air systems.

In Lavalle *et al.* (2019), we have revisited the problem over a wider parameter range (low inclination angles) and found that the Kapitza instability can indeed be suppressed for this fluid combination, e.g. a water film of  $h_0^*=0.5$  mm thickness inclined at  $\phi=3^\circ$  is fully stabilized by placing a confining plate at a distance  $H^*=1$  mm above the quiescent gas. Moreover, the stabilization is stronger when the gas flows counter-currently and increases with increasing gas velocity. These results and the underlying mechanisms are discussed in section 6.1.

- Although the relevance of surface waves for the flooding of narrow channels has been established beyond doubt (Vlachos *et al.*, 2001; Drosos *et al.*, 2006), their precise role in this catastrophic event was still largely unclear at the start of this work. Different effects of the gas flow on the nature of individual waves had been elucidated, such as wave amplification (Trifonov, 2010; Kofman *et al.*, 2017), wave reversal (Njifenju, 2010; Tseluiko & Kalliadasis, 2011), and flow reversal in the wave crests (Trifonov, 2010). But, how these effects unfold in a spatially evolving film and by what routes they bring about flooding (wave coalescence, secondary instabilities, or the loss of travelling wave solutions), remained unclear. As falling-film heat and mass exchangers are known to work best near the flooding limit, answering this question is important from a practical perspective.

In Dietze & Ruyer-Quil (2013) and Lavalle *et al.* (2020), we have uncovered three possible routes to flooding in vertically-falling liquid films. In the case of a noise-driven wave evolution, flooding is caused by coalescence events that lead to large waves obstructing the channel, and it can be suppressed by applying coherent inlet forcing. In the second case, flooding arises due to a loss of stability of TWS, which leads to spontaneous wave reversal in a spatio-temporal calculation. In the third case, when the liquid volume and not the flow rate is imposed, the gas can produce negative flooding by locally thinning the film up to the point of spinodal de-wetting. At lower gas velocities, catastrophic events are avoided, and secondary instability of TWS produces self sustained amplitude modulations that promote mixing within the liquid film. Consequently, the gas Reynolds number  $Re_2$  can be used to tailor optimal waves that maximize heat and mass transfer while avoiding flooding. This

parameter also controls the occurrence of wave-induced vortical structures in the gas (Nave, 2004), which our WRIBL model accurately predicts. Our results are discussed in section 6.2.1.

- The gas-induced linear stabilization we have observed in weakly-inclined falling liquid films (Lavalle *et al.*, 2019) suggests the possibility of wavy regimes with a reduced flooding risk, i.e. where both the linear growth rate and the nonlinear wave amplitude decrease with increasing counter-current gas flow rate. Several investigations in the literature have reported evidence suggesting the possibility of nonlinear stabilization. Samanta (2014) showed that applying a constant adverse tangential shear stress to the free-surface of a weakly inclined falling liquid film can drastically reduce the amplitude of nonlinear surface waves, although the assumption of a constant shear stress is not applicable in our strongly-confined configuration. Also, Trifonov (2020) demonstrated that the interfacial fluid velocity, mean film height, and inter-phase friction coefficient may vary non-monotonically with increasing counter-current gas velocity, although the wave amplitude in his simulations still increased monotonically.

In Lavalle *et al.* (2021), we have identified regimes where linear and nonlinear effects are either simultaneously stabilizing, simultaneously destabilizing, opposed with a linear/nonlinear stabilization/destabilization, or vice versa. In the first case, TWS resist secondary instabilities and exhibit a peculiar elongated shape with a flat top. In the latter case, the gas flow triggers secondary instabilities that alter the structure of a spatially-evolving wave train in two ways: *(i)* a coarsening dynamics via slip-streaming waves, *(ii)* a refining dynamics via wave spitting events. The slip-streaming waves decrease in amplitude as they speed up toward their leading neighbours, in contrast to the usual coarsening dynamics observed in a quiescent atmosphere (Chang *et al.*, 1996*b*). The wave splitting events reduce the wave amplitude and thus lower the flooding risk. Our results are discussed in section 6.2.2.

- Wall corrugations are a constructive means to act on the wavy liquid film, through several hydrodynamic effects, such as suppression of the Kapitza instability (Trifonov, 2014; Schörner *et al.*, 2016), resonant states, where the film surface espouses the shape of the corrugation (Bontozoglou & Papapolymerou, 1997, 1998; Dávalos-Orozco, 2007; Heining *et al.*, 2009), wave regularization (Oron & Heining, 2008) and wave selection from a noise-sustained wave evolution (Cao *et al.*, 2013), wave amplitude modulations (Trifonov, 2007*b*, 2017*b*), and increased mixing within the liquid (Trifonov, 2011). Their potential for intensifying scalar transfer is very high, but only very few studies have considered this effect (Gaskell *et al.*, 2006; Haroun *et al.*, 2010; Kohrt *et al.*, 2011), and none of them have discussed the role of surface waves.

In Dietze (2019), we have performed DNS of inter-phase scalar transfer in falling liquid films flowing over wall corrugations, in the presence of a counter-current gas (figure 4.1). We find that sinusoidal corrugations typically used in structured pack-

ings (Trifonov, 2007a), significantly intensify transfer in the high Péclet number limit (30% reduction of the required transfer surface). The same degree of intensification can be achieved through localized semicircular bumps, albeit through another mechanism. In both cases, corrugations intensify the surface renewal mechanism (Yoshimura *et al.*, 1996; Roberts & Chang, 2000) linked to the moving-frame vortex observed in large-amplitude solitary waves (figure 4.10). However, localized bumps can also trigger flooding events when the gas velocity is increased. Our results are discussed in section 6.3.

## 6.1 Gas-induced suppression of Kapitza instability

We focus on the case of a water film falling along the lower wall of an inclined channel of height  $H^*$  in contact with air<sup>2</sup>. Panel 6.2a shows how the neutral stability curve of the Kapitza instability is affected (versus the passive-gas threshold  $\text{Re}_1 = \frac{5}{6} \cot(\phi)$ ) by increasingly confining the gas, while maintaining an aerostatic pressure gradient, i.e.  $M = \sin(\phi)$ . We observe a 40% increase in the critical  $\text{Re}_1$  for the strongest confinement level ( $H^* = 1.7$  mm) and an experimentally measurable<sup>3</sup> stabilization for  $H^* = 5$  mm. Thus, for a given liquid flow rate, the Kapitza instability can be fully suppressed simply by confining the gas. Panel 6.2c demonstrates such a scenario via dispersion curves of the linear spatial growth rate  $-k_i$ , as obtained from Orr-Sommerfeld (OS) calculations (solid curves) and our WRIBL model (1.27) (symbols).

Another way to suppress the instability is by applying a counter-current gas flow and increasing its flow rate at constant gap height  $H$ , which is shown in panel 6.2d. However, this effect is highly sensitive to the inclination angle  $\phi$ , which is quite low in panels 6.2a, 6.2c, and 6.2d. Panel 6.2b demonstrates this by representing neutral stability curves in terms of  $\text{Re}_1$  and  $\text{Re}_2$  for different  $\phi$ . We see that a stabilization with increasing  $|\text{Re}_2|$  (red curves) occurs when  $\phi$  is small, whereas a destabilization (blue curves) occurs when  $\phi$  is large.

The stabilization observed at low inclination angles suggests, counter-intuitively, that the risk of wave-induced flooding can be reduced by strongly confining and shearing the falling liquid film, at least from a linear perspective. We will see in section 6.2 that the nonlinear wave dynamics may or may not conform with this conclusion.

The mechanism of the gas-induced stabilization of the Kapitza instability must emanate either from the viscous stresses (3.7g) or the pressure (3.7h) exerted by the gas at the film surface  $y=h$ . We untangle these two effects in figure 6.3. Panels 6.3a and 6.3c represent growth rate dispersion curves from OS calculations for two cases, one where the counter-current gas is stabilizing (panel 6.3a) and another where it is destabilizing (panel 6.3c). Solid curves correspond to the full problem, while red dashed ( $\Pi_\mu=0$ ) and blue dot-dashed ( $\Pi_\rho=0$ ) curves correspond to the limits where the gaseous viscous stresses

<sup>2</sup>In Lavalley *et al.* (2019), we have also considered other liquids.

<sup>3</sup>Experimental data represented by symbols in panel 6.2a were measured by Yiqin Li and Sophie Mergui. We thank Sophie Mergui for providing these data.

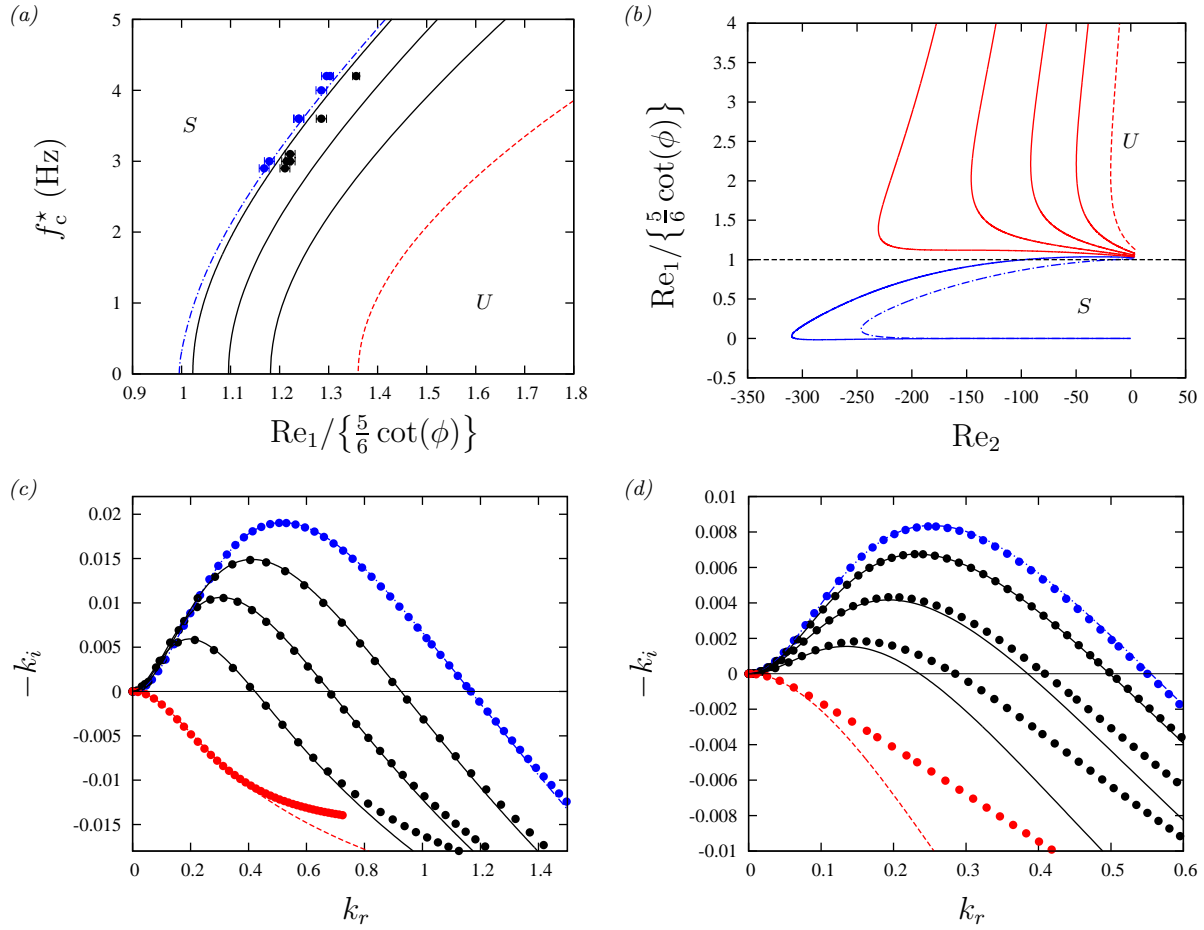


Figure 6.2: Suppression of the Kapitza instability in a confined falling liquid film. Spatial linear stability predictions from OS (lines) and WRIBL (filled symbols) calculations compared with experiments (open symbols). Water film in contact with air:  $Ka=3406.9$  (water II/air IV in table 2.1). (a) Cut-off frequency  $f_c^*$  in the case of an aerostatic pressure drop  $M=\sin(\phi)$ :  $\phi=1.69^\circ$ ,  $H^*=1.7, 2, 2.5, 5.1, \text{ and } 18$  mm (from right to left); (b) neutral stability bound in the case of a counter-current gas flow:  $H^*=2.5$  mm,  $\phi=1.5, 2, 2.5, 3, 3.5, 4.5, \text{ and } 10$  (from red dashed to blue dot-dashed curve via solid curves); (c, d) growth rate dispersion curves:  $\phi=3^\circ$ ,  $Re_1=23.9$ . (c)  $M=\sin(\phi)$ ,  $H^*=1.1, 2, 3, 4, \text{ and } 5$  mm (from bottom to top); (d)  $H^*=2.5$  mm,  $Re_2=-150, -100, -50, -20, \text{ and } 4.5$  (from bottom to top).

and gas pressure have been deactivated, either entirely in (3.2) and (3.7) (dashed and dot-dashed curves without symbols) or only in (3.7) (curves with symbols). In the latter case, only the linear perturbations of the interfacial gas stresses are neglected, while in the former case, the gas stresses are neglected entirely, i.e. also in the primary flow (3.2).

Based on panel 6.3a, perturbations of the interfacial viscous stresses are the dominant mechanism causing the gas-induced suppression of the Kapitza instability (compare red filled circles with solid black line). More precisely, it is the perturbation of the tangential



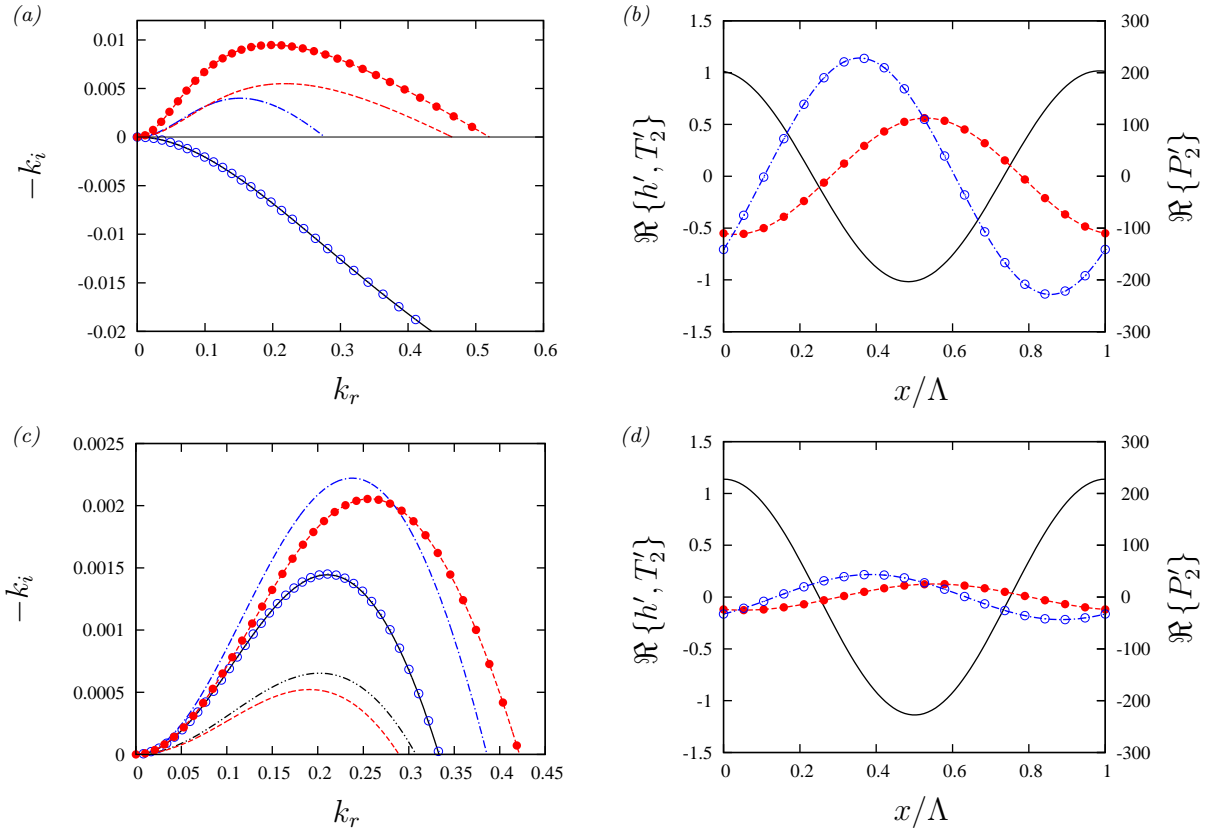


Figure 6.3: Stabilizing (*a,b*) versus destabilizing (*c,d*) effect of a counter-current gas flow:  $\phi=3^\circ$ , water film from figure 6.2. (*a*)  $H^*=2.5$  mm,  $\text{Re}_1=23.9$ ,  $\text{Re}_2=-150$ . Growth rate dispersion curves from OS calculations according to full problem (solid) and different limits. Red dashed:  $\Pi_\mu=0$  in (3.7) and (3.2); blue dot-dashed:  $\Pi_\rho=0$  in (3.7) and (3.2); filled circles:  $\Pi_\mu=0$  in (3.7); open circles:  $\Pi_\rho=0$  in (3.7); (*b*) corresponding linear perturbations of film height  $h'$  (3.6) (solid), gas shear stress  $T'_2$  (6.1) (red-dashed), and gas pressure  $P'_2$  (6.2) (dot-dashed blue):  $k_r=0.2$ ; (*c*)  $H^*=4$  mm,  $\text{Re}_1=17$ . Dispersion curves from full OS problem for  $\text{Re}_2=-10$  (dot-dot-dashed) and  $\text{Re}_2=-150$  (solid). Other curves correspond to  $\Pi_\mu=0$  and  $\Pi_\rho=0$  limits for  $\text{Re}_2=-150$ ; (*d*) corresponding linear perturbations  $k_r=0.2$ .

stress that is decisive (normal viscous stresses are negligible), whereas the gas pressure perturbation plays no role (blue open circles all but collapse with the solid black curve). Using notations from chapter 3 and following (3.5), we construct these perturbations by decomposing the interfacial tangential gas shear stress  $T_2$  and gas pressure  $P_2$ :

$$T_2 = \Pi_\mu \Pi_u \left[ S_{ij}^2 \Big|_{s=0} \cdot n_j \right] \cdot \tau_i = T_{20} + T'_2(x, t) = T_{20} + \hat{T}_2 \exp \{ ik(x - ct) \}, \quad (6.1)$$

$$P_2 = p_2 \Big|_{s=0} = P_{20} + P'_2(x, t) = P_{20} + \hat{P}_2 \exp \{ ik(x - ct) \}, \quad (6.2)$$

where the complex perturbation amplitudes  $\hat{T}_2$  and  $\hat{P}_2$  can be expressed in terms of the

stream function amplitudes  $\phi$  and  $\psi$  and their derivatives:

$$\hat{T}_2 = \left| \hat{T}_2 \right| \exp(i\beta_T) = k^2 \psi + \frac{1}{d_0^2} \left( \psi'' + \phi \frac{u_{20}''}{\tilde{c}} \right), \quad (6.3)$$

$$\begin{aligned} \hat{P}_2 = \left| \hat{P}_2 \right| \exp(i\beta_P) = & -i \frac{\psi'''}{k} \frac{1}{\text{Re}_2 d_0^3} \\ & + \frac{1}{d_0} \left\{ \psi' (i k \text{Re}_2^{-1} + c - u_{20}) + \psi u'_{20} \right\} - \frac{\phi \cos(\varphi)}{\tilde{c} \text{Fr}^2}. \end{aligned} \quad (6.4)$$

We are interested in confronting the phase shifts  $\beta_T$  and  $\beta_P$  of the perturbations  $T'_2$  and  $P'_2$  with that of the film height perturbation  $h' = \hat{h} \exp\{ik(x - ct)\}$  (3.6), which we obtain by reformulating  $\hat{h}$  based on the kinematic condition (1.9b):

$$\hat{h} = \left| \hat{h} \right| \exp(i\beta_h) = \frac{\phi}{\tilde{c}} \exp\{ik(x - ct)\}. \quad (6.5)$$

Panel 6.3b represents the three linear perturbations  $h'$ ,  $T'_2$ , and  $P'_2$  (non-dimensionalized with the natural scales (1.36)) for the water film in panel 6.3a. We focus on  $T'_2$ , which is responsible for the suppression of the Kapitza instability. Its profile (red filled circles) is shifted by half a wavelength w.r.t. the film height perturbation  $h'$  (solid black curve), so that the gas shear stress is more negative at a wave hump (where the gas cross-section is narrower) than at a wave trough (where the gas cross section is wider). As a result, the inertia-based instability mechanism discussed in figure 5.3b, which relies on a flow rate imbalance across wave extrema, is weakened.

To demonstrate this, we expand the liquid flow rate  $q_1$  up to order  $\epsilon$  in the long-wave limit (assuming  $\mathcal{O}(\text{Ka})=1/\epsilon^2$ ), following the approach for the Benney equation (5.2):

$$\begin{aligned} q_1 = & (\sin(\phi) - \epsilon \cos(\phi) \partial_x h + \epsilon^3 \text{Ka} \partial_{xxx} h) + \Pi_\mu \frac{1}{2} h^2 T_2 - \Pi_\rho \frac{1}{3} h^3 \partial_x P_2 \\ & + \epsilon \left\{ \frac{2}{15} \sin^2(\phi) h^6 \partial_x h + \Pi_\mu \left[ -\frac{5}{24} h^4 \partial_t T_2 + \sin(\phi) \left( \frac{2}{15} h^5 T_2 \partial_x h + \frac{7}{240} h^6 \partial_x T_2 \right) \right] \right. \\ & + \Pi_\rho \left[ \frac{2}{15} h^5 \partial_{xt} P_2 + \sin(\phi) \left( -\frac{4}{15} h^6 \partial_x h \partial_x P_2 - \frac{8}{315} h^7 \partial_{xx} P_2 \right) \right] \\ & - \frac{3}{40} \Pi_\mu^2 h^5 T_2 \partial_x T_2 + \Pi_\rho^2 \left[ \frac{2}{15} h^6 \partial_x h \partial_x P_2 + \frac{8}{315} h^7 \partial_x P_2 \partial_{xx} P_2 \right] \\ & \left. + \Pi_\mu \Pi_\rho \left[ -\frac{2}{15} h^5 \partial_x h T_2 \partial_x P_2 - \frac{7}{240} h^6 \partial_x T_2 \partial_x P_2 + \frac{13}{360} h^6 T_2 \partial_{xx} P_2 \right] \right\}, \end{aligned} \quad (6.6)$$

where we have employed the natural scales (1.36) for non-dimensionalization, and the effect of the gas is accounted for through  $T_2$  and  $P_2$ . Terms within the accolades are all inertia-related. Recalling that the growth rate at a wave extremum is  $\partial_t h = -\partial_x q_1$ , the only term in (6.6) representing a stabilizing effect at the wave extrema (where  $\partial_x h = 0$ ) is

$\frac{7}{240} \sin(\phi) h^6 \partial_x T_2$ . Its linear growth rate contribution  $-\frac{7}{240} \sin(\phi) h_0^6 \partial_{xx} T_2'$  varies according to the  $T_2'$  profile in panel 6.3b, i.e. it is negative at the wave hump and positive at the wave trough. The strength of this term scales with  $\sin(\phi)$ , whereas the driving term of the Kapitza instability  $\frac{2}{15} \sin^2(\phi) h^6 \partial_x h$  scales with  $\sin^2(\phi)$ . This explains why the suppression of the Kapitza instability occurs at low inclination angles (panel 6.2b). In short, stabilization occurs due to the tangential gas shear stress  $T_2$  attenuating the liquid flow rate imbalance between wave humps and wave troughs, and this weakens the inertia-induced growth mechanism of the Kapitza instability.

In the destabilizing scenario of panel 6.3c, the stabilizing effect of  $T_2'$  is not as strong because of the weaker relative confinement  $h_0/H$  (we have demonstrated the role of  $H$  in panel 2.11d), which leads to a lower perturbation amplitude  $|\hat{T}_2|$  versus  $|h'|$  (filled circles in panel 6.3c). In this case, the effect of  $T_2$  on the primary flow dominates, which is destabilizing (compare dashed red line and filled circles). Increasing  $T_{20}$  (through increasing  $|\text{Re}_2|$ ), increases the film height  $h_0$  and this favours the inertia-based driving mechanism of the Kapitza instability.

The effect of the gas pressure  $P_2$  is always stabilizing according to panels 6.3a and 6.3c (compare dot-dashed blue with solid black curves). Its linear perturbation in panels 6.3b and 6.3d is positively curved at wave maxima ( $\partial_{xx} P_2' < 0$ ), which translates into a slight stabilization through the growth rate contribution  $\frac{1}{3} \Pi_\rho h_0^3 \partial_{xx} P_2'$ . However, the role of  $P_2'$  is negligible in comparison to variations in the capillary pressure jump (open circles collapse with solid black curves). The effect of the primary flow contribution  $\partial_x P_{20} > 0$  is stabilizing on the one hand, as it counteracts the inertia-based driving mechanism through the growth rate contribution  $-\frac{4}{15} \sin(\phi) h_0^6 \partial_{xx} h' \partial_x P_{20}$ . On the other hand,  $h_0$  increases with increasing  $\partial_x P_{20}$ , which tends to destabilize the film, but this effect is weaker than for  $T_{20}$ <sup>4</sup>.

**Impact of the work and relation to the current state of the art** Our paper Lavalle *et al.* (2019) has been cited 10 times according to *Web of Science*.

In particular, Trifonov (2020), using temporal stability analysis, and Kushnir *et al.* (2021), using a spatial formulation, have confirmed our main finding that the Kapitza instability can be suppressed by strongly confining the gas. In the first work, it was further shown that no stabilization occurs for co-current gas flow. In the second work, stabilization was observed also for a recirculating gas, i.e. when the net gas flow rate  $q_{20}=0$ . In that case, the gas moves downward near the film surface and upward near the upper bounding wall. Kushnir *et al.* (2021) also confirmed the decisive role of the inclination angle observed in panel 6.2b.

Although the Gaster transformation (2.4) (Gaster, 1962) holds for the flow conditions considered here, the spatial stability formulation used by Kushnir *et al.* (2021) is more appropriate than the temporal formulation used in Lavalle *et al.* (2019). This is why we have redone our calculations for the current work (figures 6.2 and 6.3) with our spatial OS stability code (section 3). Our conclusions from Lavalle *et al.* (2019) remain unaltered.

---

<sup>4</sup>In the inertialess limit of (6.6), compare  $\frac{1}{2} \Pi_\rho h_0^2 T_{20}$  and  $-\frac{1}{3} \Pi_\rho h_0^3 \partial_x P_{20}$ .

Importantly, Kushnir *et al.* (2021) and Barmak *et al.* (2021) found that short-wave instability modes do not exist for conditions where the long-wave Kapitza instability is suppressed due to the gas effect. We have confirmed this for our configuration in section 3.1 (see figure 3.2). This means that falling liquid films can be fully stabilized in strongly confined geometries, which may be very useful in the design of real systems such as micro-reactors Lapkin & Anastas (2018) or micro-gap evaporators (Kabov *et al.*, 2011).

Mohamed *et al.* (2021) have extended our work by taking into account evaporation in a falling liquid film sheared by a counter-current gas flow. The authors confirm our observation that the Kapitza instability can be fully suppressed due to the shear stress imposed by the counter-current gas flow. However, they find that the added effect of evaporation can facilitate the transition from convective to absolute instability. In a real system, this would lead to a dry-out of the heating surface.

## 6.2 Nonlinear waves and secondary instabilities

We focus now on how a counter-current gas flow affects the nonlinear dynamics of a wavy falling liquid film flowing through a strongly-confined channel (panel 1.2a). In section 6.2.2, we will focus on inclined channels ( $\phi < 90^\circ$ ), where the gas can stabilize linearly the liquid film (as discussed in section 6.1). In the next section, 6.2.1, we will treat the vertical configuration, where this effect is negligible. In both cases, we will consider a single fluid combination defined in table 2.1, i.e. a DMSO-water solution as liquid and air II as gas. The gas flow is characterized either via the Reynolds number  $Re_2$ , which is based on the signed nominal flow rate  $\underline{q}_2^*$  (1.2) and thus negative in the counter-current configuration, or through the normalized pressure drop  $M$  (1.35), where the gas is entrained by the liquid film and  $Re_2 > 0$ . Typically, we will vary the gas flow from the aerostatic limit  $M = \sin(\phi)$  to a counter-current state with  $Re_2 < 0$ .

### 6.2.1 Vertically-falling liquid films

Figure 6.4 represents the nonlinear response of TWS to an increasingly strong counter-current gas flow, at imposed  $Re_1$  and frequency  $f$ . We consider the two channel heights  $H^* = 1$  mm and  $H^* = 1.5$  mm from panel 2.11c, where the linear response of the falling liquid film was plotted. In figure 6.4, we confront two types of nonlinear waves. Linearly-most amplified waves (blue curves), where  $f = f_{\max}$  (2.24), and low-frequency solitary waves (red and black curves), where  $f < f_{\max}$ .

For the larger channel,  $H^* = 1.5$  mm (panel 6.4a), the wave height  $h_{\max}$  is amplified under increasingly negative  $Re_2$  for both wave types, at least up to an upper limit  $h_{\max} \approx 0.75$ . For  $Re_2$  values beyond this maximum, which is reached only by the  $f^* = 16$  Hz solitary waves (black solid line with circle), the linear and nonlinear responses are opposed, i.e.  $h_{\max}$  is damped with increasing counter-current gas flow rate, whereas the linear growth rate  $-k_i$  is amplified (figure 2.11). In the rest of the parameter range, the linear and

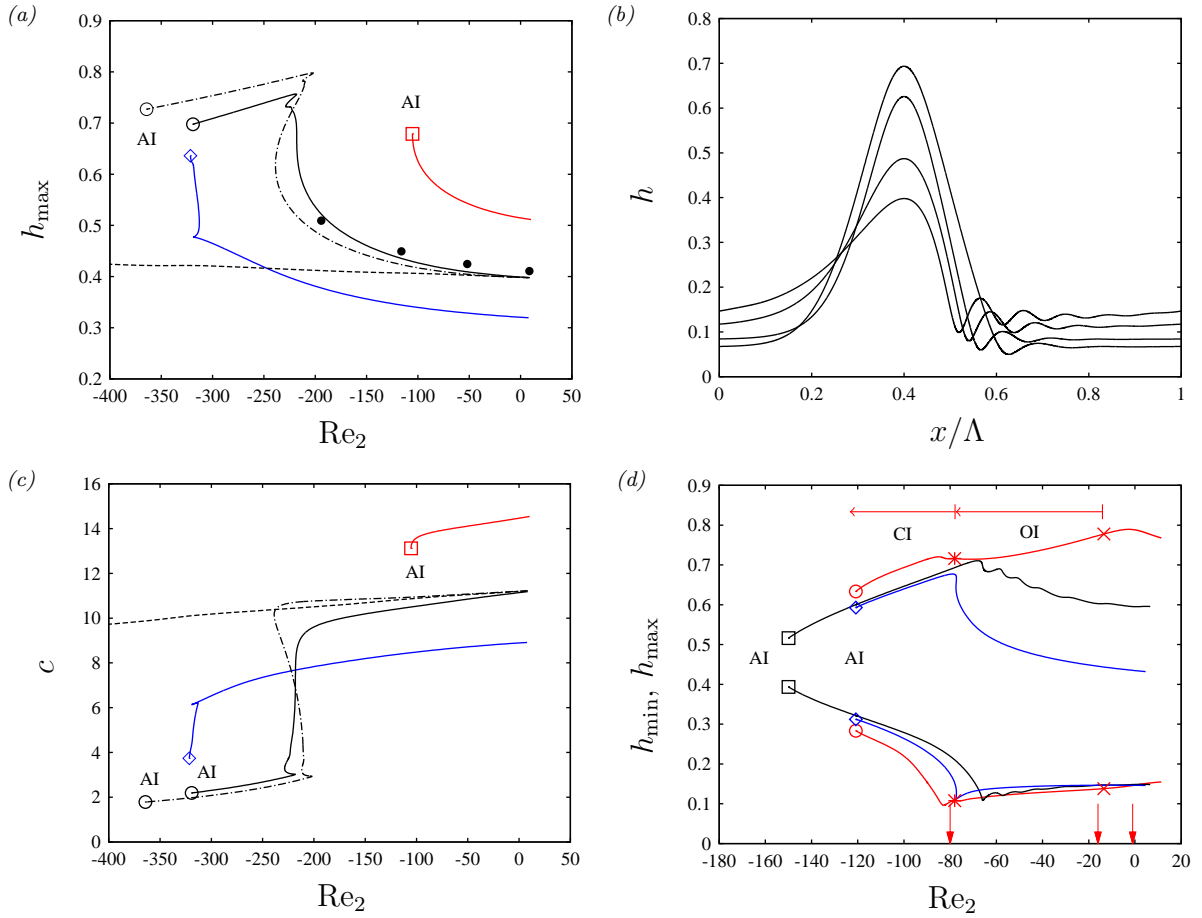


Figure 6.4: Superconfined falling liquid film in contact with a counter-current gas flow:  $\phi = 90^\circ$ ,  $Re_1 = 15$ ,  $Ka = 509.5$ . Nonlinear TWS obtained from WRIBL model (1.27). Open symbols mark linear limit of absolute instability (AI). Diamonds: most-amplified waves  $f = f_{\max}$  (2.24); open circles:  $f^* = 16 \text{ Hz} < f_{\max}$ ; squares:  $f^* = 8.7 \text{ Hz}$ . (a)  $H^* = 1.5$  mm. Wave height  $h_{\max}$ . Dashed:  $\Pi_\rho = 0$  in (1.6a); dot-dashed:  $\Pi_\mu = 0$  in (1.6a) and (1.6b); filled circles: DNS; (b) TWS profiles from panel a:  $f^* = 16 \text{ Hz}$ ;  $M = 1$ ,  $Re_2 = -174, -217, -218$ ; (c) wave celerity  $c$  for TWS from panel a; (d)  $H^* = 1.0$  mm. Asterisk ( $Re_2 = -13.5$ ) and cross ( $Re_2 = -78$ ) mark onsets of oscillatory (OI) and catastrophic instabilities (CI). Red arrows mark TWS represented in panels 6.5a, 6.5b, and 6.5c.

nonlinear responses are concordant and imply a gas-induced wave amplification.<sup>5</sup>

Panel 6.4b represents several profiles of the solitary TWS at  $f^* = 16$  Hz. The  $Re_2$  values for the different profiles correspond to the filled circles in panel 6.4a, which represent data from periodic DNS with the *interFOAM* solver (§4.2). The wave profiles show that the increase in wave height  $h_{\max}$  is accompanied by a one-by-one suppression of precursory capillary ripples (Trifonov, 2010; Kofman *et al.*, 2017). The cause for this is a drop in the

<sup>5</sup>Curves in panels 6.4a, 6.4c, and 6.4d are truncated at the linear absolute instability (AI) limit (marked by open symbols), where the concept of TWS breaks down.

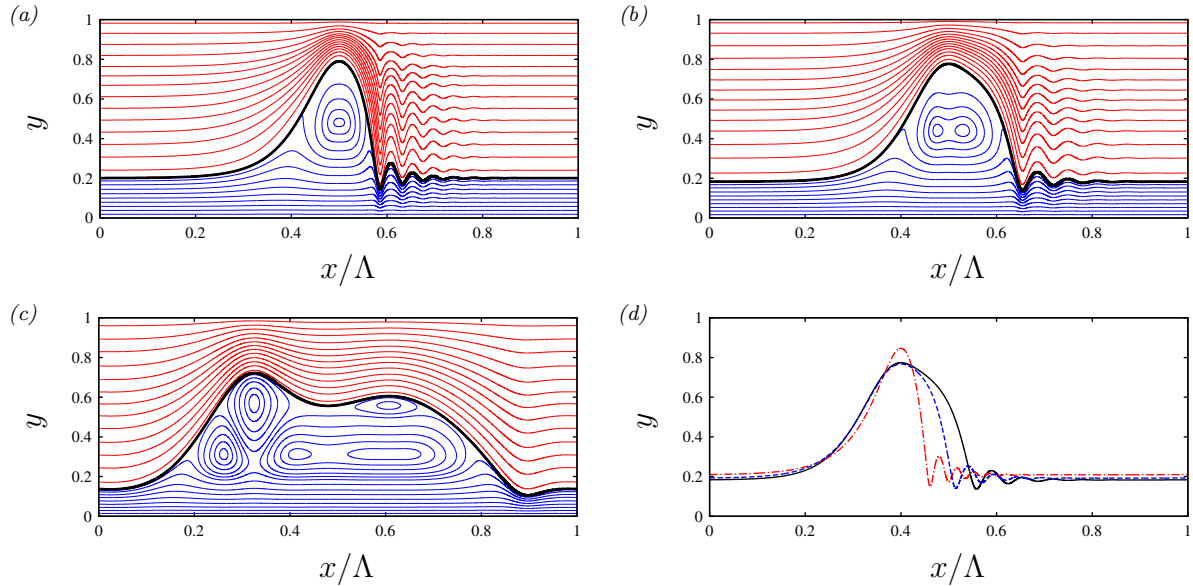


Figure 6.5: Stable and unstable TWS from panel 6.4d:  $H^*=1$  mm,  $f^*=16$  Hz. (a)  $\text{Re}_2=-1$ : stable TWS; (b)  $\text{Re}_2=-16$ : TWS subject to oscillatory instability (panel 6.6a); (c)  $\text{Re}_2=-80$ : TWS subject to catastrophic instability (figure 6.8); (d) Solution from panel *b* in different limits. Solid black line: full WRIBL model (1.27); dot-dashed red:  $\Pi_\rho=0$  in (1.6a); dashed blue:  $\Pi_\mu=0$  in (1.6b) and (1.6a).

wave celerity (panel 6.4c) under the effect of the increasingly strong counter-current gas flow. We have demonstrated in section 5.1 that slower solitary waves carry less precursory ripples.

The dashed and dot-dashed TWS curves in panels 6.4a and 6.4c pertain to the limits  $\Pi_\rho=0$  and  $\Pi_\mu=0$  in the inter-phase coupling conditions (1.6a) and (1.6b). These curves show that the nonlinear amplification and deceleration of TWS is caused by the gas pressure (deactivated via  $\Pi_\rho=0$ ) and not by the interfacial gaseous viscous stresses (deactivated via  $\Pi_\mu=0$ ). Moreover, the linear absolute instability (AI) threshold is suppressed in the  $\Pi_\rho=0$  limit.

For the narrower channel,  $H^*=1$  mm (panel 6.4d), an inversion of the  $h_{\max}$  versus  $\text{Re}_2$  trend (from wave amplification to wave damping) occurs for all wave types, well before reaching the AI limit. For the  $f^*=16$  Hz solitary waves (red curve with open circle),  $h_{\max}$  is damped almost as soon as  $\text{Re}_2<0$ . Based on this, it seems that the flooding risk can be reduced by increasing the counter-current gas flow rate. However, TWS can become prone to potentially dangerous secondary instabilities.

We demonstrate this based on the three TWS in panels 6.5a, 6.5b, and 6.5c, which lie on the red curve with circles ( $f^*=16$  Hz) in panel 6.4d, at the  $\text{Re}_2$  values marked by red arrows there. The first TWS (panel 6.5a) lies on the periodically-stable solution branch in panel 6.4d (to the right of the cross). In that case, the TWS remains unaltered in a

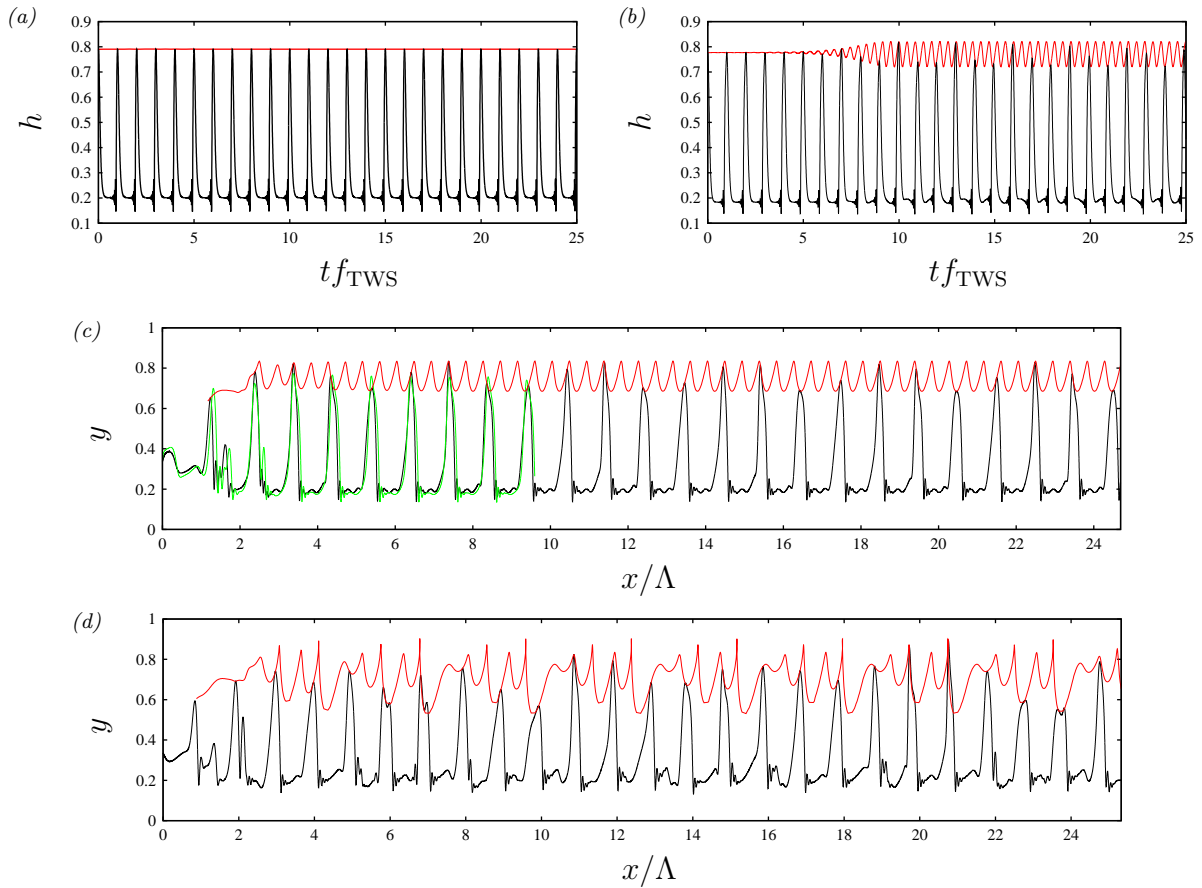


Figure 6.6: Oscillatory instability of TWS from panel 6.4d:  $H^*=1$  mm,  $\text{Re}_1=15$ ,  $f_{\text{TWS}}^*=16$  Hz. (a,b) Transient periodic computations started from TWS at  $\text{Re}_2=-1$  (stable) and  $\text{Re}_2=-16$  (oscillatory instability). Black lines: time traces of local film thickness; red lines: time traces of wave height; (c,d) open-domain computations with coherent inlet forcing at  $f=f_{\text{TWS}}$ , for  $\text{Re}_2=-19$  (panel c) and  $\text{Re}_2=-25$  (panel d). Black lines: snapshots of the film profile; red lines: paths of the wave maxima as the oscillating wave humps move through the domain; green line: DNS with **Gerris** on a shorter domain.

transient periodic computation<sup>6</sup> (panel 6.6a).

Conversely, the TWS at  $\text{Re}_2=-16$  (panel 6.5b) lies on the solution branch associated with an oscillatory secondary instability (OI), i.e. between the cross and asterisk in panel 6.4d. In a periodic transient computation (panel 6.6b), this instability produces a regular temporal modulation of the wave height  $h_{\text{max}}$ , which translates into a spatial modulation in an open-domain computation with coherent inlet forcing (2.38) at the TWS frequency  $f=f_{\text{TWS}}$  (panel 6.6c). Our WRIBL model captures this oscillation in good agreement with our own DNS using **Gerris** (green line in panel 6.6c). In panel 6.6c, the wave height modulation contains a single Fourier mode with a frequency about three times greater

<sup>6</sup>Performed with the periodic code introduced in §2.2.2, which allows using a TWS as initial condition.

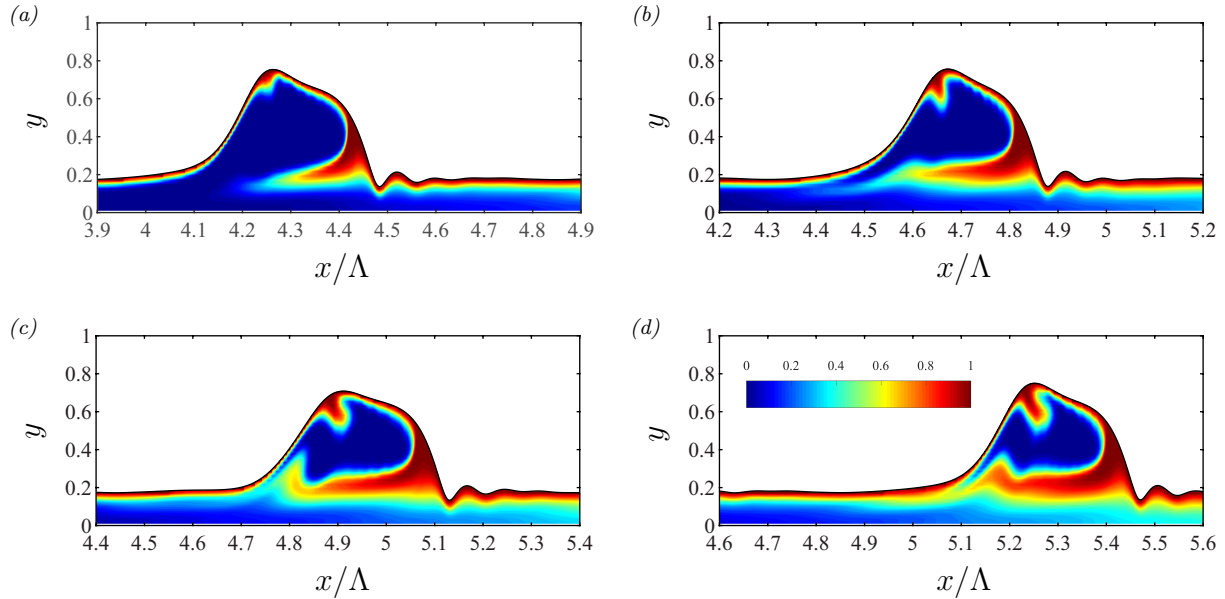


Figure 6.7: Enhanced mixing due to the oscillatory instability from panel 6.6c. DNS with **Gerris**:  $\phi=90^\circ$ ,  $H^*=1$  mm,  $\text{Re}_1^{\text{TWS}}=15$ ,  $\text{Re}_2^{\text{TWS}}=-19$ ,  $f^*=16$  Hz,  $\text{Pe}=4590$ . Contour maps of the passive scalar  $\theta$  (4.1j). (a)  $tf=62.3$ ; (b)  $tf=62.7$ ; (c)  $tf=63.0$ ; (d)  $tf=63.3$ .

than  $f_{\text{TWS}}$ . Upon increasing the counter-current gas flow rate, this mode is enriched by additional modes, but remains periodic (panel 6.6d).

The cause of the oscillatory instability seems to be the pressure coupling between the gas flow and the liquid film, and not the viscous coupling. This is supported by panel 6.5d, which compares the TWS from panel 6.5b with the limits  $\Pi_\rho=0$  (dot-dashed red line) and  $\Pi_\mu=0$  (dashed blue line), which deactivate the gas pressure ( $\Pi_\rho=0$ ) and gaseous viscous stresses ( $\Pi_\mu=0$ ) in the inter-phase coupling conditions (1.6a) and (1.6b). In particular, we see that the wave amplitude in panel 6.5d is unaffected by the gaseous viscous stresses.

The wave crest modulation caused by the oscillatory instability (panel 6.6c) periodically rearranges the flow field within the wave-fixed reference frame, which is characterized by several vortices in the wave hump (panel 6.5b). Such vortices are known to intensify inter-phase scalar transfer (Yoshimura *et al.*, 1996). However, as we will show in section 6.3, this wave-induced intensification mechanism saturates after a certain travelling distance. A way to re-initiate it is to perturb the wave humps through wall corrugations (panel 6.1b). The observed oscillatory instability represents an alternative way to achieve this, requiring minimal energy input and no costly constructive measures. Moreover, the gas flow rate provides a convenient control parameter to tune the oscillations. Figure 6.7, which represents results of our DNS from panel 6.6c, where we have additionally solved for the transport of a passive scalar  $\theta$  (4.1j), demonstrates that the oscillatory instability enhances mixing within the wave hump. In particular, the scalar plume originating at the wave front is prevented from destroying the scalar free-surface layer at the wave back, as



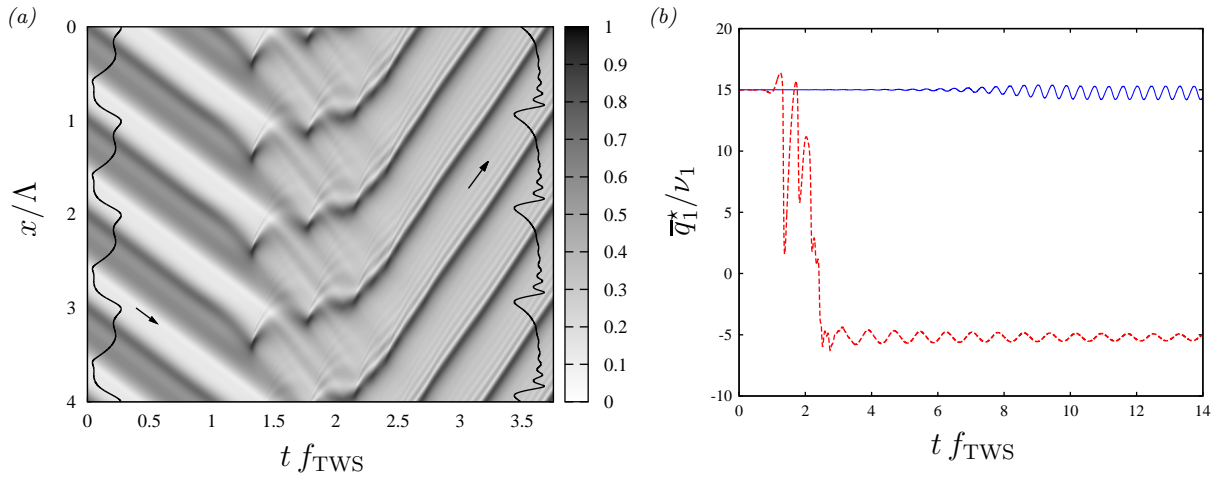


Figure 6.8: Wave reversal and liquid arrest due to catastrophic instability of TWS in panel 6.5c:  $\text{Re}_1^{\text{TWS}}=15$ ,  $f_{\text{TWS}}^*=16$  Hz,  $\text{Re}_2^{\text{TWS}}=-80$ ; (a) spatio-temporal map of film height  $h$ . Waves initially propagate downward (left profile), but are rearranged into an upward travelling train (right profile) under the effect of the counter-current gas flow; (b) time traces of normalized wave-averaged liquid flow rate  $\bar{q}_1^*/\nu_1$  (6.7). Dashed red:  $\text{Re}_2^{\text{TWS}}=-80$ ; solid blue:  $\text{Re}_2^{\text{TWS}}=-16$  (oscillatory instability from panel 6.6b).

the result of a folding mechanism that is repeated at each wave hump oscillation<sup>7</sup>.

When the counter-current gas flow rate is increased further (left of asterisk in panel 6.4d), TWS become unstable to a catastrophic secondary instability. This is the case for the TWS in panel 6.5c. As evidenced by the transient periodic computation in figure 6.8, the catastrophic instability produces a wave reversal, upon which an upward-travelling train of surface waves is established (panel 6.8a). Moreover, the normalized wave-averaged liquid flow rate  $\bar{q}_1^*/\nu_1$ , where  $\bar{q}_1^*$  is defined as:

$$\bar{q}_1^* = \frac{1}{\Lambda^*} \int_0^{\Lambda^*} q_1^* dx^*, \quad (6.7)$$

becomes negative at that time (panel 6.8b), indicating a liquid arrest, which is one of the features often associated with flooding. In a spatially-evolving film, an upward-travelling wave carrying liquid upstream will eventually collide with the inlet condition and cause a breakdown of the flow<sup>8</sup>. By contrast, in the case of the oscillatory instability (blue line in panel 6.8b),  $\bar{q}_1^*$  is modulated only slightly and remains close to the (positive) TWS value  $\bar{q}_1^*/\nu_1 = \text{Re}_1^{\text{TWS}} = 15$ .

For the larger channel,  $H^*=1.5$  mm (panel 6.4a), TWS also become periodically unstable beyond a certain  $\text{Re}_2$ . However, this threshold ( $\text{Re}_2 \approx -240$ ) lies outside the parameter range where our WRIBL model yields quantitative predictions (see §2.3.1).

<sup>7</sup>See also second supplementary movie in Lavallo *et al.* (2020).

<sup>8</sup>See first supplementary movie in Lavallo *et al.* (2020).

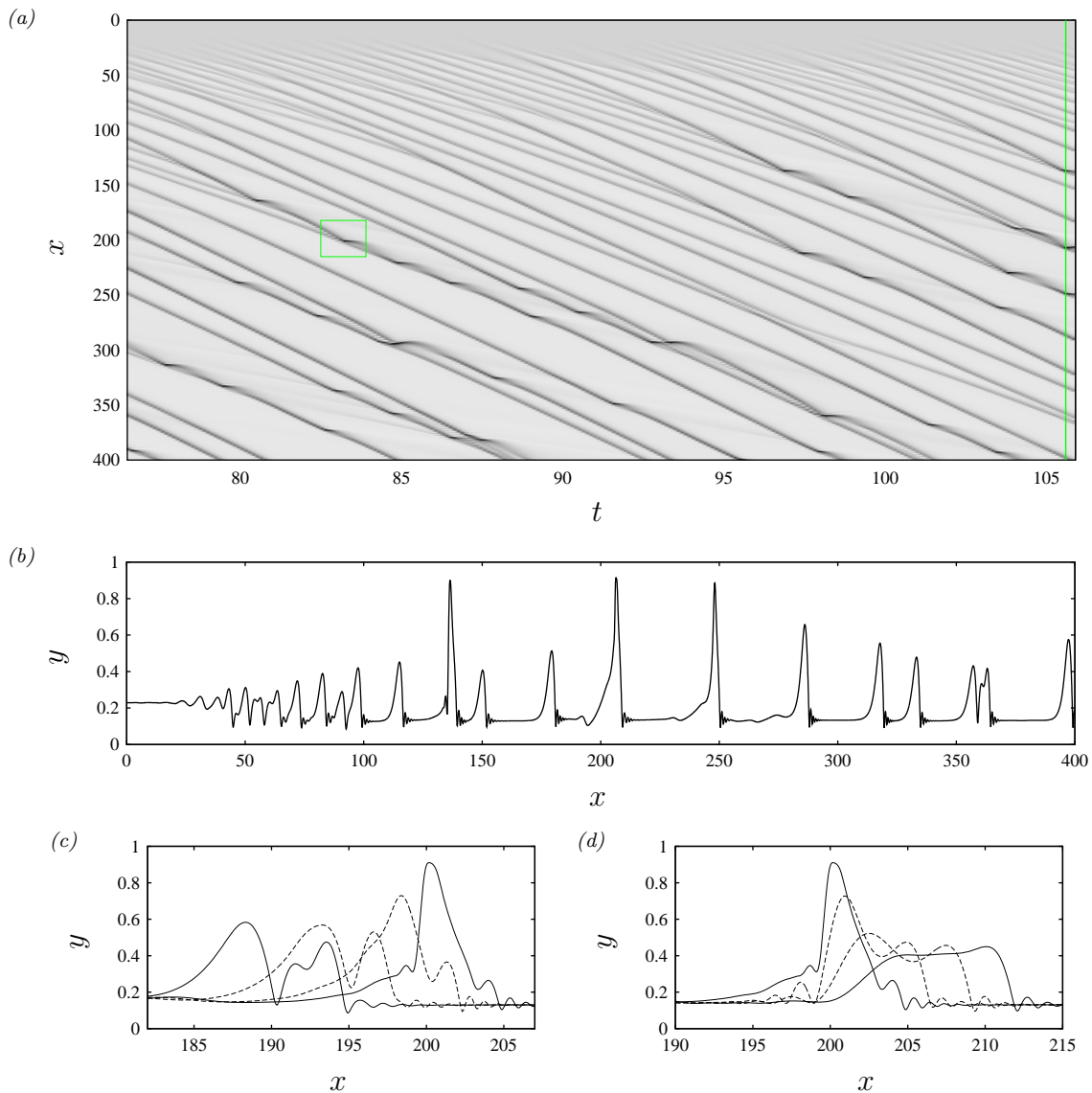


Figure 6.9: Intermittent flooding due to noise-driven wave coalescence and wave destruction in a gas-sheared vertically-falling liquid film:  $Ka=509.5$ ,  $H^*=1.5$  mm,  $Re_1=15$ ,  $Re_2=-100$ . Open-domain computation applying noisy inlet perturbation (2.38) with  $f_c=3.6$ ,  $\epsilon_1=0$ , and  $\epsilon_2=0.0002$ . (a) Space-time plot of the film height  $h$  (grey scales from 0 to 1), showing wave coalescence. Rectangle and vertical line highlight ranges of panels b, c, and d combined; (b) snapshot of the full wave profile:  $t=105.6$ ; (c) wave coalescence event forming an obstructing wave ( $t=82.5, 82.8, 83.1, 83.2$ ); (d) destruction of the obstructing wave by the counter-current gas flow ( $t=83.2, 83.5, 83.7, 83.9$ ).

Nonetheless, in the case of the most-amplified waves ( $f=f_{\max}$ ), TWS are also susceptible to the subharmonic secondary instability (panel 5.1a) observed in unconfined films (Liu & Gollub (1993)), and this can trigger a different type of flooding scenario at much

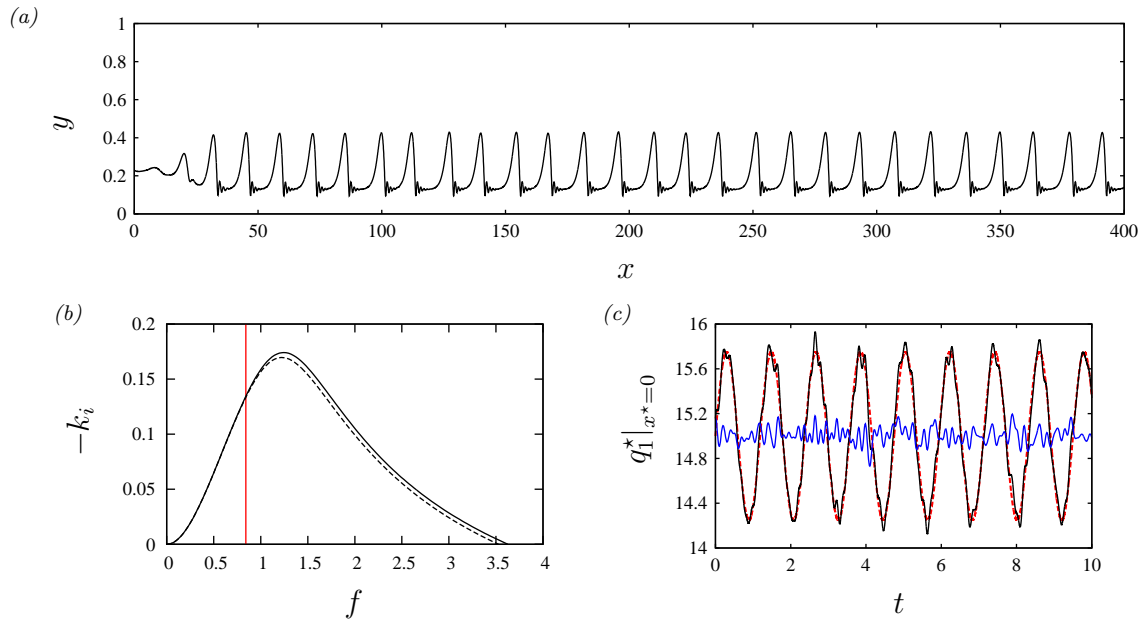


Figure 6.10: Flooding suppression through coherent inlet forcing. Parameters as in figure 6.9. (a) Open-domain computation based on panel 6.9b with additional coherent inlet forcing (2.38):  $f^*=16$  Hz,  $\epsilon_1=0.05$ ,  $f_c=3.6$ ,  $\epsilon_2=0.0002$ ; (b) linear spatial growth rate from OS (dashed) and WRIBL (solid) calculations. Red vertical line marks forcing frequency  $f$ ; (c) time traces of normalized liquid inlet flow rate  $q_1^*|_{x^*=0}/\nu_1$ . Black solid: actual perturbation (2.38); red dashed: zero noise ( $\epsilon_2=0$ ); blue solid: pure noise ( $\epsilon_1=0$ ).

lower  $|\text{Re}_2|$  (where TWS are periodically stable).

We demonstrate this in figure 6.9 via an open-domain computation based on the parameters in panel 6.4a for  $f^*=f_{\max}$  and  $\text{Re}_2=-100$ , where we have applied a noisy inlet perturbation (2.38), with  $\epsilon_1=0$ ,  $\epsilon_2=0.0002$ , and  $f_c=3.6$  (panel 6.10b). As a result of this noisy forcing, the linearly most-amplified waves ( $f=f_{\max}$ ) emerge near the liquid inlet (panels 6.9a and 6.9b). Subsequently, the subharmonic instability leads to wave coalescence events further downstream (panel 6.9c), which produce waves of much larger amplitude that locally obstruct the channel. These obstructing waves cannot resist the counter-current gas flow and are subsequently destroyed (pane 6.9d), only to re-emerge due to renewed coalescence. This sequence is repeated many times, as evidenced by the oscillations in the spatio-temporal diagram (panel 6.9a).

The *intermittent flooding* observed in figure 6.9 can be suppressed by forcing solitary waves through coherent inlet forcing. Solitary waves are not prone to the subharmonic instability, which requires direct wave interactions<sup>9</sup>. We demonstrate this based on the open-domain computation in panel 6.10a, where we have used the same settings as in panel

<sup>9</sup>Although, we will see in section 6.2.2 that the gas flow can convey long-range interactions even between solitary waves, which can lead to a different kind of secondary instability of periodically-stable TWS.

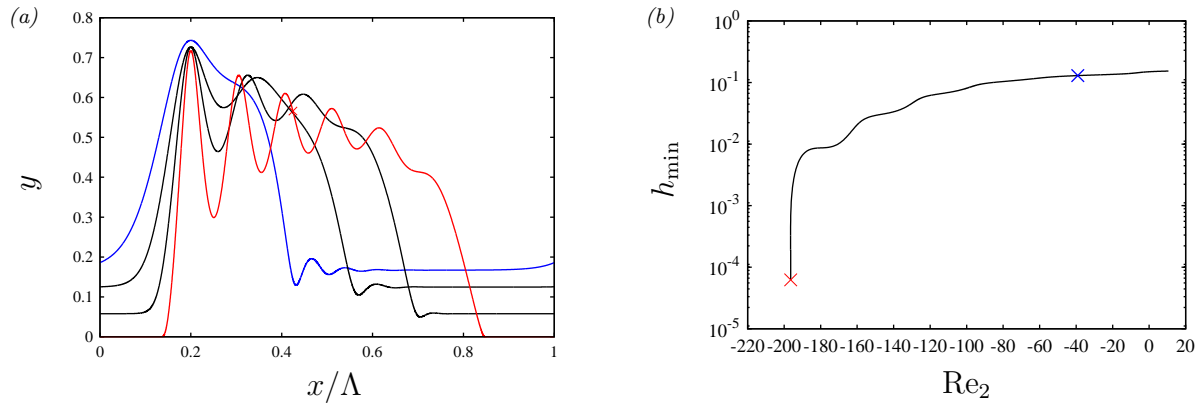


Figure 6.11: Extreme film thinning caused by a counter-current gas flow. TWS from panel 6.4d at fixed liquid volume  $V_1$  and wavelength  $\Lambda$ :  $\phi=90^\circ$ ,  $H^*=1$  mm,  $Ka=509.5$ ,  $\Lambda=46.8H$ ,  $V_1=0.31\Lambda H$ . (a) Wave profiles under an increasingly strong counter-current gas flow. From top to bottom:  $Re_2=-39.2, -78.6, -128.2,$  and  $-196.4$ ; (b) minimal film height  $h_{\min}$ . Red and blue crosses correspond to first and last profiles in panel a.

6.9b, and added a coherent inlet forcing with  $f^*=16$  Hz  $< f_{\max}^*$  (panel 6.10b) and  $\epsilon_1=0.05$  to the inlet noise  $\epsilon_2=0.0002$ . Panel 6.10c represents the time-trace of the normalized noisy liquid inlet flow rate  $q_1^*|_{x=0}/\nu_1$  resulting from this forcing. We conclude from panel 6.10a that the additional coherent inlet forcing leads to a very regular train of waves that stay well clear of obstructing the channel.

Our computations in panels 6.6, 6.8, and 6.9 were performed at fixed total flow rate  $q_{\text{tot}}$ , but the observed instabilities persist also for an imposed gas pressure drop  $\Delta p_2$  (1.34). For example, the open-domain computation in figure 23 of Dietze & Ruyer-Quil (2013), displaying the same sequence of events as figure 6.9, was performed at fixed  $M=34.4$  (1.35).

Another feature that can be associated with flooding in narrow channels is the formation of dry patches within the wavy falling liquid film under the effect of a counter-current gas flow<sup>10</sup>. Figure 6.11 demonstrates, for parameters corresponding to panel 6.4d, that the residual film of TWS at fixed wavelength  $\Lambda$  and liquid hold-up  $V_1/\Lambda/H$  can thin extremely under the effect of a counter-current gas flow (panel 6.11a). In fact, the minimal film thickness  $h_{\min}$  diverges with increasingly negative  $Re_2$ , suggesting that spinodal dewetting (Bonn, 2009) may well be achieved in an experiment<sup>11</sup>. A situation of fixed hold-up may be encountered when the gas flow is suddenly increased or in the case of very viscous fluids, such as mucus films in pulmonary airways (section 7.2).

At low values of  $|Re_2|$ , neither the amplitude nor the celerity of TWS in panel 6.4a is meaningfully affected by the gas flow, especially for the weaker confinement,  $H^*=1.5$  mm. However, surface waves can significantly affect the flow field in the gas, in particular

<sup>10</sup>Personal communication from Sophie Mergui on her experiments in inclined channels.

<sup>11</sup>See Oron (2003) and Oron (2000) on how to account for long-range van der Waals forces in long-wave models of thin liquid films.

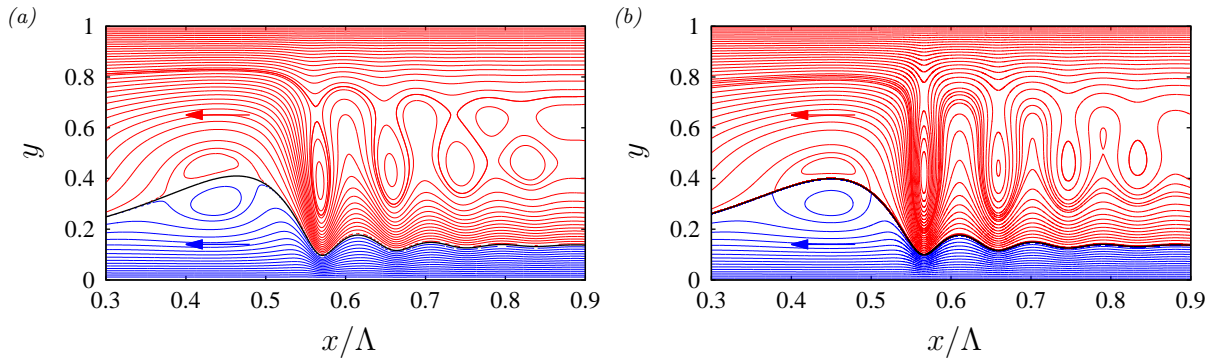


Figure 6.12: Wave-induced vortical structures in the gas. Vertically-falling liquid film in contact with a weak co-current gas flow:  $Ka=509.5$ ,  $H^*=1.5$  mm,  $Re_1=15$ ,  $Re_2=19$ ,  $f^*=16$  Hz. Streamlines in the wave-fixed reference frame. Numerical computations with periodic boundary conditions. (a) temporally converged solution of transient DNS with Gerris:  $\bar{h}=0.199$ ,  $M=-0.84$ ; (b) TWS from WRIBL model (1.27):  $\bar{h}=0.198$ ,  $M=-0.75$ .

in the wave-fixed reference frame. This is shown in figure 6.12 for the  $f^*=16$  Hz solitary TWS from panel 6.4a under a weak co-current gas flow at  $Re_2=19$ . We see a twin gas vortex that is connected to the moving-frame liquid vortex in the wave hump. Several other gas vortices are observed in the region of the precursory capillary ripples, and these force the gas flow to meander through the channel. The Prandtl and Schmidt numbers are usually quite small in gases, and thus the vortical structures in figure 6.12 will not meaningfully affect scalar transport there, which is diffusion limited. However, they may affect the distribution of small non-Brownian particles, such as bacteria or viruses.

**Impact of the work and relation to the current state of the art** Our papers Dietze & Ruyer-Quil (2013) and Lavalle *et al.* (2020) have been cited 45 and 4 times, respectively, according to *Web of Science*.

Most of these citations refer to Dietze & Ruyer-Quil (2013) as a seminal work on strongly-confined two-phase film flows:

Vellingiri *et al.* (2015); Markides *et al.* (2016); Schmidt *et al.* (2016); Saleh & Ormiston (2017); Pasquier *et al.* (2017); Miao *et al.* (2017); Dandekar *et al.* (2018); Lavalle *et al.* (2015, 2017, 2018); Denner *et al.* (2018); Mendez *et al.* (2019); Tsvlodub & Bocharov (2017, 2018, 2020); Tsvlodub *et al.* (2021); Samanta (2013, 2020); Feldmann *et al.* (2020); Pillai *et al.* (2021); Mohamed *et al.* (2021); Vakilipour *et al.* (2021).

Some of the nonlinear phenomena reported in the current section were confirmed experimentally by Kofman *et al.* (2017), albeit for much weaker confinement levels. Firstly, the one-by-one suppression of precursory capillary ripples caused by a counter-current gas flow of increasing flow rate (panel 6.4b), as well as the role of the wave speed in this phenomenon (panel 6.4c). And, secondly, the destruction of large-amplitude waves in the face of a strong counter-current gas flow (panel 6.9d).

Vakilipour *et al.* (2021) have confirmed the vortex street reported in figure 6.12 with their own DNS, using a new code based on the Arbitrary Lagrangian-Eulerian (ALE) method for interface tracking.

As we have considered very strong confinement levels here, experiments are quite difficult and require microfluidic set-ups. Nonetheless, experimental studies have shown that falling liquid films can be realized at such small scales (Zhang *et al.*, 2009). Enhancing mixing in low Reynolds number flows is a long-standing challenge. In flexible micro-channels, it has been shown that soft-wall turbulence, which sets in at much lower values of  $Re_1$  than hard-wall turbulence, can be a solution (Kumaran, 2021). The wave modulations produced by the oscillatory instability reported in panel 6.6c, should they be confirmed experimentally, may be an alternative means to achieve this.

### 6.2.2 Inclined falling liquid films

We now consider weakly-inclined falling liquid films subject to a strongly-confined counter-current gas flow. Figure 6.13 confronts the linear and nonlinear responses of such a wavy liquid film for parameters corresponding to figure 6.4, only that the film is now inclined ( $\phi=10^\circ$ ) and that the channel height is now varied in the range  $1.22 \text{ mm} \leq H^* \leq 2.35 \text{ mm}$ . Panels 6.13a and 6.13c pertain to the linearly most-amplified waves and panels 6.13b and 6.13d pertain to low-frequency solitary waves at fixed wave number  $k_r^* = \frac{2}{9} \tilde{k}_r^* = 46.68 \text{ m}^{-1}$ , where  $\tilde{k}_r$  denotes the most-amplified wave number for a passive atmosphere ( $\Pi_\mu = \Pi_\rho = 0$ ). Panels 6.13a and 6.13b represent the linear spatial growth rates and panels 6.13c and 6.13d represent the normalized maximum and minimum film heights of nonlinear TWS.

For the two strongest confinements,  $H^* = 1.22 \text{ mm}$  (open squares) and  $H^* = 1.69 \text{ mm}$  (pentagons), the counter-current gas flow stabilizes the wavy liquid film, both in terms of the linear growth rate, which reaches zero when the Kapitza instability is fully suppressed (S), and the amplitude of nonlinear waves. These regimes can be considered safe in terms of flooding. In the case of low-frequency solitary waves (panel 6.4d), TWS exhibit a peculiar shape with an elongated flat wave hump (panel 6.14b). These solutions resist periodic secondary instabilities, which are associated with dot-dashed line segments in panels 6.13c and 6.13d. The flattening of the wave hump is caused by the gas pressure and not gaseous viscous stresses, as shown in panel 6.14d, where TWS in the limits  $\Pi_\rho = 0$  (dot-dot-dashed) and  $\Pi_\mu = 0$  (dashed) are compared to the full solution (solid).

For intermediate confinements,  $H^* = 1.78 \text{ mm}$  (crosses) and  $H^* = 1.88 \text{ mm}$  (asterisks), the linear growth rates in panels 6.13a and 6.13b vary non-monotonically, first decreasing and then increasing with increasing gas velocity magnitude, until the AI limit is reached. By contrast, nonlinear TWS of the most amplified frequency (panel 6.13c) exhibit the opposite trend, and thus linear predictions can be misleading. These TWS undergo a period-halving bifurcation (PH) as  $|Re_2|$  is increased, after which they are fully suppressed by a nonlinear mechanism, i.e. when the  $h_{\min}$  and  $h_{\max}$  branches meet. The PH bifurcations are associated with the redistribution of liquid between main wave humps and capillary ripples (panel 6.14a). The nonlinear suppression of waves in panel 6.4c, which also occurs for the stronger confinements, occurs well before the linear AI and S

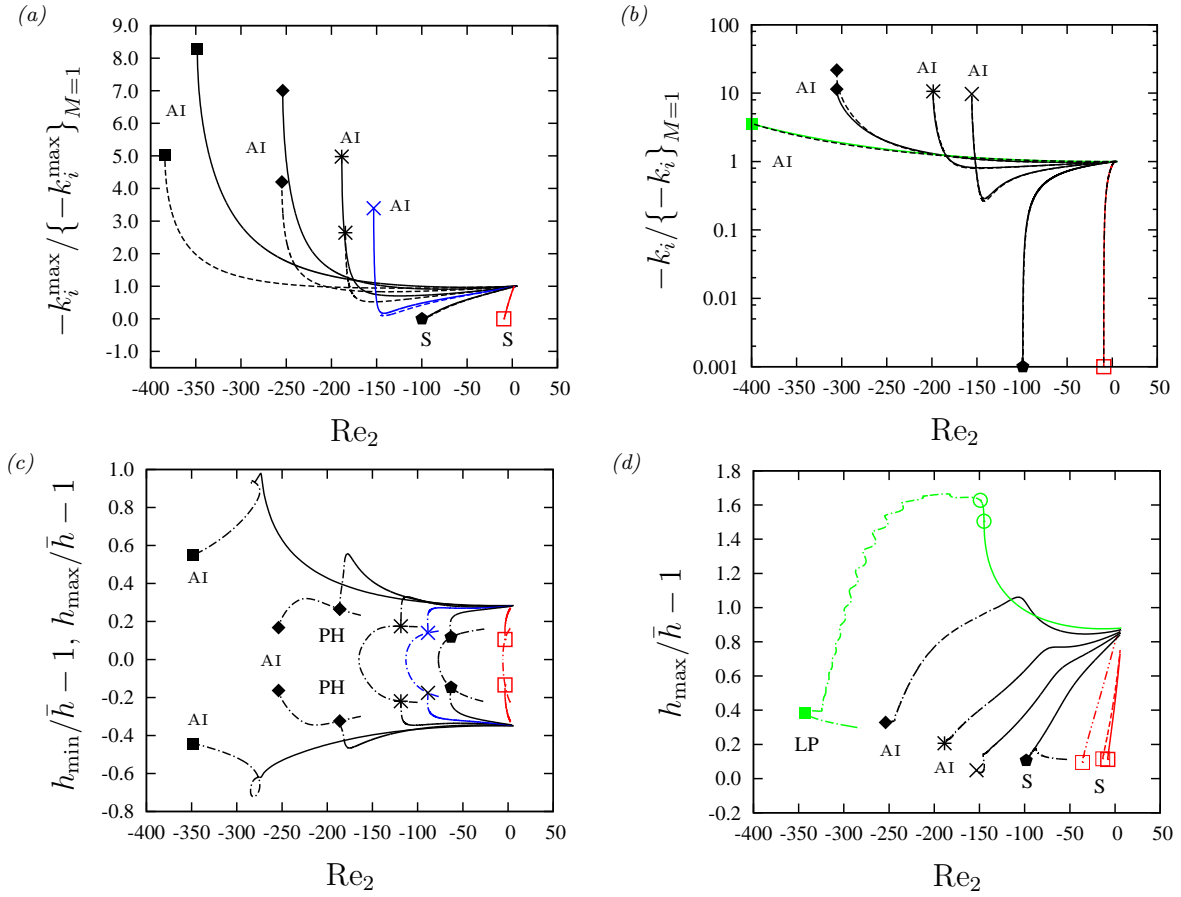


Figure 6.13: Linear (panels *a*, *b*) versus nonlinear (panels *c*, *d*) dynamics of an inclined falling liquid film subject to a strongly confined counter-current gas flow:  $Ka=509.5$  (DMSO-water and air II in table 2.1),  $\phi=10^\circ$ ,  $Re_1=15$ . Open squares:  $H^*=1.22$  mm, pentagons:  $H^*=1.69$  mm, crosses:  $H^*=1.78$  mm, asterisks:  $H^*=1.88$  mm, diamonds:  $H^*=2.07$  mm, filled squares:  $H^*=2.35$  mm. Dashed: OS, solid: WRIBL. (a) Maximum spatial growth rate; (b) spatial growth rate at fixed wave number:  $k_r^*=46.68$   $m^{-1}$ ; (c) TWS corresponding to panel *a*; (d) TWS corresponding to panel *b*. Dot-dot-dashed:  $\Pi_\rho=0$  in (1.6a), dashed:  $\Pi_\mu=0$  in (1.6a) and (1.6b). Dot-dashed segments in panels *c* and *d* correspond to periodically unstable TWS, and “PH”, “AI”, and “S” denote period-halving bifurcations, absolute instability, and full stabilization.

limits in panel 6.13a. By contrast, solitary TWS (panel 6.13d) at strong and intermediate confinements are bounded by the linear AI and S limits in panel 6.13b and follow a monotonous stabilizing trend.

For the weakest confinements,  $H^*=2.07$  mm (diamonds) and  $H^*=2.35$  mm (filled squares), the linear growth rates in panels 6.13a and 6.13b increase monotonously with  $|Re_2|$ , whereas the nonlinear wave amplitudes in panels 6.4c and 6.4d first increase and then decrease. Except for the solitary waves at  $H^*=2.07$  mm, TWS are bounded by the

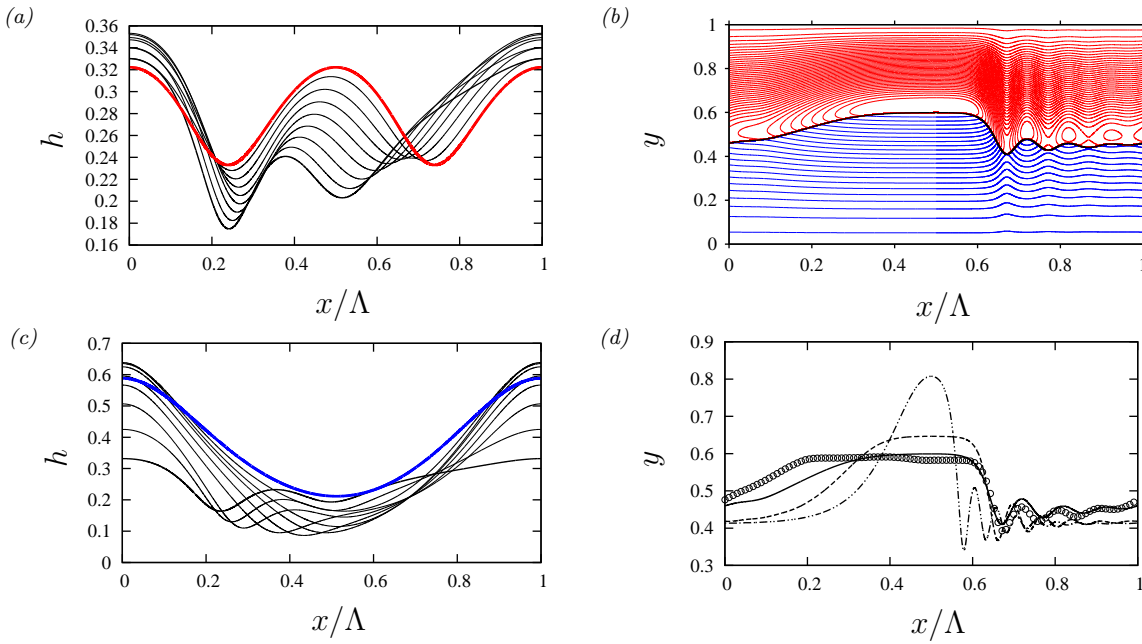


Figure 6.14: TWS from figure 6.13. (a) Approaching one of the PH bifurcations in panel 6.13c:  $H^*=1.78$  mm. Thick:  $Re_2=-37$ , blue:  $Re_2=-88$ ; (b) flat-top solitary wave from panel 6.13d:  $H^*=1.22$  mm,  $Re_2=-7$ . Streamlines in the wall-fixed reference frame; (c) suppression of capillary ripples in linearly most-amplified TWS from panel 6.13c:  $H^*=2.35$  mm. Thick:  $Re_2=-79$ , blue:  $Re_2=-348$ ; (d) TWS from panel b in different limits. Solid: full WRIBL model (1.27), dot-dot-dashed:  $\Pi_\rho=0$  in (1.6a), dashed:  $\Pi_\mu=0$  in (1.6a) and (1.6b); symbols: DNS using *Basilisk*.

AI limits in panels 6.4a and 6.4b. However, TWS become unstable w.r.t. secondary instabilities (dot-dashed line segments) before that, i.e. roughly at the point of maximum wave amplitude. For the most-amplified waves, this point is associated with the suppression of capillary ripples under the effect of the gas (panel 6.14c), similar to what was observed in panel 6.4b.

In contrast to the vertical configuration (figure 6.8), the periodic secondary instability modes corresponding to the dot-dashed line segments in panel 6.13c are not directly associated with catastrophic events. Nonetheless, they are similar to the subharmonic instability observed for liquid films falling in a quiescent atmosphere (Liu & Gollub, 1993), which leads to coalesce events that may trigger flooding in very long channels (figure 6.9). However, we have not observed such flooding events in our open-domain computations<sup>12</sup>.

By contrast, for the solitary TWS at  $H^*=2.35$  mm in panel 6.13d (filled square), we have identified two novel secondary instability modes that strongly alter the configuration of wave trains in a spatially-evolving falling liquid film. These instabilities are discussed based on panels 6.15a and 6.15c, which represent open-domain computations correspond-

<sup>12</sup>See supplementary movie 1 in Lavallo *et al.* (2021).



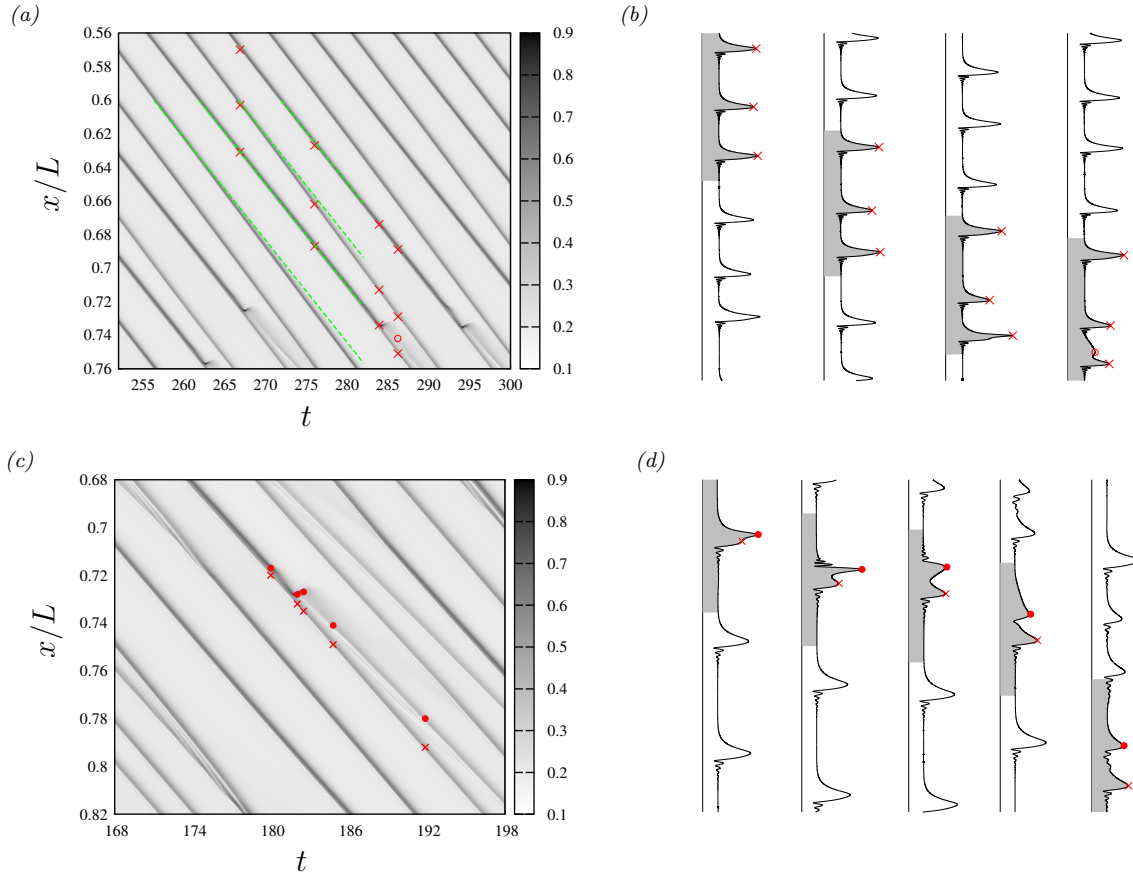


Figure 6.15: Slip streaming (panels *a, b*) and wave splitting (panels *c, d*) in solitary wave trains. WRIBL computations on an open domain of length  $L=31.4 \Lambda_{\text{TWS}}$  using coherent inlet forcing (2.38), with  $f=f_{\text{TWS}}$ ,  $\epsilon_1=0.3$ , and  $\epsilon_2=0$ . Parameters based on TWS in panel 6.13d:  $H^*=2.35$  mm. Space-time plots of film height  $h$  (panels *a, c*), and wave profile snapshots (panels *b, d*). Green dashed lines: TWS celerity. (*a, b*)  $\text{Re}_g=-145$ ,  $f_{\text{TWS}}=0.20$ ; (*c, d*)  $\text{Re}_g=-149$ ,  $f_{\text{TWS}}=0.19$ . Red symbols: primary/secondary wave maxima.

ing to the open circles in panel 6.13d. In these computations, we have applied coherent inlet forcing at the TWS frequency  $f=f_{\text{TWS}}$ .

The first instability mode occurs at a lower  $|\text{Re}_2|$ , where the TWS is periodically stable (lower open circle in panel 6.13d). Thus, this instability mode requires wave interactions. Such interactions occur in the form of individual wave humps that slipstream toward their leading neighbours while their amplitude decreases (panels 6.15a and 6.15b). This dynamics is very different from the interactions of solitary waves observed in unconfined falling liquid films (Chang *et al.*, 1996c; Pradas *et al.*, 2013), where larger-amplitude waves usually approach smaller-amplitude waves travelling in front. If the leading large-amplitude wave within the grey region of panel 6.15b would not collapse under the effect of increased exposure to the gas (thus preventing coalescence), the slip-streaming instability found here could be viewed as an inverted form of the coarsening dynamics (Chang *et al.*,

1996c) discussed w.r.t. panel 5.1a.

The second instability mode (panels 6.15c and 6.15d) is intrinsic, i.e. the corresponding TWS is periodically unstable (upper open circle in panel 6.13d). This instability is characterized by wave splitting events that refine the wavy film surface into a train of shorter, smaller-amplitude waves (panel 6.15d). In that case, the flooding risk is reduced.

**Impact of the work and relation to the current state of the art** Our paper Lavalle *et al.* (2021) was published only recently and has not been cited. Nonetheless, recent experiments of Sophie Mergui have confirmed the slipstreaming phenomenon observed in panel 6.15a, albeit for much weaker confinement ( $H^*=13$  mm). The slipstreaming phenomenon, which tends to coarsen the waviness of the film, and the wave destruction phenomenon (panel 6.15d), which tends to refine the waviness, imply that the gas flow rate may represent an effective parameter for controlling the ultimate waviness of the film. This property, which results from a cascade of instabilities.

Our computations have also shown that extreme confinement levels are not necessarily dangerous in terms of flooding. We have identified several safe wavy regimes (panels 6.14b and 6.15d), allowing to exploit the transfer intensification provided by surface waves while avoiding flooding. Such regimes are very sensitive to the confinement level (panel 6.13) and thus our computations may help to identify optimal conditions for experimentalists.

### 6.3 Scalar transfer and wall corrugations

We investigate the effect of wall corrugations on inter-phase scalar transfer between a wavy vertically-falling liquid film and a strongly-confined counter-current gas flow (Dietze, 2019). Results are based on DNS with **Gerris** according to the set-up represented in figure 4.1, where we have fixed  $H^*=1.5$  mm. We focus on the fluid combination used in section 6.2, DMSO-water and air II in table 2.1. We fix the liquid Reynolds number at  $Re_1=15$  and concentrate on convection-dominated scalar transport, considering two values for the liquid Péclet number  $Pe=RePr=\mathcal{U}_1\mathcal{L}/\alpha_1$ :  $Pe=4590$ , representative of mass transport, and  $Pe=459$ , based on the thermal diffusivity of the liquid.

We distinguish three types of wall geometries: a flat wall for reference (6.8), a sinusoidal corrugation (6.9) typically found in structured packings (Fair & Bravo, 1990; Trifonov, 2007a), and isolated semicircular bumps (6.10), which are the two-dimensional analogue of the hemispherical corrugations studied in Veremieiev *et al.* (2015). The three corrugations are defined through the profile function  $f(x)$  (see figure 4.1):

$$f(x) = 0, \tag{6.8}$$

$$f(x) = -\hat{h}_C \cos(2\pi x/\Lambda_C), \tag{6.9}$$

$$f(x) = \begin{cases} [R_C^2 - (x - x_m)^2]^{1/2} & \forall x \in [x_m - R_C, x_m + R_C] \\ 0 & \forall x \notin [x_m - R_C, x_m + R_C] \end{cases}, \tag{6.10}$$

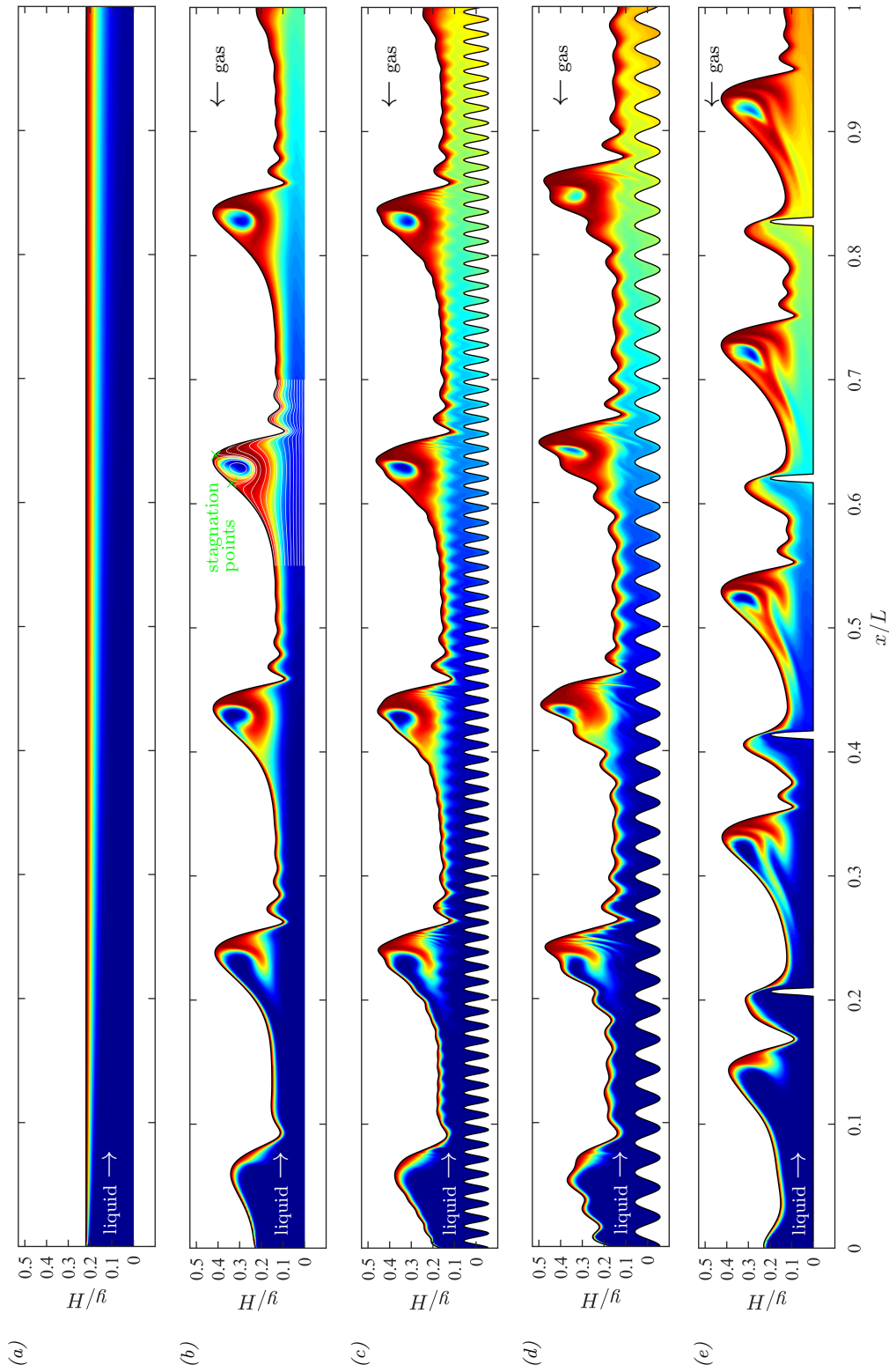


Figure 6.16: Convection-dominated scalar transport in a falling liquid film on a vertical (corrugated) wall in contact with a strongly confined counter-current air flow:  $H^*=1.5$  mm,  $\text{Ka}=509.5$ ,  $\text{Re}_1=15$ ,  $\text{Re}_2=-57$ ,  $\text{Pe}=4590$ . Periodically-forced waves (4.10):  $f^*=16$  Hz. Contours of normalized scalar  $\theta$  (4.1j) ranging from 0 (blue) to 1 (red). (a) Flat-film with  $\Pi_\mu=\Pi_\rho=0$ ; (b) flat-wall reference case. White streamlines are plotted in the moving reference frame; (c,d) sinusoidal corrugations (6.9) with  $\Lambda_C^*=1.2$ ,  $2.4$  mm and  $\hat{h}_C^*=87.5$   $\mu\text{m}$ ; (e) semicircular bumps (6.10) with  $R_C^*=0.3$  mm and  $\Lambda_C^*=20.8$  mm.

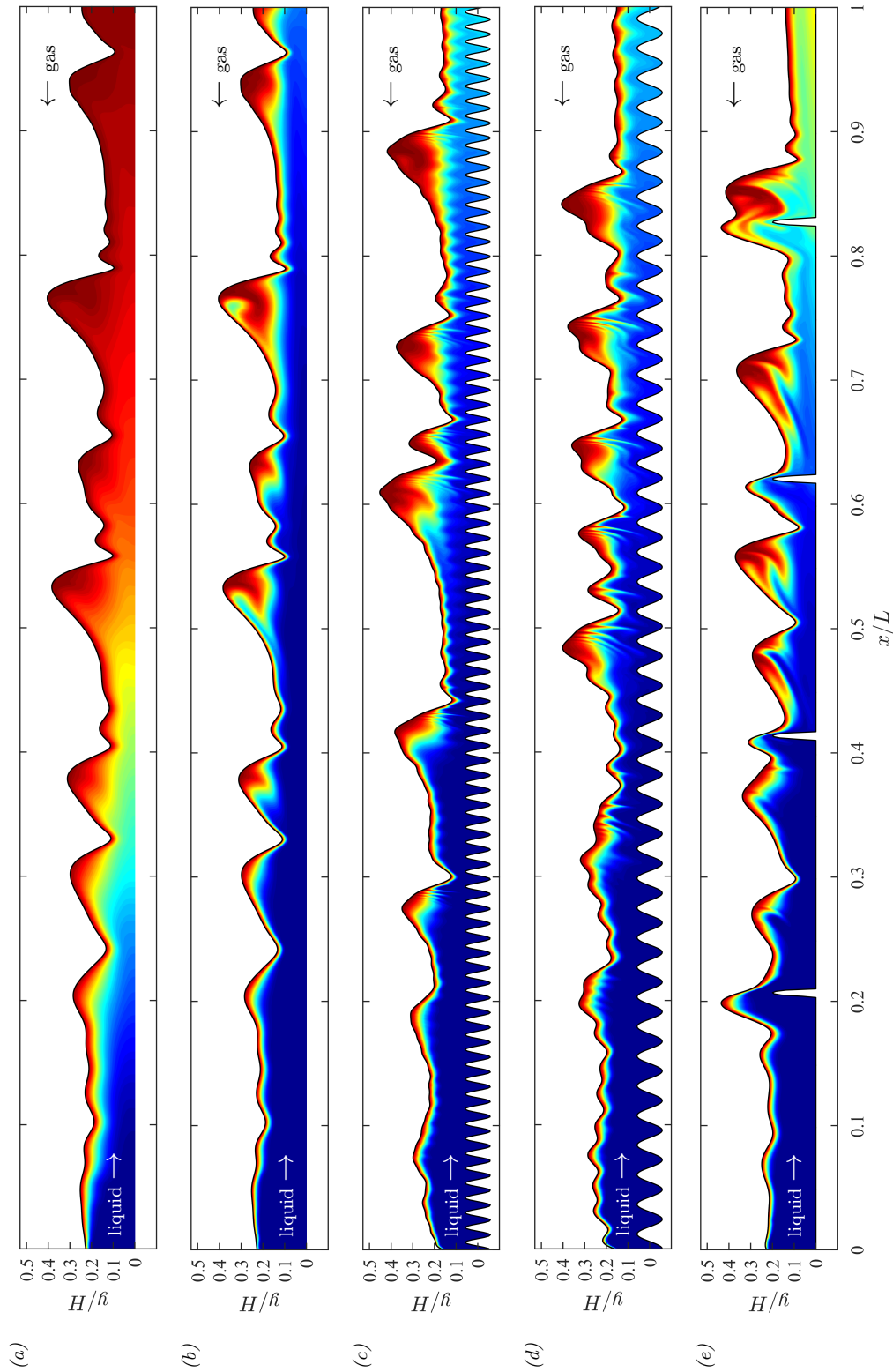


Figure 6.17: Noise-driven surface waves mimicked through random inlet forcing (4.11) with  $\epsilon_1=0.006$ . Same flow parameters and geometries as in figure 6.16. (a) Péclet number value representative of heat transport:  $Pe=459$ ,  $Pr_1=\nu_1/\alpha_1=30.6$  (DMSO-water solution in table 2.1); (b-e) Péclet number value representative of mass transport:  $Pe=4590$ ,  $Sc_1=\nu_1/\alpha_1=306$ .

where  $x_m = k \Lambda_C$  define the centres of the semicircular bumps  $k = 1, \dots, 5$ .

The corrugation amplitude  $\hat{h}_C$ , bump radius  $R_C$ , and wavelength  $\Lambda_C$  are given in figures 6.16 and 6.17, which provide an overview of our simulations. For both variants of the sinusoidal corrugation (panels 6.16d and 6.16e),  $\Lambda_C^*$  (=1.2 mm, 2.4 mm) is smaller than the cut-off wavelength of the Kapitza instability  $\Lambda_c^*=4.8$  mm ( $\Lambda_c=3.2$ ) for the flat-wall reference case (panel 6.16b).

Figure 6.16 corresponds to the case of solitary waves generated through coherent inlet forcing at frequency  $f^*=16$  Hz (4.10), whereas figure 6.17 corresponds to the case of noise-driven waves (4.11). Except for panel 6.17a, where  $Pe=459$ , all panels correspond to the larger Péclet number  $Pe=4590$ . For the lower  $Pe$  value, the scalar free-surface layer grows very rapidly, limiting the effect of the corrugations (Dietze, 2019). Thus, we will focus on the large  $Pe$  case, as well as solitary waves (figure 6.16), where the scalar transfer intensification is greatest.

Panel 6.16a represents the reference case of a flat film in contact with a quiescent gas, where the scalar convection rate in the liquid  $\dot{H}(x)$ :

$$\dot{H}(x, t) = \int_{f(x)}^{\eta(x, t)} u(x, y, t) \theta(x, y, t) dy, \quad (6.11)$$

can be obtained analytically in the limits  $Pe \rightarrow \infty$  (Higbie, 1935) and  $x \rightarrow 0$  (Brauer, 1971):

$$Pe \rightarrow \infty : \quad \dot{H}(x) = \left(\frac{6}{\pi}\right)^{1/2} \left(\frac{x}{Pe}\right)^{1/2}, \quad (6.12)$$

$$x \rightarrow \infty : \quad \dot{H}(x) = 1 - \exp\left(-x \frac{Sh}{Pe}\right). \quad (6.13)$$

This reference case will be used to gauge the transfer intensification produced by surface waves (panel 6.16b) and various corrugations (panels 6.16c to 6.16e). We do this based on panels 6.18a and 6.18b, which represent profiles of the time-averaged scalar convection rate  $\bar{\dot{H}}(x)$ :

$$\bar{\dot{H}}(x) = \frac{1}{t_2 - t_1} \int_{t_1}^{t_2} \dot{H} dt, \quad (6.14)$$

for all cases in figure 6.16. The steeper the increase in  $\bar{\dot{H}}(x)$ , the greater the rate of scalar transfer to the liquid film, and the shorter the transfer length required to reach a desired scalar content in the liquid.

Comparing the dashed blue line with the dot-dashed black line in panel 6.18a, shows that solitary waves alone (without any wall corrugations) greatly intensify inter-phase scalar transfer. This is well known and attributed to the so-called *surface renewal mechanism* (Yoshimura *et al.*, 1996), resulting from the presence of a moving-frame vortex within the large wave humps (see figure 4.10). This vortex is represented with white streamlines in panel 6.16b. The salient feature of this mechanism is the flow from the front stagnation point to the back stagnation point of the vortex, which short-circuits the

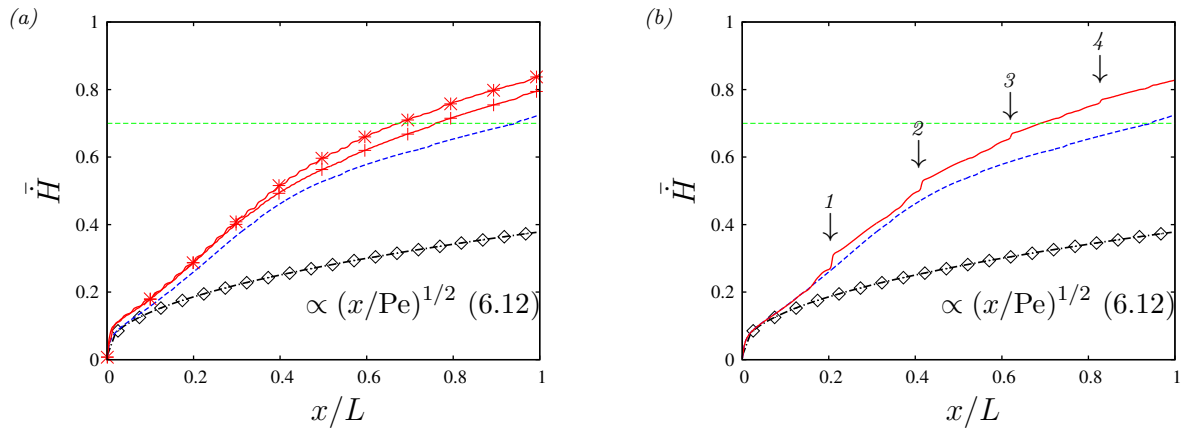


Figure 6.18: Intensification of inter-phase scalar transfer in a wavy falling liquid film due to wall corrugations. Parameters according to figure 6.16. Profiles of the time-averaged convection rate  $\bar{H}(x)$  (6.14) of the scalar  $\theta$  (4.1j) within the liquid film, as obtained from DNS with **Gerris**. Dot-dashed lines and diamonds: flat-film reference case (panel 6.16a). Data from penetration theory (6.12) (symbols) and DNS (dot-dashed lines); dashed blue lines: wavy film on flat wall (panel 6.16b); solid red: wall corrugations. (a) Sinusoidal corrugations. Plus signs:  $\Lambda_C=1.2$  mm (panel 6.16c); asterisks:  $\Lambda_C=2.4$  mm (panel 6.16d); (b) semicircular bumps (numbered 1-4) with  $R_C=0.3$  mm (panel 6.16e).

wave hump. This leads to the extraction of a scalar plume at the wave front and a compression of the scalar free-surface layer at the wave back. The latter effect greatly reduces the thickness of the scalar layer leading into the residual film, in between successive wave humps, which represents most of the transfer surface. However, this mechanism breaks down, once the scalar plume originating from the wave front has reached the wave back, i.e. roughly at  $x/L=0.4$  in panel 6.16b. This coincides with a break in the slope of the  $\bar{H}(x)$  profile in panel 6.18a (blue dashed line there).

The oscillatory secondary instability discussed in figure 6.7 is one way of extending the effect of the surface renewal mechanism, i.e. by preventing the scalar plume forming at the wave front from reaching the wave back. Wall corrugations are another way to counteract or avert the breakdown of this mechanism. In the case of the sinusoidal corrugations (figure 6.19), wave humps moving over the successive corrugation minima and maxima are modulated in their wave celerity. This causes the front stagnation point in the wave-fixed reference frame to move back and forth between the thin region of the film and the wave hump. As a result, a thin scalar plume (marked by arrows) is repeatedly extruded from the free-surface layer in the thin-film portion (panel 6.19c) and then pushed back to the wave hump (panel 6.19d), creating a sabre-tooth contour pattern there. Each of these rapid extrusion events represents a direct convection-related transport intensification, and this leads to a significant increase in inter-phase scalar transfer versus the flat-wall reference case. Comparing the red curves marked by plus signs and asterisks in panel 6.18a (sinusoidal corrugations with  $\Lambda_C^*=1.2$  mm and 2.4 mm), with the dashed blue line

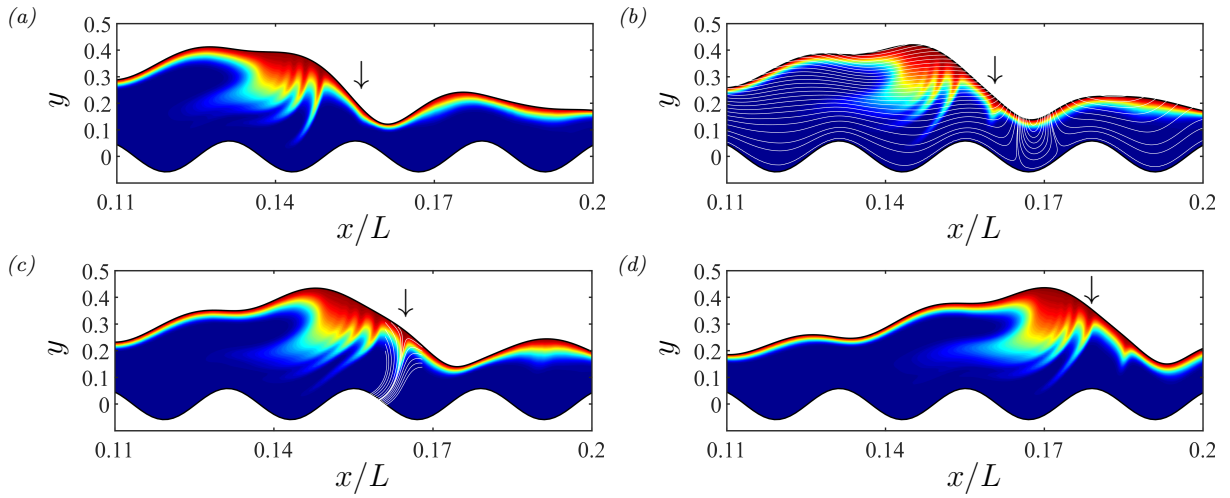


Figure 6.19: Repeated extrusion of plumes from the scalar free-surface layer within the front of a wave hump passing over a sinusoidal wall corrugation. Conditions according to panel 6.16d. (a)  $tf=60.88$ ; (b)  $tf=60.91$ . White curves represent streamlines in the wall-fixed reference frame; (c)  $tf=60.95$ . White curves represent streamlines in the wave-fixed reference frame; (d)  $tf=61.05$ . Arrows identify the same plume in all panels.

(flat wall), we see that the transfer length for reaching a scalar convection rate of  $\bar{H}=0.7$  (green line) is reduced by 30 % for the long sinusoidal corrugation (asterisks).

In the case of the semicircular bumps (panel 6.16e), the surface renewal mechanism is re-initiated every time a wave hump moves over a corrugation bump, during which the moving-frame vortex is disrupted and the liquid is redistributed within the wave. After every interaction between a wave hump and a corrugation bump, a new scalar plume forms at the wave front, pushing fresh unsaturated liquid toward the wave back, thus reinvigorating the compression of the scalar free-surface layer there (panel 6.16d).

Figure 6.20 illustrates how fresh liquid is supplied to a wave hump while moving over a corrugation bump. When the first precursory capillary trough reaches the bump (panel 6.20b), the progression of the wave hump is briefly halted, until it is lifted over the bump by the separation vortex forming at the capillary trough. During this process, fresh liquid from the wall region is pumped into the wave front, thus forming a large unsaturated region there (panel 6.20c). Once the wave front has moved over the bump, a new scalar plume forms in this region.

According to the  $\bar{H}(x)$  profiles in panel 6.18b, the transfer intensification caused by the bump-shaped corrugations (compare solid red and dashed blue curves) is comparable to that of the sinusoidal corrugations in panel 6.18a. However, it is discrete in nature, i.e. the bumps (marked by arrows in panel 6.18b) repeatedly reinitialize the surface renewal mechanism every time it has reached saturation, as evidenced by regular spikes in the  $\bar{H}(x)$  profile (red solid line).

The bumps not only provide the same transfer intensification as the sinusoidal corrugations, they also entail a lesser increase of the gas pressure drop, as reported in table

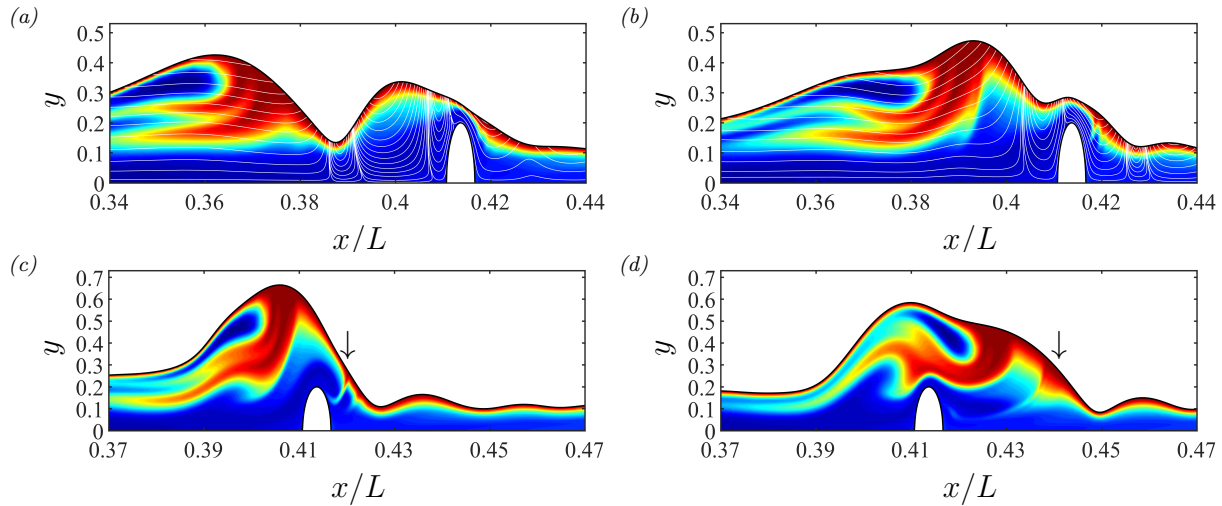


Figure 6.20: Redistribution of liquid within a wave hump moving over a bump (panels *a*, *b*), and subsequent extrusion of a new scalar plume (arrows) within the bulk of fresh liquid formed near the wave front (panels *c*, *d*). Conditions according to panel 6.16e. White curves represent streamlines in the wall-fixed reference frame, evidencing a separation vortex at the first capillary trough, which causes a liquid redistribution as it moves over the bump. (*a*)  $tf=61.10$ ; (*b*)  $tf=61.20$ ; (*c*)  $tf=61.30$ ; (*d*)  $tf=61.42$ .

2 of Dietze (2019). However, when the velocity of the counter-current gas flow is increased, bumps can trigger flooding events. This is shown in figure 6.21, representing a DNS where  $Re_2$  was varied according to four plateaus  $Re_2=-14.25$ ,  $-57$ ,  $-114$ , and  $-142.5$ . Upon reaching the last plateau,  $Re_2=-142.5$ , flooding is triggered at the third corrugation bump (panel 6.21a) as a wave hump is moving over it. The flooding event entails wave breaking and droplet formation from liquid ligaments (Fuster & Rossi, 2021) and triggers a cascade of flooding events at the other bumps<sup>13</sup>. Just before the surface wave obstructs the channel, a vortex street forms upstream of it, as a result of the strong contraction and expansion to which the gas flow is subjected (panel 6.21b). This conforms with observations that falling-film heat/mass exchangers work best near the flooding limit.

**Impact of the work and relation to the current state of the art** Our paper Dietze (2019) has been cited 13 times according to *Web of Science*.

Zhou & Prosperetti (2020b) have extended our work by performing long-time DNS of mass transport within solitary travelling waves on flat substrates at very high Schmidt number values, up to  $Sc=2000$  (compared to our maximum value  $Sc=306$ ). The authors employed a numerical method based on a fixed solution for the velocity field in the wave-fixed reference frame. The authors provide supplementary movies that confirm the breakdown of the surface renewal mechanism, which we have found in panels 6.16b and 6.18, when the scalar plume forming in the moving-frame vortex reaches the wave back.

<sup>13</sup>Supplementary movie 4 in Dietze (2019).



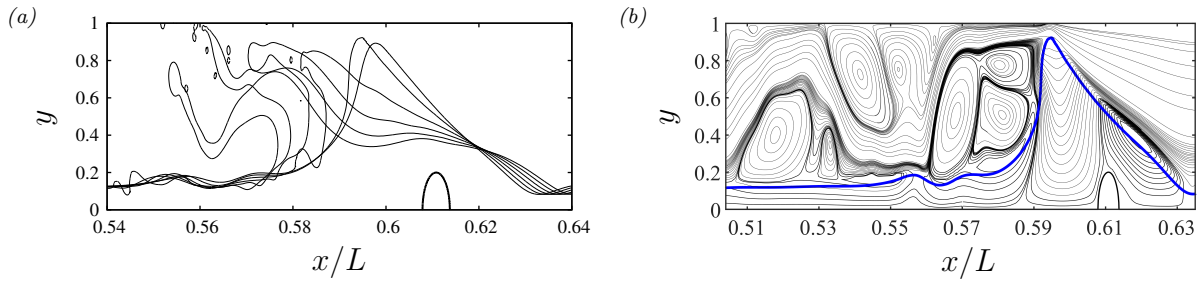


Figure 6.21: Flooding triggered by bumps upon increasing the counter-current gas flow rate. Simulation from panel 6.16e with additional stepwise variation of  $Re_2$  according to four plateaus:  $Re_2 = -14.25, -57, -114,$  and  $-142.5$ . (a) Snapshots of the film surface during a flooding event for  $Re_2 = -142.5$  at the third bump in panel 6.16e. Successive cascaded flooding events are triggered at the other bumps (supplementary movie 4 in Dietze (2019)); (b) streamlines in the wall-fixed reference frame just before the wave hump obstructs the channel.

These movies also make clear that the actual merging of the scalar plume with the scalar free-surface layer at the wave back is a diffusional effect. Indeed, in the limit  $Pe \rightarrow \infty$ , lines of constant scalar  $\theta$  would coincide with streamlines and would never merge.

Bonart *et al.* (2020) have performed DNS based on the Cahn-Hilliard Navier-Stokes equations for two phase flow and focused on the effect of isolated sharp-edged corrugations on the stability of a falling liquid film. Their results show that the wall structures can either damp and amplify the Kapitza instability.

Chen *et al.* (2021) have extended our work by performing mass transfer simulations of falling liquid films in actual corrugated micro-channels, where the confinement is even stronger than in our work ( $H^* = 100 \mu\text{m}$  versus  $H^* = 1.5 \text{ mm}$ ). Various corrugation geometries and real fluid combinations were investigated. In particular, the authors reported that sinusoidal wall corrugations can produce a 40% increase of  $CO_2$  absorption in a wavy falling water film. This is in line with our observations in panel 6.18.

# Suppression of the Kapitza instability in confined falling liquid films

Gianluca Lavallo<sup>1,†</sup>, Yiqin Li<sup>2</sup>, Sophie Mergui<sup>2</sup>, Nicolas Grenier<sup>1</sup>  
and Georg F. Dietze<sup>2</sup>

<sup>1</sup>Laboratoire LIMSI, CNRS, Univ. Paris-Sud, Université Paris-Saclay, F-91405, Orsay, France

<sup>2</sup>Laboratoire FAST, Univ. Paris-Sud, CNRS, Université Paris-Saclay, F-91405, Orsay, France

(Received 24 May 2018; revised 5 October 2018; accepted 6 November 2018)

We revisit the linear stability of a falling liquid film flowing through an inclined narrow channel in interaction with a gas phase. We focus on a particular region of parameter space, small inclination and very strong confinement, where we have found the gas to strongly stabilize the film, up to the point of fully suppressing the long-wave interfacial instability attributed to Kapitza (*Zh. Eksp. Teor. Fiz.*, vol. 18 (1), 1948, pp. 3–28). The stabilization occurs both when the gas is merely subject to an aerostatic pressure difference, i.e. when the pressure difference balances the weight of the gas column, and when it flows counter-currently. In the latter case, the degree of stabilization increases with the gas velocity. Our investigation is based on a numerical solution of the Orr–Sommerfeld temporal linear stability problem as well as stability experiments that clearly confirm the observed effect. We quantify the degree of stabilization by comparing the linear stability threshold with its passive-gas limit, and perform a parametric study, varying the relative confinement, the Reynolds number, the inclination angle and the Kapitza number. For example, we find a 30% reduction of the cutoff wavenumber of the instability for a water film in contact with air, flowing through a channel inclined at 3° and of height 2.8 times the film thickness. We also identify the critical conditions for the full suppression of the instability in terms of the governing parameters. The stabilization is caused by the strong confinement of the gas, which produces perturbations of the adverse interfacial tangential shear stress that are shifted by half a wavelength with respect to the wavy film surface. This tends to reduce flow-rate variations within the film, thus attenuating the inertia-based driving mechanism of the Kapitza instability.

**Key words:** gas/liquid flow, instability, thin films

---

## 1. Introduction

We consider a liquid film falling along the bottom wall of an inclined narrow channel, under the action of gravity and in interaction with a laminar gas flow (see figure 1). We distinguish two scenarios for the gas flow: either (i) the gas is subject to an aerostatic pressure gradient, i.e. a pressure difference which balances the weight

† Email address for correspondence: [gianluca.lavalle@limsi.fr](mailto:gianluca.lavalle@limsi.fr)

# Wavy liquid films in interaction with a confined laminar gas flow

Georg F. Dietze<sup>†</sup> and Christian Ruyer-Quil

UPMC Universitaire Paris 06, Universitaire Paris-Sud, CNRS, Laboratoire FAST, Bâtiment 502,  
Campus Universitaire d'Orsay, Orsay, F-91405, France

(Received 22 August 2012; revised 19 December 2012; accepted 14 February 2013)

A low-dimensional model capturing the fully coupled dynamics of a wavy liquid film in interaction with a strongly confined laminar gas flow is introduced. It is based on the weighted residual integral boundary layer approach of Ruyer-Quil & Manneville (*Eur. Phys. J. B*, vol. 15, 2000, pp. 357–369) and accounts for viscous diffusion up to second order in the film parameter. The model is applied to study two scenarios: a horizontal pressure-driven water film/air flow and a gravity-driven liquid film interacting with a co- or counter-current air flow. In the horizontal case, interfacial viscous drag is weak and interfacial waves are primarily driven by pressure variations induced by the velocity difference between the two layers. This produces an extremely thin interfacial shear layer which is pinched at the main and capillary wave humps, creating several elongated vortices in the wave-fixed reference frame. In the capillary wave region preceding a large wave hump, flow separation occurs in the liquid in the form of a vortex transcending the liquid–gas interface. For the gravity-driven film, a twin vortex (in the wave-fixed reference frame) linked to the occurrence of rolling waves has been identified. It consists of the known liquid-side vortex within the wave hump and a previously unknown counter-rotating gas-side vortex, which are connected by the same interfacial stagnation points. At large counter-current gas velocities, interfacial waves on the falling liquid film are amplified and cause flooding of the channel in a noise-driven scenario, while this can be delayed by forcing regular waves at the most amplified linear wave frequency. Our model is shown to exactly capture the long-wave linear stability threshold for the general case of two-phase channel flow. Further, for the two considered scenarios, it predicts growth rates and celerity of linear waves in convincing agreement with Orr–Sommerfeld calculations. Finally, model calculations of nonlinear interfacial waves are in good agreement with film thickness and velocity measurements as well as streamline patterns in both phases obtained from direct numerical simulations.

**Key words:** interfacial flows (free surface), low-dimensional models, thin films


---

## 1. Introduction


Thin liquid films flowing in the presence of a co- or counter-current and strongly confined gas flow arise in a number of technological applications. For example, cooling of miniaturized electronic equipment is performed with so-called micro-gap coolers that consist of an extremely narrow (possibly submillimetric) channel


<sup>†</sup> Email address for correspondence: [dietze@fast.u-psud.fr](mailto:dietze@fast.u-psud.fr)

**Solitary waves on superconfined falling liquid films**

Gianluca Lavallo \* and Nicolas Grenier  
*Université Paris-Saclay, CNRS, LIMSI, 91400, Orsay, France*

Sophie Mergui  
*Sorbonne Université, Université Paris-Saclay, CNRS, FAST, 91405, Orsay, France*

Georg F. Dietze †  
*Université Paris-Saclay, CNRS, FAST, 91405, Orsay, France*

 (Received 22 October 2019; accepted 11 February 2020; published 2 March 2020)

Solitary traveling waves are prominent features covering the surface of a falling liquid film and are known to promote heat and mass transfer. We focus on the little studied case where they are subject to an extremely confined countercurrent gas flow, and we identify two secondary instabilities. At high gas velocities, a catastrophic instability develops, leading to flooding through wave reversal and liquid arrest. At lower gas velocities, an oscillatory instability occurs, producing a high-frequency periodic modulation of the wave height. Conjunction of this self-sustained oscillatory state and vortices forming in the liquid is shown to enhance mixing. We also show that the gas flow can cause extreme local film thinning, leading to almost dry patches where the liquid thickness is very small.

DOI: [10.1103/PhysRevFluids.5.032001](https://doi.org/10.1103/PhysRevFluids.5.032001)

Flows through miniaturized channels are usually laminar and require active or passive methods to enhance mixing [1]. In the case of stratified two-phase flows, this can be achieved through flow structures resulting from interfacial instabilities [2]. In horizontal pressure-driven configurations, the instability is known to require a strong relative motion between the two phases [3,4]. By contrast, we study the vertical configuration of a gravity-driven falling liquid film in contact with an extremely confined gas, where the inertia-driven Kapitza instability [5] generates solitary surface waves that greatly enhance heat and mass transfer [6]. In this case, the gas velocity can be used as a free parameter to act on the waves.

Many works have studied the effect of a gas flow on the stability and dynamics of wavy falling liquid films [7–9]. Such studies have usually concentrated on weakly or moderately confined configurations. In that case, only the tangential interfacial viscous stresses exerted by the gas play a significant role, and turbulent conditions are required to affect meaningfully the liquid film [10]. By contrast, we focus on extreme confinement levels, where the gas flow and liquid film are of comparable thickness [11]. Here, gas pressure variations induced by surface waves become relevant [12], and the film is affected by the gas even under laminar conditions [13]. This configuration is bound to be more prone to flooding, i.e., occlusion of the channel by the liquid [14], wave reversal [8], or liquid arrest [10]. Yet, it is unclear how this unwanted phenomenon is provoked under extreme confinement. Does it result from a lack of saturated traveling-wave solutions or a loss of their stability? Answering such a question may produce valuable insights for the design of falling film microreactors [15–17].

---

\*Present address: Institut de Mécanique des Fluides de Toulouse (IMFT)–Univ. de Toulouse, CNRS-INPT-UPS, Toulouse, France; author to whom correspondence should be addressed: gianluca.lavalle@limsi.fr

†Author to whom correspondence should be addressed: dietze@fast.u-psud.fr



## Superconfined falling liquid films: linear versus nonlinear dynamics

Gianluca Lavallo<sup>1</sup>, Sophie Mergui<sup>2,3</sup>, Nicolas Grenier<sup>4</sup> and Georg F. Dietze<sup>2,†</sup>

<sup>1</sup>Mines Saint-Etienne, Université Lyon, CNRS, UMR 5307 LGF, Centre SPIN, 42023 Saint-Etienne, France

<sup>2</sup>Université Paris-Saclay, CNRS, FAST, 91405 Orsay, France

<sup>3</sup>Faculté des Sciences et Ingénierie, Sorbonne Université, UFR d'Ingénierie, 75005 Paris, France

<sup>4</sup>Université Paris-Saclay, CNRS, LISN, 91405 Orsay, France

(Received 19 January 2021; revised 9 April 2021; accepted 5 May 2021)

The effect of a counter-current gas flow on the linear stability of an inclined falling liquid film switches from destabilizing to stabilizing, as the flow confinement is increased. We confront this linear effect with the response of nonlinear surface waves resulting from long-wave interfacial instability. For the strongest confinement studied, the gas flow damps both the linear growth rate and the amplitude of nonlinear travelling waves, and this holds for waves of the most-amplified frequency and for low-frequency solitary waves. In the latter case, waves are shaped into elongated humps with a flat top that resist secondary instabilities. For intermediate confinement, the linear and nonlinear responses are opposed and can be non-monotonic. The linear growth rate of the most-amplified waves first decreases and then increases as the gas velocity is increased, whereas their nonlinear amplitude is first amplified and then damped. Conversely, solitary waves are amplified linearly but damped nonlinearly. For the weakest confinement, solitary waves are prone to two secondary instability modes that are not observed in unconfined falling films. The first involves waves of diminishing amplitude slipstreaming towards their growing leading neighbours. The second causes wave splitting events that lead to a train of smaller, shorter waves.

**Key words:** thin films, gas/liquid flow

### 1. Introduction

We consider a gravity-driven two-dimensional liquid film falling down a plane tilted at an angle  $\phi$  with respect to the horizontal, in contact with a counter-current gas flow that is strongly confined by an upper wall placed at  $y = H$  (figure 1). Both fluids are Newtonian,

† Email address for correspondence: [dietze@fast.u-psud.fr](mailto:dietze@fast.u-psud.fr)

# Effect of wall corrugations on scalar transfer to a wavy falling liquid film

Georg F. Dietze<sup>†</sup>

Laboratoire FAST, Univ. Paris-Sud, CNRS, Université Paris-Saclay, F-91405, Orsay, France

(Received 28 April 2018; revised 27 August 2018; accepted 17 October 2018;  
first published online 28 November 2018)

Direct numerical simulation is employed to study the effect of small-scale wall corrugations on scalar transfer through the wavy surface of a vertically falling liquid film in interaction with a strongly confined counter-current gas flow. Three wall geometries are considered: (i) a flat wall for reference; (ii) a sinusoidal corrugation typically found on structured packings in chemical engineering devices; and (iii) a heuristic design consisting of isolated semicircular bumps distanced by the wavelength of the surface waves. We consider the limiting case of a Dirichlet condition for the transported scalar (temperature or mass fraction) at the liquid–gas interface and focus on liquid-side transport. We consider convection-dominated regimes at moderate and large Péclet numbers, representative of heat and mass transfer respectively, and confront forced and noise-driven wave regimes. Our results show that sinusoidal wall corrugations increase transfer by up to 30 per cent in terms of the exchange length required to transfer a fixed amount of the transported quantity. A slightly greater intensification is achieved through the bump-shaped corrugations, which intermittently disrupt the moving-frame vortex forming within the large-amplitude solitary waves, allowing these to replenish with unsaturated liquid. However, when the velocity of the strongly confined gas flow is increased above a certain threshold, the bumps can trigger the flooding of the channel.

**Key words:** mixing, solitary waves, thin films

---

## 1. Introduction

Falling liquid films are widely used in engineering applications involving heat/mass transfer between a gas and a liquid (Alekseenko, Nakoryakov & Pokusaev 1994; Azzopardi *et al.* 2011). One example is rectification columns used e.g. for the cryogenic separation of air. In such devices, the liquid film is in contact with a counter-current gas flow inside so-called structured packings, which subdivide the cross-section of the column into millimetric channels (Fair & Bravo 1990). The sheets constituting these packings are corrugated at different levels (Valluri *et al.* 2005) in order to increase interfacial transfer (by this we mean through the mobile surface of the film). Large-scale corrugations force the liquid to meander through the packing, increasing its residence time. Small-scale corrugations, with amplitudes of the order of 100  $\mu\text{m}$  (Trifonov 2011), additionally texture the packing

<sup>†</sup> Email address for correspondence: [dietze@fast.u-psud.fr](mailto:dietze@fast.u-psud.fr)

# Chapter 7

## Liquid films in narrow tubes

Liquid films confined in cylindrical geometries and subject to an active core fluid (figure 1.3), are encountered in several practical situations. For example, evaporators for milk inspissation typically involve falling-liquid films flowing down the inner surface of long tubes that are heated from the outside via condensing steam (Jebson & Chen, 1997). Such tubular chemical engineering apparatuses are subject to the general trend of miniaturization (Seebauer *et al.*, 2012). However, increasing the radial confinement of the flow also introduces the risk of occlusion (Dao & Balakotaiah, 2000; Camassa *et al.*, 2014), when the falling film forms liquid plugs (panel 7.1a). This must be avoided in counter-current two-phase heat/mass exchangers.

Another practical example concerns mucus films in the pulmonary airways (panel 7.1c). The human respiratory network consists of over 20 generations of such airways that successively branch into increasingly narrow orifices (panel 7.1d), starting from the trachea ( $R^* \approx 10$  mm) and ending at the alveolar sacs ( $R^* \ll 1$  mm). These airways are covered by a mucus film that prevents the epithelial cells from drying out and is responsible for evacuating alien particles from the lungs (Grotberg, 1994, 2011), either via beating cilia (Bottier *et al.*, 2017) or under the effect of a cough-induced gas flow (King *et al.*, 1985). Deviations in mucus properties (Levy *et al.*, 2014), e.g. caused by respiratory diseases, can lead to occlusion (Bian *et al.*, 2010) or collapse (Heil & Hazel, 2011) of the pulmonary airways and a deterioration of oxygen transport to the lungs.

Compared to the flooding mechanisms for falling liquid films in planar channels (chapter 6), a cylindrical geometry additionally introduces the long-wave Plateau-Rayleigh instability (Plateau, 1849; Rayleigh, 1892; Goren, 1962), which can significantly increase the amplitude of travelling waves versus the planar configuration (Trifonov, 1992), and cause absolute instability (Duprat *et al.*, 2007) when the mean core radius  $\bar{d}$  becomes small. Its relevance versus the Kapitza instability is determined by the Bond number Bo:

$$\text{Bo} = \frac{\rho g \mathcal{L}^2}{\sigma} = \frac{\rho g R^{*2}}{\sigma}. \quad (7.1)$$

For liquid films in extremely narrow tubes, e.g. higher-generation pulmonary capillaries, gravity is negligible ( $\text{Bo} \ll 1$ ), and occlusion is solely due to the Plateau-Rayleigh insta-

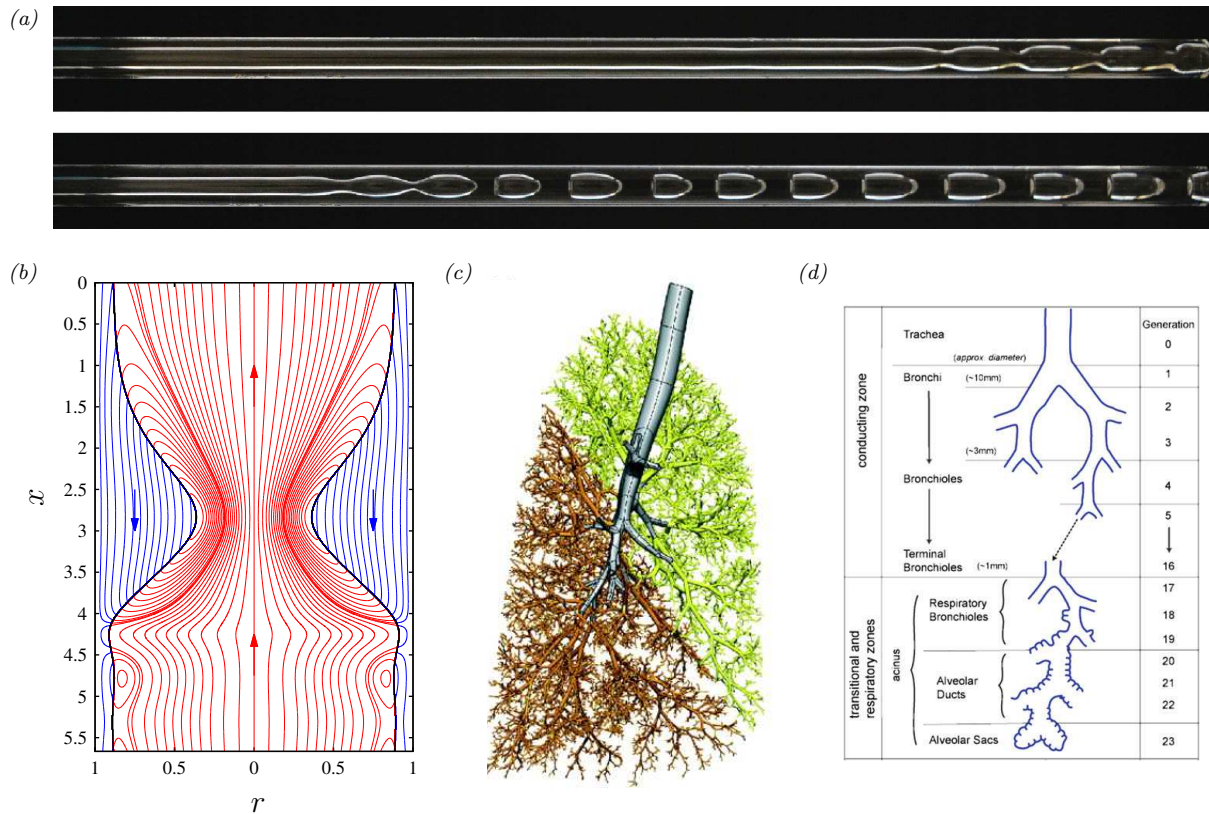


Figure 7.1: Annular liquid films in narrow cylindrical tubes in contact with a gaseous core fluid. (a) Plug formation in a vertically-falling liquid film adapted from Camassa *et al.* (2014); (b) falling liquid film subject to a counter-current air flow (Dietze *et al.*, 2020); (c) human respiratory network adapted from Burrowes *et al.* (2008); (d) generations of pulmonary airways adapted from Tu *et al.* (2013).

bility (Trifonov, 1992). In that case, as discussed in figure 2.22, occlusion sets in (provided  $\Lambda > \Lambda_C = 2\pi d_0$ ) beyond a threshold volume  $V_1/\pi/R^3 \approx 1.73$  (Everett & Haynes, 1972), which bounds the existence of *unduloids*, i.e. surfaces of revolution with constant curvature (Delaunay, 1841). For reference, in the terminal bronchioles (panel 7.1d),  $Bo \approx 0.1$  (Kamm & Schroter, 1989).

By contrast, in the case of falling liquid films ( $Bo \gtrsim 1$ ), the occlusion bound depends on an intricate interplay between the Kapitza and Plateau-Rayleigh instabilities. For example, the gravity-induced steepening of wave fronts observed in panel 5.2a favours streamwise variations in axial curvature  $\kappa_x = -\frac{1}{2}\partial_x d^2/d - \partial_{xx}d$  over streamwise variations of azimuthal curvature  $\kappa_\varphi = 1/d$ , and this can saturate the Plateau-Rayleigh instability at very small amplitudes (Frenkel *et al.*, 1987; Quéré, 1990). We will see in section 7.1 that this mechanism greatly delays the occlusion limit for falling liquid films in vertical tubes.

We have applied our cylindrical WRIBL model from section 1.2 to both types of film



flows represented in figure 7.1, i.e. falling liquid films in vertical tubes (configuration in panel 1.3a), and gravity-free mucus films in the pulmonary airways (configuration in panel 1.3b). In all cases studied, the tube radius  $R^*$  is sufficiently small to warrant the long-wave approximation underlying our WRIBL model, and we account for the effect of the core fluid (panel 7.1b), which we assume to be air. We have extended the state of the art through two works (Dietze *et al.*, 2020; Dietze & Ruyer-Quil, 2015):

- In the case of falling liquid films, the role of surface waves in the occlusion of narrow vertical tubes had not been fully understood. Dao & Balakotaiah (2000) performed comprehensive occlusion experiments for various fluids and tube diameters, but no information was provided about the nature of surface waves causing the occlusion. Nonetheless, it was conjectured that occlusion sets in when the height of TWS reaches the tube radius. The visualisation experiments of Camassa *et al.* (2014), using a high-viscosity silicone oil, later demonstrated another possible occlusion scenario, involving surface waves of regular wavelength  $\Lambda$  undergoing unbounded spatial growth. These authors found that the critical  $Re_1$  at occlusion depends on the tube length  $L$ .

Camassa *et al.* (2014) also computed TWS with a first-order asymptotic model and found that these solutions are bounded by a limit point (LP) in terms of  $Re_1$  for a given  $\Lambda$ . It was conjectured that this LP sets the occlusion bound. However,  $Re_1^{LP}$  is sensitive to  $\Lambda$  (Camassa *et al.*, 2016; Ding *et al.*, 2019), long waves being more dangerous than short ones, and agreement with the experimental occlusion bound could not be achieved for realistic values of  $\Lambda$  (Camassa *et al.*, 2016). Zhou *et al.* (2016) attempted to characterize the occlusion bound via spatially-evolving computations with a first-order IBL model. However, these computations broke down at the first occlusion event ( $d_{\min}=0$ ) and thus could not reach a developed state.

In Dietze *et al.* (2020), we identified two scenarios of wave-induced occlusion, and we reported the associated occlusion bounds for various real working liquids. Further, we determined how these bounds are affected by axial viscous diffusion, inertia, and the presence of a counter-current gas flow. In scenario I, occlusion is caused by the most-amplified surface waves emerging from linear wave selection. This regime sets in above an upper conservative bound  $Re_1 > Re_1^{\max}$ , where  $Re_1^{\max}$  corresponds to the LP of TWS at the linearly most amplified frequency  $f=f_{\max}$ . In scenario II, the most-amplified waves possess TWS, but they subsequently coalesce to form longer more-dangerous waves, as the result of coarsening dynamics (Chang *et al.*, 1996*b*). This scenario is bounded by  $Re_1^{\min} \leq Re_1 \leq Re_1^{\max}$ , where  $Re_1^{\min}$  marks the limit below which waves of all  $f$  possess TWS (Ding *et al.*, 2019). Whether occlusion occurs in a real system, depends on whether the tube is sufficiently long to accommodate the required wave dynamics. In scenario II, we found that occlusion can be prevented via coherent inlet forcing of short waves.

In the case of high-viscosity liquids, we found that axial viscous diffusion greatly precipitates the upper occlusion bound  $Re_1^{\max}$ . Accounting for this effect, allowed us

to reproduce the visualisation experiments of Camassa *et al.* (2014) (see figure 2.20) and to prove their conjecture that the experimental occlusion bound is associated with the LP of TWS (scenario I). Except for very large Bo, we found that  $d_{\min} > 0$  for TWS at  $\text{Re} = \text{Re}_1^{\max}$ , thus refuting the conjecture of Dao & Balakotaiah (2000) that occlusion occurs due to asymptotic geometrical obstruction.

Gravity strongly delays  $\text{Re}_1^{\max}$  through the axial distortion of waves (Frenkel *et al.*, 1987; Quéré, 1990). Our model accurately produces this effect and thus improves upon the work of Jensen (2000), who represented surface waves with symmetrical equilibrium shapes. Further, we found that accounting for axial viscous diffusion (high-viscosity liquids) and inertia (low-viscosity liquids) is necessary to correctly predict whether occlusion is dictated by absolute ( $\text{Bo} < 1$ ) or convective ( $\text{Bo} \geq 1$ ) instability. Our representation of liquid plugs (see section 2.2.3), either via our augmented momentum equation (1.60) or via numerical limitation of the core radius (2.45), allowed us to continue transient computations past occlusion events, until a fully-developed state was reached.

These results are discussed in section 7.1.

- In the case of gravity-free annular liquid films ( $\text{Bo} \ll 1$ ), the occlusion bound coincides with the loss of unduloid equilibrium solutions at  $V_1/\pi/R^3 \approx 1.73^1$ . Above this threshold, the only possible equilibrium shape is a liquid plug separating two spherical bubbles, and thus, the liquid film inevitably tends toward occluding the tube. However, the draining of thin-film portions (lobes) into thicker ones (collars) can take quite long, in particular on extended domains, where multiple collars and lobes interact and slide back and forth, as has been shown by Lister *et al.* (2006*b*) via simulations with a thin-film lubrication model ( $h \ll R$ ).

Johnson *et al.* (1991) successfully reproduced the unduloid/occlusion transition with a single-phase integral model for conditions representative of pulmonary airways (Kamm & Schroter, 1989). Later, Halpern & Grotberg (2003), using a lubrication model for the liquid film, accounted for the additional effect of an oscillating core gas flow via a prescribed interfacial tangential shear stress and gas pressure gradient. The authors showed that imposing a high frequency oscillation can prevent the occlusion of pulmonary airways, thus explaining the underlying physics of treatments for obstructive airway disease (Edo *et al.*, 1998). In these studies, the mucus film was modelled as a Newtonian fluid with representative values for the viscosity ( $\mu_1 \approx 10^{-3}$  Pas) and surface tension ( $\sigma \approx 20 \cdot 10^{-3}$  N/m)<sup>2</sup>.

In Dietze & Ruyer-Quil (2015), we applied our WRIBL model to various fluid combinations, including water/air, water/silicone-oil, silicone-oil/water, glycerol/silicone-oil, and mucus/air. Its novel features allow to accurately predict the dynamics of occlusion for situations where inertia (e.g. water/air) and/or inter-phase coupling

<sup>1</sup>An exact definition of this threshold involves Jacobian elliptic functions (Everett & Haynes, 1972).

<sup>2</sup>A more realistic representation of mucus rheology, accounting for viscoelasticity, was adopted in the lubrication model of Halpern *et al.* (2010).

(e.g. water/silicone-oil) are relevant. Also, it analytically predicts the occlusion onset and the cut-off wavelength  $\Lambda_C=2\pi d_0$  of the Plateau-Rayleigh instability. These validation results have been discussed in section 2.3.2.

In section 7.2, we will focus on the fluid combination of model mucus (Halpern & Grotberg, 2003) and air, for which we have discovered an alternative route to occlusion, when the liquid volume is too large to form an unduloid ( $V_1/\pi/R^3>1.73$ ) but too small to form a static liquid plug without dry patches on the tube wall ( $V_1/\pi/R^3<\Lambda/R - 4/3$ ). In that case, assuming  $\Lambda>\Lambda_C$ , occlusion is unavoidable, but the liquid film can become locally very thin as it drains into the liquid plug. The resulting thin-film portions almost arrest further growth due to increased viscous drag there, until, much later, a secondary instability causes a spontaneous sliding motion of the liquid film<sup>3</sup>. This re-initiates rapid growth and eventually leads to occlusion.

An oscillating air flow, with frequency and amplitude according to typical breathing conditions, can significantly precipitate this sliding-induced occlusion, and so does axial viscous diffusion in the liquid film. As a result of the sliding motion, the large vortices associated with the initial symmetrical growth of liquid collars (Newhouse & Pozrikidis, 1992) are broken up into a series of smaller unsymmetrical vortices.

## 7.1 Falling liquid films in vertical tubes

Figure 7.2 characterizes the upper and lower occlusion bounds  $Re_1^{\max}$  and  $Re_{10}$  for three falling liquid film configurations involving real working liquids: the high-viscosity silicone oil used in the experiments of Camassa *et al.* (2014) (panels 7.2a, 7.2b), the aqueous glycerol solution used in experimental run 13 of Dao & Balakotaiah (2000) (panel 7.2c), and a low-viscosity silicone oil (panel 7.2d). Pure water is not considered, because  $Bo \ll 1$  for the narrow tubes investigated here and thus absolute instability sets in at very low  $Re_1$ . The core fluid is air subject to an aerostatic pressure gradient,  $M=1$ .

Panel 7.2a represents TWS in terms of  $Re_1$  for the high-viscosity silicone oil at different relative wave frequencies  $f/f_{\max}$ , where the linearly most-amplified frequency  $f_{\max}$  is obtained via (2.24), using (2.9) (see section 2.2.1). The solid curve corresponds to  $f/f_{\max}=1$  and thus represents waves that are most likely to emerge in an experiment. We have already established in figure (2.7) that only occluded states, i.e. liquid plugs separated by gas bubbles, exist beyond its limit point (LP). This point marks the upper occlusion bound  $Re_1^{\max}$ , beyond which occlusion is unavoidable. We have not drawn in panel 7.2a nor in subsequent figures the solution branch associated with liquid plugs, which was discussed in panel 2.7a. This is because we are interested only in the occlusion limit here. Also, we have discovered the existence of this branch of travelling-plug solu-

---

<sup>3</sup>The same spontaneous sliding can occur in planar fluid films subject to the Rayleigh-Taylor instability (Lister *et al.*, 2006a; Dietze *et al.*, 2018), and we will explain the underlying instability in section 8.1.

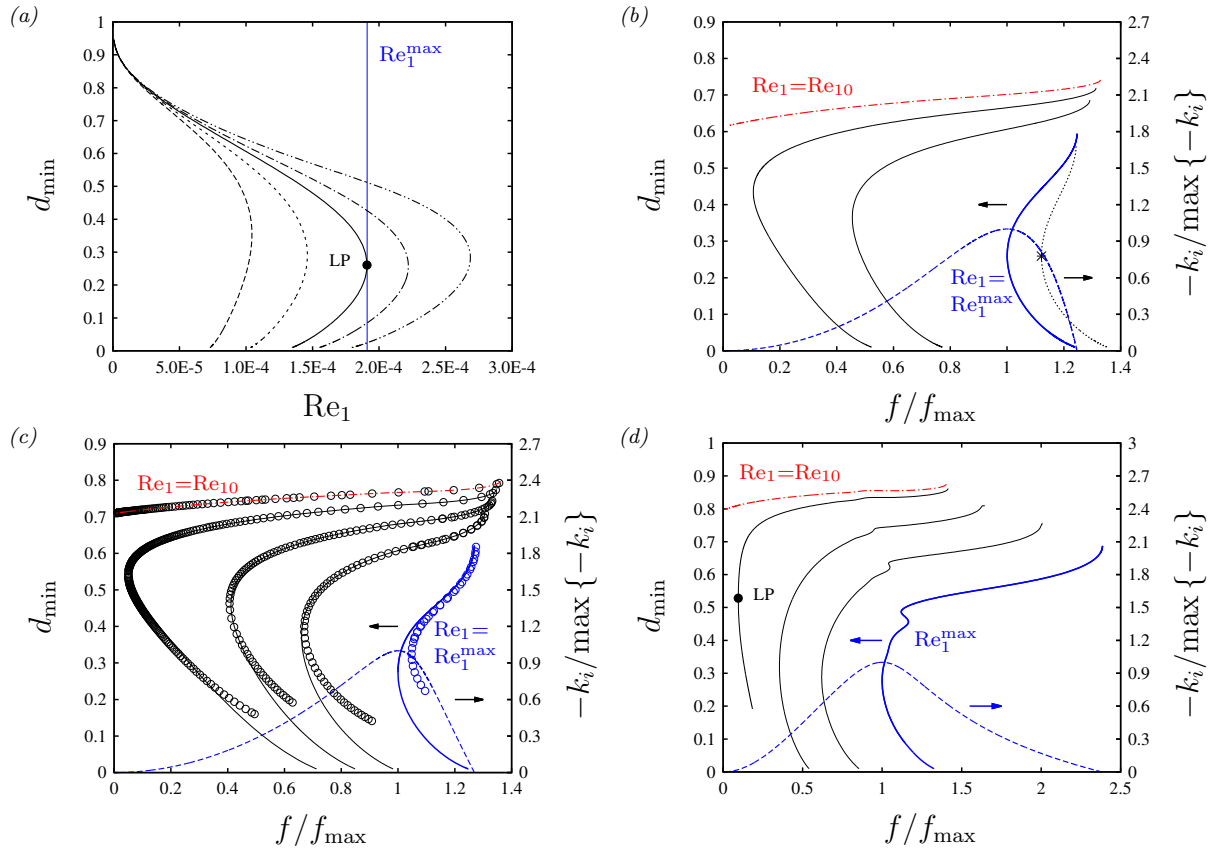


Figure 7.2: TWS for a falling liquid film within a vertical cylindrical tube in contact with a quiescent-air core:  $M=1$ . (a) Silicone oil IV from table 2.1 (Camassa *et al.*, 2014):  $Ka=3.29 \cdot 10^{-3}$ ,  $R^*=5$  mm. Long dashes:  $f/f_{\max}=0.5$ , short dashes:  $f/f_{\max}=0.8$ , solid:  $f/f_{\max}=1$ , dot-dashed:  $f/f_{\max}=1.1$ , dot-dot-dashed:  $f/f_{\max}=1.2$ . Vertical blue line marks limit point (LP) for linearly most amplified waves:  $f=f_{\max}$ ,  $Re_1=Re_1^{\max}$ ; (b-d) frequency dependence at  $Re_1=\text{const}$ . Dashed blue: linear spatial growth rate  $-k_i$  at  $Re_1=Re_1^{\max}$  (right abscissae), other: TWS at  $Re_1=\text{const}$  (left abscissae). (b) Parameters according to panel a. Dot-dashed red:  $Re_1=Re_{10}=6 \times 10^{-5}$ , thin solid:  $Re_1=7.5 \times 10^{-5}$ ,  $1 \times 10^{-4}$ , thick solid blue:  $Re_1=Re_1^{\max}=1.91 \times 10^{-4}$ , dotted with asterisk:  $Re_1=2.3 \times 10^{-4}$ ; (c) glycerol(89%)-water (Dao & Balakotaiah, 2000):  $Ka=3.532$ ,  $R^*=3.175$  mm. Dot-dashed red:  $Re_1=Re_{10}=0.075$ , thin solid:  $Re_1=0.1$ ,  $0.14$ ,  $0.2$ , thick solid:  $Re_1=Re_1^{\max}=0.393$ , open circles: DNS with passive-core ( $\Pi_\mu=\Pi_\rho=0$ ) code (Dietze *et al.*, 2020) performed by Christian Ruyer-Quil; (d) silicone oil III:  $Ka=121.4$ ,  $R^*=1.5$  mm. Dot-dashed red:  $Re_1=Re_{10}=1.5$ , thin solid:  $Re_1=2$ ,  $5$ ,  $10$ , thick blue:  $Re_1=Re_1^{\max}=18.9$ .

tions (TPS) only recently. The study of liquid plugs with our augmented model (1.60) is the subject of a new manuscript currently in preparation.

Panel 7.2b represents the TWS from panel 7.2a in terms of the wave frequency  $f$  at different fixed  $Re_1$ . This representation reveals the lower occlusion bound  $Re_{10}$  (red

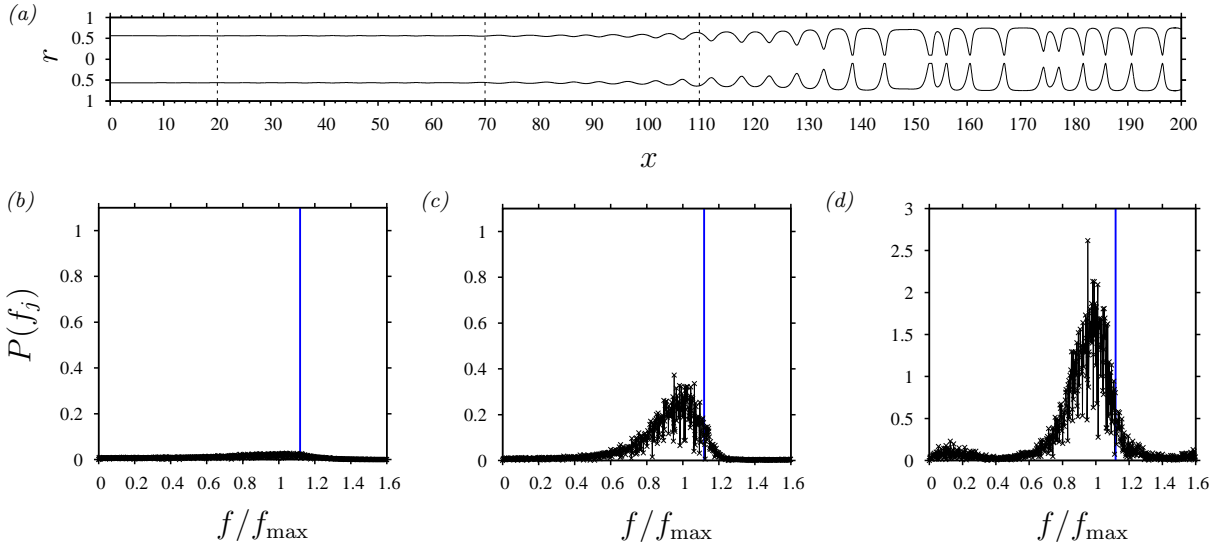


Figure 7.3: Occlusion due to noise-driven surface waves. Open-domain WRIBL computation of experiment in panel 3a of Camassa *et al.* (2014), using inlet noise (2.38):  $L^*=1$  m,  $\text{Ka}=3.29 \cdot 10^{-3}$  (silicone oil IV and air I in table 2.1),  $\text{Re}_1=2.3 \times 10^{-4}$ ,  $\epsilon_2=2 \cdot 10^{-4}$ . Numerical core radius limitation (2.45) with  $d_{\text{crit}}/R=0.2$ . (a) Snapshot of film profile; (b-d) frequency spectra at different locations: (b)  $x=20$ ; (c)  $x=70$ ; (d)  $x=110$ . Vertical blue lines at  $f/f_{\max}=1.12$  mark limit of TWS from panel 7.2b (asterisk there).

curve), below which there are TWS for all linearly unstable  $f^4$ . Occlusion is impossible below this limit. The blue curve on the right corresponds to the upper occlusion bound  $\text{Re}_1^{\max}$ , its LP occurring at  $f/f_{\max}=1$ .

Panel 7.3a represents an open-domain computation of the experiment in panel 3a of Camassa *et al.* (2014) (the second version, using a  $L^*=1$  m tube), which was performed with  $\text{Re}_1=2.3 \cdot 10^{-4}$ , i.e. slightly greater than  $\text{Re}_1^{\max}=1.91 \cdot 10^{-4}$  in panel 7.2a. Here, we have applied synthetic inlet noise (2.38) with an amplitude  $\epsilon_2$  tuned to the experiment. Also, we have used here and in other computations the numerical core radius limitation (2.45) with  $d_{\text{crit}}=0.1$ , instead of the augmented WRIBL model (1.60). This reduces the computational cost, without altering the dynamics leading up to occlusion, which is the focus of the current section<sup>5</sup>. Reducing the computational cost was particularly important for the computation in panel 7.3a, as it was run for a very long time ( $tf_{\max}=480$ ), in order to reach a statistically developed state.

Panels 7.3b, 7.3c, and 7.3d show that the spectrum of the surface waves travelling on the liquid film is dominated by the linearly most-amplified waves ( $f/f_{\max}=1$ ). These waves subsequently grow until occluding the tube (panel 7.3a). Because  $\text{Re}_1 > \text{Re}_1^{\max}$ , the linearly most-amplified waves do not possess TWS, and occlusion is inevitable. This is occlusion scenario I. In other words,  $f_{\max}$  lies below the LP of TWS at  $\text{Re}_1=2.34 \times 10^{-4}$

<sup>4</sup>The curves are bounded on the right by the cut-off frequency  $f_c$ .

<sup>5</sup>The dynamics of liquid plugs after occlusion is the subject of a new manuscript currently in preparation.

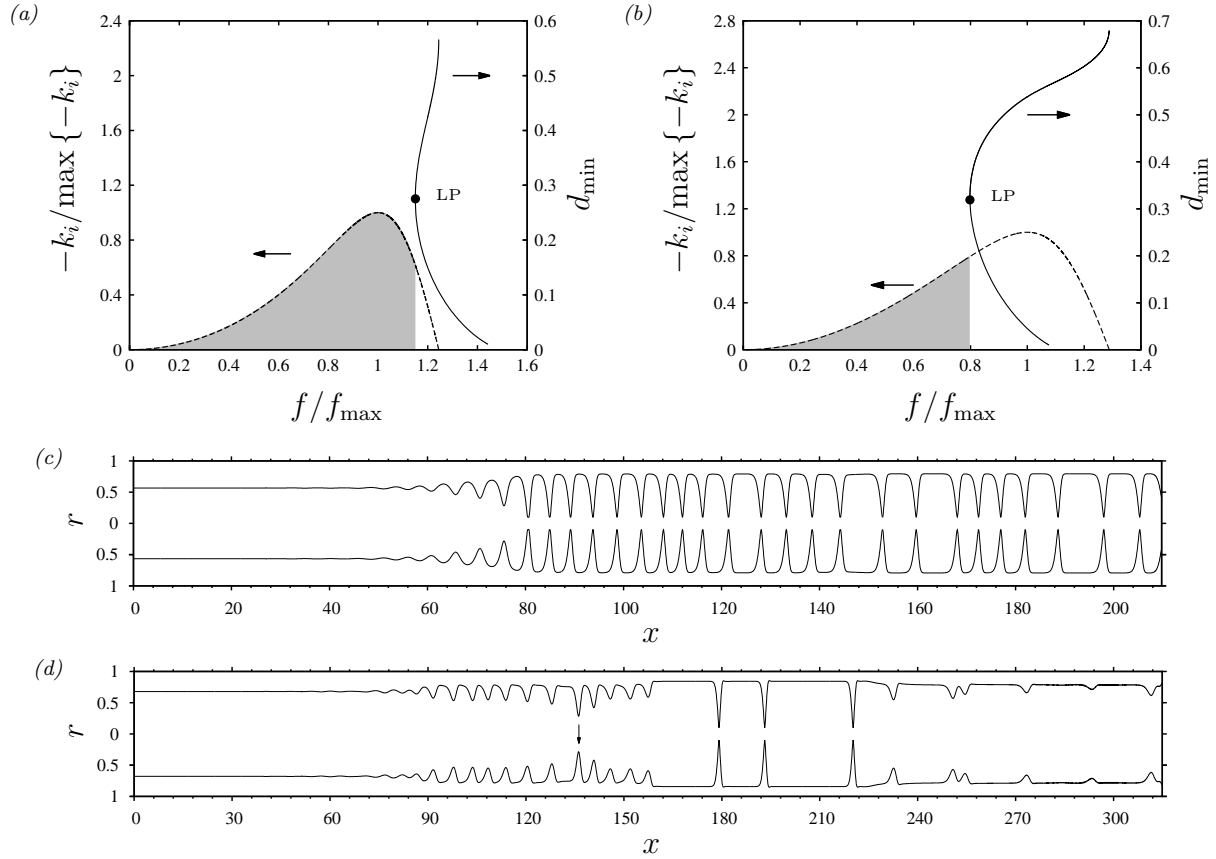


Figure 7.4: Routes to occlusion in a spatially evolving falling liquid film in contact with a quiescent air core:  $M=1$ . Computations of experimental runs 20 (panels *a,c*) and 13 (panels *b,d*) from Dao & Balakotaiah (2000). (*a,b*) TWS (right abscissae) at  $\text{Re}_1=\text{const}$ , and linear growth rate dispersion curves (left abscissae). Grey zones imply absence of TWS; (*c,d*) spatio-temporal computations on an  $L^*=1$  m domain with inlet noise (2.38) and numerical core radius limitation at  $d_{\text{crit}}/R=0.1$ ; (*a,c*) regime of certain occlusion (scenario I):  $R^*=4.765$  mm,  $\text{Ka}=0.303$  (glycerol(99%)-water and air I in table 2.1),  $\text{Re}_1=0.0497$ ,  $\epsilon_2=10^{-5}$ ; (*b,d*) regime of conditional occlusion (scenario II):  $R^*=3.175$  mm,  $\text{Ka}=3.532$  (glycerol(89%)-water and air I),  $\text{Re}_1=0.258$ ,  $\epsilon_2=10^{-5}$ . Arrow in panel *d* marks coalescence event triggering occlusion.

in panel 7.2b (asterisk on dotted curve). This limit is represented with vertical blue lines in panels 7.3b-7.3d.

Between the lower (red curve) and upper (blue curve) occlusion bounds in panel 7.2b,  $\text{Re}_{10} < \text{Re}_1 < \text{Re}_1^{\text{max}}$ , the linearly most-amplified waves possess TWS, but there is a range of low-frequency waves that do not. Occlusion in a real system thus depends on whether these waves can be accommodated, e.g. via coalescence events. In this regime, occlusion is conditional.

Panel 7.4d represents an open-domain computation (with inlet noise) that reproduces

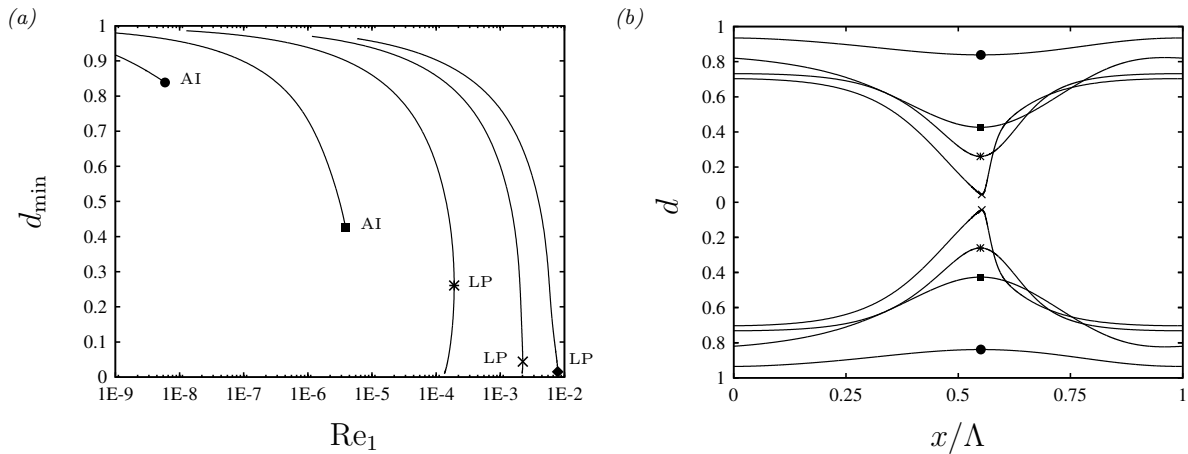


Figure 7.5: Occlusion is delayed by gravity. TWS for the fluid combination in panel 7.2a:  $Ka=3.29 \cdot 10^{-4}$ ,  $M=1$ ,  $f=f_{\max}$ . Variation of the Bond number  $Bo=\rho_1 g R^{*2}/\sigma$ . Circles:  $Bo=0.1$ ; squares:  $Bo=1$ ; asterisks:  $Bo=11.1$  (panel 7.2a); crosses:  $Bo=50$ ; diamonds:  $Bo=100$ . (a) Minimal core radius  $d_{\min}$ ; (b) surface profiles at AI and LP.

experimental run 13 from Dao & Balakotaiah (2000). Here,  $Re_1=0.258$ , which lies in the regime of conditional occlusion according to panels 7.2c and 7.4c. In this case, the linearly most-amplified waves dominate the film surface in the upper half of the tube, where the wave amplitude saturates to a safe level. However, coalescence events (marked by an arrow) generate waves of lower frequency that subsequently occlude the tube further downstream.

This is occlusion scenario II. In the current case, coalescence events result from the well known subharmonic secondary instability of high-frequency TWS, which was first discovered in plane falling liquid films (Liu & Gollub, 1993).

Panel 7.4c represents an open-domain computation reproducing experimental run 20 of Dao & Balakotaiah (2000), which, according to panel 7.4a, lies beyond the upper occlusion bound,  $Re_1 > Re_1^{\max}$ . Here, occlusion is unavoidable and results from the linearly most-amplified waves growing without bound.

We now focus on the role of different physical effects in fixing the upper occlusion bound  $Re_1^{\max}$ . Panel 7.5a represents the sensitivity of the  $f=f_{\max}$  TWS from panel 7.2a w.r.t. the Bond number  $Bo$ , which quantifies the role of gravity (7.1). For small  $Bo$  (circle and square), where the Plateau-Rayleigh instability dominates, TWS are bounded by absolute instability (AI). By contrast, for the three largest  $Bo$ , TWS are limited by non-linear effects leading to occlusion (LP). For these cases, we see that  $Re_1^{\max}$  ( $Re_1$  at the LP), is greatly delayed with increasing  $Bo$ . The underlying cause is the distortion of surface waves into an increasingly asymmetric shape, as evidenced by the film surface profiles in panel 7.5b. This mechanism, which in the cylindrical configuration favours variations of (stabilizing) axial curvature over variations in (destabilizing) azimuthal curvature, was already discussed w.r.t. planar falling liquid films in figure 5.2, and also occurs in pressure-driven core-annular flow (Frenkel *et al.*, 1987) or gravity-driven flow down a cylindrical

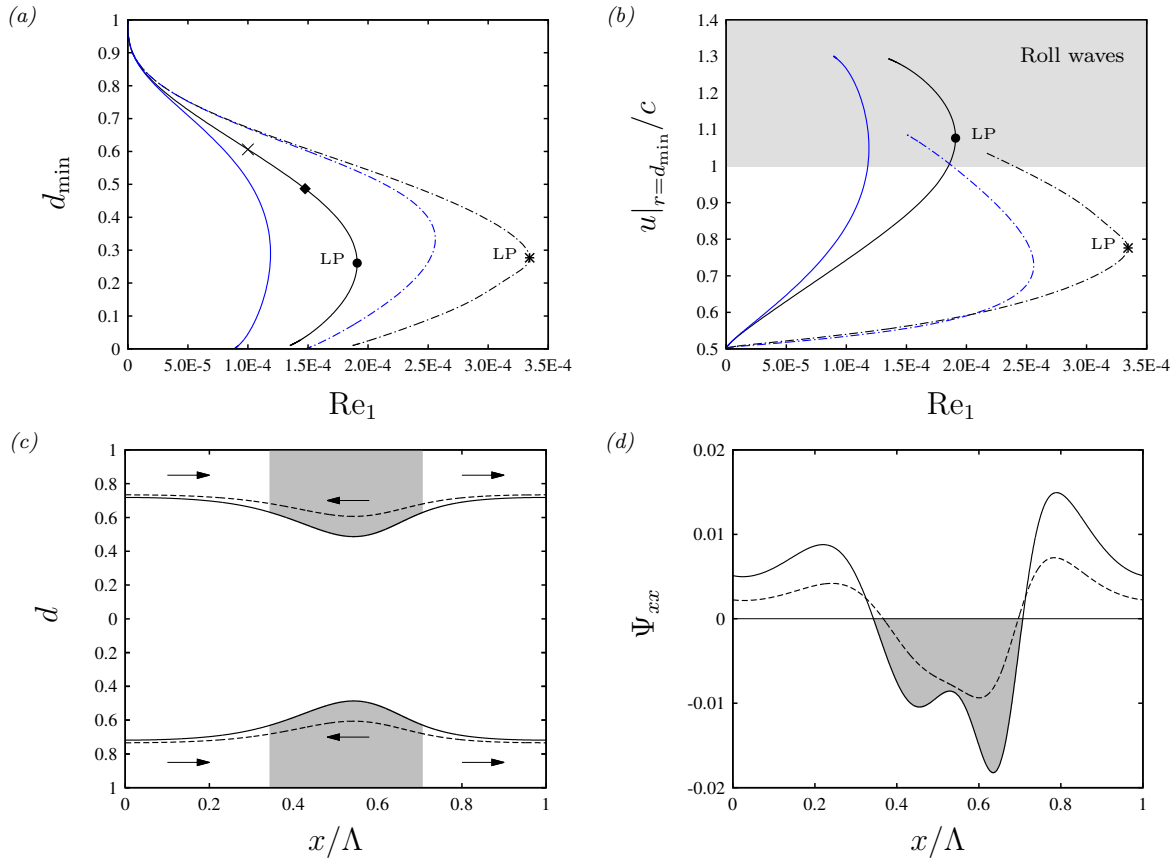


Figure 7.6: Occlusion is precipitated by axial viscous diffusion. TWS for the system in panel 7.2a:  $Ca = \mu_1 \mathcal{U} / \sigma = 0.37$ ,  $M = 1$ . Solid curves: full WRIBL model (1.48); dot-dashed:  $J_j = K_j = L_j = M_j = 0$  in (1.48) and (2.9); black curves with symbols:  $f = f_{\max}$ ; blue curves without symbols:  $\Lambda = 12.56$ . (a) Upper occlusion bounds (LP); (b) region of roll waves: interfacial fluid velocity  $u|_{r=d_{\min}}$  compared to wave speed  $c$ ; (c) surface profiles with zones of negative (grey) and positive (white)  $\Psi_{xx}$ . Solid:  $Re = 1.47 \times 10^{-4}$  (diamond in panel a); dashed:  $Re = 1.0 \times 10^{-4}$  (cross in in panel a); (d) corresponding profiles of normalized differential normal axial viscous stress  $\Psi_{xx}$  (7.2).

fibre (Quéré, 1990). The profiles in panel 7.5b correspond to the AI and LP bounds in panel 7.5a. Thus, those associated with the LP (asterisk, cross, and diamond) represent the limiting TWS in terms of occlusion. The minimal core radius  $d_{\min}$  of these solutions is still quite large, except for  $Bo = 100$ . Thus, the conjecture of Dao & Balakotaiah (2000), that occlusion sets in when the height of TWS reaches the tube axis, is only valid for large tubes ( $Bo = 100$  correspond to  $R^* = 15$  mm for the current liquid).

Figure 7.6 shows how the upper occlusion bound  $Re_1^{\max}$  is affected by axial viscous diffusion, which enters our model (1.48) via the coefficients  $J_j$ ,  $K_j$ ,  $L_j$ , and  $M_j$ . We again focus on the system from panel 7.2a, where the capillary number  $Ca = \mu_1 \mathcal{U} / \sigma = 0.37$  is not negligible and thus viscous stresses compete with surface tension. Comparing the solid



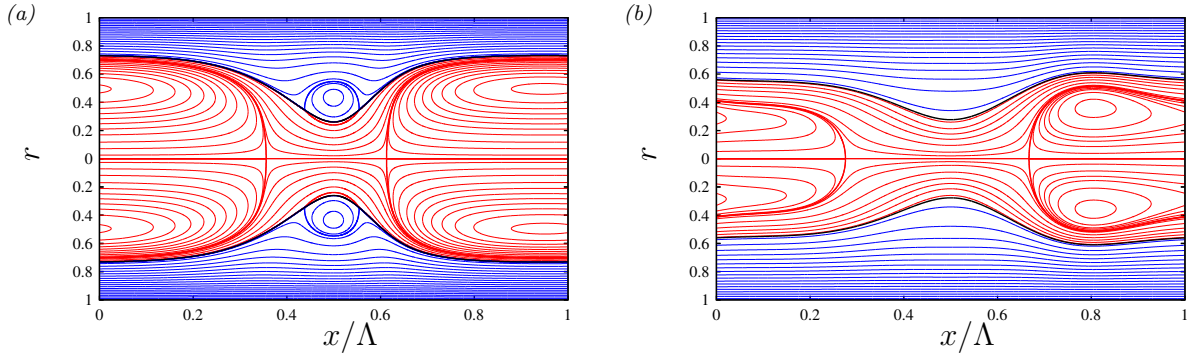


Figure 7.7: Streamlines in the wave-fixed reference frame for the marked LP in panel 7.6b. Blue lines: annular liquid film, red: core gas flow. (a) Full model (1.48). Filled circle in panel 7.6b. The wave hump contains a vortex; (b) no axial viscous diffusion:  $J_j=K_j=L_j=M_j=0$  in (1.48). Asterisk in panel 7.6b. No vortex in the wave hump.

curve marked by a filled circle in panel 7.6a with the dot-dashed curve marked by an asterisk, we find that axial viscous diffusion greatly precipitates occlusion, lowering  $\text{Re}_1^{\max}$  by roughly 70% (based on the full-model value  $\text{Re}_1^{\max}=1.9\times 10^{-4}$ ). This precipitation is due to the normal axial viscous force  $F_{xx}$  acting in the cross section of the liquid film:

$$F_{xx} = 2\pi \int_d^1 \partial_x u r dr, \quad \Psi_{xx} = \frac{\text{Fr}^2}{\text{Re}_1} \frac{\partial_x F_{xx}}{\pi(1-d^2)}, \quad (7.2)$$

which tends to make the wave hump more symmetrical. Its normalized (w.r.t. gravity) contribution  $\Psi_{xx}$  (7.2) in the differential axial force balance is plotted in panel 7.6d for the two TWS in panel 7.6c, which correspond to the open circle and asterisk in panel 7.6a. In regions where  $\Psi_{xx} < 0$ , the differential normal axial viscous force acts in upstream direction, and vice versa where  $\Psi_{xx} > 0$ . This leads to the qualitative force distribution sketched with arrows in panel 7.6c. According to this, the differential normal axial viscous force acts in upstream direction within the wave hump and in downstream direction within the residual film. This causes a compression of the wave back and an elongation of the wave front, thus counteracting the gravity-induced distortion observed in panel 7.5b.

Failing to account for axial viscous diffusion, also leads to an over-prediction of the wave celerity, and, by extension, the onset of roll waves. These TWS, which contain a vortex in the wave-fixed reference frame, correspond to the shaded region of panel 7.6b. They occur much earlier when axial viscous diffusion is accounted for, as confirmed by the streamline plots in panels 7.7a and 7.7b, which correspond to the LP in panel 7.6b.

Finally, figure 7.8 shows that, depending on the type of working liquid, axial viscous diffusion (panel 7.8a, system in panel 7.2c) or inertia (panel 7.8b, system in panel 7.2d) can determine whether TWS are bound by AI or nonlinear LPs and occlusion.

We now discuss the effect of a counter-current core gas flow on the upper occlusion bound  $\text{Re}_1^{\max}$ . We do this based on the low-viscosity silicone oil in contact with air, as considered in panel 7.2d. For all other liquids studied, the effect of the gas core is

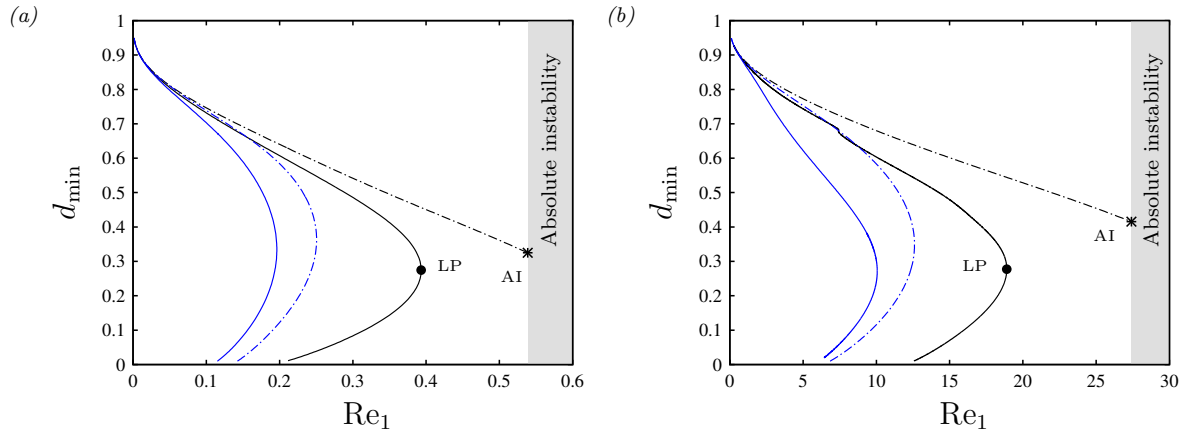


Figure 7.8: Occlusion bound (LP) versus absolute instability bound (AI). Black curves with symbols:  $f=f_{\max}$ , blue curves without symbols:  $\Lambda=12.56$ . (a) Role of axial viscous diffusion. TWS according to panel 7.2c:  $Ca=0.028$ . Solid lines: full model (1.48); dot-dashed: no axial viscous diffusion,  $J_j=K_j=L_j=M_j=0$  in (1.48) and (2.9); (b) role of inertia. TWS according to panel 7.2d:  $M=1$ . Solid: full model (1.48); dot-dashed: no inertia,  $S_i=F_{ij}=G_{ij}=0$  in (1.48) and (2.9).

negligible<sup>6</sup>, due to the large liquid viscosities. Panel 7.9a represents TWS in different limits for this system. Comparing the black solid curve marked by a filled circle ( $M=1$ ) with the dashed curve marked by an asterisk ( $Re_2=-17.27$ ), shows that a counter-current gas flow can significantly precipitate  $Re_1^{\max}$  versus the aerostatic limit. This is mainly caused by the gas pressure gradient. The role of gaseous viscous stresses is secondary, as evidenced by comparing the dot-dashed ( $\Pi_\rho=0$ ) and blue solid ( $\Pi_\mu=0$ ) curves with the full-model solution (dashed curve)<sup>7</sup>. Arrows in panel 7.9b, which represents film surface profiles for the two LP marked in panel 7.8a, indicate the action of the gas pressure gradient  $\partial_x p_2|_d$  on the liquid film. This action tends to symmetrically drain liquid toward the wave hump from the residual films on either side, thus promoting its growth.

In the conditional occlusion regime,  $Re_{10} \leq Re_1 \leq Re_1^{\max}$ , occlusion depends on what type of surface waves emerge from primary and secondary instability in a spatially evolving falling liquid film. This opens the possibility of preventing occlusion via coherent inlet forcing of non-dangerous surface waves. We validate this idea based on the open-domain computations represented in figure 7.10, which again pertain to the system in panel 7.2d. For reference, panels 7.10a and 7.10b represent computations where only inlet noise (2.38) was applied ( $\epsilon_1=0$ ,  $\epsilon_2=10^{-5}$ ) and which correspond to the regimes of impossible occlusion ( $Re_1=1.25 < Re_{10}=1.5$ ) and conditional occlusion ( $Re_{10} < Re_1=5 < Re_1^{\max}=18.9$ ), respectively. Although occlusion is precluded in panel 7.10a,  $Re_1$  is so low that surface waves are very small and thus their potential to enhance mixing is forgone. By contrast,

<sup>6</sup>At least within the parameter range accessible to our WRIBL model.

<sup>7</sup>We had also observed the dominance of gas pressure versus gaseous viscous stresses for the planar configuration (panels 6.4a and 6.5d).

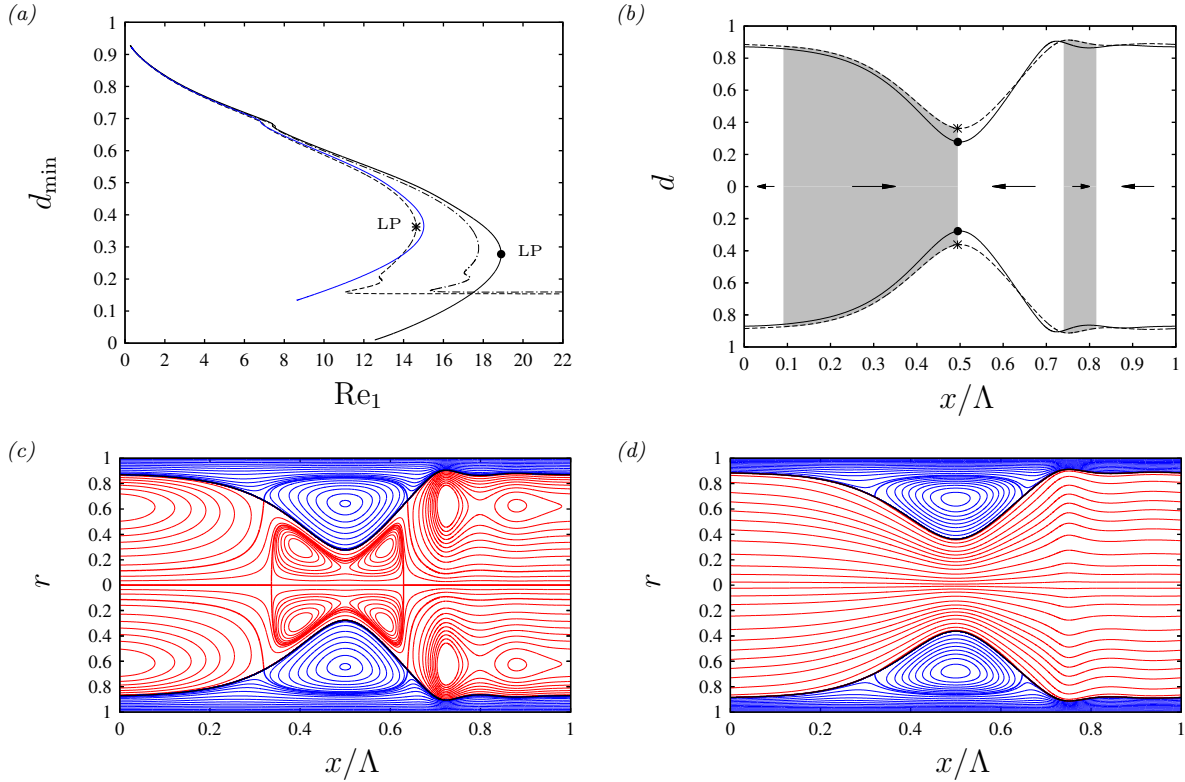


Figure 7.9: Occlusion is precipitated by a counter-current gas flow. (a) TWS according to panel 7.2d:  $f=f_{\max}$ . Solid:  $M=1$ ; dashed:  $Re_2=-17.27$ ; blue solid without symbol:  $\Pi_\mu=0$  in (1.41a) and (1.41b),  $Re_2=-17.27$ ; dot-dashed:  $\Pi_\rho=0$  in (1.41a),  $Re_2=-17.27$ ; (b) wave profiles corresponding to asterisk and filled circle in panel a. Grey/white zones between dashed profiles demarcate regions of negative/positive  $\partial_x p_2$ ; (c, d) corresponding streamlines in the wave-fixed reference frame. (c)  $M=1$ ,  $Re_1=14.6$ ,  $\Lambda=6.3$ ; (d)  $Re_2=-17.27$ ,  $Re_1=18.9$ ,  $\Lambda=5.7$ .

coherent inlet forcing via an additional monochromatic perturbation of frequency  $f$  (2.38), allows to prevent the occlusion occurring in panel 7.10b, while maintaining waves of considerable amplitude. This is shown in panel 7.10c, where we have used  $\epsilon_1=0.1$ ,  $\epsilon_2=10^{-5}$ , and  $f=0.5 f_{\max}$ .

**Impact of the work and relation to the current state of the art** Our paper Dietze *et al.* (2020) has been cited 5 times according to *Web of Science*.

By accounting for axial viscous diffusion in our WRIBL model (1.48), we were able to reproduce numerically for the first time the occlusion experiments of Camassa *et al.* (2014), via our open-domain computations (figure 2.20). Further, we have obtained a reasonable prediction of the experimental occlusion bound based on the LP of the linearly most-amplified TWS in panel 7.2a (occlusion scenario I). That approach yields  $Re_1^{\max}=1.91 \times 10^{-4}$ , whereas occlusion in the experiments was observed near the upper

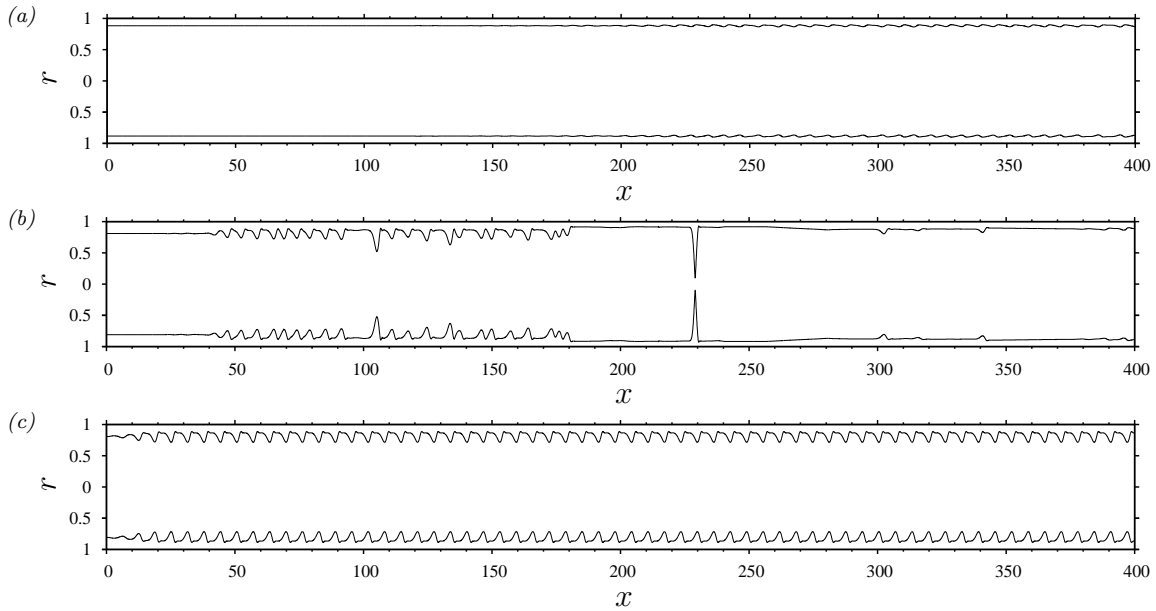


Figure 7.10: Preventing occlusion via coherent inlet forcing. Open-domain computations for the system in panel 7.2d:  $Ka=121.4$ ,  $Re_{10}=1.5$ ,  $Re_1^{\max}=18.9$ . Same level of inlet noise (2.38) for all computations:  $\epsilon_2=10^{-5}$ . (a) Regime of impossible occlusion:  $Re_1=1.25 < Re_{10}$ ,  $\epsilon_1=0$ ; (b) regime of conditional occlusion:  $Re_1=5$ ,  $\epsilon_1=0$ ; (c) additional coherent inlet forcing (2.38):  $Re_1=5$ ,  $f=0.5$   $f_{\max}=1.27$ ,  $\epsilon_1=0.1$ .

bound of the interval  $Re_1 \in [1.63 - 2.3] \times 10^{-4}$ . Further, our analysis has shown that the occlusion bound may strongly depend on what type of wave dynamics unfold in a real system (occlusion scenario II). In particular, whether the tube is long enough to accommodate the dynamics required for producing dangerous waves.

In the case of occlusion scenario I, we have shown in section 2.3.2 (figure 2.21) that TPS at  $f=f_{\max}$  provide an accurate prediction of the liquid plugs forming in a spatially evolving experiment (Camassa *et al.*, 2014), thus significantly reducing the computational cost versus open-domain WRIBL computations and DNS. These results are the subject of a new manuscript currently in preparation.

Romano *et al.* (2019); Camassa *et al.* (2021); Ogrosky (2021b); Romano *et al.* (2021), and Ogrosky (2021a) have acknowledged our contributions to predicting plug formation in annular liquid films within cylindrical tubes. Camassa *et al.* (2021) extended our work by a detailed study of the stability of nonlinear TWS. Ogrosky (2021b) extended our work by accounting for a surface-tension-reducing insoluble surfactant, and found that this effect can precipitate occlusion. Most recently, Ogrosky (2021a) developed a three-layer liquid-liquid-gas asymptotic model of core-annular flow, in order to represent the serous-mucus bilayer associated with mucociliary clearance in the pulmonary airways. The author acknowledged our finding that axial viscous diffusion strongly precipitates the occlusion onset for high-viscosity liquids (figure 7.6), as motivation for developing his

model up to second order in the long-wave parameter. Further, the author confirmed the underlying mechanism for this precipitation, which we have explained in panels 7.6c and 7.6d.

## 7.2 Mucus films in pulmonary capillaries

We now consider the configuration in panel 1.3b and focus on the model system studied by Halpern & Grotberg (2003), which is representative of the terminal bronchioles (panel 7.1d), i.e. a film of Newtonian model mucus (mucus IV in table 2.1) in contact with air, within a cylindrical tube of radius  $R^*=0.3$  mm, where gravity is negligible ( $Fr^{-1}=0$ ).

Panel 7.11a represents time traces of the minimal core radius  $d_{\min}$ , as obtained from transient periodic computations with our cylindrical WRIBL model (1.48), for different values of the liquid volume  $V_1$ , which was controlled through the initial mean core radius  $d_0$ , at fixed perturbation amplitude  $\epsilon_I d_0=0.0013$  (2.41) and fixed wavelength  $\Lambda=7.73$ . In all our computations,  $d_0$  is inferior to the unduloid threshold  $d_0^{\text{crit}}=0.88$  (corresponding to the LP at  $V_1^{\text{crit}}=1.73$  in panel 2.22a), and thus occlusion is inevitable ( $d_{\min} \rightarrow 0$ ). However, at  $d_0=0.87$  ( $V_1/\pi/R^3=1.88$ ), we observe a drastic increase in the occlusion time (rightmost curve with symbols in panel 7.11a).

This delay of occlusion is caused by a slowed drainage of liquid from the film trough forming as a result of the Plateau-Rayleigh instability. Panel 7.11b shows a blown-up view of the film surface around this trough, as it approaches the tube wall under the driving effect of the primary instability. We see that the film surface eventually buckles, sustaining further drainage via an additional outward capillary pressure gradient in the face of increasing viscous drag at the newly-formed secondary troughs. After this, growth of the deformation of the liquid film evolves degressively (red asterisk in panel 7.11a). Thus, in theory, the liquid film would require infinitely long to attain static equilibrium. Indeed, because  $V_1/\pi/R^3 < \Lambda - \frac{4}{3} = 6.4$ , there is not enough liquid to occlude the tube without rupturing the residual film lining the tube wall. This implies a complete draining of the liquid trough region in panel 7.11b, and thus a divergence of the viscous drag.

However, we do eventually observe occlusion also for this case ( $d_0=0.87$ ), albeit via a different mechanism<sup>8</sup>. As shown in panel 7.11c, occlusion is triggered by a spontaneous (leftward) sliding motion of the liquid film (from the red dashed to the solid blue curve), which re-invigorates growth of the primary instability. The logarithmic film thickness profiles  $h(x)$  in panel 7.11d allow to magnify what happens in the region of the buckled film trough during this process. According to these profiles, the loss of symmetry is associated with a thickening of the right secondary trough and a thinning of the left one. This leads to an increased overall draining rate versus a purely symmetrical evolution scenario. A detailed discussion of this effect and the secondary instability underlying the spontaneous sliding motion is provided in section 8.1, where we study the related problem

---

<sup>8</sup>It should be possible to find a universal criterion for the sliding-induced occlusion in terms of  $d_0$ , assuming  $\Lambda=\Lambda_{\max}$ .

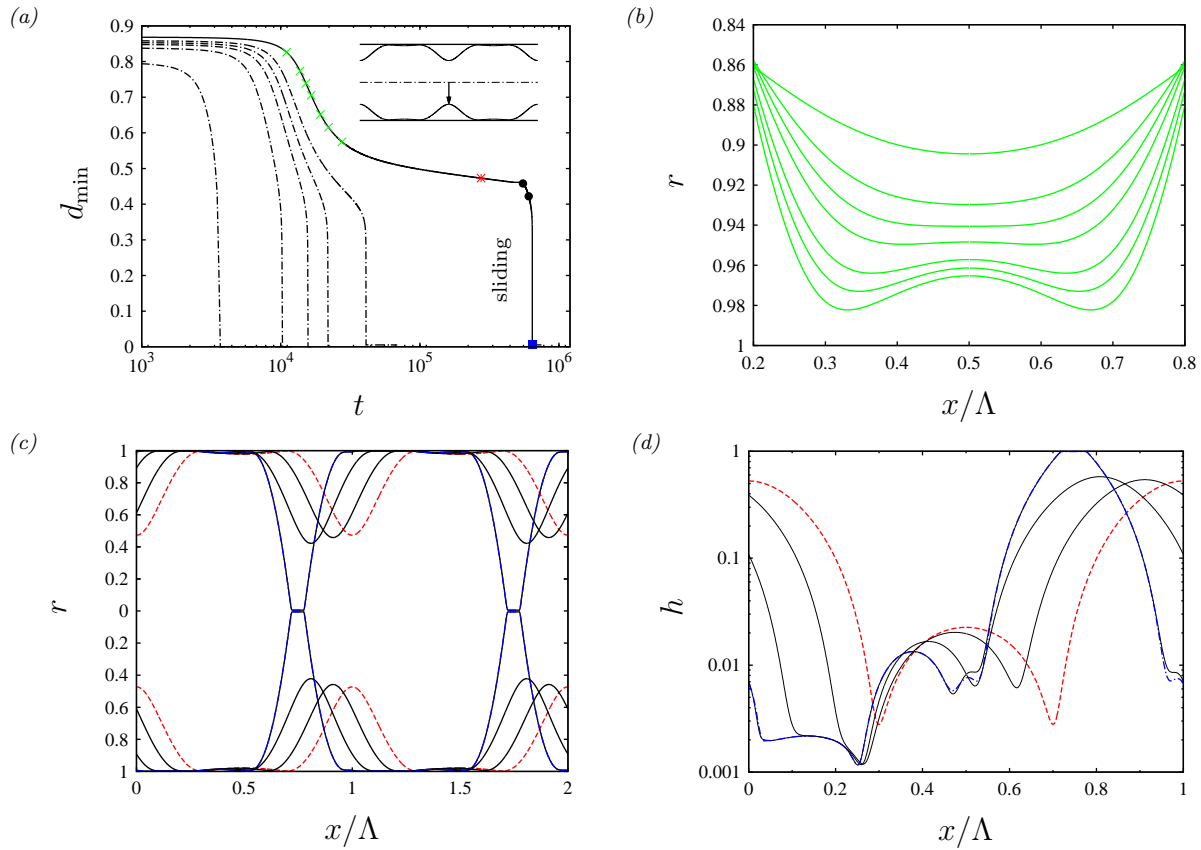


Figure 7.11: Liquid film of Newtonian model mucus in contact with air within a terminal bronchiole (Halpern & Grotberg, 2003):  $La=\sigma H^* \rho_1 / \mu_1^2=91.8$  (mucus IV and air I in table 2.1),  $R^*=0.3$  mm,  $q_{\text{tot}}=0$ ,  $Fr^{-1}=0$ . Transient periodic WRIBL computations:  $\Lambda=7.73$ ,  $\epsilon_I d_0=0.0013$  (2.41). Delay of occlusion upon approaching the unduloid threshold  $d_0^{\text{crit}}=0.88$ . (a) Time traces of the minimal core radius  $d_{\min}$ . From left to right:  $d_0=0.80$ , 0.84, 0.85, 0.855, 0.86, and 0.87; (b) buckling of the film trough (green crosses in panel a); (c) long-time occlusion triggered by spontaneous sliding:  $d_0=0.87$ . Symbols between red asterisk and blue square in panel a; (d) logarithmic profiles of film thickness  $h$  corresponding to panel c.

of a planar liquid film suspended from a ceiling subject to the Rayleigh-Taylor instability.

The spontaneous sliding motion observed in panel 7.11c also affects the core gas flow. Figure 7.12, which represents streamlines in the wall-fixed reference frame, shows that the two initial large toroidal vortices associated with symmetrical growth (panel 7.12a) are broken up into smaller vortices, once the sliding sets in (panel 7.12b).

The computations in figures 7.11 and 7.12 correspond to zero net flow ( $q_{\text{tot}}=0$ ). It is more realistic to consider a time-varying gas flow rate  $q_2$ , which mimics the breathing cycle (panel 7.13b). We implement this numerically by varying  $q_{\text{tot}}$  according to:

$$q_{\text{tot}} = q_1 + \Pi_u q_2 = 2\pi f L_T (\pi R^3) \sin(2\pi f t), \quad (7.3)$$

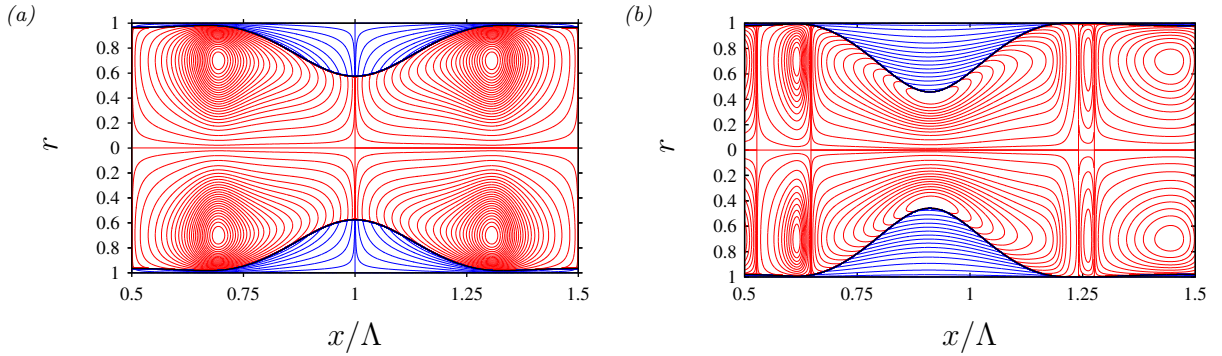


Figure 7.12: Streamlines in the wall-fixed reference frame for the sliding solution in panel 7.11a:  $d_0=0.87$ . (a) Symmetrical growth phase: last green cross in panel 7.11a, (b) after sliding onset: first black circle in panel 7.11a.

where  $f=4 \times 10^{-5}$  ( $f^*=\frac{1}{3}$  Hz) and  $L_T=\Lambda=7.73$  denote the breathing frequency and stroke length, respectively, for which we have chosen the same physiologically-relevant values as Halpern & Grotberg (2003). Because  $\Pi_\mu \ll 1$ , (7.3) amounts to imposing  $q_2$ , as evidenced by panel 7.13b, where the time traces of  $q_{\text{tot}}$  (crosses) and  $q_2$  (solid line) coincide.

Panel 7.13b compares the sliding onset for different limiting cases of the  $d_0=0.87$  computation in panel 7.11a via time traces of the axial position  $x_c$ :

$$x_c = \frac{\int_0^\Lambda \pi (1 - d^2) x dx}{\int_0^\Lambda \pi (1 - d^2) dx}, \quad (7.4)$$

of the liquid film's center of mass. The three black curves with asterisks in panel 7.13a correspond to the zero-net-flow limit  $q_{\text{tot}}=0$ . Comparing the solid (full model) and dashed ( $J_i=K_i=L_i=M_i=0$ ) curves among these, we may conclude that axial viscous diffusion greatly precipitates the sliding onset. The same is true when applying a weak amount of residual gravity (dot dashed line), as may be encountered in microgravity environments in the form of g-jitter. Gravity breaks the symmetry of the primary flow and thus reinforces the secondary instability underlying the sliding phenomenon. It also imposes a preferential direction for the sliding motion, in contrast to the gravity-free configuration, where the direction is arbitrary and thus depends on the numerical noise generated by the computation.

An oscillating core gas flow (7.3) mimicking the breathing cycle according to panel 7.13b, greatly precipitates the sliding and occlusion onsets (red line with filled circle in panel 7.13a). In this case, the asymmetrical perturbation introduced by the gas flow is quite strong, as evidenced by figure 7.14, which represents streamlines in the wall-fixed reference frame for characteristic time points during the breathing cycle (filled circles in panel 7.13b). Prior to the sliding event (panels 7.14a and 7.14b), the gas flow oscillation produces separation zones on alternating sides of the liquid hump, and this quickly leads to a symmetry loss also in the liquid film (panels 7.14c and 7.14d).

In this particular situation, the oscillatory air flow mimicking the breathing cycle increases the risk of airway occlusion. In contrast, when the liquid film is thicker and

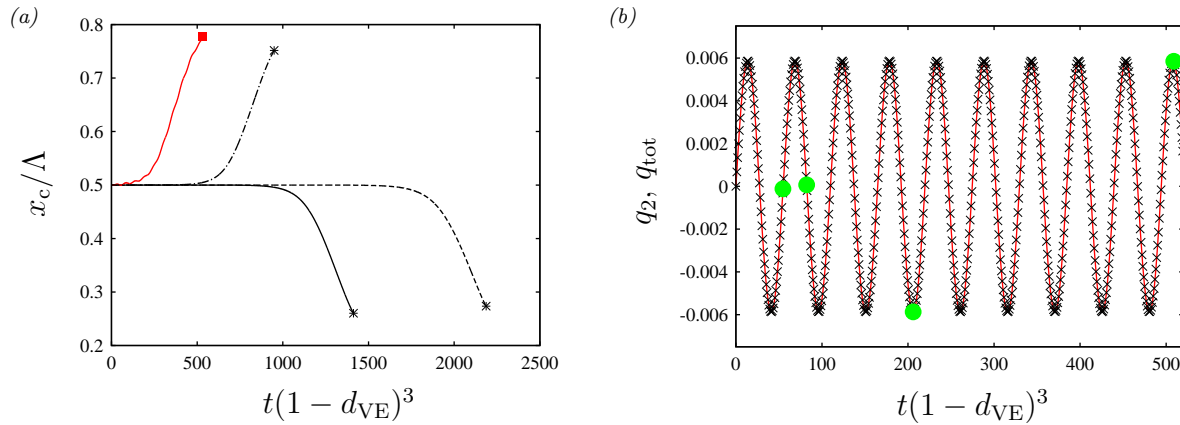


Figure 7.13: Effect of axial viscous diffusion, gravity, and breathing on the sliding onset of a mucus film in contact with air. Parameters according to the sliding solution in panel 7.11a:  $d_0=0.87$ ,  $q_{tot}=0$ ,  $Fr^{-1}=0$ . Time is normalized based on the volume-equivalent core radius  $d_{VE}=(1 - V_1/\Lambda/\pi/R^3)^{1/2}$ . (a) Axial position of the center of liquid mass  $x_c$  (7.4). Solid black line with asterisk: full model (1.48), dashed:  $J_j=K_j=L_j=M_j=0$  in (1.48), dot-dashed:  $Fr^{-1}=10^{-3} \times Fr_0^{-1}$  with  $Fr_0^{-1}=\sigma/\mu_1/\sqrt{gR^*}$ , red solid with square: oscillating  $q_{tot}(t)$  according to panel b; (b) time variation of  $q_{tot}$  (crosses) and  $q_2$  (solid line) mimicking the breathing cycle according to (7.3):  $f^*=\frac{1}{3}$  Hz,  $L_T=7.73$ .

occlusion is not thwarted by viscous drag in the draining residual film, high-frequency gas flow oscillations, such as used for the treatment of obstructive airway disease with chest wall vibrators, can delay or prevent occlusion (Halpern & Grotberg, 2003).

**Impact of the work and relation to the current state of the art** Our paper Dietze & Ruyer-Quil (2015) has been cited 26 times according to *Web of Science*. Many of these citations acknowledge our contribution to the modelling of annular liquid films and core-annular flows, as discussed at the end of section 1.2.

From a physical point of view, our work has been acknowledged w.r.t plug formation in the pulmonary airways (Magniez *et al.*, 2016; Mamba *et al.*, 2018; Romano *et al.*, 2019, 2021; Erken *et al.*, 2022) or the occlusion of micropores (Beltrame, 2018).

Further, Xu & Jensen (2017) have shown that wall roughness can thwart the sliding phenomenon observed in panel 7.11c, leading to trapped states, where the liquid film resists translation in the face of a gas shear stress or pressure gradient. Moreover, Wang (2016) showed that carefully selected wall corrugations can prevent plug formation in core annular liquid-liquid systems with zero base flow. Erken *et al.* (2022) have noted that the extreme thinness of the residual film separating two sliding humps is still prohibitive in terms of resolving this phenomenon through DNS, which underlines the usefulness of our WRIBL model.



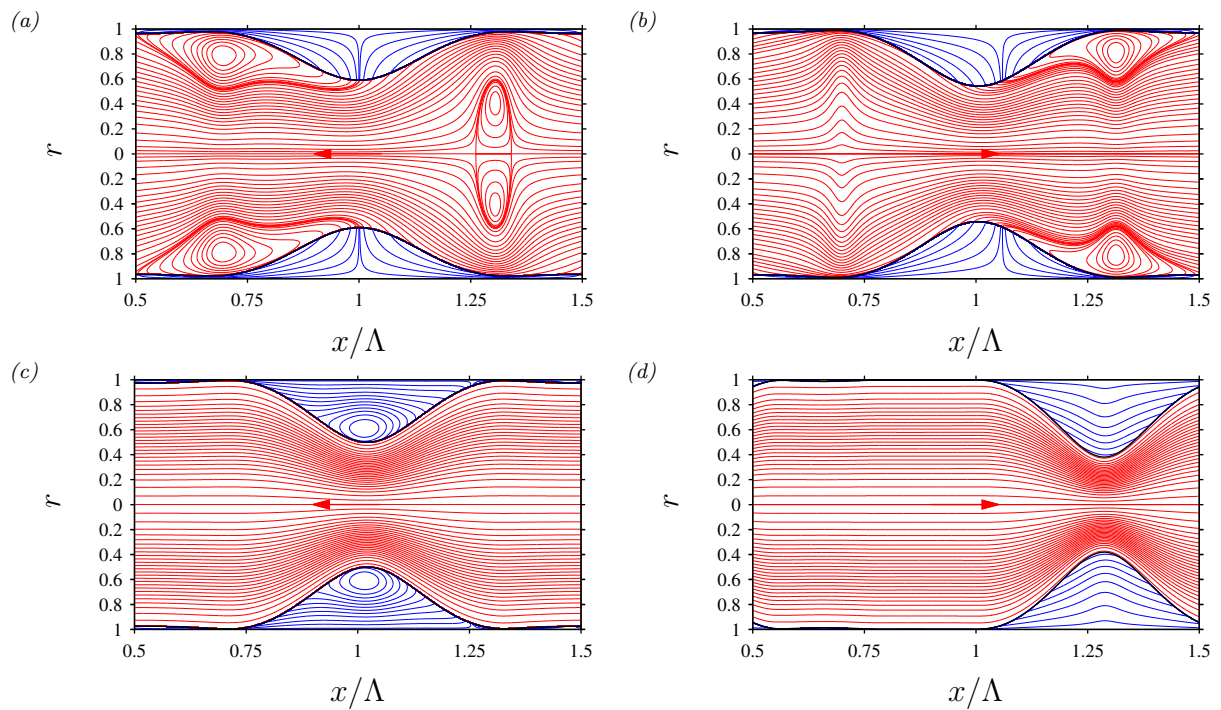


Figure 7.14: Sliding motion of a mucus film triggered by breathing (red line with square in panel 7.13a). Streamlines in the wall-fixed reference frame for selected times during the breathing cycle (green filled circles in panel 7.13b). (a)  $t(1 - d_{VE})^3 = 54.8$ ; (b)  $t(1 - d_{VE})^3 = 82.4$ ; (c)  $t(1 - d_{VE})^3 = 206.0$ ; (d)  $t(1 - d_{VE})^3 = 508.8$ .

# Falling liquid films in narrow tubes: occlusion scenarios

Georg F. Dietze<sup>1,†</sup>, G. Lavalley<sup>2,‡</sup> and C. Ruyer-Quil<sup>3</sup>

<sup>1</sup>Université Paris-Saclay, CNRS, FAST, 91405 Orsay, France

<sup>2</sup>Université Paris-Saclay, CNRS, LIMSI, 91405 Orsay, France

<sup>3</sup>Université Savoie Mont Blanc, CNRS, LOCIE, 73376 Le Bourget du Lac, France

(Received 29 October 2019; revised 26 February 2020; accepted 28 March 2020)

We study a gravity-driven wavy liquid film falling down the inner surface of a narrow cylindrical tube in the presence of an active core gas flow. We employ the model of Dietze and Ruyer-Quil (*J. Fluid Mech.*, vol. 762, 2015, pp. 68–109) to investigate the role of surface waves in the occlusion of the tube. We consider four real working liquids and reproduce several experiments from the literature, focusing on conditions where the Bond number is greater or equal to unity. We prove that occlusion is triggered by spatially growing surface waves beyond the limit of saturated travelling-wave solutions, and delimit three possible regimes for a naturally evolving wavy film: (i) certain occlusion, when the liquid Reynolds number is greater than the limit of the spatially most amplified travelling waves. Occlusion is caused by surface waves emerging from linear wave selection (scenario I); (ii) conditional occlusion, when the most amplified waves possess travelling states but longer waves do not. Occlusion is triggered by secondary instability, generating long waves through nonlinear coarsening dynamics (scenario II); and (iii) impossible occlusion, when travelling waves always exist, no matter how great their wavelength. We show that certain occlusion is delayed by gravity and precipitated by a counter-current gas flow, axial viscous diffusion (high-viscosity liquids) and inertia (low-viscosity liquids). The latter two effects are also found to determine whether the occlusion mechanism is dictated by loss of travelling-wave solutions or absolute instability. Finally, we show that occlusion can be prevented through coherent inlet forcing. As a side benefit, we introduce an augmented version of our model based on a localized additional force term that allows representing stable travelling liquid pseudo-plugs.

**Key words:** thin films, capillary flows

---

## 1. Introduction

We consider the configuration in figure 1, a thin liquid film falling down the inner surface of a vertical cylindrical tube of radius  $R^*$  under the action of the gravitational

<sup>†</sup> Email address for correspondence: [dietze@fast.u-psud.fr](mailto:dietze@fast.u-psud.fr)

<sup>‡</sup> Present address: Institut de Mécanique des Fluides de Toulouse (IMFT) - Univ. de Toulouse, CNRS-INPT-UPS, Toulouse, France

## Films in narrow tubes

Georg F. Dietze<sup>1,†</sup> and Christian Ruyer-Quil<sup>2,3</sup>

<sup>1</sup>Univ. Paris-Sud, CNRS, Lab. FAST, Bât. 502, Campus Univ., Orsay, F-91405, France

<sup>2</sup>Univ. Savoie, CNRS, LOCIE, F-73000 Chambéry, France

<sup>3</sup>Institut Universitaire de France, France

(Received 29 July 2014; revised 3 November 2014; accepted 4 November 2014)

We consider the axisymmetric arrangement of an annular liquid film, coating the inner surface of a narrow cylindrical tube, in interaction with an active core fluid. We introduce a low-dimensional model based on the two-phase weighted residual integral boundary layer (WRIBL) formalism (Dietze & Ruyer-Quil, *J. Fluid Mech.*, vol. 722, 2013, pp. 348–393) which is able to capture the long-wave instabilities characterizing such flows. Our model improves upon existing works by fully representing interfacial coupling and accounting for inertia as well as streamwise viscous diffusion in both phases. We apply this model to gravity-free liquid-film/core-fluid arrangements in narrow capillaries with specific attention to the dynamics leading to flooding, i.e. when the liquid film drains into large-amplitude collars that occlude the tube cross-section. We do this against the background of linear stability calculations and nonlinear two-phase direct numerical simulations (DNS). Due to the improvements of our model, we have found a number of novel/salient physical features of these flows. First, we show that it is essential to account for inertia and full interphase coupling to capture the temporal evolution of flooding for fluid combinations that are not dominated by viscosity, e.g. water/air and water/silicone oil. Second, we elucidate a viscous-blocking mechanism which drastically delays flooding in thin films that are too thick to form unduloids. This mechanism involves buckling of the residual film between two liquid collars, generating two very pronounced film troughs where viscous dissipation is drastically increased and growth effectively arrested. Only at very long times does breaking of symmetry in this region (due to small perturbations) initiate a sliding motion of the liquid film similar to observations by Lister *et al.* (*J. Fluid Mech.*, vol. 552, 2006, pp. 311–343) in thin non-flooding films. This kickstarts the growth of liquid collars anew and ultimately leads to flooding. We show that streamwise viscous diffusion is essential to this mechanism. Low-frequency core-flow oscillations, such as occur in human pulmonary capillaries, are found to set off this sliding-induced flooding mechanism much earlier.

**Key words:** interfacial flows (free surface), low-dimensional models, thin films

### 1. Introduction

The axisymmetric flow of an annular liquid film/fluid core within a cylindrical tube, as shown in figure 1, can be viewed in different limits. In the simplest case,

† Email address for correspondence: [dietze@fast.u-psud.fr](mailto:dietze@fast.u-psud.fr)



# Chapter 8

## Other thin film flows

### 8.1 Films subject to the Rayleigh-Taylor instability

In section 7.2, we have observed the spontaneous sliding motion of a mucus film that drains into liquid collars due to the Plateau-Rayleigh instability (panels 7.11c and 7.11d). This phenomenon is intriguing, because it occurs even though the initial condition is symmetrical, suggesting the existence of a symmetry-breaking secondary instability. In Dietze *et al.* (2018), we studied this phenomenon based on the related configuration of a fluid film subject to the Rayleigh-Taylor instability (figure 1.4), e.g. a liquid film suspended from a ceiling draining into drops (panel 1.4a), or a vapour film underneath a liquid layer forming blisters (panel 1.4b). Spontaneous sliding had been observed by Lister *et al.* (2006a) in a liquid film underneath a sedimenting liquid drop, and by Glasner (2007) in a liquid film suspended from a ceiling. Based on their observations, Lister *et al.* (2006a) suggested the existence of an instability. Other studies had demonstrated how easily liquid drops slide when the initial film is subjected to an asymmetric perturbation (Yiantsios & Higgins, 1989; Lister *et al.*, 2006b; Xu & Jensen, 2017).

In Dietze *et al.* (2018), we applied linear stability analysis to elucidate the cause of the spontaneous sliding. Thereby, we focussed mainly on the configuration of liquid drops forming on a suspended liquid film (panel 8.1a). Sliding sets in before these drops reach a static nonlinear equilibrium. To deal with this transient behaviour in our stability analysis, we employed two different approaches. First, a frozen-time approach, where the (perfectly-symmetrical) nonlinear base state is assumed to evolve much slower than the instability. This approach is limited to the late stage of the draining of the liquid film. Second, a transient analysis, where the time evolution of the nonlinear base state is accounted for in the linear stability problem (Schmid, 2007; Balestra *et al.*, 2016).

Our analyses showed that the draining liquid film is indeed subject to a secondary instability with an asymmetric most-amplified mode. This mode is present as soon as the thin residual film separating two drops has buckled, forming two extremely thin secondary troughs through which the remaining liquid must drain. However, the loss of symmetry becomes macroscopically visible only after the nonlinear growth of the base state has slowed sufficiently. Depending on the considered time horizon, the most-amplified mode

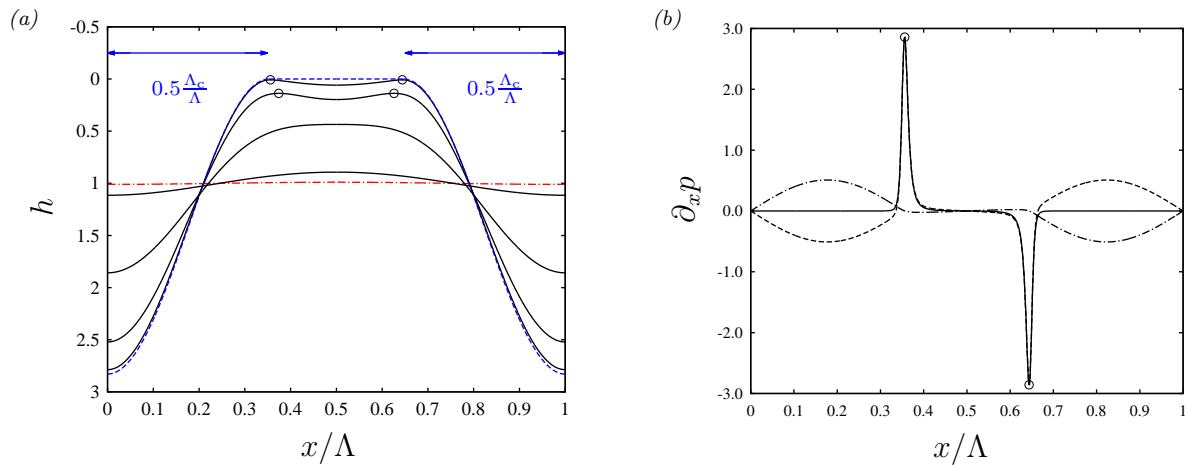


Figure 8.1: Suspended liquid film (panel 1.4a) draining into drops, as a result of the Rayleigh-Taylor instability:  $h_0^*=1$  mm,  $\text{Bo}=0.134$ ,  $\Lambda=\sqrt{2}\Lambda_c$ ,  $\Lambda_c=2\pi/\sqrt{\text{Bo}}$ . Computation based on the lubrication model (1.68) using symmetry conditions on a domain of length  $\Lambda/2$  (data mirrored onto full-wavelength domain here). (a) Film profiles (black solid lines) evolving from the initial condition (red dot-dashed line) to the lowest-energy static equilibrium state (dashed blue line):  $t=427, 641, 1068$ , and  $6.4 \times 10^4$ ; (b) profiles of the pressure gradient at  $t=6.4 \times 10^4$ . Solid line: full pressure gradient (8.1); dot-dashed: gravity-induced contribution  $\partial_x p|_g$ ; dashed: capillary contribution  $\partial_x p|_\sigma$ .

evolves from an odd pulse-like perturbation localized at the secondary troughs to a perturbation constituting a concerted translation of the entire liquid film. We have elucidated the underlying positive feedback mechanism, which is linked to the secondary troughs. From an energetic point of view, the instability can be understood by considering the viscous drag at the secondary troughs. If the left trough is slightly thinner and the right one slightly thicker, liquid drains preferentially to the right and the total draining rate is increased. Thus, an asymmetric evolution is the energetically favourable route toward the lower-energy final state.

Further, we demonstrated in Dietze *et al.* (2018) that the sliding instability also occurs in a thin vapour film underneath a liquid layer, assuming physical properties typically encountered underneath Leidenfrost drops (Burton *et al.*, 2012). Such drops are known to move autonomously on horizontal surfaces (Ma *et al.*, 2015; Bouillant *et al.*, 2018). Finally, we found that additional thermal Marangoni stresses can entirely suppress the sliding instability in suspended liquid films, by fundamentally modifying the draining mechanism at the troughs. In that case, the film undergoes a cascade of buckling events instead of sliding, similar to the traditional Marangoni problem (Boos & Thess, 1999; Oron, 2000).

We start with the suspended water film (panel 1.4a), for which panel 8.1a represents the time evolution from a weakly perturbed initial state (dot-dashed red line) toward static equilibrium (blue line). The final state consists of suspended drops separated by a portion of dry substrate, the width of the drops corresponding to the cut-off wavelength of

the Rayleigh-Taylor instability<sup>1</sup>  $\Lambda_c = 2\pi/\sqrt{\text{Bo}}$ . Our computation underlying panel 8.1a was performed with the lubrication model (1.68) on a domain of width  $\Lambda = \sqrt{2}\Lambda_c$ , i.e. the most-amplified wavelength in the passive-gas limit ( $\Pi_\mu = \Pi_\rho = 0$ ), using symmetry conditions. As a result, sliding is precluded and we obtain a perfectly symmetrical time-evolving nonlinear base state to which we apply our stability analysis.

To reach static equilibrium, the liquid between two drops must drain through an increasingly thin film, and this eventually leads to a buckling of the liquid-gas interface (panel 8.1a), similar to the annular mucus film in panel 7.11b. In this buckled state, drainage is driven by the capillary contribution  $\partial_x p|_\sigma$  to the total pressure gradient  $\partial_x p$ :

$$\partial_x p = \underbrace{-\partial_x h}_{\partial_x p|_g} - \underbrace{\frac{1}{\text{Bo}} \partial_{xxx} h}_{-\partial_x p|_\sigma}. \quad (8.1)$$

Panel 8.1b, which corresponds to the latest solid profile  $h(x)$  in panel 8.1a, shows that this contribution (dashed line) is much larger than the hydrostatic contribution  $\partial_x p|_g$  (dot dashed line) in the region of the secondary troughs (marked by open circles), where we observe large spikes of  $\partial_x p$  (solid curve) that are linked to strong variations of surface curvature. By contrast, the pressure gradient in the liquid drops is all but zero, meaning that they have virtually attained their final state. This state is neutrally stable and thus it can be translated with minimal energy input. Both of these features are necessary ingredients of the sliding instability.

Sliding is observed in computations with periodic boundary conditions, which do not force symmetry. Panel 8.2a represents time traces of the location  $x_{\min}$  of the film height minimum  $h_{\min}$  (left secondary trough after the buckling event), as obtained from two such computations for the suspended water film from figure 8.1. The solid line corresponds to the lubrication model (1.68), which we will rely on here, and the dashed line corresponds to our full model (1.64), which incorporates inertia. Both computations reach the same quasi-steady state before the onset of sliding, only that the full-model computation produces several prior oscillations<sup>2</sup>. The kinematics of the sliding phenomenon comprise four stages: rapid initial growth of the Rayleigh-Taylor instability (panel 8.2c), buckling (panel 8.2d), quasi-steady evolution (panel 8.2e), and, ultimately, loss of symmetry and sliding (panel 8.2f). The onset of the sliding motion is accompanied by a thickening of the trailing secondary trough and a thinning of the leading one (panel 8.2f).

We apply our frozen-time stability analysis (2.13) to the fully-symmetric base state obtained from our computation in panel 8.1 at time  $t = 7 \times 10^4$ , which lies in the quasi-steady regime. Panel 8.3a confronts the corresponding surface profile  $h(x)$  (solid line) with the profile obtained from our periodic computation (crosses) in panel 8.2e. The difference between these two profiles is plotted with asterisks in panel 8.3b. As the periodic computation has just lost symmetry, this profile is representative of the most-amplified linear perturbation. The solid blue and black lines in panel 8.3b represent the

<sup>1</sup>We remind the reader that the scaling from (1.66) is used for the Rayleigh-Taylor problem.

<sup>2</sup>As shown in panel 8.2b, the full-model data are in good agreement with our own DNS using **Gerris** (compare solid red and dashed black curves).

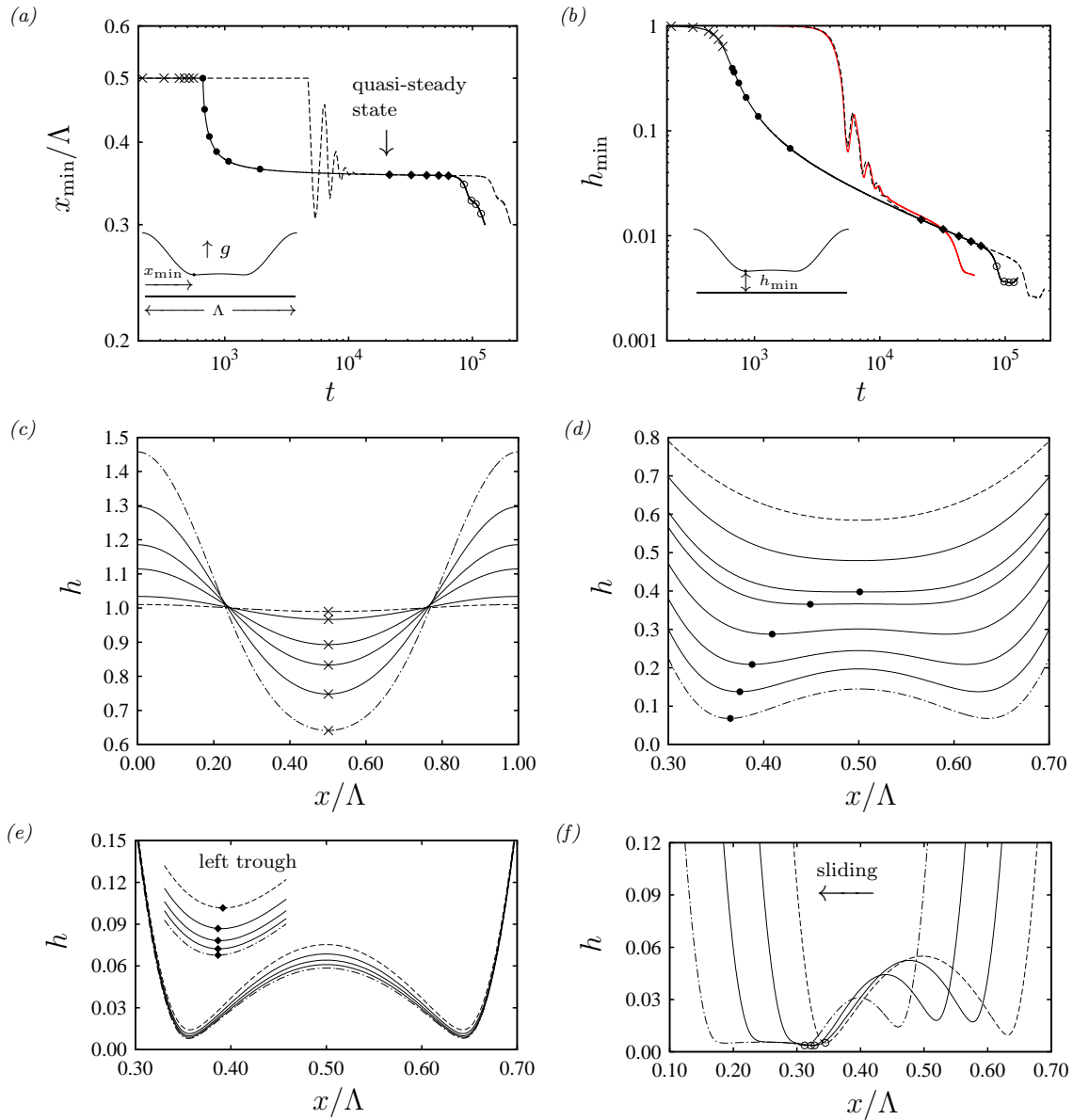


Figure 8.2: Spontaneous sliding of the water film from figure 8.1:  $h_0^* = 1$  mm,  $\text{Bo} = 0.134$ ,  $\Lambda = \sqrt{2}\Lambda_c$ ,  $\Lambda_c = 2\pi/\sqrt{\text{Bo}}$ . Computations using periodicity conditions on a domain of length  $\Lambda$ . (a,b) Position and height of film trough (left secondary trough after buckling). Dashed lines: full model (1.64), solid: (1.68), red solid: DNS with **Gerris**; (c) film surface profiles during progressive growth stage (crosses in panels a and b); (d) flattening and buckling (filled circles); (e) quasi-steady two-trough shape (diamonds, movie 1 in Dietze *et al.* (2018)); (f) loss of symmetry and sliding (open circles, movie 2).

symmetric and asymmetric eigenmodes  $\hat{h} = \eta^{-1} \partial_t h'|_{t=0}$  with the largest growth rate  $\eta$ , as obtained from our frozen-time stability analysis (2.13c).

The asymmetric mode is the only unstable one and it agrees well with the actual



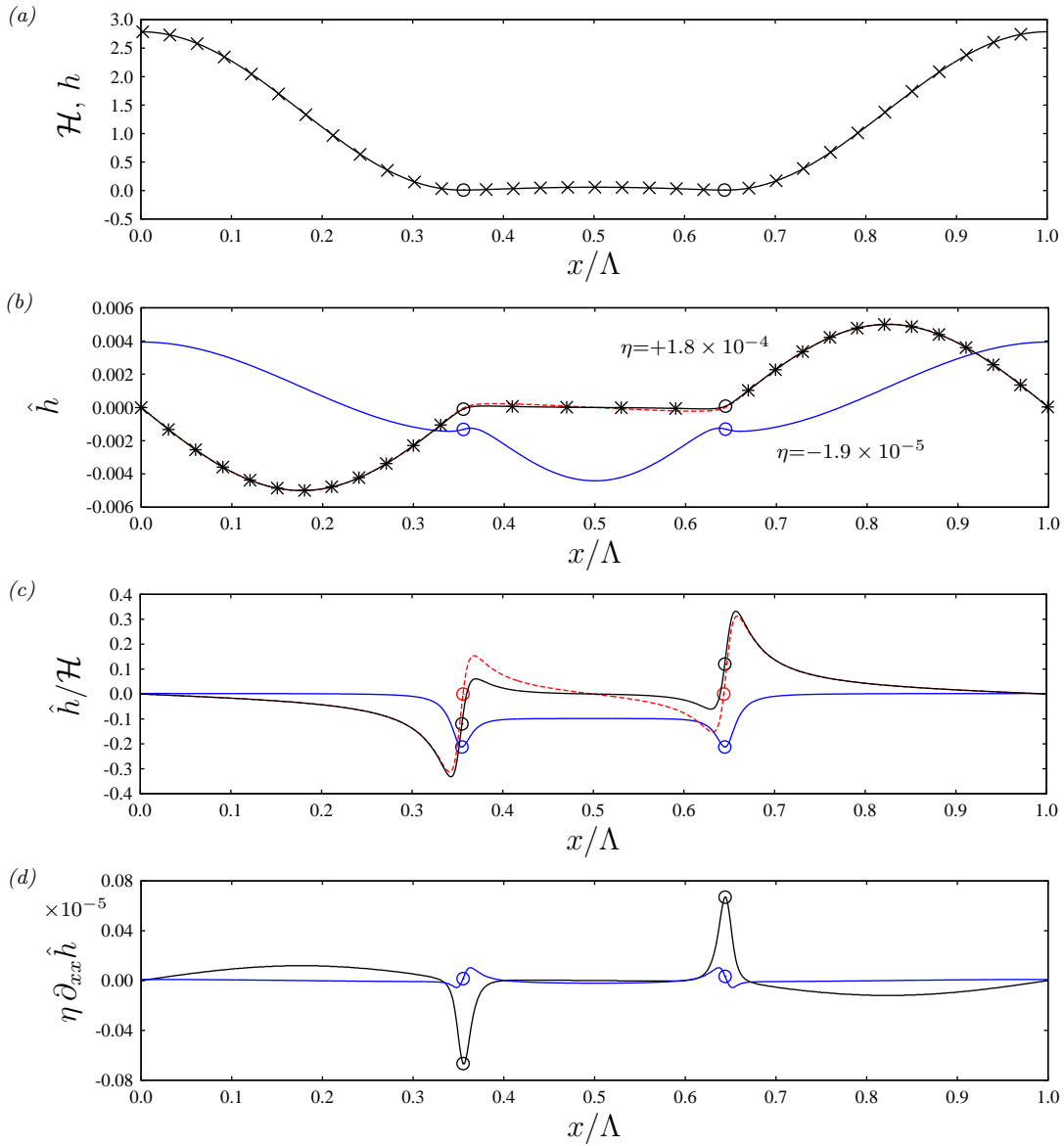


Figure 8.3: Frozen-time linear stability analysis for the suspended water film from figures 8.1 and 8.2:  $t=7 \times 10^4$ . (a) Solid line: base state  $\mathcal{H}(x)$  obtained from symmetric simulation on domain of length  $\Lambda/2$  (501 grid points) and mirrored onto full-wavelength domain; crosses: profile from periodic simulation on domain of length  $\Lambda$  (1001 grid points) slightly after loss of symmetry; (b) solid lines: most-unstable asymmetric ( $A_j=0$ ) and symmetric ( $B_j=0$ ) eigenfunctions  $\hat{h}(x)$  (2.13c) obtained from frozen-time linear stability analysis of the symmetric base state from panel (a); asterisks: actual perturbation, i.e. difference between periodic and symmetric profiles in panel (a); red-dashed line: perturbation resulting from pure translation of base profile  $\mathcal{H}(x)$  with speed  $c$ , i.e.  $\partial_t h = -c \partial_x \mathcal{H}$ ; (c) normalized perturbation profiles from panel (b); (d) time derivative of surface curvature  $\partial_t(\partial_{xx} h) = \eta \partial_{xx} \hat{h}$  associated with most-unstable eigenfunctions in panel (b).

perturbation (asterisks). The  $\hat{h}$  maxima within the liquid drops in panel 8.3b seem to imply that the instability mechanism unfolds there. However, the perturbation in these portions of the film corresponds to a pure translation, i.e.  $\partial_t h = -c \partial_x \mathcal{H}$ , represented with a dashed red line in panel 8.3b. By contrast, the region around the secondary troughs exhibits actual growth, as evidenced by panel 8.3c, which represents the profiles from panel 8.3b normalized with the base state film height  $\mathcal{H}(x)$ <sup>3</sup>. Thus, the instability mechanism must emanate from these secondary troughs.

The most-amplified perturbation  $\hat{h}$ , which is unsymmetrical, pushes down the left secondary trough and pulls up the right one (black circles in panel 8.3c). At the same time, the left trough is flattened, i.e.  $\partial_{xx} h$  is reduced, and the right one is curved, i.e.  $\partial_{xx} h$  is increased, as shown in panel 8.3d. Given the sign of the capillary pressure gradient  $\partial_x p|_\sigma$  (8.1) at the secondary troughs (panel 8.1b), this tends to increase the flow rate discrepancy across the left trough and decrease it across the right trough<sup>4</sup>. Consequently, the left trough further thins and the right one further thickens, thus amplifying the perturbation. Finally, because the  $\hat{h}/\mathcal{H}$  extrema in panel 8.3c are slightly shifted w.r.t. the secondary troughs (marked by open circles), the latter also move to the left, thus imparting a concerted sliding motion on the liquid drops, which have virtually reached static equilibrium and oppose no resistance.

Our transient stability analysis, which explicitly accounts for the time evolution of the base state  $\mathcal{H}(x, t)$  in the linear problem (2.14a) and does not rely on a normal mode decomposition, yields the same overall conclusions. Panel 8.4c represents profiles of the most-amplified linear perturbations  $h'$  (solid lines) for the three base state profiles in panel 8.4a (plotted with a logarithmic scale), as obtained from an iterative solution of the direct (2.14a) and adjoint (2.14c) linear problems, for a given time horizon  $T$ . These perturbations are pulse-like and localized at the secondary troughs, confirming that the instability mechanism emanates from these troughs. As  $t \rightarrow T$ , they evolve toward the normal mode uncovered by our frozen-time approach (dashed lines), which is also recovered when solving the direct linear problem (2.14a) starting from a noisy initial condition (panel 8.4c).

We have applied our transient stability analysis at different times in the evolution of the base state according to panel 8.1a. Instability w.r.t. to the asymmetric sliding mode is observed as soon as the residual film between two liquid drops has buckled. However, the sliding motion becomes macroscopically visible only when the evolution of the base state has slowed sufficiently. This onset also depends strongly on the noise level  $\epsilon$  applied via  $h_{\text{noise}}$  (2.15), as shown in panel 8.4d, which represents computations performed with different values of  $\epsilon$  corresponding to the surface roughness of typical materials ranging from glass to steel.

The secondary sliding instability is also observed in the case of a thin vapour film underling a liquid layer (configuration in panel 1.4b). We demonstrate this in figure 8.5,

---

<sup>3</sup>The local growth rate at  $t=0$  is given by  $\mathcal{H}^{-1} \partial_t h = \eta \frac{\hat{h}}{\mathcal{H}}$ .

<sup>4</sup>See panel 8b in Dietze *et al.* (2018) for a profile of the primary-flow curvature profile  $\partial_{xx} \mathcal{H}$  across the secondary troughs.

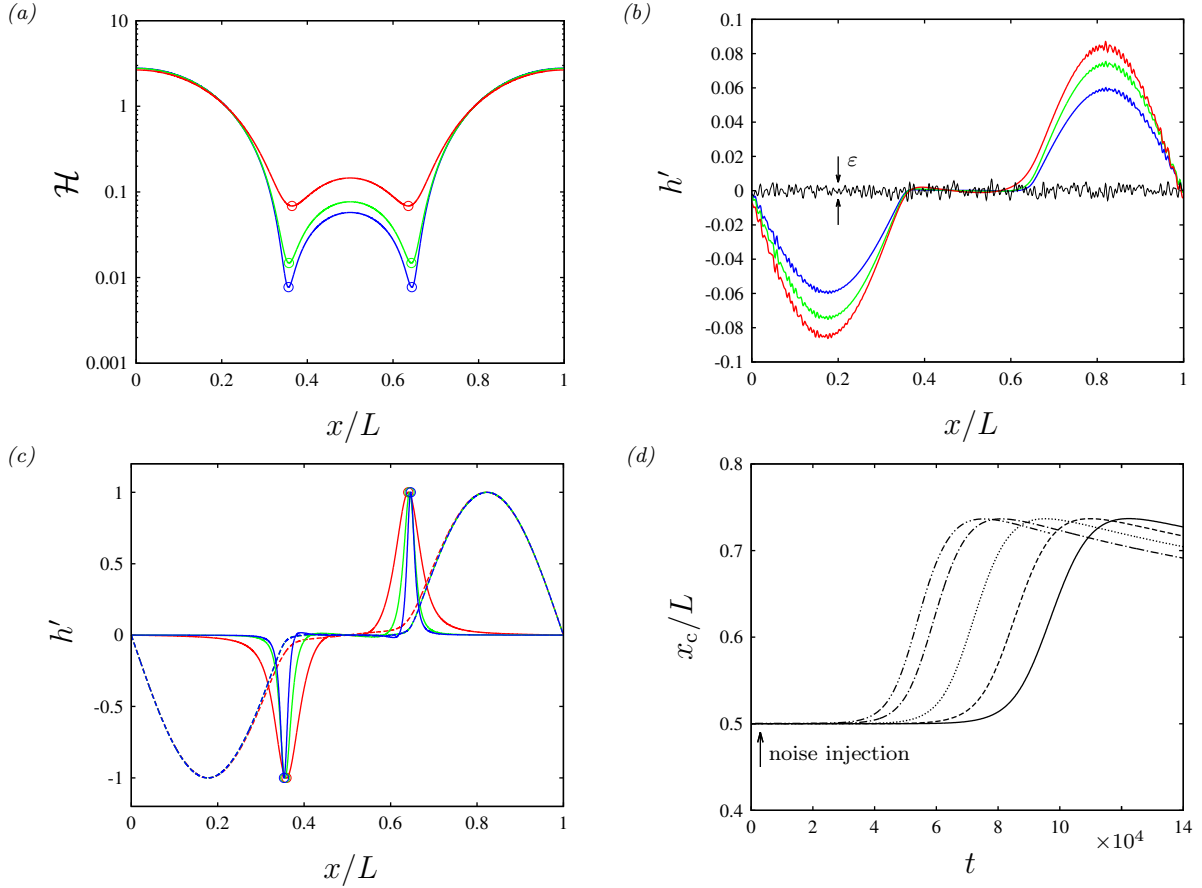


Figure 8.4: Transient stability analysis applied to the suspended water film in panel 8.2a. (a) Profiles of the symmetrical base state  $\mathcal{H}(x, t_i)$ :  $t_i=1922$  (red), 20000 (green), and 70000 (blue); (b) long-term linear responses  $h'(x, t_i + T)$  according to (2.14a) to a noisy perturbation  $h_{\text{noise}}$  (2.15) (black line) over a time horizon  $T$ . Red:  $T=2000$ , green:  $T=6000$ , blue:  $T=10000$ ; (c) most-unstable perturbations (solid lines) obtained from transient stability analysis (2.14) and linear responses at  $t=t_i+T$  (dashed lines). Red:  $T=200$ , green:  $T=1000$ , blue:  $T=1000$ ; (d) nonlinear response of the periodic computation in panel 8.2a to a noise injection at  $t=683$ . Time traces of the center of mass  $x_C$  for different noise levels  $\epsilon = \max(h_{\text{noise}}) - \min(h_{\text{noise}}) = 0$  (solid),  $1.3 \times 10^{-4}$  (dashed),  $1.3 \times 10^{-3}$  (dotted),  $1.3 \times 10^{-2}$  (dot-dashed), and 0.04 (dot-dot-dashed). These values correspond to the surface roughness of materials ranging from glass to steel.

which represents nonlinear computations performed with the lubrication model (1.68) and with our full WRIBL model (1.64). The mean film thickness  $\bar{h}=h_0$  and the fluid properties correspond to the experiments of Burton *et al.* (2012), which were performed with a Leidenfrost drop of water. The logarithmic surface profiles in panel 8.5a once again exhibit pronounced secondary troughs that deform asymmetrically when the sliding motion sets in (panel 8.5b).

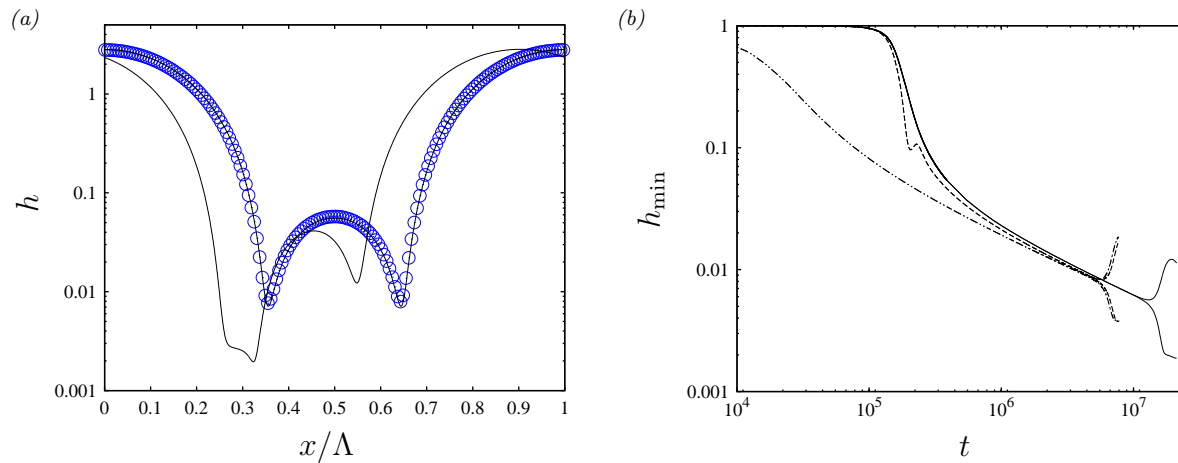


Figure 8.5: Sliding instability in the case of a vapour film underneath a liquid layer (panel 1.4b):  $h_0=100 \mu\text{m}$ ,  $\text{Bo}=0.0016$ ,  $\Lambda=2\sqrt{2} \pi/\sqrt{\text{Bo}}$ ,  $D=10$ . Fluid properties correspond to the experiments of Burton *et al.* (2012) which were performed with a Leidenfrost drop of water:  $\rho_1=0.47 \text{ kg/m}^3$ ,  $\rho_2=958.4 \text{ kg/m}^3$ ,  $\mu_1=1.8 \cdot 10^{-5} \text{ Pa s}$ ,  $\mu_2=0.28 \cdot 10^{-3} \text{ Pa s}$ ,  $\sigma=0.059 \text{ N/m}$ . (a) Surface profiles. Solid black lines: just before and just after the onset of sliding; circles: suspended water film from figure 8.1; (b) time traces of the film thickness at the left and right secondary troughs. Solid: full model (1.64), dashed:  $\Pi_\mu=0$ , dot-dot-dashed: lubrication model (1.68).

Both for the suspended water film (panel 8.4a) and for the thin vapour film (panel 8.5a), the minimal film thickness  $h_{\min}$  upon sliding is at least two orders of magnitude greater than the range of long-range van der Waals forces, which is of the order of 10 nm (Bonn, 2009; Israelachvili, 2011). Thus, sliding should be observed in an experiment well before the occurrence of spinodal dewetting.

In case of the suspended water film (configuration in panel 1.4a), the sliding instability can be suppressed via thermal Marangoni stresses by heating the liquid from the wall, i.e. for  $\text{Ma}<1$  and  $|\text{Ma}|$  sufficiently large. This is shown in figure 8.6, which represents a computation based on the augmented lubrication model (1.69). Instead of reaching a quasi-steady state, the liquid film continues undergoing buckling events (panel 8.6a), i.e. secondary troughs form tertiary troughs (panel 8.6b) which in turn split into quaternary troughs (panel 8.6c) and so forth, eventually leading to film rupture in an experiment. This repeated buckling results from the thermocapillary drain rate contribution  $q|_{\text{Ma}}$  in (1.69):

$$q_1 = \underbrace{\frac{1}{3}h^3\partial_x h}_{q|_g} + \underbrace{\frac{1}{3}\text{Bo}^{-1}h^3\partial_{xxx} h}_{q|_\sigma} + \underbrace{-\frac{1}{2}\frac{\text{Ma}}{\text{Bo}}h^2\partial_x h \frac{\text{Bi}}{(1+\text{Bi}h)^2}}_{q|_{\text{Ma}}}, \quad (8.2)$$

which is symmetric about the troughs (dashed line in panel 8.6d), i.e. Marangoni stresses pull liquid away from a trough in both directions. This thermocapillary flow rate survives in the face of viscous drag even at small  $h$  ( $q|_{\text{Ma}} \propto h^2$ ), in contrast to the gravitational contribution ( $q|_g \propto h^3$ ). On the inside of a given trough (e.g. the left tertiary trough

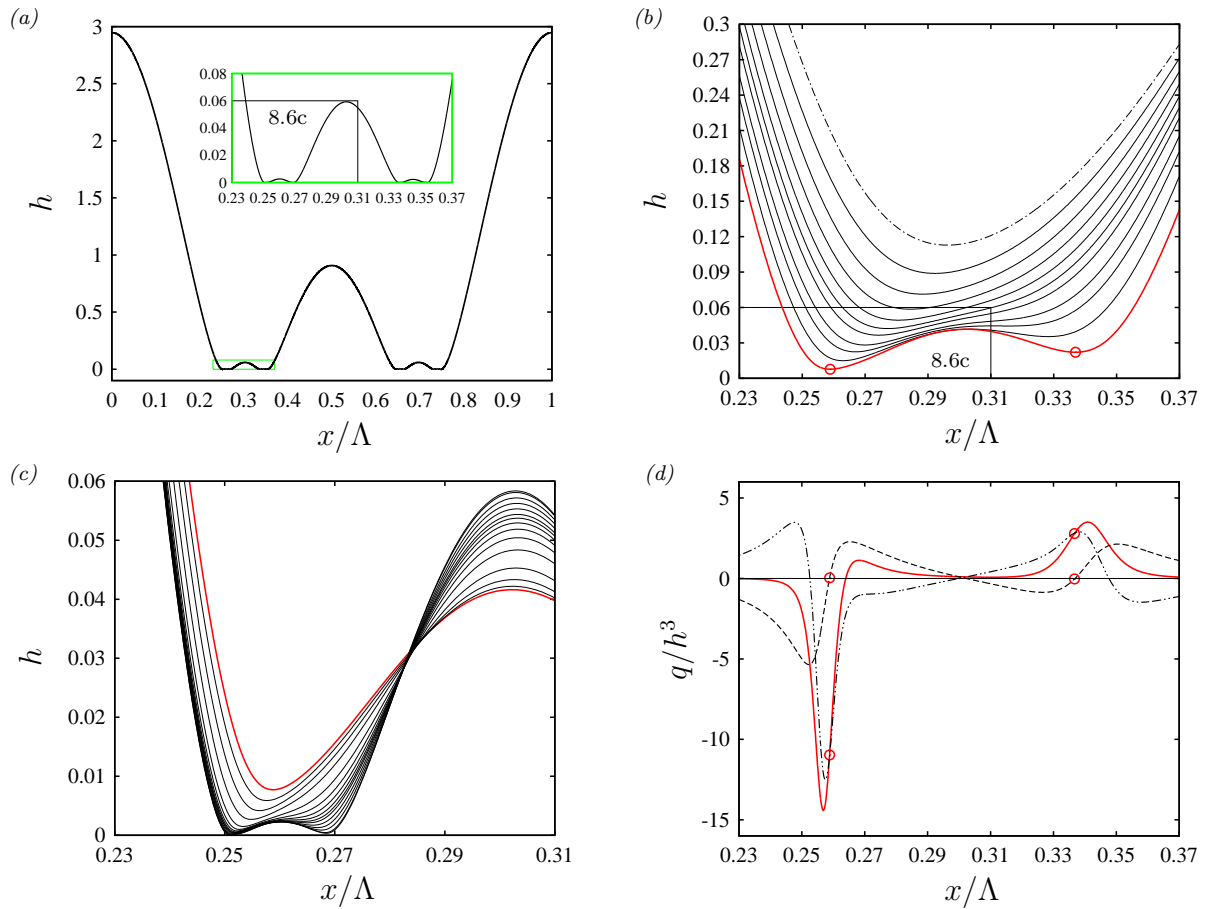


Figure 8.6: Suppression of sliding due to thermal Marangoni stresses. Suspended water film from figure 8.2 with additional heating from the wall. Numerical computation based on (1.69):  $Ma=-0.2$ ,  $Bi=1.0$ . (a) Surface profile after three buckling events ( $t=2 \cdot 10^4$ ). Inset shows enlarged view of boxed region around left tertiary hump; (b) second buckling event leading to tertiary hump; (c) third buckling event leading to leftmost quaternary hump; (d) normalized flow rate contributions (8.2) for thick red profile in panel b. Open circles mark loci of tertiary troughs. Thick red solid line: total flow rate  $q$ ; dashed: thermocapillary contribution  $q|_{Ma}$  (8.2); dot-dot-dashed: capillary contribution  $q|_{\sigma}$ .

in panel 8.6b, marked by an open circle in panel 8.6d),  $q|_{Ma}$  counteracts the capillary drain rate  $q|_{\sigma}$ , which is always directed outward from the smallest hump. This leads to a divergence point (red solid line in panel 8.6d changes sign), where the next-generation trough will develop.

Thus, new troughs always develop on the inside of an existing one and this counteracts the peeling mechanism required for the sliding instability (panel 8.2f). Also, the thermocapillary draining mechanism resists the surface perturbation associated with the sliding mode (panels 8.3c and 8.3d). Considering the (nonlinear) thermocapillary growth rate

contribution:

$$h^{-1} \partial_t h|_{\text{Ma}} = -h^{-1} \partial_x q|_{\text{Ma}} \approx \frac{\text{Ma Bi}}{\text{Bo}} (\partial_x h)^2 + \frac{1}{2} \frac{\text{Ma Bi}}{\text{Bo}} h \partial_{xx} h, \quad (8.3)$$

Marangoni stresses ( $\text{Ma} < 0$ ) reduce the thinning rate of a trough that has been flattened (decreased in  $h_{xx}$ ) and increase the thinning rate of a trough that has been curved (increased in  $h_{xx}$ ). These two thermocapillary effects explain why sliding is suppressed when the liquid film is heated from the wall.

**Impact of the work and relation to the current state of the art** Our work Dietze *et al.* (2018) has been cited 3 times according to *Web of Science*.

Pillai & Narayanan (2018*b*), who studied dielectric liquid films subject to the Rayleigh-Taylor instability under additional transient electrostatic forcing, observed an oscillatory sliding regime, where the minimal film thickness is reduced after each period. Pillai & Narayanan (2020) have shown that the transition from sliding to cascaded buckling (compare panels 8.2f and 8.6a), which occurs due to Marangoni stresses in our case, can also be brought about via applying a steady electrical field to a film of dielectric liquid. In that case, sliding is favoured by normal Maxwell stresses acting at the film surface, whereas tangential stresses promote repeated buckling. Lerisson *et al.* (2020) have invoked our work w.r.t to the formation of rivulets on a liquid film flowing underneath an inclined wall.

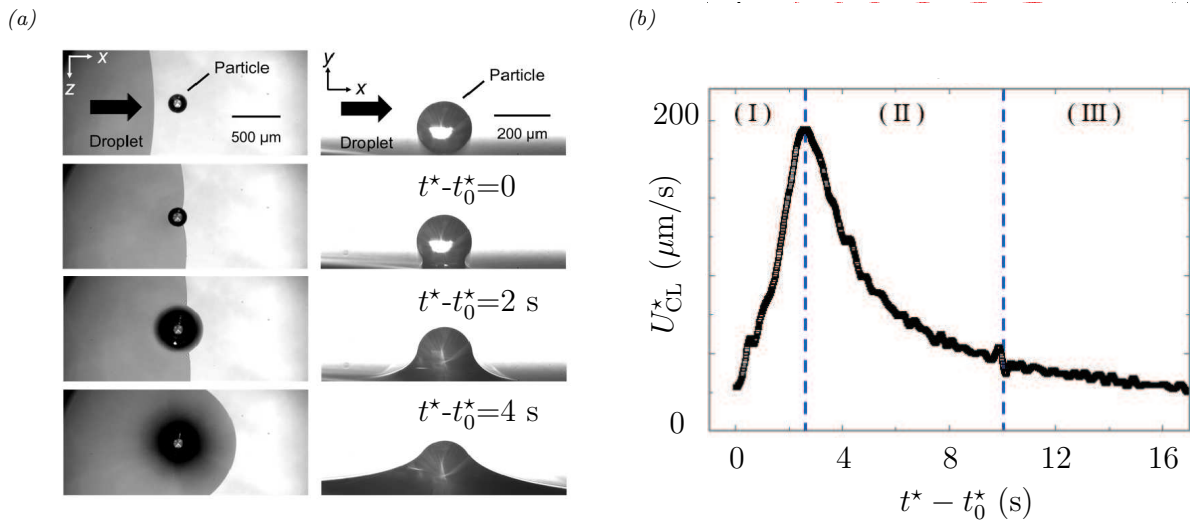


Figure 8.7: Experiment conducted at Tokyo University of Science (Nakamura *et al.*, 2020b). Contact line at the front of a liquid drop of silicone oil spreading on a smooth substrate and entering into contact with a spherical particle of radius  $R^*=25 \mu\text{m}$ :  $\nu_1=2 \times 10^{-6} \text{ m}^2/\text{s}$ ,  $\rho_1=873 \text{ kg}/\text{m}^3$   $\sigma=0.0183 \text{ N}/\text{m}$ . The static contact angles on the substrate and particle are  $\beta_s=5^\circ$  and  $\beta_p=20^\circ$ . (a) Top-view and side-view photographs at different times; (b) contact line velocity obtained from image processing, evidencing an accelerated spreading rate shortly after contact with the particle at time  $t_0$ .

## 8.2 Drops spreading around microparticles

The results presented in this section were obtained in the context of an international project “Fluid dynamics in the vicinity of a macroscopic contact line in interaction with microparticles” lead by Ichiro Ueno at Tokyo University of Science. My role in this project was to introduce a numerical approach to reproduce experiments on liquid-particle interaction that were well under way at that time (figure 8.7). The basis for this was laid with a Masters student, Motochika Inoue, who visited FAST for a 4 month period in 2015. Subsequent simulations (figures 8.8 and 8.9) used in our publications (Nakamura *et al.*, 2020b,a) were performed by another student, Hayate Nakamura, at Tokyo University of Science between 2019 and 2020. My contribution to the results presented here was mainly in a supervising role.

We consider a liquid drop that spreads on a smooth horizontal substrate and comes into contact with an individual micro-particle (figure 8.7). We assume a regime of partial wetting, i.e.  $S < 0$ , where  $S$  denotes the spreading parameter:

$$S = \sigma_{SG} - \sigma_{SL} - \sigma = \sigma \{ \cos(\beta_0) - 1 \}, \quad (8.4)$$

introducing the solid/liquid and solid/gas interfacial tensions  $\sigma_{SL}$  and  $\sigma_{SG}$ , and the equilibrium contact angle  $\beta_0$ . In a broader sense, this configuration corresponds to the wetting of rough surfaces, although the isolated-particle situation is clearly a limiting case.

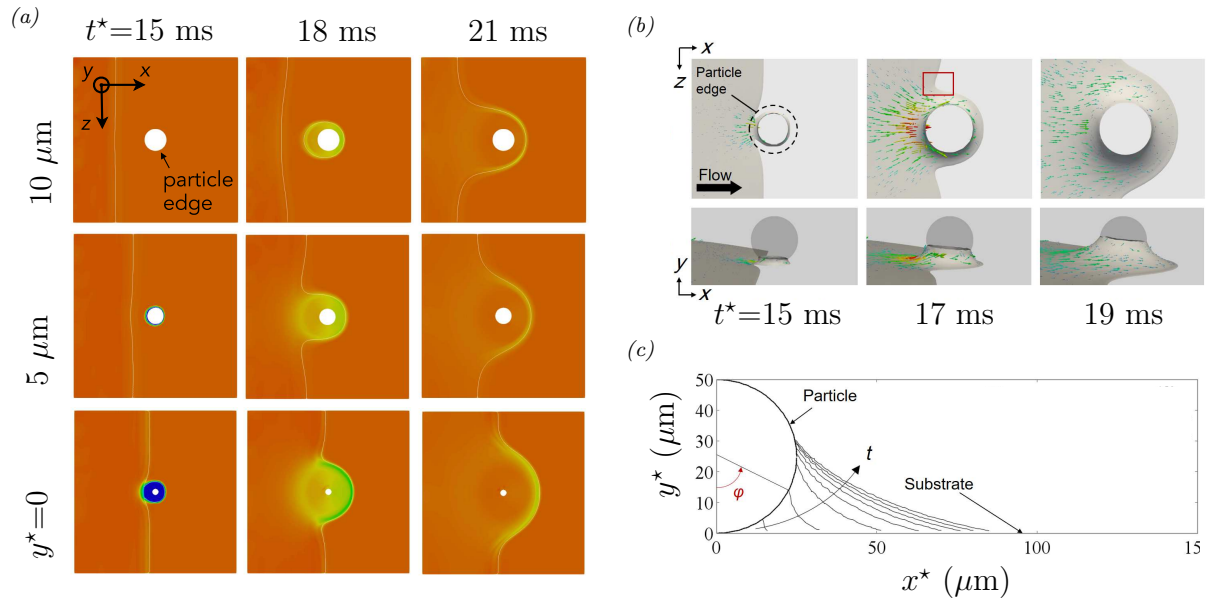


Figure 8.8: Numerical simulation of the experiment in figure 8.7. Dynamic contact angle  $\beta$  (4.44) imposed on the substrate and particle, with  $\beta_0 = \beta_s = 5^\circ$  and  $\beta_0 = \beta_p = 20^\circ$ . The simulation was performed with the `interFOAM` solver (Rusche, 2002) at Tokyo University of Science (Nakamura *et al.*, 2020b). (a) Pressure field at different wall distances; (b) top and side views of the liquid spreading around the particle; (c) time evolution of the liquid meniscus on the downstream side of the particle.

Adding small-scale structures is known to enhance the wetting characteristics of a given substrate material (Quéré, 2005): omniphobic (hydrophobic in the case of water) substrates become super-omniphobic (Onda *et al.*, 1996) and omniphilic substrates become super-omniphilic (Bico *et al.*, 2001). We are interested in the latter case, where  $\beta_0 < \frac{\pi}{2}$ , and micro-structures accelerate liquid spreading (Cazabat & Stuart, 1986).

From a technological point of view, such a behaviour is useful for liquid transport in small-scale two-phase systems, e.g. heat pipes (Jouhara *et al.*, 2017) or labs on a chip (Blanchard *et al.*, 1996), and can be functionalized by appropriately designing the topography of the micro-structure (Courbin *et al.*, 2007). Conversely, the forces exerted by the liquid on the particle are relevant for the cleaning of contaminated surfaces (Aramrak *et al.*, 2013; Zoueshtiagh *et al.*, 2014).

Many studies have investigated the spreading of liquids on ordered arrays of structure elements such as micro-pillars (Quéré, 2005; Bonn, 2009). Here, we focus on the interaction between an advancing contact line and a single or a series of two isolated particles, in order to elucidate the mechanisms underlying enhanced spreading.

Figure 8.7 displays results from an experiment at Tokyo University of Science, where a droplet of low-viscosity silicone oil spreads on a smooth plane substrate and comes into contact with an isolated spherical micro-particle of radius  $R$ . When the contact line constituting the front of the spreading droplet has reached the particle, a meniscus is formed around the foot of the latter. This meniscus, of initially very large curvature,



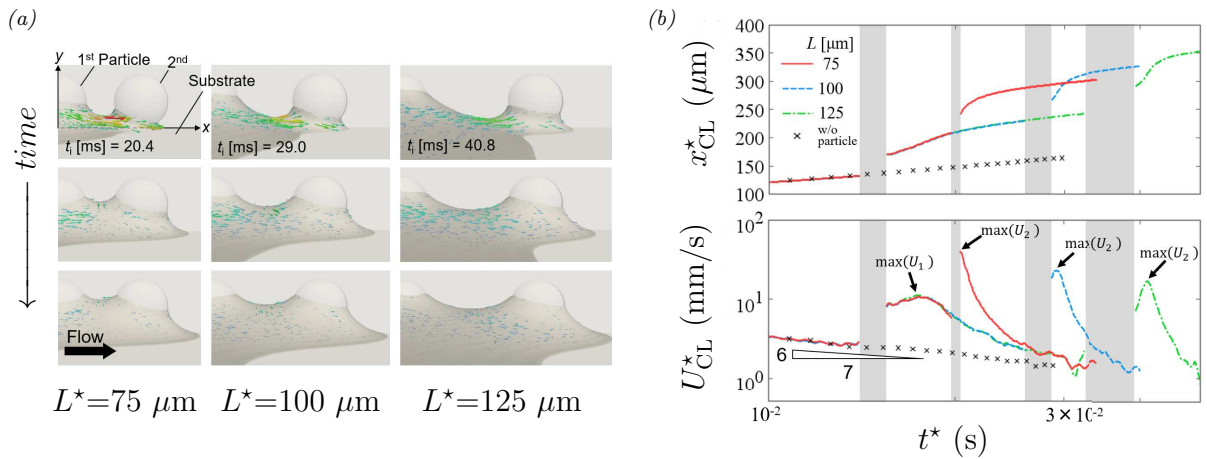


Figure 8.9: Same numerical simulation as in figure 8.8 with an additional second particle placed at a distance  $L^*$ . (a) Formation of a liquid meniscus between the two particles for  $L^*=75$ , 100, and 125  $\mu\text{m}$ ; (b) time evolution of the contact line position (top) and contact line velocity (bottom). Red solid:  $L^*=75$   $\mu\text{m}$ , blue dashed:  $L^*=100$   $\mu\text{m}$ , green dot-dashed:  $L^*=125$   $\mu\text{m}$ . Grey zones highlight the time spans during which the contact line moves around the first and second particle.

sucks liquid toward it and rapidly rises until attaining a quasi-steady shape. As a result, the thickness of the liquid film around the particle is considerably increased versus the situation prior to first contact (panel 8.7a). At the same time, the spreading velocity  $U_{\text{CL}}^*$  of the contact line, which is now located downstream of the particle, is strongly increased (panel 8.7b).

In Nakamura *et al.* (2020b), we reproduced the experiment from figure 8.7 via DNS with the `interFOAM`<sup>5</sup> solver (see section 4.1.3), in order to elucidate the mechanism underlying contact line acceleration (figure 8.8). These DNS reproduce the dynamics of the meniscus formation and the contact line acceleration in good agreement with the experiment (compare panels 8.8b and 8.7a). The mechanism of this acceleration relies on two ingredients, which both result from the rise of the meniscus around the particle. Firstly, the increased thickness of the liquid film around the particle reduces viscous drag. Secondly, the increased slope of the film front at the contact line downstream of the particle (panel 8.8c) projects the system back into a regime of faster liquid spreading. This is evidenced by panel 8.8a, which represents pressure contours within wall-parallel planes of different  $y$ . In particular, we observe a pronounced pressure minimum behind the particle, once the contact line has reached there (last two images from the lowest row). This minimum is much lower than the pressure along the portions of the contact line that are further away from the particle.

In Nakamura *et al.* (2020a), we applied the same numerical procedure to a two-particle system (figure 8.9), where two identical particles were placed one behind the other at a separation distance  $L^*$ . In this case, the contact line acceleration is repeated at the

<sup>5</sup>Version 5 of the `OpenFOAM` package.

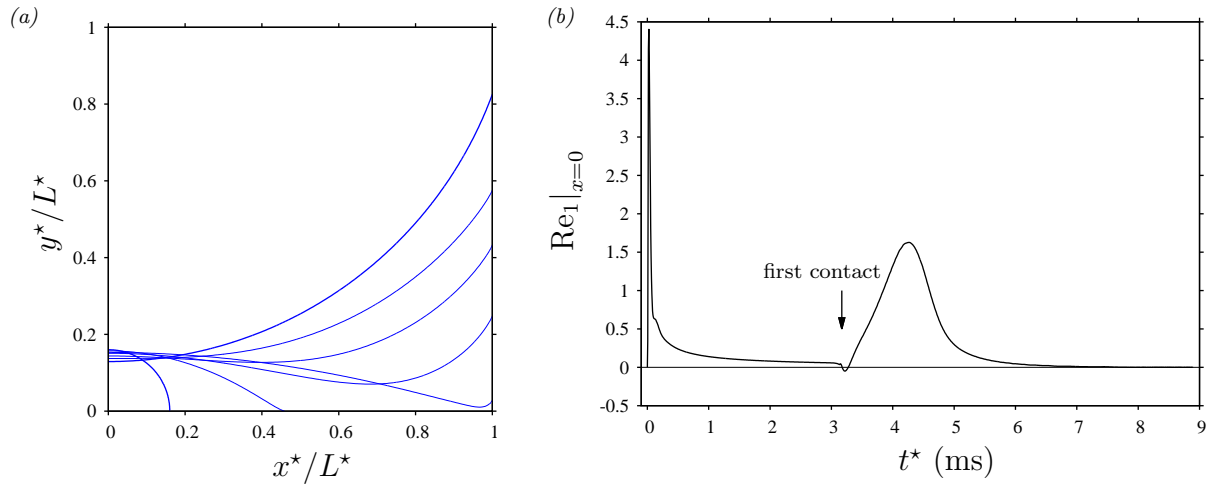


Figure 8.10: Two-dimensional meniscus pump: liquid film spreading on a horizontal substrate then rising on a vertical wall. DNS with **Gerris**:  $\beta_0^s=5^\circ$ ,  $\beta_0^p=20^\circ$ ,  $R_0^*=0.755$  mm,  $Bo=2.6 \cdot 10^{-5}$  (silicone oil 2 in table 2.1). Dynamic contact angle  $\beta$  according to (4.25) with  $c=10$ ,  $L_e^*=R_0^*$ , and  $L_i^*=100 \mu\text{m}$ . Adaptive grid refinement with  $RL_{\max}=8$  based on  $\underline{L}^*=L^*=0.125$  mm. (a) Snapshots of the liquid-gas interface at  $t^*=0, 0.12, 3.09, 3.66, 4.12, 4.43,$  and  $9.16$  ms; (b) time trace of the liquid Reynolds number  $Re_1|_{x=0}$  at the left domain boundary, where homogeneous Neumann boundary conditions are applied.

second particle. Moreover, the acceleration caused by the second particle results in a larger maximum of  $U_{\text{CL}}^*$  than the one caused by the first, as shown in panel 8.9b. Here, we have plotted time traces of the contact line position  $x_{\text{CL}}^*$  and spreading velocity  $U_{\text{CL}}^*$  for three values of  $L^*$ . Grey zones in these plots correspond to time spans where the contact line is located underneath the equator of a given particle, their width depending on the current spreading velocity  $U_{\text{CL}}^*$ . We conclude from these data that the magnitude of the second  $U_{\text{CL}}^*$  maximum depends on the separation distance  $L^*$ . When  $L^*$  is too large, the inter-particle meniscus becomes too deep (panel 8.9a), which increases viscous drag within the liquid film. By contrast, when  $L^*$  is too small (not shown here), the inter-particle meniscus becomes too curved, which reduces the driving pressure drop across the second particle.

Figure 8.10 represents a two-dimensional DNS performed with **Gerris**, which allows to quantify the strength of the meniscus pump at the origin of the meniscus rise and the resulting contact line acceleration observed in figures 8.8 and 8.9. In panel 8.10a, a liquid film spreads on a horizontal plane substrate ( $\beta_s=5^\circ$ ) and then climbs up a vertical pillar ( $\beta_p=20^\circ$ ) placed at the right domain boundary. Our simulation is started from an initial condition representing a circular liquid drop of radius  $R_0^*=0.755$  mm, and we use the same liquid properties as in the experiment of figure 8.7 (silicone oil II in table 2.1). At the left domain boundary,  $x=0$ , we impose homogeneous Neumann conditions on all variables. Thus, liquid can enter or leave the domain freely at this position, depending on the spreading dynamics. Panel 8.10b represents the time trace of the liquid Reynolds

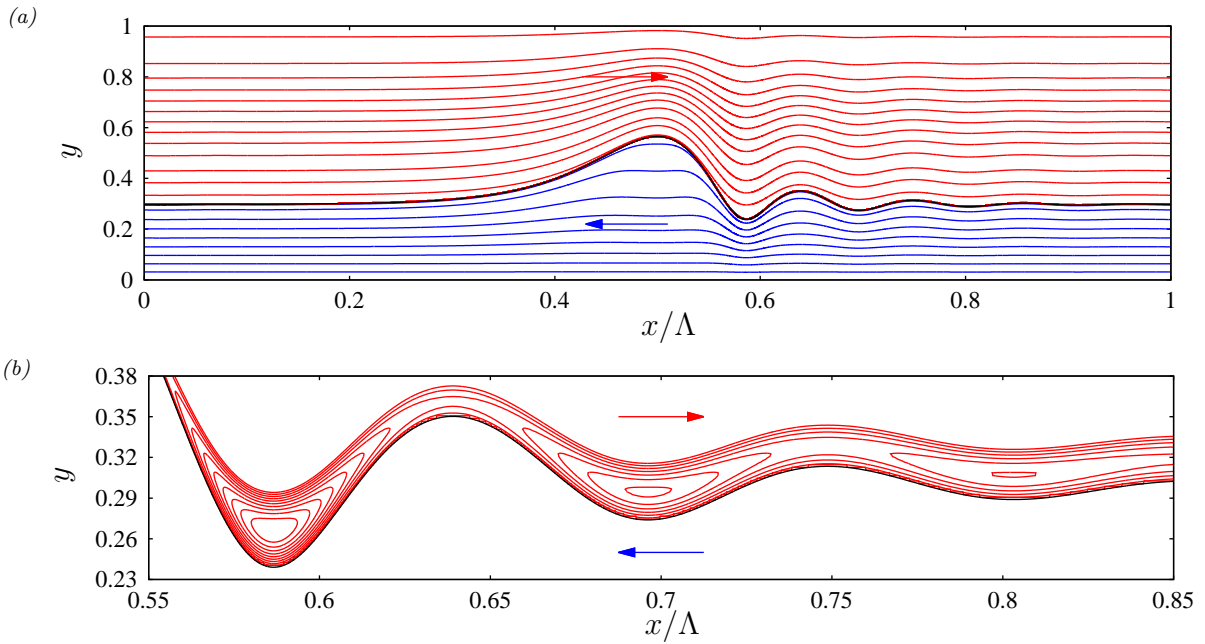


Figure 8.11: Pressure-driven stratified water/air flow through a narrow channel in zero-gravity environment. TWS from panel 2.14a:  $H^*=0.39$  mm,  $Ka=3592.3$  (water I and air III in table 2.1),  $\Lambda=200/3$ ,  $\bar{h}=1/3$ ,  $M=-256.0$ ,  $Re_1=5.97$ ,  $Re_2=33.86$ . Streamlines in the wave-fixed reference frame. (a) Full view; (b) blown up view of the shear layer near the liquid-gas interface.

number  $Re_1|_{x=0}=q_1^*|_{x=0}/\nu_1$  at this position. At the time when the film moves onto the pillar ( $t^* \approx 3.1$  ms),  $Re_1|_{x=0}$  strongly increases, due to the sucking action of the meniscus forming at the pillar foot. Then, it reaches a maximum and decreases again, attaining zero when the meniscus has reached its static shape. The height of the  $Re_1|_{x=0}$  maximum is a measure of the pumping strength of the meniscus, which is considerable in our system. Indeed,  $Re_1|_{x=0}$  increases by one order of magnitude versus the spreading regime of the film before contact with the pillar.

### 8.3 Pressure-driven liquid films in microgaps

Pressure-driven stratified liquid/gas flows through microgaps constitute an effective means for the cooling of semiconductor devices in terrestrial and microgravity applications (Kabov *et al.*, 2011). In this configuration (panel 1.2b), a liquid film and gas flow co-currently under the effect of an imposed pressure drop, and the film surface is subject to the Yih instability (Yih, 1967), leading to the formation of nonlinear travelling waves (Frank, 2008). We have shown in section 2.3.1 that our WRIBL model (1.27) captures these waves accurately (figure 2.14). Here, we introduce several insights that we have gained from computations with this model (Dietze & Ruyer-Quil, 2013), which are based

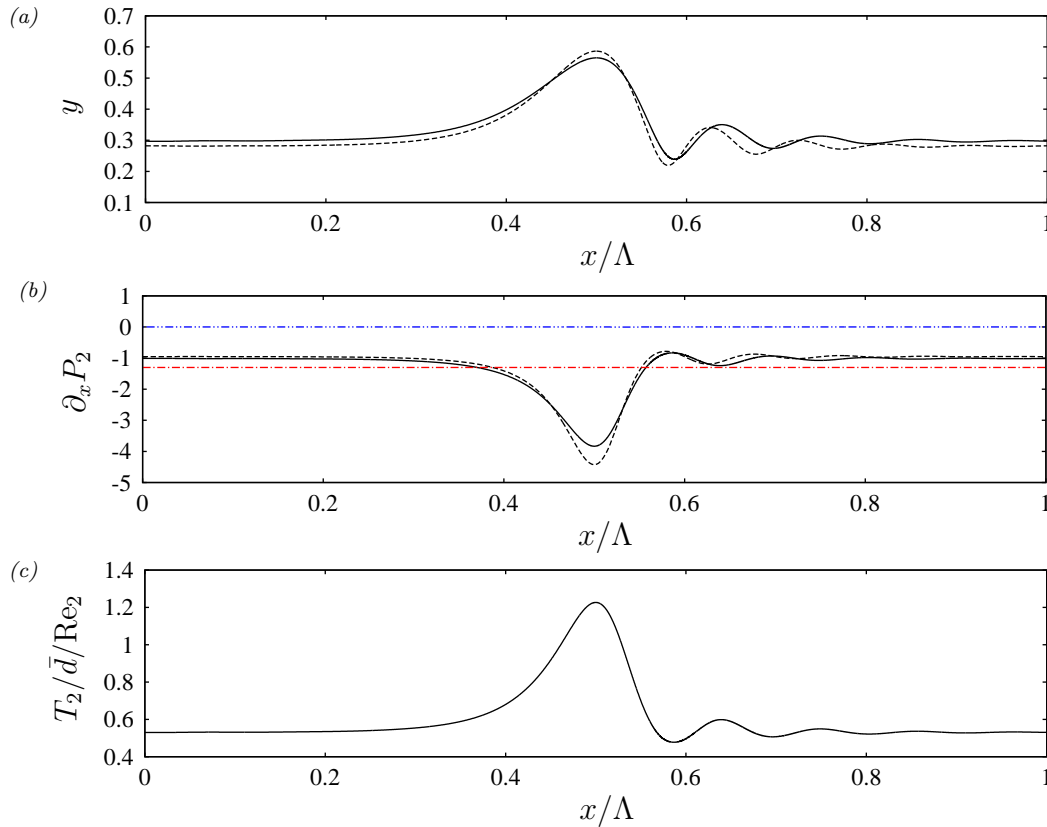


Figure 8.12: Gas-liquid coupling for the TWS in figure 8.11. Solid lines: full WRIBL model (1.27), dashed:  $\Pi_\mu=0$ . (a) Wave profiles; (b) streamwise derivative of interfacial gas pressure  $P_2$  (8.5a). Red dot-dashed: average over  $\Lambda$ , blue dot-dot-dashed: contribution of dynamic pressure  $\frac{1}{2}(q_2/d)^2$ ; (c) gaseous interfacial tangential viscous stress  $T_2$  (8.5b).

on the zero-gravity superconfined water/air system studied by Frank (2008) (figures 8.11, 8.12, and 8.13).

Figure 8.11 represents streamlines in the wave-fixed reference frame for the TWS from panel 2.14a. As shown in the blown up view from panel 8.11b, the discrepancy in superficial velocity between the liquid ( $Re_1=5.97$ ) and gas ( $Re_2=33.86$ ) is reconciled within an extremely thin shear layer around the film surface, which contains several elongated vortices that are linked to the capillary ripples.

The mechanism underlying the surface waves can be identified based on figure 8.12. There, we have plotted profiles of the streamwise derivative of the gas pressure  $P_2$  (panel 8.12b) and the gaseous tangential viscous stress  $T_2$  (panel 8.12c) acting at the film surface:

$$P_2 = p_2|_h, \quad (8.5a)$$

$$T_2 = T_2^* \frac{\mathcal{L}}{\mu_2 \mathcal{U}_2} = \{ -(\partial_y \hat{u}_2 + \partial_x \hat{v}_2) + 4 \partial_x h \partial_x \hat{u}_2 \}_h, \quad (8.5b)$$

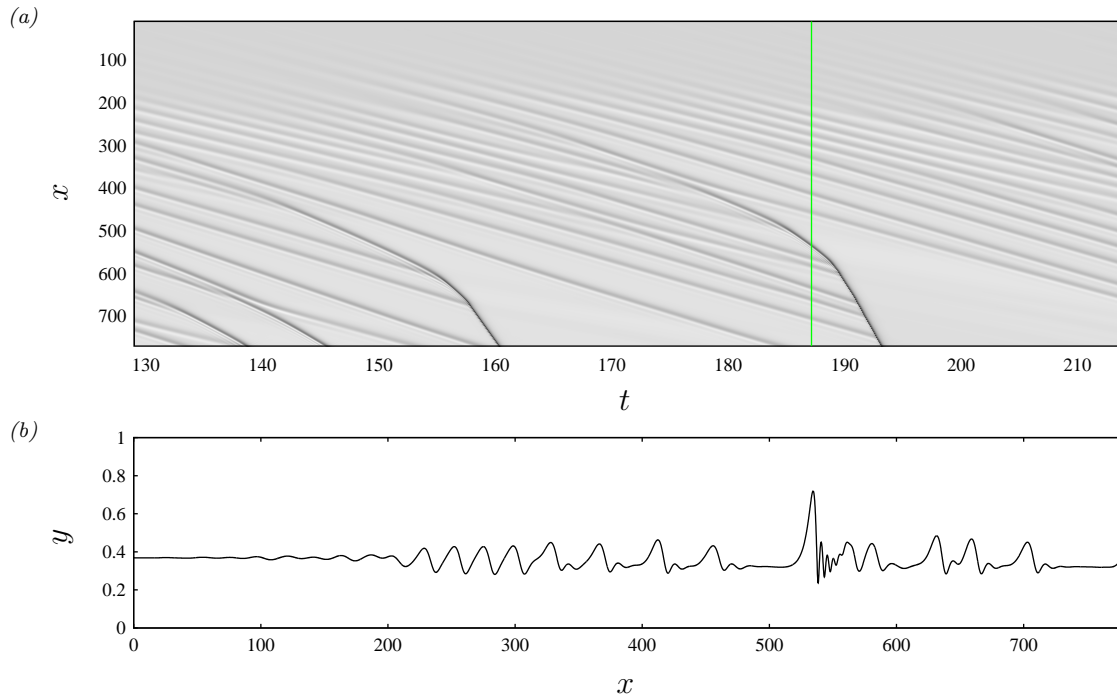


Figure 8.13: Self-excited tsunami waves for the pressure-driven water/air flow from figure 8.11:  $H^*=0.39$  mm,  $Ka=3592.3$  (water I and air III in table 2.1),  $L^*=0.3$  m,  $Re_1=5.97$ ,  $Re_2=33.86$ . Spatio-temporal computation on a domain of length  $L^*=0.3$  m using inlet outlet/outlet conditions. A noisy perturbation (2.38) is applied at the inlet:  $\epsilon_1=0$ ,  $\epsilon_2=4 \cdot 10^{-4}$ . (a) Spatio-temporal diagram of the film height  $h$ ; (b) film profile at  $t=187.1$  (green line in panel a).

where  $P_2$  is obtained from the pressure equation (1.33) and consistent at order  $\epsilon^2$ , and  $T_2$  is obtained from the RHS of (1.6b) when dropping the velocity corrections  $u_2^{(1)}$ .

According to panel 8.12a, gaseous viscous stresses play only a minor role in shaping the surface waves. Comparing the TWS profile obtained from our full model (1.27) (solid line) with the solution in the limit  $\Pi_\mu=0$  (dashed line), where viscous inter-phase coupling is inactive, we observe only a very slight variation in wave amplitude and no alteration in the general shape of the film profile. Thus, the pressure gradient (panel 8.12b) is the necessary ingredient for the instability. Firstly, it drives the mean flow and thus mimics the role of gravity in falling liquid films (section 5.1). Where the film is thicker, it produces a larger liquid flow rate  $q_1$  and vice versa where the film is thinner. The resulting flow rate discrepancies lead to an inertia-induced instability mechanism, similar to the one discussed in panel 5.3b. Also, humps travel faster than troughs, leading to a compression of the wave front and an elongation of the wave back. These features, along with the occurrence of precursory capillary ripples (panel 8.12a), are very similar to those observed in falling films subject to the Kapitza instability.

Secondly, variations in film height  $h$  considerably increase the pressure gradient at

the wave hump (solid line in panel 8.12b), and this amplifies the instability mechanism. This variation in pressure gradient is not due to a variation in dynamic pressure, the contribution of which we have approximated by  $P_2 = \frac{1}{2}(q_2/d)^2$  (blue dot-dot-dashed line in panel 8.12b), but due to variations in viscous drag, as a result of variations in the gas layer thickness.

In figure 8.13, we demonstrate the fate of these surface waves in a spatially evolving film, as obtained from a WRIBL computation with inlet/outlet conditions on an extended domain ( $L^* = 0.3$  m). Surface waves are excited through a purely noisy perturbation at the liquid inlet, i.e.  $\epsilon_1 = 0$  and  $\epsilon_2 = 4 \cdot 10^{-4}$  in (2.38). The spatio-temporal diagram in panel 8.13 shows that the train of surface waves is repeatedly disrupted by very large amplitude tsunami waves that self-excite as a result of coalescence events. These waves travel extremely fast and absorb all smaller waves travelling in front, leading to a repeated and complete renewal of the film surface. This mechanism could be beneficial for scalar inter-phase transfer, as it entails a renewal of the scalar boundary layer developing at the film surface<sup>6</sup>.

---

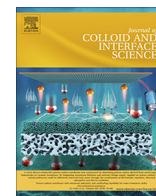
<sup>6</sup>In some ways, this is similar to the effect of bump-shaped corrugations discussed in figure 6.20.





Contents lists available at ScienceDirect

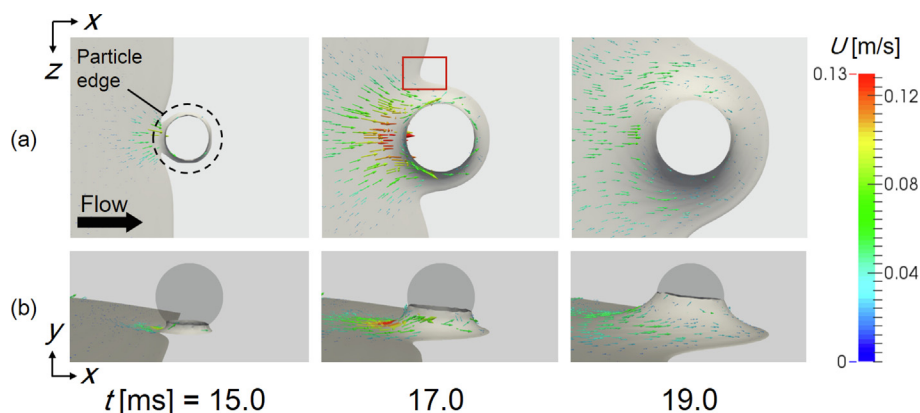
## Journal of Colloid and Interface Science

journal homepage: [www.elsevier.com/locate/jcis](http://www.elsevier.com/locate/jcis)

## Pumping effect of heterogeneous meniscus formed around spherical particle

Hayate Nakamura<sup>a</sup>, Tetsuya Ogawa<sup>a</sup>, Motochika Inoue<sup>a</sup>, Takuma Hori<sup>b</sup>, Lizhong Mu<sup>c</sup>, Harunori N. Yoshikawa<sup>d,\*</sup>, Farzam Zoueshtiagh<sup>e</sup>, Georg Dietze<sup>f</sup>, Takahiro Tsukahara<sup>g,h</sup>, Ichiro Ueno<sup>g,h,\*</sup><sup>a</sup> Division of Mechanical Engineering, Graduate School of Science and Technology, Tokyo University of Science, 2641 Yamazaki, Noda, Chiba 278-8510, Japan<sup>b</sup> Division of Advanced Mechanical Systems Engineering, Institute of Engineering, Tokyo University of Agriculture and Technology, 2-24-16 Koganei City, Naka Town, Tokyo 184-8588, Japan<sup>c</sup> Key Laboratory of Ocean Energy Utilization and Energy Conservation of Ministry of Education, School of Energy and Power Engineering, Dalian University of Technology, China<sup>d</sup> Université Côte d'Azur, CNRS, Institut de Physique de Nice, France<sup>e</sup> Université Lille, CNRS, ECLille, ISEN, Univ. Valenciennes, UMR 8520 - IEMN, F-59000 Lille, France<sup>f</sup> Université Paris-Sud, CNRS, Lab. FAST, Bât. 502, Campus Univ., Orsay F-91405, France<sup>g</sup> Department of Mechanical Engineering, Faculty of Science and Technology, Tokyo University of Science, 2641 Yamazaki, Noda, Chiba 278-8510, Japan<sup>h</sup> Research Institute for Science and Technology (RIST), Tokyo University of Science, 2641 Yamazaki, Noda, Chiba 278-8510, Japan

## GRAPHICAL ABSTRACT



## ARTICLE INFO

## Article history:

Received 17 September 2019

Revised 30 November 2019

Accepted 2 December 2019

Available online 9 December 2019

2010 MSC:

00-01

99-00

## Keywords:

Dynamic wetting

## ABSTRACT

**Hypothesis:** A disturbance such as a microparticle on the pathway of a spreading droplet has shown the tremendous ability to accelerate locally the motion of the macroscopic contact line (Mu et al., 2017). Although this ability has been linked to the particle-liquid interaction, the physical mechanisms behind it are still poorly understood despite its academic interest and the scope of numerous industrial applications in need of fast wetting.

**Experiments:** In order to better understand the mechanisms behind the particle-liquid interaction, we numerically investigate the pressure and velocity fields in the liquid film. The results are compared to experiments assessing the temporal shape variation of the liquid-film meniscus from which pressure difference around the particle is evaluated.

**Findings:** The particle-induced acceleration of the film front depends both on the shape of the meniscus that forms around the particle foot and the liquid “reservoir” in the film that can be pumped thanks to the

\* Corresponding authors at: Department of Mechanical Engineering, Faculty of Science and Technology, Tokyo University of Science, 2641 Yamazaki, Noda, Chiba 278-8510, Japan (I. Ueno).

E-mail addresses: [Harunori.YOSHIKAWA@univ-cotedazur.fr](mailto:Harunori.YOSHIKAWA@univ-cotedazur.fr) (H.N. Yoshikawa), [ich@rs.tus.ac.jp](mailto:ich@rs.tus.ac.jp) (I. Ueno).



## Enhancement of Meniscus Pump by Multiple Particles

Hayate Nakamura, Victor Delafosse, Georg F. Dietze, Harunori N. Yoshikawa, Farzam Zoueshtiagh, Lizhong Mu, Takahiro Tsukahara, and Ichiro Ueno\*



Cite This: *Langmuir* 2020, 36, 4447–4453



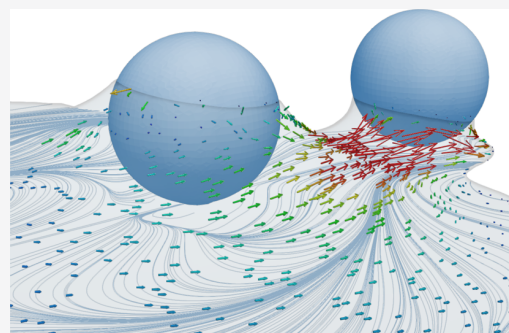
Read Online

ACCESS |

Metrics & More

Article Recommendations

**ABSTRACT:** We numerically investigate the behavior of a droplet spreading on a smooth substrate with multiple obstacles. As experimental works have indicated, the macroscopic contact line or the three-phase boundary line of a droplet exhibits significant deformation resulting in a local acceleration by successive interactions with an array of tiny obstacles settled on the substrate (Mu et al., *Langmuir* 2019, 35). We focus on the menisci formation and the resultant pressure and velocity fields inside a liquid film in a two-spherical-particle system to realize an optimal design for the effective liquid-transport phenomenon. Special attention is paid to the meniscus formation around the second particle, which influences the liquid supply related to the pressure difference around the first particle as a function of the distance between the two particles. We find that the meniscus around the first particle plays an additional role as the reservoir of the liquid supplied toward the second particle, which is found to enhance the total pumping effect.



### INTRODUCTION

Wetting is ubiquitous in nature, and nature exploits wetting. For example, lotus leaves repel water droplets owing to their microstructures,<sup>1</sup> and certain insects move freely on a water surface by deforming the free surface with their feet.<sup>2</sup> Wetting characteristics have been applied to numerous industrial products such as inkjet printing,<sup>3</sup> self-cleaning,<sup>4,5</sup> fluid management,<sup>6,7</sup> antioil-fouling,<sup>8</sup> self-assembly,<sup>9,10</sup> and food processing.<sup>11,12</sup> In particular, to improve industrial equipment such as heat pipes<sup>13</sup> and “lab on a chip devices,”<sup>14</sup> which are designed to efficiently transport liquids, it is essential to have a physical understanding of the spreading of liquids on solid surfaces and to control this efficiently.

Liquid spreading is evaluated by monitoring the behavior of a contact line (CL), which is a three-phase interface on a solid surface. In particular, a visually confirmed CL is known as a macroscopic CL (M-CL). Several studies have confirmed that the correlation between the spreading radius  $R$  and spreading time  $t$  of a liquid film on a smooth horizontal substrate can be expressed as  $R \approx t^a$ . The exponent  $a$  depends on the dominant force acting on the liquid film; the exponent becomes  $a = 1/10$  in a surface tension-dominant regime,<sup>15</sup> and  $a = 1/8$  in a gravity-dominant regime.<sup>16</sup> In particular, the exponent becomes  $a = 1/7$  when the surface tension is dominant in two-dimensional spreading where the liquid film spreads in only one direction.<sup>15</sup>

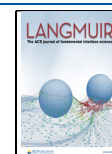
The spreading of a liquid film on a rough substrate has also been investigated. Cazabat and Cohen Stuart<sup>17</sup> conducted a series of experiments on a liquid spreading on a hydrophilic

rough glass surface and determined that the presence of the roughness made the liquid film more susceptible to spreading on the substrate. In recent years, a number of studies have been conducted on the phenomenon where water droplets deposit on a superhydrophilic surface where numerous cylinders and prismatic structures are arranged, and the liquid penetrates into the gaps between the structures (hemiwicking).<sup>18–23</sup> Courbin et al.<sup>18</sup> demonstrated that a water droplet on a superhydrophilic surface changes its shape to polygons such as a square or an octagon in the process of spreading. Several studies have attributed this phenomenon to the complex microscopic behavior of the liquid between the rows of individual columns (zipping).<sup>19,22</sup> Based on the above results, Kim et al.<sup>23</sup> constructed a scaling law to estimate the hemiwicking velocity on a rough substrate for different pillar arrangements by both macroscopic and microscopic approaches. They described the correlation from the equilibrium equations of capillary driving force and viscous drag force generated between the structure and the liquid film. Thus, to understand macroscopic liquid behavior, it is important to understand the microscopic, that is, the influence of individual structures on liquid spreading.

Received: December 3, 2019

Revised: January 21, 2020

Published: February 12, 2020





## Chapter 9

# Ongoing work: falling liquid films sheared by a turbulent gas

Several industrial applications, such as compact reflux condensers (Vlachos *et al.*, 2001) or structured packings in distillation columns (Valluri *et al.*, 2005), involve falling liquid films sheared by a counter-current gas flow within a plane channel at intermediate confinement levels, i.e.  $H^* \geq 5$  mm. At such confinement levels, in contrast to the strongly-confined films discussed in chapter 6, the effect of the gas pressure gradient  $\partial_x P_2$  on the liquid film (which enters via equation 1.76) becomes less relevant in relation to the tangential shear stress  $T_2$ . Based on the notations in figure 1.5, and assuming primary flow, the contributions of these two quantities to the liquid-side force balance are related as follows:

$$\frac{T_2}{h_0 \partial_x P_2} = \frac{d_0}{h_0} \left\{ 1 + \frac{\text{Re}_2}{\text{Fr}^2} \frac{1}{\partial_x P_2} \right\}, \quad (9.1)$$

where the second term on the RHS relates gravitational and pressure forces in the gas and is usually small. According to (9.1), the contribution of  $T_2$  thus becomes dominant as  $d_0/h_0$  is increased.

Further, large gas velocities, typically involving turbulent flow conditions, are required to significantly affect the falling liquid film, in particular when the configuration is vertical (Trifonov, 2010). Although a geometrical obstruction of the channel due to large-amplitude surface waves may still occur for moderate  $H^*$  (Vlachos *et al.*, 2001), flooding is usually associated with wave reversal (Kofman *et al.*, 2017) and/or atomization (Zapke & Kröger, 2000). However, the mechanisms underlying these catastrophic events, which clearly involve surface waves, have not been fully understood.

In the PhD. thesis of Misa Ishimura, we have modelled this flow (figure 1.5) via the approach introduced in section 1.4, which couples the WRIBL method of Ruyer-Quil & Manneville (1998), applied to the falling liquid film, with the asymptotic method of Camassa *et al.* (2017), applied to the gas flow. We have used this model to study the effect of a confined turbulent gas flow on the linear and nonlinear dynamics of surface waves, with the aim of identifying catastrophic events associated with flooding.

Samanta (2014), who employed a WRIBL model imposing a constant gas shear stress

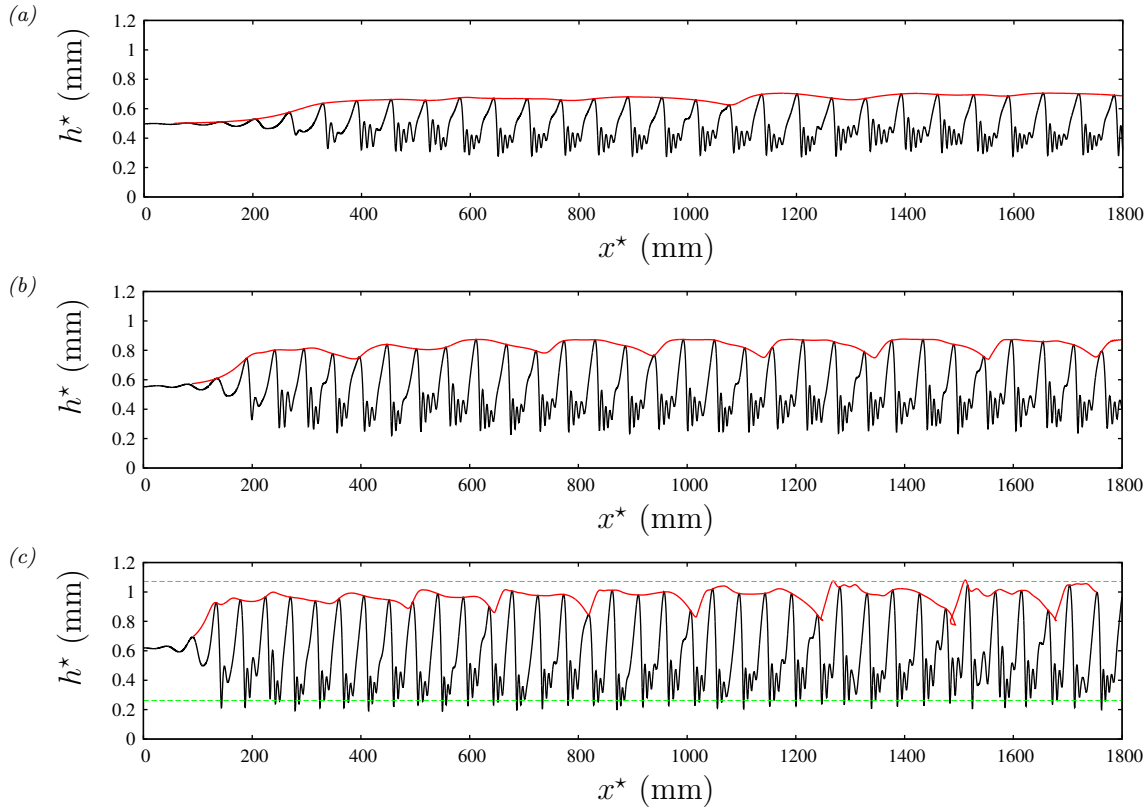


Figure 9.1: Inclined falling liquid film in contact with a counter-current turbulent gas flow. Open-domain computations with our model (1.76) applying coherent inlet forcing at frequency  $f$ . Experimental conditions from figure 4.10 in Kofman (2014):  $Ka=3174.3$  (water IV and air V in table 2.1),  $\phi=5^\circ$ ,  $H^*=19$  mm,  $Re_1=32.7$ ,  $f^*=2.8$  Hz. (a) Passive-gas reference case ( $T_2=\partial_x P_2=0$ ); (b)  $Re_2=-4123$ ; (c)  $Re_2=-6713$ .

$T_2=\text{const}$ , observed a reduction in wave amplitude under the effect of a counter-current gas flow. However, his model neglects the effect of the local instantaneous film surface position  $d$  and its inclination  $\partial_x d$  on the gas shear stress. As shown by the simulations of Tseluiko & Kalliadasis (2011), which evidence an increase in wave height with increasing counter-current gas flow rate, these effects can play a role even in the limit  $H^* \rightarrow \infty$ .

In this limit, the gas velocity profile  $u_2$  is insensitive to  $H^*$ , and the pressure gradient  $\partial_x P_2$  is negligible in the liquid-side problem. For the confinement levels studied in our work ( $10 \leq H^*/h_0^* \leq 40$ ), this approximation is not always applicable and thus the confinement level, entering via  $H^*$  in our model (1.76), comes into play.

We recall that our gas-side model was developed in the limit  $\underline{\epsilon}=\mathcal{L}_2/\Lambda^* \ll 1$ . Although we have chosen  $\mathcal{L}_2=H^*$ , this does not necessarily imply that our model is invalid for  $H^*>\Lambda^*$ . Indeed, for a fully turbulent gas flow, the main wall-normal variation of the velocity contributions  $U_0$  (1.95) and  $U_1$  (1.96) occurs over a distance much shorter than  $H^*$  (panel 2.9a). Thus,  $\mathcal{L}_2=H^*$  is a conservative estimate for the length scale of wall-

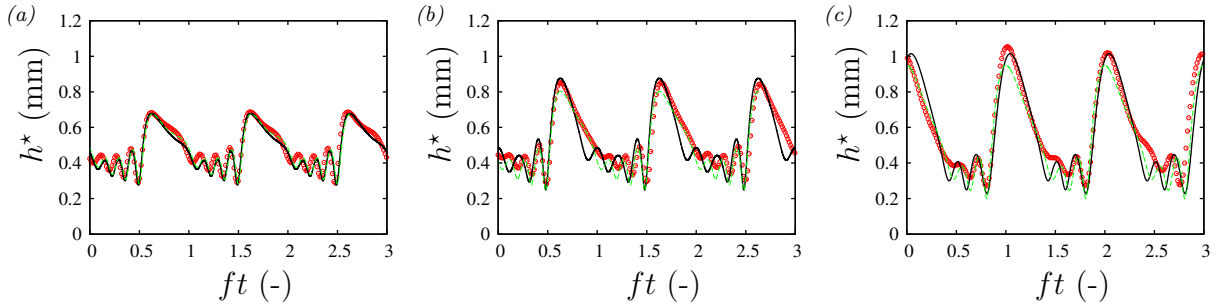


Figure 9.2: Comparison of our WRIBL model (1.76) with the experiments of Kofman (2014). Conditions according to figure 9.1. Time traces of film thickness  $h$  at a fixed streamwise position  $x$ . Red symbols: experiment; solid black lines: open-domain computations from figure 9.1; dashed green lines: TWS from figure 9.3. (a) Quiescent gas ( $T_2 = \partial_x P_2 = 0$  in the computations); (b)  $\text{Re}_2 = -4123$ ; (c)  $\text{Re}_2 = -6713$ .

normal gradients and our model is expected to work also for  $H^* > \Lambda^*$ .

Figure 9.1 represents numerical computations performed on an open-domain with our model (1.76). Conditions correspond to the experiments in figure 4.10 of Kofman (2014), which were performed in a weakly-inclined channel of height  $H^* = 19$  mm using water and air, and applying coherent inlet forcing at  $f^* = 2.8$  Hz. The counter-current gas flow rate is increased, starting from the quiescent-gas reference case (panel 9.1a), until reaching fully-turbulent conditions in the gas, i.e.  $\text{Re}_1 = -4123$  (panel 9.1b) and  $\text{Re}_1 = -6713$  (panel 9.1c). In all three panels, we observe spatial modulations of the wave height, which are due to a secondary side-band instability first identified by Liu & Gollub (1993) in the limit of a quiescent gas. Here, we see that the amplitude of these modulations increases, as the counter-current gas flow is increased (from panel 9.1a to 9.1c). In figure 9.2, we have confronted film thickness time traces obtained from these computations (solid black curves) with the measurement data (red open circles) of Kofman (2014). According to this, our model accurately captures both the increase in wave height and the suppression of capillary ripples, caused by an increasingly-strong gas flow. The dashed green curves in the same panels correspond to TWS obtained with `Auto07P` (figure 9.3), which constitute the attractors around which the modulations of the side-band instability are organized.

Figure 9.3 represents different branches of TWS in terms of the gas Reynolds number  $\text{Re}_2$ . The solid black (2 CR), dashed red (3 CR), and dot-dot-dashed green (4 CR) curves correspond to TWS at  $f^* = 2.8$  Hz with different numbers of capillary ripples (CR). These different branches coexist and it is the fastest-moving solution, as identified by the wave speed curves in panel 9.3b, that will prevail at large distances. For example, in the passive-gas computation of panel 9.1a, the wave train moves from 3 CR to 4 CR. However, when the counter-current gas flow rate is increased, the 4 CR branch in figure 9.3 disappears, and 2 CR and 3 CR waves dominate from there on (panels 9.1b and 9.1c).

The dot-dot-dashed curves in figure 9.3 correspond to 2 CR TWS at the linearly most-amplified frequency  $f = f_{\max}$ . As  $|\text{Re}_2|$  is increased, these most-amplified solutions move

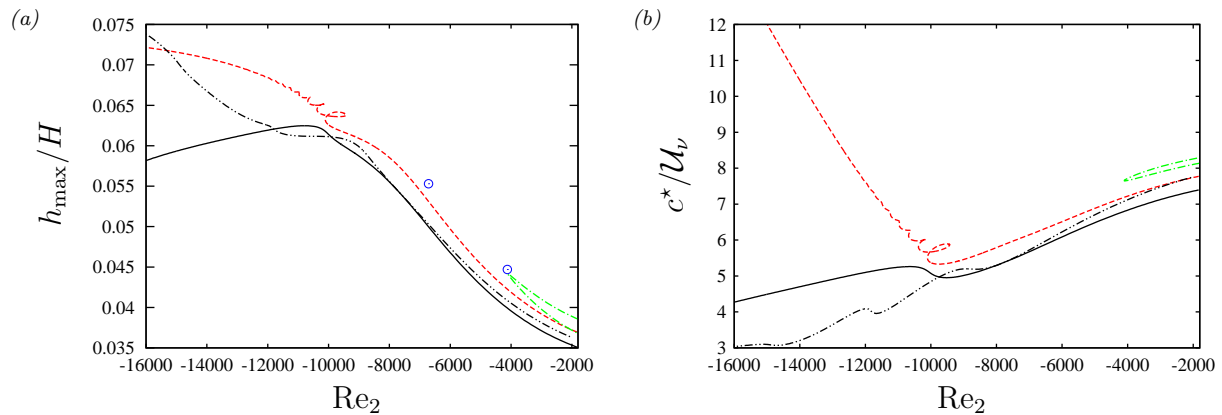


Figure 9.3: TWS obtained with our WRIBL model (1.76) for conditions corresponding to figure 9.1:  $Re_1=32.7$ ,  $f^*=2.8$  Hz. Different curves correspond to different numbers of capillary ripples (CR). Dot-dashed green: 4 CR; dashed red: 3 CR; solid black: 2 CR; dot-dot-dashed black:  $f=f_{\max}$ , 2 CR; blue open circles: experimental data from figure 9.2. (a) Wave height; (b) wave celerity.

from the 3 CR to the 2 CR branch of the TWS at  $f^*=2.8$  Hz (red dashed and black solid curves in panel 9.3b). Thus, the 2 CR TWS at  $f=2.8$  Hz become privileged from the point of view of linear growth, although their nonlinear speed is lower. This is in line with the wave forms in panel 9.1c. Of course, at long distances, the speed advantage of 3 CR solutions will prevail in an experiment. The speed discrepancy between 2 CR and 3 CR waves in panel 9.3 becomes very large starting from  $Re_2=-10^4$ . Beyond this point, the wave speed of the 3 CR branch (red dashed curve in panel 9.3b) increases, whereas that of the 2 CR branch (solid black curve) keeps decreasing.

The increase in wave speed evidenced by the dashed red curve in panel 9.3b is accompanied by an accumulation of more and more new capillary ripples, which eventually become so pronounced that they would be destroyed by spanwise capillary instability (Kofman *et al.*, 2014) in an experiment. The streamwise streaks in the experimental photographs represented in panels 3c and 3d of Kofman *et al.* (2017), could be evidence of such a 3-dimensional disintegration of capillary ripples. Thus, in our current case of a falling water film, where capillary ripples are very pronounced due to the large Kapitza number ( $Ka=3174.3$ ), our two-dimensional WRIBL model does not seem equipped to study regimes at large  $|Re_2|$ .

Instead, we consider the DMSO-water solution ( $Ka=509.5$ ) from section 6.2.1, for which we had identified an oscillatory instability in the case of superconfined vertically-falling liquid films (figure 6.6). We focus on the same liquid-side flow conditions as in panel 6.6, i.e.  $Re_1=15$  and  $f^*=16$  Hz, but we use a much larger channel height ( $H^*=10$  mm) and a fully-turbulent gas flow ( $Re_2<-1800$ ).

Panel 9.4a represents linear growth rate dispersion curves for these conditions, as  $|Re_2|$  is increased toward the AI limit  $Re_2=-8552$ . Panel 9.4b represents TWS. Black solid (1 CR) and dashed (0 CR) curves correspond to the linearly most-amplified waves

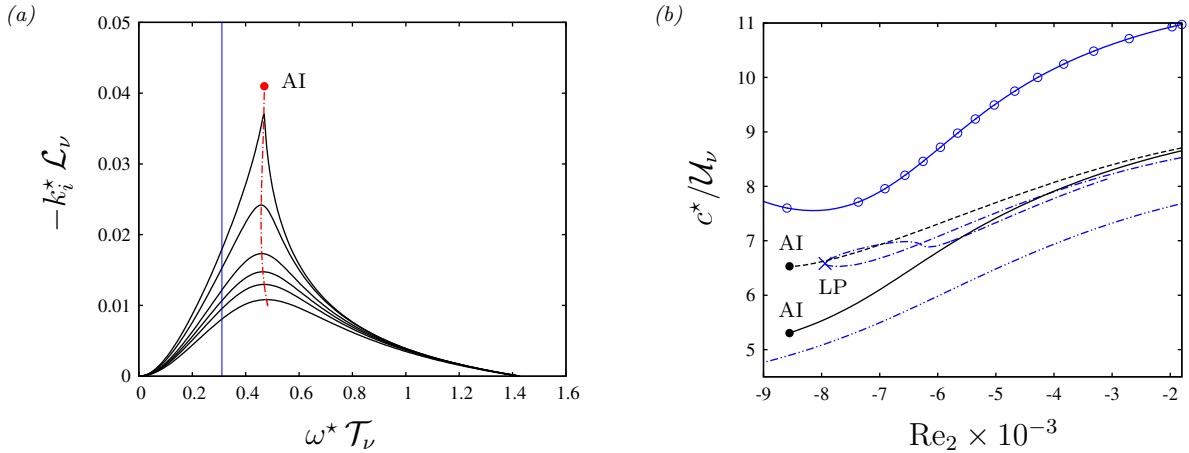


Figure 9.4: Vertically-falling liquid film from figure 6.6 subject to a turbulent gas flow in a wide channel:  $Ka=509.5$  (DMSO-water and air II in table 2.1),  $Re_1=15$ ,  $H^*=10$  mm. (a) Linear spatial growth rate. From bottom to top:  $Re_2=-2000$ ,  $-4000$ ,  $-5000$ ,  $-6000$ ,  $-7500$ , and  $-8500$ . Red dot-dashed curve: maximum growth rate until AI limit  $Re_2^{AI}=-8552$ . Vertical line:  $f^*=16$  Hz; (b) TWS at  $f=f_{\max}$  (black solid and dashed curves) and  $f^*=16$  Hz (blue dot-dashed, dot-dot-dashed, and open circles). Dashed/dot-dot-dashed: 0 capillary ripples (CR), solid: 1 CR, dot-dashed: 2 CR, open circles:  $>1$  CR.

at  $f=f_{\max}$ , whereas the blue dot-dashed curves (2 CR), dot-dot-dashed curves (0 CR), and curves with open circles (several CR) correspond to solitary waves at  $f^*=16$  Hz. TWS on the two  $f=f_{\max}$  solution branches (black curves) exist up to the AI limit, similar to our observations for superconfined films (panel 6.4). The solitary TWS at  $f^*=16$  Hz (blue curves) extend beyond the AI limit, and they can be bounded by a nonlinear limit point (LP). However, their linear growth rate diminishes w.r.t. that of the most-amplified waves as  $|Re_2|$  is increased (panel 9.4a), and thus they become less likely to prevail in an experiment.

Figure 9.5 represents results of an open-domain computation with our WRIBL model for the system in figure 9.4. In this computation, we have forced solitary waves through coherent inlet forcing at  $f^*=16$  Hz, and incrementally increased the counter-current gas flow rate toward the AI bound  $Re_2^{AI}=-8552$ . Sufficiently far from the AI bound ( $Re_2=-6500$ ), the liquid film responds well to the inlet forcing, leading to a regular train of solitary waves (panel 9.4a). By contrast, for  $Re_2=-7500$  (panels 9.5b to 9.5e), a train of high frequency waves develops near the liquid inlet (panels 9.5a and 9.5d). These waves still propagate downstream, but their spatial growth rate is extremely large, so that they saturate within one wavelength (panel 9.5b).

They result from noise-sustained linear wave selection, and thus the wave train exhibits small defects that lead to coalescence events and coarsening dynamics (Chang *et al.*, 1996c) further downstream (panel 9.5b). The resulting large-amplitude tsunami waves are separated by long portions of residual film. It is here that absolute instability takes hold to form rapidly growing (in time) secondary waves, which are almost standing. This can

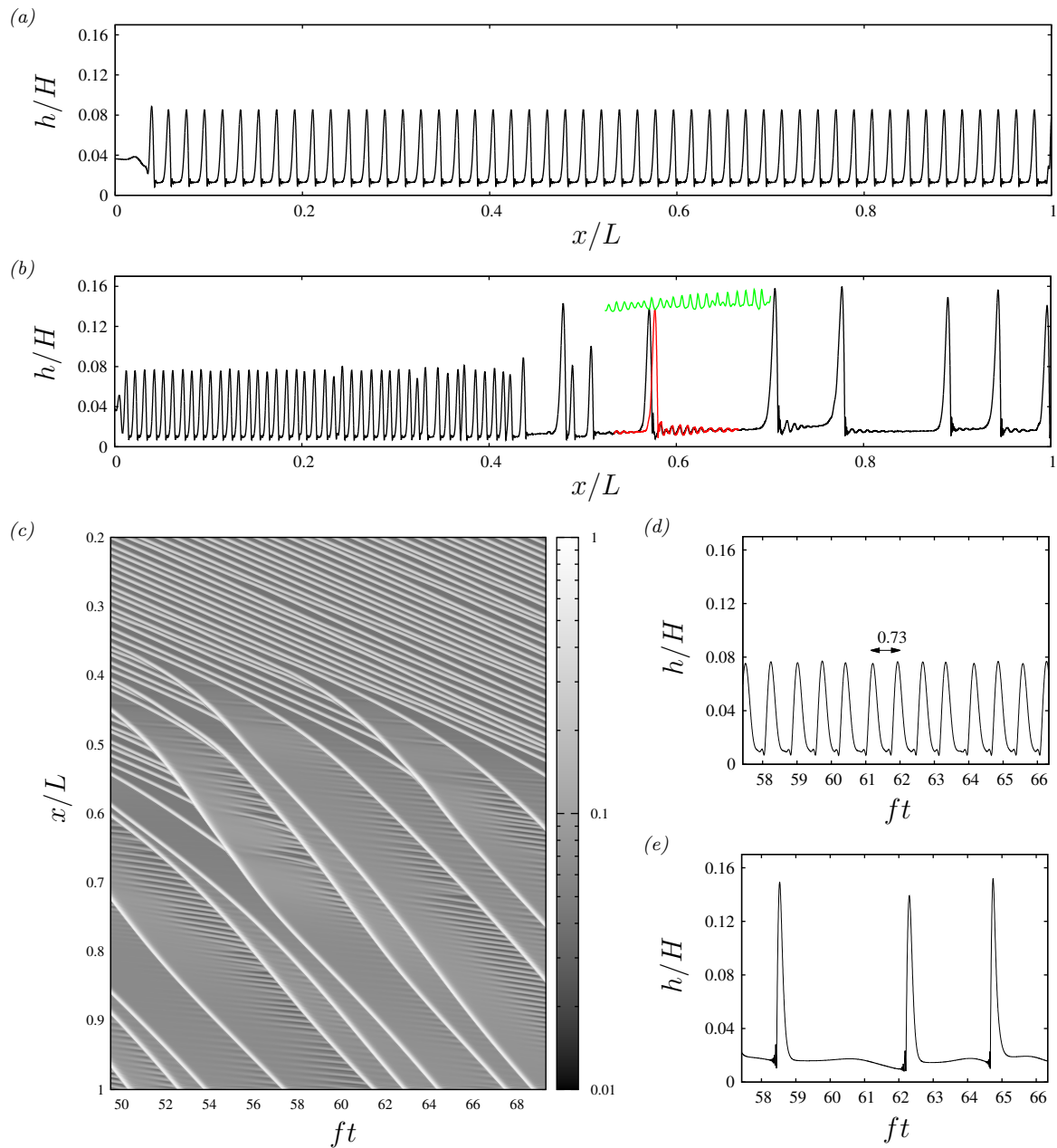


Figure 9.5: Vertically-falling liquid film from figure 9.4 leading up to the AI limit:  $Ka=509.46$ ,  $H^*=10$  mm,  $Re_1=15$ ,  $Re_2^{AI}=-8552$ . WRIBL computations on an open domain of length  $L^*=0.843$  m, using coherent inlet forcing (2.38):  $f^*=16$  Hz,  $\epsilon_1=0.01$ ,  $\epsilon_2=0$ . (a)  $Re_2=-6500$ ; (b-e)  $Re_2=-7500$ . (a,b) Snapshots of the fully developed film profile  $h(x)$ . Red segment corresponds to slightly later time and green curve indicates spatial oscillation undergone by the large wave crests; (c) spatio-temporal diagram of normalized film height  $h/h_{\max}$ ; (d,e) film height time traces  $h(t)$  at  $x/L=0.1$  and  $x/L=0.6$ .

be deduced by confronting the spatial and temporal film height profiles in panels 9.5b and



9.5e. In the spatio-temporal plot of panel 9.5c, these secondary waves appear as almost horizontal streaks connecting to the downward sloping fronts of the tsunami waves. This structure is similar to the ripples observed experimentally in panel 20b of Kofman *et al.* (2017), although those ripples moved upward. The experiments of Kofman *et al.* (2017) were conducted in a weakly-inclined channel using water. For such configurations, we have found that the liquid flow rate  $q_1$  in the residual film in between large waves can become negative, thus allowing for a transition from downward-convective to upward-convective instability via absolute instability (Vellingiri *et al.*, 2015; Schmidt *et al.*, 2016). This may explain the difference between the experimental observation of Kofman *et al.* (2017) and the downward-travelling ripples observed in our vertically-falling liquid film (panel 9.5c).

Having said this, the ripples observed in panel 9.5c move extremely slowly, i.e. they are much slower than the tsunami waves. This can be observed by comparing the full profile in panel 9.5b (solid black line) with the red profile segment, which corresponds to a slightly later time. During the time span separating these two profiles, the tsunami waves have visibly moved, while the ripples have not. As a result of this speed discrepancy, the large wave humps move over the ripples and this causes a strong modulation of their amplitude (green curve tracking one of the wave maxima in panel 9.5b). Although the cause for these modulations is quite different from that for the oscillatory instability in panel 6.6c, their effect on heat and mass transfer is expected to be equally beneficial. Based on the result in figure 9.5, it seems that wave regimes leading up to the AI limit are not necessarily dangerous, and may even be useful.

The assumptions underlying the representation of turbulence in our WRIBL model from section 1.4 are quite crude. We use a mixing-length model to represent the turbulent viscosity, we assume that the liquid-gas interface behaves like a wall from the point of view of the gas (turbulent fluctuations at the liquid-gas interface are neglected), and, due to our first-order long-wave formulation, only the  $\rho_2 \overline{u_2'v_2'}$  Reynolds stress is accounted for. Although our comparisons with the experiments of Kofman *et al.* (2017) (figure 9.2) give some confidence in our approach, it would be helpful to check our assumptions against numerical simulations based on the full unsteady RANS equations, large eddy simulations (LES), or DNS. For example, Adjoua (2010) have developed a two-phase VOF solver within the JADIM code, where turbulence is resolved through the LES approach. This code has been applied to the simulation of horizontal liquid films driven by a co-current turbulent gas flow (Adjoua & Magnaudet, 2009). Based on their results, the authors concluded that the liquid-gas interface can be considered as a solid wall from the point of view of the gas.





# Appendix A

## Coefficients of WRIBL models

The expressions for all coefficients reported in this appendix have been inserted into the current L<sup>A</sup>T<sub>E</sub>X document automatically from the corresponding *Mathematica* source files using the *Splice* command. This avoids manual transcription errors. As a result of the automatic transcription, the notation for derivatives is different than in the main body of the document. For functions of the form  $w(y)$  and  $f(y, h)$  with  $h=h(x, t)$ , the following definitions apply:

$$\begin{aligned} w'(y) &= \partial_y w, \\ f^{(n,0)}(y, h) &= (\partial_y)^n f, \quad f^{(0,n)}(y, h) = (\partial_h)^n f, \quad f^{(1,1)}(h, h) = (\partial_{yh} f)|_{y=h}. \end{aligned} \tag{A.1}$$

### A.1 Planar model

The coefficients  $f_{ki}$  of the streamwise velocity component's base profile  $\hat{u}_k$  (1.17) are as follows:

$$f_{11} = \frac{3y(y(-4h\Pi_\mu + h - H) + 2h(h(2\Pi_\mu - 1) + H))}{2h^3(h(\Pi_\mu - 1) + H)} \tag{A.2a}$$

$$f_{12} = \frac{3y(2h - 3y)\Pi_\mu\Pi_u}{2h(h - H)(h(\Pi_\mu - 1) + H)} \tag{A.2b}$$

$$f_{21} = -\frac{3(H - y)(2h + H - 3y)}{2h(h - H)\Pi_u(h(\Pi_\mu - 1) + H)} \tag{A.2c}$$

$$f_{22} = -\frac{3(H - y)(-2h^2(\Pi_\mu - 2) + h(H + y)(\Pi_\mu - 4) + 4Hy)}{2(h - H)^3(h(\Pi_\mu - 1) + H)} \tag{A.2d}$$

The coefficients  $g_{k1}$ ,  $g_{k2}$ ,  $g_{k3}$ , and  $g_{k4}$  of the wall-normal velocity component's base profile  $\hat{v}_k$  (1.22) are as follows. For the liquid ( $k=1$ ):

$$\begin{aligned} g_{11} &= - \int_0^y f_{11}^{(0,1)}(\tilde{y}, h) d\tilde{y}, & g_{12} &= - \int_0^y f_{12}^{(0,1)}(\tilde{y}, h) d\tilde{y}, \\ g_{13} &= - \int_0^y f_{11}(\tilde{y}, h) d\tilde{y}, & g_{14} &= - \int_0^y f_{12}(\tilde{y}, h) d\tilde{y}, \end{aligned} \tag{A.3a}$$

and for the gas ( $k=2$ ):

$$\begin{aligned} g_{21} &= \int_y^H f_{21}^{(0,1)}(\tilde{y}, h) d\tilde{y}, & g_{22} &= \int_y^H f_{22}^{(0,1)}(\tilde{y}, h) d\tilde{y}, \\ g_{23} &= \int_y^H f_{21}(\tilde{y}, h) d\tilde{y}, & g_{24} &= \int_y^H f_{22}(\tilde{y}, h) d\tilde{y}. \end{aligned} \tag{A.3b}$$

The coefficients  $S_i$ ,  $F_{ij}$ ,  $G_{ij}$ ,  $C_i$ ,  $J_i$ ,  $K_i$ ,  $L_i$ , and  $M_i$  of the momentum equation (1.27) are defined on the next pages.

$$S_1 = \Pi_\rho \Pi_u^2 \left( \int_h^H w_2(y) f_{21}(y, h) dy \right) + \int_0^h w_1(y) f_{11}(y, h) dy$$

$$S_2 = \Pi_\rho \Pi_u^2 \left( \int_h^H w_2(y) f_{22}(y, h) dy \right) + \int_0^h w_1(y) f_{12}(y, h) dy$$

$$\begin{aligned} F_{11} = & \Pi_\rho \Pi_u^3 \left( \int_h^H w_2(y) f_{21}^{(1,0)}(y, h) g_{23}(y, h) dy + \int_h^H w_2(y) f_{21}(y, h)^2 dy \right) \\ & + \int_0^h w_1(y) f_{11}^{(1,0)}(y, h) g_{13}(y, h) dy \\ & + \int_0^h w_1(y) f_{11}(y, h)^2 dy - \int_0^h w_1(y) f_{11}^{(0,1)}(y, h) dy \end{aligned}$$

$$\begin{aligned} F_{12} = & \Pi_\rho \Pi_u^3 \left( \int_h^H w_2(y) f_{21}^{(1,0)}(y, h) g_{24}(y, h) dy + \int_h^H w_2(y) f_{21}(y, h) f_{22}(y, h) dy \right) \\ & + \int_0^h w_1(y) f_{11}^{(1,0)}(y, h) g_{14}(y, h) dy \\ & + \Pi_\rho \Pi_u^2 \left( \int_h^H w_2(y) f_{21}^{(0,1)}(y, h) dy \right) + \int_0^h w_1(y) f_{11}(y, h) f_{12}(y, h) dy \end{aligned}$$

$$\begin{aligned} F_{21} = & \Pi_\rho \Pi_u^3 \left( \int_h^H w_2(y) f_{22}^{(1,0)}(y, h) g_{23}(y, h) dy + \int_h^H w_2(y) f_{21}(y, h) f_{22}(y, h) dy \right) \\ & + \int_0^h w_1(y) f_{12}^{(1,0)}(y, h) g_{13}(y, h) dy \\ & + \int_0^h w_1(y) f_{11}(y, h) f_{12}(y, h) dy - \int_0^h w_1(y) f_{12}^{(0,1)}(y, h) dy \end{aligned}$$

$$\begin{aligned} F_{22} = & \Pi_\rho \Pi_u^3 \left( \int_h^H w_2(y) f_{22}^{(1,0)}(y, h) g_{24}(y, h) dy + \int_h^H w_2(y) f_{22}(y, h)^2 dy \right) \\ & + \int_0^h w_1(y) f_{12}^{(1,0)}(y, h) g_{14}(y, h) dy \\ & + \Pi_\rho \Pi_u^2 \left( \int_h^H w_2(y) f_{22}^{(0,1)}(y, h) dy \right) + \int_0^h w_1(y) f_{12}(y, h)^2 dy \end{aligned}$$

$$\begin{aligned} G_{11} = & \Pi_\rho \Pi_u^3 \left( \int_h^H w_2(y) f_{21}^{(1,0)}(y, h) g_{21}(y, h) dy + \int_h^H w_2(y) f_{21}(y, h) f_{21}^{(0,1)}(y, h) dy \right) \\ & + \int_0^h w_1(y) f_{11}^{(1,0)}(y, h) g_{11}(y, h) dy + \int_0^h w_1(y) f_{11}(y, h) f_{11}^{(0,1)}(y, h) dy \end{aligned}$$

$$\begin{aligned}
G_{12} &= G_{21} \\
&= \frac{1}{2} \Pi_\rho \Pi_u^3 \left( \int_h^H w_2(y) f_{21}^{(1,0)}(y, h) g_{22}(y, h) dy + \int_h^H w_2(y) f_{22}^{(1,0)}(y, h) g_{21}(y, h) dy \right. \\
&\quad \left. + \int_h^H w_2(y) f_{22}(y, h) f_{21}^{(0,1)}(y, h) dy + \int_h^H w_2(y) f_{21}(y, h) f_{22}^{(0,1)}(y, h) dy \right) \\
&\quad + \frac{1}{2} \left( \int_0^h w_1(y) f_{11}^{(1,0)}(y, h) g_{12}(y, h) dy + \int_0^h w_1(y) f_{12}^{(1,0)}(y, h) g_{11}(y, h) dy \right. \\
&\quad \left. + \int_0^h w_1(y) f_{12}(y, h) f_{11}^{(0,1)}(y, h) dy + \int_0^h w_1(y) f_{11}(y, h) f_{12}^{(0,1)}(y, h) dy \right) \\
G_{22} &= \Pi_\rho \Pi_u^3 \left( \int_h^H w_2(y) f_{22}^{(1,0)}(y, h) g_{22}(y, h) dy + \int_h^H w_2(y) f_{22}(y, h) f_{22}^{(0,1)}(y, h) dy \right) \\
&\quad + \int_0^h w_1(y) f_{12}^{(1,0)}(y, h) g_{12}(y, h) dy + \int_0^h w_1(y) f_{12}(y, h) f_{12}^{(0,1)}(y, h) dy \\
C_1 &= \text{Re}_2^{-1} \Pi_\rho \Pi_u^3 \left( \int_h^H w_2(y) f_{21}^{(2,0)}(y, h) dy \right) + \text{Re}_1^{-1} w_1(h) \Pi_\mu \Pi_u f_{21}^{(1,0)}(h, h) \\
&\quad + \text{Re}_1^{-1} \left( -\Pi_u f_{21}(h, h) w_1'(h) + \int_0^h w_1(y) f_{11}^{(2,0)}(y, h) dy + f_{11}(h, h) w_1'(h) \right. \\
&\quad \left. - w_1(h) f_{11}^{(1,0)}(h, h) \right) \\
C_2 &= \text{Re}_2^{-1} \Pi_\rho \Pi_u^3 \left( \int_h^H w_2(y) f_{22}^{(2,0)}(y, h) dy \right) + \text{Re}_1^{-1} w_1(h) \Pi_\mu \Pi_u f_{22}^{(1,0)}(h, h) \\
&\quad + \text{Re}_1^{-1} \left( -\Pi_u f_{22}(h, h) w_1'(h) + \int_0^h w_1(y) f_{12}^{(2,0)}(y, h) dy + f_{12}(h, h) w_1'(h) \right. \\
&\quad \left. - w_1(h) f_{12}^{(1,0)}(h, h) \right) \\
J_1 &= \text{Re}_1^{-1} \Pi_\mu \Pi_u \left( -2w_1(h) f_{21}^{(0,1)}(h, h) + 2g_{21}^{(1,1)}(h, h) \left( \int_0^h w_1(y) dy \right) \right. \\
&\quad \left. + 2g_{21}^{(2,0)}(h, h) \left( \int_0^h w_1(y) dy \right) + w_1(h) g_{21}^{(0,1)}(h, h) + 2w_1(h) g_{21}^{(1,0)}(h, h) \right) \\
&\quad + \text{Re}_1^{-1} \left( 2 \int_0^h w_1(y) f_{11}^{(0,2)}(y, h) dy + f_{11}^{(0,2)}(h, h) \left( \int_0^h w_1(y) dy \right) \right. \\
&\quad \left. + f_{11}^{(1,1)}(h, h) \left( \int_0^h w_1(y) dy \right) + 4w_1(h) f_{11}^{(0,1)}(h, h) - w_1(h) g_{11}^{(0,1)}(h, h) \right) \\
&\quad + \text{Re}_2^{-1} \Pi_\rho \Pi_u^3 \left( 2 \int_h^H w_2(y) f_{21}^{(0,2)}(y, h) dy - f_{21}^{(0,2)}(h, h) \left( \int_h^H w_2(y) dy \right) \right. \\
&\quad \left. - f_{21}^{(1,1)}(h, h) \left( \int_h^H w_2(y) dy \right) \right)
\end{aligned}$$

$$\begin{aligned}
J_2 = & \operatorname{Re}_1^{-1} \Pi_\mu \Pi_u \left( -2w_1(h) f_{22}^{(0,1)}(h, h) + 2g_{22}^{(1,1)}(h, h) \left( \int_0^h w_1(y) dy \right) \right. \\
& \left. + 2g_{22}^{(2,0)}(h, h) \left( \int_0^h w_1(y) dy \right) + w_1(h) g_{22}^{(0,1)}(h, h) + 2w_1(h) g_{22}^{(1,0)}(h, h) \right) \\
& + \operatorname{Re}_1^{-1} \left( 2 \int_0^h w_1(y) f_{12}^{(0,2)}(y, h) dy + f_{12}^{(0,2)}(h, h) \left( \int_0^h w_1(y) dy \right) \right. \\
& \left. + f_{12}^{(1,1)}(h, h) \left( \int_0^h w_1(y) dy \right) + 4w_1(h) f_{12}^{(0,1)}(h, h) - w_1(h) g_{12}^{(0,1)}(h, h) \right) \\
& + \operatorname{Re}_2^{-1} \Pi_\rho \Pi_u^3 \left( 2 \int_h^H w_2(y) f_{22}^{(0,2)}(y, h) dy - f_{22}^{(0,2)}(h, h) \left( \int_h^H w_2(y) dy \right) \right. \\
& \left. - f_{22}^{(1,1)}(h, h) \left( \int_h^H w_2(y) dy \right) \right)
\end{aligned}$$

$$\begin{aligned}
K_1 = & \operatorname{Re}_1^{-1} \Pi_\mu \Pi_u \left( -2w_1(h) f_{21}(h, h) + 2g_{21}^{(1,0)}(h, h) \left( \int_0^h w_1(y) dy \right) \right. \\
& \left. + 2g_{23}^{(1,1)}(h, h) \left( \int_0^h w_1(y) dy \right) + 2g_{23}^{(2,0)}(h, h) \left( \int_0^h w_1(y) dy \right) + w_1(h) g_{21}(h, h) \right. \\
& \left. + w_1(h) g_{23}^{(0,1)}(h, h) + 2w_1(h) g_{23}^{(1,0)}(h, h) \right) + \operatorname{Re}_1^{-1} \left( 4 \int_0^h w_1(y) f_{11}^{(0,1)}(y, h) dy \right. \\
& \left. + 2f_{11}^{(0,1)}(h, h) \left( \int_0^h w_1(y) dy \right) + f_{11}^{(1,0)}(h, h) \left( \int_0^h w_1(y) dy \right) + 4w_1(h) f_{11}(h, h) \right. \\
& \left. - w_1(h) g_{11}(h, h) - w_1(h) g_{13}^{(0,1)}(h, h) \right) + \operatorname{Re}_2^{-1} \Pi_\rho \Pi_u^3 \left( 4 \int_h^H w_2(y) f_{21}^{(0,1)}(y, h) dy \right. \\
& \left. - 2f_{21}^{(0,1)}(h, h) \left( \int_h^H w_2(y) dy \right) - f_{21}^{(1,0)}(h, h) \left( \int_h^H w_2(y) dy \right) \right)
\end{aligned}$$

$$\begin{aligned}
K_2 = & \operatorname{Re}_1^{-1} \Pi_\mu \Pi_u \left( -2w_1(h) f_{22}(h, h) + 2g_{22}^{(1,0)}(h, h) \left( \int_0^h w_1(y) dy \right) \right. \\
& \left. + 2g_{24}^{(1,1)}(h, h) \left( \int_0^h w_1(y) dy \right) + 2g_{24}^{(2,0)}(h, h) \left( \int_0^h w_1(y) dy \right) + w_1(h) g_{22}(h, h) \right. \\
& \left. + w_1(h) g_{24}^{(0,1)}(h, h) + 2w_1(h) g_{24}^{(1,0)}(h, h) \right) + \operatorname{Re}_1^{-1} \left( 4 \int_0^h w_1(y) f_{12}^{(0,1)}(y, h) dy \right. \\
& \left. + 2f_{12}^{(0,1)}(h, h) \left( \int_0^h w_1(y) dy \right) + f_{12}^{(1,0)}(h, h) \left( \int_0^h w_1(y) dy \right) + 4w_1(h) f_{12}(h, h) \right. \\
& \left. - w_1(h) g_{12}(h, h) - w_1(h) g_{14}^{(0,1)}(h, h) \right) + \operatorname{Re}_2^{-1} \Pi_\rho \Pi_u^3 \left( 4 \int_h^H w_2(y) f_{22}^{(0,1)}(y, h) dy \right. \\
& \left. - 2f_{22}^{(0,1)}(h, h) \left( \int_h^H w_2(y) dy \right) - f_{22}^{(1,0)}(h, h) \left( \int_h^H w_2(y) dy \right) \right)
\end{aligned}$$



$$\begin{aligned}
L_1 &= \operatorname{Re}_1^{-1} \left( 2 \int_0^h w_1(y) f_{11}^{(0,1)}(y, h) dy + f_{11}^{(0,1)}(h, h) \left( \int_0^h w_1(y) dy \right) - w_1(h) g_{11}(h, h) \right) \\
&\quad + \operatorname{Re}_2^{-1} \Pi_\rho \Pi_u^3 \left( 2 \int_h^H w_2(y) f_{21}^{(0,1)}(y, h) dy - f_{21}^{(0,1)}(h, h) \left( \int_h^H w_2(y) dy \right) \right) \\
&\quad + \operatorname{Re}_1^{-1} \Pi_\mu \Pi_u \left( 2 g_{21}^{(1,0)}(h, h) \left( \int_0^h w_1(y) dy \right) + w_1(h) g_{21}(h, h) \right) \\
L_2 &= \operatorname{Re}_1^{-1} \left( 2 \int_0^h w_1(y) f_{12}^{(0,1)}(y, h) dy + f_{12}^{(0,1)}(h, h) \left( \int_0^h w_1(y) dy \right) - w_1(h) g_{12}(h, h) \right) \\
&\quad + \operatorname{Re}_2^{-1} \Pi_\rho \Pi_u^3 \left( 2 \int_h^H w_2(y) f_{22}^{(0,1)}(y, h) dy - f_{22}^{(0,1)}(h, h) \left( \int_h^H w_2(y) dy \right) \right) \\
&\quad + \operatorname{Re}_1^{-1} \Pi_\mu \Pi_u \left( 2 g_{22}^{(1,0)}(h, h) \left( \int_0^h w_1(y) dy \right) + w_1(h) g_{22}(h, h) \right) \\
M_1 &= \operatorname{Re}_1^{-1} \left( 2 \int_0^h w_1(y) f_{11}(y, h) dy + f_{11}(h, h) \left( \int_0^h w_1(y) dy \right) - w_1(h) g_{13}(h, h) \right) \\
&\quad + \operatorname{Re}_2^{-1} \Pi_\rho \Pi_u^3 \left( 2 \int_h^H w_2(y) f_{21}(y, h) dy - f_{21}(h, h) \left( \int_h^H w_2(y) dy \right) \right) \\
&\quad + \operatorname{Re}_1^{-1} \Pi_\mu \Pi_u \left( 2 g_{23}^{(1,0)}(h, h) \left( \int_0^h w_1(y) dy \right) + w_1(h) g_{23}(h, h) \right) \\
M_2 &= \operatorname{Re}_1^{-1} \left( 2 \int_0^h w_1(y) f_{12}(y, h) dy + f_{12}(h, h) \left( \int_0^h w_1(y) dy \right) - w_1(h) g_{14}(h, h) \right) \\
&\quad + \operatorname{Re}_2^{-1} \Pi_\rho \Pi_u^3 \left( 2 \int_h^H w_2(y) f_{22}(y, h) dy - f_{22}(h, h) \left( \int_h^H w_2(y) dy \right) \right) \\
&\quad + \operatorname{Re}_1^{-1} \Pi_\mu \Pi_u \left( 2 g_{24}^{(1,0)}(h, h) \left( \int_0^h w_1(y) dy \right) + w_1(h) g_{24}(h, h) \right)
\end{aligned}$$

## A.2 Cylindrical model

The coefficients  $f_{ki}$  of the streamwise velocity component's base profile  $\hat{u}_k$  (1.49) are as follows (where “log” refers to the natural logarithm):

$$f_{11} = \frac{\log(R) ((8d^2 - 8r^2) \Pi_\mu - 4d^2)}{\Xi} + \frac{\log(r) ((8R^2 - 8d^2) \Pi_\mu + 4d^2)}{\Xi} \quad (\text{A.4a})$$

$$+ \frac{\log(d) \Pi_\mu (8r^2 - 8R^2)}{\Xi} + \frac{2R^2 - 2r^2}{\Xi},$$

$$f_{12} = \frac{\Pi_\mu \Pi_u \log(R) \left( \frac{4R^4}{d^2} + 4d^2 - 8r^2 \right)}{\Xi} + \frac{\Pi_\mu \Pi_u \left( \frac{4r^2 R^2}{d^2} - \frac{4R^4}{d^2} - 4r^2 + 4R^2 \right)}{\Xi} \quad (\text{A.4b})$$

$$+ \frac{\left( -\frac{4R^4}{d^2} - 4d^2 + 8R^2 \right) \Pi_\mu \Pi_u \log(r)}{\Xi} + \frac{\log(d) \Pi_\mu \Pi_u (8r^2 - 8R^2)}{\Xi},$$

$$f_{21} = \frac{\frac{4r^2 R^2}{d^2} + 2d^2 - 4r^2 - 2R^2}{\Xi \Pi_u} + \frac{(4d^2 - 8r^2) \log(R)}{\Xi \Pi_u} + \frac{(8r^2 - 4d^2) \log(d)}{\Xi \Pi_u}, \quad (\text{A.4c})$$

$$f_{22} = \frac{\log(d) \left( \left( 4d^2 - \frac{4R^4}{d^2} \right) \Pi_\mu - 8d^2 + 8r^2 \right)}{\Xi} + \frac{\log(R) \left( \left( \frac{4R^4}{d^2} - 4d^2 \right) \Pi_\mu + 8d^2 - 8r^2 \right)}{\Xi}$$

$$+ \frac{-\frac{2r^2 R^4}{d^4} + \left( -\frac{4R^4}{d^2} - 4d^2 + 8R^2 \right) \Pi_\mu + \frac{8r^2 R^2}{d^2} + \frac{2R^4}{d^2} + 6d^2 - 6r^2 - 8R^2}{\Xi}, \quad (\text{A.4d})$$

where we have extracted the common factor  $\Xi$ :

$$\Xi = \pi \log(d) \left( (4d^4 - 4R^4) \Pi_\mu - 4d^4 \right) + \pi \log(R) \left( (4R^4 - 4d^4) \Pi_\mu + 4d^4 \right) \quad (\text{A.4e})$$

$$+ \pi \left( -4d^4 + 8d^2 R^2 - 4R^4 \right) \Pi_\mu + \pi \left( 3d^4 - 4d^2 R^2 + R^4 \right).$$

The coefficients  $g_{k1}$ ,  $g_{k2}$ ,  $g_{k3}$ , and  $g_{k4}$  of the wall-normal velocity component's base profile  $\hat{v}_k$  (1.50) are as follows. For the liquid film ( $k=1$ ):

$$g_{11} = \frac{\int_r^R \tilde{r} f_{11}^{(0,1)}(\tilde{r}, d) d\tilde{r}}{r}, \quad g_{12} = \frac{\int_r^R \tilde{r} f_{12}^{(0,1)}(\tilde{r}, d) d\tilde{r}}{r}, \quad (\text{A.5a})$$

$$g_{13} = \frac{\int_r^R \tilde{r} f_{11}(\tilde{r}, d) d\tilde{r}}{r}, \quad g_{14} = \frac{\int_r^R \tilde{r} f_{12}(\tilde{r}, d) d\tilde{r}}{r},$$

and for the core fluid ( $k=2$ ):

$$g_{21} = -\frac{\int_0^r \tilde{r} f_{21}^{(0,1)}(\tilde{r}, d) d\tilde{r}}{r}, \quad g_{22} = -\frac{\int_0^r \tilde{r} f_{22}^{(0,1)}(\tilde{r}, d) d\tilde{r}}{r}, \quad (\text{A.5b})$$

$$g_{23} = -\frac{\int_0^r \tilde{r} f_{21}(\tilde{r}, d) d\tilde{r}}{r}, \quad g_{24} = -\frac{\int_0^r \tilde{r} f_{22}(\tilde{r}, d) d\tilde{r}}{r}.$$

The coefficients  $S_i$ ,  $F_{ij}$ ,  $G_{ij}$ ,  $C_i$ ,  $J_i$ ,  $K_i$ ,  $L_i$ , and  $M_i$  of the momentum equation (1.48) are defined on the next pages.

$$S_1 = \Pi_\rho \Pi_u^2 \left( \int_0^d r w_2(r) f_{21}(r, d) dr \right) + \int_d^R r w_1(r) f_{11}(r, d) dr$$

$$S_2 = \Pi_\rho \Pi_u^2 \left( \int_0^d r w_2(r) f_{22}(r, d) dr \right) + \int_d^R r w_1(r) f_{12}(r, d) dr$$

$$\begin{aligned} F_{11} = & \Pi_\rho \Pi_u^3 \left( \int_0^d r w_2(r) f_{21}^{(1,0)}(r, d) g_{23}(r, d) dr + \int_0^d r w_2(r) f_{21}(r, d)^2 dr \right) \\ & + \int_d^R r w_1(r) f_{11}^{(1,0)}(r, d) g_{13}(r, d) dr \\ & + \int_d^R r w_1(r) f_{11}(r, d)^2 dr + \frac{\int_d^R r w_1(r) f_{11}^{(0,1)}(r, d) dr}{2\pi d} \end{aligned}$$

$$\begin{aligned} F_{12} = & \Pi_\rho \Pi_u^3 \left( \int_0^d r w_2(r) f_{21}^{(1,0)}(r, d) g_{24}(r, d) dr + \int_0^d r w_2(r) f_{21}(r, d) f_{22}(r, d) dr \right. \\ & \left. - \frac{\int_0^d r w_2(r) f_{21}^{(0,1)}(r, d) dr}{2\pi d} \right) \\ & + \int_d^R r w_1(r) f_{11}^{(1,0)}(r, d) g_{14}(r, d) dr + \int_d^R r w_1(r) f_{11}(r, d) f_{12}(r, d) dr \end{aligned}$$

$$\begin{aligned} F_{21} = & \Pi_\rho \Pi_u^3 \left( \int_0^d r w_2(r) f_{22}^{(1,0)}(r, d) g_{23}(r, d) dr + \int_0^d r w_2(r) f_{21}(r, d) f_{22}(r, d) dr \right) \\ & + \int_d^R r w_1(r) f_{12}^{(1,0)}(r, d) g_{13}(r, d) dr \\ & + \int_d^R r w_1(r) f_{11}(r, d) f_{12}(r, d) dr + \frac{\int_d^R r w_1(r) f_{12}^{(0,1)}(r, d) dr}{2\pi d} \end{aligned}$$

$$\begin{aligned} F_{22} = & \Pi_\rho \Pi_u^3 \left( \int_0^d r w_2(r) f_{22}^{(1,0)}(r, d) g_{24}(r, d) dr + \int_0^d r w_2(r) f_{22}(r, d)^2 dr \right. \\ & \left. - \frac{\int_0^d r w_2(r) f_{22}^{(0,1)}(r, d) dr}{2\pi d} \right) \\ & + \int_d^R r w_1(r) f_{12}^{(1,0)}(r, d) g_{14}(r, d) dr + \int_d^R r w_1(r) f_{12}(r, d)^2 dr \end{aligned}$$

$$\begin{aligned} G_{11} = & \Pi_\rho \Pi_u^3 \left( \int_0^d r w_2(r) f_{21}^{(1,0)}(r, d) g_{21}(r, d) dr + \int_0^d r w_2(r) f_{21}(r, d) f_{21}^{(0,1)}(r, d) dr \right) \\ & + \int_d^R r w_1(r) f_{11}^{(1,0)}(r, d) g_{11}(r, d) dr + \int_d^R r w_1(r) f_{11}(r, d) f_{11}^{(0,1)}(r, d) dr \end{aligned}$$

$$\begin{aligned}
G_{12} &= G_{21} \\
&= \frac{1}{2} \Pi_\rho \Pi_u^3 \left( \int_0^d r w_2(r) f_{21}^{(1,0)}(r, d) g_{22}(r, d) dr + \int_0^d r w_2(r) f_{22}^{(1,0)}(r, d) g_{21}(r, d) dr \right. \\
&\quad \left. + \int_0^d r w_2(r) f_{22}(r, d) f_{21}^{(0,1)}(r, d) dr + \int_0^d r w_2(r) f_{21}(r, d) f_{22}^{(0,1)}(r, d) dr \right) \\
&\quad + \frac{1}{2} \left( \int_d^R r w_1(r) f_{11}^{(1,0)}(r, d) g_{12}(r, d) dr + \int_d^R r w_1(r) f_{12}^{(1,0)}(r, d) g_{11}(r, d) dr \right. \\
&\quad \left. + \int_d^R r w_1(r) f_{12}(r, d) f_{11}^{(0,1)}(r, d) dr + \int_d^R r w_1(r) f_{11}(r, d) f_{12}^{(0,1)}(r, d) dr \right) \\
G_{22} &= \Pi_\rho \Pi_u^3 \left( \int_0^d r w_2(r) f_{22}^{(1,0)}(r, d) g_{22}(r, d) dr + \int_0^d r w_2(r) f_{22}(r, d) f_{22}^{(0,1)}(r, d) dr \right) \\
&\quad + \int_d^R r w_1(r) f_{12}^{(1,0)}(r, d) g_{12}(r, d) dr + \int_d^R r w_1(r) f_{12}(r, d) f_{12}^{(0,1)}(r, d) dr \\
C_1 &= 2\pi \left( \text{Re}_2^{-1} \Pi_\rho \Pi_u^3 \left( \int_0^d w_2(r) f_{21}^{(1,0)}(r, d) dr + \int_0^d r w_2(r) f_{21}^{(2,0)}(r, d) dr \right) \right. \\
&\quad \left. + \text{Re}_1^{-1} \left( \int_d^R w_1(r) f_{11}^{(1,0)}(r, d) dr + \int_d^R r w_1(r) f_{11}^{(2,0)}(r, d) dr \right) \right) \\
C_2 &= 2\pi \left( \text{Re}_2^{-1} \Pi_\rho \Pi_u^3 \left( \int_0^d w_2(r) f_{21}^{(1,0)}(r, d) dr + \int_0^d r w_2(r) f_{21}^{(2,0)}(r, d) dr \right) \right. \\
&\quad \left. + \text{Re}_1^{-1} \left( \int_d^R w_1(r) f_{11}^{(1,0)}(r, d) dr + \int_d^R r w_1(r) f_{11}^{(2,0)}(r, d) dr \right) \right) \\
J_1 &= \text{Re}_1^{-1} \left( -\frac{2g_{11}(d, d) \left( \int_d^R r w_1(r) dr \right)}{d^2} + 2 \int_d^R r w_1(r) f_{11}^{(0,2)}(r, d) dr \right. \\
&\quad \left. + f_{11}^{(0,2)}(d, d) \left( \int_d^R r w_1(r) dr \right) + f_{11}^{(1,1)}(d, d) \left( \int_d^R r w_1(r) dr \right) \right. \\
&\quad \left. + \frac{2g_{11}^{(0,1)}(d, d) \left( \int_d^R r w_1(r) dr \right)}{d} + \frac{2g_{11}^{(1,0)}(d, d) \left( \int_d^R r w_1(r) dr \right)}{d} \right) \\
&\quad + \text{Re}_1^{-1} \Pi_\mu \Pi_u^2 \left( 2dw_2(d) f_{21}^{(0,1)}(d, d) - dw_2(d) g_{21}^{(0,1)}(d, d) - 2dw_2(d) g_{21}^{(1,0)}(d, d) \right) \\
&\quad + \text{Re}_1^{-1} \Pi_u \left( -4dw_2(d) f_{11}^{(0,1)}(d, d) - 2w_2(d) g_{11}(d, d) + dw_2(d) g_{11}^{(0,1)}(d, d) \right) \\
&\quad + \text{Re}_2^{-1} \Pi_\rho \Pi_u^3 \left( 2 \int_0^d r w_2(r) f_{21}^{(0,2)}(r, d) dr - f_{21}^{(0,2)}(d, d) \left( \int_0^d r w_2(r) dr \right) \right. \\
&\quad \left. - f_{21}^{(1,1)}(d, d) \left( \int_0^d r w_2(r) dr \right) \right) \\
&\quad + \text{Re}_1^{-1} \Pi_\mu \Pi_u \left( 2g_{21}^{(1,1)}(d, d) \left( \int_d^R r w_1(r) dr \right) + 2g_{21}^{(2,0)}(d, d) \left( \int_d^R r w_1(r) dr \right) \right)
\end{aligned}$$

$$\begin{aligned}
J_2 = & \operatorname{Re}_1^{-1} \left( -\frac{2g_{12}(d, d) \left( \int_d^R r w_1(r) dr \right)}{d^2} + 2 \int_d^R r w_1(r) f_{12}^{(0,2)}(r, d) dr \right. \\
& + f_{12}^{(0,2)}(d, d) \left( \int_d^R r w_1(r) dr \right) + f_{12}^{(1,1)}(d, d) \left( \int_d^R r w_1(r) dr \right) \\
& \left. + \frac{2g_{12}^{(0,1)}(d, d) \left( \int_d^R r w_1(r) dr \right)}{d} + \frac{2g_{12}^{(1,0)}(d, d) \left( \int_d^R r w_1(r) dr \right)}{d} \right) \\
& + \operatorname{Re}_1^{-1} \Pi_\mu \Pi_u^2 \left( 2dw_2(d) f_{22}^{(0,1)}(d, d) - dw_2(d) g_{22}^{(0,1)}(d, d) - 2dw_2(d) g_{22}^{(1,0)}(d, d) \right) \\
& + \operatorname{Re}_1^{-1} \Pi_u \left( -4dw_2(d) f_{12}^{(0,1)}(d, d) - 2w_2(d) g_{12}(d, d) + dw_2(d) g_{12}^{(0,1)}(d, d) \right) \\
& + \operatorname{Re}_2^{-1} \Pi_\rho \Pi_u^3 \left( 2 \int_0^d r w_2(r) f_{22}^{(0,2)}(r, d) dr - f_{22}^{(0,2)}(d, d) \left( \int_0^d r w_2(r) dr \right) \right. \\
& \quad \left. - f_{22}^{(1,1)}(d, d) \left( \int_0^d r w_2(r) dr \right) \right) \\
& + \operatorname{Re}_1^{-1} \Pi_\mu \Pi_u \left( 2g_{22}^{(1,1)}(d, d) \left( \int_d^R r w_1(r) dr \right) + 2g_{22}^{(2,0)}(d, d) \left( \int_d^R r w_1(r) dr \right) \right) \\
K_1 = & \operatorname{Re}_1^{-1} \left( -\frac{2g_{13}(d, d) \left( \int_d^R r w_1(r) dr \right)}{d^2} - 4dw_2(d) \Pi_u^2 f_{21}(d, d) \right. \\
& + 4 \int_d^R r w_1(r) f_{11}^{(0,1)}(r, d) dr + 2f_{11}^{(0,1)}(d, d) \left( \int_d^R r w_1(r) dr \right) \\
& + \frac{2g_{11}(d, d) \left( \int_d^R r w_1(r) dr \right)}{d} + \frac{2g_{13}^{(0,1)}(d, d) \left( \int_d^R r w_1(r) dr \right)}{d} \\
& \left. + \frac{2g_{13}^{(1,0)}(d, d) \left( \int_d^R r w_1(r) dr \right)}{d} \right) \\
& + \operatorname{Re}_1^{-1} \Pi_\mu \Pi_u \left( f_{21}^{(1,0)}(d, d) \left( \int_d^R r w_1(r) dr \right) + 2g_{21}^{(1,0)}(d, d) \left( \int_d^R r w_1(r) dr \right) \right. \\
& \quad \left. + 2g_{23}^{(1,1)}(d, d) \left( \int_d^R r w_1(r) dr \right) + 2g_{23}^{(2,0)}(d, d) \left( \int_d^R r w_1(r) dr \right) \right) \\
& + \operatorname{Re}_1^{-1} \Pi_\mu \Pi_u^2 \left( 2dw_2(d) f_{21}(d, d) - dw_2(d) g_{21}(d, d) - dw_2(d) g_{23}^{(0,1)}(d, d) \right. \\
& \quad - 2dw_2(d) g_{23}^{(1,0)}(d, d) + \operatorname{Re}_2^{-1} \Pi_\rho \Pi_u^3 \left( 4 \int_0^d r w_2(r) f_{21}^{(0,1)}(r, d) dr \right. \\
& \quad \left. - 2f_{21}^{(0,1)}(d, d) \left( \int_0^d r w_2(r) dr \right) - f_{21}^{(1,0)}(d, d) \left( \int_0^d r w_2(r) dr \right) \right) \\
& \left. + \operatorname{Re}_1^{-1} \Pi_u \left( dw_2(d) g_{11}(d, d) - 2w_2(d) g_{13}(d, d) + dw_2(d) g_{13}^{(0,1)}(d, d) \right) \right)
\end{aligned}$$

$$\begin{aligned}
K_2 = & \operatorname{Re}_1^{-1} \left( -\frac{2g_{14}(d, d) \left( \int_d^R r w_1(r) dr \right)}{d^2} - 4dw_2(d) \Pi_u^2 f_{22}(d, d) \right. \\
& + 4 \int_d^R r w_1(r) f_{12}^{(0,1)}(r, d) dr + 2f_{12}^{(0,1)}(d, d) \left( \int_d^R r w_1(r) dr \right) \\
& + \frac{2g_{12}(d, d) \left( \int_d^R r w_1(r) dr \right)}{d} + \frac{2g_{14}^{(0,1)}(d, d) \left( \int_d^R r w_1(r) dr \right)}{d} \\
& \left. + \frac{2g_{14}^{(1,0)}(d, d) \left( \int_d^R r w_1(r) dr \right)}{d} \right) \\
& + \operatorname{Re}_1^{-1} \Pi_\mu \Pi_u \left( f_{22}^{(1,0)}(d, d) \left( \int_d^R r w_1(r) dr \right) + 2g_{22}^{(1,0)}(d, d) \left( \int_d^R r w_1(r) dr \right) \right. \\
& \left. + 2g_{24}^{(1,1)}(d, d) \left( \int_d^R r w_1(r) dr \right) + 2g_{24}^{(2,0)}(d, d) \left( \int_d^R r w_1(r) dr \right) \right) \\
& + \operatorname{Re}_1^{-1} \Pi_\mu \Pi_u^2 \left( 2dw_2(d) f_{22}(d, d) - dw_2(d) g_{22}(d, d) - dw_2(d) g_{24}^{(0,1)}(d, d) \right. \\
& \left. - 2dw_2(d) g_{24}^{(1,0)}(d, d) \right) + \operatorname{Re}_2^{-1} \Pi_\rho \Pi_u^3 \left( 4 \int_0^d r w_2(r) f_{22}^{(0,1)}(r, d) dr \right. \\
& \left. - 2f_{22}^{(0,1)}(d, d) \left( \int_0^d r w_2(r) dr \right) - f_{22}^{(1,0)}(d, d) \left( \int_0^d r w_2(r) dr \right) \right) \\
& + \operatorname{Re}_1^{-1} \Pi_u \left( dw_2(d) g_{12}(d, d) - 2w_2(d) g_{14}(d, d) + dw_2(d) g_{14}^{(0,1)}(d, d) \right) \\
L_1 = & \operatorname{Re}_1^{-1} \left( 2 \int_d^R r w_1(r) f_{11}^{(0,1)}(r, d) dr + f_{11}^{(0,1)}(d, d) \left( \int_d^R r w_1(r) dr \right) \right. \\
& \left. + dw_2(d) \Pi_u g_{11}(d, d) + \frac{2g_{11}(d, d) \left( \int_d^R r w_1(r) dr \right)}{d} \right) \\
& + \operatorname{Re}_2^{-1} \Pi_\rho \Pi_u^3 \left( 2 \int_0^d r w_2(r) f_{21}^{(0,1)}(r, d) dr - f_{21}^{(0,1)}(d, d) \left( \int_0^d r w_2(r) dr \right) \right) \\
& + \operatorname{Re}_1^{-1} \Pi_\mu \left( 2 \Pi_u g_{21}^{(1,0)}(d, d) \left( \int_d^R r w_1(r) dr \right) - dw_2(d) \Pi_u^2 g_{21}(d, d) \right)
\end{aligned}$$

$$\begin{aligned}
L_2 &= \text{Re}_1^{-1} \left( 2 \int_d^R r w_1(r) f_{12}^{(0,1)}(r, d) dr + f_{12}^{(0,1)}(d, d) \left( \int_d^R r w_1(r) dr \right) \right. \\
&\quad \left. + d w_2(d) \Pi_u g_{12}(d, d) + \frac{2g_{12}(d, d) \left( \int_d^R r w_1(r) dr \right)}{d} \right) \\
&\quad + \text{Re}_2^{-1} \Pi_\rho \Pi_u^3 \left( 2 \int_0^d r w_2(r) f_{22}^{(0,1)}(r, d) dr - f_{22}^{(0,1)}(d, d) \left( \int_0^d r w_2(r) dr \right) \right) \\
&\quad + \text{Re}_1^{-1} \Pi_\mu \left( 2 \Pi_u g_{22}^{(1,0)}(d, d) \left( \int_d^R r w_1(r) dr \right) - d w_2(d) \Pi_u^2 g_{22}(d, d) \right) \\
M_1 &= \text{Re}_1^{-1} \left( \Pi_u f_{21}(d, d) \left( \int_d^R r w_1(r) dr \right) + 2 \int_d^R r w_1(r) f_{11}(r, d) dr + d w_2(d) \Pi_u g_{13}(d, d) \right. \\
&\quad \left. + \frac{2g_{13}(d, d) \left( \int_d^R r w_1(r) dr \right)}{d} \right) \\
&\quad + \text{Re}_2^{-1} \Pi_\rho \Pi_u^3 \left( 2 \int_0^d r w_2(r) f_{21}(r, d) dr - f_{21}(d, d) \left( \int_0^d r w_2(r) dr \right) \right) \\
&\quad + \text{Re}_1^{-1} \Pi_\mu \left( 2 \Pi_u g_{23}^{(1,0)}(d, d) \left( \int_d^R r w_1(r) dr \right) - d w_2(d) \Pi_u^2 g_{23}(d, d) \right) \\
M_2 &= \text{Re}_1^{-1} \left( \Pi_u f_{22}(d, d) \left( \int_d^R r w_1(r) dr \right) + 2 \int_d^R r w_1(r) f_{12}(r, d) dr + d w_2(d) \Pi_u g_{14}(d, d) \right. \\
&\quad \left. + \frac{2g_{14}(d, d) \left( \int_d^R r w_1(r) dr \right)}{d} \right) \\
&\quad + \text{Re}_2^{-1} \Pi_\rho \Pi_u^3 \left( 2 \int_0^d r w_2(r) f_{22}(r, d) dr - f_{22}(d, d) \left( \int_0^d r w_2(r) dr \right) \right) \\
&\quad + \text{Re}_1^{-1} \Pi_\mu \left( 2 \Pi_u g_{24}^{(1,0)}(d, d) \left( \int_d^R r w_1(r) dr \right) - d w_2(d) \Pi_u^2 g_{24}(d, d) \right)
\end{aligned}$$





# Curriculum vitae

## Georg Dietze, born 11/27/1979 in Gerolstein, Germany

Current position: CNRS Research Associate (class of 2012)  
Laboratoire FAST, UMR 7608  
CNRS, Université Paris-Saclay

Web page: <http://www.fast.u-psud.fr/~dietze>

Researcher ID: [D-2172-2013](https://orcid.org/0000-0003-1495-5505)

ORCID ID: [orcid.org/0000-0003-1495-5505](https://orcid.org/0000-0003-1495-5505)

h-index: h=11 in Web of Science

## Degrees

- 2010 PhD in Mechanical Engineering, Dr.-Ing. (summa cum laude)  
RWTH Aachen University, Aachen, Germany  
Diploma: July 9th 2010, Aachen  
Jury: W. Schröder, C. Tropea, R. Kneer, M. Zeller
- 2005 Master of Engineering, Dipl.-Ing. (cum laude)  
RWTH Aachen University, Aachen, Germany

## Academic career

- since 2016 CNRS research associate, rank CR1  
Laboratoire FAST, UMR 7608  
CNRS, Université Paris-Saclay
- 2012-2016 CNRS research associate, rank CR2  
Laboratoire FAST, UMR 7608  
CNRS, Université Paris-Sud
- 2011-2012 Post-doctoral scholar (DAAD)  
Université Pierre et Marie Curie
- 2010-2011 Post-doctoral researcher, group leader  
RWTH Aachen University

## Scholarships and awards

- 2020 Outstanding research award, Heat Transfer Society of Japan
- 2015 Invited scholar, University of Florida
- 2011 DAAD post-doctoral scholarship, Université Pierre et Marie Curie
- 2011 Friedrich-Wilhelm award for PhD. thesis, RWTH Aachen
- 2011 Borchers medal, RWTH Aachen

2006 Friedrich-Wilhelm award for Master thesis, RWTH Aachen

### Post-doctoral scholars supervised

- |  |  |
|--|--|
| Anjishnu Choudhury<br><i>since 09/2021</i> | LaSIPS project mucusFILM<br>Co-supervision with Marcel Filoche (École Polytechnique) and Nicolas Grenier (LISN)  |
| Gianluca Lavallo<br><i>02/2017-11/2018</i> | ANR project wavyFILM<br>Co-supervision with Nicolas Grenier (LIMSI)<br><a href="#">Lavallo et al., <i>J. Fluid Mech.</i>, 2019, 860, 608-639</a><br><a href="#">Lavallo et al., <i>Phys. Rev. Fluids</i>, 2020, 5, 032001(R)</a><br><a href="#">Lavallo et al., <i>J. Fluid Mech.</i>, 2021, 919, R2</a><br><a href="#">Dietze et al., <i>J. Fluid Mech.</i>, 2020, 894, A17</a> |
| Yiqin Li<br><i>05/2017-03/2019</i>         | ANR project wavyFILM<br>Co-supervision with Sophie Mergui (FAST)<br><a href="#">Lavallo et al., <i>J. Fluid Mech.</i>, 2019, 860, 608-639</a>  |

### Doctoral students supervised

- |   |   |
|---|---|
| Igin Ignatius<br><i>since 07/2021</i>       | University of Florida<br>Chateaubriand scholarship for 4-month stay at FAST in 2022<br>Co-supervision with Ranga Narayanan (University of Florida)  |
| Misa Ishimura<br><i>will defend in 2022</i> | Université Savoie Mont Blanc (2 years at FAST),<br>MESRI scholarship<br>Co-supervision with Christian Ruyer-Quil (LOCIE) and Sophie Mergui (FAST)   |
| Jason Picardo<br><i>defended in 2017</i>    | IIT Madras<br>Fulbright scholarship at University of Florida<br>Co-supervision with Ranga Narayanan (University of Florida)<br><a href="#">Dietze et al., <i>J. Fluid Mech.</i>, 2018, 857, 111-141</a>   |
| Wilko Rohlfs<br><i>defended in 2015</i>     | RWTH Aachen University<br>Co-supervision with Reinhold Kneer (RWTH Aachen University)<br><a href="#">Dietze et al., <i>J. Fluid Mech.</i>, 2014, 743, 75-123</a><br><a href="#">Rohlfs et al., <i>Eur. Phys. J. Special Topics</i>, 2013, 219, 111</a><br><a href="#">Rohlfs et al., <i>Exp. Fluids</i>, 2012, 53, 1045-1056</a><br><a href="#">Rohlfs et al., <i>J. Comp. Phys.</i>, 2012, 231, 4454</a> |
| Nicolas Kofman<br><i>defended in 2014</i>   | Université Pierre et Marie Curie, CIFRE scholarship<br>Co-supervision with Guillaume Mougine (Air Liquide), Sophie Mergui (FAST), and Christian Ruyer-Quil (FAST)   |

## Master students supervised

Kogen Ozawa	2021, Tokyo University of Science
Hayate Nakamura	2020, Tokyo University of Science <a href="#">Nakamura et al., <i>Langmuir</i>, 2020, 857, 111-141</a> <a href="#">Nakamura et al., <i>J. Coll. Int. Sci.</i>, 2020, 857, 111-141</a>
Mayu Kiriki	2018, Tokyo University of Science
Sarah Christin	2018, Université Paris-Sud
Motochika Inoue	2017, Tokyo University of Science
Clément Mendy	2016, Université Paris-Sud
Jean Saint-Vil	2016, Université de Lille
Houssein Mazloum	2014, Université Paris-Sud
Norman Lahann	2010, RWTH Aachen University
Wilko Rohlf	2009, RWTH Aachen University
Martin Horsky	2009, RWTH Aachen University

## Membership in PhD. evaluation committees

Examiner 2020	PhD. candidate: Sanghasri Mukhopadhyay Université Savoie Mont Blanc
Examiner 2018	PhD. candidate: Nicolas Cellier Université Savoie Mont Blanc

## Research grants

Project Partner <i>since 2021</i>	ANR project FEFS: “Fluid Engineering for Food Security.” Partners: Université de Lille, INRA, Tokyo University of Science, Université de Nice
Principal Investigator <i>since 2021</i>	LaSIPS project mucusFILM: “Low-dimensional modelling of a viscoelastic mucus film in an individual pulmonary airway” Partners: Laboratoire LISN, École Polytechnique Grant: 57.500 EUR
Principal Investigator 2016-2019	ANR project wavyFILM: “Harnessing waves on liquid films to optimize distillation processes” Partners: Laboratoire LIMSI, Air Liquide Grant: 323.000 EUR
Project Partner <i>since 2016</i>	Tokyo University of Science exchange program: “Fluid dynamics in the vicinity of a macroscopic contact line in interaction with microparticles.”

	Partners: Tokyo University of Science, Université de Lille, Université Côte d'Azur, Technion Israel Institute of Technology
Principal Investigator 2014-2015	INSIS project DYNAFILM: "Excitation spatiale de la dynamique non-linéaire d'un film liquide tombant : application à l'optimisation des échangeurs à films ruisselants" Partners: Université Savoie Mont Blanc Grant: 15.000 EUR
Principal Investigator 2017	Industrial consulting contract Partner: Air Liquide Grant: 4.000 EUR
Principal Investigator 2013	Industrial consulting contract Partner: Air Liquide Grant: 10.000 EUR

## Referee activities

International journals	J. Fluid Mech.; Phys. Fluids; Phys. Rev. Fluids; Phys. Rev. E; Exp. Fluids; Eur. J. Mech. B.; Meccanica; Fluid Dyn. Res.; Int. J. Multiphase Flow; J. Comp Phys.; J. Eng. Math.; Int. J. Numer. Methods Fluids; Can. J. Chem. Eng.; Int. J. Heat Mass Transfer; Int. J. Therm. Sci.; Ind. Eng. Chem. Res.; J. Process Mech. Eng.; NPJ microgravity; Transp. Porous Media; IJST-T Mech. Eng.
Funding agencies	Review of 1 PRC proposal for Agence Nationale de la Recherche (2013)

## Research activities

- **Integral boundary layer modelling of slender multiphase flows**  
Development of low-dimensional models based on the Weighted Residual Integral Boundary Layer (WRIBL) approach. Collaboration with: C. Ruyer-Quil (Université Savoie Mont Blanc).
- **Direct numerical simulation of interfacial instabilities**  
Simulations with solvers based on the Volume of Fluid (VOF) and Continuum Surface Force (CSF) approaches (Gerris, Basilisk, OpenFOAM); high-performance computing.
- **Experiments in two-phase flows using optical measurement techniques**  
Collaboration with: Sophie Mergui (FAST). PhD. students: W. Rohlf's (RWTH Aachen University), N. Kofman (Université Pierre et Marie Curie).
- **Hydrodynamics of falling liquid films**  
Collaboration with: R. Kneer (RWTH Aachen University) and Benoit Scheid (Uni-

versité Libre de Buxelles). PhD. students: W. Rohlf's (RWTH Aachen University).

- **Falling liquid films in strongly-confined channels**  
Collaboration with: C. Ruyer-Quil (Université Savoie Mont Blanc), S. Mergui (Sorbonne Universités), and N. Grenier (Université Paris-Saclay). Postdoctoral scholars: G. Lavalle, Y. Li. PhD. students: Misa Ishimura (Université Savoie Mont Blanc, FAST).
- **Falling liquid films in narrow tubes**  
Collaboration with: C. Ruyer-Quil (Université Savoie Mont Blanc).
- **Heat/mass transfer intensification in wavy falling liquid films**  
Collaboration with: M. Gisclon, D. Bresch, and C. Ruyer-Quil (Université Savoie Mont Blanc).
- **Mucus films in pulmonary airways**  
Collaboration with: Marcel Filoche (École Polytechnique), Nicolas Grenier (Université Paris-Saclay), C. Ruyer-Quil (Université Savoie Mont Blanc). Postdoctoral scholars: A. Choudhury.
- **Thin films subject to Rayleigh-Taylor and Marangoni instabilities**  
Collaboration with: R. Narayanan (University of Florida). PhD. students: I. Ignatius, J. Picardo (University of Florida).
- **Spreading films and microparticles**  
Collaboration with: I. Ueno (Tokyo University of Science), F. Zoueshtiagh (Université de Lille), and H. Yoshikawa (Université de Nice).
- **Falling liquid films formed by condensation**  
Collaboration with: J. Seiwert (Air Liquide), C. Ruyer-Quil (Université Savoie Mont Blanc), and S. Mergui (FAST). PhD. students: W. Combaluzier (Université Paris-Saclay).

## Teaching activities

2015	Lectures on low-dimensional modelling of thin film flows; graduate students; 20 hours. University of Florida
2012	Lecture at “Summer School on Wave Patterns and Interactions in Advection-Dominated Flows”; graduate students. University of Thessaly
2012-2013	Tutorials in Heat and Mass Transfer; third year students; 32 hours. Polytech Université Pierre et Marie Curie
2007-2010	Lectures in Heat and Mass Transfer; third year students; 58.5 hours. RWTH Aachen University
2005-2007	Tutorials in Heat and Mass Transfer; third year students; 36 hours. RWTH Aachen University

**Institutional responsibilities**

- since 2019 Member of steering committee of GDR 2042 TRANSINTER. Co-chair of topic 2: “Falling films and associated transfer”.
- since 2013 Co-organizer of joint mechanics seminar at Laboratoires LISN and FAST
- since 2017 “Correspondant partenariat et innovation” for INSIS
- since 2017 “Correspondant relations internationales” for Université Paris-Saclay
- 2014-2016 Organizer of internal seminar at Laboratoire FAST

# List of publications

The number in front of each listed paper corresponds to the number of citations registered by the search engine *Web of Science*. This currently indicates an h-index of 11 for my publications. Hyperlinks coloured in blue link to the respective papers on the website of the journal.

## 23 peer-reviewed papers in international journals

- 0 Lavalley, G., Grenier, N., Mergui, S., Dietze, G. F. **2021** : Superconfined falling liquid films : linear versus nonlinear dynamics. *Journal of Fluid Mechanics* **919**, R2.
- 5 Dietze, G. F., Lavalley G., Ruyer-Quil, C. **2020** : Falling liquid films in narrow tubes : occlusion scenarios. *Journal of Fluid Mechanics* **894**, A17.
- 2 Nakamura, H., Delafosse, V., Dietze, G. F., Yoshikawa, H. N., Zoueshiagh, F., Mu, L., Tsukahara, T., Ueno, I. **2020** : Enhancement of Meniscus Pump by Multiple Particles. *Langmuir* **36**, 4447-4453.
- 4 Lavalley, G., Grenier, N., Mergui, S., Dietze, G. F. **2020** : Solitary waves on superconfined falling liquid films. *Physical Review Fluids* **5(3)**, 032001(R).
- 3 Nakamura, H., Ogawa, T., Inoue, M., Hori, T., Mu, L., Yoshikawa, H. N., Zoueshiagh, F., Dietze, G. F., Tsukahara, T. and Ueno, I. **2020** : Pumping effect of heterogeneous meniscus formed around spherical particle. *Journal of Colloid and Interface Science* **562**, 133-141.
- 10 Lavalley, G., Li, Y., Mergui, S., Grenier, N. and Dietze, G. F. **2019** : Suppression of the Kapitza instability in confined falling liquid films. *Journal of Fluid Mechanics* **860**, 608-639.
- 13 Dietze, G. F. **2019** : Effect of wall corrugations on scalar transfer to a wavy falling liquid film. *Journal of Fluid Mechanics* **859**, 1098-1128.
- 3 Dietze, G. F., Picardo, J. R. and Narayanan, R. **2018** : Sliding instability of draining fluid films. *Journal of Fluid Mechanics* **857**, 111-141.
- 17 Dietze, G. F. **2016** : On the Kapitza instability and the generation of capillary waves. *Journal of Fluid Mechanics* **789**, 368-401.
- 26 Dietze, G. F. and Ruyer-Quil, C. **2015** : Films in narrow tubes. *Journal of Fluid Mechanics* **762**, 68-109.
- 27 Dietze, G. F., Rohlf, W., Kneer, R. and Scheid, B. **2014** : Three-dimensional flow structures in laminar falling liquid films. *Journal of Fluid Mechanics* **743**, 75-123.



- 45 Dietze, G. F. and Ruyer-Quil, C. **2013** : Wavy liquid films in interaction with a confined laminar gas flow. *Journal of Fluid Mechanics* **722**, 348-393.
- 7 Haustein, H. D., Gany, A., Dietze, G. F., Elias, E. and Kneer, R. **2013** : The Dynamics of Bubble Growth at Medium-High Superheat : Boiling in an Infinite Medium and on a Wall. *Journal of Heat Transfer* **135**, 111-119.
- 3 Rohlf, W., Dietze, G. F., Haustein, H. D. and Kneer, R. **2013** : Experimental investigation of 3-dimensional wavy liquid films under the coupled influence of thermocapillary and electrostatic forces. *European Physical Journal Special Topics* **219**, 111-119.
- 10 Rohlf, W., Dietze, G. F., Haustein, H. D., Tselodub, O. and Kneer, R. **2012** : Experimental investigation into three-dimensional wavy liquid films under the influence of electrostatic forces. *Experiments in Fluids* **53**, 1045-1056.
- 11 Rohlf, W., Dietze, G. F., Haustein, H. D. and Kneer, R. **2012** : Two-phase electrohydrodynamic simulations using a volume-of-fluid approach : A comment. *Journal of Computational Physics* **231**, 4454-4463.
- 18 Dietze, G. F. and Kneer, R. **2011** : Flow separation in falling liquid films. *Frontiers in Heat and Mass Transfer* **2** (3), 033001.
- 65 Dietze, G. F., Al-Sibai, F. and Kneer, R. **2009** : Experimental study of flow separation in laminar falling liquid films. *Journal of Fluid Mechanics* **637**, 73-104.
- 65 Dietze, G. F., Leefken, A. and Kneer, R. **2008** : Investigation of the backflow phenomenon in falling liquid films. *Journal of Fluid Mechanics* **595**, 435-459.
- 11 Bardow, A., Bischof, C. H., Bücke, M. H., Dietze, G., Kneer, R., Leefken, A., Marquardt, W., Renz, U. and Slusanschi, E. **2008** : Sensitivity-based analysis of the k-epsilon model for the turbulent flow between two plates. *Chemical Engineering Science* **63**, 4763-4775.
- 52 Lel, V. V., Kellermann, A., Dietze, G., Kneer, R. and Pavlenko, A. N. **2008** : Investigations of the Marangoni effect on the regular structures in heated wavy liquid films. *Experiments in Fluids* **44**, 341-354.
- 7 Lel, V. V., Dietze, G., Stadler, H., Al-Sibai, F. and Kneer **2007** : Investigation of the thermal entry length in laminar wavy falling films. *Microgravity Science and Technology* **19**, 66-68.
- 37 Schagen, A., Modigell, M., Dietze, G. and Kneer, R. **2006** : Simultaneous measurement of local film thickness and temperature distribution in wavy liquid films using a luminescence technique. *International Journal of Heat and Mass Transfer* **49**, 5049-5061.

### 1 patent

- Dietze, G., Flock, D., Schmachtenberg, E. **2011** : Geothermiesonde und Verfahren

zu deren Betrieb. Deutsches Patent- und Markenamt. [DE102009040476A1](https://patent.de/patent/DE102009040476A1).

### 9 invited talks (symposia/workshops/summer schools)

Dietze, G. F. **2021** : Contrôle d'ondes interfaciales au sein de films liquides tombants pour l'optimisation de procédés de distillation. *Webinaire ADEME-ANCRE-ANR - Innovations de rupture pour la décarbonation de l'industrie chimique*.

Dietze, G. F. **2018** : Effect of wall corrugations on scalar transfer to a wavy falling liquid film. *WMS2018 International Symposium of Water Frontier Science and Technology Research Center*, Tokyo University of Science.

Dietze, G. F., Ruyer-Quil, C., Picardo, J. and Narayanan, R. **2018** : Integral boundary layer modeling applied to three examples of thin film interfacial instability. *Symposium in honor of Lewis Johns*, University of Florida.

Dietze, G. F. **2018** : Effect of wall corrugations on scalar transfer to a wavy falling liquid film. *IUTAM Symposium on Dynamics and Stability of Fluid Interfaces*, University of Florida.

Dietze, G. F. **2015** : Liquid films in confined geometries. *PHC-Sakura Symposium*, Université de Lille 1.

Dietze, G. F. **2015** : Wave-induced momentum transport in falling liquid films : simulations, experiments and modeling. *3rd I2plus International Symposium on Thermo-Fluid Dynamics*, Tokyo University of Science.

Dietze, G. F. **2014** : Wave dynamics and flow patterns in falling liquid films. *Workshop on Fluid Patterns for Science and Technology*, University of Florida.

Dietze, G. F. **2013** : Mesures d'épaisseur, vélocimétrie et thermométrie optique au sein de films liquides tombants. *34ème journée thématique de l'AFVL*, CNRS Bellevue, Meudon.

Dietze, G. F. **2010** : Heat and Mass Transfer in Falling Liquid Films. *Summer School on Wave Patterns and Interactions in Advection-Dominated Flows*, University of Thessaly.

### 8 peer-reviewed papers in international conference proceedings

Lavalle, G., Li, Y., Mergui, S., Grenier, N. and Dietze, G. F. **2019** : Falling liquid films in interaction with a confined counter-current gas. *CFM - 24ème Congrès Français de Mécanique*.

Rohlf, W., Dietze, G. F., Haustein, H. D., Lel, V. V. and Kneer, R. **2011** : Experimental investigation of 3-dimensional wavy liquid films under the influence of electrostatic forces. *Proceedings of the sixth International Conference on Two-Phase Systems for Ground and Space Applications*.

Dietze, G. F. and Kneer, R. **2011** : Séparation de l'écoulement dans un film liquide et laminaire. **CFM - 20ème Congrès Français de Mécanique**.

Haustein, H. D., Dietze, G. F. and Kneer, R. **2011** : A new empirical model for bubble growth : Boiling in an infinite medium and on a wall at high superheat. **ASME/JSME - 8th Thermal Engineering Joint Conference**, AJTEC2011-44429. ISBN 978-0-7918-3892-1.

Dietze, G. F. and Kneer, R. **2010** : Capillary flow separation in 2- and 3-dimensional laminar falling liquid films. **IHTC 14 - Proceedings of the 14th International Heat Transfer Conference**, 753-768. ISBN 978-0-7918-4938-5.

Karalashvili, M., Bischof, C., Bücker, M., Dietze, G., Kneer, R., Mhamdi, A., Vehreschild, A. and Marquardt, W. **2009** : Sensitivity-analysis and identification of an effective heat transport model in wavy liquid films. *Progress in Computational Heat and Mass Transfer*, 644-651.

Dietze, G., Lel, V. V. and Kneer, R. **2006** : Modelling of heat transfer in stable wavy film flow based on effective thermal diffusivity. **IHTC 13 - Proceedings of the 13th International Heat Transfer Conference**, Nr. CSN-13. ISBN 1-56700-226-9.

Lel, V. V., Kellermann, A., Dietze, G., Kneer, R. and Pavlenko, A. N. **2006** : Experimental investigations of metastable quasiregular structures in heated wavy liquid films. **IHTC 13 - Proceedings of the 13th International Heat Transfer Conference**, Nr. CSN-12. ISBN 1-56700-226-9.

### 3 papers in conference proceedings with peer-review of only the abstract

Rohlf, W., Dietze, G. F., Haustein, H. D. and Kneer, R. **2011** : Experimental investigation of 3-dimensional wavy liquid films under the influence of electrostatic forces. *Proceedings of the sixth International Berlin Workshop (IBW6) on Transport Phenomena with Moving Boundaries*, (ed. F.-P. Schindler), *Fortschritt-Berichte VDI Reihe 3*, **929**. VDI Verlag. ISBN 978-3-18-392903-0.

Dietze, G. F., Horsky, M., Lel, V. V., Al-Sibai, F. and Kneer, R. **2011** : Selected transport phenomena in falling liquid films. *Fifth International Berlin Workshop (IBW5) on Transport Phenomena with Moving Boundaries* (ed. F.-P. Schindler), *Fortschritt-Berichte VDI Reihe 3*, **920**, 107-150. VDI Verlag. ISBN 978-3-18-392003-7.

Dietze, G., Lel, V. V. and Kneer, R. **2005** : Experimental investigation and modeling of wavy film flow. *Proceedings of the third International Berlin Workshop (IBW3) on Transport Phenomena with Moving Boundaries* (ed. F.-P. Schindler), 159-173.

### 11 presentations at international conferences without proceedings

Lavalle, G., Li, Y., Mergui, S., Grenier, N. and Dietze, G. F. **2019** : Falling liquid films in interaction with a confined counter-current gas. **IUTAM Symposium - Computational modelling of instabilities and turbulence in separated two-phase flows**.

Lavalle, G., Li, Y., Mergui, S., Grenier, N. and Dietze, G. F. **2019** : Falling liquid films in confined channels. **ICMF 2019** - *10th International Conference on Multiphase Flow*.

Lavalle, G., Li, Y., Mergui, S., Grenier, N. and Dietze, G. F. **2018** : On the stability of inclined liquid films with confined counter-current gas. **APS 2018** - *71th Annual Meeting of the Division of Fluid Dynamics*.

Lavalle, G., Li, Y., Mergui, S., Grenier, N. and Dietze, G. F. **2018** : Suppression of the Kapitza instability in falling liquid films by confining the gas phase. **EFMC12** - *12th European Fluid Dynamics Conference*.

Li, Y., Mergui, S., Lavalle, G., Grenier, N. and Dietze, G. F. **2018** : Influence of confinement on the linear stability of a falling liquid film. **IMA9** - *9th Conference of the International Marangoni Association*.

Lavalle, G., Li, Y., Mergui, S., Grenier, N. and Dietze, G. F. **2017** : Instability of thin liquid films in strongly confined channels. **APS 2017** - *70th Annual Meeting of the Division of Fluid Dynamics*.

Lavalle, G., Li, Y., Mergui, S., Grenier, N. and Dietze, G. F. **2017** : Wave dynamics in counter-current gas-liquid flows for distillation process applications. **Multiphase 2017** - *17th International workshop on trends in numerical and physical modeling for industrial multiphase flows*.

Dietze, G. F. and Ruyer-Quil, C. **2015** : Thin liquid films in confined geometries. **BIFD 2015** - *Sixth International Symposium on Bifurcations and Instabilities in Fluid Dynamics*.

Dietze, G. F., Rohlf, W., Nährich, K., Kneer, R. and Scheid, B. **2014** : Direct and model-based simulations of three-dimensional falling liquid films : surface waves and associated flow structures. **IMA 7** - *Seventh Conference of the International Marangoni Association*.

Dietze, G. F. and Ruyer-Quil, C. **2013** : Wavy liquid films in interaction with a strongly confined laminar gas flow : modeling and direct numerical simulations. **APS 2013** - *66th Annual Meeting of the Division of Fluid Dynamics*.

Dietze, G. F. and Ruyer-Quil, C. **2013** : Wavy liquid films interacting with a confined laminar gas flow : modelling and DNSs. **Euromech Colloquium No. 555** - *Small-scale numerical methods for multi-phase flows*.

## 5 presentations at national conferences and workshops without proceedings

Dietze, G. F., Rohlf, W., Nährich, K. and Scheid, B. **2014** : Simulation dreidimensionaler Fallfilme : Strömungsstruktur und Wellendynamik. *Jahrestreffen der ProcessNet-Fachausschüsse Mehrphasenströmungen und Wärme- und Stoffübertragung*.

Dietze, G. F. and Ruyer-Quil, C. **2012** : Rieselfilme unter dem Einfluss einer Gasströmung :

ein integrales Grenzschichtmodell. *Jahrestreffen des ProcessNet-Fachausschusses für Wärme- und Stoffübertragung.*

Rohlf, W., Lahann, N., Dirgayasa, A., Dietze, G. and Kneer, R. **2010** : Numerische und experimentelle Untersuchungen von Rayleigh-Bénard Konvektion in einer geschlossenen Zelle. *Jahrestreffen der ProcessNet-Fachausschüsse Computational Fluid Dynamics und Wärme- und Stoffübertragung.*

Dietze, G. and Kneer, R. **2009** : Experimentelle Untersuchung der Strömungsablösung in laminaren Rieselfilmen. *Jahrestreffen der ProcessNet-Fachausschüsse Mehrphasenströmungen und Wärme- und Stoffübertragung.*

Dietze, G. F. and Kneer, R. **2008** : Experimentelle und numerische Untersuchungen von Transportprozessen in laminaren Rieselfilmen. *Jahrestreffen des ProcessNet-Fachausschusses Wärme- und Stoffübertragung.*

## 12 invited seminars at research laboratories

Dietze, G. F. **2017** : Sliding instability of draining fluid films. *Department of Chemical Engineering, University of Florida.*

Dietze, G. F. **2017** : On the Kapitza instability and the generation of capillary waves. *Department of Mechanical Engineering, Ueno Research group, Tokyo University of Science.*

Dietze, G. F. **2017** : Sliding instability of draining fluid films. *Department of Mechanical Engineering, Ueno Research group, Tokyo University of Science.*

Dietze, G. F. **2015** : Wave-induced momentum transport in falling liquid films : simulations, experiments and modeling. *Department of Mechanical Engineering, Ueno Research group, Tokyo University of Science.*

Dietze, G. F. **2014** : Wave-induced momentum transport in falling liquid films : simulations, experiments and modeling. *Nonlinear Physical Chemistry Unit, Université Libre de Bruxelles.*

Dietze, G. F. **2014** : Ondes de surface et dynamique de films liquides (tombants) : simulation, expériences et modélisation. *Laboratoire de Mathématiques, Université de Chambéry.*

Dietze, G. F. **2013** : Ondes de surface et dynamique de films liquides : simulations, expériences et modélisation. *ArcelorMittal, Maizières-lès-Metz.*

Dietze, G. F. **2013** : Wave-Induced Momentum Transport in Falling Liquid Films. *Department of Chemical Engineering, University of Florida.*

Dietze, G. F. **2011** : Flow separation in the capillary wave region of a falling liquid film. *Institut Jean Le Rond d'Alembert, Université Pierre et Marie Curie, Paris.*

Dietze, G. F. **2011** : Séparation de l'écoulement dans la région capillaire d'un film

liquide tombant. *Service TIPs (Transferts, Interfaces et Procédés)*, Université Libre de Bruxelles.

Dietze, G. F. **2010** : Séparation de l'écoulement dans la région capillaire d'un film liquide laminaire. *Laboratoire FAST, Orsay*.

Dietze, G. F. **2010** : Strömungsablösung in laminar-welligen Rieselfilmen. *Center for Smart Interfaces, Technische Universität Darmstadt*.

## **12 talks at informal meetings of the research networks [GDR 3373](#) and [GDR 2042](#)**

Dietze G. F., Lavallo, G., Li, Y., Mergui, S. et Grenier, N. **2021** : Effect of wall corrugations on scalar transfer to a wavy falling liquid film. *Institut Jean le Rond d'Alembert, Paris*.

Lavallo, G., Li, Y., Mergui, S., Grenier, N. and Dietze, G. F. **2019** : Instability of thin liquid films in strongly confined channels. *Centre Paul Langevin, Aussois*.

Dietze, G. F., Picardo, J. R. and Narayanan, R. **2017** : Symmetry loss of thinning fluid films. *Centre Paul Langevin, Aussois*.

Dietze, G. F. **2015** : On the Kapitza instability and the generation of capillary waves. *Centre Paul Langevin, Aussois*.

Dietze, G. F. **2014** : Films liquides fortement confinés au sein de géométries cylindriques. *Laboratoire de Mécanique des Fluides et d'Acoustique, Lyon*.

Dietze, G. F. **2013** : Capillary and inertial flow structures in 3-dimensional wavy liquid films. *Domaine de l'Asnee, Nancy*.

Dietze, G. F. **2013** : Dissection of the velocity field in three-dimensional falling liquid films based on DNS. *Centre Paul Langevin, Aussois*.

Dietze, G. F. **2012** : Heat and mass transfer in falling liquid films. *CAES du CNRS, Fréjus*.

Dietze, G. F. **2012** : Films liquides en interaction avec un écoulement gazeux et confiné : un modèle intégral. *Institut de Mécanique des Fluides de Toulouse, Toulouse*.

Dietze, G. F. **2012** : Wavy liquid films in interaction with a strongly confined laminar gas flow : an integral model. *Université Pierre et Marie Curie, Paris*.

Dietze, G. F. **2011** : Films liquide cisailles par un écoulement gazeux : un état de l'art. *Centre Paul Langevin, Aussois*.

Dietze, G. F. **2011** : Séparation de l'écoulement dans la région capillaire d'un film liquide et laminaire. *Université Pierre et Marie Curie, Paris*.

## **1 manuscript**

Dietze, G. F. **2010** : Flow Separation in Falling Liquid Films. PhD. thesis, RWTH Aachen. Sierke Verlag. [ISBN 978-3-86844-259-5](#).



# Bibliography

- A., KVON., KHARLAMOV, S., BOBYLEV, A. & GUZANOV, V. 2022 Investigation of the flow structure in three-dimensional waves on falling liquid films using light field camera. *Experimental Thermal and Fluid Science* **132**, 110553.
- ADJOUA, S. 2010 Développement d'une méthode de simulation de films liquides cisailés par un courant gazeux. PhD thesis, Université de Toulouse.
- ADJOUA, S. & MAGNAUDET, J. 2009 Développement d'une méthode de simulation d'écoulements diphasiques turbulents. In *Congrès Français de Mécanique*.
- ADOMEIT, P. & RENZ, U. 2000 Hydrodynamics of three-dimensional waves in laminar falling films. *International Journal of Multiphase Flow* **26**, 1183–1208.
- AFKHAMI, S. & BUSSMANN, M. 2009 Height functions for applying contact angles to 3d vof simulations. *International Journal for Numerical Methods in Fluids* **61** (8), 827–847.
- ÅKESJÖ, A., GOURDON, M., VAMLING, L., INNINGS, F. & SASIC, S. 2018 Experimental and numerical study of heat transfer in a large-scale vertical falling film pilot unit. *International Journal of Heat and Mass Transfer* **125**, 53–65.
- AKSEL, N. & SCHÖRNER, M. 2018 Films over topography: from creeping flow to linear stability, theory, and experiments, a review. *Acta Mechanica* **229** (1453-1482).
- ALBA, K., LAURE, P. & KHAYAT, R. E. 2011 Transient two-layer thin-film flow inside a channel. *Physical Review E* **84** (2), 1–14.
- ALBERT, C., MARSCHALL, H. & BOTHE, D. 2014 Direct numerical simulation of interfacial mass transfer into falling films. *International Journal of Heat and Mass Transfer* **69**, 343–357.
- ALEKSEENKO, S., ANTIPIN, V., GUZANOV, V., KHARLAMOV, S. & MARKOVIC, D. 2007a Evolution of solitary three-dimensional waves on vertically falling liquid films. In *6th International Conference on Multiphase Flow*.
- ALEKSEENKO, S. V., AKTERSHEV, S. P., CHERDANTSEV, A. V., KHARLAMOV, S. M. & MARKOVICH, D. M. 2009 Primary instabilities of liquid film flow sheared by turbulent gas stream. *International Journal of Multiphase Flow* **35**, 617–627.



- ALEKSEENKO, S. V., ANTIPIN, V. A., BOBYLEV, A. V. & MARKOVICH, D. M. 2007b Application of PIV to velocity measurements in a liquid film flowing down an inclined cylinder. *Experiments in Fluids* **43** (2-3), 197–207.
- ALEKSEENKO, S. V., ANTIPIN, V. A., GUZANOV, V. V., KHARLAMOV, S. M. & MARKOVICH, D. M. 2005 Three-dimensional solitary waves on falling liquid film at low Reynolds numbers. *Physics of Fluids* **17** (121704), 1–4.
- ALEKSEENKO, S. V., GUZANOV, V. V., MARKOVICH, D. M. & KHARLAMOV, S. M. 2012 Specific features of a transition from the regular two-dimensional to three-dimensional waves on falling liquid films. *Technical Physics Letters* **38** (8), 739–742.
- ALEKSEENKO, S. V. & NAKORYAKOV, V. E. 1995 Instability of a liquid film moving under the effect of gravity and gas flow. *International Journal of Heat and Mass Transfer* **38** (11), 2127–2134.
- ALEKSEENKO, S. V., NAKORYAKOV, V. E. & POKUSAEV, B. G. 1994 *Wave Flow of Liquid Films*. New York: Begell House.
- ALEXEEV, A. & ORON, A. 2007 Suppression of the Rayleigh-Taylor instability of thin liquid films by the Marangoni effect. *Physics of Fluids* **19** (8), 082101.
- ALLEY, M. 2018 *The Craft of Scientific Writing*. Berlin: Springer.
- AMAUCHE, M., MEHIDI, N. & AMATOUSSE, N. 2007 Linear stability of a two-layer film flow down an inclined channel: A second-order weighted residual approach. *Physics of Fluids* **19**, 084106.
- AMATOUSSE, N., AIT ABDERRAHMANE, H. & MEHIDI, N. 2012 Traveling waves on a falling weakly viscoelastic fluid film. *International Journal of Engineering Science* **54**, 27–41.
- ARAMRAK, S., FLURY, M., HARSH, J. B., ZOLLARS, R. L. & DAVIS, H. P. 2013 Does colloid shape affect detachment of colloids by a moving air-water interface? *Langmuir* **29** (19), 5770–5780.
- AUL, R. W. & OLBRICHT, W. L. 1990 Stability of a thin annular film in pressure-driven, low-reynolds-number flow through a capillary. *Journal of Fluid Mechanics* **215**, 585–599.
- AZZOPARDI, B. J., MUDDE, R. F., LO, S., MORVAN, H., YAN, Y. & ZHAO, D. 2011 *Hydrodynamics of Gas-Liquid Reactors: Normal Operation and Upset Conditions*. John Wiley & Sons.
- BAI, R., KELKAR, K. & JOSEPH, D. D. 1996 Direct simulation of interfacial waves in a high-viscosity-ratio and axisymmetric core-annular flow. *Journal of Fluid Mechanics* **327**, 1–34.

- BALESTRA, G., BRUN, P.-T. & GALLAIRE, F. 2016 Rayleigh-Taylor instability under curved substrates: An optimal transient growth analysis. *Physical Review Fluids* **1**, 083902.
- BARMAK, I., GELFGAT, A., VITOSHKIN, H., ULLMAN, A. & BRAUNER, N. 2016 Stability of stratified two-phase flows in horizontal channels. *Physics of Fluids* **28**, 044101.
- BARMAK, I., KUSHNIR, R., GELFGAT, A., ULLMANN, A. & BRAUNER, N. 2021 Instability of a gravity-driven liquid film confined in an inclined rectangular duct. *Interfacial Phenomena and Heat Transfer* **9** (3), 17–42.
- BARTHELET, P., CHARRU, F. & FABRE, J. 1995 Experimental study of interfacial long waves in a two-layer shear flow. *Journal of Fluid Mechanics* **303**, 23–53.
- BELTRAME, P. 2018 Partial and complete wetting in a micro-tube. *Europhysics Letters* **121**, 64002.
- BENNEY, D. J. 1966 Long waves on liquid films. *Journal of Mathematics and Physics* **45**, 150–155.
- BIAN, S., TAI, C.-F., HALPERN, D., ZHENG, Y. & GROTBORG, J. B. 2010 Experimental study of flow fields in an airway closure model. *Journal of Fluid Mechanics* **647**, 391–402.
- BICO, J., TORDEUX, C. & QUÉRÉ, D. 2001 Rough wetting. *Europhysics Letters* **55** (2), 214–220.
- BLANCHARD, A. P., KAISER, R. J. & HOOD, L. E. 1996 High-density oligonucleotide arrays. *Biosensors and Bioelectronics* **11**, 687–690.
- BONART, H., RAJES, S., JUNG, J. & REPKE, J.-U. 2020 Stability of gravity-driven liquid films overflowing microstructures with sharp corners. *Physical Review Fluids* **5**, 094001.
- BONN, D. 2009 Wetting and spreading. *Review of Modern Physics* **81** (2), 739–805.
- BONTOZOGLOU, V. & PAPAPOLYMEROU, G. 1997 Laminar film flow down a wavy incline. *International Journal of Multiphase Flow* **23** (1), 69–79.
- BONTOZOGLOU, V. & PAPAPOLYMEROU, G. 1998 Wall-triggered interfacial resonance in laminar gas-liquid flow. *International Journal of Multiphase Flow* **24** (1), 131–143.
- BOOMKAMP, P. A. M., BOERSMA, B. J., MIESEN, R. H. M. & BEIJNON, G. V. 1997 A Chebyshev collocation method for solving two-phase flow stability problems. *Journal of Computational Physics* **132**, 191–200.

- BOOMKAMP, P. A. M. & MIESEN, R. H. M. 1996 Classification of instabilities in parallel two-phase flow. *International Journal of Multiphase Flow* **22**, 67–88.
- BOOS, W. & THESS, A. 1999 Cascade of structures in long-wavelength marangoni instability. *Physics of Fluids* **11** (6), 1484–1494.
- BOTTIER, M., PEÑA FERNÁNDEZ, M., PELLE, G., ISABEY, D., LOUIS, B., GROTBORG, J. B. & FILOCHE, M. 2017 A new index for characterizing micro-bead motion in a flow induced by ciliary beating: Part ii, modeling. *PLoS Comput. Biol.* **13** (7), e1005552.
- BOUILLANT, A., MOUTERDE, T., BOURRIANE, P., LAGARDE, A., CLANET, C. & QUÉRÉ, D. 2018 Leidenfrost wheels. *Nature Physics* **14**, 1188–1192.
- BOYD, J. P. 1989 *Chebyshev & Fourier Spectral Methods*. Springer-Verlag Berlin Heidelberg.
- BRACKBILL, J. U., KOTHE, D. B. & ZEMACH, C. 1992 A continuum method for modelling surface tension. *Journal of Computational Physics* **100**, 335–354.
- BRAUER, H. 1956 Strömung und Wärmeübergang bei Rieselfilmen. *VDI-Forschungsheft* **457** (22), 1–40.
- BRAUER, H. 1971 *Stoffaustausch einschließlich chemischer Reaktion*. Aarau: Verlag Sauerländer.
- BREVDÓ, L., LAURE, P., DIAS, F. & BRIDGES, T. J. 1999 Linear pulse structure and signalling in a film flow on an inclined plane. *Journal of Fluid Mechanics* **396**, 37–71.
- BROCK, R. R. 1970 Periodic permanent roll waves. *Journal of Hydraulic Engineering* **96** (12), 2565–2580.
- BROOKE BENJAMIN, T. 1957 Wave formation in laminar flow down an inclined plane. *Journal of Fluid Mechanics* **2**, 554–574.
- BURROWES, K. S., SWAN, A. J., WARREN, N. J. & TAWHAI, M. H. 2008 Towards a virtual lung: multi-scale, multi-physics modelling of the pulmonary system. *Phil. Trans. R. Soc. A* **366**, 3247–3263.
- BURTON, J. C., SHARPE, A. L., VAN DER VEEN, R. C. A., FRANCO, A. & NAGEL, S. R. 2012 Geometry of the vapor layer under a Leidenfrost drop. *Physical Review Letters* **109**, 074301.
- CALHOUN, D. 1999 A Cartesian grid method for solving the streamfunction-vorticity equations in irregular geometries. PhD thesis, University of Washington.

- CAMASSA, R., MARZUOLA, J. L., OGROSKY, H. R. & SWYGERT, S. 2021 On the stability of traveling wave solutions to thin-film and long-wave models for film flows inside a tube. *Physica D* **415**, 132750.
- CAMASSA, R., MARZUOLA, J. L., OGROSKY, H. R. & VAUGHN, N. 2016 Traveling waves for a model of gravity-driven film flows in cylindrical domains. *Physica D* **333**, 254–265.
- CAMASSA, R., OGROSKY, H. R. & OLANDER, J. 2014 Viscous film-flow coating the interior of a vertical tube. part 1. gravity-driven flow. *Journal of Fluid Mechanics* **745**, 682–715.
- CAMASSA, R., OGROSKY, H. R. & OLANDER, J. 2017 Viscous film-flow coating the interior of a vertical tube. part 2. air-driven flow. *Journal of Fluid Mechanics* **825**, 1056–1090.
- CAO, Z., VLACHOGIANNIS, M. & BONTOZOGLOU, V. 2013 Experimental evidence for a short-wave global mode in film flow along periodic corrugations. *Journal of Fluid Mechanics* **718**, 304–320.
- CAZABAT, A. M. & STUART, M. A. COHEN 1986 Dynamics of wetting: Effects of surface roughness. *Journal of Physical Chemistry* **90** (22), 5845–5849.
- CHANDRASEKHAR, S. 1981 *Hydrodynamic and Hydromagnetic Stability*. Dover.
- CHANG, H. C. 1994 Wave evolution on a falling film. *Annual Review of Fluid Mechanics* **26**, 103–136.
- CHANG, H. C. & DEMEKHIN, E. A. 2002 *Complex Wave Dynamics on thin Films. Studies in Interface Science* 14. Amsterdam: Elsevier.
- CHANG, H. C., DEMEKHIN, E. A. & KALADIN, E. 1996a Simulation of noise-driven wave dynamics on a falling film. *AIChE Journal* **42** (6), 1553–1568.
- CHANG, H. C., DEMEKHIN, E. A., KALADIN, E. & YE, Y. 1996b Coarsening dynamics of falling-film solitary waves. *Physical Review E* **54** (2), 1467–1477.
- CHANG, H. C., DEMEKHIN, E. A. & KOPELEVICH, D. I. 1996c Local stability theory of solitary pulses in an active medium. *Physica D* **97**, 353–375.
- CHARRU, F. & HINCH, E. J. 2000 Phase diagram of interfacial instabilities in a two-layer couette flow and mechanism of the long-wave instability. *Journal of Fluid Mechanics* **414**, 195–223.
- CHEN, K., BAI, R. & JOSEPH, D. D. 1990 Lubricated pipelining. part 3 Stability of core-annular flow in vertical pipes. *Journal of Fluid Mechanics* **214**, 251–286.

- CHEN, K. P. & JOSEPH, D. D. 1991 Long wave and lubrication theories for core-annular flow. *Physics of Fluids* **3** (11), 2627–2679.
- CHEN, S., ZHANG, T., L., LV., CHEN, Y. & TANG, S. 2021 Simulation of the hydrodynamics and mass transfer in a falling film wavy microchannel. *Chinese Journal of Chemical Engineering* **34**, 97–105.
- CHORIN, A. J. 1968 Numerical solution of the Navier-Stokes equations. *Math. Comp.* **22**, 745–762.
- COLLIGNON, R., CABALLINA, O., LEMOINE, F. & CASTANET, G. 2021 Temperature distribution in the cross section of wavy and falling thinliquid films. *Experiments in Fluids* **62**, 115.
- COURBIN, L., DENIEUL, E., DRESSAIRE, E., ROPER, M., AJDARI, A. & STONE, H. A. 2007 Imbibition by polygonal spreading on microdecorated surfaces. *Nature Materials* **6**, 661–664.
- CRASTER, R. V. & MATAR, O. K. 2009 Dynamics and stability of thin liquid films. *Reviews of Modern Physics* **81**, 1131–1198.
- DANDEKAR, R., PICARDO, J. R. & PUSHPAVANAM, S. 2018 Layered two-phase flows in microchannels with arbitrary interface-wall contact angles. *Chemical Engineering Science* **182**, 1058–1070.
- DAO, E. K. & BALAKOTAIAH, V. 2000 Experimental study of wave occlusion on falling films in a vertical pipe. *AIChE Journal* **46** (7), 1300–1306.
- DÁVALOS-OROZCO, L. A. 2007 Nonlinear instability of a thin film flowing down a smoothly deformed surface. *Physics of Fluids* **19**, 074103.
- DELAUNAY, C. 1841 Sur la surface de révolution dont la courbure moyenne est constante. *Journal de Mathématiques Pures et Appliquées* **6**, 309–320.
- DEMEKHIN, E. A. 1981 Nonlinear waves in a liquid film entrained by a turbulent gas stream. *Fluid Dynamics* **16**, 188–193.
- DEMEKHIN, E. A., KALAININ, E. N., KALLIADASIS, S. & VLASKIN, S. YU. 2007a Three-dimensional localized coherent structures of surface turbulence. I. scenarios of two-dimensional-three-dimensional transition. *Physics of Fluids* **19** (114103), 114103.
- DEMEKHIN, E. A., KALAININ, E. N., KALLIADASIS, S. & VLASKIN, S. YU. 2007b Three-dimensional localized coherent structures of surface turbulence. II. solitons. *Physics of Fluids* **19** (114103), 114104.
- DENNER, F. 2016 Frequency dispersion of small-amplitude capillary waves in viscous fluids. *Physical Review E* **94**, 023110.

- DENNER, F., CHAROGIANNIS, A., PRADAS, M., MARKIDES, C. N. VAN WACHEM, B. G. M. & KALLIADASIS, S. 2018 Solitary waves on falling liquid films in the inertia-dominated regime. *Journal of Fluid Mechanics* **837**, 491–519.
- DENNER, F., PARÉ, G. & ZALESKI, S. 2017 Dispersion and viscous attenuation of capillary waves with finite amplitude. *Eur. Phys. J. Special Topics* **226**, 1229–1238.
- DIETZE, G. F. 2010 Flow Separation in Falling Liquid Films. PhD thesis, RWTH Aachen University. ISBN 978-3-86844-259-5.
- DIETZE, G. F. 2016 On the Kapitza instability and the generation of capillary waves. *Journal of Fluid Mechanics* **789**, 368–401.
- DIETZE, G. F. 2019 Effect of wall corrugations on scalar transfer to a wavy falling liquid film. *Journal of Fluid Mechanics* **859**, 1098–1128.
- DIETZE, G. F., AL-SIBAI, F. & KNEER, R. 2009 Experimental study of flow separation in laminar falling liquid films. *Journal of Fluid Mechanics* **637**, 73–104.
- DIETZE, G. F. & KNEER, R. 2011 Flow separation in falling liquid films. *Frontiers of Heat and Mass Transfer* **2** (3), 033001.
- DIETZE, G. F., LAVALLE, G. & RUYER-QUIL, C. 2020 Falling liquid films in narrow tubes: occlusion scenarios. *Journal of Fluid Mechanics* **894**, A17.
- DIETZE, G. F., LEEFKEN, A. & KNEER, R. 2008 Investigation of the backflow phenomenon in falling liquid films. *Journal of Fluid Mechanics* **595**, 435–459.
- DIETZE, G. F., PICARDO, J. R. & NARAYANAN, R. 2018 Sliding instability of draining fluid films. *Journal of Fluid Mechanics* **857**, 111–141.
- DIETZE, G. F., ROHLFS, W., NÄHRICH, K., KNEER, R. & SCHEID, B. 2014 Three-dimensional flow structures in laminar falling liquid films. *Journal of Fluid Mechanics* **743**, 75–123.
- DIETZE, G. F. & RUYER-QUIL, C. 2013 Wavy liquid films in interaction with a confined laminar gas flow. *Journal of Fluid Mechanics* **722**, 348–393.
- DIETZE, G. F. & RUYER-QUIL, C. 2015 Films in narrow tubes. *Journal of Fluid Mechanics* **762**, 68–109.
- DINESH, B., CORBIN, T. & NARAYANAN, R. 2022 Thin-film rayleigh-taylor instability in the presence of a deep periodic corrugated wall. *Journal of Fluid Mechanics* **931**, R5.
- DING, Z., LIU, Z., LIU, R. & YANG, C. 2019 Thermocapillary effect on the dynamics of liquid films coating the interior surface of a tube. *International Journal of Heat and Mass Transfer* **138**, 524–533.

- DOEDEL, E. J. 2008 AUTO07P: Continuation and bifurcation software for ordinary differential equations. *Montreal Concordia University* .
- DROSOS, E. I. P., PARAS, S. V. & KARABELAS, A. J. 2006 Counter-current gas-liquid flow in a vertical narrow channel - liquid film characteristics and flooding phenomena. *International Journal of Multiphase Flow* **32**, 51–81.
- DUPRAT, C., RUYER-QUIL, C., KALLIADASIS, S. & GIORGIUTTI-DAUPHINÉ, F. 2007 Absolute and convective instabilities of a viscous film flowing down a vertical fiber. *Physical Review Letters* **98**, 244502.
- EDO, H., KIMURA, H., NIIJIMA, M., SAKABE, H., SHIBUYA, M., KANAMARU, A., HOMMA, I. & KURIYAMA, T. 1998 Effects of chest wall vibration on breathlessness during hypercapnic ventilatory response. *Journal of Applied Physiology* **84**, 1487–1491.
- ERKEN, O., ROMANÒ, F., GROTBORG, J.B. & MURADOGLU, M. 2022 Capillary instability of a two-layer annular film: an airway closure model. *Journal of Fluid Mechanics* **934**, A7.
- EVERETT, D. H. & HAYNES, J. M. 1972 Model studies of capillary condensation. *Journal of Colloid and Interface Science* **38** (1), 125–137.
- FAIR, J. R. & BRAVO, J. L. 1990 Distillation columns containing structured packing. *Chemical Engineering Progress* **86** (1), 19–29.
- FELDMANN, J., ROISMANN, I. V. & TROPEA, C. 2020 Dynamics of a steady liquid flow in a rim bounding a falling wall film: Influence of aerodynamic effects. *Physical Review Fluids* **5**, 064001.
- FILOCHE, M., TAI, C.-F. & GROTBORG, J. B. 2015 Three-dimensional model of surfactant replacement therapy. *Proc. Natl. Acad. Sci. U.S.A.* **112** (30), 9287–9292.
- FLORYAN, J. M., DAVIS, S. H. & KELLY, R. E. 1987 Instabilities of a liquid film flowing down a slightly inclined plane. *Physics of Fluids* **30** (4), 983–989.
- FRANCOIS, M. M., CUMMINS, S. J., DENDY, E. D., KOTHE, D. B., SICILIAN, J. M. & WILLIAMS, M. W. 2006 A balanced-force algorithm for continuous and sharp interfacial surface tension models within a volume tracking framework. *Journal of Computational Physics* **213**, 141–173.
- FRANK, A. M. 2008 Numerical simulation of gas driven waves in a liquid film. *Physics of Fluids* **20**, 122102.
- FRENKEL, A. L., BABCHIN, A. J., LEVICH, B. G., SHLANG, T. & SIVASHINSKY, G. I. 1987 Annular flows can keep unstable films from breakup: nonlinear saturation of capillary instability. *Journal of Colloid and Interface Science* **115** (1), 225–233.

- FUSTER, D. & ROSSI, M. 2021 Vortex-interface interactions in two-dimensional flows. *International Journal of Multiphase Flow* **143**, 103757.
- GASKELL, P. H., JIMACK, P. K., SELIER, M. & THOMPSON, H. M. 2006 Flow of evaporating, gravity-driven thin liquid films over topography. *Physics of Fluids* **18**, 013601.
- GASTER, M. 1962 A note on the relation between temporally increasing and spatially increasing disturbances in hydrodynamic stability. *Journal of Fluid Mechanics* **14**, 222–224.
- GAUGLITZ, P. A. & RADKE, C. J. 1988 An extended evolution equation for liquid film breakup in cylindrical capillaries. *Chemical Engineering Science* **43** (7), 1457–1465.
- GEORGANTAKI, A., VATTEVILLE, J., VLACHOGIANNIS, M. & BONTOZOGLOU, V. 2011 Measurements of liquid film flow as a function of fluid properties and channel width: Evidence for surface-tension-induced long-range transverse coherence. *Physical Review E* **84**, 026325.
- GJEVIK, B. 1970 Occurrence of finite-amplitude surface waves on falling liquid films. *The Physics of Fluids* **13** (8), 1918–1925.
- GLASNER, K. 2007 The dynamics of pendant droplets on a one-dimensional surface. *Physics of Fluids* **19** (10), 102104.
- GOREN, S. L. 1962 The instability of an annular thread of fluid. *Journal of Fluid Mechanics* **12** (2), 309–319.
- GOVINDARAJAN, R. & SAHU, K. C. 2014 Instabilities in viscosity-stratified flow. *Annual Review of Fluid Mechanics* **46**, 331–353.
- GROTBERG, J. 1994 Pulmonary flow and transport phenomena. *Annual Review of Fluid Mechanics* **26**, 529–571.
- GROTBERG, J. 2011 Respiratory fluid mechanics. *Physics of Fluids* **23**, 021301.
- GRÜNDING, D., SMUDA, M., ANTRITTER, T., FRICKE, M., RETTENMAIER, D., KUMMER, F., STEPHAN, P., MARSCHALL, H. & BOTHE, D. 2020 A comparative study of transient capillary rise using direct numerical simulations. *Applied Mathematical Modelling* **86**, 142–165.
- GUZANOV, V. V., A.V., BOBYLEV., HEINZ, O. M., KHARLAMOV, S. M., KVON, A. Z. & MARKOVICH, D. M. 2018 Characterization of 3-d wave flow regimes on falling liquid films. *International Journal of Multiphase Flow* **99**, 474–484.
- HALPERN, D., FUJIOKA, H. & GROTBERG, J. B. 2010 The effect of viscoelasticity on the stability of a pulmonary airway liquid layer. *Physics of Fluids* **22**, 011901.



- HALPERN, D. & GROTBORG, J. B. 2003 Nonlinear saturation of the rayleigh-instability due to oscillatory flow in a liquid-lined tube. *Journal of Fluid Mechanics* **492**, 251–270.
- HAMMOND, P. S. 1983 Nonlinear adjustment of a thin annular film of viscous fluid surrounding a thread of another within a circular cylindrical pipe. *Journal of Fluid Mechanics* **137**, 363–384.
- HAROUN, Y., LEGENDRE, D. & RAYNAL, L. 2010 Direct numerical simulation of reactive absorption in gas-liquid flow on structured packing using interface capturing method. *Chemical Engineering Science* **65**, 351–356.
- HAUSTEIN, H. D., GANY, A., DIETZE, G. F., ELIAS, E. & KNEER, R. 2013 The dynamics of bubble growth at medium-high superheat: Boiling in an infinite medium and on a wall. *Journal of Heat Transfer* **135** (7), 111–119.
- HEIL, M. & HAZEL, A. L. 2011 Fluid-structure interaction in internal physiological flows. *Annual Review of Fluid Mechanics* **43**, 141–162.
- HEINING, C., BONTOZOGLOU, V., AKSEL, N. & WIERSCHEM, A. 2009 Nonlinear resonance in viscous films on inclined wavy planes. *International Journal of Multiphase Flow* **35**, 78–90.
- HICKOX, C. E. 1971 Instability due to viscosity and density stratification in axisymmetric pipe flow. *Physics of Fluids* **14** (2), 251–262.
- HIGBIE, R. 1935 The rate of absorption of a pure gas into a still liquid during short periods of exposure. *Transactions of the American Institute of Chemical Engineers* **31**, 365–389.
- HINCH, E. J. 1984 A note on the mechanism of the instability at the interface between two shearing fluids. *Journal of Fluid Mechanics* **144**, 463–465.
- HIRT, C. W. & NICHOLS, B. D. 1981 Volume of fluid (VOF) method for the dynamics of free boundaries. *Journal of Computational Physics* **39**, 201–225.
- HOOPER, A. P. & BOYD, W. G. C. 1983 Shear-flow instability at the interface between two viscous fluids. *Journal of Fluid Mechanics* **128**, 507–528.
- ISHIGAI, S., NAKANISI, S., KOIZUMI, T. & OYABU, Z. 1972 Hydrodynamics and heat transfer of vertically falling liquid films. *Bulletin of the JSME* **15** (83), 594–601.
- ISRAELACHVILI, J. 2011 *Intermolecular and Surface Forces*. Academic Press.
- JEBSON, R. S. & CHEN, H. 1997 Performances of falling film evaporators on whole milk and a comparison with performance on skim milk. *Journal of Dairy Research* **64**, 57–67.

- JENSEN, O. E. 2000 Draining collars and lenses in liquid-lined vertical tubes. *Journal of Colloid and Interface Science* **221**, 38–49.
- JOHNSON, M., KAMM, R. D., HO, L. W., SHAPIRO, A. & PEDLEY, T. J. 1991 The nonlinear growth of surface-tension-driven instabilities of a thin annular film. *Journal of Fluid Mechanics* **233**, 141–156.
- JOO, S. W. & DAVIS, S. H. 1992 Instabilities of three-dimensional viscous falling films. *Journal of Fluid Mechanics* **242**, 529–547.
- JOSEPH, D. D., CHEN, K. P. & RENARDY, Y. Y. 1997 Core-annular flows. *Annual Review of Fluid Mechanics* **29**, 65–90.
- JOUHARA, H., CHAUHAN, A., NANNOU, T., ALMAHMOUD, S., DELPECH, B. & WROBEL, L. C. 2017 Heat pipe based systems - advances and applications. *Energy* **128**, 729–754.
- JURMAN, L. A., BRUNO, K. & MCCREADY, J. 1989 Periodic and solitary waves on thin, horizontal, gas-sheared liquid films. *International Journal of Multiphase Flow* **15** (3), 371–384.
- JURMAN, L. A. & MCCREADY, M. J. 1989 Study of waves on thin liquid films sheared by turbulent gas flows. *Physics of Fluids A* **1** (3), 522–536.
- KABOV, O. A., ZAITSEV, D.V., V.V., CHEVERDA & BAR-COHEN, A. 2011 Evaporation and flow dynamics of thin, shear-driven liquid films in microgap channels. *Experimental Thermal and Fluid Science* **35**, 825–831.
- KALLIADASIS, S., RUYER-QUIL, C., SCHEID, B. & VELARDE, M. G. 2012 *Falling Liquid Films*, Applied Mathematical Sciences, vol. 176. Springer.
- KAMM, R. D. & SCHROTER, R. C. 1989 Is airway closure caused by a liquid film instability? *Respiration Physiology* **75**, 141–156.
- KAPITZA, P. L. 1948 Wave flow of thin layer of viscous fluid (in Russian). *Zhurn. Eksper. Teor. Fiz.* **18** (1), 3–28.
- KAPITZA, P. L. & KAPITZA, S.P. 1949 Wave flow of thin layers of viscous fluid (in Russian). *Zhurn. Eksper. Teor. Fiz.* **19** (2), 105–120.
- KAPITZA, P. L. & KAPITZA, S. P. 1965 Wave flow on thin layers of a viscous fluid. In *Collected papers of P. L. Kapitza* (ed. D. Ter Haar), , vol. 2, pp. 662–709. Oxford: Pergamon Press.
- KERCHMAN, V. 1995 Strongly nonlinear interfacial dynamics in core-annular flows. *Journal of Fluid Mechanics* **290**, 131–166.

- KHARLAMOV, S. M., GUZANOV, V. V., BOBYLEV, A. V., ALEKSEENKO, S. V. & MARKOVICH, D. M. 2015 The transition from two-dimensional to three-dimensional waves in falling liquid films: Wave patterns and transverse redistribution of local flow rates. *Physics of Fluids* **27**, 114106.
- KHODAPARAST, S., KIM, M. K., SILPE, J. E. & STONE, H. A. 2017 Bubble-driven detachment of bacteria from confined microgeometries. *Environmental Science & Technology* **51** (3), 1340–1347.
- KILLION, J. D. & GARIMELLA, S. 2004 Simulation of pendant droplets and falling films in horizontal tube absorbers. *Journal of Heat Transfer* **126**, 1003–1013.
- KING, M., BROCK, G. & LUNDELL, C. 1985 Clearance of mucus by simulated cough. *Journal of Applied Physiology* **58** (6), 1776–1782.
- KOFMAN, N. 2014 Films liquides tombants avec ou sans contre-écoulement de gaz: application au problème de l'engorgement dans les colonnes de distillation. PhD thesis, Université Pierre et Marie Curie.
- KOFMAN, N., MERGUI, S. & RUYER-QUI, C. 2014 Three-dimensional instabilities of quasi-solitary waves in a falling liquid film. *Journal of Fluid Mechanics* **757**, 854–887.
- KOFMAN, N., MERGUI, S. & RUYER-QUIL, C. 2017 Characteristics of solitary waves on a falling liquid film sheared by a turbulent counter-current gas flow. *International Journal of Multiphase Flow* **95**, 22–34.
- KOVRT, M., AUSNER, I., WOZNY, G. & REPKE, J.-U. 2011 Texture influence on liquid-side mass transfer. *Chemical Engineering Research and Design* **89**, 1405–1413.
- KOURIS, C. & TSAMOPOULOS, J. 2001 Dynamics of axisymmetric core-annular flow in a straight tube. I. the more viscous fluid in the core, bamboo waves. *Physics of Fluids* **13** (4), 841–858.
- KUMARAN, V. 2021 Stability and the transition to turbulence in the flow through conduits with compliant walls. *Journal of Fluid Mechanics* **924**, P1.
- KUNUGI, T. & KINO, C. 2005 DNS of falling film structure and heat transfer via MARS method. *Computers & Structures* **83** (6-7), 455–462.
- KUSHNIR, R., BARMAK, I., ULLMANN, A. & BRAUNER, N. 2021 Stability of gravity-driven thin-film flow in the presence of an adjacent gas phase. *International Journal of Multiphase Flow* **135**, 103443.
- KVON, A. Z., BOBYLEV, A. V., GUZANOV, V. V., MARKOVICH, D. M. & KHARLAMOV, S. M. 2016 Simultaneous film thickness and 3d-2c velocity measurements using lif and light-field ptv methods in a 3dwave on a falling liquid film. *Interfacial Phenomena and Heat Transfer* **4** (4), 253–258.

- LAMSTAES, C. & EGGERS, J. 2017 Arrested bubble rise in a narrow tube. *Journal of Statistical Physics* **167**, 656–682.
- LAPKIN, A. & ANASTAS, P. T., ed. 2018 *Green Chemical Engineering, Handbook of Green Chemistry*, vol. 12. Wiley-VHC.
- LAVALLE, G., GRENIER, N., MERGUI, S. & DIETZE, G. F. 2020 Solitary waves on superconfined falling liquid films. *Physical Review Fluids* **5** (3), 032001(R).
- LAVALLE, G., LI, Y., MERGUI, S., GRENIER, N. & DIETZE, G. F. 2019 Suppression of the kapitza instability in confined falling liquid films. *Journal of Fluid Mechanics* **860**, 608–639.
- LAVALLE, G., LUCQUIAUD, M., WEHRLI, M. & VALLURI, P. 2018 Cross-flow structured packing for the process intensification of post-combustion carbon dioxide capture. *Chemical Engineering Science* **178**, 284–296.
- LAVALLE, G., MERGUI, S., GRENIER, N. & DIETZE, G. F. 2021 Superconfined falling liquid films: linear versus nonlinear dynamics. *Journal of Fluid Mechanics Rapids* **919**, R2.
- LAVALLE, G., VILA, J.-P., BLANCHARD, G., LAURENT, C. & CHARRU, F. 2015 A numerical reduced model for thin liquid films sheared by a gas flow. *Journal of Computational Physics* **301**, 119–140.
- LAVALLE, G., VILA, J.-P., LUCQUIAUD, M. & VALLURI, P. 2017 Ultraefficient reduced model for countercurrent two-layer flows. *Physical Review Fluids* **2** (1), 014001.
- LERISSON, G., LEDDA, P. G., BALESTRA, G. & GALLAIRE, F. 2020 Instability of a thin viscous film flowing under an inclined substrate: steady patterns. *Journal of Fluid Mechanics* **898**, A6.
- LEVY, R., HILL, D. B., FOREST, G. & GROTBORG, J. B. 2014 Pulmonary fluid flow challenges for experimental and mathematical modeling. *Integrative and Comparative Biology* **54** (6), 985–1000.
- LISTER, J. R., MORRISON, N. F. & RALLISON, J. M. 2006a Sedimentation of a two-dimensional drop towards a rigid horizontal plate. *Journal of Fluid Mechanics* **552**, 345–351.
- LISTER, J. R., RALLISON, J. M., KING, A. A., CUMMINGS, L. J. & JENSEN, O. E. 2006b Capillary drainage of an annular film: the dynamics of collars and lobes. *Journal of Fluid Mechanics* **552**, 311–343.
- LIU, J. & GOLLUB, J. P. 1993 Onset of spatially chaotic waves on flowing films. *Physical Review Letters* **70** (15), 2289–2292.

- LIU, J. & GOLLUB, J. P. 1994 Solitary wave dynamics of film flows. *Physics of Fluids* **6** (5), 1702–1712.
- LIU, J., SCHNEIDER, J.B. & GOLLUB, J. P. 1995 Three-dimensional instabilities of film flows. *Physics of Fluids* **7** (1), 55–67.
- LIU, L. & DING, Z. 2020 Instabilities and bifurcations of liquid films flowing down a rotating fibre. *Journal of Fluid Mechanics* **899**, A14.
- LIU, R. & DING, Z. 2017 Stability of viscous film flow coating the interior of a vertical tube with a porous wall. *Physical Review E* **95** (5), 053101.
- MA, X., LIÉTOR-SANTOS, J.-J. & BURTON, J. C. 2015 The many faces of a leidenfrost drop. *Physics of Fluids* **27**, 091109.
- MAGNIEZ, J. C., BAUDOIN, M., C., LIU. & ZOUESHTIAGH, F. 2016 Dynamics of liquid plugs in prewetted capillary tubes: from acceleration and rupture to deceleration and airway obstruction. *Soft Matter* **12**, 8710–8717.
- MALAMATARIS, N. A. & BALAKOTAIAH, V. 2008 Flow structure underneath the large amplitude waves of a vertically falling film. *AIChE Journal* **54** (7), 1725–1740.
- MALAMATARIS, N. A., VLACHOGIANNIS, M. & BONTOZOGLOU, V. 2002 Solitary waves on inclined films: Flow structure and binary interactions. *Physics of Fluids* **14** (3), 1082–1094.
- MAMBA, S. S., MAGNIEZ, J. C., ZOUESHTIAGH, F. & BAUDOIN, M. 2018 Dynamics of a liquid plug in a capillary tube under cyclic forcing: memory effects and airway reopening. *Journal of Fluid Mechanics* **838**, 165–191.
- MARKIDES, C. N., MATHIE, R. & A., CHAROGIANNIS 2016 An experimental study of spatiotemporally resolved heat transfer in thin liquid-film flows falling over an inclined heated foil. *International Journal of Heat and Mass Transfer* **93**, 872–888.
- MASCARENHAS, N. & MUDAWAR, I. 2013 Study of the influence of interfacial waves on heat transfer in turbulent falling films. *International Journal of Heat and Mass Transfer* **67**, 1106–1121.
- MATAR, O. K., LAWRENCE, C. J. & SISOEV, G. M. 2007 Interfacial dynamics in pressure-driven two-layer laminar channel flow with high viscosity ratios. *Phys. Rev. E* **75**, 056314.
- MATHEMATICA 2014 *Version 10.0.2.0*. Wolfram Research, Inc., Champaign, IL.
- MATLAB 2015 *Version 8.6 (R2015b)*. Natick, Massachusetts: The MathWorks Inc.
- MEHIDI, N. & AMATOUSSE, N. 2009 Modélisation d'un écoulement coaxial en conduite circulaire de deux fluides visqueux. *C. R. Mécanique* **337**, 112–118.

- MENDEZ, M. A., GOSSET, A. & BUCHLIN, J.-M. 2019 Experimental analysis of the stability of the jet wiping process, part ii: Multiscale modal analysis of the gas jet-liquid film interaction. *Experimental Thermal and Fluid Science* **106**, 48–67.
- MIAO, S., HENDRICKSON, K. & LIU, Y. 2017 Computation of three-dimensional multiphase flow dynamics by fully-coupled immersed flow (fcif) solver. *Journal of Computational Physics* **350**, 97–116.
- MIYARA, A. 1999 Numerical analysis on flow dynamics and heat transfer of falling liquid films with interfacial waves. *Heat and Mass Transfer* **35**, 298–306.
- MIYARA, A. 2001 Flow dynamics and heat transfer of wavy condensate film. *Journal of Heat Transfer* **123**, 492–500.
- MOHAMED, O. A. A., DALLASTON, M. C. & BIANCOFIORE, L. 2021 Spatiotemporal evolution of evaporating liquid films sheared by a gas. *Phys. Rev. Fluids* **6**, 114002.
- MOISY, F. & RABAUD, M. 2014 Mach-like capillary-gravity wakes. *Physical Review E* **90**, 023009.
- MUKHOPADHYAY, S., CHHAY, M. & RUYER-QUIL, C. 2017 Modelling transitional falling liquid films. In *Congrès Français de Mécanique*.
- NAKAMURA, H., DELAFOSSE, V., DIETZE, G. F., YOSHIKAWA, H. N., ZOUESHTIAGH, F., MU, L., TSUKAHARA, T. & UENO, I. 2020a Enhancement of meniscus pump by multiple particles. *Langmuir* **36**, 4447–4453.
- NAKAMURA, H., OGAWA, T., INOUE, M., HORI, T., MU, L., YOSHIKAWA, H. N., ZOUESHTIAGH, F., DIETZE, G. F., TSUKAHARA, T. & UENO, I. 2020b Pumping effect of heterogeneous meniscus formed around spherical particle. *Journal of Colloid and Interface Science* **562**, 133–141.
- NÀRAIGH, L. Ó., SPELT, P. D. M., MATAR, O. K. & ZAKI, T. A. 2011 Interfacial instability in turbulent flow over a liquid film in a channel. *International Journal of Multiphase Flow* **37**, 812–830.
- NAVE, J.-C. 2004 Direct numerical simulation of liquid films. PhD thesis, University of California.
- NAVON, I. M. 1987 PENT: A periodic pentadiagonal systems solver. *Communications in Applied Numerical Methods* **3**, 63–69.
- NEWHOUSE, L. A. & POZRIKIDIS, C. 1992 The capillary instability of annular layers and liquid threads. *Journal of Fluid Mechanics* **242**, 193–209.
- NJIFENJU, K. 2010 Gouttes et films liquides en aérodynamique automobile. PhD thesis, Université Pierre et Marie Curie.

- NOSOKO, T., YOSHIMURA, P. N., NAGATA, T. & OYAKAWA, K. 1996 Characteristics of two-dimensional waves on a falling liquid film. *Chemical Engineering Science* **51** (5), 725–732.
- NOVBARI, E. & ORON, A. 2009 Energy integral method for the nonlinear dynamics of an axisymmetric thin liquid film falling on a vertical cylinder. *Physics of Fluids* **21**, 062107.
- NUSSELT, W. 1916 Die Oberflächenkondensation des Wasserdampfes. *VDI-Zeitschrift* **60**, 541–546.
- NUSSELT, W. 1923 Der Wärmeaustausch am Berieselungskühler. *VDI-Zeitschrift* **67**, 206–210.
- OGROSKY, H. R. 2021*a* Impact of viscosity ratio on falling two-layer viscous film flow inside a tube. *Physical Review Fluids* **6**, 104005.
- OGROSKY, H. R. 2021*b* Linear stability and nonlinear dynamics in a long-wave model of film flows inside a tube in the presence of surfactant. *Journal of Fluid Mechanics* **908**, A23.
- ONDA, T., SHIBUICHI, S., SATOH, N. & TSUJII, K. 1996 Super-water-repellent fractal surfaces. *Langmuir* **12**, 2125–2127.
- ORON, A. 2000 Nonlinear dynamics of three-dimensional long-wave Marangoni instability in thin liquid films. *Physics of Fluids* **12** (7), 1633–1645.
- ORON, A. 2000 Three-dimensional nonlinear dynamics of thin liquid films. *PHYSICAL REVIEW LETTERS* **85** (10), 2108–2111.
- ORON, A. 2003 Short commentary: Theory of thin liquid films: some questions and challenges. *The European Physical Journal E* **12**, 455–458.
- ORON, A. & BANKOFF, S. G. 2001 Dynamics of a condensing liquid film under conjoining/disjoining pressures. *PHYSICS OF FLUIDS* **13** (5), 1107–1117.
- ORON, A., DAVIS, S. H. & BANKOFF, S. G. 1997 Long-scale evolution of thin liquid films. *Reviews of Modern Physics* **69** (3), 931–980.
- ORON, A. & GOTTLIEB, O. 2004 Subcritical and supercritical bifurcations of the first- and second-order Benney equations. *Journal of Engineering Mathematics* **50** (2-3), 121–140.
- ORON, A., GOTTLIEB, O. & NOVBARI, E. 2009 Numerical analysis of a weighted-residual integral boundary-layer model for nonlinear dynamics of falling liquid films. *European Journal of Mechanics B-Fluids* **28** (1), 1–36.

- ORON, A. & HEINING, C. 2008 Weighted-residual integral boundary-layer model for the nonlinear dynamics of thin liquid films falling on an undulating vertical wall. *Physics of Fluids* **20** (082102).
- PARK, C. D. & NOSOKO, T. 2003 Three-dimensional wave dynamics on a falling film and associated mass transfer. *AIChE Journal* **49** (11), 2715–2727.
- PASQUIER, S., QUINTARD, M. & DAVIT, Y. 2017 Modeling flow in porous media with rough surfaces: Effective slip boundary conditions and application to structured packings. *Chemical Engineering Science* **165**, 131–146.
- PATANKAR, S. V. 1980 *Numerical Heat Transfer and Fluid Flow*. Taylor & Francis.
- PETVIASHVILI, V. I. & TSVELODUB, D. Y. 1978 Horseshoe-shaped solitons on a flowing viscous film of fluid. *Soviet Physics Doklady* **23**, 117.
- PFENNIG, A. 2018 On the strong influence of molecular interactions over large distances. *The European Physical Journal D* **72** (45).
- PILLAI, D. & NARAYANAN, R. 2018a Interfacial dynamics of a confined liquid-vapour bilayer undergoing evaporation. *Journal of Fluid Mechanics Rapids* **857**, 1–37.
- PILLAI, D. & NARAYANAN, R. 2018b Nonlinear dynamics of electrostatic Faraday instability in thin films. *Journal of Fluid Mechanics Rapids* **855**, R4.
- PILLAI, D. S. & NARAYANAN, R. 2020 Electrostatic forcing of thin leaky dielectric films under periodic and steady fields. *Journal of Fluid Mechanics* **890**, A20.
- PILLAI, D. S., SAHU, K. C. & NARAYANAN, R. 2021 Electrowetting of a leaky dielectric droplet under a time-periodic electric field. *Physical Review Fluids* **6**, 073701.
- PIROIRD, K., CLANET, C. & QUÉRÉ, D. 2011 Detergency in a tube. *Soft Matter* **7**, 7498–7503.
- PLATEAU, J. P. 1849 Recherches expérimentales et théoriques sur les figures d'équilibre d'une masse liquide sans pesanteur. *Mémoires de l'Académie Royale des Sciences, des Lettres et des Beaux-Arts de Belgique* **23**, 1–150.
- POHLHAUSEN, K. 1921 Zur näherungsweise Integration der Differentialgleichung der laminaren Grenzschicht. *Z. angew. Math. Mech.* **1**, 252–268.
- POPE, S. B. 2000 *Turbulent Flows*. Cambridge University Press.
- POPINET, S. 2009 An accurate adaptive solver for surface-tension-driven interfacial flows. *Journal of Computational Physics* **228**, 5838–5866.
- POPINET, S. 2015 A quadtree-adaptive multigrid solver for the serre-green-naghdi equations. *Journal of Computational Physics* **302**, 336–358.



- POZRIKIDIS, C. 1998 Gravity-driven creeping flow of two adjacent layers through a channel and down a plane wall. *Journal of Fluid Mechanics* **371**, 345–376.
- PRADAS, M., KALLIADASIS, S., NGUYEN, P.-K. & BONTOZOGLOU, V. 2013 Bound-state formation in interfacial turbulence: direct numerical simulations and theory. *Journal of Fluid Mechanics* **716**, R2.
- PRADAS, M., KALLIADASIS, S. & TSELUIKO, D. 2012 Binary interactions of solitary pulses in falling liquid films. *IMA Journal of Applied Mathematics* **77** (3), 408–419.
- PRADAS, M., TSELUIKO, D. & KALLIADASIS, S. 2011 Rigorous coherent-structure theory for falling liquid films: Viscous dispersion effects on bound-state formation and self-organization. *Physics of Fluids* **23**, 044104.
- PRANDTL, L. 1925 Bericht über Untersuchungen zur ausgebildeten Turbulenz. *Zeitschrift für angewandte Mathematik und Mechanik* **5**, 136–139.
- PREZIOSI, L., CHEN, K. P. & JOSEPH, D. D. 1989 Lubricated pipelining - stability of core annular flow. *Journal of Fluid Mechanics* **201**, 323–356.
- PROSPERETTI, A. & TRYGGVASON, G., ed. 2007 *Computational Methods for Multiphase Flow*. Cambridge University Press.
- PUMIR, A., MANNEVILLE, P. & POMEAU, Y. 1983 On solitary waves running down an inclined plane. *Journal of Fluid Mechanics* **135**, 27–50.
- QUÉRÉ, D. 1990 Thin films flowing on vertical fibers. *Europhysics Letters* **13** (8), 721–726.
- QUÉRÉ, D. 2005 Non-sticking drops. *Reports on the Progress of Physics* **68**, 2495–2532.
- RAPHAËL, E. & DE GENNES, P.-G. 1996 Capillary gravity waves caused by a moving disturbance: Wave resistance. *Physical Review E* **53**, 3448.
- RASTATURIN, A., DEMEKHIN, E. & KAL Aidin, E. 2006 Optimal regimes of heat-mass transfer in a falling film. *Journal of Non-Equilibrium Thermodynamics* **31**, 1–10.
- RAYLEIGH, LORD 1892 On the instability of cylindrical fluid surfaces. *Philosophical Magazine* **34** (207), 177–180.
- RENARDY, Y. 1985 Instability at the interface between two shearing fluids in a channel. *Physics of Fluids* **28** (12), 3441–3443.
- RENARDY, Y. & RENARDY, M. 2002 PROST: A parabolic reconstruction of surface tension for the Volume-of-Fluid method. *Journal of Computational Physics* **183** (2), 400 – 421.

- RICHARD, G., RUYER-QUIL, C. & VILA, J. P. 2016 A three-equation model for thin films down an inclined plane. *Journal of Fluid Mechanics* **804**, 162–200.
- ROBERTS, R. M. & CHANG, H.-C. 2000 Wave-enhanced interfacial transfer. *Chemical Engineering Science* **55**, 1127–1141.
- ROHLFS, W., CAMMIADE, L. M. F., RIETZ, M. & SCHEID, B. 2021 On the effect of electrostatic surface forces on dielectric falling films. *Journal of Fluid Mechanics* **906**, A18.
- ROHLFS, W., DIETZE, G. F., HAUSTEIN, H. & KNEER, R. 2013 Experimental investigation of 3-dimensional wavy liquid films under the coupled influence of thermo-capillary and electrostatic forces. *Eur. Phys. J. Special Topics* **219** (4), 111–119.
- ROHLFS, W., DIETZE, G. F., HAUSTEIN, H., TSVELODUB, O. & KNEER, R. 2012*a* Experimental investigation into three-dimensional wavy liquid films under the influence of electrostatic forces. *Experiments in Fluids* **53** (4), 1045–1056.
- ROHLFS, W., DIETZE, G. F., HAUSTEIN, H. D. & KNEER, R. 2012*b* Two-phase electrohydrodynamic simulations using a volume-of-fluid approach: A comment. *Journal of Computational Physics* **231** (12), 4454–4463.
- ROMANO, F., FUJIOKA, H., MURADOGLU, M. & GROTBORG, J. B. 2019 Liquid plug formation in an airway closure model. *Physical Review Fluids* **4**, 093103.
- ROMANO, F., MURADOGLU, M., FUJIOKA, H. & GROTBORG, J. B. 2021 The effect of viscoelasticity in an airway closure model. *Journal of Fluid Mechanics* **913**, A31.
- RUDMAN, M. 1997 Volume-tracking methods for interfacial flows calculations. *International Journal for Numerical Methods in Fluids* **24** (7), 671–691.
- RUSCHE, H. 2002 Computational fluid dynamics of dispersed two-phase flows at high phase fractions. PhD thesis, Imperial College, University of London.
- RUYER-QUIL, C. 2012 Instabilities and modeling of falling film flows. PhD thesis, Université Pierre et Marie Curie.
- RUYER-QUIL, C., CHAKRABORTY, S. & DANDAPAT, B. S. 2012 Wavy regime of a power-law film flow. *Journal of Fluid Mechanics* **692**, 220–256.
- RUYER-QUIL, C. & MANNEVILLE, P. 1998 Modeling film flows down inclined planes. *European Physical Journal B* **6** (2), 277–292.
- RUYER-QUIL, C. & MANNEVILLE, P. 2000 Improved modeling of flows down inclined planes. *European Physical Journal B* **15** (2), 357–369.

- RUYER-QUIL, C. & MANNEVILLE, P. 2002 Further accuracy and convergence results on the modeling of flows down inclined planes by weighted-residual approximations. *Physics of Fluids* **14** (1), 170–183.
- RUYER-QUIL, C., TREVELYAN, P., GIORGIUTTI-DAUPHINE, F., DUPRAT, C. & KALLIADASIS, S. 2008 Modelling film flows down a fibre. *Journal of Fluid Mechanics* **603**, 431–462.
- SALAMON, T. R., ARMSTRONG, R. C. & BROWN, R. A. 1994 Traveling waves on vertical films: Numerical analysis using the finite element method. *Physics of Fluids* **6**, 2202–2220.
- SALEH, ESAM A. & ORMISTON, SCOTT J. 2017 A sharp-interface elliptic numerical model of laminar two-phase gas-liquid downward flow in a vertical parallel plate channel. *The Canadian Journal of Chemical Engineering* **95** (3), 568–577.
- SALIN, D. & TALON, L. 2019 Revisiting the linear stability analysis and absolute-convective transition of two fluid core annular flow. *J. Fluid Mech.* **865**, 743–761.
- SAMANTA, A. 2013 Effect of surfactant on two-layer channel flow. *Journal of Fluid Mechanics* **735**, 519–552.
- SAMANTA, A. 2014 Shear-imposed falling film. *Journal of Fluid Mechanics* **753**, 131–149.
- SAMANTA, A. 2020 Optimal disturbance growth in shear-imposed falling film. *AIChE Journal* **66** (5), 0001–1541.
- SAMANTA, A., RUYER-QUIL, C. & GOYEAU, B. 2011 A falling film down a slippery inclined plane. *Journal of Fluid Mechanics* **684**, 353–383.
- SAPRYKIN, S., KOOPMANS, R. J. & S., KALLIADASIS. 2007 Free-surface thin-film flows over topography: influence of inertia and viscoelasticity. *Journal of Fluid Mechanics* **578**, 271–293.
- SCHEID, B., KALLIADASIS, S., RUYER-QUIL, C. & COLINET, P. 2008 Interaction of three-dimensional hydrodynamic and thermocapillary instabilities in film flows. *Physical Review E* **78**, 066311.
- SCHEID, B., RUYER-QUIL, C. & MANNEVILLE, P. 2006 Wave patterns in film flows: modelling and three-dimensional waves. *Journal of Fluid Mechanics* **562**, 183–222.
- SCHLICHTING, H. & GERSTEN, K. 2001 *Boundary-Layer Theory*, eight edn. Mc Graw-Hill: New York.
- SCHMID, P. J. 2007 Nonmodal stability theory. *Annual Review of Fluid Mechanics* **39**, 129–162.

- SCHMIDT, P., NÁRAIGH, L. Ó., LUCQUIAUD, M. & VALLURI, P. 2016 Linear and nonlinear instability in vertical counter-current laminar gas-liquid flows. *Physics of Fluids* **28**, 042102.
- SCHÖRNER, M., RECK, D. & AKSEL, N. 2016 Stability phenomena far beyond the nusselt flow - revealed by experimental asymptotics. *Physics of Fluids* **28**, 022102.
- SEDAGHAT, M. H., FARNOUD, A., SCHMID, O. & ABOUALI, O. 2022 Nonlinear simulation of mucociliary clearance: A three-dimensional study. *Journal of Non-Newtonian Fluid Mechanics* **300**, 104727.
- SEEBAUER, F., POECHLAUER, P., BRAUNE, S. & STEINHOFER, S. 2012 Tube bundle falling film microreactor for performing gas liquid reactions. *US Patent* **8221708B2**.
- SHKADOV, V. YA. 1967 Wave flow regimes of a thin layer of viscous fluid subject to gravity. *Fluid Dynamics* **2** (1), 29–34.
- SINGH, A. 2014 Chebyshev collocation code for solving two phase Orr-Sommerfeld eigenvalue problem. MATLAB Central File Exchange.
- SIRWAH, M. A. & ZAKARIA, K. 2019 Dynamics of surface waves of a ferrofluid film. *Wave Motion* **84**, 8–31.
- SISOEV, G. M., MATAR, O. K. & LAWRENCE, C. J. 2009 Wave regimes in two-layer microchannel flow. *Chemical Engineering Science* **64**, 3094–3102.
- SNOEIJER, J. & ANDREOTTI, B. 2013 Moving contact lines: Scales, regimes, and dynamical transitions. *Annual Review of Fluid Mechanics* **45**, 269–292.
- SPAGNOLIE, S. E., ed. 2015 *Complex Fluids in Biological Systems - Experiment, Theory, and Computation*. New York: Springer.
- SUI, Y., DING, H. & SPELT, P. D. M. 2014 Numerical simulations of flows with moving contact lines. *Annual Review of Fluid Mechanics* **46**, 97–119.
- SURESH, V. & GROTBORG, J. B. 2005 The effect of gravity on liquid plug propagation in a two-dimensional channel. *Physics of Fluids* **17** (3), 031507, arXiv: <https://doi.org/10.1063/1.1863853>.
- TAI, C.-F., BIAN, S., HALPERN, D., ZHENG, Y., FILOCHE, M. & GROTBORG, J. B. 2011 Numerical study of flow fields in an airway closure model. *Journal of Fluid Mechanics* **677**, 483–502.
- TANNER, L. H. 1979 The spreading of silicone oil drops on horizontal surfaces. *Journal of Physics D* **12**, 1474–1484.
- THIELE, U., VELARDE, M. G., NEUFFER, K & POMEAU, Y. 2001 Sliding drops in the diffuse interface model coupled to hydrodynamics. *Physical Review E* **64** (6), 061601.

- TIHON, J., SERIFI, K., ARGYRIADI, K. & BONTOZOGLU, V. 2006 Solitary waves on inclined films: their characteristics and the effects on wall shear stress. *Experiments in Fluids* **41**, 79–89.
- TILLEY, B. S., DAVIS, S. H. & BANKOFF, S. G. 1994a Linear stability theory of two-layer fluid flow in an inclined channel. *Physics of Fluids* **6** (12), 3906–3922.
- TILLEY, B. S., DAVIS, S. H. & BANKOFF, S. G. 1994b Nonlinear long-wave stability of superposed fluids in an inclined channel. *Journal of Fluid Mechanics* **277**, 55–83.
- TREFETHEN, L. N. 2000 *Spectral methods in MATLAB*. Philadelphia: SIAM.
- TREVELYAN, P. M. J., SCHEID, B., RUYER-QUIL, C. & KALLIADASIS, S. 2007 Heated falling films. *Journal of Fluid Mechanics* **592**, 295–334.
- TRIFONOV, Y. Y. 1992 Steady-state traveling waves on the surface of a viscous liquid film falling down on vertical wires and tubes. *AIChE Journal* **38** (6), 821–834.
- TRIFONOV, Y. Y. 2007a Stability and nonlinear wavy regimes in downward film flows on a corrugated surface. *Journal of Applied Mechanics and Technical Physics* **48** (1), 91–100.
- TRIFONOV, Y. Y. 2007b Stability of a viscous liquid film flowing down a periodic surface. *International Journal of Multiphase Flow* **33**, 1186–1204.
- TRIFONOV, YU. YA. 2010 Counter-current gas-liquid wavy film flow between the vertical plates analyzed using the Navier-Stokes equations. *AIChE Journal* **56** (8), 1975–1987.
- TRIFONOV, Y. Y. 2011 Counter-current gas-liquid flow between vertical corrugated plates. *Chemical Engineering Science* **66**, 4851–4866.
- TRIFONOV, Y. Y. 2014 Stability of a film flowing down an inclined corrugated plate: The direct Navier-Stokes computations and Floquet theory. *Physics of Fluids* **26**, 114101.
- TRIFONOV, Y. Y. 2017a Instabilities of a gas-liquid flow between two inclined plates analyzed using the Navier-Stokes equations. *International Journal of Multiphase Flow* **95**, 144–154.
- TRIFONOV, Y. Y. 2017b Nonlinear waves on a liquid film falling down an inclined corrugated surface. *Physics of Fluids* **29**, 054104.
- TRIFONOV, Y. Y. 2020 Linear and nonlinear instabilities of a co-current gas-liquid flow between two inclined plates analyzed using the Navier-Stokes equations. *International Journal of Multiphase Flow* **122**, 103159.
- TSELUIKO, D., BLYTH, M. G. & PAPAGEORGIOU, D. T. 2013 Stability of film flow over inclined topography based on a long-wave nonlinear model. *Journal of Fluid Mechanics* **729**, 638–671.

- TSELUIKO, D. & KALLIADASIS, S. 2011 Nonlinear waves in counter-current gas-liquid film flow. *Journal of Fluid Mechanics* **673**, 19–59.
- TSVELODUB, O. Y., ARKHIPOV, D. G. & VOZHAKOV, I. S. 2021 Investigating waves on the surface of a thin liquid film entrained by a turbulent gas flow: modeling beyond the quasi-laminar approximation. *Thermophysics and Aeromechanics* **28**, 223–236.
- TSVELODUB, O. YU. & BOCHAROV, A. A. 2017 Modeling nonlinear wave regimes in a falling liquid film entrained by a gas flow. *Chaos, Solitons and Fractals* **104**, 580–587.
- TSVELODUB, O. YU. & BOCHAROV, A. A. 2018 Simulating solitary waves on a flowing down liquid film entrained by a gas stream. *European Journal of Mechanics B* **72**, 449–455.
- TSVELODUB, O. YU. & BOCHAROV, A. A. 2020 Studying the topological structure of steady-state travelling solutions for the model of film flow of a viscous fluid entrained by a gas flow. *European Journal of Mechanics B* **81**, 15–22.
- TU, J., INTHAVONG, K. & AHMADI, G. 2013 *Computational Fluid and Particle Dynamics in the Human Respiratory System*, chap. The Human Respiratory System. Springer, Dordrecht.
- UBAL, S., CAMPANA, D. M., GIAVEDONI, M. D. & SAITA, F. A. 2008 Stability of the steady-state displacement of a liquid plug driven by a constant pressure difference along a prewetted capillary tube. *Industrial & Engineering Chemistry Research* **47**, 6307–6315.
- UMA & USHA 2006 Dynamics of a thin viscoelastic film on an inclined plane. *International Journal of Engineering Science* **44**, 1449–1481.
- VAKILIPOUR, S., MOHAMMADI, M. & ORMISTON, S. 2021 A fully coupled ale interface tracking method for a pressure-based finite volume solver. *Journal of Computational Physics* **427**, 110054.
- VALLURI, P., MATAR, O. K., HEWITT, G. F. & MENDES, M. A. 2005 Thin film flow over structured packings at moderate Reynolds numbers. *Chemical Engineering Science* **60**, 1965–1975.
- VAN DRIEST, E. R. 1956 On turbulent flow near a wall. *Journal of the Aeronautical Sciences* **23** (11), 1007–1011, arXiv: <https://doi.org/10.2514/8.3713>.
- VELLINGIRI, R., TSELUIKO, D. & KALLIADASIS, S. 2015 Absolute and convective instabilities in counter-current gas-liquid film flows. *Journal of Fluid Mechanics* **763**, 166–201.
- VEREMIEIEV, S., THOMPSON, H. M. & GASKEL, P. H. 2015 Free-surface film flow over topography: Full three-dimensional finite element solutions. *Computers and Fluids* **122**, 66–82.

- VLACHOS, N. A., PARAS, S. V., MOUZA, A. A. & KARABELAS, A. J. 2001 Visual observations of flooding in narrow rectangular channels. *International Journal of Multiphase Flow* **27**, 1415–1430.
- VON KÁRMÁN, T. 1921 Über laminare und turbulente Reibung. *Z. angew. Math. Mech.* **1**, 233–252.
- WANG, Q. 2016 Stability and breakup of liquid threads and annular layers in a corrugated tube with zero base flow. *SIAM Journal of Applied Mathematics* **76** (2), 500–524.
- WANG, Q. & PAPAGEORGIOU, D. T. 2018 Using electric fields to induce patterning in leaky dielectric fluids in a rod-annular geometry. *IMA Journal of Applied Mathematics* **83** (1), 24–52.
- WANG, R., JIA, H. & DUAN, R. 2020 Experimental observation of flow reversal in thin liquid film flow falling on an inclined plate. *Coatings* **10**, 599.
- WHITAKER, S. 1968 *Introduction to Fluid Mechanics*. Englewood Cliffs, N.J.: Prentice Hall.
- WIERSCHEM, A., POLLAK, T., HEINING, C. & AKSEL, N. 2010 Suppression of eddies in films over topography. *Physics of Fluids* **22**, 113603.
- XIE, X., LIU, H., HE, C., ZHANG, B., CHEN, Q. & PAN, M. 2019 Deciphering the heat and mass transfer behaviors of staggered tube bundles in a closed wet cooling tower using a 3-d vof model. *Applied Thermal Engineering* **161**, 114202.
- XU, F. & JENSEN, O. 2017 Trapping and displacement of liquid collars and plugs in rough-walled tubes. *Physical Review Fluids* **2**, 094004.
- YIANTSIOS, S. G. & HIGGINS, B. G. 1988 Linear stability of plane poiseuille flow of two superposed fluids. *Physics of Fluids* **31** (11), 3225–3238.
- YIANTSIOS, S. G. & HIGGINS, B. G. 1989 Rayleigh-Taylor instability in thin viscous films. *Physics of Fluids A* **1**, 1484–1501.
- YIH, C.-S. 1955 Stability of two-dimensional parallel flows for three-dimensional disturbances. *Quarterly of Applied Mathematics* **12**, 434–435.
- YIH, C. -S. 1963 Stability of liquid flow down an inclined plane. *The Physics of Fluids* **6** (3), 321–334.
- YIH, C.-S. 1967 Instability due to viscosity stratification. *Journal of Fluid Mechanics* **27** (2), 337–352.
- YOSHIMURA, P. N., NOSOKO, P. & NAGATA, T. 1996 Enhancement of mass transfer into a falling laminar liquid film by two-dimensional surface waves-some experimental observations and modeling. *Chemical Engineering Science* **51** (8), 1231–1240.

- YOUNGS, D. L. 1982 *Numerical Methods for Fluid Dynamics*, chap. Time-dependent multi-material flow with large fluid distortion, pp. 273–285. New York: Academic Press.
- ZAKARIA, K. 2012 Long interfacial waves inside an inclined permeable channel. *International Journal of Non-Linear Mechanics* **47**, 42–48.
- ZAPKE, A. & KRÖGER, D. G. 2000 Countercurrent gas-liquid flow in inclined and vertical ducts - I: Flow patterns, pressure drop characteristics and flooding. *International Journal of Multiphase Flow* **26**, 1439–1455.
- ZHANG, H., CHEN, G., YUE, J. & YUAN, Q. 2009 Hydrodynamics and mass transfer of gas-liquid flow in a falling film microreactor. *AIChE Journal* **55** (5), 1110–1120.
- ZHOU, G. & PROSPERETTI, A. 2020a Capillary waves on a falling film. *Physical Review Fluids* **5**, 114005.
- ZHOU, G. & PROSPERETTI, A. 2020b A numerical study of mass transfer from laminar liquid films. *Journal of Fluid Mechanics* **902** (A10).
- ZHOU, Z.-Q., PENG, J. & ZHANG, Y.-J. ZHUGE, W.-L. 2016 Viscoelastic liquid film flowing down a flexible tube. *Journal of Fluid Mechanics* **802**, 583–610.
- ZIENKIEWICZ, O. C., TAYLOR, R. L. & ZHU, J. Z. 2013 *The Finite Element Method: Its Basis and Fundamentals*. Elsevier.
- ZOUESHTIAGH, F., BAUDOIN, M. & GUERRIN, D. 2014 Capillary tube wetting induced by particles: towards armoured bubbles tailoring. *Soft Matter* **10**, 9403–9412.